Marine Cybernetics

Towards
Autonomous Marine Operations and Systems

Lecture Notes

Asgeir J. Sørensen
Department of Marine Technology
Norwegian University of Science and Technology

Report UK-18-76

Preface

Marine Cybernetics is a multidisciplinary education and research program offered by the Department of Marine Technology in cooperation with the Department of Engineering Cybernetics, the Norwegian University of Science and Technology (NTNU).

Marine Cybernetics is the science about techniques and methods for analysis, monitoring and control of marine systems. The specialization provides insight and knowledge in *Mathematical modeling*, *Control engineering* and *Information and communication technology*.

The material presented is intended for use as Lecture notes in the NTNU course entitled *TMR4240 Marine Control Systems* and partly in *TMR4515 Marine Control Systems, Specialization Course*. The courses are given on graduate level for MSc degree for specialization in *Marine Cybernetics*. Besides several dedicated courses on dynamics, hydrodynamics, machinery systems, guidance and control, optimization, artificial intelligence, instrumentation systems and computer science are given.

Learning outcome: The lecture notes will provide the reader knowledge in the development of mathematical models and design control systems for propulsion and motion controllers for ships, underwater vehicles and other floating structures based on fundamental physical laws and observed relations.

It is assumed that the students already have acquired themselves fundamental knowledge in automatic control theory and mathematical modeling of mechanical systems.

This is the fourth version of the lecture notes and contains several updates from the previous one issued in 2013. In particular, the research on autonomous marine operations and systems addressed in the NTNU Centre of Excellence (NTNU AMOS) has provided advances in various aspects related to autonomy and more intelligent marine systems. We may regard autonomy as the next step in automation by automating the mission and guidance layers in conjunction to the control execution layer, as well as expanding the control execution layer to cope with even larger variability in the environmental and operational conditions. Equally important, interdisciplinary knowledge fields bridging technology, science and end-user needs are also enabler for autonomous systems. This is ongoing research and more will evolve in the years to come as indicated by the subtitle - *Towards autonomous marine operations and systems*.

The students are greatly acknowledged for comments providing continuously improvements.

Asgeir J. Sørensen
Trondheim, Norway
August 2018.

Acknowledgements

Several of the chapters are results from joint research between the author and colleagues from the Norwegian University of Science and Technology (NTNU), former colleges in ABB Marine and Marine Cybernetics (now DNV GL) and new partners in the industry.

The lecture notes has evolved from extensive research at the research centers of excellence: Centre for Ships and Ocean Structures (CeSOS) and Centre for Autonomous Marine Operations and Systems (NTNU AMOS). All the colleagues are greatly acknowledged.

The following coauthors are acknowledged for cooperation and contributions to the Lecture Notes:

- Professor Thor I. Fossen, Dr. Jann Peter Strand and Dr. Trong Dong Nguyen for contributions to the Chapter on *Dynamic Positioning Control System*.
- Dr. Øyvind Smogeli, Dr. Marit Ronæss, Dr. Vegar Johansen, Dr. Jon Refsnes, Dr. Tristan Perez and Dr. Svein Ersdal for contributions to the Chapter on *Mathematical Modeling*.
- Dr. Øyvind Smogeli and Dr. Eivind Ruth for contributions to the Chapter on *Propulsion Control*.
- Professor Bernt Leira and Professor Carl M. Larsen for contributions to the Section on *Control of Drilling Riser Angles by Dynamic Positioning of Surface Vessels*.
- Dr. Anne Marthine Rustad for writing the Section on *Modeling and Control Top Tensioned*. Professor Carl M. Larsen is also acknowledged for his contributions here.
- Dr. Astrid H. Brodtkorb for writing the Section on *Hybrid Control*.

Finally, the author is grateful for the contributions to all the PhD candidates and MSc students I have had the pleasure to supervise and being enlightened tenfold in return. They are all listed on my NTNU homepage. Here you can also download the lecture notes.

http://folk.ntnu.no/assor/

Contents

Chapter 1

Introduction

This chapter gives a short introduction to the field of marine cybernetics and the organization of the book. *Marine control systems* or *Marine cybernetics* is defined to be the science about techniques and methods for analysis, monitoring and control of marine systems. Marine cybernetics provides knowledge in *mathematical modeling*, *control engineering* and *information and communication technology*. We will in the following go into details in all these three knowledge fields. In addition, we will by several examples show the importance of the interdisciplinary approach being successful in the design of marine control systems. We may simply state that you need knowledge about the process or plant you are aiming to control as well as the business.

1.1 Ocean Industries - The Blue Economy

The main application fields for marine control systems are the three big marine industries: *Sea transportation (shipping)*, *offshore oil and gas exploration and exploitation*, and *fisheries and aquaculture*. New emerging fields are offshore renewable energy, coastal infrastructure, marine mining, ocean science and management, and tourism. All of these belong to a super cluster called the *Ocean industries - The blue economy*, see Figure 1.1. The value chain in the blue economy contains numerous of stake holders such as designers, engineering companies, yards, system and equipment vendors, ship owners and offshore contractors, energy companies, fish farmers, asset and good owners, independent class societies, governmental agencies, brokers, insurance companies in addition to navy academies, colleges, universities, research institutes and non-governmental agencies. The methods and best practice learned in one field should quite easily be possible to transfer between the various fields and stake holders. This is also quite common as you find many of the same stake holders operating across the ocean industries and into other industrial areas.

So far most of the examples are collected from the mature industries such as shipping and offshore oil and gas exploration and exploitation. It is believed that these industries will be even more technology demanding with focus on safe and cost effective solutions in the years to come. More of the offshore activities is assumed to take place in deeper water based on floating solutions in combination with underwater installations. The need for conducting all-year marine operations in the *ocean space* with varying complexity will increase and motivate to the development of underwater robotics with increased autonomy. Due to increased industrialization within the fisheries and aquaculture, the industrial content and thereby the introduction of advanced technology is increased here as well.

With the rapid development of enabling technologies such as information and communication technology, micro- and nano technology, material technology, autonomy and artificial intelligence we also see a clear trend towards more intelligent operations and systems. Unmanned systems or reduced manning motivate for increased autonomy.

Finally, there is no other option that sustainability must be the most important target for any industrial area and management policy. The humanity is facing increasing global challenges such as global warming, deteriorating ecosystems, population explosion and lack of energy, food, water and minerals. Solutions to global challenges can also be found by proper management and utilization of the resources found in the oceans.

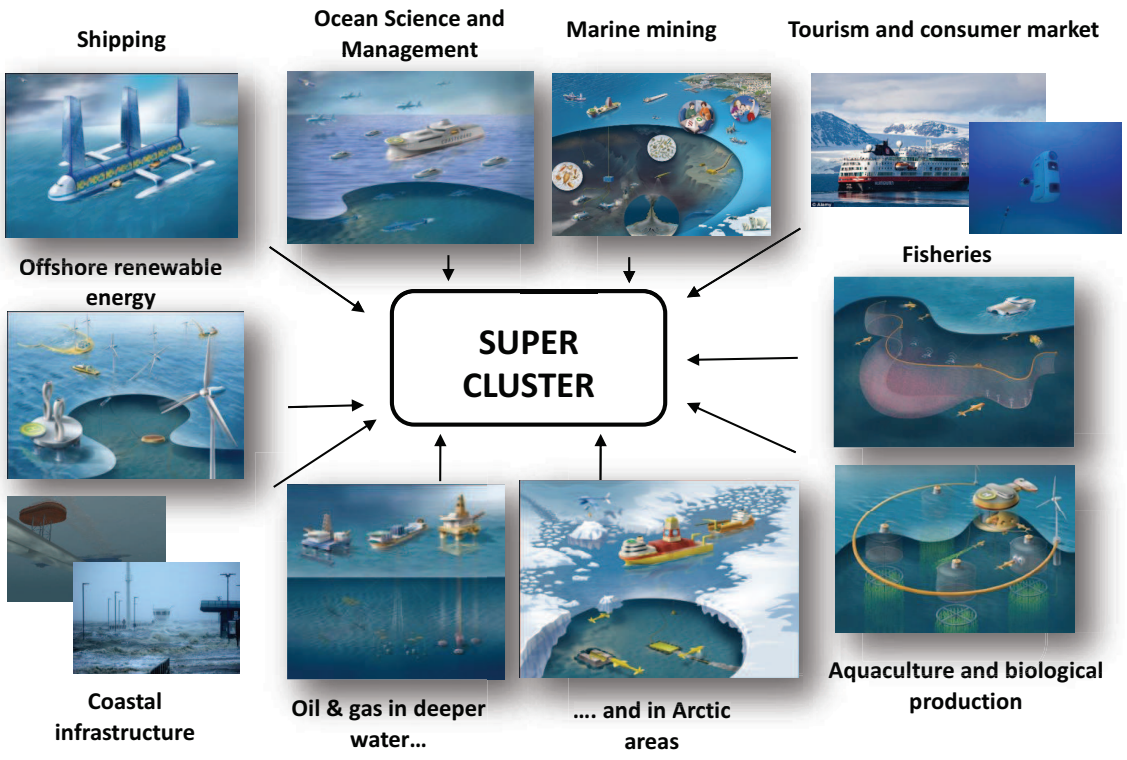

Figure 1.1: Ocean industries- the blue economy.

1.2 Marine Control Architecture

Concerning marine control systems it is suggested to divide the *control structure* into three main layers: *mission layer*, *guidance and optimization layer*, and *control execution* , see Figure 1.2. The control execution layer is as shown in Figure 1.2 divided into *low-level actuator control* and *high-level plant control*. Setpoints to the high-level plant control are provided by the *guidance and optimization layer* which again is receiving its commands from the mission layer. The mission commands may be given by an human pilot or by the system itself if it is operating in autonomous mode. An autonomous system should be able to plan and re-plan its mission subject to mission

objective, risk exposure and any operational and environmental constraints that may happen as the operation goes. We will in the text use demonstrating examples from the offshore oil and gas industry and ocean science and management. In particular, examples with *dynamically positioned (DP)* offshore vessels will be used. A DP vessel maintains its position (fixed location or pre-determined track) exclusively by means of active thrusters. Position keeping means maintaining a desired position in the horizontal-plane within the normal excursions from the desired position and heading.

The real-time control structure for a DP system may then consist of:

- *Actuator control*: The actuators for DP systems are normally thrusters, propellers, and rudders. Local control of propellers and thrusters may be done by controlling e.g. the speed (rpm), pitch, torque, and power or combinations of these. Dependent on the actuators are mechanically, hydraulically and/or electrically driven controllers with different properties will be used.

- *Plant control*: In station keeping operations the DP system is supposed to counteract the disturbances like wave (mean and slowly varying), wind and currents loads acting on the vessel. The plant controller calculates the commanded surge and sway forces and yaw moment needed to compensate the disturbances. A multivariable output controller often of PID type using linear observers e.g. Kalman filter or nonlinear passive observers may be used. Setpoints to the thrusters are provided by the thruster allocation scheme.

- *Guidance and optimization*: Depending of the actual marine operation the DP vessel is involved in optimization of desired setpoint in conjunction with appropriate reference models for e.g. drilling operations, weather vaning, pipe laying, tracking operations, etc. are used.

As the controllers rely on proper measurements to work on, *signal processing* is of vital importance for the stability and robustness of the control system. This will be the first topic of the text.

1.3 Main Topics

The topics covered here are:

- Chapter 2 chapter gives an overview of marine control systems exemplified by DP vessels with electrical propulsion systems. Design aspects related to high-level vessel control such as power management and DP are shown. Rules and regulations including testing and verification of marine control systems based on Hardware-In-the-Loop (HIL) testing will also be introduced.

- Chapter 3 introduces the reader to the basics in linear system theory and computer-controlled systems. Today most of the control systems are implemented in computers run by digital processors. Computers will operate on continuous-time processes at discrete-time sampling instants. Therefore, computer-controlled systems can be regarded as discrete control systems. Discrete systems could in many cases be viewed as approximations of analog systems. Computer-controlled systems may introduce deteriorations of the control objective, if not accounting for the fact that they operate on discrete instants of processes which are time-continuous by nature.

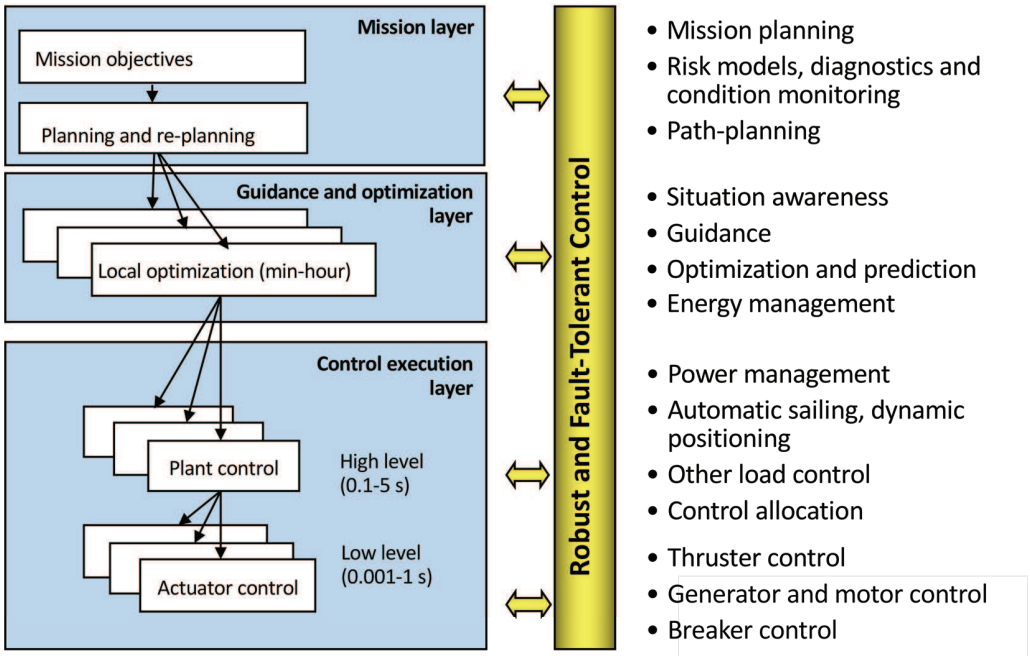

Figure 1.2: Control structure.

- In Chapter 4 the most common analog and digital filters in addition to observer theory are presented. The Kalman filter is also derived. Kalman filters have successfully been used in marine control systems since the late 1970s.

- Chapter 5 is about signal quality control and fault detection. All industrial control systems contains several functions for signal quality checking. The performance of the control system depends on these functions operate properly. In this chapter the most important signal processing properties for the purpose of control will be treated.

- In Chapter 6 the mathematical models used in the design of marine control systems such as DP systems and thruster assisted position mooring systems are formulated. To readers unfamiliar with hydrodynamics, the models may look difficult. However, the intention here is to focus on the structural properties of the models important for control, rather than going into details about calculation of the hydrodynamic coefficients. If the reader is inspired to enter this field any further, the author is convinced that this will improve the control system designs even more.

- Chapter 7 contains a comprehensive introduction to dynamic positioning (DP) and thruster assisted position mooring (PM) including design of observers and controllers.

- Chapter 8 on propulsion and thruster controls show the importance of considering low-level control designs of the actuators ensuring that the high-level control demands are fulfilled according to the control objective.

- Chapter 9 gives an introduction to hybrid control systems with performance monitoring and switching logic, and gives examples of applications of hybrid theory to marine control systems. Real industrial control systems contain a bank of controllers and observers serving different control objectives and changes in environmental and operational conditions including fault handling. Switching between the different controllers are often done by *ad hock methods*. Hybrid systems theory provides a formalism for the integration of multi-functional controllers combining discrete events and continuous control.

- Chapter 10 presents a new field of research concerning marine control systems applied on ocean structures. In particular, various marine operations involving slender flexible structures and marine vessels are studied.

- Chapter 11 is about motion control of high speed craft. In particular the chapter presents how flexibility in the air cushion pressure dynamics will have impact on the design of a ride control system for motion damping of a high speed craft called Surface Effect Ships (SES).

Chapter 2

Overview of Marine Control Systems

This chapter gives an overview of marine control systems exemplified by DP vessels with electrical propulsion systems. Design aspects related to high-level vessel control such as power management and DP are shown. Rules and regulations including testing and verification of marine control systems based on Hardware-In-the-Loop (HIL) testing will also be introduced.

Learning outcome of the chapter: The reader shall have an overview of:

- The fundamental architecture in marine control systems from low-level control of motors and propellers to high-level control subject to the particular marine operation, desired behavior and constraints.
- The power, automation and dynamic positioning (DP) systems on electrically driven ships.
- The fundamental safety requirements from class societies and authorities for testing, verification and certification of marine control systems. Here, additional teaching material is supported by the class society - DNV GL.

2.1 Introduction

The history of automated closed-loop ship control started with Elmer Sperry (1860-1930), who constructed the first automatic ship steering mechanism in 1911 for course keeping (Bennet, 1979). This device is referred to as the "Metal Mike", and it was capturing much of the behavior of a skilled pilot or a helmsman. "Metal Mike" did compensate for varying sea states by using feedback control and automatic gain adjustments. Later in 1922, Nicholas Minorsky (1885-1970), presented a detailed analysis of a position feedback control system where he formulated a three-term control law which today is refereed to as Proportional-Integral-Derivative (PID) control (Minorsky, 1922). These three different behaviors were motivated by observing the way in which a helmsman steered a ship.

This chapter gives an overview of marine control systems exemplified by *dynamically positioned* (DP) vessels with electrical propulsion systems. Design aspects related to high-level vessel control such as power management and DP are shown. Design requirements and ability for reconfiguration accounting for physical segregation and redundancy of power, propulsion and automation systems will be presented. Rules and regulations including testing and verification of marine control systems based on Hardware-In-the-Loop (HIL) testing will also be introduced.

Other marine control systems; propulsion control systems, control of slender ocean structures, motion control systems for high speed crafts and details on DP systems will be presented in separate chapters later in the text. The design steps combining software (SW) and hardware (HW) architecture, modeling, sensor processing, controller design, simulation and testing will more or less follow the same principles. However, requirements to performance and redundancy, and thereby complexity, may differ for the various marine control system applications.

Offshore exploration and exploitation of hydrocarbons have opened up an era of DP vessels. Currently, there are more than 2000 DP vessels of various kind operating worldwide. DP systems are used for a wide range of vessel types and marine operations:

- **Offshore oil and gas industry:** Typical applications in the offshore market are offshore service vessels, drilling rigs and drilling ships, shuttle tankers, cable and pipe layers, floating production off-loading and storage units (FPSOs), crane and heavy lift vessels, geological survey vessels and multi-purpose vessels. Cable and pipe laying are typical operations which also need tracking functionality.

- **Shipping:** Currently there is a trend towards more automatic control of marine/merchant vessels, beyond the conventional autopilot. This involves guidance systems coupled to automatic tracking control systems, either at high or low speed. In addition, more sophisticated weather routing and weather planning systems are expected. Automatic docking systems, and a need for precise positioning using DP systems when operating in confined waters will become more used.

- **Cruise ships and yachts:** The cruise and yacht market also make use of more automatic positioning control. In areas where anchors are not allowed due to vulnerable coral reefs, DP systems are used for station keeping. Precise positioning is also required for operating in harbors and confined waters.

- **Fisheries:** Application of more sophisticated guidance, navigation and control systems for ships during fishing are motivated by the need for precise positioning, reduced fuel consumption and intelligent selective fishing.

Electric propulsion is not a very new concept. It has been used as early as in the late 19th century. However, only in few vessels until the 1920s where the electric shaft line concept enabled the design of the largest Trans-Atlantic passenger liners. Variable speed propulsion was used in some few applications during the 1950s and 1960s, while, first when the semiconductor technology became available in large scale commercial applications, this technology became acceptable for a wide range of applications. The introduction of AC drives and podded propulsors was another shift in technology that led to a rapid increase in the use of electric propulsion through the last 15-20 years. Typically, ships with electric propulsion tend to have more system functionality implemented in integrated automation systems, partially because such functions are regarded to be necessary for safe and optimal operation, but also because the electric propulsion plant enables the use of such functions. In the commercial market the offshore vessels in addition to cruise ships and ice breakers have been technology drivers concerning automation, power and propulsion systems. They are characterized by the required ability to conduct complex marine operations, operational availability, safety focus, cost effectiveness and flexibility in operational profile concerning transit, station keeping, maneuverability and to some extent also a significant vessel or process load system. These rather complex power plants opened up for an increasing

use of fully all-electric ships and the introduction of fully integrated computer-controlled systems in order to operate safely and cost efficiently. Such concepts are today applied in an increasing number of ship applications.

Consequently, the complexity has also increased with a variety of solutions consisting of stand-alone systems, partly integrated systems to fully physical and functional integrated systems. Up to now integrated automation systems have been proprietary with a limited number of vendors. However, in the automation industry it is a trend towards openness in communication protocols and network. How this will influence on the technology solutions and responsibilities for multi-vendor integration systems is still a subject for discussion. During the late 1990s the introduction of low-cost off-shelf computers not originally designed for automation purposes have also been taken more into use. This development is driven by the need to make more cost efficient solutions. Nevertheless it also creates new issues of concern:

- New procedures for design and specification that considers compatibility and integration aspects.
- Failure analysis and test methods, adequate to ensure fault-tolerance in the overall system.

2.2 System Overview

A DP offshore vessel, in this case a drilling rig as illustrated in Figure 2.1, may comprise the following sub-systems:

- *Power system.*
- *Marine control* or *automation system.*
- *Positioning systems* comprise *dynamic positioning (DP) system* for automatic station keeping and low speed manoeuvring of free floating vessels or *thruster assisted position mooring (PM) system* for anchored vessels. Sensors and position reference systems. Hardware, software and sensors to supply information and/or corrections necessary to give e.g. accurate vessel motion, position and heading measurements.
- *Automatic sailing system* and *nautical system* including autopilot, radar, automatic identification system (AIS), and GPS for automatic course keeping and course changing for transit operations.
- *Joystick system* for manual control of the thruster system for positioning of the vessel in surge, sway and yaw/heading. Often automatic heading control function is included. One should notice that the operator does not control each thruster individually. The operator command a desired thrust in surge, sway and yaw. Then the thruster allocation algorithm map the desired thrust in surge, sway and yaw to individual thrust set-points of the enabled thruster.
- *Manual thruster control system* includes individual control of each thrusters.
- *Propulsion and thruster system* involves all components and systems necessary to supply a vessel with thrust for dynamic positioning, maneuvering and transit. For details the reader is referred to Chapter 8.

- Equipment packages and systems for e.g. drilling, off-loading, crane operations, oil and gas production.
- Mooring system (applicable for moored vessels only). Generally, a mooring system consists of n lines connected to the structure and horizontally spread out in a certain pattern. At the seabed the lines are connected to anchors. *Spread mooring* systems are used both for semi-submersibles and turret-anchored ships. In the latter case the anchor lines are connected to a *turret* on the ship, which can be rotated relative to the ship. The number of anchor lines may vary, typically from 6 to 12. The length of the anchor lines are adjusted by winches and determines the pre-tension and thus the stiffness of the mooring system.
- Safety systems.
- Auxiliary systems, such at heating, ventilation and air condition (HVAC), water cooling, hydraulic systems, etc.

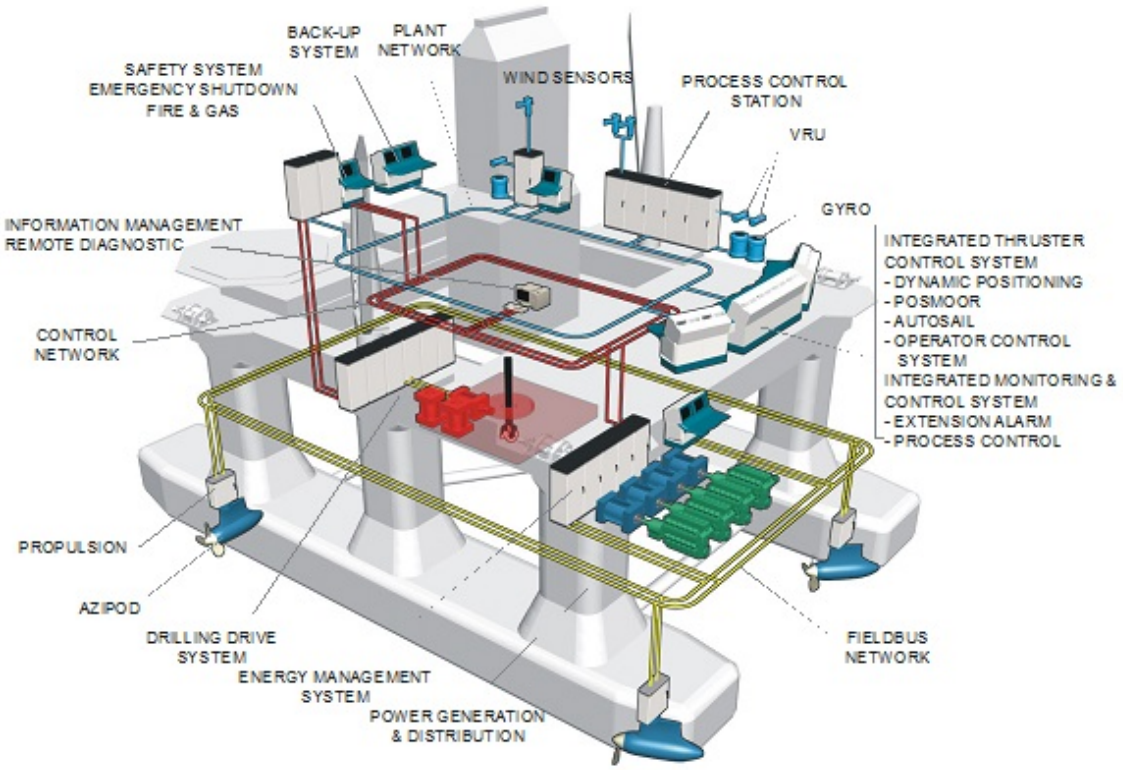

Figure 2.1: Illustration of different systems and components in a large, integrated plant (Courtesy ABB Marine).

2.3 Power System

Power system comprises all units necessary to supply the vessel with power. The power generation and distribution systems are divided into the following main parts, see also Hansen (2000), Radan (2008) and Miyazaki (2017) for more details:

- A power generation plant with prime mover and generators. In commercial vessels, the prime movers are typically medium speed diesel engines, due to high efficiency and cost efficiency. Gas turbines, and also steam turbines, are used in some ship applications due to their advantages in weight and size. There are intensive research and development in the field of LNG and feasible fuel cells, which in some future also can be applied in a wider scale than of today. In addition, combined power plants are also looked more into.
- An electric power distribution system with main and distribution switchboards. The distribution system is typically split in two, three or four sections, with the possibility to connect and split the sections by use of bus ties or bus feeders. With a proper protection system and operational philosophy, such systems may have the flexibility of operating in a common, connected mode for optimizing the energy production in normal modes, while isolating faulty parts of the system and obtain the intended redundancy without loss of maneuverability or station keeping ability by automatic splitting and segregation of the system.
- Transformers for feeding of alternate voltage levels in main or low voltage switchboards and motor control centers.
- Uninterruptible power supply of sensitive equipment and automation systems.
- Rotating converters for frequency conversion and clean power supply.
- Cabling, including cable routing and segregation.

In many ships there is a vessel or process plant system, which is critically dependent on the electrical power system. Such systems can be:

- Hotel loads, e.g. for cruise and passenger vessels.
- Crane and winch systems, e.g. for support vessels.
- Drilling systems, e.g. for drilling rigs.
- Oil and gas production, for FPSOs.
- Load/cargo handling systems, for cargo vessels and tankers.

Even though these systems may not be directly critical for the safe maneuverability of the vessel, there may be serious consequences by loss of controllability, both with concern to safety, environmental or economical consequences. Hence, redundancy and segregation in the process and automation systems may be equally important as in the electrical power and propulsion system. This can be explained by the redundant configuration of a drilling drive system, with dual independent power feeding and possibility to segregate into independent sections either in normal or faulty conditions, as shown in Figure 2.2. The definitions of some of the electrotechnical terms are found in Appendix C.

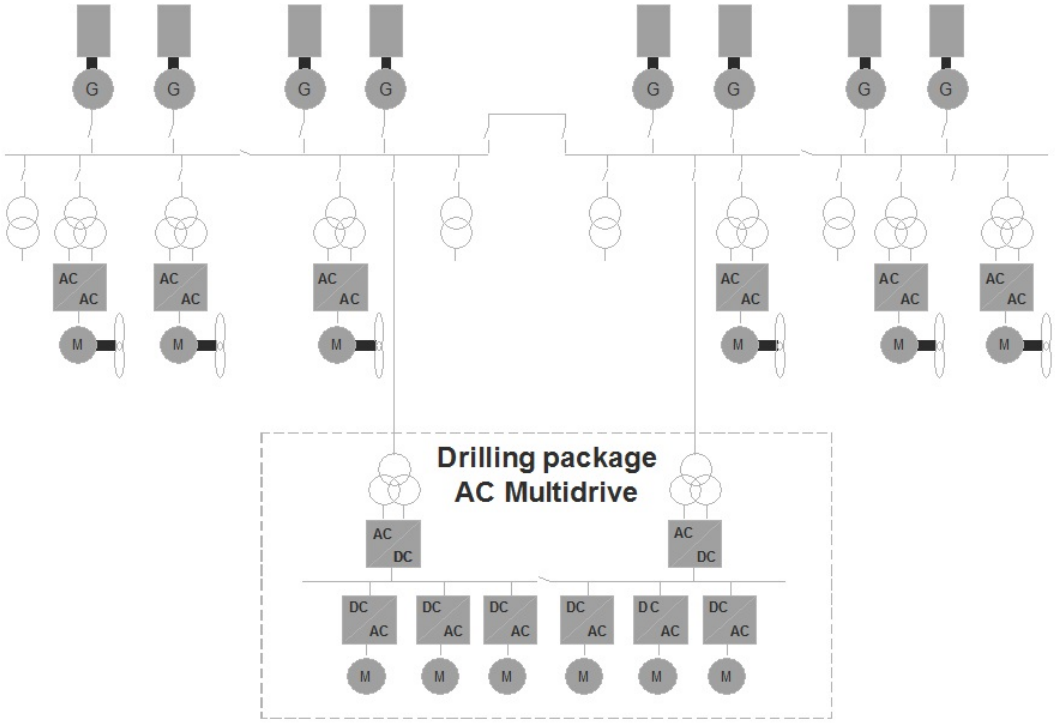

Figure 2.2: Single line diagram of a drilling rig.

2.4 Propulsion System

The propulsion system consists typically of prime movers as diesel engines, generators, transmissions and thrusters. A *thruster* is here defined as the general expression for a propeller unit. A ship can be equipped with several types of thrusters. Conventional ships typically have a main propulsion unit located aft. Traditionally, shaft line propulsion with controllable pitch or fixed pitch propellers is applied, with rudders to direct the thrust. Another common type is the *tunnel* thruster which is a propeller inside a tunnel that goes through the hull and produces a fixed-direction transverse force. A third type is the *azimuth* (rotatable) thruster, which can produce thrust in any direction. While the main and the tunnel thrusters have fixed force directions, the direction of the azimuth thruster can be changed, either manually by the operator or automatically by the positioning control system. Rudders in combination with main propellers can also be used actively in the positioning system to produce a transverse force acting on the stern. In positioning systems the main objective is to control the thruster's force. However, since this resulting force cannot be measured directly, it is common to control the thruster revolution speed (RPM control), the pitching of the propeller blades (pitch control), or by these in the combination (consolidated control). The servo mechanisms for the propulsion devices must be designed to give accurate and fast response. This is often referred to as *low-level* thrust control, which will be treated in more detail in the Chapter 8.

2.5 Marine Automation System

2.5.1 Overview

In marine industry, there are two main directions of solutions for automation systems:

- Integrated automation systems.
- Stand-alone automation systems.

The two different classes of solutions are found in most kind of vessels. However, since complex functions and tasks are handled better by the integrated solutions, this is more often found in the vessels with complex and advanced propulsion and station keeping installations. In the following integrated automation system is treated.

Marine automation or vessel control system comprises:

- Control functions for e.g. HVAC control, cargo and ballast control, emergency shutdown and fire and gas detection, off-loading control, engine control, etc.
- Power management system (PMS) for handling of generators, black-out prevention, power limitation, load sharing and load shedding. For advanced vessels more sophisticated energy management systems may be used for intelligent power planning and allocation.
- The operator's user interface to the automation system is through the Human-Machine Interface (HMI) with display systems and operator panels, often denoted as operator stations.
- Centralized computers with scalable CPU processing and I/O capacities, often denoted as controllers or process control stations (Figure 2.3).
- Distributed computers or PLCs, typically with local control and interfaces to process and to centralized computers.
- Communication buses at the different levels of control.
- Associated cabling, segregation and cable routing.

With today's standardization on communication in automation systems, it is relatively easy to connect various sub systems into a network communication system. The evolution of interconnecting systems in such networks has, today, developed to be an international standard of many new buildings. It is a challenge of designers, to distinguish between the essential and important communication, and to define the right level of redundancy and inter-dependency of sub-systems.

2.5.2 Data Network and Process Stations

On larger systems the power, automation and the various parts of the positioning system are connected by data networks, and the positioning control systems are implemented in the local process stations. It is important that these systems meet the necessary redundancy level and communication real-time requirements, such that the positioning system is reliable. Today it has been common to integrate all automation system into a common plant network (Figure 2.3).

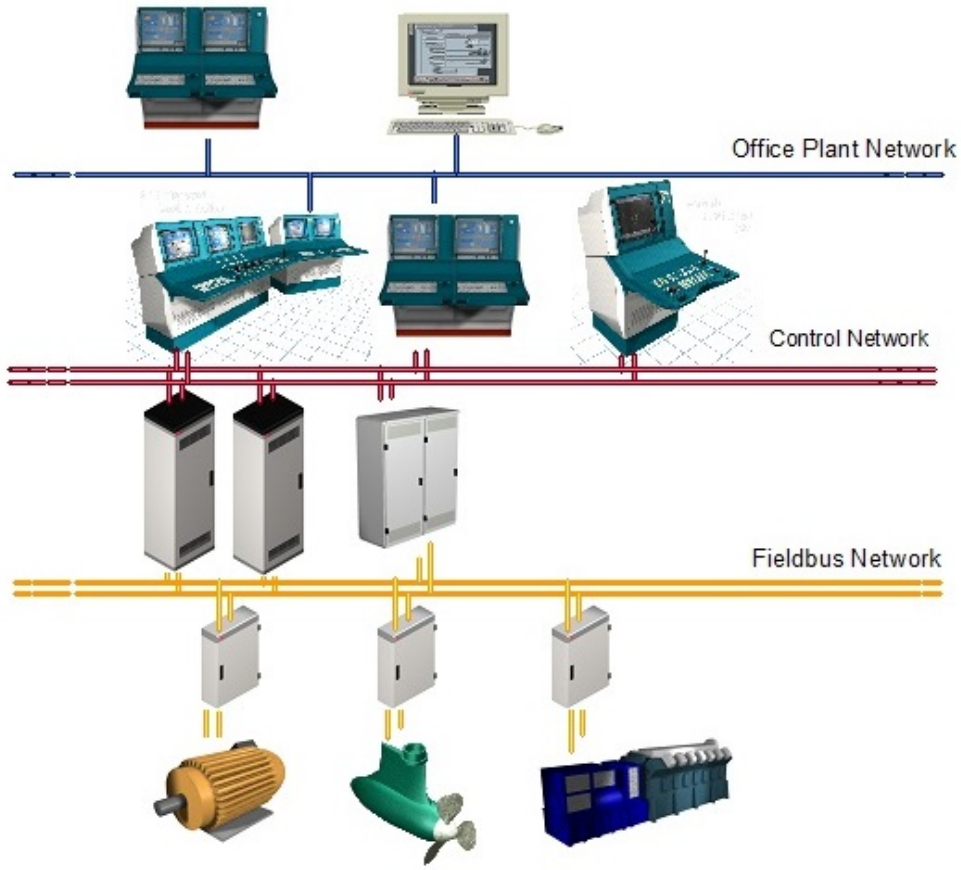

Figure 2.3: Automation plant.

2.5.3 Operator Stations and HMI

The operator's link to the positioning system is through the Human-Machine Interface (HMI) on the operator stations. On the operating stations, it is common to arrange a joystick system, giving the operator the opportunity to direct control the thruster forces in surge and sway and moment in yaw. The HMI should be user-friendly and sufficient information should be presented for the operator so that correct decisions can be made.

2.5.4 Integration Aspects

Physical integration based on standardized communication protocols ensure connectivity of devices and integration of controllers and operator stations into three network levels (Figure 2.3): *Real time field bus network* communication on low level between devices and controllers, *real time control network* connecting controllers and operator stations, and *office plant network* to various office systems and information management systems. The last level opens up for satellite communication to land offices at ship operators or vendors. It is common to characterize

the automation system by the number of I/Os and dividing the applications into low-end or high-end segments. For a drilling rig as shown in Figure 2.1 the number of I/O signals may be up to 10-15000. For a conventional supply vessel the I/O number is typically lower than 1500 - 2000 signals.

2.6 Dynamic Positioning (DP) System

In the 1960s systems for automatic control of horizontal position in addition to the course were developed. Such systems for simultaneously control of three horizontal motions (surge, sway and yaw motion) are today known as *dynamic positioning (DP) systems.* Description of DP systems including the early history can be found in Fay Fay (1989). In the 1960s the first DP system was using single-input single-output PID control algorithms in combination with low-pass and/or notch filter. In the 1970s more advanced output control methods based on multivariable optimal control and Kalman filter theory was proposed. Later on nonlinear control was also applied (Sørensen, 2011). More details are given in Chapter 7.

Definition 2.1 *A DP vessel is by the class societies e.g. DNVGL (2018) defined as a vessel that maintains its position and heading (fixed location or pre-determined track) exclusively by means of active thrusters. This is obtained either by installing tunnel thrusters in addition to the main screw(s), or by using azimuthing thrusters, which can produce thrust in different directions.*

Other class societies such as American Bureau of Shipping (ABS) and Lloyd's Register (LRS or Lloyd's) have similar rules. While in DP operated ships the thrusters are the sole source of station keeping, the assistance of thrusters are only complementary to the mooring system in the case of *thruster assisted position mooring (PM) systems.* Here, most of the position keeping is provided by a deployed anchor system. In severe environmental conditions the thrust assistance is used to minimize the vessel excursions and line tension by mainly increasing the damping in terms of velocity feedback control. For turret anchored ships, see Figures 2.4 and 2.5, without natural weather-vaning properties the thrusters are also used to automatic control of the heading, similarly to DP operated vessels. In this text, a *marine positioning system* is either defined as a *dynamic positioning* (DP) system or a *thruster assisted position mooring* (PM) system.

DP systems have traditionally been a *low-speed* application, where the basic DP functionality is either to keep a fixed position and heading or to move slowly from one location to another. In addition specialized tracking functions for cable and pipe-layers, and remote operated vehicle (ROV) operations have been available. The traditional *autopilot* functionality has over the years become more sophisticated. Often a course correction function is available for correction of course set-point due to environmental disturbances and drifting, such that the vessel follows a straight line. Way-point tracking is used when a vessel is supposed to follow a pre-defined track e.g. defined by several way-point coordinates. The trend today is that typical high-speed operation functionality merges with the DP functionality, giving *one unified system* for all speed ranges and types of operations. Further research on hybrid control will enable this.

2.6.1 Position Reference Systems and Sensors

It is common to divide the different measurements used by a positioning system into position reference systems and sensor systems. The most commonly used position reference systems are:

Figure 2.4: Marine operations in offshore oil and gas exploration.

- **Global Navigation Satellite Systems (GNSS):** The most commonly used navigation system for marine vessels is Navstar GPS, which is a US satellite navigation system with world coverage. An alternative system is the Russian system Glonass, which only covers certain regions of the globe. An European system, *Galileo*, is currently under construction. For local area operations it is now possible to achieve meter accuracy by using *Differential* GPS (DGPS), and sub-decimeter accuracy by using *Carrier Differential* GPS (CDGPS). The development of *wide area augmentation systems* (WAAS) is expected to give meter accuracy across entire continents. When using a satellite navigation system, at least four satellites must be visible in order to compute a reliable position estimate (three for sea level navigation). If the ship is entering a shadowed region, and redundant signals are not

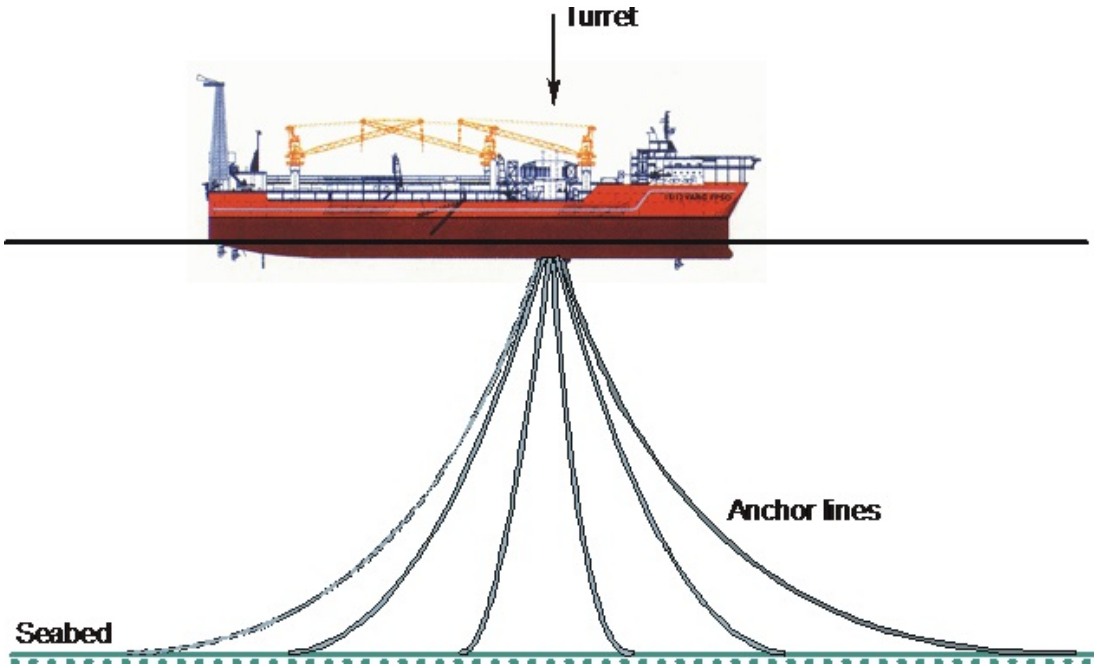

Figure 2.5: Turret anchored FPSO.

available, there will be a loss of position measurement. Other causes for degraded position measurements (or in the worst case loss or measurement) are ionospheric disturbances, reflections in the water surface, etc. For DGPS the accuracy is typically within 1 meter radius with 95 % probability. Recently, the forced signal distortion (SA) on the GPS signal has been removed, such that the accuracy of the GPS itself without differential correction is dramatically improved. Depending of antennas and signal receivers, typical accuracy is within $\pm 10\, m$. This opens up for even more cost effective navigation equipment within the field of marine positioning.

- **Hydroacoustic Position Reference (HPR) Systems:** By using one or several transponders located on fixed position on the seabed and one or several transducer mounted under the hull, the position of the vessel is measured. The accuracy of such systems depends on the water depth and the horizontal distance between the transponder and the transducer. There are different principles for performing measurements, where the most common used are super short baseline (SBL), super ultra short baseline (S/USBL) or long baseline (LBL).

- **Taut Wire:** A *taut wire* system is used to measure the relative position of a floating vessel at rest. This system consists of a heavy load located at the sea floor. The load is connected to the vessel by a wire cord or heavy metal chain which is hold in constant tension by using a winch onboard the vessel. Furthermore the angles at the top and bottom of the wire are measured, and the length of the wire. Hence, the relative position (x, y, z) can be computed by solving three geometric equations with three unknowns.

Other position reference systems can be microwave systems (ARTEMIS, MICRORAGER, MICRO FIX), Radiowave systems (SYLEDIS), optical systems (laser beams), and riser angle

position measurement systems. The latter system is based on instrumentation on a marine riser attached to the vessel when performing drilling operations.

The sensor systems may comprise:

- Gyrocompass and/or magnetic compass, which measures the heading of the vessel.
- Vertical reference unit (VRU), which at minimum measures the vessel heave, roll and pitch motions. Angular velocities are also often available. One of the main functions for the VRU is to adjust the position measurements provided by GPS, hydroacoustic position reference (HPR) systems, etc. for roll and pitch motions. For deepwater DP operations the accuracy of the roll and pitch signals must be high providing accurate HPR position measurements.
- An IMU typically contains gyros and accelerometers in 3-axes that can be used to measure the body-fixed accelerations in surge, sway and heave, the angular rates in roll, pitch and yaw and the corresponding Euler angles (Fossen, 2011). The IMU can be integrated in a filter (observer) with DGPS and HPR measurements for instance in order to produce accurate velocity estimates. In most cases only the IMU Euler angles are used in conjunction with DGPS. This is a minimum configuration since the Euler angles are needed in order to transform the measured GPS position corresponding to the GPS antenna down to the vessel fixed coordinate system usually located in the centerline of the ship.
- Wind sensors, which measures the wind velocity and direction relative to the vessel.
- Draft sensors (used for vessels which is operated over a wide range of drafts).
- Environmental sensors: wave sensors (significant wave height , direction, peak frequency), current sensors (velocity and direction at sea surface and at different depths). Environmental sensors are not a class requirement. These sensors are quite common on the most sophisticated offshore installation.
- Other sensors dependent on type of operation, e.g. for pipe layers pipe tension is also measured an utilized by the DP system.

In many installations redundant measurements are available, and the number and types of measurements required are specified by certain class rules, see for example DNVGL (2018). Redundant measurements increases the safety and availability of the positioning system.

The heading of the vessel is usually measured by one or several gyrocompasses, which dynamically are accurate. During rapid turning operations, however, the gyros will produce a steady-state offset which gradually decreases to zero when the course is constant again. By using two GPS antennas, the heading can be measured even more accurately, without the drifting effect. In the case of anchored vessels, measurements of line length and tension are usually interfaced to the PM control system. *Any* positioning system requires measurement of the vessel position and heading. Wind sensors, measuring the wind speed and relative direction, are commonly used for wind feedforward control. In most commercial systems measurements of surge and sway velocities are *not* available with sufficient accuracy and must be estimated on-line. A guidance rule by DNVGL (2018) is that the accuracy of the position reference data is generally to be within a radius of 2% of the water depth for bottom-based systems, and within a radius of 3 meters for surface-based systems.

A minimum sensor and navigation configuration for a DP system typically consist of at least one position reference system, one gyro compass, one VRU for roll and pitch measurement and one wind sensor. The redundancy of the DP system can of course be increased by multiple measurement devices. However, one should also consider using systems based on different measurement principles, giving full redundancy not only in hardware configuration.

The trend today is integration between sensor systems and position reference systems. Over the last years the price of accurate inertial motion units (IMU's) have been reduced. This trend opens for integration between inertial navigation systems (which are based on the IMU sensor units) and other position reference systems e.g. GPS.

2.6.2 Modes of Operation

The DP and PM control functionality are closely connected to the surge, sway and yaw degrees of freedom (DOF), which can be viewed as independent of the actual thruster configuration, as long as there are enough thrust capacity to fulfill the force and moment demands. The various DOFs can individually be controlled in the following modes of operation:

- **Manual Control:** By using a joystick and a rotation knob the operator of the ship can generate force set-points in surge and sway and a moment set-point in yaw for manual control of the ship.
- **Damping Control:** Feedback is produced from estimated low-frequency vessel velocities and the objective is to regulate the vessel in the specific axis towards zero. This mode is especially applicable for anchored vessels, where effective damping will reduce possible large oscillatory motions, experienced about the resonance period of the anchored vessel, and thus reduce the stress on the mooring system. Damping is also useful in DP for obtaining a smooth transition between transit speed and fixed position operations.
- **Set-point Control:** Feedback is produced from both estimated low-frequency velocities and position/yaw angle. The objective is to keep the actual axis at the specified set-point position or heading.
- **Tracking Control:** The vessel tracks a reference trajectory which is computed from the old to the new position or heading set-point.

The most common DP operation is naturally set-point control in all three axes, often referred to as *station keeping*. Other fully automatic modes of operation can be station keeping with weather optimal positioning, and roll- pitch damping. In the first case the vessel automatically tends to the heading where the effect of the environmental loads are minimized. In the latter case the roll and pitch motion is suppressed by proper action of the horizontal thrust components. A combination between different modes are common, e.g. semi-automatic mode where a joystick is used for manual surge and sway control, while the heading is automatically controlled. Other tailor made DP functions exist for tracking operations like cable and pipe laying, ROV operations, etc.

The combination of damping control in surge and sway and set-point control of heading is often used in PM systems, especially in bad weather. Moreover, the vessel will tend to an equilibrium position where the mean environmental forces are balanced by the mooring forces. Assuming a proper heading set-point, this equilibrium position will be optimal with respect to

the thrust usage and the fuel consumption. For turret-moored ships automatic heading control is often the most important function. By keeping the heading optimally against the weather the effect of the environmental loads, and thereby the stress on the mooring system, will be minimized.

2.6.3 Functionality and Modules

The various DP vendors may differ in design methods. However, the basic DP functionality are more or less based on the same principles, as outlined in Figure 2.6.

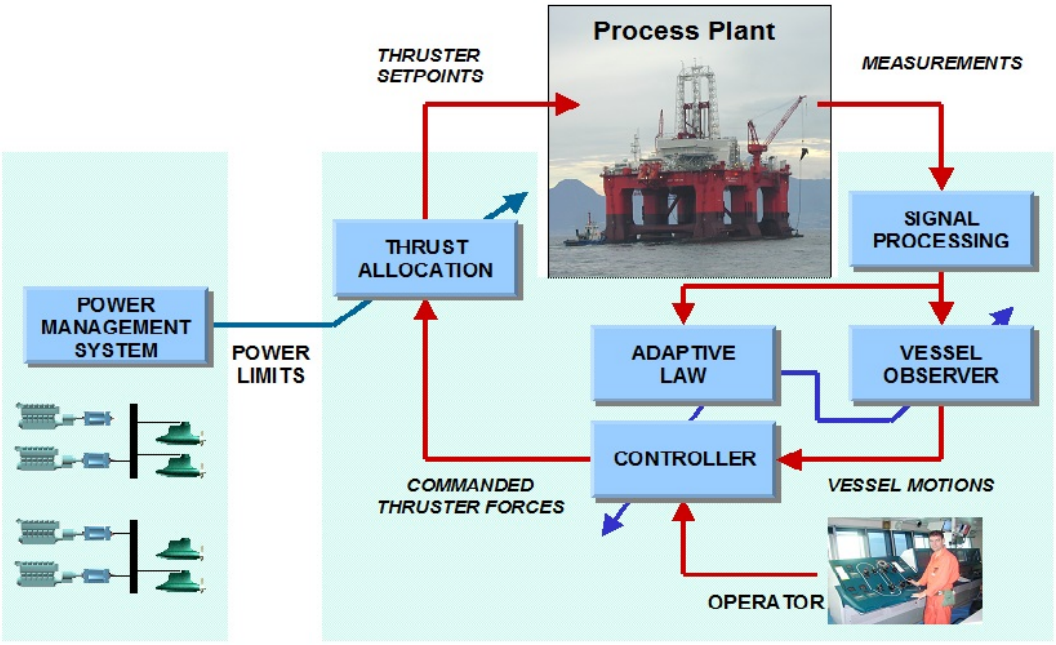

Figure 2.6: DP SW modules integrated with the power management system.

Signal processing

All signals from external sensors should be thoroughly analyzed and checked in a separate signal processing module. This comprises testing of the individual signals and sensor signal voting and weighting when redundant measurements are available. The individual signal quality verification should include tests for signal range and variance, frozen signals and signal wild points. If an erroneous signal is detected, the measurement is rejected and not used by the positioning system. The weighted signals from each sensor group should not contain any steps or discontinuities when utilized further in the system ensuring a safe operation.

Vessel observer

Filtering and state estimation are important features of a positioning system. In most cases today, accurate measurements of the vessel velocities are not available. Hence, estimates of the

velocities must be computed from noisy position and heading measurements through a state *observer*. The position and heading measurements are corrupted with colored noise, mainly caused by wind, waves and ocean currents. However, only the slowly-varying disturbances should be counteracted by the propulsion system, whereas the oscillatory motion due to the waves (1st-order wave-loads) should *not* enter the feedback loop. The so-called wave-frequency modulation of the thrusters will cause unnecessary wear and tear of the propulsion equipment. In the observer so-called *wave filtering* techniques are used, which separates the position and heading measurements into a low-frequency (LF) and a wave-frequency (WF) part. The estimated LF position, heading and velocities are utilized by the feedback controller. The observer is also needed when the position or heading measurements temporarily are unavailable. This situation is called *dead reckoning*, and in this case the *predicted* estimates from the observer are used in the control loop. Another feature of the observer is that it estimates the unmodeled and unmeasured slowly-varying forces and moments, mainly due to second-order wave loads and ocean current.

Controller logic

The positioning system can be operated in different modes of operation, see Section 2.6.2. All kind of internal system status handling and mode transitions, model adaptation etc. are governed by the controller logic. This includes smooth transitions between the different modes of operation, issue alarm and warnings, and operator interactions.

Feedback control law

The positioning controllers are often of the PD type (multivariable or decoupled in surge, sway and yaw), where feedback is produced from estimated LF position and heading deviations and estimated LF velocities. The underlying control methods may, however, vary. Traditionally, decoupled controllers and linear quadratic controllers have been popular. In addition to the PD part, integral action is needed to compensate for the static (or slowly-varying) part of the environmental loads. The controller should be optimized with respect to positioning accuracy, fuel consumption, and wear and tear of the propulsion system. In the design of positioning controller, the control inputs are forces in surge, sway and moment in yaw. In the context of positioning systems, this may be regarded as *high-level control*, since the actual control inputs are shaft speed (RPM control) or the pitching of the propeller blades (pitch control), which indirectly controls the developed force. In the case of azimuth thrusters, the direction of each thrust device are additional control inputs.

Guidance system and reference trajectories

In tracking operations, where the ship moves from one position and heading to another, a reference model is needed for achieving a smooth transition. In the most basic case the operator specifies a new desired position and heading, and a reference model generates smooth reference trajectories/paths for the vessel to follow. A more advanced guidance system involves way-point tracking functionality, optimal path planning and weather routing for long distance sailing. The guidance system could be interfaced to electric map systems.

Feedforward control laws

The most common feedforward control term is *wind feedforward*. Based on measurements of wind speed and direction, estimates of wind forces and moment acting on the ship are computed. As a consequence, a fast disturbance rejection with respect to varying wind loads can be obtained. In order to improve the performance of the system during tracking operations, a *reference feedforward* is computed. This is done by using a model of the ship dynamics, reference accelerations and velocities, given by the reference model. In PM systems wind feedforward is normally enabled in yaw only, since stationary wind loads in surge and sway should be compensated by the mooring system. In addition, a line break detection algorithm is monitoring the line tension signals and the corresponding vessel motions, in order to automatically detect break in the anchor lines. When a line break is detected, the line break feedforward controller will be activated in order to have the thrusters compensating for the lost forces and moment produced by the broken line. This will ease the load in the surrounding lines and thus preventing yet another line break.

Thrust allocation

The high-level feedback and feedforward controllers compute commanded forces in surge and sway and moment in yaw. The *thrust allocation* module computes the corresponding force and direction commands to each thrust device. The low-level thruster controllers will then control the propeller pitch, speed, torque, and power satisfying the desired thrust demands. The thrust allocation algorithm should be optimized for fuel consumption, wear and tear of the thruster devices and for obtaining the commanded thrust in surge, sway and yaw. In addition, the function should take into account saturation of the rpm/pitch inputs and forbidden directional sectors. The thrust allocation module is also the main link between the positioning system and the power management system (PMS). The positioning system has a very high priority as a power consumer. In any case, the thrust allocation must handle power limitation of the thrusters in order to avoid power system overload or blackout. The thrust allocation module receives continuously updated inputs from the PMS about available power and prevailing power plant configuration with status on the bus ties and generators. This should prevent power black-out and undesired load shedding of other important power consumers.

Model adaptation

The parameters in the mathematical model describing the vessel dynamics will vary with different operational and environmental conditions. In a model-based observer and controller design, the positioning system should automatically provide the necessary corrections of the vessel model and controller gains subject to changes in vessel draught, wind area and variations in the sea state. This can be obtained either by gain-scheduling techniques or continuously by using nonlinear and adaptive formulations. In addition other adaptive control and estimation methods may be applied, either run in batches or processing on-line.

2.6.4 Advisory and Surveillance Systems

Use of advisory systems for diagnostics, simulation and analysis of future operational requirements, subject to varying environmental and operational conditions, becomes of increasing im-

portance for optimal operational planning. Such systems are integrated with the positioning system and typical features are described below:

- **DP and PM vessel motion simulators.** Such simulators include mathematical models of the environment and the vessel motion, and the operator can simulate the performance of the positioning system, either using the prevailing environmental conditions or specify any environmental condition. In addition, different types of failure scenarios can be simulated, such as power or thruster failure, drive- and drift off. In PM systems failures in one or several lines can be simulated as well.

- **Consequence Analysis.** This is an advanced version of a position capability analysis, which continuously verifies that the vessel is capable of keeping position and heading for different failure scenarios during the prevailing conditions. This can be loss of one or several thrusters, one engine room or mooring lines (if applicable). In many cases a similar off-line version is also available, where *any* environmental condition, operation or failure situation can be simulated, by request from the operator.

2.6.5 DP Capability

The main purpose of a DP system is to keep position (and heading) within a certain excursion limits within a specified weather window, or so-called design environment. In order to meet the designed positioning capability, the system components should be reliable and the necessary redundancy requirements should be met. During the design phase it is important to verify that the amount of power and thrust capacity installed on a vessel will provide the necessary holding capacity. This can be done either by static or dynamic analysis. In a static analysis only the mean slowly varying forces due to wind, current and waves are considered. The items of data required in such a study include:

- Main vessel particulars, such as displacement, length, breadth and operating draft.

- Directional dependent wind, current and wave-drift coefficients, from which the corresponding forces and moments can be computed.

- The maximum environmental conditions in which the vessel should operate in dynamic positioning (wind speed, significant wave height and current speed). Important parameters are dominating wave period and the statistical description of the waves, usually described by wave spectrum formulations such as the Bretscheider spectrum, the Pierson-Moskowitz spectrum or the Joint North Sea Wave Project (JONSWAP) spectrum.

A rule of thumb is that the most loaded thruster should not use more than 80% of the maximum thrust in the design environment to compensate for the static loads, (API). The 20% margin is then left for compensation of dynamic variations. The results of such a static analysis can be presented as a *capability plot* (Figure 2.7). The sectors about $120^\circ - 133^\circ$ and $240^\circ - 250^\circ$ where the "butterfly-shape" curvature crosses the unity circle, indicate lack of thrust capability to maintain the position and the heading for the environmental loads acting in these directions. The environmental load data is given to the right on Figure 2.7. The butterfly-shape curvature results from rotating the environmental loads 360° about the vessel. The load directions given to the right are the prevailing directions from a real DP operation.

The static analysis with 20% margin is often too conservative. This suggests that the capability analysis should be complemented with dynamic (time domain) simulations, where the thrust allocation, the inherent thruster dynamics and dynamic thruster losses, forbidden azimuthing sectors and the whole control loop is taken into account in the final verification. In the traditional capability simulations the effect of power limitation is often neglected, which in fact often is the most limiting factor in failure situations. A capability analysis with power limitation is also important in the design of the power plant; how many power buses, amount of power generation on each bus, which thruster to be connected to the different buses, etc.

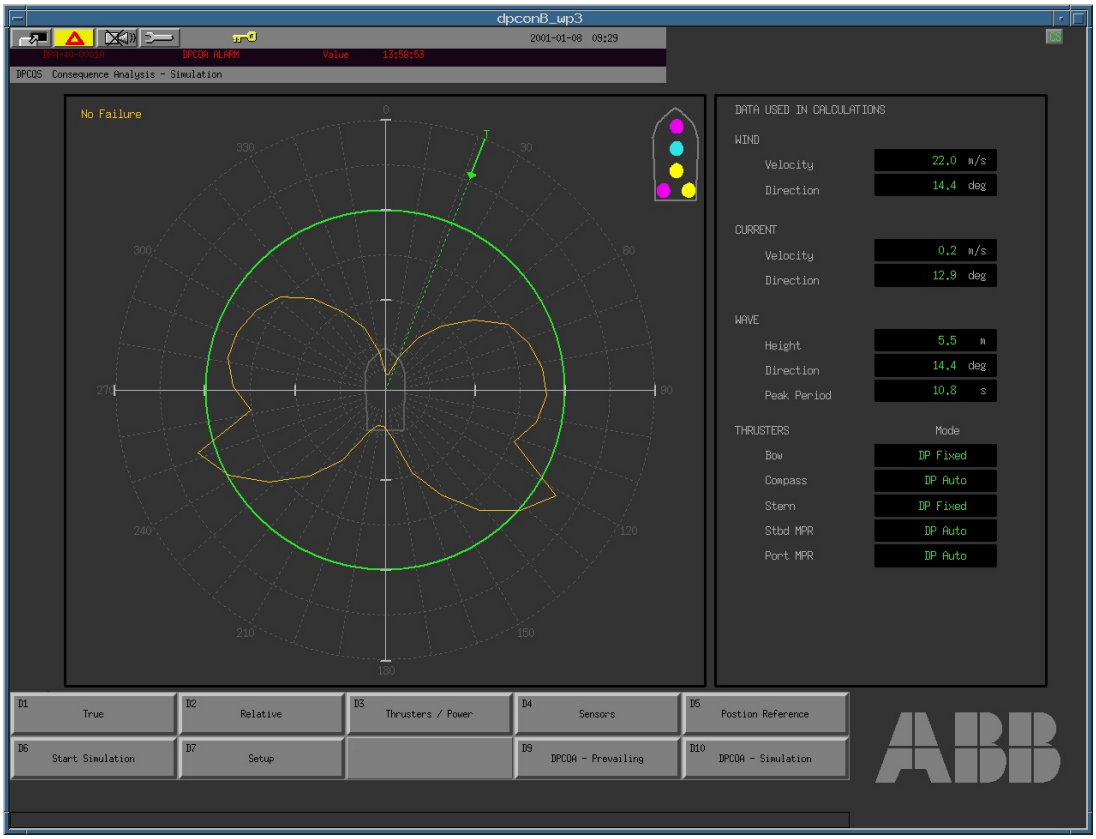

Figure 2.7: Typical DP capability plot for a supply ship - DP consequence analysis.

2.7 Power and Energy Management

In a system of electrical power installations, vessel and process automation system, DP system, and the other parts of the automation system controls their parts of the power system, e.g. the DP system controls the thruster drives, the off-loading control system use cargo pump drives, the process control system interacts with the compressors and cooling/heating systems etc. The interconnecting point for all the installed power equipment is the power distribution system. By starting and inrush transients, load variations, and network disturbances from harmonic effects, the load and generators are interacting and influencing each other. Optimum operation and control of the power system is essential for safe operation with a minimum of fuel consumption. As it is the energy control system (power/energy management system – PMS/EMS), which

monitors and has the overall control functionality of the power system, it will be the integrating element in a totally integrated power, automation and DP system.

The purpose of the PMS is to ensure that there is sufficient available power for the actual operating condition. This is obtained by monitoring the load and status of the generator sets and the power system. If the available power becomes too small, either due to increased load or fault in a running generator set, the PMS will automatically start the next generator set in the start sequence. A PMS can also have extended functionality by monitoring and control of the energy flow in a way that utilizes the installed and running equipment with optimum fuel efficiency. Such systems can be EMS. Energy management is a new approach to control and monitor the energy flow in marine, oil and gas systems. The EMS extends the concept of power management in the direction of controlling and coordinating the energy generation and consumption. In addition to optimize the instantaneous power flow, the historical energy usage and future energy demands are considered. EMS will then be the integrating element in a totally integrated power, automation and DP system. For PMS and EMS, the main functions can be grouped into:

- Power generation management: Overall control with frequency and voltage monitoring with active and passive load sharing monitoring and possibly control, and load dependent start and stop of generator sets. Since control logic and interlocking functions are a significant part of the power system switchboard design, the functionally of these systems must be coordinated.

- Load management: Load power monitoring and coordination of power limitation functions in other systems, load shedding and start interlock of heavy consumers based on available power monitoring.

- Distribution management: Configuration and sequence control for reconfiguration of the power distribution system. The distribution system should be configured to fit the requirements in the actual operational mode for the vessel.

The new generation production vessels and also drill ships/rigs have a complex power system configuration with advanced protection and relaying philosophies. There are close connections between the functional design and performance of the PMS and the power protection system functions. It is a challenge for involved parties to obtain an optimal and functional solution with several suppliers involved and a yard being responsible for all the coordination.

2.7.1 Blackout Restoration

Blackout of the power generating system is the most severe fault that can happen in an electric propulsion system. Should a blackout occur, and it does unfortunately happen from time to time, there will normally be required to have a system for sequence control of start-up and reconfiguration of the power system. This is implemented at the system control level, and includes sequences for starting and synchronizing generator sets and loads. There will normally also be a set of predefined operation modes, e.g. transit mode, station keeping mode, maneuvering mode, etc. with automatic sequence control for power system reconfiguration. A typical sequence for:

Automatic start and connection of emergency generator control. Separate control system - not part of the overall vessel control system.

- Automatic start/reconnection of standby generator(s).
- Reconnection of transformer breakers, distribution breakers.
- Tie breakers remain open if tripped.
- Restart of fuel and cooling pumps.
- Restart of other pumps and fans in sequence.
- Restart of thrusters, if required.

2.7.2 Load Reduction and Blackout Prevention

The diesel-electrical power system has better performance and fuel economy if the PMS controls the number of running engines in the power plant to match the load demand with high loading of the diesel engine. The optimal load with respect to fuel consumption, tear and wear, and maintenance is typically about 85% of maximum continuous rating (MCR). With a high load at the running engines, the system gets more vulnerable to faults in the system, such as a sudden trip of one diesel engine generator. The remaining, healthy engines will experience a step load increase and possible overloading, and in worst case, under frequency trip unless the functionality in the system reduces the load power in accordance with the generating capacity. In a modern drilling vessel, this load reduction and blackout prevention function is distributed and handled by several subsystems like:

- Power management's load management and blackout prevention functions.
- DP system's power limitation functions.
- Thruster drive's load reduction and load phase back functions.
- Drilling drive's load reduction and load phase back functions.

The ability to withstand such faults is also highly depending on the design and engineering methods and solutions, such as:

- Load capability and dynamics of the diesel engine.
- Governor and AVR configuration and settings.
- Generator and switchboard protection relay settings.
- Critical equipment should be fault-tolerant with loss of power ride-through functionality.

In DP vessels with high efficient speed controlled fixed pitch thrusters, the total load under normal operation is so low that the power plant runs optimal with few, often only two running diesel engines. In order to utilize this saving potential, the challenge is to design and tune the system to be capable of handling fault scenarios within a time frame not compromising the stability of the power supply.

Figure 2.8 shows, for illustration, the diesel engines capability to maintain the frequency for the load step associated with the loss of a parallel run engine. In typical installations, it has

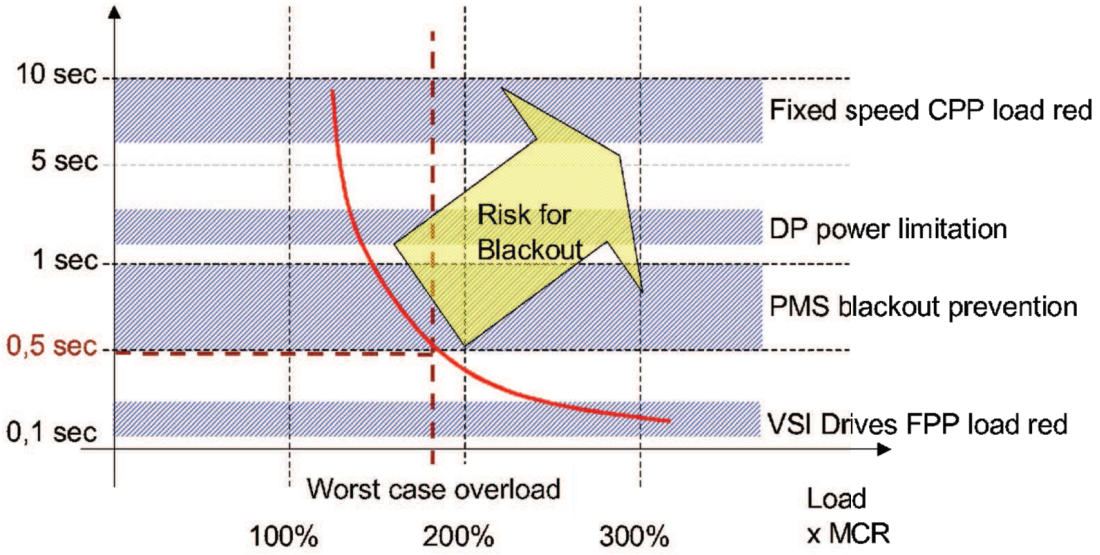

Figure 2.8: Regulation time constants for power reduction, with maximum response time in the order of 500ms (Illustrative only).

been seen that the actions of load reduction and blackout prevention must be effective within less than 500ms in order to not compromise the power system stability and limit the flexibility of operation. Several solutions are in use and the operators and owners have different preferences. However, some common conclusions can be made on what is typically required for the blackout prevention functionality:

- *Thruster and thruster drives:* Variable speed FPP thrusters must have a load reduction scheme, either monitoring the network frequency and/or receiving a fast load reduction signal from the PMS, either as a power phase-back signal, maximum power limitation signal, or – if well coordinated – fast RPM reference reduction. In order to avoid instabilities in the network frequency, the load reduction should be as precise as possible in order to dampen potential oscillations. Fixed speed CPP thrusters do not have fast enough response time for blackout prevention. These must be included in the power management's load shedding scheme.
- *Drilling drives:* Similar to the requirements of the thruster drives, with built-in priorities for the individual drilling drives.
- *PMS:* By class requirements, the PMS must include blackout prevention with load reduction/load shedding functionality. It was observed earlier, that the response time in this

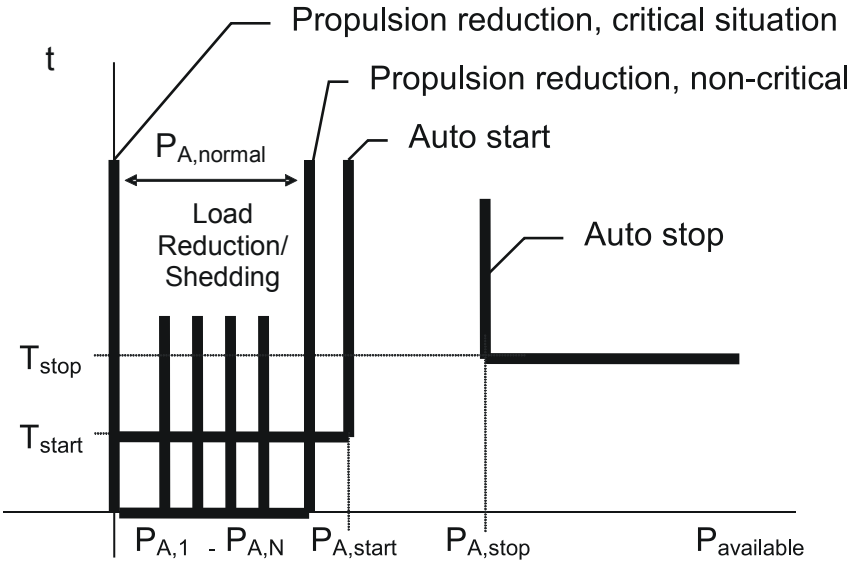

Figure 2.9: Coordination of auto start/stop and blackout prevention functions (example).

system was too long to obtain the desired level of fault-tolerance without a fast acting, stand-alone load reduction scheme in the thruster drives. With the knowledge of today, this has been claimed solved by use of fast acting, and possibly event-trigged load reduction algorithms.

- *DP system:* The DP system is also equipped with a power limitation function, normally based on a permitted maximum power consumption signal from the PMS. Generally, this has shown to be effective in avoiding overloading of the running plant, but not fast enough to handle faults and loss of diesel-generator sets. Of importance is also that the power limitation in manual and joystick control of the thrusters.

Based on experience, it is recommended that all load reduction and blackout prevention functions described above are installed and well coordinated, tuned and tested during commissioning and sea trial. Also, the need for retuning and testing must also be considered after modifications in the installation that may affect the coordination.

A typical coordination diagram is shown in Figure 2.9. Auto start and auto stop limits shows the level and time settings for load dependent automatic start and shutdown of the engines. Available power will under normal operations be within these limits. Upon faults, and sudden loss of engine, the available power is being reduced. The power reduction functions of the DP can be distinguished between critical or non-critical situations, allowing the DP to take all available power after possible load reduction and load shedding of non-essential consumers or consumers with lower priority.

2.7.3 Diesel Engine Governor and AVR Fault Tolerance

Although the rules and regulations have allowed for DP operations with closed bus ties in the electrical power system and one commonly connected power plant, the practices were until mid 1990s to split the network into two or more separated sections in DP 2 or 3 operations. With

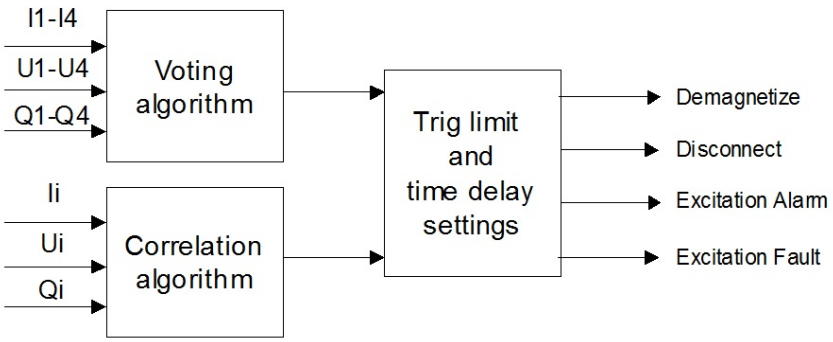

Figure 2.10: A monitoring scheme for AVR fault detection.

the developments on switchboard protection relays, and thruster drives together with new PMS with more precise and faster load reduction and blackout prevention functions, this has changed and it is now more common to operate with normally closed bus tie breakers and also with closed ring main bus. This development is motivated by the benefits of better and more flexible utilization of the installed generating capacity and to gain an improved fuel economy. The fuel savings for optimized loading of running engines have shown to be significant.

In such systems, it has been observed that under some load and operating conditions, certain faults in the governors and automatic voltage regulators, AVRs, can be difficult to identify with a regular protection scheme. In worst case, faults have shown to interfere with healthy equipment causing undesired shutdowns, and in some cases, even blackout. Developments in digital generator protection relays with multifunction and programmable protection logics have enabled a possibility to combine protection functions in new manners, and to include logic and algebraic functionality into the protection scheme. This has significantly improved the protection relay's ability to detect governor and AVR faults, and improved the system's fault tolerance to such faults. Figure 2.10 shows a possible monitoring scheme for AVR, including correlation functions of multiple variable and voting functions for multiple gensets. Such functions can be installed in the modern, programmable multifunction generator protection relays, or in separate logic controllers for retrofit and upgrades.

2.8 Maritime Industrial IT

We will in this chapter also shortly address aspects related to the information flow between the real time systems ensuring on- line control and the management systems optimizing the operations and the business processes. This includes fleet allocation related to transport logistics, supply chain management, monitoring and diagnostics of technical condition of equipment and systems.

As reported in Rensvik et al. (2003) systems for operational management such as condition monitoring and diagnostics systems, supply chain management systems, enterprise management systems, etc. have increased the possibility to improve operational performance, productivity and life cycle optimization of the assets related to operation of the installations.

Lately, the automation vendors, mainly in land-based industry sectors, have started the next step to physically and functionally integrate the real time control systems with the operational management systems. This has been denoted as *industrial IT*. The introduction of industrial IT

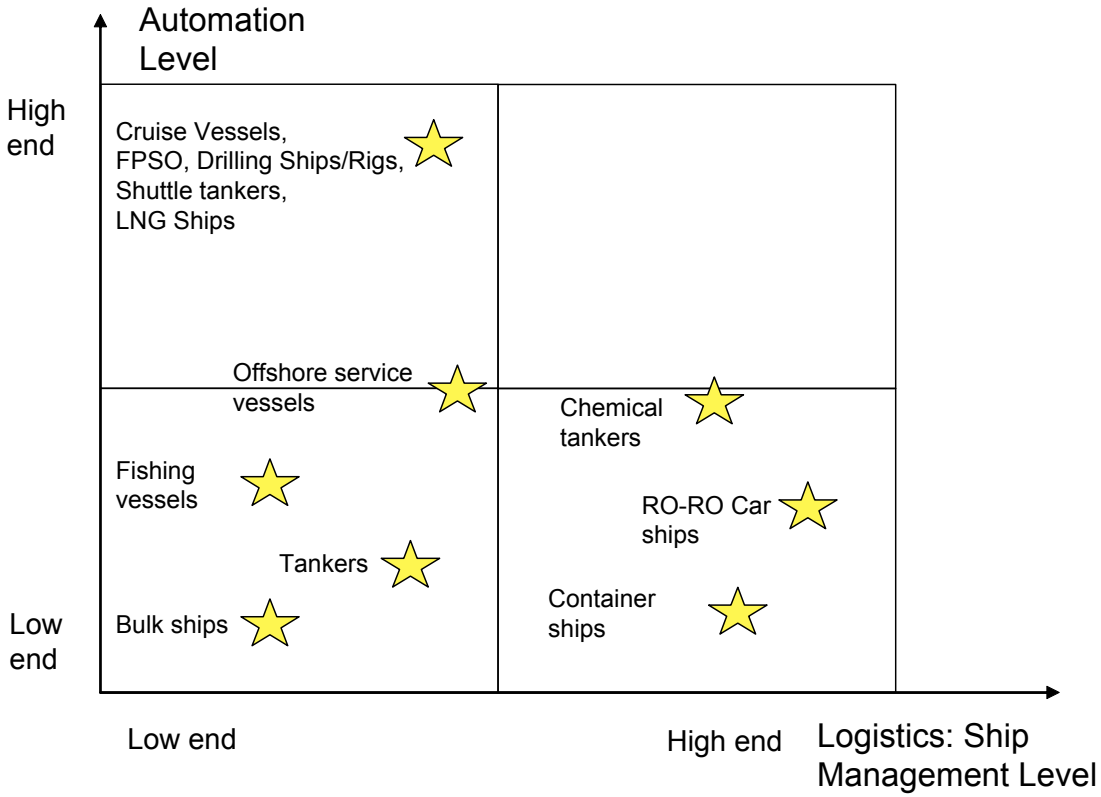

Figure 2.11: Low-end and high-end market segments within automation and ship management.

into marine applications has yet only started, and is still an area of research and development. For vendors and ship operators it is a challenge to take out the potential this shift of technology gives.

Maritime industrial IT solutions for the various marine market segments will be dependent on type of trade and charter, vessel complexity, safety and availability requirements, size of fleet, etc. Concerning vessel automation we will here focus on ships and vessels characterized as advanced and specialized with high number of input/outputs (I/O) and rather complicated operational functions. This is denoted as the high-end market; see also Figure 2.11. Examples are ships (Figure 2.4) and rigs (Figure 2.1) for oil and gas exploration and exploitation, passenger and cruise vessels. Typical applications in the offshore market are service vessels, drilling rigs and ships, shuttle tankers, cable and pipe layers, floating production off-loading and storage units (FPSOs), crane and heavy lift vessels, geological survey vessels and multi-purpose vessels.

As a part of enabling industrial IT solutions some vendors have installed condition monitoring and control functions locally on the power equipment and field devices as indicated in Figure 2.3 with the possibility for remote monitoring and diagnostics.

In many installations redundant systems are available, and the number and types of measurements required are specified by certain class rules. Physical integration based on standardized communication protocols ensure connectivity of devices and integration of controllers and operator stations into three network levels (Figure 2.3) real time field bus network communication on low level between devices and controllers, real time control network connecting controllers and operator stations, and office plant network to various office systems and information man-

agement systems. The last level opens up for satellite communication to land offices at ship operators or vendors, see also Figure 2.12.

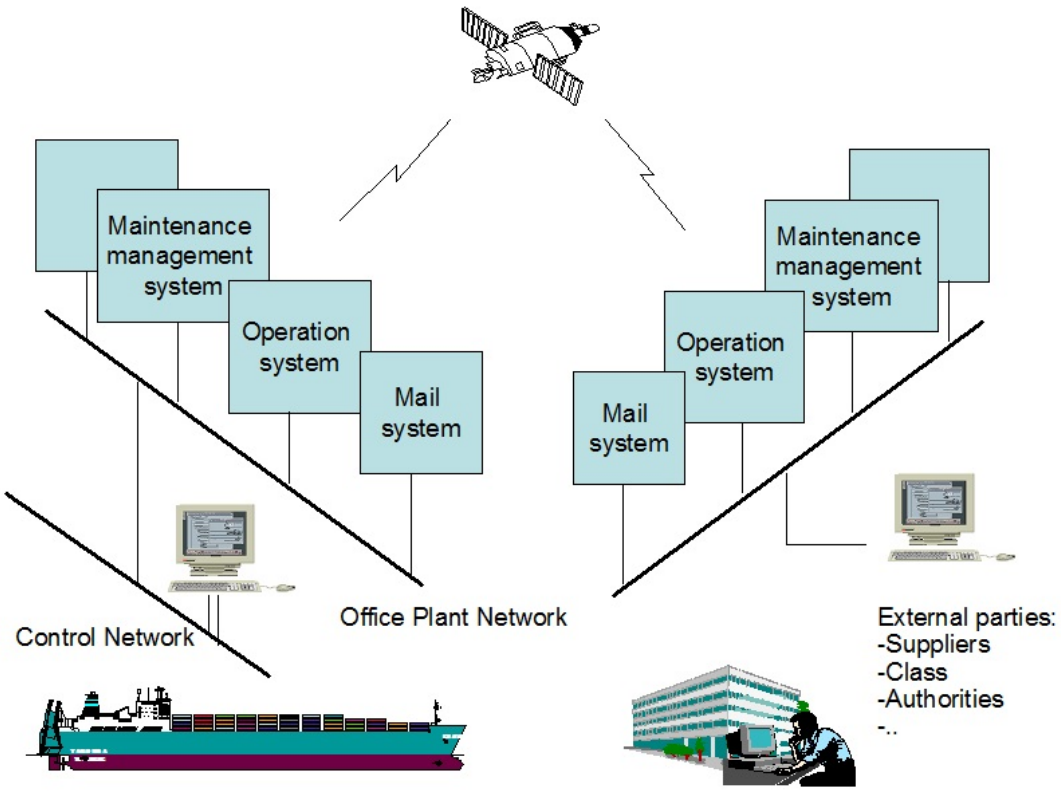

Figure 2.12: Distributed information systems ships – shore for flexible information flow and sharing.

Industrial IT is supposed to increase the integration of vessel plant data with the business management systems ensuring optimized asset management and operation of each vessel in particular and the whole fleet on corporate level, see Figure 2.13

As cost on the vessel-to-land satellite communication is reduced (Figure 2.14) and the maritime information technology architecture is improved this kind of information flow is expected to be working seamless in real time, as opposed today, where a limited amount of date is transferred at discrete events.

Up to now integrated automation systems have been proprietary with a limited number of vendors. However, in the automation industry it is a trend towards openness in communication protocols and network. How this will influence on the technology solutions and responsibilities for multi-vendor integration systems is still a subject for discussion.

Condition monitoring and RCM (Reliability Centered Maintenance) are well known concepts in many industries. These concepts have now also been incorporated in ship maintenance management systems. Today, ships in many trades have only very short loading and discharging periods in port. This means that maintenance that only can be performed in port including flag state and class surveys have to be carried out during these short periods to avoid down-

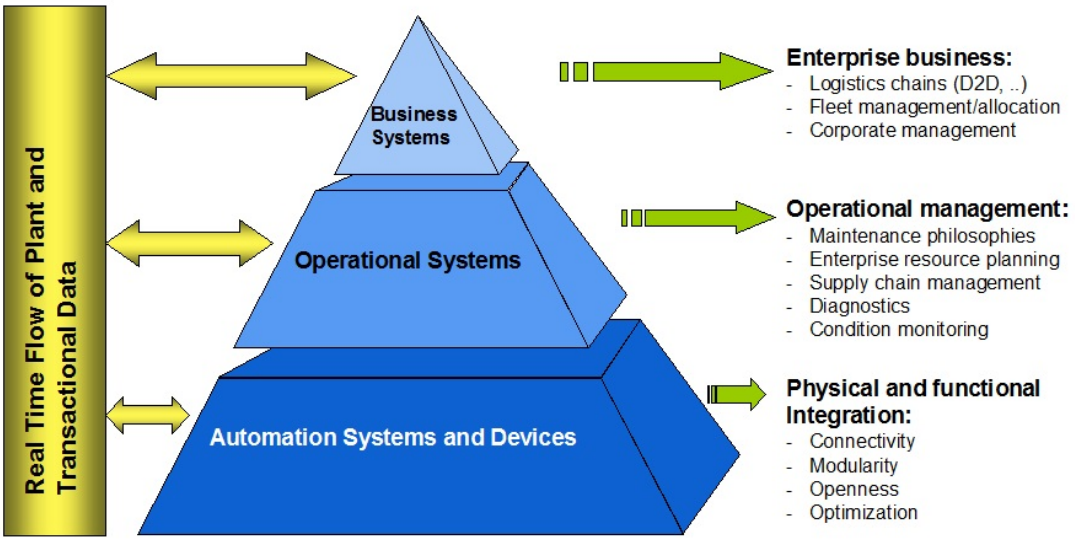

Figure 2.13: Industrial IT architecture.

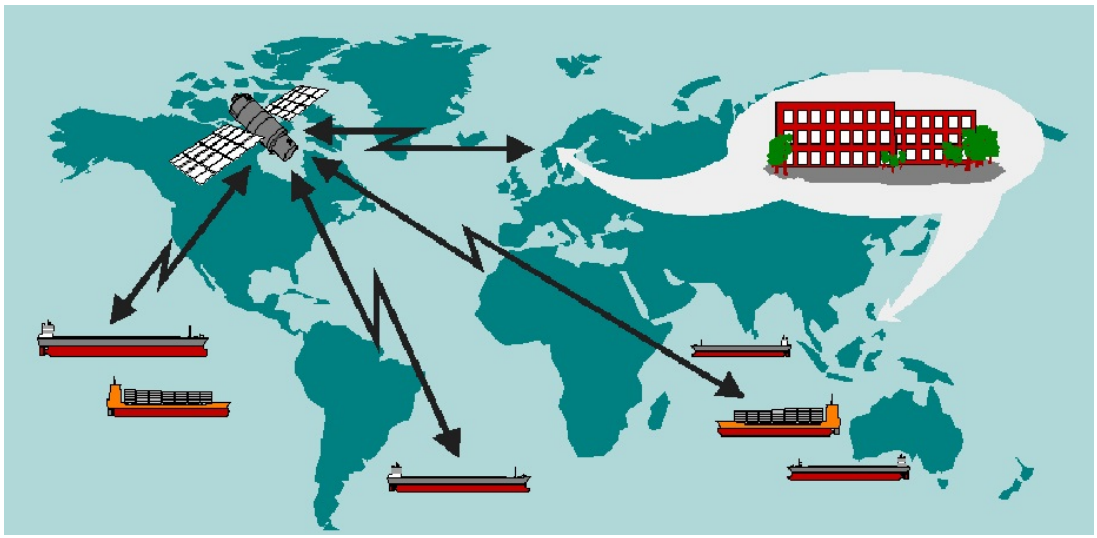

Figure 2.14: Fleet allocation and operations managed on cooperate level.

time. To improve such a harmonization, analysis and planning methods have to be available to monitor the status of the vessel, to schedule surveys and to predict the future state of the ship based on frequent reporting and continues monitoring of technical condition for structures and equipment (Figure 2.15). This concept can further be developed into a "continues" risk analysis based on this technical condition information, and adapted to highlight risk equipment related to the different operational mode of the ship, i.e. a way to enhance safety measures. Frequent tools in technical monitoring is the use of signal processing techniques such as spectrum analysis and other statistical methods. Examples are acceleration measurements for vibration analysis, temperature measurements for overheating, etc. Lately, the use of observers for state estimation

may also be used.

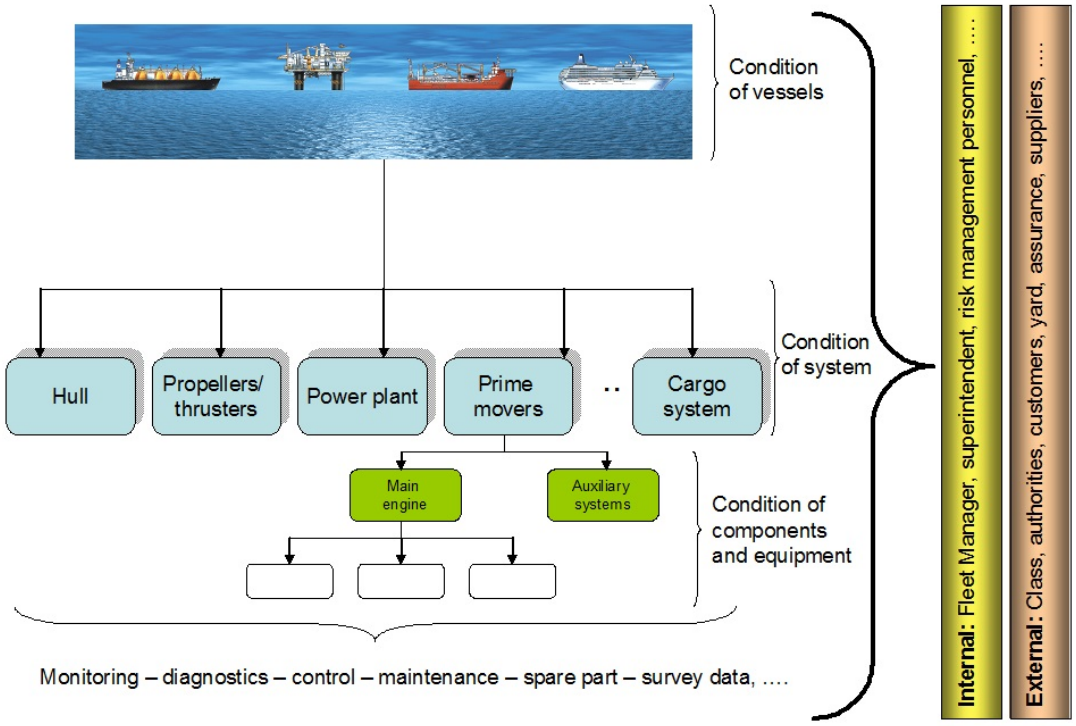

Figure 2.15: Technical condition philosophy.

2.9 Rules and Regulations

2.9.1 Class Requirements

In many cases it is up to the owners to decide which type of classification (or to seek for class approval at all) for the positioning system installed. Three examples of class societies that have rules for classification of DP systems are DNV GL (DNVGL, 2018), ABS and LRS . The International Marine Organization (IMO) has also developed Guidelines for Dynamic Positioning, in order to provide an international standard for DP systems on all types of new vessels. The purpose of the Guidelines and class rules is to recommend design criteria, necessary equipment, operating requirements, and a test and documentation system for DP systems to reduce the risk to personnel, the vessel itself, other vessels and structures, sub-sea installations and the environment while operating under dynamic positioning control. Taking into consideration that DP operated vessels often operate in different parts of the world, such a standardization provides a useful tool for the different Costal states to specify the local rules and regulations, defining levels of safety requirements, requirements for redundancy and operations for DP vessels. For moored vessels using automatic thruster assistance, IMO does not have any guidelines. DNV has the class notation called POSMOOR ATA, DNVGL (2018) and Lloyd's Register of Shipping has the notation PM or PM T1, LRS .

The requirements for hardware and software on DP systems are closely connected to the level of redundancy, which is defined as:

Definition 2.2 (Redundancy) *Redundancy means ability of a component or system to maintain or restore its function when a single fault has occurred. This property can be obtained by installation of multiple components, systems, or alternative means of performing a function.*

A DP system consists of components and systems acting together to achieve sufficiently reliable positioning keeping capability. The necessary reliability of such systems is determined by the consequence of a loss of position keeping capability. The larger the consequence, the more reliable the DP system should be. To achieve this philosophy the requirements have been grouped into three different equipment classes. The equipment class depends on the specific DP operation, which may be governed by Coastal state rules and regulations or in agreement between the DP operator company and their customers. A short description of the different classes is given below.

Class 1 For equipment class 1, loss of position may occur in the event of a single fault, e.g. the DP control system need *not* to be redundant.

Class 2 For equipment class 2, loss of position is not to occur in the event of a single fault in any active component or system. The DP control system must have redundancy in all active components, e.g. the hardware must consist of at least two independent computer systems with self-checking routines and redundant data transfer arrangements and plant interfaces. At least three independent position reference systems and three sensor systems for vertical motion measurement, three gyrocompasses and three wind sensors.

Class 3 Same as DP class 2, with additional requirements on redundancy in technical design and physical arrangement.

IMO Equipment Class	DNV GL	LRS	ABS
Not applicable	Dynpos AUTS	DP CM	DPS-0
Class 1	Dynpos AUT	DP AM	DPS-1
Class 2	Dynpos AUTR	DP AA	DPS-2
Class 3	Dynpos AUTRO	DP AAA	DPS-3

Table 2.1: Mapping table of DP class notation by IMO, DnV, Lloyds and ABS.

Class 2 or 3 system should include the function "Consequence analysis", which continuously verifies that the vessel will remain in position even if the worst single failure occurs. The IMO Guidelines also specifies relationship between equipment class and type of operation. DP drilling operations and production of hydrocarbons, for instance, requires equipment Class 3, according to IMO. In Table 2.1 the coherence for DP class notations by DNV GL, LRS, ABS and IMO are shown.

In Figure 2.16 DNVGL (2018) has listed up the minimum requirements for DP class notation.

2.9.2 Reliability and Redundancy

From a safety point of view a DP system can be viewed as four different sub-systems. Each sub-system can then be further split recursively into sub-sub systems. For instance:

- Level 1: Power system. Level 2: Power generation, power distribution, drives, etc.
- Level 1: Propulsion system. Level 2: Main screw, tunnel thrusters, azimuth thrusters.
- Level 1: Positioning control system. Level 2: Computer and I/O, Operator HMI, UPS, Operator interaction.
- Level 1: Sensor system. Level 2: Gyros, Position reference systems, Wind sensors.

Starting from the bottom, the reliability of each sub-component can be specified and depending on the level of redundancy, the reliability and availability of the total system can be computed using statistical methods. Each component can be characterized by:

- Failure rate λ, defined Maximum number of failures per million hours.
- Mean time between failures (MTBF), for one component given by

$$MTBF = \frac{1}{\lambda}$$

- Total down time, T_d, of a component, including mean time to repair (MTTR).
- Availability, A, defined as

$$A = \frac{MTBF}{MTBF + T_d}$$

The above characteristics are specified for each component or each level in a reliability analysis and will at the top level characterize the whole plant.

Table 7 System arrangement

Subsystem or component			*Minimum requirements for class notations*			
			DYNPOS(AUTS)	***DYNPOS(AUT)*** ***DPS(1)***	***DYNPOS(AUTR)*** ***DPS(2)***	***DYNPOS(AUTRO)*** ***DPS(3)***
Electrical power system	Electrical system		No redundancy [3]	No redundancy [3]	Redundancy in technical design	Redundancy in technical design and physical separation (separate compartments)
	Main switchboard		1[3]	1[3]	1	2 in separate compartments
	Bus-tie breaker		0[3]	0[3]	1	2, 1 breaker in each MSB
	Distribution system		Non-redundant[3]	Non-redundant [3]	Redundant	Redundant, through separate compartments
	Power management		No	No	**DYNPOS (AUTR)** :Yes **DPS(2)**: No	**DYNPOS (AUTRO)**: Yes **DPS(3)**: No
Thrusters	Arrangement of thrusters		No redundancy	No redundancy	Redundancy in technical design[4]	Redundancy in technical design and physical separation (separate compartments)
	Single levers for each thruster at main DP-control centre		Yes	Yes	Yes	Yes
Positioning control system	Automatic control; number of computer systems		1	1	2	2 + 1 in back-up control centre
	Manual control; independent joystick system with automatic heading control [2]		No	Yes	Yes	Yes
Sensors	Position reference systems		1	2	3	3 whereof 1 in back-up control centre
	External sensors	Wind	1	1	**DYNPOS (AUTR)**: 3 **DPS(2)**: 2	**DYNPOS (AUTRO)**: 3 **DPS(3)**: 2 whereof 1 connected to back-up control system
		Heading reference system[1]	1	1	3	3 whereof 1 in back-up control centre
		Vertical reference sensor (VRS)	1	1	**DYNPOS (AUTR)**: 3 **DPS(2)**: 2[5]	3 whereof 1 in back-up control centre
UPS			0	1	2	2 + 1 in back-up control centre
Printer			Yes[6]	Yes[6]	Yes[6]	Yes[6]
Back-up control centre for dynamic positioning control back-up system			No	No	No	Yes

1) The heading reference system(s) shall comply with IMO Res. A424(XI) performance standards for gyro-compasses. When three heading reference systems are required one of the three may be replaced by a heading measuring device based upon another principle, as long as this heading device is type approved as a THD (transmitting heading device) as specified in IMO Res. MSC.116(73). For notations **DYNPOS (AUTRO)** and **DPS(3)** this is not to be the gyro placed in the back-up control centre.

Heading sensors based on other principles may be accepted upon special considerations. When such considerations are made the total heading device installation shall be considered in view of redundancy, robustness and failure tolerance, both with respect to the number of heading devices installed, principles used, and the installation of the equipment with respect to signal transmission, power supply and physical installation (including separation when required).

2) The heading input may be taken from any of the required heading input devices.

3) When this is part of the ship normal electrical power system (i.e. used for normal ship systems, not only the DP system), then Pt.4 Ch.8 applies.

4) For **DPS(2)** see also [4.3.2].

5) Where necessary for the correct functioning of position reference systems, at least three vertical reference sensors shall be provided for notation **DPS(2)**. If the DP-control system can position the ship within the operating limits without VRS corrections, only 2 VRSs are required.

6) Dynamic positioning systems. The printer may be replaced by a separate electronic data logger, provided the data is stored on redundant electronic media (the DP-control system operator stations may be used as redundant storage media) and the data logger has UPS supply in compliance with [8]. The data logger shall have HMI and functionality in place for the operator to access and view the stored date in an efficient manner. The data logger shall have capacity for storage of data for minimum 7 days of operation. It shall be possible to upload to offline storage media, for data storage longer than the logger capacity. (The data logger should preferably be time synchronised with other alarm and logging systems to support performance and incident analysis.)

Figure 2.16: Minimum DNV GL requirements (2018) for DP class notation.

The redundancy concept of the electrical power and propulsion plant will be based on the required ability for maneuvering and propulsion after faults in the system. In commercial vessels, these requirements are determined by national and international legislation, and specified by the classification societies by the different class notations. A typical redundancy diagram for a DP class 2/3 drilling rig is indicated in Figure 2.17. Each block represents a part of the system which is susceptible to a single failure.

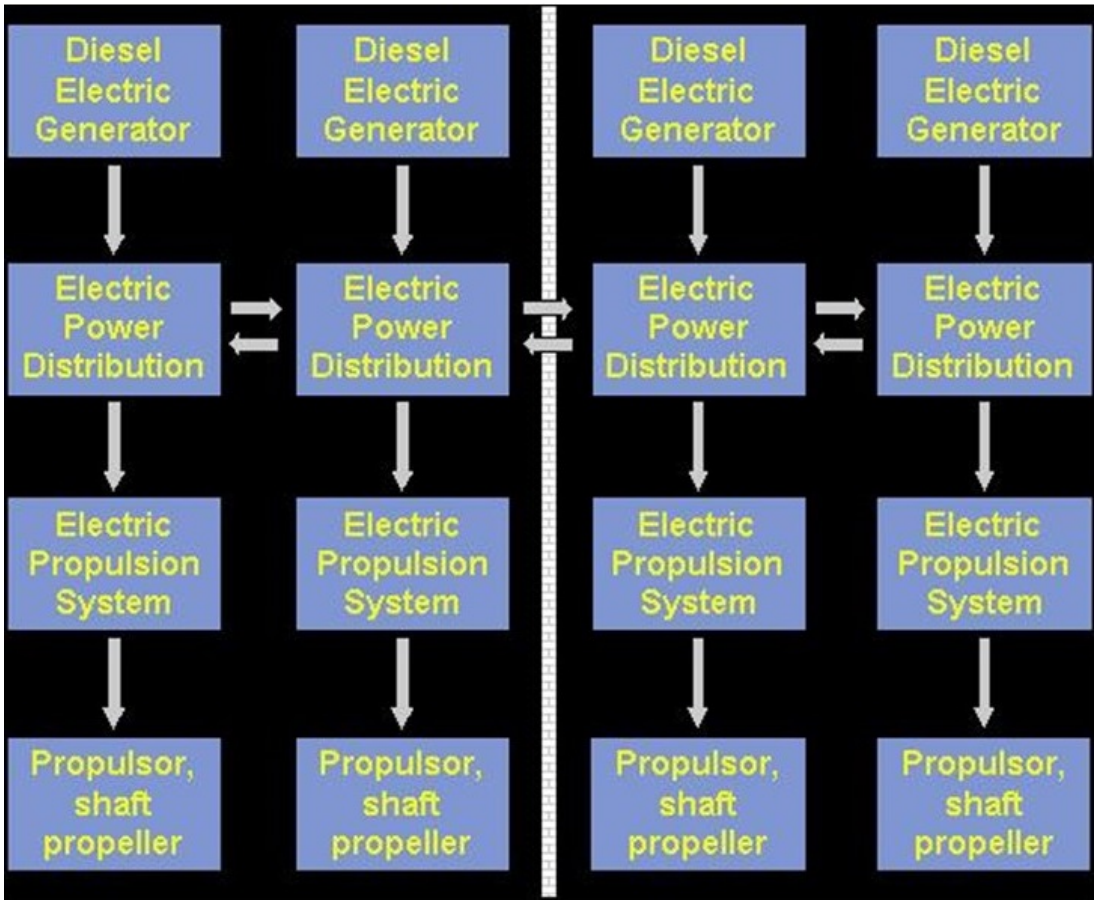

Figure 2.17: Each block represents a part of system which is sensitive to a single failure.

At higher level of controls the redundancy concept is different and achieved by the duplication of the control systems in hot back-up configuration, as seen in Figure 2.18 for a typical DP 3 drilling rig.

The vessel control system must follow the same redundancy and segregation principles as the electric system. Principally, this is achieved by designing the vessel control structure as a mirror image of the electrical power plant, as shown in Figure 2.19.

2.9.3 Failure Analysis

The cost of making design changes during the initial project phase is small, but as the project progresses the cost of design changes increases significantly. Minor changes in a system can cause project delays and huge additional costs during the commissioning and sea trials. During

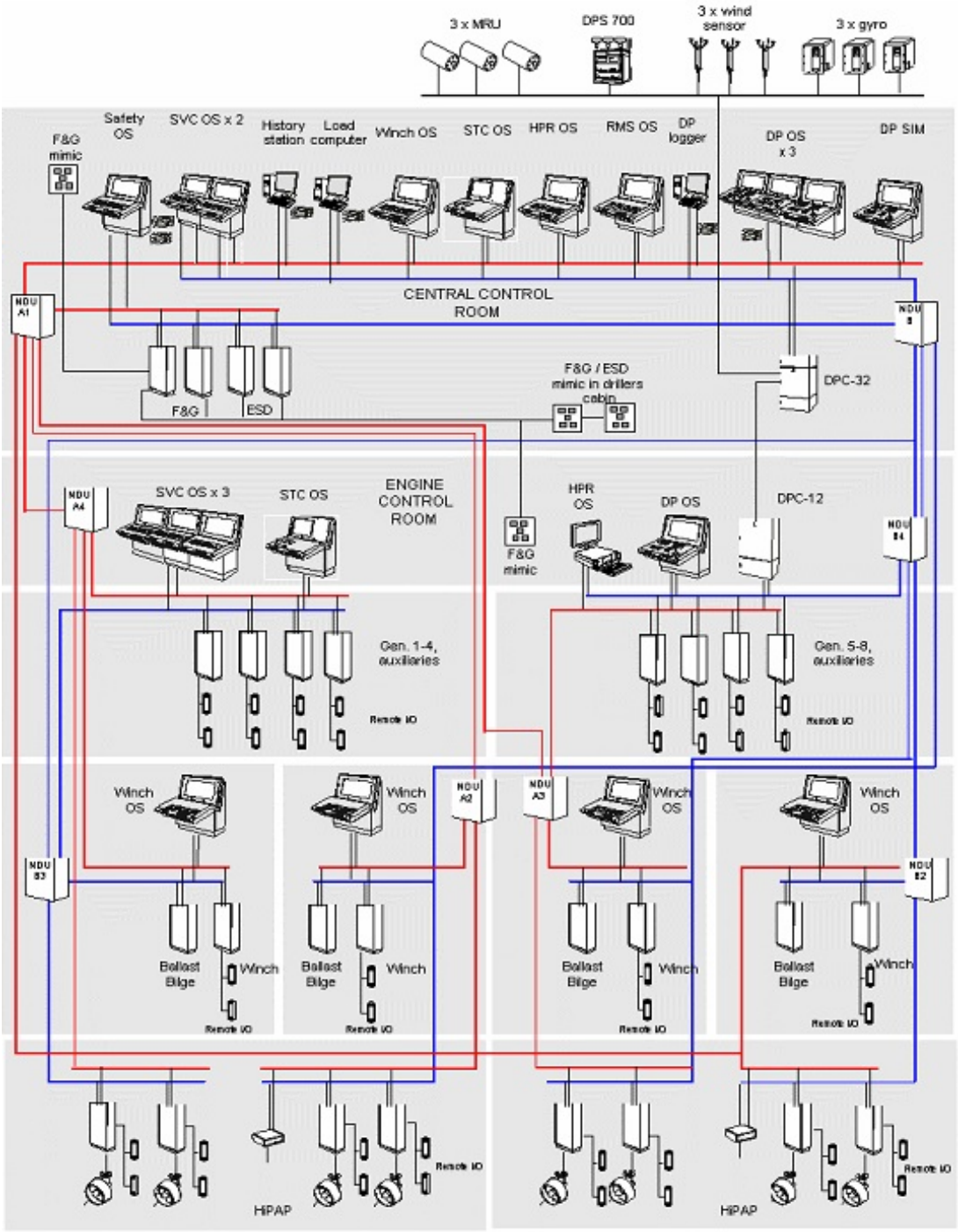

Figure 2.18: A total integrated vessel control system for drilling vessels (Courtesy of Kongsberg Maritime).

the whole design phase of newbuildings, the reliability of the total system can be thoroughly investigated by different reliability methodologies, in order to detect system design errors and

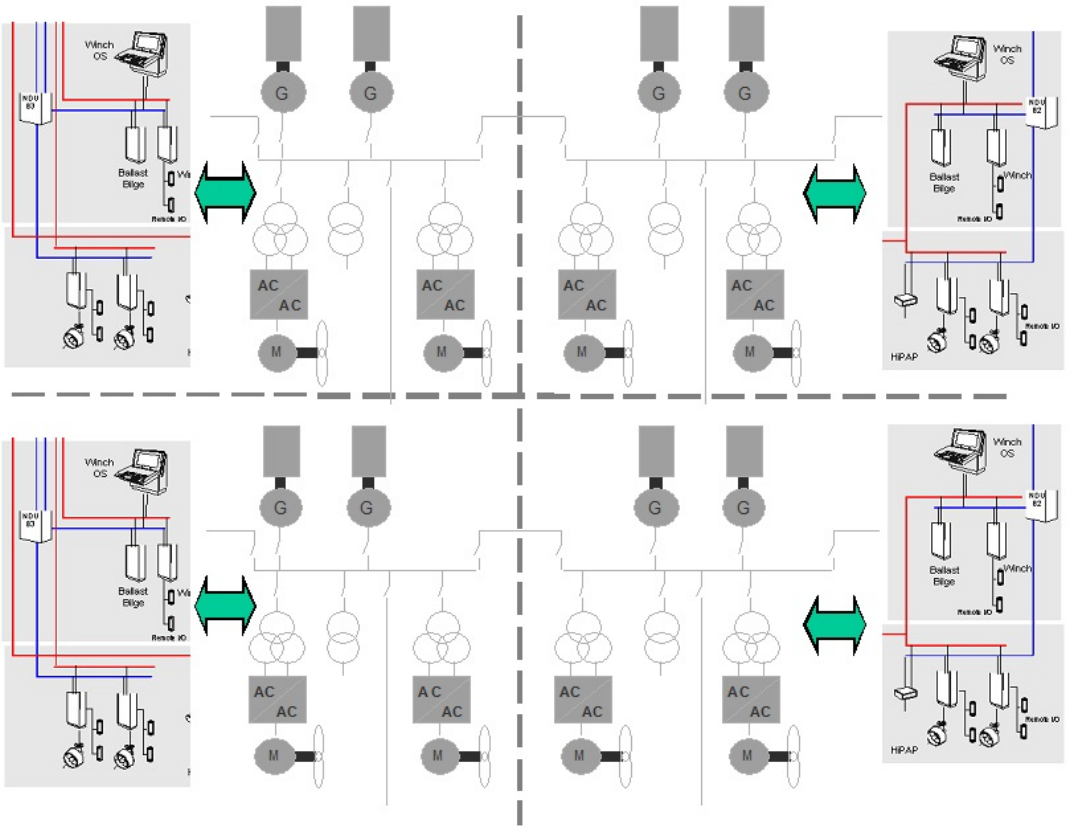

Figure 2.19: Mirror image design of the vessel control system ensures to achieve a unified redundancy and segregation philosophy.

thus minimize the risk. Such analysis of DP system and it's subsystems is not required by the class societies or the IMO Guidelines. However, the Coastal states, oil companies or customers may require it, in addition to classification approval. There are different methods available for assessing the reliability of such complex systems.

One common methodology is the Failure Mode and Effect Analysis (FMEA). This is a qualitative reliability technique for systematically analyzing each possible failure mode within a system and identifying the resulting effect on that system, the mission and personnel. This analysis can be extended by a criticality analysis (CA), a quantitative procedure which ranks failure modes by their probability and consequence.

2.10 Simulation

For years numerical simulators have been used as tools in system design and analysis, both in academia and in the industry. The simulator may use models of various fidelity to reconstruct the real physical properties of a dynamic system, Sørensen et al. (2003). For control system design and testing purposes it is convenient to develop a real-time system simulator, Figure 2.20 In order to operate in real-time often simplified or equivalent models of fast dynamic systems like power electronics, complex systems like multi-dimensional finite element method (FEM)

models of structures and panel methods of hydrodynamics must be used. Model reduction and simplifications must be done with care such that important structural information and properties of the dynamic system are not lost

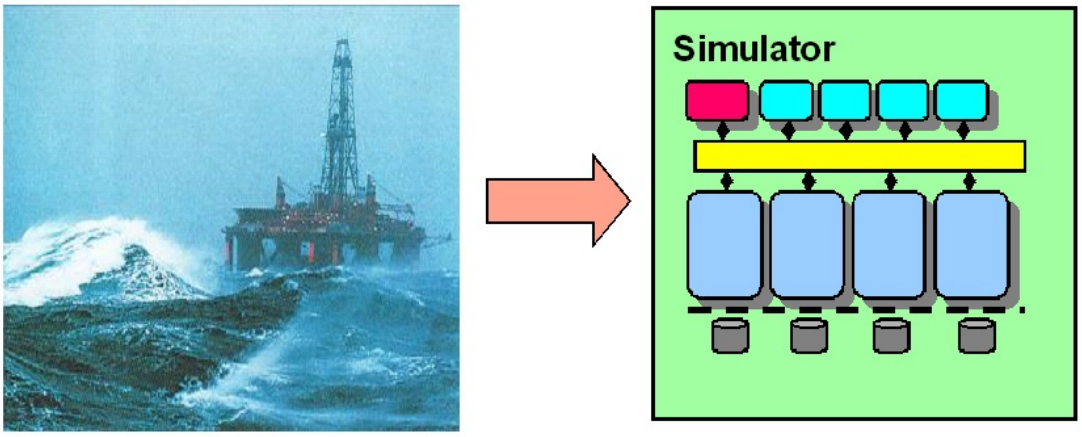

Figure 2.20: Mathematical software models of ship, equipment and its systems are implemented and analyzed subject to varying environmental loads, operational requirements and scenarios.

At NTNU a marine system simulator illustrated in Figure 2.21, Marine Systems Simulator (Fossen and Perez (2004)), based on MATLAB/SIMULINK. MSS integrates the disciplines hydrodynamics, structural mechanics, marine machinery, electric power generation and distribution, navigation and automatic control of marine vessels. The main purpose of MSS is to improve the accumulation and reuse of knowledge and thereby the quality of the education and research. The simulator will be continuously developed by students and researchers, and will serve a diversity of applications. This necessitates a modular structure, in which each module is a self-contained unit with a well-defined interface and functionality.

2.10.1 Simulator Structure

The core of the simulator is the *process plant models or simulation models*, which give the necessary detailed description of the vessel dynamics, systems and components and its surroundings, see Figure 2.21. The other main parts of the simulator are the control systems interfaced with the sensor and actuator modules. The control systems may for instance be DP system, thruster assisted position-mooring system, tracking controllers and autopilots, local thrust controllers, PMS, crane control systems, etc. MSS is made partly as open-source SW.

2.10.2 Module Hierarchy

Depending on the development stage and required accuracy of the operation and application studied, a hierarchy in module complexity is allowed. For any application, several modules of varying technical complexity, built-in functionality and release levels may exist. These should all cover the same basic functionality and have the same interfaces, and may therefore easily be interchanged. Figure 2.22 shows a module hierarchy example, where module complexity is plotted versus release level and application.

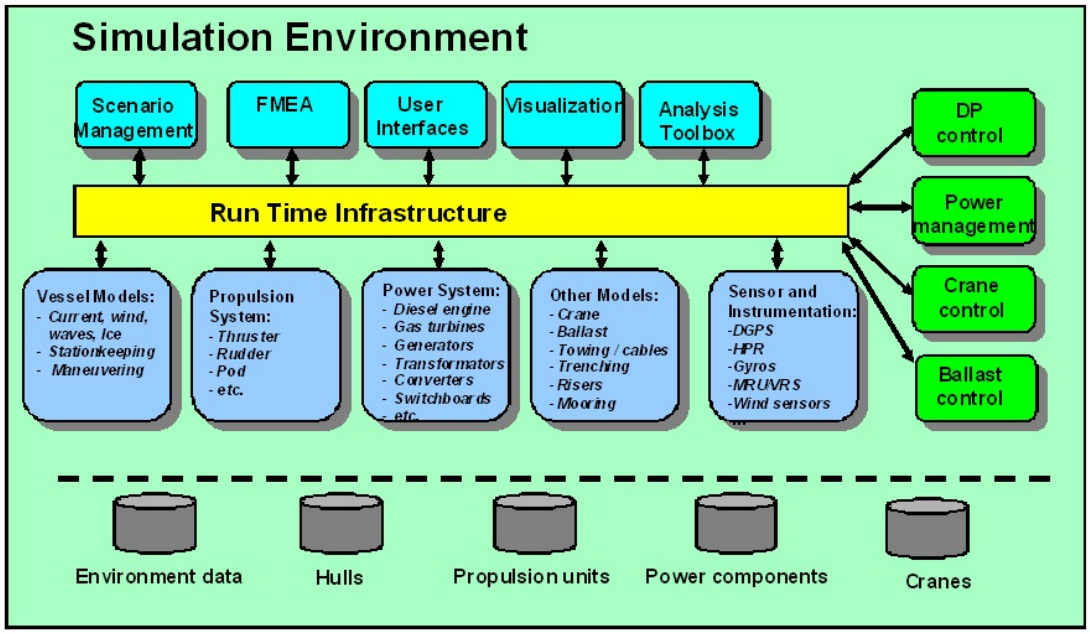

Figure 2.21: Marine Systems Simulator, NTNU.

2.10.3 Hardware and Software Platform

The simulator is currently being developed in a MATLAB/SIMULINK environment on the Windows PC platform. SIMULINK was chosen for running the main simulation loop because of its flexibility towards several programming languages. Applications written in MATLAB, C, C++, and Fortran may easily be linked to the simulation by use of S-functions. This is convenient for generating simulator modules from existing code, and makes development of new modules more user-friendly.

2.10.4 Hardware-In-the-Loop Testing

As the DP vessels become more demanding and complex, safety, reliability and integration aspects with the navigation system, power plant, vessel automation, propulsion system and other consumers become more important. In order to reduce these risks, regulatory bodies, class societies and independent consultants have been continuously addressing advances in rules and regulations and testing and verification methodologies. In this context the safety and verification regime for DP systems may be seen as an example to be followed for other mission critical control systems as well.

The successful operation of DP vessels such depends more and more on advanced integrated functionality of software-based control systems. Consequently, software related problems, often in conjunction with hardware and/or human errors, may lead to vessel construction delays, downtime during operation, reduced income for clients, increased cost, and reduced safety. In order to reduce these risks, independent third party Hardware-In-the-loop (HIL) simulator testing has recently been applied for extensive software testing and verification of DP systems on several offshore vessels. In the work of Johansen and Sørensen (2009) and Smogeli (2010) the concept of HIL testing is described, and the experiences and findings statistics are reported from

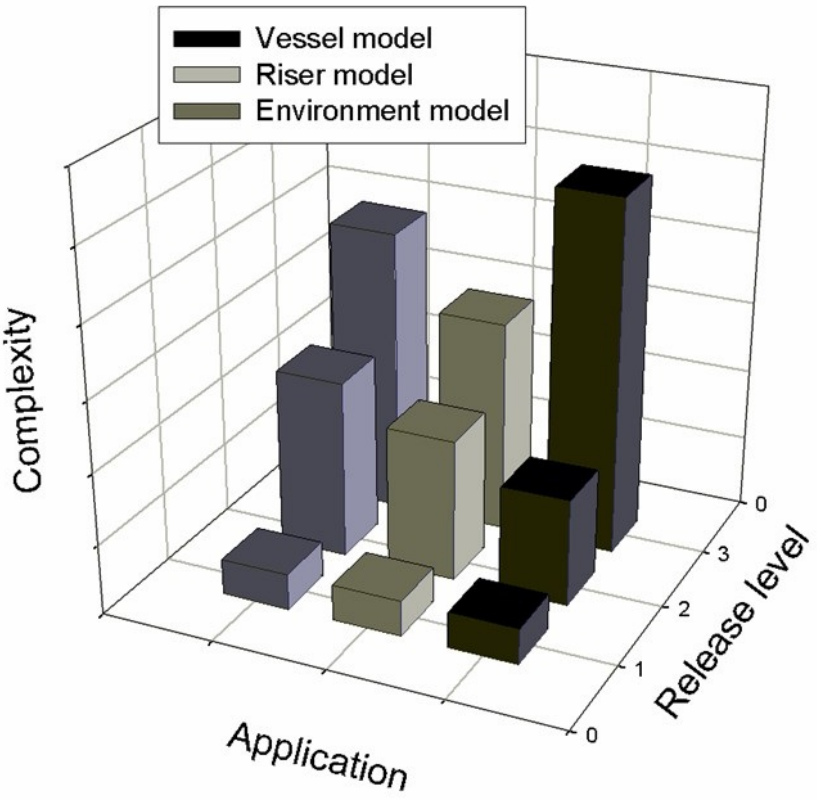

Figure 2.22: Module hierarchy example.

HIL testing of DP computer systems, power management systems and steering, propulsion and thruster control systems on drilling vessels, offshore service and construction vessels, and shuttle tankers. The main idea is testing and verification of the computer software using a vessel specific simulator (Figure 2.23) capable of simulating the dynamic response of the vessel, thruster and propulsion system, sensors, position reference systems, power generation, distribution, main consumers, and other relevant equipment (Sørensen et al., 2003). The simulator is connected via network or bus interfaces to the targeted control system such that all relevant feedback and command signals are simulated. In order to achieve the test objective, the simulator is capable of simulating a wide range of realistic scenarios defined by operational modes, operational tasks and single, common mode and multiple failure modes in order to verify correct functionality and performance during normal, abnormal and faulty conditions.

HIL testing may be conducted in several phases of a new-building or retrofit, where the first phase is usually an extensive software test conducted at factory or a lab facility. By using HIL simulator technology a virtual sea trial with thorough testing is conducted before the vessel is built. The objective is fully functional and failure testing of the software before the commissioning and integration starts, ensuring that the software will be more finalized and ready for commissioning. Follow-up system and integration testing is normally conducted during commissioning, and a final verification of the integrated functionality is conduced aboard the vessel at the end of commissioning.

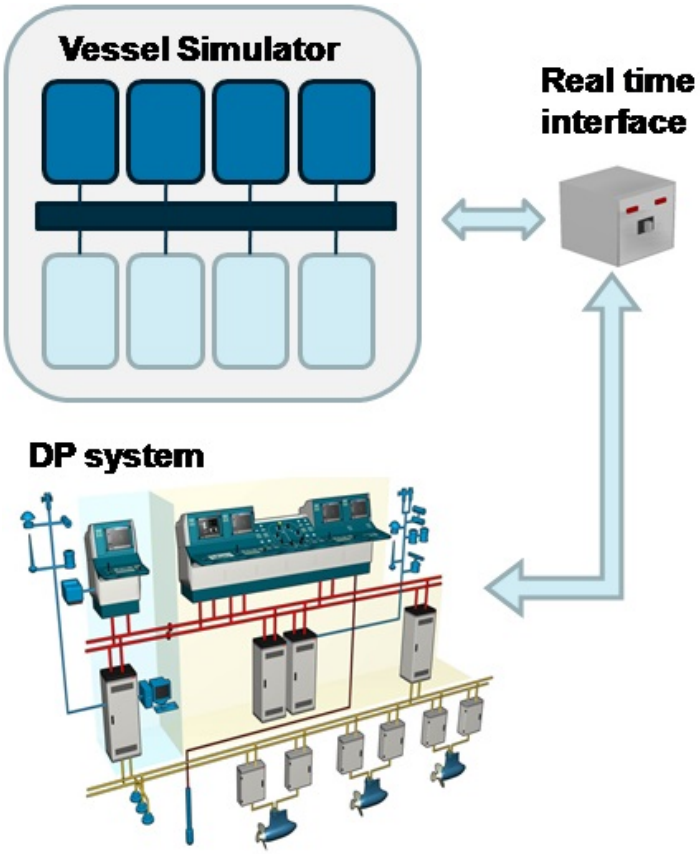

Figure 2.23: HIL Testing.

Chapter 3

Computer-Controlled Systems

This chapter introduces the reader to the basics in linear system theory and computer-controlled systems. Today most of the control systems are implemented in computers run by digital processors. Computers will operate on continuous-time processes at discrete-time sampling instants. Therefore, computer-controlled systems can be regarded as discrete control systems. Discrete systems could in many cases be viewed as approximations of analog systems. Computer-controlled systems may introduce deterioration of the control objective, if not accounting for the fact that they operate on discrete instants of processes which are time-continuous by nature.

Learning outcome of the chapter: The reader shall understand:

- The principles of computer-controlled systems and linear system theory.
- How to carry out discrete-time approximation of continuous-time differential systems using the simplest form for numerical methods based on backwards such as Euler, forward Euler, and Tustins methods.
- Stability issues that may occur in numerical approximation as well as Nyquist frequency and Shannons sampling theorem.
- The principles of shift-operator calculus and z-transform.

3.1 Introduction

Today most of the control systems are implemented in computers run by digital processors. For the applications studied here, computers will operate on *continuous-time* processes at *discrete-time* sampling instants. Therefore, computer-controlled systems can be regarded as discrete control systems. Discrete systems could in many cases be viewed as approximations of analog systems. However, it is important to be aware of that computer-controlled systems may also open up new possibilities that were not possible in analog systems. On the other hand computer-controlled systems may also introduce deteriorations of the control objective, if not accounting for the fact that they operate on discrete instants of processes which are time-continuous by nature. Some important aspects to consider in computer-controlled systems are:

- *Signal sampling and reconstruction of time-continuous signals.* In computer based control systems discrete-time approximations of continuous signals have to be done before they can

be processed by the computer. The discrete-time approximation is based on the division of the time axis into sufficient small time increments. The effect of the discrete-time approximations on the control system design will be discussed.

- *Signal detection and quality checking* and *handling of multiple signals* Each sensor signal has to be checked for errors subject to certain criteria before processed by the control system. If several sensors provide measurements of the same state variable, weighting and voting mechanism must be introduced. Signal detection and handling of multiple signals will be treated in Chapter 5.

This chapter will present the basic properties of linear system theory and computer-controlled systems. Most of the theory presented is general and valid for almost all kind of industrial control problems.

The fundamental theory presented in this chapter is a short extract from well recognized text books in this field. Fore more thoroughly presentation the reader is referred to Johansson (1993), Christiansen (1996), Oppenheim and Willsky (2013), Åstrøm and Wittenmark (1997), Dorf and Bishop (1998), Egeland and Gravdahl (2002), Chen (2004) and Chen (2014).

The class of systems studied in this text will have input and output terminals as shown in Figure 3.1.

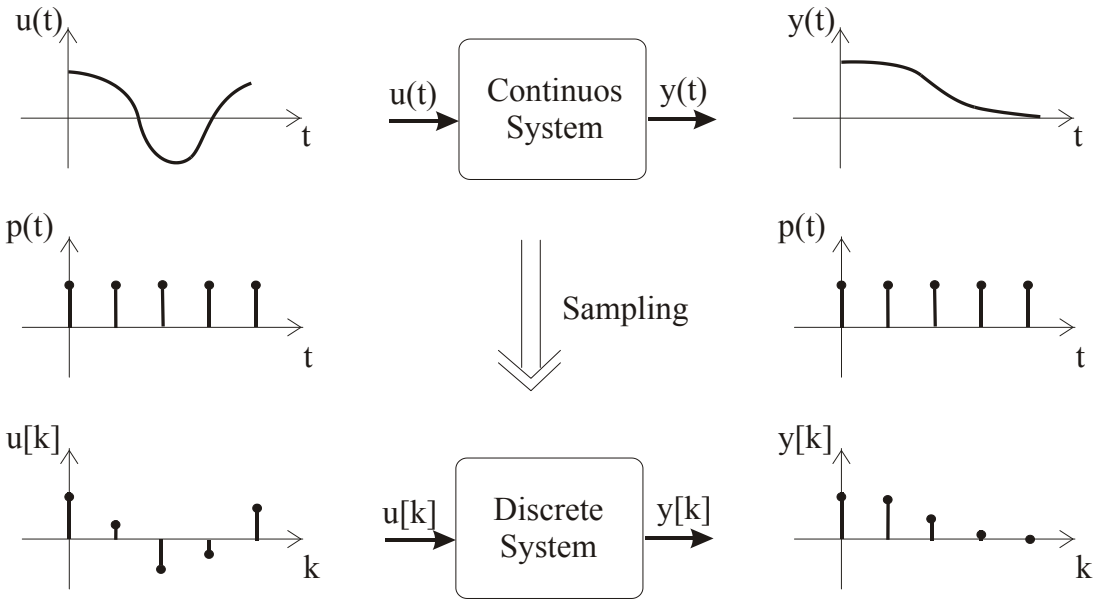

Figure 3.1: Continuous-time and discrete-time systems.

It is assumed that the relation between excitation/cause and response/effect can be formulated by either single-input single-output (SISO or monovariable) systems or by multi-input multi-output (MIMO or multivariable) systems. The input and output signals of monovariable systems are denoted by $u(t)$ and $y(t)$, while multivariable systems will be defined by the input and output vectors $\mathbf{u}(t)$ and $\mathbf{y}(t)$. A system is called a *continuous-time* system, if it accepts continuous-time signals as its input and generates continuous-time signals as its output. Similarly, a system is a *discrete-time* system, if the input and output relation is described by discrete inputs and outputs.

Today computer-controlled systems as shown in Figure 3.2 are widely used in many industrial control applications including marine control systems. Sensor measurements are often provided by digital signals in form of serial signals and are thereby discrete. Analog (continuous-time) measurements will be made discrete by a so-called analog-to-digital (AD) converter before processed by the computer. The calculated outputs of the controller will be made analog by a digital-to-analog (D/A) converter before acting the process plant. A computer-controlled system consists of:

- The real process denoted as process plant.
- Sampler with analog-to-digital (AD) converter is converting the analog output signal of the real process into finite digital numbers. The resolution is dependent on how many bits that are used. The sampling process is quantized by the clock.
- Digital-to-analog (DA) converter with hold circuit. In Figure 3.2 a DA converter with Zero-Order-Hold (ZOH) circuit is used to convert and translate the digital signal into a continuous-time signal that is applied to the real process.
- Computer with clock and software (SW) for real-time control applications and interrupt handling. The control algorithms are implemented in a SW program and work with input data that are quantized in time and in level.
- Communication network. One should notice that in a distributed automation system as shown in Chapter 2 there are several computers with clocks that need to be synchronized with hard constraints achieving a real-time control system.
- Operator station with graphical user interface to the operator.

The process of converting a sequence of numbers into a continuous-time signal is called *signal reconstruction*. Hence, the calculations in the computer will be on the discretized signals. The discrete systems treated here will be discretized version of physically continuous systems as shown in the Figure 3.2. Sampling means that a continuous-time signal is replaced by a sequence of numbers representing the signal at certain times. Let $Z = \{..., -2, -1, 0, 1, 2, ..\}$ define the positive and negative integers, and let $\{t_k : k \in Z\}$ be a subset of the real numbers called the sampling instants. Then, the sampled version of the signal $y(t)$ is the sequence

$$\{y(t_k) : k \in Z\}. \tag{3.1}$$

For the systems studied here negative integers of k will not be considered. Sampling is a linear operation and the sampling instants are often equally spaced in time such that

$$t_k = kT, \tag{3.2}$$

where T is the *sampling period* or *the sampling time*. The discrete-time model between the input sequence $\{u(t_k)\}$ and the output sequence $\{y(t_k)\}$ is called a *stroboscopic model* since it gives the relationship between the system variables at the sampling instant only.

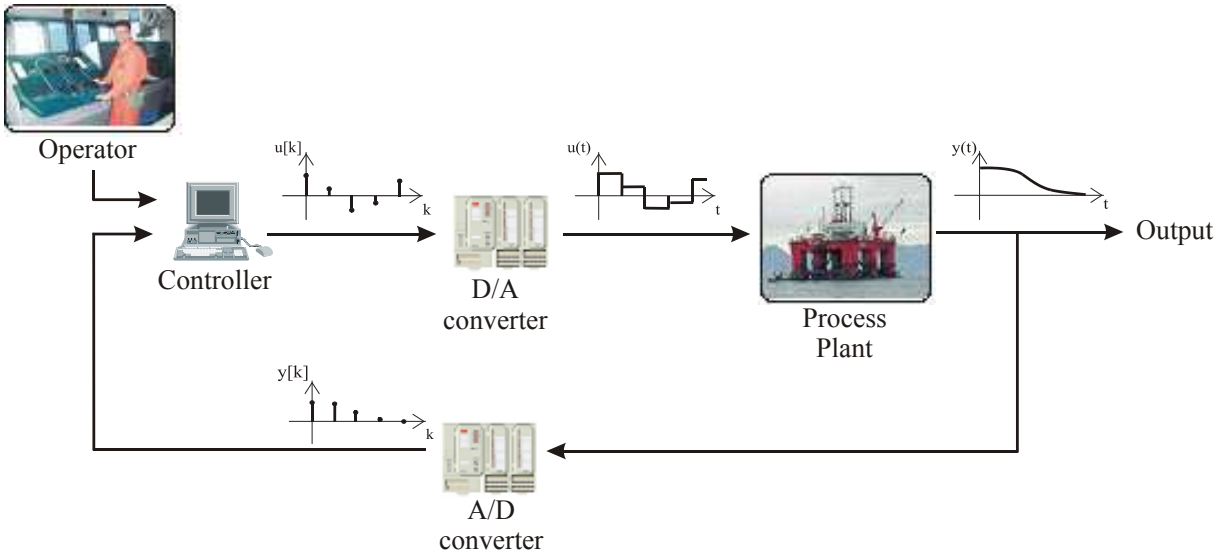

Figure 3.2: Computer-controlled system.

3.2 Basics in Linear System Theory

3.2.1 Causality and State Definition

We will in this text only consider systems that current output depends on past and current inputs, hence, not future inputs. Then the system is said to be *causal* or *nonanticipatory* system. A noncausal system can predict what will be applied in the future by the fact that current output will depend on future input. This capability is not possible for physical systems, which then are said to be causal.

By the definition of *state vector* denoted by $\mathbf{x}(t)$, a causal system's output can be properly defined for inputs going back to $-\infty$ to the current time t.

Definition 3.1 *Chen (2014). The state $\mathbf{x}(t_o)$ of a system at time t_o is the information at t_o that, together with the input $\mathbf{u}(t)$, for $t \geq t_o$, determines uniquely the output $\mathbf{y}(t)$ for all $t \geq t_o$.*

By definition, by knowing the state $\mathbf{x}(t)$ at t_o there is no need to know the input $\mathbf{u}(t)$ applied before t_o in determining the output $\mathbf{y}(t)$ after t_o. The state summarize the effect of the past input on the future output or represents the *memory* that the dynamic system has of its past. Furthermore, a dynamic system is said to be *lumped,* if the state vector has finite number of state variables. A dynamic system is called a *distributed* system, if its state vector has infinitely many state variables.

3.2.2 Continuous-time State Space Model

A general dynamic continuous-time nonlinear process plant may be described by the state space model consisting of a finite number n of coupled first-order differential equations according to

$$\dot{\mathbf{x}} = \mathbf{f}(t, \mathbf{x}, \mathbf{u}, \mathbf{w}), \tag{3.3}$$

$$\mathbf{y} = \mathbf{h}(t, \mathbf{x}, \mathbf{u}, \mathbf{v}), \tag{3.4}$$

where $\dot{\mathbf{x}}$ denotes the time derivatives of $\mathbf{x}$ with respect to the time variable t. The functions $\mathbf{f} \in \mathbb{R}^n$ and $\mathbf{h} \in \mathbb{R}^q$ are assumed to be smooth. The states variables are defined by the n-dimensional vector $\mathbf{x}$, $\mathbf{u}$ is the control input vector of dimension p, $\mathbf{w}$ is the r-dimensional process disturbances vector, $\mathbf{y}$ the output vector of dimension q comprises variables of particular interest in the analyses of the dynamic system, and $\mathbf{v}$ is the q-dimensional noise vector. Here, the output vector $\mathbf{y}$ is regarded as physically measured variables.

Eq. (3.3) and (3.4) may be further linearized about the vector (operation points) $\mathbf{x}_o$. Then, for linear time-variant (LTV) systems (3.3) and (3.4) takes the form

$$\dot{\mathbf{x}} = \mathbf{A}(t)\mathbf{x} + \mathbf{B}(t)\mathbf{u} + \mathbf{E}(t)\mathbf{w}, \tag{3.5}$$

$$\mathbf{y} = \mathbf{C}(t)\mathbf{x} + \mathbf{D}(t)\mathbf{u} + \mathbf{v}, \tag{3.6}$$

where $\mathbf{A} = \frac{\partial \mathbf{f}}{\partial \mathbf{x}}|_{\mathbf{x}_o}$ is the $n \times n$ dimensional system matrix, $\mathbf{B} = \frac{\partial \mathbf{f}}{\partial \mathbf{u}}|_{\mathbf{x}_o}$ is the $n \times p$ dimensional input matrix, $\mathbf{E} = \frac{\partial \mathbf{f}}{\partial \mathbf{w}}|_{\mathbf{x}_o}$ is the $n \times r$ dimensional disturbance matrix, $\mathbf{C} = \frac{\partial \mathbf{h}}{\partial \mathbf{x}}|_{\mathbf{x}_o}$ is the $q \times n$ dimensional measurement matrix, and $\mathbf{D} = \frac{\partial \mathbf{h}}{\partial \mathbf{u}}|_{\mathbf{x}_o}$ is an $q \times r$ dimensional matrix. If these matrices have constant coefficients, the system described in (3.5) and (3.6) is defined to be linear time-invariant (LTI) and will be written

$$\dot{\mathbf{x}} = \mathbf{A}\mathbf{x} + \mathbf{B}\mathbf{u} + \mathbf{E}\mathbf{w}, \tag{3.7}$$

$$\mathbf{y} = \mathbf{C}\mathbf{x} + \mathbf{D}\mathbf{u} + \mathbf{v}. \tag{3.8}$$

Consider the simplified LTI system where process disturbance and sensor noise are disregarded

$$\dot{\mathbf{x}} = \mathbf{A}\mathbf{x} + \mathbf{B}\mathbf{u}, \tag{3.9}$$

$$\mathbf{y} = \mathbf{C}\mathbf{x} + \mathbf{D}\mathbf{u}. \tag{3.10}$$

From linear control theory it is well known that the solution of (3.9) is

$$\mathbf{x}(t) = e^{\mathbf{A}(t-t_0)}\mathbf{x}(t_0) + \int_{t_0}^{t} e^{\mathbf{A}(t-\tau)}\mathbf{B}\mathbf{u}(\tau)d\tau. \tag{3.11}$$

Let us define the transition matrix to be $\mathbf{\Phi}(t)=e^{\mathbf{A}t}$. Furthermore, the transition matrix can be represented by a Taylor series according to

$$\mathbf{\Phi}(t)=e^{\mathbf{A}t} = \mathbf{I} + \mathbf{A}t + \frac{1}{2!}\mathbf{A}^2t^2 + ... + \frac{1}{i!}\mathbf{A}^it^i + ... \tag{3.12}$$

This representation will be used later in the text when making an approximated time-discrete formulation of (3.7) and (3.8).

Definition 3.2 *Chen (2014). The state equations (3.9) and (3.10) are said to be* observable *if for any unknown initial state* $\mathbf{x}(0)$*, there exists a finite time* $t_1 > 0$ *such that the knowledge of the input* $\mathbf{u}$ *and the output* $\mathbf{y}$ *over* $[0, t_1]$ *suffices to determine uniquely the initial state* $\mathbf{x}(0)$*. Otherwise (3.9) and (3.10) are said to be unobservable.*

Theorem 3.1 *Chen (2014). The n-dimensional pair* $(\mathbf{A}, \mathbf{C})$ *is* observable *if the* $nq \times n$ *observability matrix* $\mathbf{Q}_o$ *has full column rank n, where*

$$\mathbf{Q}_o= [\mathbf{C}^T, \mathbf{A}^T\mathbf{C}^T, \quad .. \quad , (\mathbf{A}^T)^{n-1}\mathbf{C}^T]^T. \tag{3.13}$$

Definition 3.3 *Chen (2014). The state equation (3.9) or the pair* $(\mathbf{A}, \mathbf{B})$ *is said to be* controllable *if for any initial state* $\mathbf{x}(0) = \mathbf{x}_0$ *and any final state* $\mathbf{x_1}$*, there exists an input that transfers* $\mathbf{x}_0$ *to* $\mathbf{x_1}$ *in a finite time. Otherwise (3.9) or the pair* $(\mathbf{A}, \mathbf{B})$ *is said to be uncontrollable.*

Theorem 3.2 *Chen (2014). The n-dimensional pair* $(\mathbf{A}, \mathbf{B})$ *is controllable if the* $n \times np$ *controllability matrix* $\mathbf{Q}_c$ *has full row rank n, where*

$$\mathbf{Q}_c = [\mathbf{B},\ \mathbf{AB},\quad ..\quad ,(\mathbf{A})^{n-1}\mathbf{B}]. \tag{3.14}$$

Remark 3.1 *In Matlab the controllability and observability matrices can be generated by calling* `ctrb` *and* `obsv` *respectively.*

Remark 3.2 *A sufficient and necessary condition for that the* $n \times n$ *matrix* $\mathbf{Q}$ *has full rank is that* $\mathbf{Q}^{-1}$ *exists.*

Remark 3.3 *When the vector* $\mathbf{x}$ *consists of n real numbers, it is said to be n-dimensional. Mathematically we can also write* $\mathbf{x} \in \mathbb{R}^n$*. When the matrix* $\mathbf{A}$ *consists of n rows and n columns of elements of real numbers, it is said to be* $n \times n$ *dimensional, or simply* $n \times n$*. Mathematically we can write* $\mathbf{A} \in \mathbb{R}^{n \times n}$*. In this text both notations will be used.*

Example 3.1 *Consider the state equations*

$$\begin{aligned} \dot{\mathbf{x}} &= \begin{bmatrix} 2 & 1 & 0 \\ 2 & 0 & 1 \\ 0 & 2 & -1 \end{bmatrix} \mathbf{x} + \begin{bmatrix} 0 & 1 \\ 1 & 0 \\ 0 & 0 \end{bmatrix} \mathbf{u}, \\ y &= \begin{bmatrix} 1 & 0 & 1 \end{bmatrix} \mathbf{x}. \end{aligned}$$

Controllability and observability can be evaluated by the following Matlab script:

```
A=[2  1  0;  2  0  1;  0  2  -1];  B=[0  1;  1  0;  0  0];
C=[1  0  1];
CO=CTRB(A,B);  OB=OBSV(A,C);
rank(CO);   rank(OB);
```

The state equations are both observable and controllable as Matlab returns:

$$\begin{aligned} CO &= \begin{bmatrix} 0 & 1 & 1 & 2 & 2 & 6 \\ 1 & 0 & 0 & 2 & 4 & 4 \\ 0 & 0 & 2 & 0 & -2 & 4 \end{bmatrix}, OB = \begin{bmatrix} 1 & 0 & 1 \\ 2 & 3 & -1 \\ 10 & 0 & 4 \end{bmatrix}, \\ rank(CO) &= 3, rank(OB) = 3. \end{aligned}$$

3.2.3 Basic Functions

We will here define some of the most used basic functions applied in control system design and analyses.

Step function

Consider the sequence of functions $\{z_n(t)\}$,where

$$z_n(t) = \begin{cases} 0, & t < -\frac{1}{2n} \\ nt + 1/2, & -\frac{1}{2n} \leq t \leq \frac{1}{2n} \\ 1, & \frac{1}{2n} < t \end{cases}, \tag{3.15}$$

where n is an integer. As seen in Figure 3.3 for $n \to \infty$ the sequence $\{z_n(t)\}$ converges to the *step function*, also called *Heaviside function*, by

$$f(t) = \begin{cases} 0 & t < 0 \\ 1/2 & t = 0 \\ 1 & t > 0 \end{cases}. \tag{3.16}$$

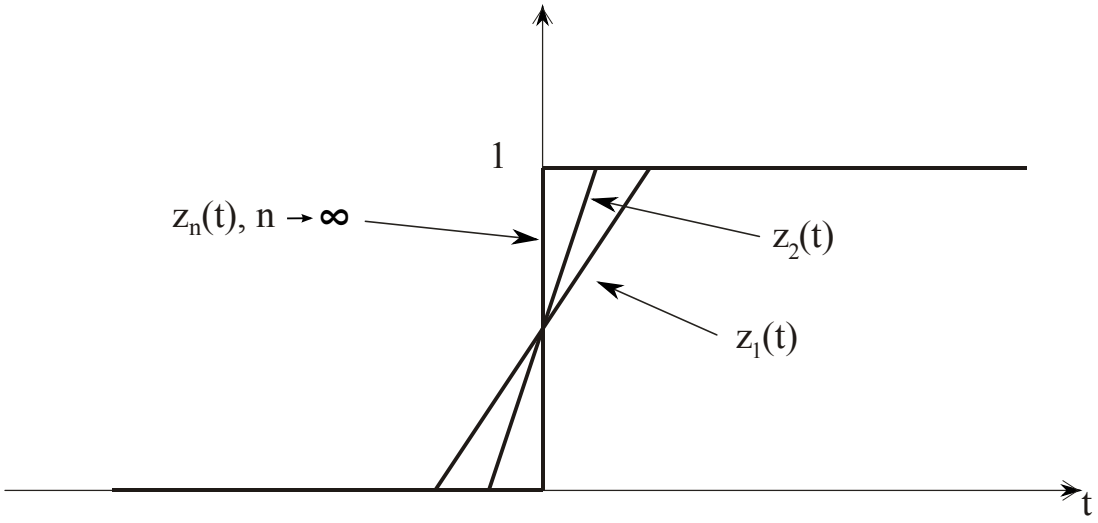

Figure 3.3: Step function.

Impulse function

The impulse function can be thought as the derivative of the step function such that

$$s_n = \frac{dz_n(t)}{dt} \underset{n\to\infty}{\to} \delta(t). \tag{3.17}$$

The unit impulse $\delta(t)$, see Figure 3.4, also known as the *Dirac function* or *delta function* is defined to have zero duration and infinite amplitude. The Dirac function is assumed to have the property

$$\int_{t=0^-}^{t=0^+} \delta(t)dt = 1. \tag{3.18}$$

The Dirac impulse function is a mathematical abstraction which cannot be realized in practice since no physical signal can have infinite amplitude with zero duration.

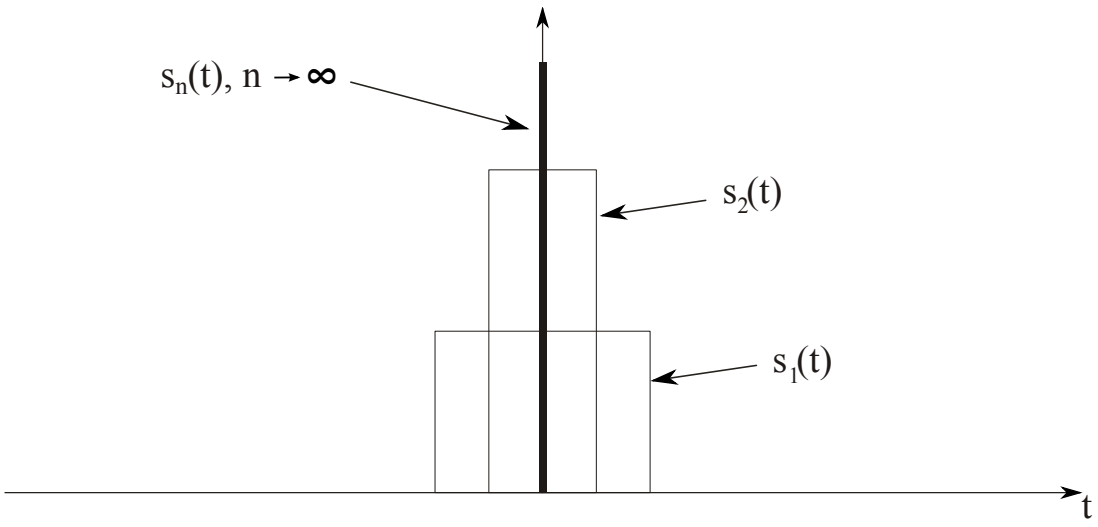

Figure 3.4: Impulse function.

Ramp and parabolic functions

The unity ramp function, see Figure 3.5, can be regarded as the integral of the step function

$$r(t) = \begin{cases} \int_{-\infty}^{t} f(t)dt = t, & t > 0 \\ 0, & t \leq 0 \end{cases}. \tag{3.19}$$

The unity parabolic function, see Figure 3.5, can be regarded as the integral of the ramp function according to

$$p(t) = \begin{cases} \int_{-\infty}^{t} r(t)dt = t^2, & t > 0 \\ 0, & t \leq 0 \end{cases}. \tag{3.20}$$

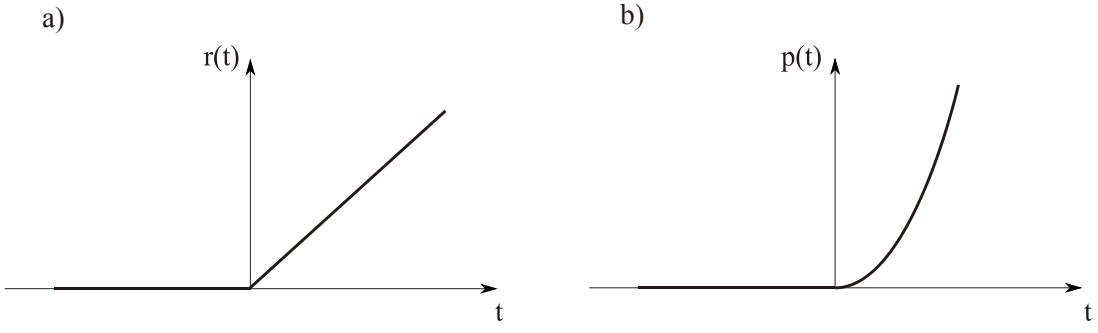

Figure 3.5: (a) Ramp function and (b) parabolic function.

3.2.4 Laplace Transform

The two-sided Laplace transformation $F(s)$ of a continuous signal $f(t)$ defined for all time t is defined as

$$F(s) = \mathcal{L}\{f(t)\} = \int_{-\infty}^{\infty} f(t)e^{-ts}dt, \tag{3.21}$$

where the argument $s = \sigma + j\omega$ is the complex frequency. The inverse Laplace transform is defined to be

$$f(t) = \mathcal{L}^{-1}\{F(s)\} = \frac{1}{2\pi j}\int_{\sigma-j\infty}^{\sigma+j\infty} F(s)e^{ts}ds. \tag{3.22}$$

For the case $f(t)$ only takes values for $t > 0$, it is customary to restrict the Laplace transform to the be one-sided according to

$$\mathcal{L}\{f(t)\} = F(s) = \int_0^\infty f(t)e^{-ts}dt. \tag{3.23}$$

The one-sided Laplace transform will be identical to the two-sided only when $f(t) = 0$ for $t \leq 0$. In control problems we normally deal with one-sided Laplace transforms.

Tables of the most used Laplace transforms are found in Dorf and Bishop (1998) or in mathematical text books covering Laplace transforms.

3.2.5 Fourier Transform

A *spectrum* is defined as the Fourier transform of a signal $f(t)$ and is given

$$F(j\omega) = \mathcal{F}\{f(t)\} = \int_{-\infty}^\infty f(t)e^{-j\omega t}dt. \tag{3.24}$$

The inverse Fourier transform is defined

$$f(t) = \mathcal{F}^{-1}\{F(j\omega)\} = \frac{1}{2\pi}\int_{-\infty}^\infty F(j\omega)e^{j\omega t}d\omega. \tag{3.25}$$

Remark 3.4 *Assume that the Fourier and Laplace transform exists, that is, take finite values (remain bounded), then the Fourier transform and the Laplace transform coincide for the choice $s = j\omega$, where ω can be regarded as the angular frequency [rad/s]. The major difference between the Laplace and Fourier transforms is that the Laplace transform is valuable for analysis of transient behavior, whereas the Fourier transform is mainly applicable to periodic signals.*

Remark 3.5 *Alternatively $s \triangleq \frac{d}{dt}, s^2 \triangleq \frac{d^2}{dt^2}, s^3 \triangleq \frac{d^3}{dt^3}, ...,$ could also be considered to be the time differential operator which is convenient to apply in manipulation of linear differential equations with constant coefficients. Notice that an operator should not be confused with the complex variable in the Laplace transformation theory.*

3.3 Sampler and Zero-Order Hold

A continuous-time signal may be discretized by a sampler. A sampler is basically a switch that closes every T second for one instant of time. Let $r(t)$ be a continuous signal, where $r(t) = 0$ for $t < 0$. Let the input to the sampler be $r(t)$, then the output of the sampler is denoted $r^*(t)$. We define kT to be the current sample time, where the current value of $r^*(t)$ is $r(kT)$. By introducing a periodic impulse train $p_T(t)$ and multiply it with the continuous signal, the series of impulses can be represented by

$$r^*(t) = r(t)p_T(t), \tag{3.26}$$

where $p_T(t)$ is often referred to as the *sampling function* and is defined to be

$$p_T(t) = \sum_{k=0}^{\infty} \delta(t - kT),\ t > 0. \tag{3.27}$$

$\delta(t-kT)$ is the Dirac impulse function at $t-kT$. This mechanism is also known as *impulse-train sampling.*

Remark 3.6 *Notice that multiplying $r(t)$ by a unit impulse samples the value of the signal at the point at which the impulse is located. Hence, $r(t)\delta(t-kT) = r(kT)\delta(t-kT)$.*

Remark 3.7 *T is denoted as the* sampling period *and $\omega_s = \frac{2\pi}{T}$ is the fundamental frequency of $p_T(t)$, denoted as the* sampling frequency *in rad/s. $f_s = \frac{1}{T}$ is the sampling frequency in Hz.*

We can now rewrite (3.26) such that

$$r^*(t) = r(kT) \sum_{k=0}^{\infty} \delta(t - kT). \tag{3.28}$$

In control application it is required that the sampled signal will be kept constant over the sampling interval. This may be done by a *ZOH* circuit in the digital-to-analog (D/A) converter. The D/A converter is often installed on separate Input/Output (I/O) boards. Thus a sampler together with a ZOH is introduced, see Figure 3.6. This will convert the sampled signal $r^*(t)$ to a continuous signal $p(t)$.The transfer function of the ZOH circuit is given by

$$G_o(s) = \frac{1}{s} - \frac{1}{s}e^{-Ts} = \frac{(1 - e^{-sT})}{s}, \tag{3.29}$$

where s is the complex variable known from Laplace transformation theory. The ZOH circuit holds the value of $r(kT)$ constant for $kT \leq t < (k+1)T$. In Figure 3.6 (b) this is shown for the case the impulse input $r(kT) = 1$ for $k = 0$ and $r(kT) = 0$ for $k \neq 0$, so that $r^*(t) = r(0)\delta(t)$.

3.4 Discrete-time State Space Model

3.4.1 ZOH Equivalent of Continuous-time State Space Model

Let us define the sampling instants, $t_k = kT$, as the times when the control input $\mathbf{u} \in \mathbb{R}^p$ changes. The zero-order-hold will result in a discontinuous control signal. We will adopt the convention that the control signal is kept constant in the time interval $t_k \leq t \leq t_{k+1}$ and continuous from the right. The state $\mathbf{x} \in \mathbb{R}^n$ at time t of (3.9) is thus given by Åstrøm and Wittenmark (1997))

$$\begin{aligned}
\mathbf{x}(t) &= e^{\mathbf{A}(t-t_k)}\mathbf{x}(t_k) + \int_{t_k}^{t} e^{\mathbf{A}(t-s')}\mathbf{B}\mathbf{u}(s')ds', \\
&= e^{\mathbf{A}(t-t_k)}\mathbf{x}(t_k) + \int_{t_k}^{t} e^{\mathbf{A}(t-s')}ds'\mathbf{B}\mathbf{u}(t_k), \\
&= e^{\mathbf{A}(t-t_k)}\mathbf{x}(t_k) + \int_{0}^{t-t_k} e^{\mathbf{A}s}ds\mathbf{B}\mathbf{u}(t_k),\ s = t - s' \\
&= \mathbf{\Phi}(t, t_k)\mathbf{x}(t_k) + \mathbf{\Delta}(t, t_k)\mathbf{u}(t_k).
\end{aligned} \tag{3.30}$$

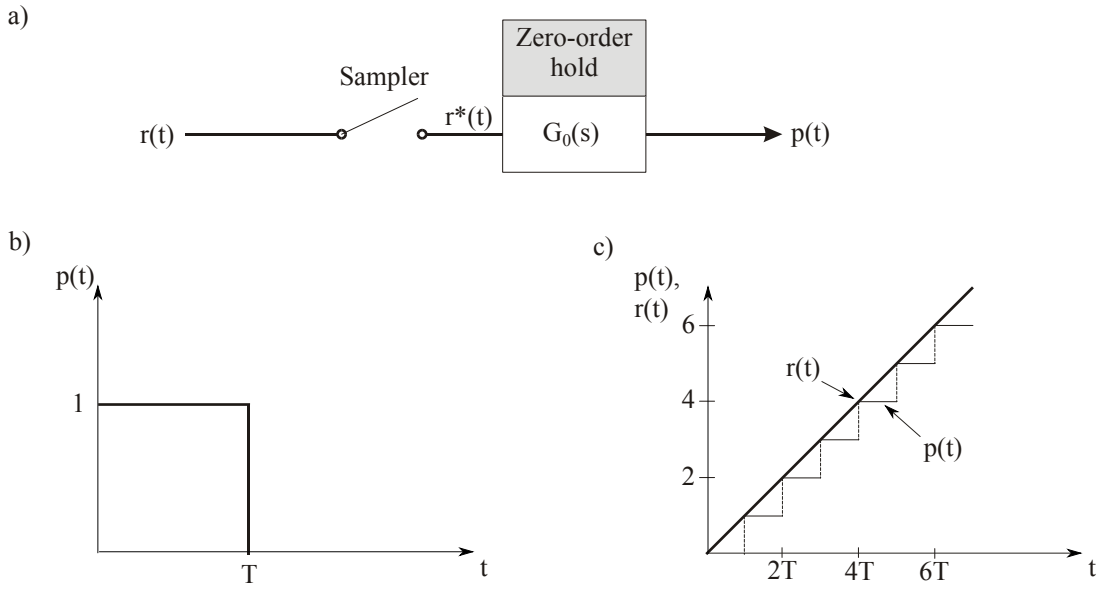

Figure 3.6: Sampler and ZOH circuit, (b) response of a ZOH to an impulse input $r(kT)$, which equals 1 when $k = 0$ and equals 0 when $k \neq 0$, so that $r^*(t) = r(0)\delta(t)$, and (c) response of a sampler and ZOH for a ramp input $r(t) = t$.

The state vector $\mathbf{x}(t)$ at time t is thus a linear function of $\mathbf{x}(t_k)$ and $\mathbf{u}(t_k)$. If the AD and DA converters are perfectly synchronized and if the conversion times are negligible, the input $\mathbf{u}(t_k)$ and output $\mathbf{y}(t_k) \in \mathbb{R}^q$ can be regarded as being at the same instants such that the system equation of the sampled system at the sampling instants is given by the *linear difference equation*

$$\begin{aligned} \mathbf{x}(t_{k+1}) &= \mathbf{\Phi}(t_{k+1}, t_k)\mathbf{x}(t_k) + \mathbf{\Delta}(t_{k+1}, t_k)\mathbf{u}(t_k), && (3.31) \\ \mathbf{y}(t_k) &= \mathbf{C}\mathbf{x}(t_k) + \mathbf{D}\mathbf{u}(t_k), && (3.32) \end{aligned}$$

where

$$\begin{aligned} \mathbf{\Phi}(t_{k+1}, t_k) &= e^{\mathbf{A}(t_{k+1}-t_k)}, && (3.33) \\ \mathbf{\Delta}(t_{k+1}, t_k) &= \int_0^{t_{k+1}-t_k} e^{\mathbf{A}s} ds \mathbf{B}, && (3.34) \end{aligned}$$

and $\mathbf{\Phi} \in \mathbb{R}^{n\times n}$, $\mathbf{\Delta} \in \mathbb{R}^{n\times p}, \mathbf{C} \in \mathbb{R}^{q\times n}$ and $\mathbf{D} \in \mathbb{R}^{q\times p}$. The zero-order-hold solution (3.31) and (3.32) gives the exact values of the state variables because the control input is constant between the sampling instants. The intersample behavior of the system, that is the state vector between the sampling instants, can be investigated by using (3.30). For periodic sampling interval, $t_k = kT$ where $k = 0, 1, 2, 3, ...$, the model described by (3.31) and (3.32) simplifies to a linear time-invariant system according to

$$\begin{aligned} \mathbf{x}[(k+1)T] &= \mathbf{\Phi}\mathbf{x}[kT] + \mathbf{\Delta}\mathbf{u}[kT], && (3.35) \\ \mathbf{y}[kT] &= \mathbf{C}\mathbf{x}[kT] + \mathbf{D}\mathbf{u}[kT], && (3.36) \end{aligned}$$

where

$$\mathbf{\Phi} = e^{\mathbf{A}T}, \tag{3.37}$$

$$\mathbf{\Delta} = \int_0^T e^{\mathbf{A}s} ds \mathbf{B}. \tag{3.38}$$

3.4.2 Discrete-time Approximation

A discrete-time approximation based on *Euler's method* for integration of the state space equations may be found by approximating the derivative with a difference

$$\dot{\mathbf{x}} = \frac{\mathbf{x}(t_k + T) - \mathbf{x}(t_k)}{T}. \tag{3.39}$$

As above, let k be an integer index so that $k = 0, 1, 2, 3, ...$ If we assume small sampling periods, a discrete-time approximation of (3.7) may be written

$$\mathbf{x}(t + T) \approx (T\mathbf{A} + \mathbf{I})\mathbf{x}(t) + T\mathbf{B}\mathbf{u}(t) + T\mathbf{E}\mathbf{w}(t). \tag{3.40}$$

Introducing discrete notation (3.40) is written as

$$\mathbf{x}[(k + 1)T] \approx (\mathbf{I} + T\mathbf{A})\mathbf{x}[kT] + T\mathbf{B}\mathbf{u}[kT] + T\mathbf{E}\mathbf{w}[kT]. \tag{3.41}$$

We can now recognize that $(\mathbf{I}+T\mathbf{A})$ is the same as the first two terms of (3.12). If we assume small T, the transition matrix can be approximated by $\mathbf{\Phi}(T) \approx (\mathbf{I}+T\mathbf{A})$. Similarly, the control input and disturbance matrices become $\mathbf{\Delta} = T\mathbf{B}$ and $\mathbf{\Gamma} = T\mathbf{E}$. By omitting T in the arguments such that $\mathbf{x}(t) = \mathbf{x}(kT) \triangleq \mathbf{x}[k]$, (3.41) can be rewritten

$$\mathbf{x}[k + 1] = \mathbf{\Phi}\mathbf{x}[k] + \mathbf{\Delta}\mathbf{u}[k] + \mathbf{\Gamma}\mathbf{w}[k], \tag{3.42}$$

and the corresponding discrete-time formulation of (3.8) becomes

$$\mathbf{y}[k] = \mathbf{C}\mathbf{x}[k] + \mathbf{D}\mathbf{u}[k] + \mathbf{v}[k]. \tag{3.43}$$

Remark 3.8 *The control input matrix is often written*

$$\mathbf{\Delta} = \mathbf{A}^{-1}(e^{\mathbf{A}T} - \mathbf{I})\mathbf{B}. \tag{3.44}$$

Remark 3.9 *In several textbooks and Matlab, the discrete-time state space formulation is written using the same matrix symbols as for time-continuous systems. This means that for LTI systems (3.42) and (3.43) are reformulated according to*

$$\mathbf{x}[k + 1] = \mathbf{A}\mathbf{x}[k] + \mathbf{B}\mathbf{u}[k] + \mathbf{E}\mathbf{w}[k], \tag{3.45}$$

$$\mathbf{y}[k] = \mathbf{C}\mathbf{x}[k] + \mathbf{D}\mathbf{u}[k] + \mathbf{v}[k]. \tag{3.46}$$

The corresponding discrete-time version for a LTV system is given by

$$\mathbf{x}[k + 1] = \mathbf{A}[k]\mathbf{x}[k] + \mathbf{B}[k]\mathbf{u}[k] + \mathbf{E}[k]\mathbf{w}[k], \tag{3.47}$$

$$\mathbf{y}[k] = \mathbf{C}[k]\mathbf{x}[k] + \mathbf{D}[k]\mathbf{u}[k] + \mathbf{v}[k]. \tag{3.48}$$

3.4.3 Solution of Discrete-time System Equation

Consider the following difference equation

$$\begin{aligned} \mathbf{x}[k+1] &= \mathbf{\Phi}\mathbf{x}[k] + \mathbf{\Delta}\mathbf{u}[k], && (3.49)\\ \mathbf{y}[k] &= \mathbf{C}\mathbf{x}[k]. && (3.50) \end{aligned}$$

A solution of (3.49) can be found by assuming that the initial condition $\mathbf{x}[k_0]$ and the input sequence $\mathbf{u}[k], \mathbf{u}[k_0+1], ..$ are known. Thus by iteration we have

$$\begin{aligned} \mathbf{x}[k_0+1] &= \mathbf{\Phi}\mathbf{x}[k_0] + \mathbf{\Delta}\mathbf{u}[k_0],\\ \mathbf{x}[k_0+2] &= \mathbf{\Phi}\mathbf{x}[k_0+1] + \mathbf{\Delta}\mathbf{u}[k_0+1],\\ &= \mathbf{\Phi}^2\mathbf{x}[k_0] + \mathbf{\Phi}\mathbf{\Delta}\mathbf{u}[k_0] + \mathbf{\Delta}\mathbf{u}[k_0+1],\\ \mathbf{x}[k_0+3] &= \mathbf{\Phi}\mathbf{x}[k_0+2] + \mathbf{\Delta}\mathbf{u}[k_0+2],\\ &= \mathbf{\Phi}\left(\mathbf{\Phi}^2\mathbf{x}[k_0] + \mathbf{\Phi}\mathbf{\Delta}\mathbf{u}[k_0] + \mathbf{\Delta}\mathbf{u}[k_0+1]\right) + \mathbf{\Delta}\mathbf{u}[k_0+2],\\ &= \mathbf{\Phi}^3\mathbf{x}[k_0] + \mathbf{\Phi}^2\mathbf{\Delta}\mathbf{u}[k_0] + \mathbf{\Phi}\mathbf{\Delta}\mathbf{u}[k_0+1] + \mathbf{\Delta}\mathbf{u}[k_0+2],\\ &\ \ \vdots\\ &\ \ \vdots\\ \mathbf{x}[k_0+k'] &= \mathbf{\Phi}^{k'}\mathbf{x}[k_0] + \sum_{i=0}^{k'-1} \mathbf{\Phi}^{k'-i-1}\mathbf{\Delta}\mathbf{u}[i+k_0]. && (3.51) \end{aligned}$$

Let us define $k = k_0 + k'$ and $j = i + k_0$, then (3.51) can be reformulated

$$\begin{aligned} \mathbf{x}[k] &= \mathbf{\Phi}^{k-k_0}\mathbf{x}[k_0] + \sum_{i=0}^{k-k_0-1} \mathbf{\Phi}^{k-(i+k_0)-1}\mathbf{\Delta}\mathbf{u}[i+k_0],\\ \mathbf{x}[k] &= \mathbf{\Phi}^{k-k_0}\mathbf{x}[k_0] + \sum_{j=k_0}^{k-1} \mathbf{\Phi}^{k-j-1}\mathbf{\Delta}\mathbf{u}[j]. && (3.52) \end{aligned}$$

We can observe that the first part depends on the initial condition, while the second part is a weighted sum of the input signals. It is also seen that the eigenvalues of $\mathbf{\Phi}$ obtained from the *characteristic equation*

$$\det(\lambda\mathbf{I} - \mathbf{\Phi}) = 0. \quad (3.53)$$

will determine the properties of the solution (3.52).

Theorem 3.3 *Asymptotic stability of linear systems (Åstrøm and Wittenmark (1997)). A discrete-time linear time-invariant system on the form* $\mathbf{x}[k+1] = \mathbf{\Phi}\mathbf{x}[k]$ *is asymptotically stable if and only if all eigenvalues of* $\mathbf{\Phi}$ *are strictly inside the unit disk, that is* $|\lambda_i| < 1$ *for* $i = 1, 2, ..., n$.

Remark 3.10 *In general for discrete-time systems the stability is defined for a particular solution and not for the system, and is thus a local concept. However, for linear time invariant discrete-time systems, stability is also a property of the system.*

3.4.4 Controllability and Observability of Discrete-time Systems

Let us define $k_0 = 0$ and $k = n$ in (3.52) such that

$$\begin{aligned}\mathbf{x}[n] &= \mathbf{\Phi}^n\mathbf{x}[0]+\sum_{j=0}^{n-1}\mathbf{\Phi}^{n-j-1}\mathbf{\Delta}\mathbf{u}[j],\\ &= \mathbf{\Phi}^n\mathbf{x}[0]+\mathbf{\Phi}^{n-1}\mathbf{\Delta}\mathbf{u}[0]+\mathbf{\Phi}^{n-2}\mathbf{\Delta}\mathbf{u}[1]+\mathbf{\Phi}^{n-3}\mathbf{\Delta}\mathbf{u}[2]+...+\mathbf{\Delta}\mathbf{u}[n-1],\\ &= \mathbf{\Phi}^n\mathbf{x}[0]+\mathbf{Q}_{dc}\mathbf{U}, \qquad (3.54)\end{aligned}$$

where

$$\mathbf{Q}_{dc} = [\mathbf{\Delta},\, \mathbf{\Phi\Delta},\quad ..\quad ,(\mathbf{\Phi})^{n-1}\mathbf{\Delta}], \qquad (3.55)$$

$$\mathbf{U} = [\mathbf{u}^T[n-1],\quad ..\quad ,\mathbf{u}^T[0]]^T. \qquad (3.56)$$

If $\mathbf{Q}_{dc}$ has full row rank n, it is possible to find n equations from which the control signal can be found such that the initial state is transferred to the desired final state $x[n]$.

Definition 3.4 *Chen (2014). The discrete LTI equations (3.49) and (3.50) with $n \times n$ state $\mathbf{\Phi}$ and $n \times p$ control $\mathbf{\Delta}$ matrices described by the pair $(\mathbf{\Phi}, \mathbf{\Delta})$ are defined to be be controllable if for any initial state $\mathbf{x}[0] = x_0$ and any final state $\mathbf{x}[n] = x_n$, there exists an input sequence of finite length that transfers $\mathbf{x}[0]$ to $\mathbf{x}[n]$. Otherwise the discrete LTI equations (3.49) and (3.50) or the pair $(\mathbf{\Phi}, \mathbf{\Delta})$ are said to be uncontrollable.*

Theorem 3.4 *Chen (2014). The n-dimensional pair $(\mathbf{\Phi}, \mathbf{\Delta})$ is controllable if the $n \times np$ controllability matrix $\mathbf{Q}_{dc}$ has full row rank n, where*

$$\mathbf{Q}_{dc} = [\mathbf{\Delta},\, \mathbf{\Phi\Delta},\quad ..\quad ,(\mathbf{\Phi})^{n-1}\mathbf{\Delta}]. \qquad (3.57)$$

Chen (2014) defines three different controllability definitions:

1. Transfer any state to any other state in finite time, as adopted here.
2. Transfer any state to the zero state in finite time, called *controllability to the origin.*
3. Transfer the zero state to any state in finite time, called *controllability from the origin* or, more often, *reachability.*

Remark 3.11 *In the literature, there are different definitions of controllability and reachability. In Åstrøm and Wittenmark (1997) definition 1 is called* reachability*, while definition 2 is called* controllability.

Remark 3.12 *Controllability definitions 1 and 2 are equivalent if $\mathbf{\Phi}$ is invertible. Definition 2 does not imply definition 1. If $\mathbf{\Phi}^n\mathbf{x}[0] = \mathbf{0}$, then the origin of (3.54)will be reached with zero input, but the system is not necessarily controllable.*

Consider (3.49) and (3.50), and for simplicity assume that the control input is equal to zero, $\mathbf{u}[k] = \mathbf{0}$ for all k. This gives the following set of equations

$$\begin{aligned}\mathbf{y}[0] &= \mathbf{C}\mathbf{x}[0],\\ \mathbf{y}[1] &= \mathbf{C}\mathbf{x}[1] = \mathbf{C}\mathbf{\Phi}\mathbf{x}[0],\\ &\vdots\\ \mathbf{y}[n-1] &= \mathbf{C}\mathbf{\Phi}^{n-1}\mathbf{x}[0], \qquad (3.58)\end{aligned}$$

or on vector form

$$\begin{aligned}\left[\mathbf{C}^T,(\mathbf{C}\mathbf{\Phi})^T,...,(\mathbf{C}\mathbf{\Phi}^{n-1})^T\right]^T\mathbf{x}[0] &= \left[\mathbf{y}^T[0],\mathbf{y}^T[1],..,\mathbf{y}^T[n-1]\right]^T,\\ \mathbf{Q}_{do}\mathbf{x}[0] &= \left[\mathbf{y}^T[0],\mathbf{y}^T[1],..,\mathbf{y}^T[n-1]\right]^T. \end{aligned} \tag{3.59}$$

Definition 3.5 *Chen (2014). The discrete LTI equations (3.49) and (3.50) with $n \times n$ state matrix $\mathbf{\Phi}$ and $q \times n$ output matrix $\mathbf{C}$ described by the pair $(\mathbf{\Phi}, \mathbf{C})$ are defined to be be observable if for any unknown initial state $\mathbf{x}[0]$, there exists a finite integer $k_1 > 0$ such that the knowledge of the input sequence $\mathbf{u}[k]$ and output sequence $\mathbf{y}[k]$ from $k = 0$ to k_1 suffices to determine uniquely the initial state $\mathbf{x}[0]$. Otherwise the discrete LTI equations (3.49) and (3.50) or the pair $(\mathbf{\Phi}, \mathbf{C})$ are said to be unobservable.*

Theorem 3.5 *Chen (2014). The n-dimensional pair $(\mathbf{\Phi}, \mathbf{C})$ is observable if the $nq \times n$ observability matrix $\mathbf{Q}_{do}$ has full column rank n, where*

$$\mathbf{Q}_{do} = [\mathbf{C}^T, \mathbf{\Phi}^T\mathbf{C}^T, \quad .. \quad , (\mathbf{\Phi}^T)^{n-1}\mathbf{C}^T]^T. \tag{3.60}$$

Definition 3.6 *Åstrøm and Wittenmark (1997)). The discrete LTI equations (3.49) and (3.50) is detectable if the only unobservable states are such that they decay to the origin. That is, the corresponding eigenvalues are stable.*

3.5 Discrete-time Approximation Methods

A solution of (3.49) was found by iteration and was given in (3.52). An advantage of this method is that stability problems due to discretization may be avoided providing accurate calculation of $\mathbf{\Phi}$. However, the main limitation is that this method in practice is only applicable for linear systems with constant coefficients. We will here briefly present three alternative numerical integration schemes often used in control applications. Numerous of other numerical methods exist, whereof the so-called Runge Kutta methods often are favorable with respect to accuracy, see Egeland and Gravdahl (2002) for details.

We will here consider a system on the form

$$\dot{\mathbf{x}} = \mathbf{f}(t, \mathbf{x}, \mathbf{u}). \tag{3.61}$$

3.5.1 Euler's Method

The Euler's method is based on the assumption that the derivative is approximated by the forward difference according to

$$\dot{\mathbf{x}} = \frac{\mathbf{x}(t+T) - \mathbf{x}(t)}{T} = \mathbf{f}(t, \mathbf{x}, \mathbf{u}). \tag{3.62}$$

We introduce the discrete notation $t = kT$, then the integration method is written

$$\mathbf{x}[k+1] = \mathbf{x}[k] + T\mathbf{f}(\mathbf{x}[k], \mathbf{u}[k], k). \tag{3.63}$$

Euler's method is an explicit 1-step method. An explicit difference equation means that $\mathbf{x}[k+n]$ can be recursively calculated, since all terms on the right hand side are calculated in previous

sampling instants, that is for $k+n-1$, $k+n-2$, ... The method is denoted to be 1-step, since only values of the previous sampling is included. This method has local interrupt error proportional to T^2, often written $O(T^2)$. Euler's method is suitable in simulation of simple systems, where the requirements to the accuracy is not strict. The accuracy is of course sensitive to the sampling interval. It can be shown that Euler's method is stable for systems with its poles λ_p within the circle $|1 + T\lambda_p| = 1$. For systems with real poles in the left-hand plane, a requirement for stability is

$$T < \frac{2}{|\lambda_{\max}|}. \tag{3.64}$$

3.5.2 Backward Euler's Method

The backward Euler's method is based on the assumption that the derivative is approximated by the backward difference according to

$$\dot{\mathbf{x}} = \frac{\mathbf{x}(t) - \mathbf{x}(t-T)}{T} = \mathbf{f}(t, \mathbf{x}, \mathbf{u}). \tag{3.65}$$

Using discrete notation

$$\mathbf{x}[k] = \mathbf{x}[k-1] + T\mathbf{f}(\mathbf{x}[k], \mathbf{u}[k],k), \tag{3.66}$$

or

$$\mathbf{x}[k+1] = \mathbf{x}[k] + T\mathbf{f}(\mathbf{x}[k+1], \mathbf{u}[k+1],k). \tag{3.67}$$

Also this method is having local interrupt error of order $O(T^2)$. Euler's method is an implicit 1-step method. An implicit difference equation means that $\mathbf{x}[k+n]$ cannot be recursively calculated, since terms on the right hand side are also given at the time instant $k+n$. The region of stability for backward Euler's method is $\frac{1}{|1-T\lambda_p|} < 1$.

3.5.3 Combined Backward and Forward Euler's Method

An appropriate method for integration of second order systems with complex conjugated poles is the combined backward and forward Euler's method. Consider the following second order system on phase-variable form

$$\dot{\mathbf{x}}_1 = \mathbf{x}_2, \tag{3.68}$$

$$\dot{\mathbf{x}}_2 = \mathbf{f}(t, \mathbf{x}, \mathbf{u}). \tag{3.69}$$

Let us apply Euler's method to integrate (3.69) and backwards Euler's method on (3.68) according to

$$\mathbf{x}_2[k+1] = \mathbf{x}_2[k] + T\mathbf{f}(\mathbf{x}_1[k], \mathbf{x}_2[k], \mathbf{u}[k],k), \tag{3.70}$$

$$\mathbf{x}_1[k+1] = \mathbf{x}_1[k] + T\mathbf{x}_2[k+1]. \tag{3.71}$$

We avoid the problem with the implicit equation (3.71) since of $\mathbf{x}_2[k+1]$ is known from the previous calculation given in (3.70). Hence, we can solve the integration recursively.

3.5.4 Trapezoidal (Tustin's) Method

The trapezoidal method is an implicit 2-step method and is written

$$\mathbf{x}[k+1] = \mathbf{x}[k] + \frac{T}{2}\left[\mathbf{f}(\mathbf{x}[k], \mathbf{u}[k], k) + \mathbf{f}(\mathbf{x}[k+1], \mathbf{u}[k+1], k+1)\right]. \tag{3.72}$$

Condition for stability is

$$\left|\frac{1 + \frac{T\lambda_p}{2}}{1 - \frac{T\lambda_p}{2}}\right| < 1, p = 1, ..., n \tag{3.73}$$

where λ_p is the poles of the system. If $Re(\lambda_p) < 0$, then $Re(T\lambda_p) < 0$ provided $T > 0$. The trapezoidal method is stable for all $T > 0$, and is having local interrupt error of order $O(T^3)$.

3.5.5 Second Order System

In the following examples we will show how Tustin's method subject to smaller sampling periods converge to the real solution, and then a comparison is done for backward Eulers, forward Euler's and Tusin's methods for discretization. Let us consider the following second order system

$$\ddot{x} + 2\zeta\omega_0\dot{x} + \omega_0^2 x = \frac{1}{m}F, \tag{3.74}$$

where m=10 kg, ζ=0,2, $\omega_0 = \frac{2\pi}{T_n} = \frac{2\pi}{2}$ and F=10 N. The eigenvalues are λ_p = -0.6283 ± 3.0781i.

Example 3.2 *Let us consider Tustin's method for discretization of (3.74) with increasing sampling periods from T=0.01s, 0.05s, 0.1s, 0.2s, and 0.5s. As seen in Figure 3.7 for $T \leq 0.1s$ the system becomes well approximated. For $T \geq 0.2s$, the approximation becomes oscillatory.*

Example 3.3 *Let us compare backward Eulers, forward Euler's and Tusin's methods for discretization of (3.74) with T= 0.1s. As seen in Figure 3.8 forward Euler is as expected less accurate.*

3.6 Nyquist Frequency

Assume that a continuous signal is band limited, that is the Fourier transform is zero outside a finite band of frequencies. If the samples of the continuous signal are taken sufficiently close together in relation to the highest frequency of the band, then the samples will uniquely reconstruct the signal. Stable continuous LTI systems have the property that the steady-state response to sinusoidal excitations is sinusoidal with the frequency of the excitation signal (usually with some phase lag). However, discrete systems will create signals with new frequencies. A discrete control system operates on process variables at discrete times only. Achieving satisfactory performance and stability of the discrete control system, appropriate choice of the sampling period is crucial. The main concern is under what condition will the discrete value recover the continuous signal. In order to have a minimum fair representation of sinusoidal signals with frequency ω_M, Nyquist showed that it was necessary to sample at least twice per period, $T < \frac{\pi}{\omega_M}$.

Consider the spectrum of the sampled signal $r^*(t)$ obtained as the discrete Fourier transform

$$R_d(j\omega) = \mathcal{F}\{r^*(t)\} = \mathcal{F}\{r(t)\} * \mathcal{F}\{p_T(t)\} = R(j\omega) * P(j\omega), \tag{3.75}$$

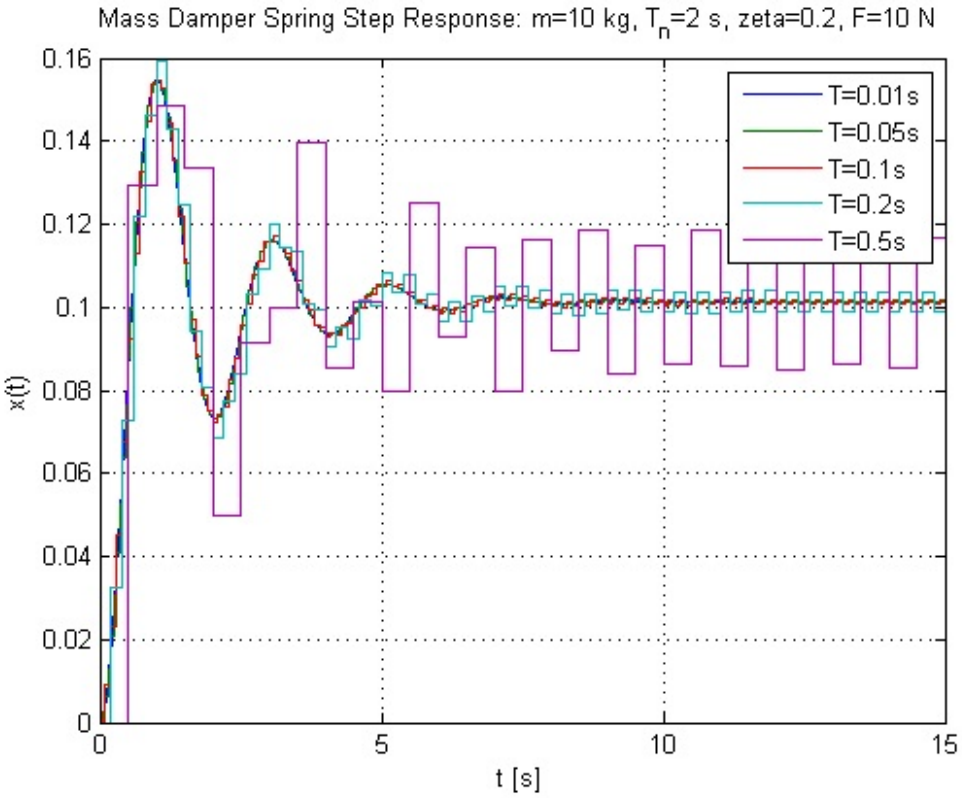

Figure 3.7: Step response of second order system using Tustin's method with increasing sampling period.

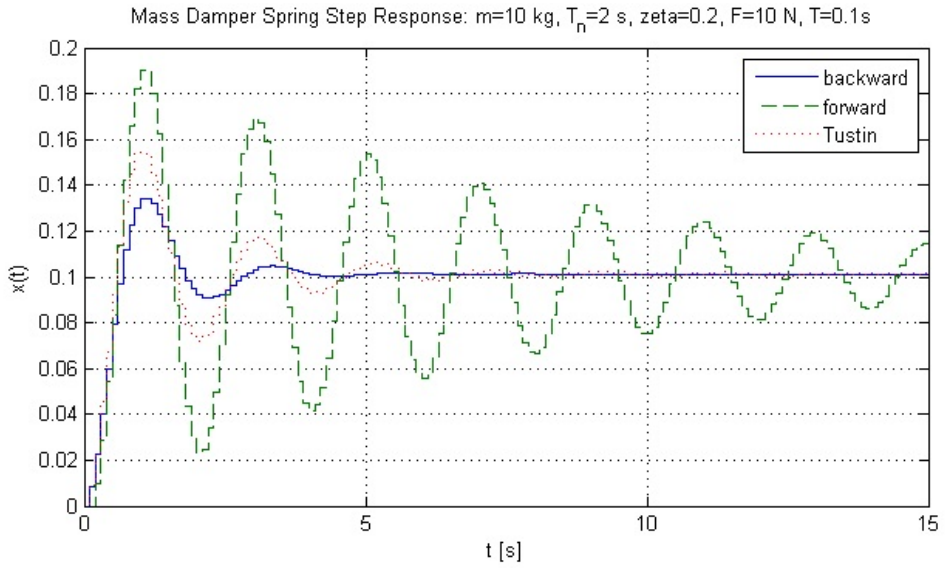

Figure 3.8: Step response of second order system using backward Euler's,forward Euler's and Tustin's methods.

where

$$P(j\omega) = \mathcal{F}\left\{\sum_{k=0}^{\infty}\delta(t-kT)\right\} = \frac{2\pi}{T}\sum_{k=0}^{\infty}\delta(\omega - \frac{2\pi}{T}k). \tag{3.76}$$

Hence, since convolution with impulses shifts a signal, we have

$$R_d(j\omega) = \frac{1}{T}\sum_{k=0}^{\infty}R(j(\omega - \frac{2\pi}{T}k)). \tag{3.77}$$

Hence, $R_d(j\omega)$ is a periodic function of the sampling frequency ω_s, see Figure 3.9 (a) and (b). In Figure 3.9 (c) we can see that if $\omega_M < (\omega_s - \omega_M)$ or $\omega_s > 2\omega_M$, there is no overlap between the shifted replicas of $R(j\omega)$ and is thus properly recovered by $R_d(j\omega)$. However, if the signal to be sampled contains frequency components larger than half the sampling frequency $\omega_s < 2\omega_M$, the sampling process itself will create low frequency components in the sampled signal Sampling of a signal with frequency ω_M creates signal components with frequencies

$$\omega_{samp} = n\omega_s \pm \omega_M$$

where n is an arbitrary integer. The phenomenon that the frequency process creates new frequency components is called *aliasing*, see Figure 3.9 (d). The frequency that is half of the sampling frequency ω_s is called the *Nyquist frequency*

$$\omega_n = \frac{1}{2}\omega_s = \frac{\pi}{T}. \tag{3.78}$$

To avoid aliasing it is important that all frequency components of signal higher than the Nyquist frequency are removed before the sampling. This could be done by introducing a *presampling filter* or *antialiasing filter,* which will be of lowpass characteristics. This is often done by an analog low pass filter in the front of the sampler. The lowpass filter must have a cut-off frequency equal or less the Nyquist frequency, $\omega_c \leq \omega_n$. In Figure 3.10 we can see the recovery of a time-continuous signal from its samples using ideal lowpass filter.

Theorem 3.6 *Shannon's sampling theorem. A continuous-time signal with a Fourier transform that is zero outside the interval $(-\omega_M, \omega_M)$ is given uniquely by its value in equidistant points if the sampling frequency is higher than $2\omega_M$.*

Remark 3.13 *The Fourier transform $R_d(j\omega)$ of a sampled signal is a periodic function of the original spectrum $R(j\omega)$ along the frequency axis with the period equal to the sampling frequency ω_s.*

3.7 The z-Transform

3.7.1 Definition

Let us define

$$z = e^{Ts}, \tag{3.79}$$

$$\Updownarrow$$

$$z^{-1} = e^{-Ts}. \tag{3.80}$$

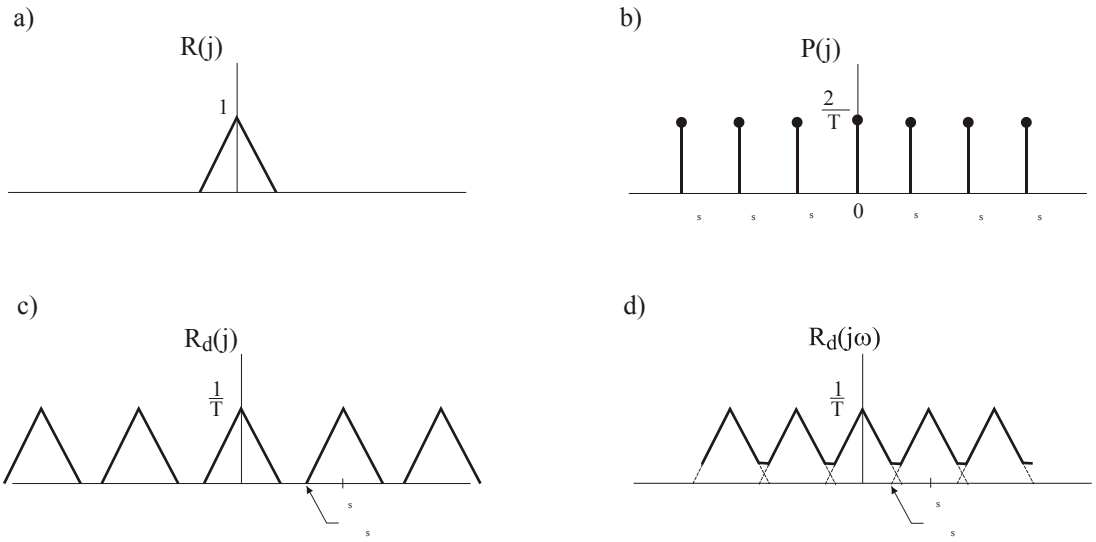

Figure 3.9: (a) Power spectrum of continuous-time signal, (b) power spectrum of sampling function, (c) power spectrum of sampled signal with $\omega_s > 2\omega_M$, and (d) power spectrum of sampled signal with $\omega_s < 2\omega_M$ resulting in aliasing.

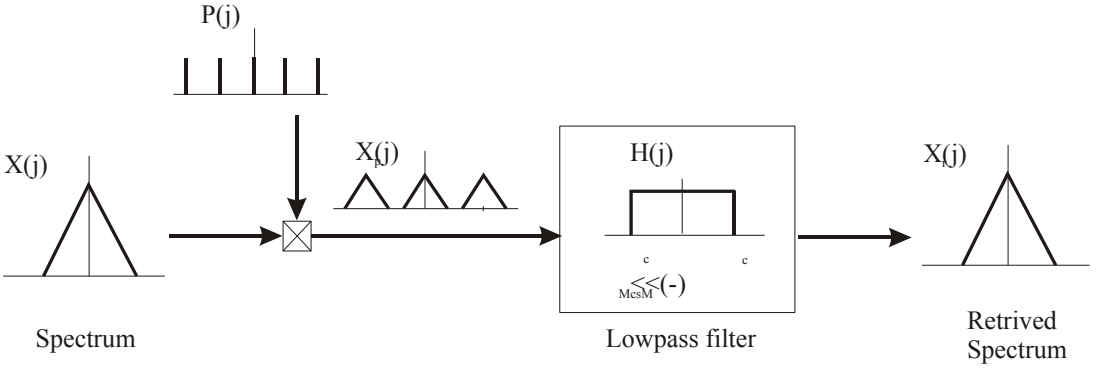

Figure 3.10: Recovery of a time-continuous signal from its samples using ideal lowpass filter.

The z-transform maps a semi-infinite time sequence (only a sequence of positive integers) into a function of a complex variable z. Applying Laplace transform on (3.28) we have

$$\mathcal{L}\{r^*(t)\} = \sum_{k=0}^{\infty} r(kT)e^{-kTs}. \tag{3.81}$$

A new z-transform is then defined, so that for a general function $r(t)$ the z-transform is found to be

$$Z\{r(t)\} = Z\{r^*(t)\} = R(z) = \sum_{k=0}^{\infty} r(kT)z^{-k}. \tag{3.82}$$

Tables of the most used z-transforms are found in Åstrøm and Wittenmark (1997) and Dorf and Bishop (1998).

Definition 3.7 *For a discrete signal $f[k]$ a similar transformation as the Laplace transformation, which is defined as the z-transform $F(z)$ can be found by*

$$F(z) = Z\{f[k]\} = \sum_{k=0}^{\infty} f[k]z^{-k}. \tag{3.83}$$

Example 3.4 *Consider the exponential function*

$$f(t) = e^{-at}, \;\; t \geq 0. \tag{3.84}$$

The z-transform is determined to be

$$Z\{e^{-at}\} = F(z) = \sum_{k=0}^{\infty} e^{-akT} z^{-k} = \sum_{k=0}^{\infty} \left(ze^{aT}\right)^{-k}, \tag{3.85}$$

which can be rewritten in closed form as

$$F(z) = \frac{1}{1 - (ze^{aT})^{-1}} = \frac{z}{z - e^{-aT}}. \tag{3.86}$$

Example 3.5 *Consider the step function $f(t)$ given in (3.16). The z-transform is determined to be*

$$Z\{f(t)\} = F(z) = \sum_{k=0}^{\infty} z^{-k}, \tag{3.87}$$

which can be rewritten in closed form as

$$F(z) = \frac{1}{1 - z^{-1}} = \frac{z}{z - 1}. \tag{3.88}$$

3.7.2 Stability Properties

Consider $z = e^{Ts}$, where $s = \sigma + j\omega$. We then find

$$z = e^{Ts} = e^{(\sigma + j\omega)T}, \tag{3.89}$$

where

$$|z| = e^{\sigma T}, \tag{3.90}$$

$$\measuredangle z = \omega T. \tag{3.91}$$

We observe that the left-half plane in the s-domain with $\sigma \leq 0$ will in the z-domain correspond to

$$0 < |z| = e^{\sigma T} \leq 1. \tag{3.92}$$

Hence the left-half plane in the the s-domain corresponds to the unit circle in the z-domain. Stable roots in the s-domain will in the z-domain be within the unit circle, see Figure 3.11.

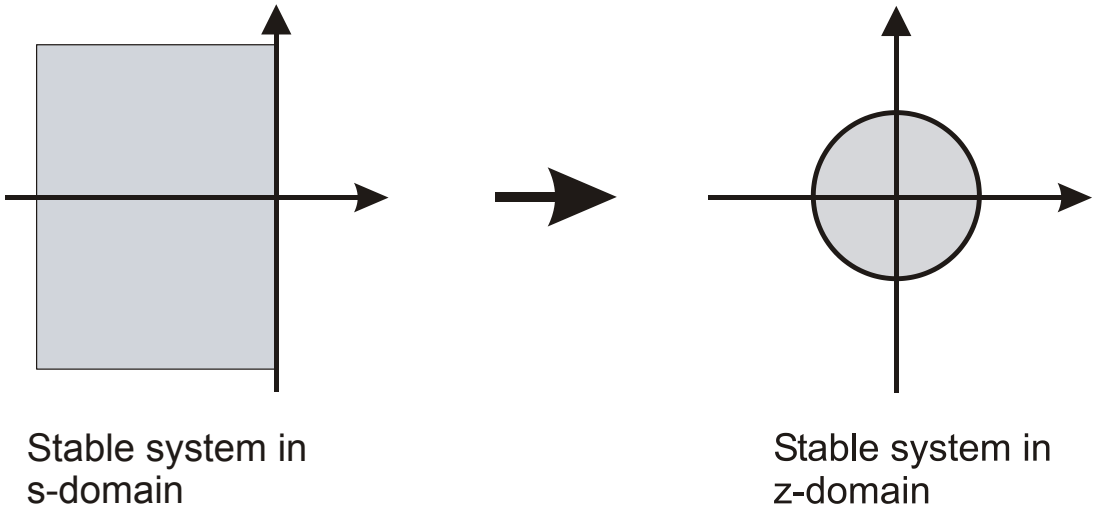

Figure 3.11: Correspondence between stability regions in s -domain and z-domain.

3.8 The Pulse-Transfer Function and the Pulse Response

3.8.1 Pulse-transfer Function

Consider the LTI system on the form

$$\begin{aligned} x[k+1] &= \mathbf{\Phi}x[k] + \mathbf{\Delta}u[k], && (3.93)\\ y[k] &= \mathbf{C}x[k] + \mathbf{D}u[k]. && (3.94) \end{aligned}$$

The z-transform gives

$$\sum_{k=0}^{\infty} z^{-k}x\left[k+1\right] = z\left(\sum_{k=0}^{\infty} z^{-k}x\left[k\right] - x\left[0\right]\right) = \sum_{k=0}^{\infty} \mathbf{\Phi}z^{-k}x\left[k\right] + \sum_{k=0}^{\infty} \mathbf{\Delta}z^{-k}u\left[k\right]. \tag{3.95}$$

Hence,

$$\begin{aligned} z\left(X(z) - x\left[0\right]\right) &= \mathbf{\Phi}X(z) + \mathbf{\Delta}U(z), && (3.96)\\ &\Updownarrow \\ X(z) &= \left(z\mathbf{I} - \mathbf{\Phi}\right)^{-1}\left(zx(0) + \mathbf{\Delta}U(z)\right). && (3.97) \end{aligned}$$

and

$$Y(z) = \mathbf{C}\left(z\mathbf{I} - \mathbf{\Phi}\right)^{-1} zx(0) + \Big(\mathbf{C}\left(z\mathbf{I} - \mathbf{\Phi}\right)^{-1}\mathbf{\Delta} + \mathbf{D}\Big)U(z). \tag{3.98}$$

The pulse-transfer function is defined as

$$H(z) = \mathbf{C}\left(z\mathbf{I} - \mathbf{\Phi}\right)^{-1}\mathbf{\Delta} + \mathbf{D}. \tag{3.99}$$

3.8.2 Pulse Response

Let $\delta[k-n]$ describe the discrete impulse sequence defined by

$$\delta[k-n] \triangleq \begin{cases} 1, & k = n \\ 0, & k \neq n \end{cases}, \tag{3.100}$$

where k and n are both integers. $\delta[k-n]$ is the discrete counterpart of the Dirac function (3.17). When the input $u[n] = \delta[0]$ acts on a LTI system, the discrete impulse response $h[k]$ appears. When a input signal $u[n]$ act on a LTI system with impulse response $h[k]$, then the discrete output $y[k]$ is defined as the discrete convolution integral according to

$$\begin{aligned} y[k] &= h[k]u[0] + h[k-1]u[1] + ... + h[1]u[k-1] + h[0]u[k], \\ &= \sum_{n=0}^{k} h[k-n]u[n] = \sum_{n=0}^{k} h[n]u[k-n] = h[k] * u[k]. \end{aligned} \tag{3.101}$$

If we substitute (3.101) into (3.82) and let $k \to \infty$, we can find the discrete pulse response function

$$\begin{aligned} Y[z] &= \sum_{k=0}^{\infty} \left(\sum_{n=0}^{\infty} h[k-n]u[n] \right) z^{-k} = \sum_{k=0}^{\infty} \left(\sum_{n=0}^{\infty} h[k-n]u[n] \right) z^{-(k-n)} z^{-n}, \\ &= \sum_{n=0}^{\infty} \left(\sum_{k=0}^{\infty} h[k-n] z^{-(k-n)} \right) u[n] z^{-n} = \left(\sum_{l=0}^{\infty} h[l] z^{-l} \right) \left(\sum_{n=0}^{\infty} u[n] z^{-n} \right), \\ &\triangleq H(z)U(z). \end{aligned} \tag{3.102}$$

where $l = k - n$ and $h[l] = 0$ for $l < 0$. As for continuous systems, we can see that convolution in the time domain (t-continuous/k-discrete) corresponds to multiplication in the frequency domain (s-continuous/z-discrete).

Theorem 3.7 *The pulse response (3.102) and the pulse-transfer function (3.99) are a z-transform pair, that is*

$$Z\{h[k]\} = H(z). \tag{3.103}$$

Example 3.6 *For a continuous SISO system*

$$\dot{x} = -ax + bu, \tag{3.104}$$

where $x(t) = 0$ for $t \leq 0$, the corresponding convolution integral will be

$$y(t) = \int_0^t h(t-\tau)u(\tau)d\tau = h(t) * u(t), \tag{3.105}$$

where $h(t-\tau) = e^{-a(t-\tau)}b$.

Example 3.7 *Consider the unit-sampling-time delay system defined by*

$$y[k] = u[k-1]. \tag{3.106}$$

The output equals the input delayed by one sampling period. Its impulse response is $h[k] = \delta[k-1]$ and its discrete transfer function is

$$H(z) = Z\{\delta[k-1]\} = z^{-1} = \frac{1}{z}. \tag{3.107}$$

One should notice that every continuous system involving time delay is a distributed system. This is not the so in the discrete case, where $H(z)$ is a rational function in z. Similarly the discrete transfer function of $h[k] = \delta[k-m]$ is

$$H(z) = Z\{\delta[k-m]\} = z^{-m}. \tag{3.108}$$

Remark 3.14 *Notice that if $h[k] \neq 0$ for only a finite number of k, the system is called a* finite impulse-response *(FIR) system. This means that the output only will be influence by a finite number of inputs.*

3.9 Shift-operator Calculus

For continuous systems differential-operator calculus, where $s \triangleq \frac{d}{dt}, s^2 \triangleq \frac{d^2}{dt^2}, s^3 \triangleq \frac{d^3}{dt^3}, ...$, is a helpful tool for manipulating linear differential equations with constant coefficients. For discrete systems a similar equivalent shift-operator calculus can be defined for linear difference equations with constant coefficients. All signals to be considered has to be defined by double sequences according to

$$\{y[k] : k = ... - 2, -1, 0, 1, 2, ...\}. \tag{3.109}$$

3.9.1 Shift Operator

The *forward-shift operator* is here denoted by z such that

$$zu[k] = u[k + 1]. \tag{3.110}$$

Remark 3.15 *Notice that in some literature such as Åstrøm and Wittenmark (1997) the letter q is used in order to have a clear distinguish from the z-transform which is a complex variable which also take initial conditions into consideration. However, here we will use z as long as it is clear from the text which purpose z is used. Forward-shift operator is often used in relation to stability analysis related to the characteristic equation.*

Example 3.8 *Åstrøm and Wittenmark (1997). Consider the difference equation*

$$y[k + 1] - ay[k] = u[k], \tag{3.111}$$

where $|a| < 1$. In operator notation the equation can be written as

$$(z - a)y[k] = u[k]. \tag{3.112}$$

A solution is

$$y[k] = \frac{1}{z - a}u[k] = \frac{z^{-1}}{1 - az^{-1}}u[k]. \tag{3.113}$$

Since z^{-1} has unit norm, the right-hand side can be represented as a convergent series according to

$$\begin{aligned} y[k] &= z^{-1}(1 + az^{-1} + a^2z^{-2} + ...)u[k], \\ &= \sum_{i=1}^{\infty} a^{i-1}u[k - i]. \end{aligned} \tag{3.114}$$

If $y[k_0] = y_0$ it follows from (3.52) that the solution is

$$\begin{aligned} y[k] &= a^{k-k_0}y_{k_0} + \sum_{j=k_0}^{k-1} a^{k-j-1}u[j], \\ &= a^{k-k_0}y_{k_0} + \sum_{i=1}^{k-k_0} a^{i-1}u[k - i]. \end{aligned} \tag{3.115}$$

It is clear that (3.114) is equal to (3.115) only if it is assumed that $y_0 = 0$ or that $k - k_0 \to \infty$.

The inverse of the forward-shift operator is called the *backward-shift operator* or the *delay operator,* and is denoted by z^{-1} such that

$$z^{-1}u[k] = u[k-1]. \tag{3.116}$$

If the range is not double infinite sequences, the inverse of the the forward-shift operator may not exist. The backward-shift operator is often used in relation to causality considerations.

3.9.2 Pulse-transfer Operator

Consider the LTI system on the form

$$\begin{aligned} x[k+1] &= \mathbf{\Phi}x[k] + \mathbf{\Delta}u[k], & (3.117)\\ y[k] &= \mathbf{C}x[k] + \mathbf{D}u[k]. & (3.118) \end{aligned}$$

An input-output relationship is obtained by

$$zx\left[k\right] = \mathbf{\Phi}x\left[k\right] + \mathbf{\Delta}u\left[k\right]. \tag{3.119}$$

Hence,

$$x[k] = \left(z\mathbf{I} - \mathbf{\Phi}\right)^{-1}\mathbf{\Delta}u\left[k\right], \tag{3.120}$$

and

$$y\left[k\right] = \left(\mathbf{C}\left(z\mathbf{I} - \mathbf{\Phi}\right)^{-1}\mathbf{\Delta} + \mathbf{D}\right)u\left[k\right]. \tag{3.121}$$

The pulse-transfer operator is defined as

$$H(z) = \mathbf{C}\left(z\mathbf{I} - \mathbf{\Phi}\right)^{-1}\mathbf{\Delta} + \mathbf{D} = \frac{\mathbf{B}(z)}{\mathbf{A}(z)}. \tag{3.122}$$

The poles of (3.122) is given by the zeros of the characteristics polynomial $\mathbf{A}(z)$.

3.10 Stability Regions

Some important aspects concerning stability, when applying the different approximation methods for integration as presented in Section 3.5, appears nicely by applying the shift-operator calculus. This will be demonstrated by examples.

Example 3.9 *Consider the LTI on the form*

$$\dot{\mathbf{x}} = \mathbf{A}\mathbf{x}. \tag{3.123}$$

Let us then apply the trapezoidal method given by (3.72) according to

$$\mathbf{x}[k+1] = \mathbf{x}[k] + \frac{T}{2}\left[\mathbf{A}\mathbf{x}[k] + \mathbf{A}\mathbf{x}[k+1])\right]. \tag{3.124}$$

If we apply the shift-operator calculus, we have

$$\begin{aligned} z\mathbf{x}[k] &= \mathbf{x}[k] + \frac{T}{2}\left[\mathbf{A}\mathbf{x}[k] + z\mathbf{A}\mathbf{x}[k])\right], && (3.125)\\ &\Updownarrow \\ \frac{2}{T}\left(\frac{z-1}{z+1}\right)\mathbf{x}[k] &= \mathbf{A}\mathbf{x}[k]. && (3.126) \end{aligned}$$

Alternatively (3.126) can be rewritten

$$\frac{2}{T}\left(\frac{1-z^{-1}}{1+z^{-1}}\right)\mathbf{x}[k] = \mathbf{A}\mathbf{x}[k]. \quad (3.127)$$

Example 3.10 *Let us then apply Euler's method based on forward difference (3.63) on (3.123) according to*

$$\mathbf{x}[k+1] = \mathbf{x}[k] + T\mathbf{A}\mathbf{x}[k]. \quad (3.128)$$

If we apply the shift-operator calculus, we have

$$\begin{aligned} z\mathbf{x}[k] &= \mathbf{x}[k] + T\mathbf{A}\mathbf{x}[k], && (3.129)\\ &\Updownarrow \\ \left(\frac{z-1}{T}\right)\mathbf{x}[k] &= \mathbf{A}\mathbf{x}[k]. && (3.130) \end{aligned}$$

Example 3.11 *Let us then apply Euler backward method (3.66) on (3.123) according to*

$$\mathbf{x}[k+1] = \mathbf{x}[k] + T\mathbf{A}\mathbf{x}[k+1]. \quad (3.131)$$

If we apply the shift-operator calculus, we have

$$\begin{aligned} z\mathbf{x}[k] &= \mathbf{x}[k] + Tz\mathbf{A}\mathbf{x}[k], && (3.132)\\ &\Updownarrow \\ \left(\frac{z-1}{zT}\right)\mathbf{x}[k] &= \mathbf{A}\mathbf{x}[k]. && (3.133) \end{aligned}$$

Remark 3.16 *Transformation from the s-domain to the z-domain may appear by using one of the following approximations*

$$\begin{aligned} s &= \frac{2(1-z^{-1})}{T(1+z^{-1})}, && (3.134)\\ s &= \frac{z-1}{T}, && (3.135)\\ s &= \frac{z-1}{zT}. && (3.136) \end{aligned}$$

Eq. (3.134) is known as the bilinear transformation or Tustin's approximation often used in stability analysis of discrete controllers in the so-called q-domain. This transformation maps the imaginary axis in the s-domain to the unit circle in the z-domain. Thus, stable poles in the left-hand plane in the s-domain correspond to poles within the unit circle in the z-domain.

Example 3.12 *Consider the second order system given by*

$$\dot{x}_1 = x_2, \tag{3.137}$$
$$\dot{x}_2 = -\omega_0^2 x_1 - 2\zeta\omega_0 x_2 + v, \tag{3.138}$$

where ζ is the damping ratio, ω_0 is the resonance frequency and v is the disturbance. Applying Euler's method of integration gives

$$x_1[k+1] = x_1[k] + Tx_2[k], \tag{3.139}$$
$$x_2[k+1] = x_2[k] + T\left(-\omega_0^2 x_1[k] - 2\zeta\omega_0 x_2[k] + v[k]\right). \tag{3.140}$$

By using shift-operator calculus we have the z-domain formulation

$$\frac{(z-1)}{T}x_1[k] = x_2[k], \tag{3.141}$$
$$\frac{(z-1)}{T}x_2[k] = \left(-\omega_0^2 x_1[k] - 2\zeta\omega_0 x_2[k] + v[k]\right). \tag{3.142}$$

Assume $\zeta = 0$, by setting the expression for $x_2[k]$ given by (3.141) into (3.142), the the z-domain formulation appears to be

$$\frac{x_1}{v}(z) = \frac{T^2}{z^2 - 2z + 1 + T^2\omega_0^2}. \tag{3.143}$$

Notice that this expression has poles for $z_{1,2} = 1 \pm jT\omega_0$. Thus, the poles is outside the unit circle, such that the discretized system is unstable for all T.

Example 3.13 *Consider the second order system given by (3.137) and (3.138). Applying combined forward and backwards Euler's method of integration gives*

$$x_2[k+1] = x_2[k] + T\left(-\omega_0^2 x_1[k] - 2\zeta\omega_0 x_2[k] + v[k]\right), \tag{3.144}$$
$$x_1[k+1] = x_1[k] + Tx_2[k+1]. \tag{3.145}$$

The shift-operator calculus gives

$$x_2[k] = \frac{T}{(z-1)}\left(-\omega_0^2 x_1[k] - 2\zeta\omega_0 x_2[k] + v[k]\right), \tag{3.146}$$
$$x_1[k] = \frac{Tz}{(z-1)}x_2[k]. \tag{3.147}$$

Assume $\zeta = 0$, by setting (3.147) into (3.146) yields the z-domain formulation

$$\frac{x_1}{v}(z) = \frac{z^2 - 2z + 1}{z^2 + (T^2\omega_0^2 - 2)z + 1}. \tag{3.148}$$

Notice that this expression has poles for $z_{1,2} = 1 - \frac{T^2\omega_0^2}{2} \pm T\omega_0\sqrt{\frac{T^2\omega_0^2}{4} - 1}$. The poles are complex conjugated for $T < \frac{2}{\omega_0}$ such that

$$z_{1,2} = 1 - \frac{T^2\omega_0^2}{2} \pm T\omega_0\sqrt{1 - \frac{T^2\omega_0^2}{4}}j = a \pm jb, \tag{3.149}$$

where $a = 1 - \frac{T^2\omega_0^2}{2}$ and $b = T\omega_0\sqrt{1 - \frac{T^2\omega_0^2}{4}}$. Since $z_1 z_2 = a^2 + b^2 = 1$ this indicates that the poles are on the unit circle, which corresponds to the poles on the imaginary axis in the s-domain. Hence, stability is ensured.

In Figure 3.12 it is shown how the stability region for $Re(s) < 0$ is mapped on the z-plane for Euler's method (3.135), backwards Euler (3.136) and trapezoidal method (3.134). We observe that Euler's method may map the time-continuous system into an unstable region in the discrete-time system, that is outside the unit circle. For systems with complex conjugated poles with small damping Euler's method may cause stability problems as we noticed in the example above. When the backward approximation is used a stable continuous-time system always give a stable discrete-time system. Unfortunately, some unstable continuous-time systems may be transformed into stable discrete systems. Tustin's approximation or the trapezoidal method has the advantage that the left-hand of the s-plane is transformed into the whole unit circle. Hence, stable (unstable) continuous-time systems are transformed into stable (unstable) discrete systems.

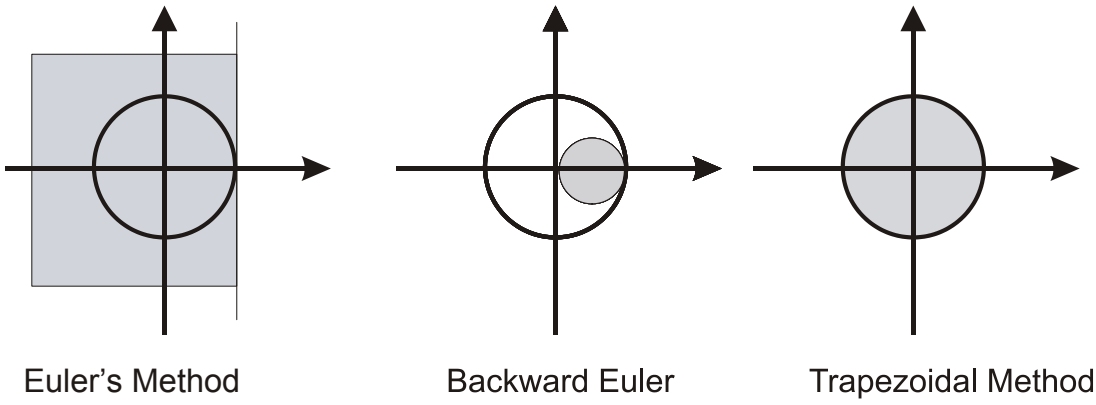

Figure 3.12: Mapping of stability regions in the s-domain on the z-domain using Euler's method, backward Euler and trapezoidal (Tustin's) method for difference approximation.

3.11 Order of the System

Let a difference equation be written as

$$y[k+n_a] + a_1 y[k+n_a-1] + ... + a_{n_a} y[k] = b_0 u[k+n_b] + b_1 u[k+n_b-1] ... + b_{n_b} u[k], \quad (3.150)$$

where the *order* of the (3.150) is defined to be equal to the poles, that is n_a. The zeros is defined to be n_b. We also assume that $n_a \geq n_b$. The pole excess is defined to be $d = n_a - n_b$. Applying forward-shift operator on (3.150) gives

$$\left(z^{n_a} + a_1 z^{n_a-1} + a_2 z^{n_a-2} + ... + a_{n_a}\right) y[k] = \left(b_0 z^{n_b} + b_1 z^{n_b-1} + b_2 z^{n_b-2} + ... + b_{n_b}\right) u[k]. \quad (3.151)$$

Let us define the polynomials

$$A(z) = z^{n_a} + a_1 z^{n_a-1} + a_2 z^{n_a-2} + ... + a_{n_a}, \quad (3.152)$$

and

$$B(z) = b_0 z^{n_b} + b_1 z^{n_b-1} + b_2 z^{n_b-2} + ... + b_{n_b}. \quad (3.153)$$

Hence, (3.150) can be reformulated as

$$A(z) y[k] = B(z) u[k]. \quad (3.154)$$

It is also possible to reformulate 3.150 such that

$$\begin{aligned} y[k] + a_1 y[k-1] + ... + a_{n_a} y[k-n_a] &= b_0 u[k+n_b-n_a] + & (3.155)\\ & \quad b_1 u[k+n_b-n_a-1] + ... + b_{n_b} u[k-n_a] & (3.156) \end{aligned}$$

By reversing the order of the coefficients of $A(z)$, the *reciprocal polynomial* $A^*(z)$ is defined

$$\begin{aligned} A^*(z) &= 1 + a_1 z + a_2 z^2 + ... + a_{n_a} z^{n_a}, & (3.157)\\ &= z^{n_a}(z^{-n_a} + a_1 z^{-(n_a-1)} + a_2 z^{-(n_a-2)} + ... + a_{n_a}),\\ &= z^{n_a} A\left(z^{-1}\right). \end{aligned}$$

Notice that

$$\begin{aligned} A^*(z^{-1}) &= 1 + a_1 z^{-1} + a_2 z^{-2} + ... + a_{n_a} z^{-n_a}, & (3.158)\\ &= z^{-n_a}(z^{n_a} + a_1 z^{n_a-1} + a_2 z^{n_a-2} + ... + a_{n_a}),\\ &= z^{-n_a} A\left(z\right), \end{aligned}$$

and

$$A(z) = z^{n_a} A^*(z^{-1}). \tag{3.159}$$

For $B(z)$ we have similarly

$$B(z) = z^{n_b} B^*(z^{-1}). \tag{3.160}$$

Using reciprocal polynomials (3.154) can be written

$$\begin{aligned} A(z)y[k] &= B(z)u[k],\\ &\Updownarrow\\ z^{n_a} A^*(z^{-1})y[k] &= z^{n_b} B^*(z^{-1})u[k],\\ &\Updownarrow\\ A^*(z^{-1})y[k] &= z^{n_b-n_a} B^*(z^{-1})u[k],\\ &\Updownarrow\\ A^*(z^{-1})y[k] &= B^*(z^{-1})u[k+n_b-n_a]. \end{aligned} \tag{3.161}$$

Notice that $A^{**}(z)$ is not necessarily the same as $A(z)$. The polynomial $A(z)$ is said to be self-reciprocal if

$$A^*(z) = A(z). \tag{3.162}$$

Example 3.14 *Let $A(z) = z$ Then the reciprocal is $A^*(z) = z \cdot z^{-1} = 1$. The reciprocal of $A^*(z)$ is $A^{**}(z) = 1$, which of course is different from $A(z)$.*

3.12 Relation Between Shift-Operator Calculus and z-Transform

Calculation with z-transform and shift-operator calculus are related to each other. However, it is important to be aware of that in shift-operator calculus z denotes an operator that acts on a double sequences, while in z-transform z denotes a complex variable. Due to this several authors make a distinction between by using q instead of z in shift-operator calculus. Consider the following example from Åstrøm and Wittenmark (1997) about pole-zero cancellations:

Example 3.15 *Consider the difference equation*

$$y[k+1] + ay[k] = u[k+1] + au[k], \tag{3.163}$$

where a can be an arbitrary real number. The difference equation of (3.163) has the solution

$$y[k] = (-a)^k y[0] + u[k]. \tag{3.164}$$

The pulse-transfer function, see (3.99), of (3.163) is

$$H(z) = \frac{z+a}{z+a} = 1. \tag{3.165}$$

The last equality is obtained because z is a complex variable. We may misled to believe that (3.163) is identical to

$$y[k] = u[k]. \tag{3.166}$$

This is only true if the initial condition $y[0] = 0$. If shift-operator calculus is used in solving (3.163), we achieve

$$(z+a)y[k] = (z+a)u[k]. \tag{3.167}$$

Since z here is an operator we can not formally divide by $(z+a)$.

Remark 3.17 *Hence, in z-transform calculus it is allowed to divide with an arbitrary expression. However, this is not allowed in shift-operator calculus unless special assumptions are made i.e. initial condition is equal to zero.*

Chapter 4

Filtering and State Estimation

This chapter will present the basic properties of the most used conventional analog and digital filters, and model based filters (also called observers) used in control system design. Most of the theory presented is general and valid for almost all kind of industrial control problems. However, certain filtering and state estimation problems a more characteristics for marine applications. These will be paid more attention to later in the text in Chapter 7. The chapter is organized as follows: Section 4.2 will handle conventional analog and digital filtering techniques. In Section 4.3 model based state space filtering techniques also called observers will be presented.

The theory presented in this chapter is solely based on earlier text books. For more thoroughly presentation the reader is referred to Johansson (1993), Christiansen (1996), Oppenheim and Willsky (2013) and Åstrøm and Wittenmark (1997). Concerning diagnostics and fault-tolerant control the reader is referred to Blanke et al. (2003)..

Learning outcome of the chapter: The reader shall understand:

- The principles of analog and digital filtering.
- The objective and formulation of low pass, notch and high pass filters.
- The objective and formulation of state estimation using deterministic observes and stochastic filters including the certainty equivalence principle connecting state estimation to control.
- The main concept of stochastic state estimation, Kalman filtering, based on minimum variance filtering (stochastic).

4.1 Introduction

In order to be successful in the design of industrial control system in addition to appropriate signal processing, filtering of signals are essential. Topics considered in this chapter are basic introduction to:

- *Filtering of measurement noise.* Most sensor signals are contaminated by some noise caused by external disturbances and internal properties of the sensor itself. The noise may have negative impact on the controller performance, if no precaution is taken. By filtering

we achieve a change in the relative amplitudes of the frequency components in a signal or even elimination of some frequency components entirely.

- *Reconstruction of non-measured data.* For many applications important process states are not measured. Typical reasons for this could be that no convenient sensors exists, or simply that cost reasons motivate to not to install the sensor. In such cases sophisticated model based filtering techniques - state estimation - can be applied. The main purpose of the state estimator (observer) is to reconstruct unmeasured signals and perform filtering before the signals are used in a feedback control system. The input to the state estimator in a dynamic positioning system is sensor data e.g. from an inertial measurement unit (IMU) measuring the vessel's heave, roll and pitch motions, a compass or gyro measuring the vessel's heading and a position reference system like the satellite navigation system DGPS (differential global positioning system) measuring the vessel's North and East position coordinates, see Chapter 2 for more description of these sensors.

- *Dead reckoning.* All kind of equipment will fail according to some failure rate. Experience from industrial applications has shown that the most frequent control system failure are caused by sensor failures. In safety critical marine applications a sudden drop-out of the control system may lead to dangerous situations, if not an adequate signal substitution will take place. Applying model based filters the predicted sensor signal may, at least for some period of time, replace the measured signal. Then only the mathematical model of the process and the sensor device itself is used to predict the signal to be used by the control system. Using only model prediction for calculation of state signal is called dead reckoning. Use of observers for the purpose of diagnostics and in the design of so-called virtual sensors for fault-tolerant control is an increasing field of research

4.2 Analog and Digital Filtering

According to Oppenheim and Willsky (2013) Linear time-invariant (LTI) systems that change the shape of the systems power spectrum are referred to as *frequency-shaping filters.* Filters that are designed to pass some frequencies essentially undistorted and significantly attenuate or eliminate others are called *frequency-selective filters.* Due to the broad field of applications we will below first concentrate on frequency-selective filters. Several basic types of filters has been designed, and they are given name indicating their main function. The most common ideal filters are:

- *Lowpass filter* passes low frequencies of signals from zero to cut-off frequency and attenuate or reject all higher frequencies.

- *Highpass filter* passes the high frequencies of signals and attenuate or reject all low frequencies from zero to cut-off frequency.

- *Bandpass filter* passes a band of frequencies between lower and upper cut-off frequencies and attenuate frequencies higher and lower than those defined by the band.

- *Bandstop filter* (or reject filter) stops signal frequencies between its lower and upper cut-off frequencies, and transmits all other signals.

- *All-pass filter* transmits all signal frequencies and produces a predictable phase shift.

Example 4.1 *A continuous-time ideal lowpass filter is a LTI system that passes complex exponential $e^{j\omega t}$ for values of ω in the range of $-\omega_c \leq \omega \leq \omega_c$ and rejects all other frequencies, where ω_c is the cut-off frequency. Hence, the frequency response is given on the form:*

$$h(j\omega) = \begin{cases} 1, & |\omega| \leq \omega_c \\ 0, & |\omega| > \omega_c \end{cases} . \tag{4.1}$$

Adopting the complex exponential signal $e^{j\omega t}$, ideal filters are usually defined to have symmetrical frequency response about $\omega = 0$, where $|h(j\omega)| = 1$.

Ideal filters is useful to describe idealized system configurations. However, they are not realizable and must be approximated in real applications as nonideal filters. Nonideal filters do have a gradual transition band from passband to stopband. The acceptable deviation limits in the passband and the stopband are often described by δ_1 and δ_2, see Figure 4.1. The amount by which the frequency response differs from unity in the passband is referred to as passband ripple, and corresponding deviation from zero in the stopband is referred to as stopband ripple. In addition, especially for control purposes the phase characteristics of the filter is of importance. For nonideal lowpass filters, there is a trade-off between the width of the transition band (frequency domain) and the rise time, delay time and overshoot (time domain) of the step response.

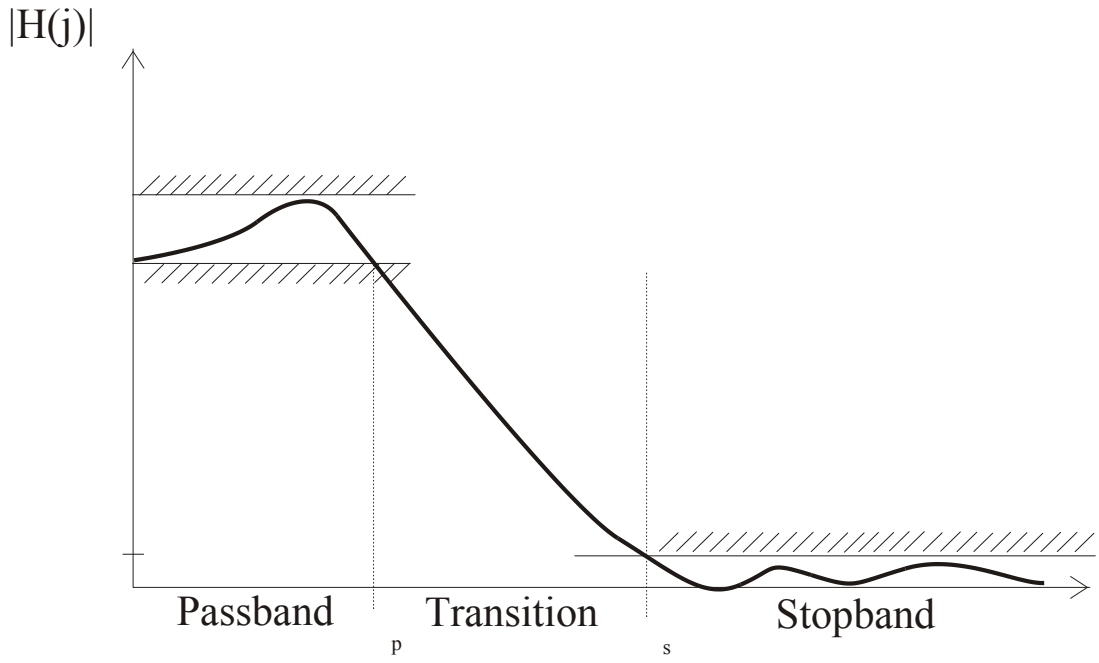

Figure 4.1: Tolerances for magnitude characteristics of a lowpass filter.

4.2.1 Nonideal Lowpass Filter

A widely-used class of LTI systems for lowpass filtering (Oppenheim and Willsky, 2013) is the so-called nth-order Butterworth filters. In the frequency domain for $n = 1, 2$ and 3

$$n = 1 : b(s) = \frac{\omega_c}{s + \omega_c}, \tag{4.2}$$

$$n = 2 : b(s) = \frac{\omega_c^2}{\left(s^2 + \sqrt{2}\omega_c s + \omega_c^2\right)}, \tag{4.3}$$

$$n = 3 : b(s) = \frac{\omega_c^3}{\left(s^2 + \omega_c s + \omega_c^2\right)(s + \omega_c)}. \tag{4.4}$$

The corresponding filters may also be written in time domain according to

$$n = 1 : \dot{x}_f + \omega_c x_f = \omega_c x, \tag{4.5}$$

$$n = 2 : \ddot{x}_f + \sqrt{2}\omega_c \dot{x}_f + \omega_c^2 x_f = \omega_c^2 x, \tag{4.6}$$

$$n = 3 : \dddot{x}_f + 2\omega_c \ddot{x}_f + 2\omega_c^2 \dot{x}_f + \omega_c^3 = \omega_c^3 x, \tag{4.7}$$

where x is the signal to be filtered (input), x_f is the filtered signal (output) and ω_c is the cut-off frequency. The Butterworth filters have a frequency response which is optimized to give as flat amplitude as possible in the passband, see Figure 4.2. Similarly other classes of lowpass filter exist, where the most known are Chebyshev filter, Bessel filter, Legendre-Papoulis filter and Elliptic filter, see Part 16 in Christiansen (1996) for more details. The Elliptic filter does also have zeros that may differ from infinite.

4.2.2 Nonideal Highpass Filter

A highpass filter may be designed by substituting

$$s \to \frac{1}{s}, \tag{4.8}$$

in the equations describing the lowpass filter.

4.2.3 Notch Filter

Cascaded notch filter is an often used bandstop filter and is written

$$h_n = \prod_{i=1}^{r} \frac{s^2 + 2\varsigma_{ni}\omega_i s + \omega_i^2}{s^2 + 2\varsigma_{di}\omega_i s + \omega_i^2}. \tag{4.9}$$

where ω_i is the center frequencies of the filter, r is the number of center frequencies, and $\varsigma_{ni} \ll 1$ and $0 < \varsigma_{di}$ are the damping ratios in the numerator and the denominator, respectively. A typical choice could be $\varsigma_{ni} = 0.1$ and $\varsigma_{di} = 1$. Notch filter in cascade with lowpass filter have often in the past been used for wave filtering. An appropriate number of center frequencies, typically 3, with a distribution about the domination wave frequency is chosen, see Figure 4.3.

4.2.4 Digital Filtering

Digital filters provide many of the same frequency selective services as analog filters. Digital filters are often defined in terms of equivalent analog filters. However, many digital filters are

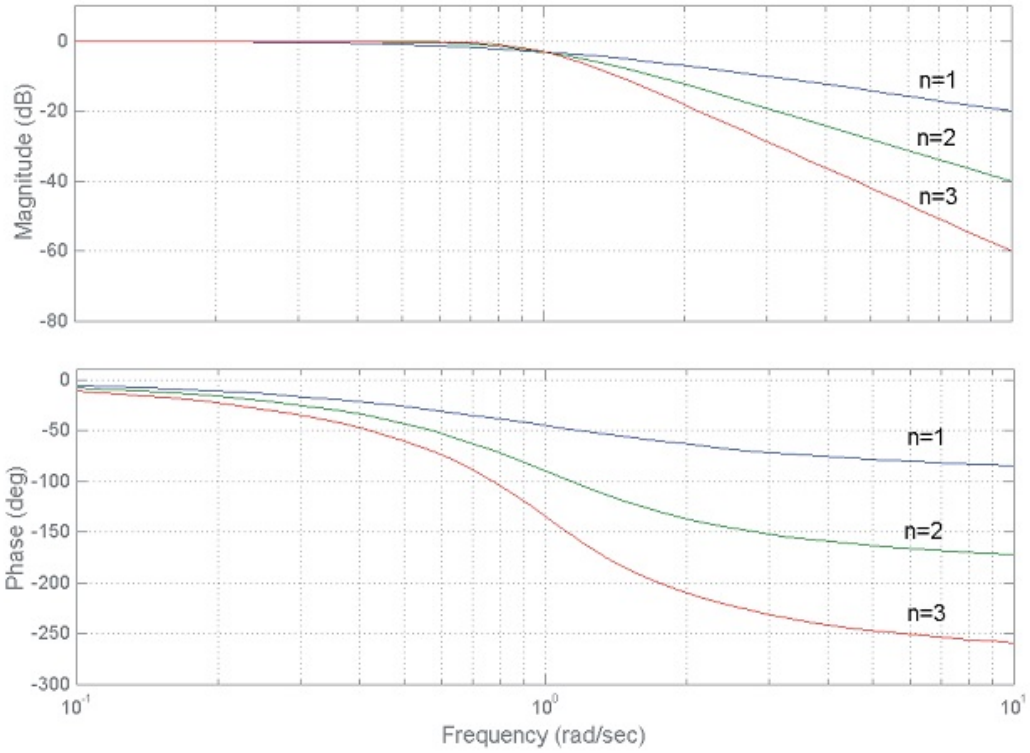

Figure 4.2: Bode plot of Butterworth filter.

designed using properties that are unique to this technology. Compared to analog filters, digital filters generally have the advantages that the stability of certain classes can be guaranteed, coefficients can easily be altered, they can operate over a wide range of frequencies with wide dynamic range and with high precision.

Consider the equation

$$\dot{x} = u. \tag{4.10}$$

Approximation of this equation could be

$$\frac{x[k+1] - x[k]}{T} = (u[k+1] + u[k])\frac{1}{2}. \tag{4.11}$$

Applying z-transform gives

$$\begin{aligned} \frac{(z-1)x[z]}{T} &= \frac{1}{2}(z+1)u[z], \\ &\Updownarrow \\ x[z] &= \frac{T(z+1)}{2(z-1)}u[z]. \end{aligned} \tag{4.12}$$

Hence, once an analog filter $h(s)$ is defined, the discrete filter $H(z)$ based on trapezoidal approx-

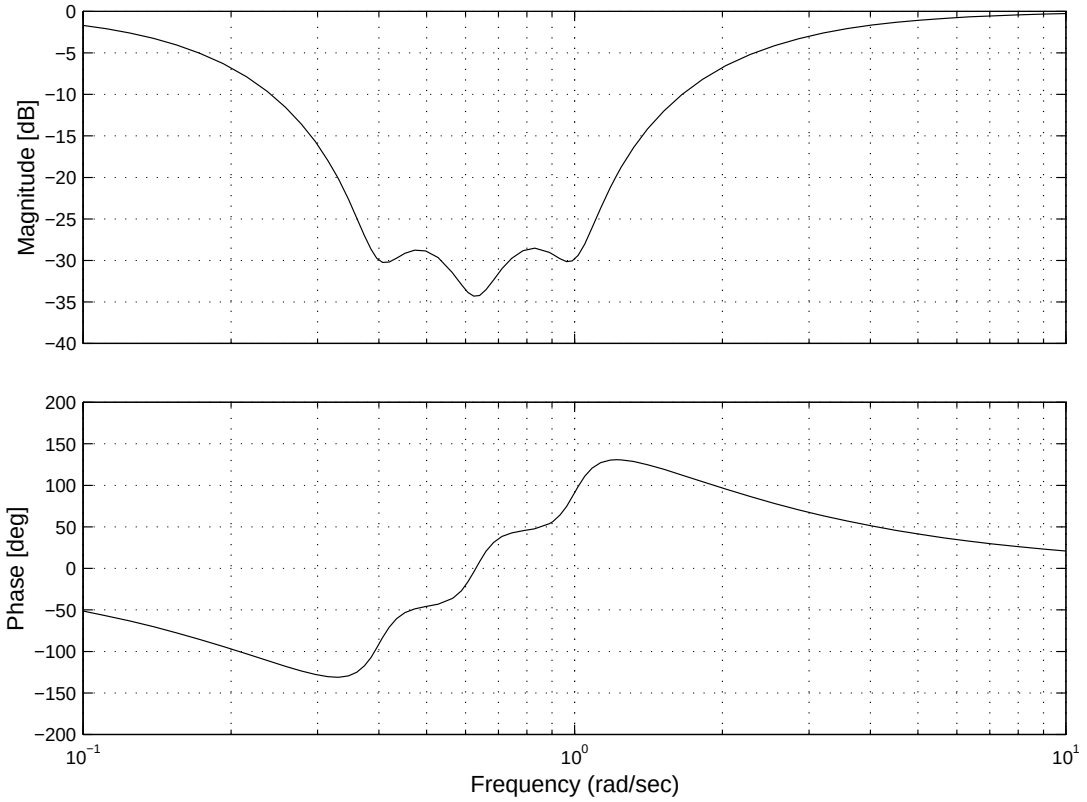

Figure 4.3: Notch filter where $\varsigma_{ni} = 0.1$ and $\varsigma_{di} = 1$, $\omega_1 = 0.4$ $[rad/s]$, $\omega_2 = 0.63$ $[rad/s]$ and $\omega_3 = 1.0$ $[rad/s]$.

imation method could be constructed by replacing s in $h(s)$ by

$$s = \frac{2(z-1)}{T(z+1)}. \tag{4.13}$$

Setting $z = e^{i\omega T}$ in (4.13) gives

$$s = \frac{2(e^{i\omega T}-1)}{T(e^{i\omega T}+1)} = i\frac{2}{T}\tan\left(\frac{\omega T}{2}\right) = iv, \tag{4.14}$$

where v is the discrete frequency corresponding to ω. When $\frac{\omega T}{2} \to \frac{\pi}{2}$, $v \to \infty$. As noticed in (3.78) $\omega = \frac{\pi}{T}$ is known as the Nyquist frequency, which is the absolute upper limit for the discrete filter to approximate the analog filter.

Linear constant coefficients filters can be categorized into two main classes known as finite impulse-response (FIR) filter or infinite impulse-response (IIR) filters.

Finite Impulse-Response (FIR) filter

FIR filters can be expressed as

$$\begin{aligned} y[k] &= b_0u[k] + b_1u[k-1] + ... + b_nu[k-n], \\ &= \sum_{i=0}^{n} b_iu[k-i], \end{aligned} \tag{4.15}$$

where the coefficients $\{b_i\}$ are called filter tap weights. In terms of z-transform the filter discrete transfer function is written

$$H(z) = \sum_{i=0}^{n} b_i z^{-i}. \tag{4.16}$$

The filter's transfer function consists of zeroes only (i.e. no poles). Because of this the FIR filter is referred to as an all-zero or transversal filter. If the filter input is bounded (i.e. $|u(i)| \leq 1$ for all i), the maximum value of the output $y(i)$ is $\sum |b_i|$. If all the tap weights $\{b_i\}$ are bounded, the filters output is likewise bounded and, as result, stability is guaranteed. Furthermore, the phase of $H(z)$, when plotted with respect to frequency, is linear with constant slope.

Example 4.2 *For moving average filter it is convenient to apply a FIR formulation, where the output $y[k]$ for any k, i.e. k_0, is an average of values $u[k]$ in the vicinity of k_0. An example of a two-point average filter is*

$$y[k] = \frac{1}{2}\left(u[k-1] + u[k]\right). \tag{4.17}$$

Three-point moving average filter may be

$$y[k] = \frac{1}{3}u[k-1] + u[k] + u[k+1]. \tag{4.18}$$

Infinite Impulse-Response (IIR) filter

IIR filters can be expressed as

$$y[k] = -a_1 y[k-1] - a_2 y[k-2] - ... - a_n y[k-n] + b_0 u[k] + b_1 u[k-1] + ... + b_n u[k-n], \tag{4.19}$$

where the the coefficients $\{a_i\}$ and $\{b_i\}$ are the filter tap weights. IIR filter generally satisfies a given magnitude frequency response design objective with a lower order filter compared to a corresponding FIR filter. However the phase characteristics does not generally exhibit linear phase. FIR filter can only be realized in digital form, while IIR filter may be realized analog.

The most known IIR filters are Tsjebyscheff, Elliptic and Butterworth. The discrete IIR version of a Butterworth filter may be derived putting (4.13) into (4.2)-(4.4).

4.3 State Estimation

Analog filters are not always suitable for all control applications. In many cases the signals to be separated do not appear in totally disjoint frequency bands. A disadvantage concerning control is that undesired phase lag often is introduced by filters. This consequently reduce the control performance and stability margins in terms of bandwidth reduction, and by less gain and phase margin. Thus for the purpose of control especially higher order lowpass filter or cascades of filters should be used with care. Very often the signals of interest consists of frequency components in different frequency band slightly overlapping each others. This is in particular the case for many marine applications.

In industrial control systems many of the states of interest concerning control are impossible to measure, or if possible, the cost for installing the sensors may be too high. It is therefore of importance to determine or *reconstruct* those states from the available measurements. This is called *state estimation* and is provided by so-called *observers*.

Definition 4.1 *An observer or state estimator produces the state of a system from measurements of inputs and outputs.*

In positioning of marine vessels, the main purpose of the observer (Figure 4.4) is to estimate velocities and current and wave drift forces from position measurements. Later in the text in Section 7.2 we will see that, in addition, 1st-order wave disturbances should be filtered out e.g. by using a notch filter suppressing wave-induced disturbances close to the peak frequency of the wave spectrum. The position and heading measurements are corrupted with colored noise caused by wind, waves and ocean currents. However, only the slowly-varying disturbances should be counteracted by the propulsion system whereas the oscillatory motion due to the waves (1st-order wave-induced disturbances) should *not* enter the feedback loop. This is done by using so-called *wave filtering* techniques, which separates the position and heading measurements into a low-frequency (LF) and a wave-frequency (WF) position and heading part, see Figure 6.20. Even though accurate measurements of the vessel velocities are available when using differential GPS systems or Doppler log, a state estimator must be designed in order to satisfy the classification rules for the positioning systems. In the case of temporarily loss of position and heading measurements, the observer must be able to operate in a *dead reckoning* mode implying that *predicted* observer velocity, position and heading is used for feedback. A temporarily loss of these measurements will not affect the positioning accuracy. When the necessary signals reappear, the estimated values will give a smooth transition back to the true position and heading.

Before we address the marine applications any further, basic introduction to the most used linear observers will be given in this chapter.

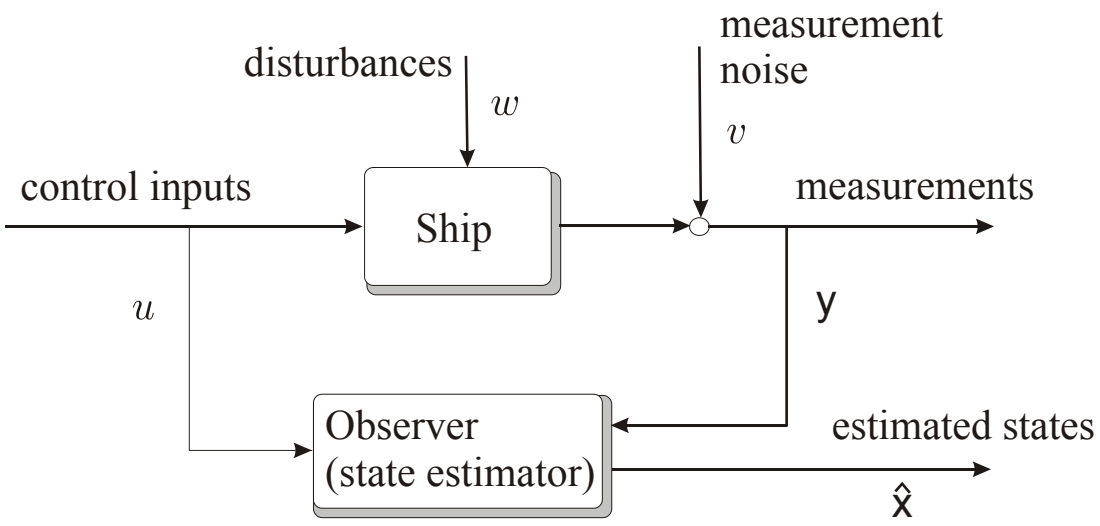

Figure 4.4: Block diagram showing the principle of state estimation.

4.3.1 Deterministic State Estimation

In the ideal situation when there are no uncertainties in the system with regards to modeling parameters and noise, the system is called deterministic. For this simplified case, a deterministic estimator may be constructed to illustrate the concept of state estimation. In the realistic case

with modeling uncertainties and noise on measurements and control signals, stochastic theory may be applied in the observer design. The best known stochastic estimator is the Kalman filter, which will be treated subsequently.

Continuous-time deterministic estimator

Consider the following *control plant model* of the linear time-invariant (LTI) system of the form

$$\dot{\mathbf{x}} = \mathbf{A}\mathbf{x} + \mathbf{B}\mathbf{u}, \tag{4.20}$$

$$\mathbf{y} = \mathbf{D}\mathbf{x}. \tag{4.21}$$

This system is completely deterministic, and it is assumed that the pair $[\mathbf{A}, \mathbf{D}^T]$ is observable (actually, detectability is sufficient). This means that it is possible to estimate the system states from its inputs and outputs. A first attempt at constructing an estimator might be to require that the estimator copies the control plant model exactly

$$\dot{\hat{\mathbf{x}}} = \mathbf{A}\hat{\mathbf{x}} + \mathbf{B}\mathbf{u}, \tag{4.22}$$

$$\hat{\mathbf{y}} = \mathbf{D}\hat{\mathbf{x}}, \tag{4.23}$$

where $\hat{\mathbf{x}}$ is the estimated state vector. But if the initial conditions $\mathbf{x}(t_o)$ and $\hat{\mathbf{x}}(t_o)$ differ, the estimator will not reproduce the correct states. To correct this, an injection term using the difference between the measured output $\mathbf{y}$ and the estimated output $\hat{\mathbf{y}}$ is added to the estimator

$$\dot{\hat{\mathbf{x}}} = \mathbf{A}\hat{\mathbf{x}} + \mathbf{B}\mathbf{u} + \mathbf{K}_e(\mathbf{y} - \hat{\mathbf{y}}) = \mathbf{A}\hat{\mathbf{x}} + \mathbf{B}\mathbf{u} + \mathbf{K}_e\mathbf{D}(\mathbf{x} - \hat{\mathbf{x}}). \tag{4.24}$$

The state-feedback gain matrix $\mathbf{K}_e$ may then be used for tuning the estimator. The error dynamics is found by subtracting (4.24) from (4.20)

$$\frac{d}{dt}\tilde{\mathbf{x}} = \dot{\mathbf{x}} - \dot{\hat{\mathbf{x}}} = \mathbf{A}(\mathbf{x} - \hat{\mathbf{x}}) - \mathbf{K}_e\mathbf{D}(\mathbf{x} - \hat{\mathbf{x}}) = (\mathbf{A} - \mathbf{K}_e\mathbf{D})(\mathbf{x} - \hat{\mathbf{x}}) = (\mathbf{A} - \mathbf{K}_e\mathbf{D})\tilde{\mathbf{x}}. \tag{4.25}$$

Hence, the error $\tilde{\mathbf{x}}$ will exponentially approach zero if the eigenvalues of $(\mathbf{A} - \mathbf{K}_e\mathbf{D})$ have negative real parts. Figure 4.5 shows a block diagram of this estimator.

If $\mathbf{K}_e$ is chosen only with respect to obtaining fast convergence of $\hat{\mathbf{x}}$ to $\mathbf{x}$, the poles will be moved far away into the left half-plane. This will increase the bandwidth of the estimator, which means that $\hat{\mathbf{x}}$ will be more sensitive to noise in $\mathbf{u}$ and $\mathbf{y}$. The choice of $\mathbf{K}_e$ is thus a trade-off between fast estimation and noise-rejection properties, where the best compromise is achieved by an optimal estimator (Anderson and Moore, 1989).

Discrete-time deterministic estimator

Consider the *control plant model* of the discrete system

$$\mathbf{x}[k+1] = \mathbf{\Phi}\mathbf{x}[k] + \mathbf{\Delta}\mathbf{u}[k], \tag{4.26}$$

$$\mathbf{y}[k] = \mathbf{C}\mathbf{x}[k]. \tag{4.27}$$

The estimator can found by copying the control plant model such that

$$\hat{\mathbf{x}}[k+1] = \mathbf{\Phi}\hat{\mathbf{x}}[k] + \mathbf{\Delta}\mathbf{u}[k] + \mathbf{L}(\mathbf{y}[k] - \hat{\mathbf{y}}[k]), \tag{4.28}$$

$$\hat{\mathbf{y}}[k] = \mathbf{C}\hat{\mathbf{x}}[k], \tag{4.29}$$

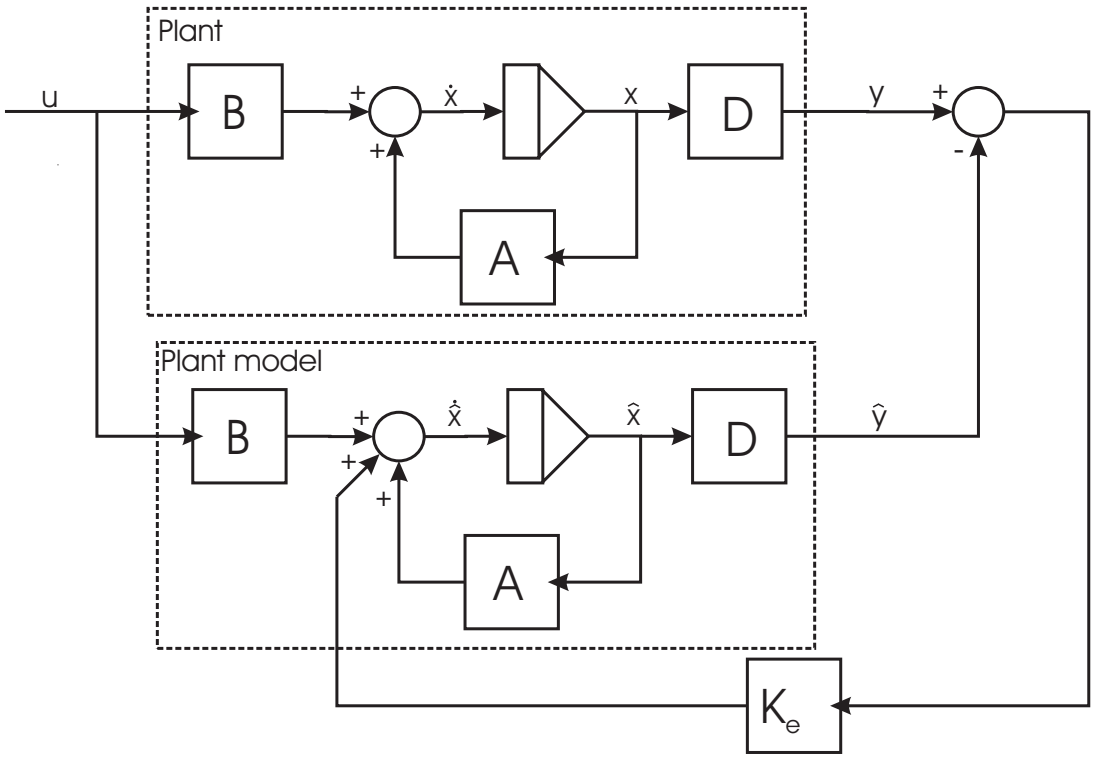

Figure 4.5: Deterministic estimator illustrating the plant model concept.

where $\mathbf{L}$ is the state-feedback gain matrix, and $\hat{\mathbf{x}}$ is the estimate of $\mathbf{x}$. The error dynamics become (with $\tilde{\mathbf{x}} = \mathbf{x} - \hat{\mathbf{x}}$)

$$\tilde{\mathbf{x}}[k+1] = \mathbf{\Phi}\tilde{\mathbf{x}}[k] - \mathbf{L}(\mathbf{y}[k] - \hat{\mathbf{y}}[k]) = \mathbf{\Phi}\tilde{\mathbf{x}}[k] - \mathbf{LC}(\mathbf{x}[k] - \hat{\mathbf{x}}[k]) = (\mathbf{\Phi} - \mathbf{LC})\tilde{\mathbf{x}}[k]. \tag{4.30}$$

Now $\mathbf{L}$ must be chosen such that (4.30) is asymptotically stable, which means that the magnitude of the eigenvalues of $(\mathbf{\Phi} - \mathbf{LC})$ must be within the unit circle. This is again only possible if the system is observable.

4.3.2 Certainty Equivalence Principle

If a dynamic system is defined by (4.26) and (4.27), a feedback control law may be defined by using a complete state information and the positive gain matrix $\mathbf{G} > 0$ such that

$$\mathbf{u}[k] = -\mathbf{G}\mathbf{x}[k], \tag{4.31}$$

$$\mathbf{x}[k+1] = \mathbf{\Phi}\mathbf{x}[k] - \mathbf{\Delta G}\mathbf{x}[k] = (\mathbf{\Phi} - \mathbf{\Delta G})\mathbf{x}[k]. \tag{4.32}$$

If the complete state information is unavailable, the observer defined in (4.28) may be used, and the estimated state vector $\hat{\mathbf{x}}$ replaces $\mathbf{x}$ in the calculation of the control input according to $\mathbf{u} = -\mathbf{G}\hat{\mathbf{x}}[k]$. This is in the literature denoted as the *certainty equivalence principle* or *separation theorem*. The closed loop error dynamics of the complete feedback system becomes

$$\begin{aligned} \mathbf{x}[k+1] - \hat{\mathbf{x}}[k+1] &= (\mathbf{\Phi} - \mathbf{\Delta G})\mathbf{x}[k] - (\mathbf{\Phi} - \mathbf{\Delta G})\hat{\mathbf{x}}[k] - \mathbf{LC}\tilde{\mathbf{x}}[k] \\ &= (\mathbf{\Phi} - \mathbf{LC} - \mathbf{\Delta G})\tilde{\mathbf{x}}[k]. \end{aligned} \tag{4.33}$$

This system is of order $2n$ (with n as the order of the control plant model). The eigenvalues of the matrix $eig(\mathbf{\Phi} - \mathbf{\Delta G})$ is the eigenvalues of the closed-loop pole-placement problem with full state information. The eigenvalues of the matrix $eig(\mathbf{\Phi} - \mathbf{LC})$ of the observer is assumed to be faster than those of the controller, typical one decade. The solution of these two problems are dual, and the stability of the two systems may be analyzed separately (Åstrøm and Wittenmark, 1997).

Remark 4.1 *The Certainty equivalence principle is used for both linear deterministic and linear stochastic state estimation in conjunction to control. This principle may be extended to more complex combinations of nonlinear controllers and observers, and is a subject for research.*

4.3.3 Stochastic State Estimation: Least Squares Estimation

The state vector $\mathbf{x}$ of a static, linear stochastic process may be estimated from the measurement vector $\mathbf{y}$ and an a priori estimate of the state vector $\bar{\mathbf{x}}$, made prior to the time of the measurement. Let the measurement be described by

$$\mathbf{y} = \mathbf{Cx} + \mathbf{v}, \tag{4.34}$$

where $\mathbf{C}$ is a known matrix, and $\mathbf{v}$ is the measurement noise, which is assumed statistically independent of $\mathbf{x}$ with a known, positive definite covariance matrix $\mathbf{V}$ and expectation value equal to 0 such that

$$E[\mathbf{v}] = 0, \quad cov[\mathbf{v}] = E[\mathbf{v}\mathbf{v}^T] = \mathbf{V} > 0, \quad E[\mathbf{x}\mathbf{v}^T] = 0. \tag{4.35}$$

The uncertainty of the a priori estimate $\bar{\mathbf{x}}$, which also is the expectation value of the corrected state vector $\mathbf{x}$, is given by the covariance matrix $\bar{\mathbf{X}}$

$$E[\mathbf{x}] = \bar{\mathbf{x}}, \quad cov[\mathbf{x}] = E[(\mathbf{x} - \bar{\mathbf{x}})(\mathbf{x} - \bar{\mathbf{x}})^T] = \bar{\mathbf{X}} > 0. \tag{4.36}$$

A weighted least squares method for finding $\mathbf{x}$ from $\bar{\mathbf{x}}$ and $\mathbf{y}$ is given by

$$J = \frac{1}{2}[(\mathbf{x} - \bar{\mathbf{x}})^{\mathbf{T}}\mathbf{P}(\mathbf{x} - \bar{\mathbf{x}}) + (\mathbf{y} - \mathbf{Cx})^T\mathbf{Q}(\mathbf{y} - \mathbf{Cx})], \tag{4.37}$$

where $\mathbf{P}$ and $\mathbf{Q}$ are appropriately chosen positive semidefinite and positive definite weighting matrices, respectively. By requiring the derivative of J to be zero, the value $\hat{\mathbf{x}}$ of $\mathbf{x}$ which minimizes J may be found

$$\left.\frac{dJ}{d\mathbf{x}}\right|_{(\mathbf{x}=\hat{\mathbf{x}})} = \mathbf{P}(\hat{\mathbf{x}} - \bar{\mathbf{x}}) - \mathbf{C}^T\mathbf{Q}(\mathbf{y} - \mathbf{C}\hat{\mathbf{x}}) = 0, \tag{4.38}$$

$$(\mathbf{P} + \mathbf{C}^T\mathbf{QC})\hat{\mathbf{x}} = \mathbf{P}\bar{\mathbf{x}} + \mathbf{C}^T\mathbf{Qy} = (\mathbf{P} + \mathbf{C}^T\mathbf{QC})\bar{\mathbf{x}} + \mathbf{C}^T\mathbf{Q}(\mathbf{y} - \mathbf{C}\bar{\mathbf{x}}), \tag{4.39}$$

$$\hat{\mathbf{x}} = \bar{\mathbf{x}} + (\mathbf{P} + \mathbf{C}^{\mathbf{T}}\mathbf{QC})^{-1}\mathbf{C}^T\mathbf{Q}(\mathbf{y} - \mathbf{C}\bar{\mathbf{x}}) = \bar{\mathbf{x}} + \mathbf{K}(\mathbf{y} - \mathbf{C}\bar{\mathbf{x}}). \tag{4.40}$$

$\hat{\mathbf{x}}$ is the improved estimate of $\mathbf{x}$ after the measurement has been made, is termed the *corrected* or *aposteriori* estimate of $\mathbf{x}$. The uncertainty of $\hat{\mathbf{x}}$ is given by the covariance of the estimation

error $\tilde{\mathbf{x}} = \mathbf{x} - \hat{\mathbf{x}}$, which is termed $\hat{\mathbf{X}}$ according to

$$\begin{aligned}
\hat{\mathbf{X}} &= E[\tilde{\mathbf{x}}\tilde{\mathbf{x}}^T] = E[(\mathbf{x}-\hat{\mathbf{x}})(\mathbf{x}-\hat{\mathbf{x}})^T] \\
&= E[(\mathbf{x}-\bar{\mathbf{x}}-\mathbf{K}(\mathbf{y}-\mathbf{C}\bar{\mathbf{x}}))(\mathbf{x}-\bar{\mathbf{x}}-\mathbf{K}(\mathbf{y}-\mathbf{C}\bar{\mathbf{x}}))^T] \\
&= E[(\mathbf{x}-\bar{\mathbf{x}}-\mathbf{K}(\mathbf{C}\mathbf{x}+\mathbf{v}-\mathbf{C}\bar{\mathbf{x}}))(\mathbf{x}-\bar{\mathbf{x}}-\mathbf{K}(\mathbf{C}\mathbf{x}+\mathbf{v}-\mathbf{C}\bar{\mathbf{x}}))^T] \\
&= E[(\mathbf{x}-\bar{\mathbf{x}}-\mathbf{K}\mathbf{C}(\mathbf{x}-\bar{\mathbf{x}})-\mathbf{K}\mathbf{v}))(\mathbf{x}-\bar{\mathbf{x}}-\mathbf{K}\mathbf{C}(\mathbf{x}-\bar{\mathbf{x}})-\mathbf{K}\mathbf{v}))^T] \\
&= E[((\mathbf{I}-\mathbf{K}\mathbf{C})(\mathbf{x}-\bar{\mathbf{x}})-\mathbf{K}\mathbf{v}))((\mathbf{I}-\mathbf{K}\mathbf{C})(\mathbf{x}-\bar{\mathbf{x}})-\mathbf{K}\mathbf{v}))^T] \\
&= E[(\mathbf{I}-\mathbf{K}\mathbf{C})(\mathbf{x}-\bar{\mathbf{x}})(\mathbf{x}-\bar{\mathbf{x}})^T(\mathbf{I}-\mathbf{K}\mathbf{C})^T - \mathbf{K}\mathbf{v}(\mathbf{x}-\bar{\mathbf{x}})^T(\mathbf{I}-\mathbf{K}\mathbf{C})^T... \\
&\quad -(\mathbf{I}-\mathbf{K}\mathbf{C})(\mathbf{x}-\bar{\mathbf{x}})\mathbf{v}^T\mathbf{K}^T + \mathbf{K}\mathbf{v}\mathbf{v}^T\mathbf{K}^T] \\
&= (\mathbf{I}-\mathbf{K}\mathbf{C})E[(\mathbf{x}-\bar{\mathbf{x}})(\mathbf{x}-\bar{\mathbf{x}})^T](\mathbf{I}-\mathbf{K}\mathbf{C})^T + \mathbf{K}E[\mathbf{v}\mathbf{v}^T]\mathbf{K}^T... \\
&\quad -\mathbf{K}E[\mathbf{v}(\mathbf{x}-\bar{\mathbf{x}})^T](\mathbf{I}-\mathbf{K}\mathbf{C})^T - (\mathbf{I}-\mathbf{K}\mathbf{C})E[(\mathbf{x}-\bar{\mathbf{x}})\mathbf{v}^T]\mathbf{K}^T \\
&= (\mathbf{I}-\mathbf{K}\mathbf{C})\bar{\mathbf{X}}(\mathbf{I}-\mathbf{K}\mathbf{C})^T + \mathbf{K}\mathbf{V}\mathbf{K}^T, \qquad (4.41)
\end{aligned}$$

because $E[\mathbf{v}] = E[\mathbf{x}\mathbf{v}^T] = 0$. One (important) way of choosing $\mathbf{P}$ and $\mathbf{Q}$ is to minimize the sum of diagonal terms in the covariance matrix $\hat{\mathbf{X}}$. It can be shown that this is achieved by the choice

$$\mathbf{P} = \bar{\mathbf{X}}^{-1}, \quad \mathbf{Q} = \mathbf{V}^{-1}. \qquad (4.42)$$

The gain matrix $\mathbf{K}$ is then given by

$$\mathbf{K} = (\bar{\mathbf{X}}^{-1} + \mathbf{C}^{\mathbf{T}}\mathbf{V}^{-1}\mathbf{C})^{-1}\mathbf{C}^T\mathbf{V}^{-1} = \bar{\mathbf{X}}\mathbf{C}^T(\mathbf{C}\bar{\mathbf{X}}\mathbf{C}^T + \mathbf{V})^{-1}. \qquad (4.43)$$

It may be shown that the estimator $\hat{\mathbf{x}}$ is unbiased, which means that the expectation value of the a-posteriori estimate equals the a priori expectation value

$$E[\hat{\mathbf{x}}] = E[\mathbf{x}] = \bar{\mathbf{x}}.$$

These results may now be used to develop the discrete Kalman Filter.

4.3.4 Stochastic State Estimation: Discrete Kalman Filter

Consider the following discrete LTI system on the form

$$\begin{aligned}
\mathbf{x}[k+1] &= \mathbf{\Phi}\mathbf{x}[k] + \mathbf{\Delta}\mathbf{u}[k] + \mathbf{\Gamma}\mathbf{w}[k], \qquad (4.44) \\
\mathbf{y}[k] &= \mathbf{C}\mathbf{x}[k] + \mathbf{v}[k], \qquad (4.45)
\end{aligned}$$

where it is assumed that the system is observable.

Let us assume that the process noise $\mathbf{w}[k]$ and the sensor noise $\mathbf{v}[k]$ are discrete Gaussian *white noise* processes with known covariance matrices.

That is, $\mathbf{w}[k] \sim N(\bar{\mathbf{w}}, \mathbf{W}[k])$ and $\mathbf{v}[k] \sim N(\bar{\mathbf{v}}, \mathbf{V}[k])$. The mean value of the process disturbance is defined as

$$\mathbf{E}[\mathbf{w}[k]] = \bar{\mathbf{w}}. \qquad (4.46)$$

The covariance matrix of the process disturbance is positive definite (Appendix A) and is defined as

$$\mathbf{E}[(\mathbf{w}[k]-\bar{\mathbf{w}})(\mathbf{w}[k]-\bar{\mathbf{w}})^T] = \mathbf{W}[k]\delta_{kj}, \qquad (4.47)$$

where $\delta_{kj} = 1$ if $k = j$ and $\delta_{kj} = 0$ if $k \neq j$. The mean value of the sensor noise is defined as

$$\mathbf{E}[\mathbf{v}[k]] = \bar{\mathbf{v}} = \mathbf{0}. \tag{4.48}$$

The covariance matrix of the sensor noise is positive definite and defined as

$$\mathbf{E}[(\mathbf{v}[k] - \bar{\mathbf{v}})(\mathbf{v}[k] - \bar{\mathbf{v}})^T] = \mathbf{V}[k]\delta_{kj}. \tag{4.49}$$

Assume that the process disturbance and measurement noise are uncorrelated:

$$\mathbf{E}[\mathbf{v}[k]\mathbf{w}[k]^T] = \mathbf{0}. \tag{4.50}$$

The expectation value of the initial condition of the state is defined as

$$\mathbf{E}[\mathbf{x}[0]] = \bar{\mathbf{x}}(0). \tag{4.51}$$

The corresponding covariance matrix of the initial condition of the state is positive definite and is defined as

$$\mathbf{E}[(\mathbf{x}[0] - \bar{\mathbf{x}}(0))(\mathbf{x}[0] - \bar{\mathbf{x}}(0))^T] = \bar{\mathbf{X}}_0. \tag{4.52}$$

Assume that the process disturbance and the sensor noise is uncorrelated with the initial condition according to

$$\mathbf{E}[(\mathbf{x}[0] - \bar{\mathbf{x}}(0))\mathbf{w}[k]^T] = 0, \tag{4.53}$$

$$\mathbf{E}[(\mathbf{x}[0] - \bar{\mathbf{x}}(0))\mathbf{v}[k]^T] = 0. \tag{4.54}$$

Remark 4.2 *Notice that if the real disturbance is not a Gaussian process, it can be reformulated in a disturbance model (approximation) which is driven by white noise. The disturbance model is then included in an augmented state vector.*

Assume that the data

$$\mathbf{Y}_k = \{\mathbf{y}[i], \mathbf{u}[i] \mid i \leq k\}, \tag{4.55}$$

is known. Using $\mathbf{Y}_k$ it is possible to have three cases for estimation (Figure 4.6) of $\mathbf{x}[k+m]$:

- Smoothing for $m < 0$.
- Filtering for $m = 0$.
- Prediction for $m > 0$.

We will first consider the case when $m = 1$.This is a so-called *one-step prediction*. Then the filtering case with $m = 0$ will be shown.

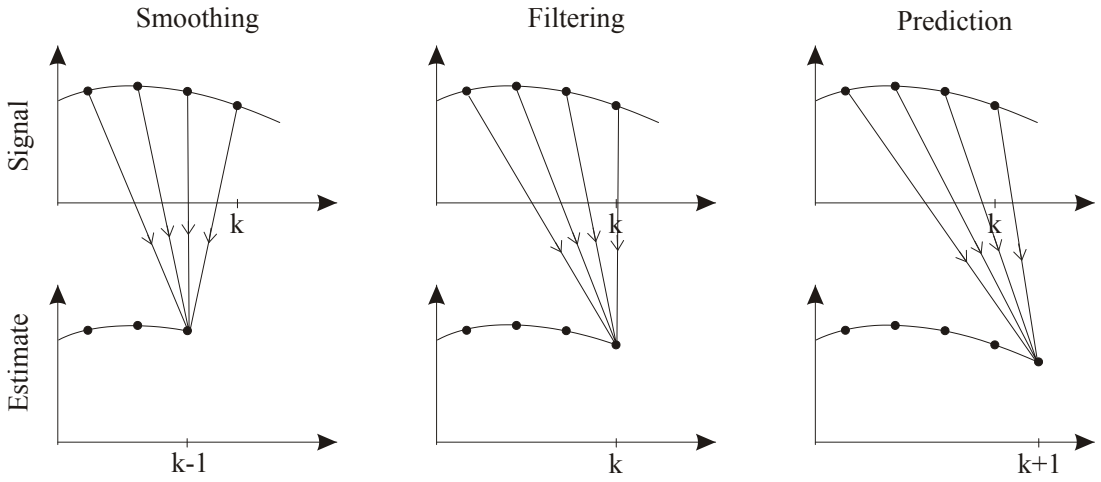

Figure 4.6: Smoothing, filtering and prediction.

Kalman filter - prediction case

Let us denote the vector $\hat{\mathbf{x}}$ to be the *state estimate* of the state vector $\mathbf{x}$. Consider the system given by (4.44) and (4.45) and assume that the estimated state vector is a function of past inputs according to

$$\begin{aligned} \hat{\mathbf{x}}[k+1|k] &= \mathbf{\Phi}\,\hat{\mathbf{x}}[k|k-1] + \mathbf{\Delta}\mathbf{u}[k] + \mathbf{\Gamma}\,\bar{\mathbf{w}}[k] + \mathbf{K}[k]\,(\mathbf{y}[k] - \hat{\mathbf{y}}[k])\,, & (4.56)\\ \hat{\mathbf{y}}[k] &= \mathbf{C}\,\hat{\mathbf{x}}[k|k-1]. & (4.57) \end{aligned}$$

A new feedback term $\mathbf{K}[k]\,(\mathbf{y}[k] - \hat{\mathbf{y}}[k])$ is introduced. $\mathbf{K}[k]$ is a $n \times n$ gain matrix and is also called *Kalman filter* gain matrix if it is chosen subject to some principles as we will see later in the text. The notation $\hat{\mathbf{x}}[k+1|k]$ is used to indicate that is is an estimate of $\mathbf{x}[k+1]$ based on measurements available at time k. As long as the predicted measurement vector $\hat{\mathbf{y}}[k]$ coincides exactly with the measurement vector $\mathbf{y}[k]$ the feedback term will give no contribution. We often call the difference $\mathbf{y}[k] - \hat{\mathbf{y}}[k]$ to be the *innovation*. Eq. (4.56) and (4.57) is an *observer* of the LTI system (4.44) and (4.45).

The *error dynamics* of the reconstruction (estimation) can be found by subtracting (4.44) from (4.56) according to

$$\begin{aligned} \tilde{\mathbf{x}}[k+1|k] &= \mathbf{x}[k+1] - \hat{\mathbf{x}}[k+1|k], & (4.58)\\ &\Updownarrow & \\ \tilde{\mathbf{x}}[k+1|k] &= \mathbf{\Phi}\,\tilde{\mathbf{x}}[k|k-1] + \mathbf{\Gamma}(\mathbf{w}[k] - \bar{\mathbf{w}}[k]) - \mathbf{K}[k]\,(\mathbf{y}[k] - \hat{\mathbf{y}}[k])\,, & (4.59)\\ &\Updownarrow & \\ \tilde{\mathbf{x}}[k+1|k] &= (\mathbf{\Phi} - \mathbf{K}[k]\mathbf{C})\;\tilde{\mathbf{x}}[k|k-1] + \mathbf{\Gamma}(\mathbf{w}[k] - \bar{\mathbf{w}}[k]) - \mathbf{K}[k]\mathbf{v}[k], & (4.60)\\ &\Updownarrow & \\ \tilde{\mathbf{x}}[k+1|k] &= (\mathbf{I} - \mathbf{K}[k])\left(\begin{pmatrix} \mathbf{\Phi} \\ \mathbf{C} \end{pmatrix}\tilde{\mathbf{x}}[k|k-1] + \begin{pmatrix} \mathbf{\Gamma}(\mathbf{w}[k] - \bar{\mathbf{w}}[k]) \\ \mathbf{v}[k] \end{pmatrix}\right). & (4.61) \end{aligned}$$

Remark 4.3 *If we disregard the effect of* $\mathbf{\Gamma}\,(\mathbf{w}[k] - \bar{\mathbf{w}}[k]) - \mathbf{K}[k]\mathbf{v}[k]$, *we observe that the choice of* $\mathbf{K}[k]$ *can be made such that (4.61) is asymptotically stable. Thus, the* error dynamics *converges*

to zero even if the system itself is unstable providing that the pair $(\mathbf{\Phi}, \mathbf{C})$*, the criterion for observability is fulfilled. Hence, the* $n \times n$ *observability matrix* $\mathbf{Q}_{do}$ *has full rank, see (3.60) in Section 3.4.*

However, we will here take the properties of the noise into account in the design of $\mathbf{K}[k]$ minimizing the variance of the error dynamics, which is denoted as

$$\bar{\mathbf{X}}[k] = \mathbf{E}[(\tilde{\mathbf{x}}[k] - \mathbf{E}(\tilde{\mathbf{x}}[k]))(\tilde{\mathbf{x}}[k] - \mathbf{E}(\tilde{\mathbf{x}}[k]))^T]. \tag{4.62}$$

The expectation value of the error $\tilde{\mathbf{x}}$ is

$$\mathbf{E}[\tilde{\mathbf{x}}[k+1]] = (\mathbf{\Phi} - \mathbf{K}[k]\mathbf{C})\ \mathbf{E}[\tilde{\mathbf{x}}[k]]. \tag{4.63}$$

Let $\mathbf{E}[\mathbf{x}[0]] = \bar{\mathbf{x}}(0)$. If $\hat{\mathbf{x}}[0] = \bar{\mathbf{x}}(0)$, then $\mathbf{E}[\tilde{\mathbf{x}}[0]] = \mathbf{0}$. Thus the mean value of the error dynamics is zero for all $k \geq 0$ independent of $\mathbf{K}[k]$. Since $\mathbf{E}[\tilde{\mathbf{x}}[k]]$ is assumed to be independent of $\mathbf{w}[k]$ and $\mathbf{v}[k]$,(4.61) gives

$$\begin{aligned}
\bar{\mathbf{X}}[k+1] &= \mathbf{E}[(\tilde{\mathbf{x}}[k+1] - \mathbf{E}(\tilde{\mathbf{x}}[k+1]))(\tilde{\mathbf{x}}[k+1] - \mathbf{E}(\tilde{\mathbf{x}}[k+1]))^T], \qquad (4.64)\\
&= \mathbf{E}[\tilde{\mathbf{x}}[k+1]\tilde{\mathbf{x}}[k+1]^T],\\
&= (\mathbf{I} - \mathbf{K}[k]) \left(\begin{pmatrix} \mathbf{\Phi} \\ \mathbf{C} \end{pmatrix} \bar{\mathbf{X}}[k] \begin{pmatrix} \mathbf{\Phi} \\ \mathbf{C} \end{pmatrix}^T + \begin{pmatrix} \mathbf{\Gamma}\mathbf{W}[k]\mathbf{\Gamma}^T & \mathbf{0}_{n\times n} \\ \mathbf{0}_{n\times n} & \mathbf{V}[k] \end{pmatrix} \right) \begin{pmatrix} \mathbf{I}_{n\times n} \\ -\mathbf{K}[k]^T \end{pmatrix}.
\end{aligned}$$

Further $\bar{\mathbf{X}}[0] = \bar{\mathbf{X}}_0$. From (4.64) it follows that if $\bar{\mathbf{X}}[k]$ is positive semidefinite, then $\bar{\mathbf{X}}[k+1]$ is also positive semidefinite.

Let us first define a general principle called the completion of squares (Åstrøm and Wittenmark, 1997), where the quadratic loss function is defined as

$$J(\mathbf{x} - \hat{\mathbf{x}}, \mathbf{y} - \hat{\mathbf{y}}) = \left((\mathbf{x} - \hat{\mathbf{x}})^T, (\mathbf{y} - \hat{\mathbf{y}})^T \right) \begin{pmatrix} \mathbf{Q}_x & \mathbf{Q}_{xy} \\ \mathbf{Q}_{xy}^T & \mathbf{Q}_y \end{pmatrix} \begin{pmatrix} \mathbf{x} - \hat{\mathbf{x}} \\ \mathbf{y} - \hat{\mathbf{y}} \end{pmatrix}, \tag{4.65}$$

where $\mathbf{Q}_y > 0$ is a symmetric positive definite matrix and $\mathbf{Q}_x \geq 0$ is a symmetric positive semidefinite matrix. The minimum of (4.65) with respect to $\mathbf{x}$ is found by

$$\left. \frac{\partial J(\mathbf{x} - \hat{\mathbf{x}}, \mathbf{y} - \hat{\mathbf{y}})}{\partial \mathbf{x}} \right|_{\mathbf{x}=\hat{\mathbf{x}}} = 0. \tag{4.66}$$

Then there exists an $\mathbf{K}$ satisfying

$$\mathbf{Q}_y \mathbf{K}\mathbf{C} = \mathbf{Q}_{xy}^T, \tag{4.67}$$

such that (4.65) can be rewritten

$$\begin{aligned}
J(\mathbf{x} - \hat{\mathbf{x}}, \mathbf{y} - \hat{\mathbf{y}}) &= (\mathbf{x} - \hat{\mathbf{x}})^T \left(\mathbf{Q}_x - (\mathbf{K}\mathbf{C})^T \mathbf{Q}_y \mathbf{K}\mathbf{C} \right) (\mathbf{x} - \hat{\mathbf{x}}) + \qquad (4.68)\\
&\quad (\mathbf{y} - \hat{\mathbf{y}} + \mathbf{K}\mathbf{C}(\mathbf{x} - \hat{\mathbf{x}}))^T \mathbf{Q}_y \left(\mathbf{y} - \hat{\mathbf{y}} + \mathbf{K}\mathbf{C}(\mathbf{x} - \hat{\mathbf{x}}) \right). \qquad (4.69)
\end{aligned}$$

Because (4.68) is quadratic in $\mathbf{y} - \hat{\mathbf{y}}$ and both terms are greater or equal to zero, it is seen that (4.68) is minimized for

$$\mathbf{y} - \hat{\mathbf{y}} = -\mathbf{K}\mathbf{C}(\mathbf{x} - \hat{\mathbf{x}}). \tag{4.70}$$

Thus, it can be shown that $\mathbf{K}$ is unique since $\mathbf{Q}_y > 0$. The minimum is therefore

$$J(\mathbf{x}-\hat{\mathbf{x}}, \mathbf{y}-\hat{\mathbf{y}}) = (\mathbf{x}-\hat{\mathbf{x}})^T \left(\mathbf{Q}_x - (\mathbf{KC})^T \mathbf{Q}_y \mathbf{KC}\right)(\mathbf{x}-\hat{\mathbf{x}}). \tag{4.71}$$

By using the idea of completion of squares, it follows that $\alpha^T \bar{\mathbf{X}}[k+1]\alpha$ is minimized by $\mathbf{K}[k]$ satisfying

$$\mathbf{K}[k]\left(\mathbf{V}[k] + \mathbf{C}\bar{\mathbf{X}}[k]\mathbf{C}^T\right) = \mathbf{\Phi}\bar{\mathbf{X}}[k]\mathbf{C}^T, \tag{4.72}$$

for any α. If $\mathbf{V}[k] + \mathbf{C}\bar{\mathbf{X}}[k]\mathbf{C}^T$ is positive definite then

$$\mathbf{K}[k] = \mathbf{\Phi}\bar{\mathbf{X}}[k]\mathbf{C}^T\left(\mathbf{V}[k] + \mathbf{C}\bar{\mathbf{X}}[k]\mathbf{C}^T\right)^{-1}. \tag{4.73}$$

This inserted into (4.64) gives

$$\bar{\mathbf{X}}[k+1] = \mathbf{\Phi}\bar{\mathbf{X}}[k]\mathbf{\Phi}^T + \mathbf{\Gamma}\mathbf{W}[k]\mathbf{\Gamma}^T - \mathbf{\Phi}\bar{\mathbf{X}}[k]\mathbf{C}^T\left(\mathbf{V}[k] + \mathbf{C}\bar{\mathbf{X}}[k]\mathbf{C}^T\right)^{-1}\mathbf{C}\bar{\mathbf{X}}[k]\mathbf{\Phi}^T. \tag{4.74}$$

Theorem 4.1 *Åstrøm and Wittenmark (1997). The Kalman filter predictor case is defined by (4.56) and (4.57). It is optimal with respect to minimum variance of the error dynamics if* $\left(\mathbf{V}[k] + \mathbf{C}\bar{\mathbf{X}}[k]\mathbf{C}^T\right)$ *is positive definite, the disturbance and measurement error are Gaussian, and if the Kalman filter gain matrix is chosen as (4.73), where the covariance matrix of the error dynamics* $\bar{\mathbf{X}}[k+1]$ *is found by (4.74).*

Remark 4.4 *As long as* $\mathbf{E}[\mathbf{v}[k]] = \mathbf{0}$ *it is possible to show that the an unbiased estimate is possible to achieve.*

Remark 4.5 *Another notation of (4.74) is* $\bar{\mathbf{X}}[k|k-1]$*, indicating that the measurements up to and including* $k-1$ *are used. The term* $\mathbf{\Phi}\bar{\mathbf{X}}[k-1]\mathbf{\Phi}^T$ *shows the influence of system dynamics on the covariance matrix of the error dynamics.* $\mathbf{\Gamma}\mathbf{W}[k]\mathbf{\Gamma}^T$ *shows that the covariance matrix will increase for increasing process disturbance. The term*

$$-\mathbf{\Phi}\bar{\mathbf{X}}[k-1]\mathbf{C}^T\left(\mathbf{V}[k-1] + \mathbf{C}\bar{\mathbf{X}}[k-1]\mathbf{C}^T\right)^{-1}\mathbf{C}\bar{\mathbf{X}}[k-1]\mathbf{\Phi}^T, \tag{4.75}$$

shows how the variance is decreased accounting for information obtained through the measurements.

Remark 4.6 *Since* $\bar{\mathbf{X}}[k|k-1]$ *does not depend on any measurements and all other terms are assumed to be known, it is possible to precompute (4.73) and* $\bar{\mathbf{X}}[k|k-1]$.

Remark 4.7 *For LTI where* $\mathbf{\Phi}$ *,* $\mathbf{\Delta}$*,* $\mathbf{\Gamma}$ *and* $\mathbf{C}$ *are constant stationary solution of (4.73) can be found, where* $\bar{\mathbf{X}}[k+1] \to \bar{\mathbf{X}}_\infty$ *such that* $\mathbf{K}[k] \to \mathbf{K}_\infty$.

Kalman filter - filter case

Consider the LTI process given by (4.56) and (4.57). If the matrix $\left(\mathbf{V}[k] + \mathbf{C}\bar{\mathbf{X}}[k|k-1]\mathbf{C}^T\right)$ is positive definite, then the optimal filter can be found. The so-called *corrector* or *aposteriori estimate* is given by

$$\hat{\mathbf{x}}[k|k] = \bar{\mathbf{x}}[k|k-1] + \mathbf{K}_f[k]\left(\mathbf{y}[k] - \mathbf{C}\,\bar{\mathbf{x}}[k|k-1]\right). \tag{4.76}$$

The *predictor* or *apriori estimate* is given by

$$\begin{aligned}\bar{\mathbf{x}}[k+1|k] &= \mathbf{\Phi}\,\hat{\mathbf{x}}[k|k] + \mathbf{\Delta u}[k] + \mathbf{\Gamma}\bar{\mathbf{w}}[k|k], \\ &= \mathbf{\Phi}\,\bar{\mathbf{x}}[k|k-1] + \mathbf{\Delta u}[k] + \mathbf{\Gamma}\bar{\mathbf{w}}[k|k] + \mathbf{K}[k]\left(\mathbf{y}[k] - \mathbf{C}\,\bar{\mathbf{x}}[k|k-1]\right), \end{aligned} \tag{4.77}$$

where

$$\mathbf{K}_f[k] = \bar{\mathbf{X}}[k|k-1]\mathbf{C}^T\left(\mathbf{V}[k] + \mathbf{C}\bar{\mathbf{X}}[k|k-1]\mathbf{C}^T\right)^{-1}, \tag{4.78}$$

$$\mathbf{K}[k] = \mathbf{\Phi}\mathbf{K}_f[k]. \tag{4.79}$$

The covariance matrix of the estimation error dynamics is given by a so-called *Ricatti equation* according to

$$\bar{\mathbf{X}}[k+1|k] = \mathbf{\Phi}\bar{\mathbf{X}}[k|k-1]\mathbf{\Phi}^T + \mathbf{\Gamma}\mathbf{W}[k]\mathbf{\Gamma}^T - \mathbf{K}[k]\left(\mathbf{V}[k] + \mathbf{C}\bar{\mathbf{X}}[k|k-1]\mathbf{C}^T\right)\mathbf{K}[k]^T \tag{4.80}$$

$$\bar{\mathbf{X}}[k|k] = \bar{\mathbf{X}}[k|k-1] - \bar{\mathbf{X}}[k|k-1]\mathbf{C}^T\left(\mathbf{V}[k] + \mathbf{C}\bar{\mathbf{X}}[k|k-1]\mathbf{C}^T\right)^{-1}\mathbf{C}\bar{\mathbf{X}}[k|k-1] \tag{4.81}$$

$$\bar{\mathbf{X}}[0|-1] = \bar{\mathbf{X}}_0. \tag{4.82}$$

In Figure 4.7 the Kalman filter is illustrated graphically.

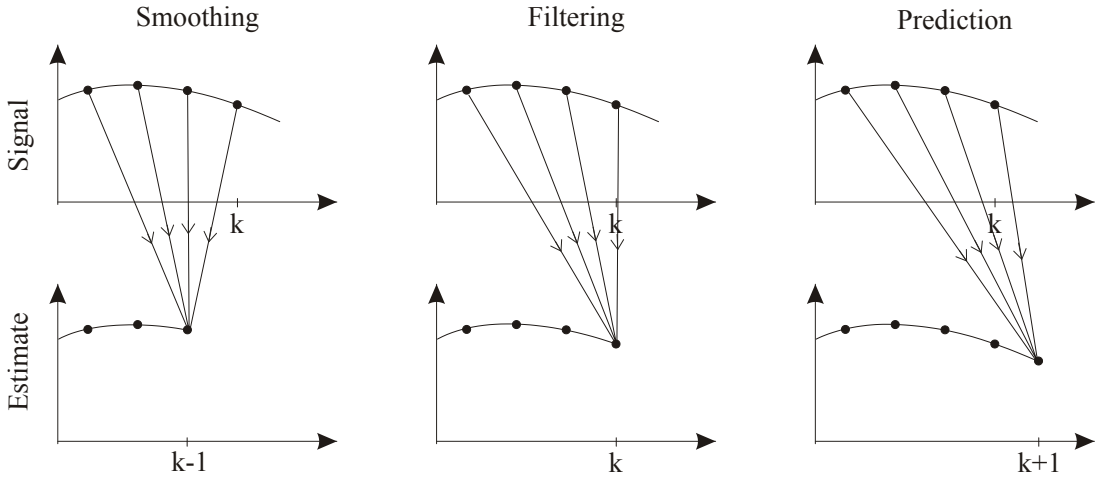

Figure 4.7: Discrete Kalman filter.

Remark 4.8 *The notation* $\bar{\mathbf{X}}[k|k-1]$ *is used to specify the available data. Notice that* $\bar{\mathbf{X}}[k|k]$ *is the variance of the estimation error dynamics at time* k *given* $\mathbf{Y}_k$*.*

Remark 4.9 *The innovation given by* $\epsilon[k] = \mathbf{y}[k] - \hat{\mathbf{y}}[k] = \mathbf{y}[k] - \mathbf{C}\bar{\mathbf{x}}[k|k-1]$ *will be white noise in a Kalman filter given as above.*

Remark 4.10 *In dead reckogning (with a failure in sensor* i *and thus loss of* $y_i[k]$*) the corresponding innovation will be set to* $\epsilon_i[k] = 0$*. Hence, only the predictor (4.77) will be active. Usually the predicted state* $\bar{x}_i[k]$ *becomes less noisy and sluggish without the corrector. Depending on the external disturbances and the accuracy of the model, the control performance may be satisfactory for quite long time. In dynamic positioning dead reckogning with satisfactory control performance up to several minutes has been experienced.*

4.3.5 Stochastic Nonlinear State Estimation: Extended Kalman Filtering

In the previous section we assumed that the process dynamics could be described by a LTI system. However, in many cases the process will be nonlinear. In marine applications conduction dynamic positioning the kinematics relating Earth-fixed coordinates to vessel-fixed coordinates represents such an nonlinearity. This will be explained more in detail later on. A common way to circumvent the problem of nonlinearities is to introduce a so-called *extended Kalman filter*, which is briefly described in the following. Consider a nonlinear time-variant state-space model on discrete form

$$\begin{aligned} \mathbf{x}[k+1] &= \mathbf{f}_k(\mathbf{x}[k], \mathbf{u}[k]) + \mathbf{\Gamma}\mathbf{w}[k] \\ \mathbf{y}[k] &= \mathbf{h}_k(\mathbf{x}[k]) + \mathbf{v}[k] \end{aligned} \tag{4.83}$$

In the extended Kalman filter, linearizations of the nonlinear dynamics $\mathbf{f}[k]$ and measurement $\mathbf{h}[k]$ are made about the current state estimate according to

$$\mathbf{\Phi}[k] = \left.\frac{\partial \mathbf{f}_k(\mathbf{x}[k], \mathbf{u}[k])}{\partial \mathbf{x}[k]}\right|_{\mathbf{x}[k]=\hat{\mathbf{x}}[k]} \tag{4.84}$$

$$\mathbf{C}[k] = \left.\frac{\partial \mathbf{h}_k(\mathbf{x}[k])}{\partial \mathbf{x}[k]}\right|_{\mathbf{x}[k]=\hat{\mathbf{x}}[k]} \tag{4.85}$$

$\mathbf{\Phi}[k]$ and $\mathbf{C}[k]$ may then be substituted for $\mathbf{\Phi}$ and $\mathbf{C}$ in the equations for the discrete Kalman filter (see above) such that the Kalman filter gain matrix $\mathbf{K}$ must be updated for each linearization, see above. In practice, we often make local linearized models about a set of predefined operating points and then apply individual precalculated Kalman filters for each model. By using proper gain scheduling techniques the correct filter model will be applied. The reader is referred to Bagchi (1993) for details.

Chapter 5

Signal Quality Checking and Fault Detection

All industrial control systems contains several functions for signal quality checking. The performance of the control system including state estimation and control depends on that these functions operate properly. In this chapter the most important signal processing properties for the purpose of control will be treated.

Learning outcome of the chapter: The reader shall understand:

- Why signal testing of sensor measurements is important for the control system.
- Testing and signal quality control of individual sensor signals.
- Handling of redundant sensor signals.

5.1 Introduction

Accurate control performance depends on reliable sensor signals. Unreliable signals from the sensors will influence the control systems capability for accurate and safe performance. Therefore poor signal quality should be detected, and the available information should be utilized in an optimal way, see Figure 5.1. Each signal should be checked for errors and bad signals should be rejected in a *signal processing module*. For many safety critical marine operations redundancy in instrumentation is required by the authorities. This means that two or more sensors measuring the same state are installed and interfaced to the control system. The redundant sensors could be of same type, or they could be different. For instance in dynamic positioning having redundancy in measuring the vessel position in North-East coordinates, two Differential Global Positioning Systems (DGPS) may be installed. The GPS is a satellite based positioning system. Even better, one DGPS and one hydroacoustic positioning reference (HPR) system could be installed. The HPR is an underwater based positioning system. In the last case redundancy is also achieved both in hardware, software and in the measuring principle. As we will see in Section 2.9 the authorities requires three or more number of sensors for conducting dynamic positioning in the most safety critical operations where loss of position could cause fatal accidents, severe pollution or damages with major economic consequences. This is defined as *equipment* or *consequence class 3* operation. This means that if one of the three sensors fails, the dynamic positioning operation

must be stopped. In order to increase the overall availability and reduce the days of off-hire, the ship owner then may decide to install a fourth and even a fifth system. Having redundant sensor signals available put additional requirements to the signal processing concerning signal weighting (which one should be trusted most), and signal drifting (signal voting may be used to reject a sensor with large deviation). Hence, handling of multiple signals in an consistent manner is crucial ensuring a safe and optimal operation.

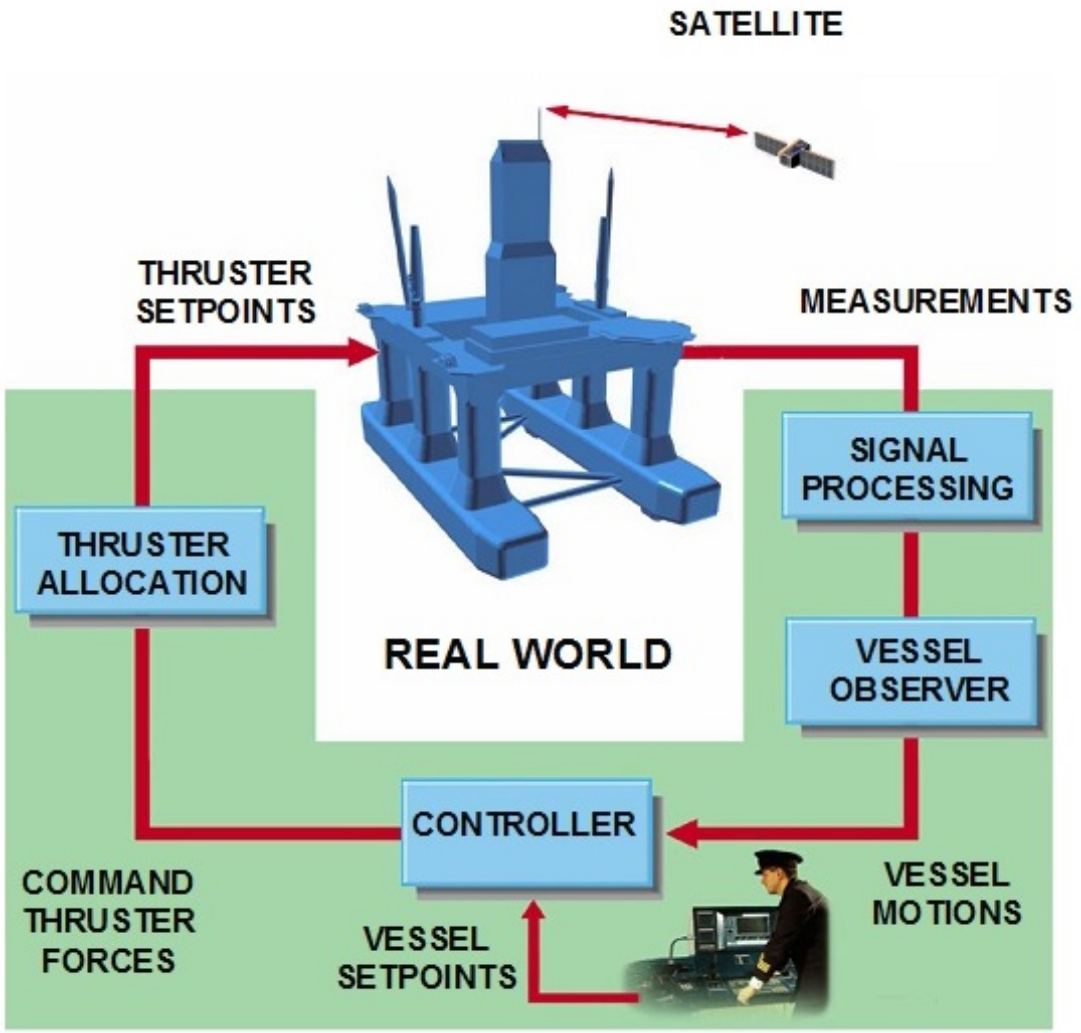

Figure 5.1: Controller architecture.

5.2 Testing of Individual Signals

A signal processing module (Figure 5.1) should perform quality checking of all sensor signals, position reference system signals and thrust device feedback signals. Single signal quality checking will include different tests such as:

- Signal range testing.

- Variance testing.
- Wild point testing.

The set of the tests above may be performed for every signal. If a failure situation is detected, the signal is unusable and the signal should be rejected.

5.2.1 Windowing

Different formulas based on different techniques for *windowing* for calculating a signal variance can be used. Windowing is the operation of taking a signal $x[k]$ and multiplying it by a finite-duration *window* signal $w[k]$. That is,

$$p[k] = x[k]w[k]. \tag{5.1}$$

Then $p[n]$ is also of finite duration. In practice we are only able to measure a signal $x[k]$ over a finite time interval, *time window*. The actual signal available for analysis is then

$$p[k] = \begin{cases} x[k], & -M \leq k \leq M \\ 0, & \text{otherwise,} \end{cases} \tag{5.2}$$

where $-M \leq k \leq M$ is the time window.

Using a rectangular window the finite-duration window signal is written

$$w[k] = \begin{cases} 1, & -M \leq k \leq M \\ 0, & \text{otherwise.} \end{cases} \tag{5.3}$$

One of the problems using rectangular window is that it may introduce ripples on the Fourier transform. This is related to the so-called Gibbs phenomenon. Other techniques using exponential window and Hanning window may improve this situation. For details Oppenheim and Willsky (2013) and Christiansen (1996).

5.2.2 Signal Range Testing

Most of the signals available have a defined range. An example of this is the gyro sensor, whose heading output is in the range of $0 - 360^{\text{o}}$. If the signal processing module receives a gyro signal outside this range, it assumes that the sensor signal is faulty and will therefore reject it. Thus it is required that the signal is within a set of allowed values defined by a minimum value $x_{\min}$ and a maximum value $x_{\max}$ according to

$$x[k] \in [x_{\min}, x_{\max}]. \tag{5.4}$$

5.2.3 Variance Testing

The signal variance gives an indication about the variations in amplitude and frequency of a signal. For instance, a high level of measurement noise gives high variance and vice versa. However, the signal variance may also be high due to a high level of process noise, i.e. heavy seas. This is not a failure situation and should therefore be reflected in the calculations.

Consider the sequence $\{x[k]\}$ at $t = k$ consisting of the signal itself and $n-1$ historical values according to

$$\{x[i] : i = k - (n-1), ..., k-1, k\}. \tag{5.5}$$

The average value of the sequence $\bar{x}_k$ can be calculated to be

$$\bar{x}_k = \frac{1}{n} \sum_{i=k-(n-1)}^{k} x[i]. \tag{5.6}$$

The corresponding variance is then found to be

$$\sigma_k^2 = \frac{1}{n-1} \left(\sum_{i=k-(n-1)}^{k} x[i]^2 - n\bar{x}_k^2 \right). \tag{5.7}$$

Let us define

$$y[k] = \frac{1}{n} \sum_{i=k+1-(n-1)}^{k} x[i]^2. \tag{5.8}$$

On recursive form (5.7) can be written as

$$\sigma_{k+1}^2 = \frac{n}{n-1} \left(y[k+1] - (\bar{x}[k+1])^2 \right), \tag{5.9}$$

where

$$y[k+1] = y[k] + \frac{1}{n} \left((x[k+1])^2 - (x[k-(n-1)])^2 \right). \tag{5.10}$$

High variance may be a symptom of a sensor failure or inaccurate measurement. A frozen signal can indicate a failure in a sensor, leading to zero variance. Hence, both an upper and a lower limit is considered in the variance test, see Figure 5.2.

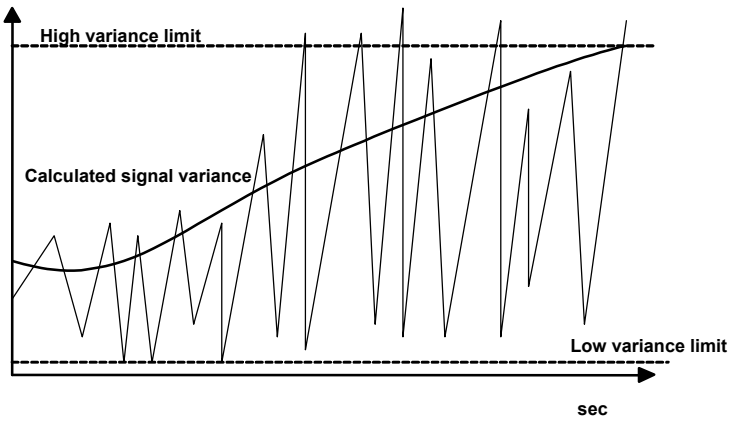

Figure 5.2: Signal variance test.

5.2.4 Wild Point Testing

If a wild point is detected, this measurement should be rejected for one sample. A wild point is a measurement that deviates considerably from the previous measurements, that is, it is outside a certain band about the estimated mean signal, see Figure 5.3. The sampled value $x[k]$ may be accepted if

$$x[k] \in [\bar{x}_k - a\sigma, \bar{x}_k + a\sigma], \tag{5.11}$$

where a often is set to be in the interval $3 - 9$. Normally, the wild point is replaced by a calculated value. This could be the value from the previous sample, the mean value or an estimated minimum variance value.

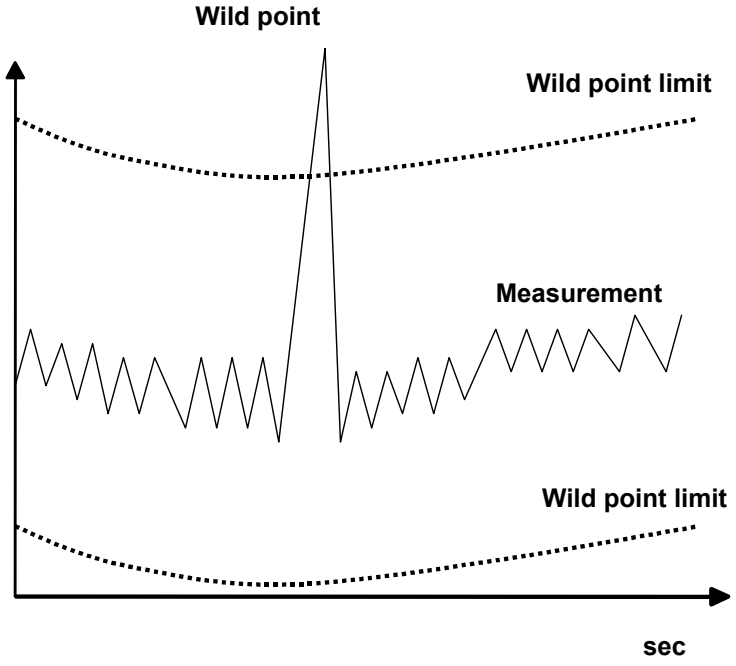

Figure 5.3: Wild point test.

5.3 Handling of Redundant Measurements

For redundant sensor or position reference system configurations, the possibilities for fault detection, weighting and voting are improved. Signals from different sensors or position reference systems are compared and the difference between them will indicate a failure situation. Weighting principles are used for calculation of optimal input data to the controller algorithm.

5.3.1 Voting

The signal processing module provides two levels of voting for detection of drifting of sensors and position reference systems.

If two sensors or position reference systems are available, the signal processing module can detect drifting (bias) between the two sources. However, it is not able to detect which sensor or position reference system that has failed unless an individual signal erroneous situation is detected. Anyway, the operator receives a warning that a signal is detected.

If three or more sensors are available, the signal processing module is also able to carry out voting in order to detect whether one of the signals are truly drifting. Figure 5.4 illustrates this situation. The three measurements are different, but it seems that sensor no 2 deviates from sensor no 1 and no 3. The voting algorithm will reject sensor no 2 when the deviation exceeds a defined limit.

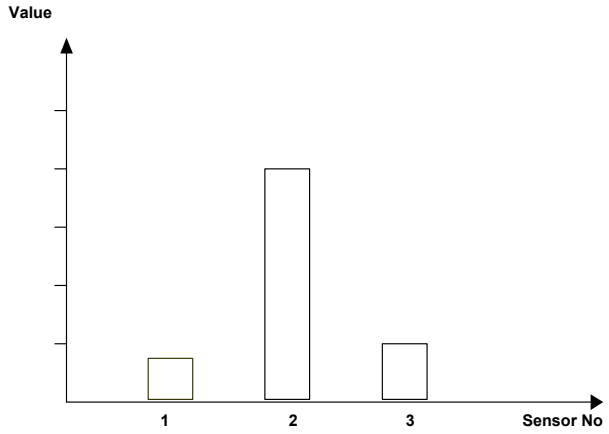

Figure 5.4: Voting of redundant measurements.

5.3.2 Weighting

For redundant sensor or position reference system configurations the signal processing module performs a weighting of the individual signal before in order to calculate the optimal average signals. The individual signal weighting factors are either calculated automatically based on the signal variance or set manually. A sensor which has high variance compared to the other sensors will, in the automatic case, have a correspondingly low weighting factor and influence on the weighted signal. However, if the variance is too low (frozen signal) the signal is discarded from the weighting calculation.

The equation below illustrates calculation of a weighted sensor measurement, x_w. Assume that three sensor measurements are available, x_1, x_2 and x_3, with weighting factors w_1, w_2 and w_3, then the weighted measurement becomes

$$x_w = \frac{w_1 x_1 + w_2 x_2 + w_3 x_3}{w_1 + w_2 + w_3}. \tag{5.12}$$

Consider an unbiased estimated signal consisting of a sum of n independent weighted signal according to

$$\hat{x} = \sum_{i=1}^{n} s_i x_i, \tag{5.13}$$

where

$$\sum_{i=1}^{n} s_i = 1. \tag{5.14}$$

The weighting factors can be set manually by an operator or automatically calculated based on the principle of minimum variance. For manual weighting we have

$$s_i = \frac{w_i}{\sum_{k=1}^{n} w_k}. \tag{5.15}$$

For automatic weighting consisting of two measurements the weights become

$$s_1 = \frac{\sigma_2^2}{\sigma_1^2 + \sigma_2^2}, \tag{5.16}$$

$$s_2 = \frac{\sigma_1^2}{\sigma_1^2 + \sigma_2^2}. \tag{5.17}$$

Notice that a higher variance in one of the signals results in higher weight in the remaining signal. The general automatic weighting algorithm for n signals can be written

$$s_i = \frac{\prod_{j \neq i} \sigma_j^2}{\sum_{k=1}^{n} \prod_{j \neq k} \sigma_j^2}. \tag{5.18}$$

5.3.3 Enabling and Disabling of Sensors

Operator initiated disabling or an abrupt loss of a sensor can lead to the signal deviation effect shown in Figure 5.5. This can be avoided by filtering the signal average a specific time period after the loss of signal has occurred, illustrated by Figure 5.6. The filter should be activated subject to an *event* indicating the loss of the sensor signal. An appropriate time period T_f depending on a signal difference and a maximum change rate should be specified. A change in the average value is inevitable after a signal loss but the filtering will prevent the unwanted response.

Let y_w denote the new calculated weighted signal after the failure situation. Then, the filtered weighted signal y_{fw} entering the control system could be found by solving the lowpass equation below

$$\dot{y}_{fw} = -\frac{1}{T_f} y_{fw} + \frac{1}{T_f} y_w. \tag{5.19}$$

The filtering should not inflict a phase change of the measurement too much. When enabling a sensor, the signal will remain smooth and no filtering is necessary.

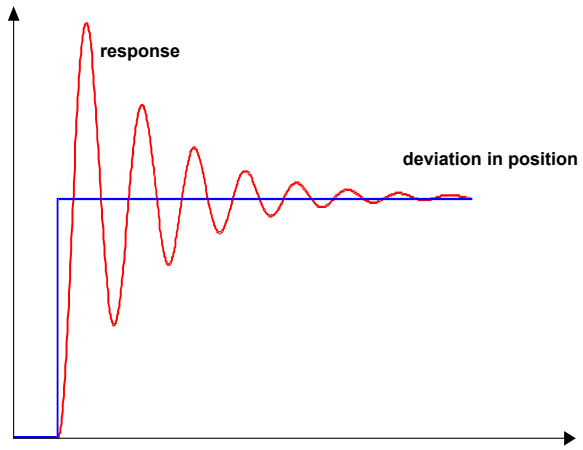

Figure 5.5: Effect of step in position measurement.

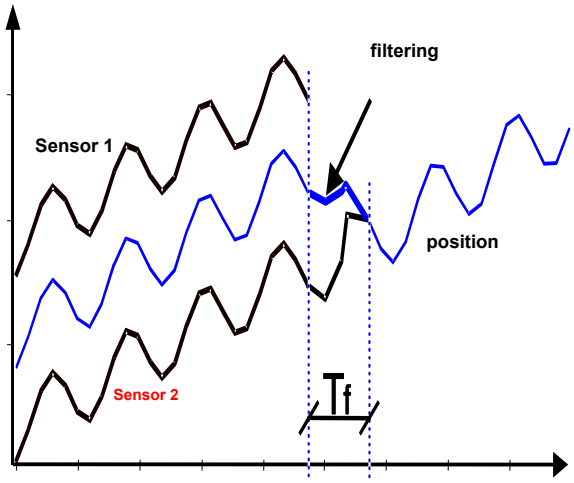

Figure 5.6: Filtering of position average.

Chapter 6

Mathematical Modeling: Hydrodynamics

In this chapter the mathematical models used in the design of marine control systems such as dynamic positioning systems and thruster assisted position mooring systems are formulated. The intention here is to focus on the structural properties of the models important for control, rather than going into details about calculation of the hydrodynamic models and coefficients.

Learning outcome of the chapter: The reader shall understand:

- The purpose of mathematical modeling including why we formulate models with different complexity or fidelity.
- How to formulate environmental models of wind, wave and wave behaviors.
- How to formulate kinematic relations between the various reference frames used in modeling and control of floating vessels, structures and underwater vehicles.
- How to formulate mathematical models of loads and motions of floating vessels, structures and underwater vehicles.
- How to formulate cable models based on catenary equations. Cables models may be used in marine operations to describe mooring systems and suspended loads handled by cranes.

6.1 Introduction

Depending on the operational conditions the vessel models may briefly be classified into *station keeping,* low velocity and high velocity models (Figure 6.1). Considering vessel motions in waves is defined as *sea keeping* and will here apply both for station keeping (zero speed) and forward speed. Dynamically positioning (DP) of vessels or thruster assisted position mooring (PM) of anchored marine vessels can in general be regarded as station keeping and low velocity or low Froude number applications. This assumption will particularly be used in the formulation of mathematical models used in conjunction with the controller design. Notice that the manoeuvring models often assumes low-frequency motions only, where the effect of wave-frequency motions is included afterwards by linear superposition.

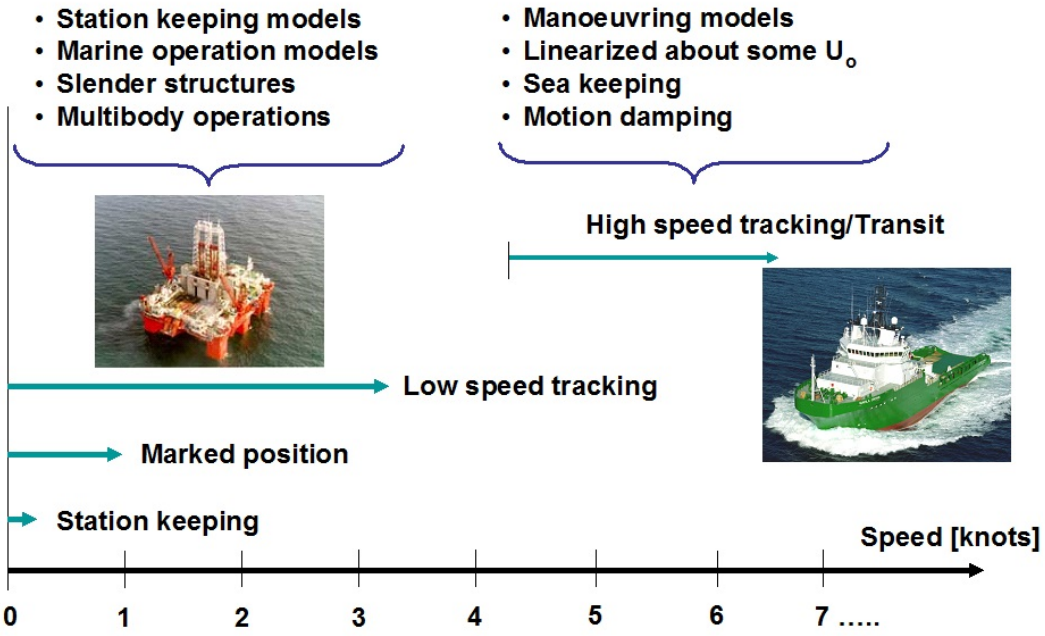

Figure 6.1: Modeling properties.

Easy access to computer capacity, and the presence of efficient control system design toolboxes, such as Matlab, Simulink and others, have motivated more extensive use of numerical simulations for design and verification of control systems. Essential in being successful in this is the ability to make sufficiently detailed mathematical models of the actual plant or process. From an industrial point of view, the same tendency is driven by the fact that control system safety and performance testing by hardware-in-the-loop (HIL) simulations contribute to reduced time for tuning during commissioning and sea trials and, not at least, reduced risk for incidents during operation caused by software bugs and erroneous control system configurations.

In controller design it is important to consider any coupling effects between the different degrees of freedom and subsystems, in addition to the natural periods (resonances) of the dynamic system, e.g. vessel, riser and mooring in open-loop (without control) and closed-loop (with control). The coupling effects and natural periods may be excited by the environmental loads or unintentionally by the control system itself if not properly accounted for in the design process. In Figure 6.2, typical natural periods for ships, semisubmersibles, risers and mooring system are given in addition to periods of wave loads. The working range or the bandwidth of a DP system is also indicated.

For the purpose of model-based observer and controller design, it is sufficient to derive a simplified mathematical model, which nevertheless is detailed enough to describe the main physical characteristics of the dynamic system. Then, structural information of the physical properties of the dynamic system is incorporated in the controller design in order to achieve a

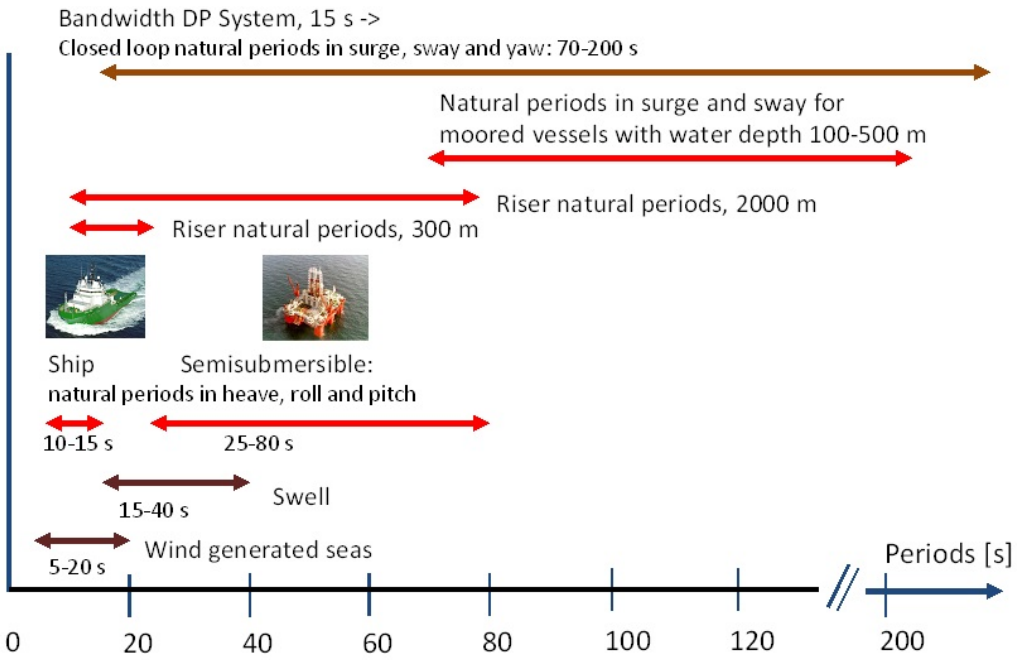

Figure 6.2: Periods of interest.

better performance and robustness compared to the conventional PID control design methods. For processes dominated by nonlinearities, it has also been experienced that nonlinear model-based control design will simplify the overall control algorithm since linearizations about different working points is avoided.

Hence, the mathematical models may be formulated in two complexity levels:

- *Control plant model* s a simplified mathematical description containing only the main physical properties of the process or plant. This model may constitute a part of the controller. The control plant model is also used in analytical stability analysis based on e.g. Lyapunov stability and passivity.

- *Process plant model* or *simulation model* is a comprehensive description of the actual process and should be as detailed as needed using high fidelity models. The main purpose of this model is to simulate the real plant dynamics. The process plant model is used in numerical performance and robustness analysis and testing of the control systems.

Due to the lack of process knowledge and thereby proper models, control plant models are often used as process plant models. This may result in bad controller designs, since "perfect"

models are assumed. In some control literature *calibration model* is used to describe the process plant model and *nominal or control model* is used to describe the control plant model.

This section will focus on the formulation of *process plant models*. In this context it means mathematical models of the vessel dynamics and external forces and moments, in terms of environmental loads, thruster/propeller forces and mooring forces (if any), acting on the vessel. Description of the *control plant models* will be presented in the controller design sections.

6.2 Environmental Models

Environmental models are essential for achieving realistic simulations of a marine vessel. Section 6.4 describes the environmental loads on the vessel, whereas this section describes environmental models for waves, wind and current.

6.2.1 Waves

Irregular waves are commonly described by a wave spectrum $S(\omega, \psi)$, which in general is a function of both frequency ω and direction ψ (Faltinsen, 1993). The wave spectrum is often divided in a frequency spectrum $S(\omega)$ and a directional spreading function $D(\psi, \omega)$, such that

$$S(\omega, \psi) = S(\omega)D(\psi, \omega). \tag{6.1}$$

The integral over all frequencies and directions represents the total energy in the sea state S_{tot}

$$S_{tot} = \int_0^\infty \int_0^{2\pi} S(\omega, \psi) d\psi d\omega. \tag{6.2}$$

Linearity is assumed, so that the harmonic wave components extracted from the spectrum may be superposed.

Frequency spectrum

The frequency spectrum $S(\omega)$ describes the energy distribution of the sea state over different frequencies, with the integral over all frequencies representing the total energy of the sea state. From a given spectrum, a set of harmonic wave components representing the total energy may be extracted by choosing a set of frequencies (ω_q) and frequency intervals ($\Delta\omega_q$) such that the whole area below the spectral curve is covered, see Figure 6.3. In the limiting case, where the number of wave components $n \to \infty$, and such $\Delta\omega_q \to 0$, this approaches the Riemann integral over $S(\omega)$. The amplitude ζ_{aq} of one wave is determined from the spectral value $S(\omega_q)$ by the formula

$$\zeta_{aq} = \sqrt{2S(\omega_q)\Delta\omega_q}. \tag{6.3}$$

In the following we will use a constant frequency interval $\Delta\omega$. The harmonic waves are assumed to have phase angles (ϕ_q) that are evenly distributed between 0 and 2π. Each component is then described by

$$\zeta_q(t) = \zeta_{aq} \cos(\omega_q t + \phi_q). \tag{6.4}$$

Note that these harmonic waves represent the total wave energy with waves in only one direction. To include different wave directions, a spreading function must be added. The maximum

frequency included in the realization of the wave spectra is denoted $\omega_{\max}$. The frequency spectrum is commonly defined in terms of the significant wave height H_s and the peak frequency ω_p. H_s is the average height of the 1/3 largest waves in the sea state, and ω_p is the frequency that contains the most energy in the sea state (i.e. defines the peak of the frequency spectrum). Notice that the wave height is defined as the distance from the bottom of a wave trough to the top of a wave peak, and hence is twice the wave amplitude.

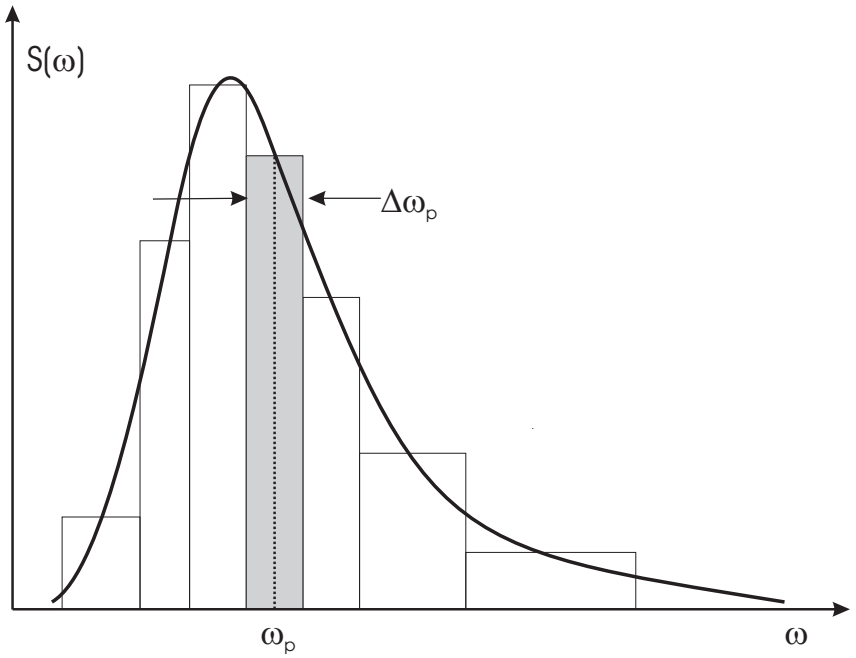

Figure 6.3: Wave spectrum as function of frequency.

Spreading function

The spreading function $D(\psi, \omega)$ gives the directional distribution of wave energy, spanned about the mean wave direction ψ_o. It is in general a function of both direction and frequency, but is often simplified to be a function of only direction. The integral over all directions $(-\pi, \pi)$ must be unity, so that the total wave energy in the sea state is kept unchanged. To obtain "scaling factors" for the wave amplitudes in different directions, a set of directions (ψ_r) and direction intervals $(\Delta\psi_r)$ must be chosen such that the whole area below the curve is covered, in the same way as with the frequency spectrum, see Figure 6.4. In the following we will use a constant direction interval $\Delta\psi$.

Wave spectrum

The wave spectrum $S(\omega, \psi)$, composed of the frequency spectrum and spreading function as in (6.1), now represents the energy distribution over both frequencies and directions. The integral over all directions equals the frequency spectrum $S(\omega)$, and the double integral over all directions

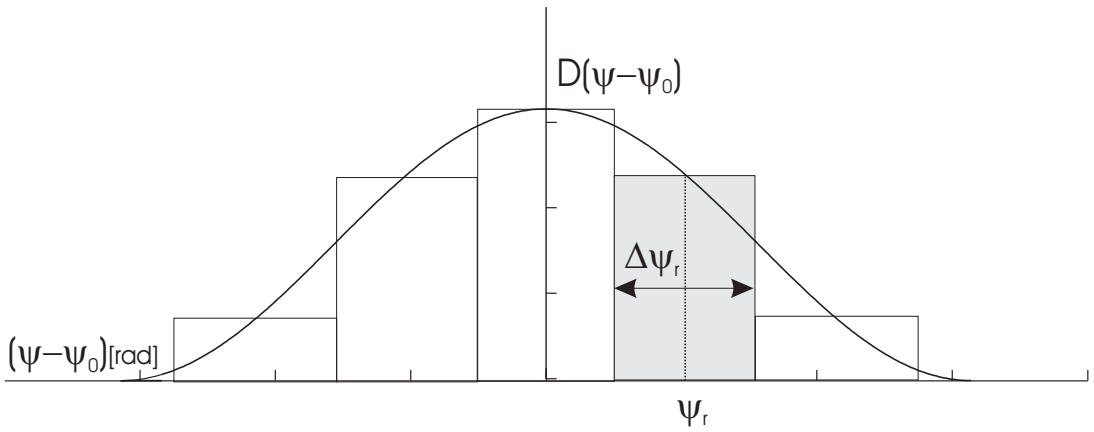

Figure 6.4: Spreading function.

and frequencies equals the total wave energy

$$\int_0^\infty \int_{\psi_0-\pi}^{\psi_0+\pi} S(\omega,\psi)d\psi d\omega = \int_0^\infty S(\omega)d\omega. \tag{6.5}$$

Figure 6.5 shows a wave spectrum , where each square composed of a $\Delta\omega$ and a $\Delta\psi$ represents one harmonic wave amplitude. The wave amplitude ζ_{aqr} is found by a modification of (6.3)

$$\zeta_{aqr} = \sqrt{2S(\omega_q,\psi_r)\Delta\omega\Delta\psi}. \tag{6.6}$$

One harmonic wave component is now represented by four parameters: Direction ψ_r, frequency ω_q, amplitude ζ_{aqr} and phase angle ϕ_{qr}. Note that the phase angles of *all* wave components are evenly distributed between 0 and 2π. In an Earth-fixed coordinate system, the surface elevation in the coordinate (x, y) will be given as

$$\zeta_{qr}(x,y,t) = \zeta_{aqr}\sin[\omega_q t + \phi_{qr} - k_q(x\cos\psi_r + y\sin\psi_r)]. \tag{6.7}$$

k_q is the wave number, which equals $2\pi/\lambda_q$, where λ_q is the wave length. For deep water, the dispersion relation $\omega_q^2 = kg$, where g is the acceleration of gravity, gives the wave number from the wave frequency. The coordinate system is defined so that waves with zero heading ($\psi_r = 0$) are propagating towards north. The total surface elevation of all wave components at the point (x, y) at time t for N frequencies and M directions will then be

$$\zeta(x,y,t) = \sum_{q=1}^{N}\sum_{r=1}^{M}\sqrt{2S(\omega_q,\psi_r)\Delta\omega\Delta\psi}\sin(\omega_q t + \phi_{qr} - k_q(x\cos\psi_r + y\sin\psi_r)). \tag{6.8}$$

Remark 6.1 *Please notice that similar equations in e.g. Faltinsen (1993) are given with different coordinate system conventions, and thus differ from the equation above.*

Implementation considerations

Several modifications of the wave spectrum defined by (6.8) can be made in order to facilitate more realistic simulations when it is desired to keep the number of wave components as low as possible (and hence reduce computational effort).

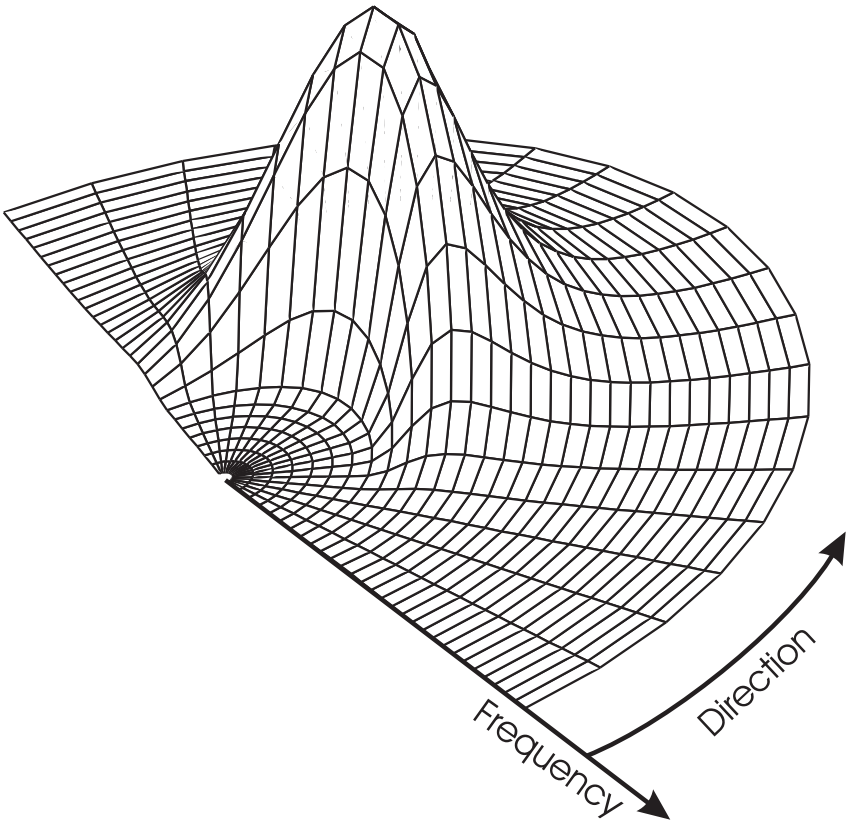

Figure 6.5: Wave spectrum as function of frequency and direction.

Random frequencies and directions The expression in (6.8) will repeat itself after the time $T = 2\pi/\Delta\omega$. This means that a large number of wave components should be used, but as this is computationally demanding, a better solution is to choose a random frequency within each frequency interval $(\omega_q - \Delta\omega/2, \omega_q + \Delta\omega/2)$ (Faltinsen, 1993). To further increase realism, the direction may also be chosen at random within each direction interval $(\psi_r - \Delta\psi/2, \psi_r + \Delta\psi/2)$. The number of wave components is according to Faltinsen still recommended to be as high as 1000.

Removing insignificant components If implementing (6.8), with or without random frequencies and directions, the total number of harmonic wave components n_{grid} is the product of the number of directions in the grid and the number of frequencies in the grid, $n_{grid} = N \cdot M$. However, both for high and low frequencies, as well as for directions far from the mean wave directions, the wave spectrum contains little energy. This means that the wave components generated from the these areas have small amplitudes, and hence contribute little to the total sea state.

A way of reducing computational effort is therefore to avoid having too many wave components with close to zero amplitude. A first step at solving this is to choose the maximum frequency of the realization of the spectrum, $\omega_{\max}$, as low as possible, see Figure 6.3, and thereby avoid including insignificant wave components from the tail of the frequency spectrum. An easy way of implementing this for varying peak frequencies in the spectrum is to define a frequency

cutoff factor ξ such that

$$\omega_{\max} = \xi\omega_p. \tag{6.9}$$

ξ would typically be in the interval $(2, 3)$. A second step is to replace the outer limits of the direction spectrum $(\psi_0 - \pi, \psi_0 + \pi)$ with user-defined limits $(\psi_0 - \psi_{\lim}, \psi_0 + \psi_{\lim})$, see Figure 6.4, and thereby avoid including insignificant wave components from the outer limits of the direction spectrum. $\psi_{\lim}$ can be chosen larger for spreading functions with most energy centered about the mean direction than for spreading functions with much energy far from the mean direction. A typical maximum value for $\psi_{\lim}$ would be approximately 65°.

A more effective way of removing the insignificant wave components is to do a test of the energy content of each wave component, and then discard the components with little energy. Two ways of doing this is:

1. Choose a fixed number of waves, n_{waves}, which naturally must satisfy $n_{waves} \leq n_{grid}$. Find the energy $S(\omega_q, \psi_r)$ of each wave component and sort them in descending order. Then choose the n_{waves} first components for the simulation. The upside to this approach is that you get a user-defined number of waves. The downside is that you have no guarantee of not loosing any significant wave components. If $n_{waves} = n_{grid}$, all wave components are used.

2. Choose a relative wave component energy limit $\kappa \in (0, 1)$ and discard all wave components which contain less than this ratio of the total sea state energy S_{tot}:

$$\frac{S(\omega_q, \psi_r)}{S_{tot}} < \kappa \Rightarrow \text{component discarded.} \tag{6.10}$$

   The upside to this approach is that you are guaranteed that all components with energy above the user-defined limit is kept. The downside is that you don't have control over the number of waves. If $\kappa = 0$, all wave components are used.

Common wave spectra

Common frequency spectra are the Pierson-Moskowitz (PM) spectrum, the ITTC/ISSC spectrum , the JONSWAP spectrum. and the more recent doubly peaked spectrum by Torsethaugen.

PM/ITTC/ISSC spectra The PM type spectra have the general form

$$S(\omega) = \frac{A}{\omega^5} \exp(-\frac{B}{\omega^4}). \tag{6.11}$$

They apply to fully developed sea states in open seas. The PM spectrum is given from wind speed V at 19.5 meters height

$$A = 0.0081g^2; \quad B = 0.74(g/V)^4. \tag{6.12}$$

The peak frequency of the spectrum, ω_p, may be used in place of the wind speed, giving

$$A = 0.0081g^2; \quad B = \frac{5}{4}\omega_p^4. \tag{6.13}$$

The ITTC and ISSC spectra are identical for open seas, and given by the significant wave height H_s and peak wave frequency ω_p

$$A = 0.31H_s^2\omega_p^4; \quad B = 1.25\omega_p^4. \tag{6.14}$$

H_s and ω_p are interdependent and must be chosen with care.

JONSWAP spectrum The JONSWAP spectrum may according to Faltinsen (1993) be formulated as

$$S(\omega) = \alpha \frac{g^2}{\omega^5} \exp[-\frac{5}{4}(\frac{\omega_p}{\omega})^4]\gamma^{\exp[-\frac{1}{2}(\frac{\omega-\omega_p}{\sigma\omega_p})^2]}, \tag{6.15}$$

α, γ and σ are parameters to be determined, and ω_p is the peak frequency of the spectrum. γ is a peak parameter, and may vary between 1 and 7. For $\alpha = 0.0081$ and $\gamma = 1$, the JONSWAP spectrum is identical to the PM spectrum. The JONSWAP spectrum was developed after measurements in an area of the North Sea which is relatively shallow and close to land. It is a spectrum for not fully developed seas, with a much sharper peak than the PM type spectra. Increasing γ gives a sharper peak of the spectrum. Faltinsen (1993) recommends the following values for the JONSWAP parameters

$$\gamma = 3.3, \quad \sigma = \begin{cases} 0.07 & \omega \leq \omega_p \\ 0.09 & \omega \geq \omega_p \end{cases} \quad ; \quad \alpha = 0.2\frac{H_s^2\omega_p^4}{g^2}. \tag{6.16}$$

To keep within the validity area of the spectrum it is suggested the following constriction on H_s and ω_p

$$1.25/\sqrt{H_s} < \omega_p < 1.75/\sqrt{H_s}. \tag{6.17}$$

If no information on γ is available, DNV GL proposes the following γ based on H_s and ω_p :

$$k = \frac{2\pi}{\omega_p\sqrt{H_s}},$$

$$\begin{array}{ll} k \leq 3.6 \Rightarrow & \gamma = 5, \\ k \leq 5.0 \Rightarrow & \gamma = e^{(5.75-1.15k)}, \\ k > 5.0 \Rightarrow & \gamma = 1. \end{array} \tag{6.18}$$

Doubly peaked (Torsethaugen) spectrum The spectra presented above may all be termed wind generated, and have been criticized for not giving a good representation of the low-frequency wave energy, or swell. Torsethaugen developed a doubly peaked wave spectrum; a low frequency peak due to swell, and a high frequency peak due to locally wind generated waves. The spectrum was developed by curve fitting of experimental data from the North Sea, and was standardized under Norsok (2018). All parameters are found by the significant wave height and spectral peak period. The total wave spectrum is a sum of two spectral peaks, called primary and secondary. For fully developed seas, the secondary peak vanishes, and the wave energy is centered in a narrow peak about the spectral peak period $T_p = 2\pi/\omega_p$. For the same significant wave height H_s, primary peak periods higher than the value for fully developed seas can only be due to swell components, with a secondary peak of locally wind generated waves. For lower primary peak periods, the total energy cannot be set up by local winds alone, and an additional secondary swell peak is needed. For $T_p > 6.6H_s$, the primary peak is in the swell generated, and for $T_p < 6.6H_s$, the primary peak is in the wind generated. When the sea state is dominated by swell, the shape of the wave specter will differ significantly from the JONSWAP and PM wave spectra The formulation of the doubly peaked spectrum is not presented here, but it is implemented in the Marine Systems Simulator Fossen and Perez (2004) GNC Toolbox as $[\omega, S] = torset(H_s, \omega_p, \omega_{\max}, N)$, where $\omega_{\max}$ is the maximum frequency and N the number of wave components.

Comparison of the spectra Figure 6.6 shows a comparison of the PM, ITTC and JONSWAP spectra, all for $H_s = 6$ and $\omega_p = 1.5/\sqrt{H_s} \approx 0.61$. The PM spectrum does not account for the actual wave height, and contains less energy than the two others. The ITTC and JONSWAP spectra contains approximately the same amount of energy, but the JONSWAP spectrum has more of this energy close to ω_p. Figure 6.7 shows how the doubly peaked spectrum varies with the peak frequency for constant H_s. The two spectra with thick lines are examples of a primary swell spectrum (largest peak for low frequencies) and a primary wind-generated spectrum.

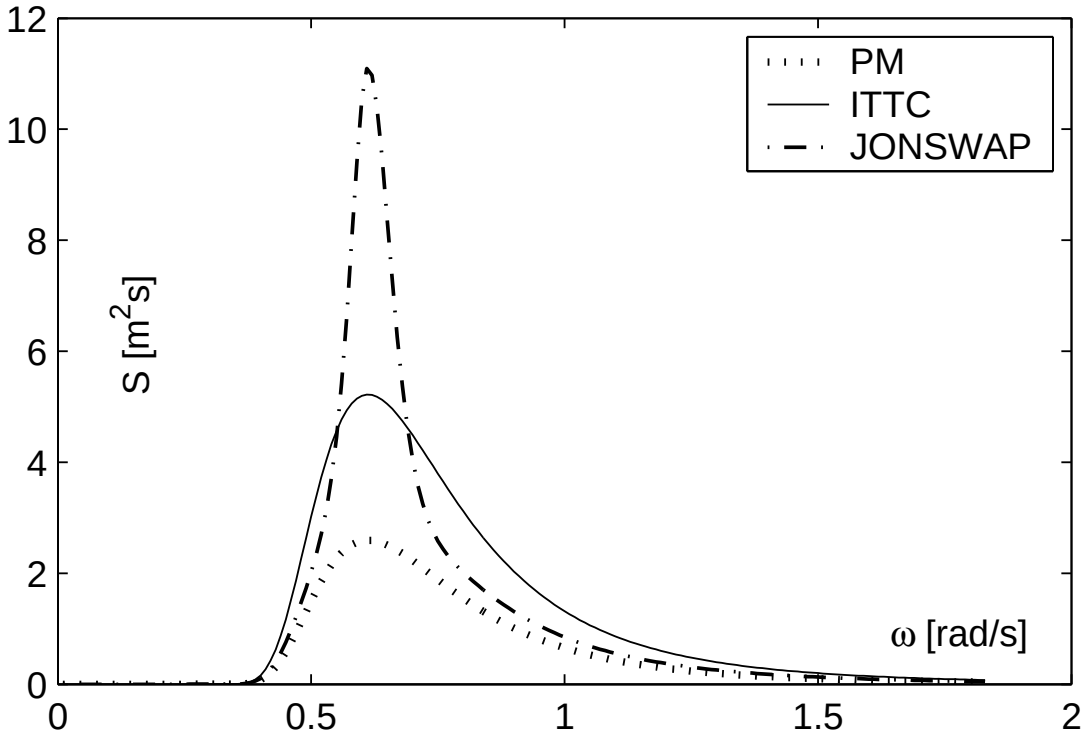

Figure 6.6: Comparison of PM, ITTC and JONSWAP spectra.

Linear wave theory limitations Linear wave theory only considers non-breaking waves. A rule-of-thumb for modeling of non-breaking waves is

$$\begin{aligned} h/\lambda &\leq 1/7, \\ &\Downarrow \\ \lambda &\geq 7h, \end{aligned} \tag{6.19}$$

where h is the wave height (peak-to-peak) and λ the wave length. λ is related to the wave number k by

$$k = \frac{1}{\lambda}. \tag{6.20}$$

In deep water, the dispersion relation is

$$k = \frac{\omega^2}{g}, \tag{6.21}$$

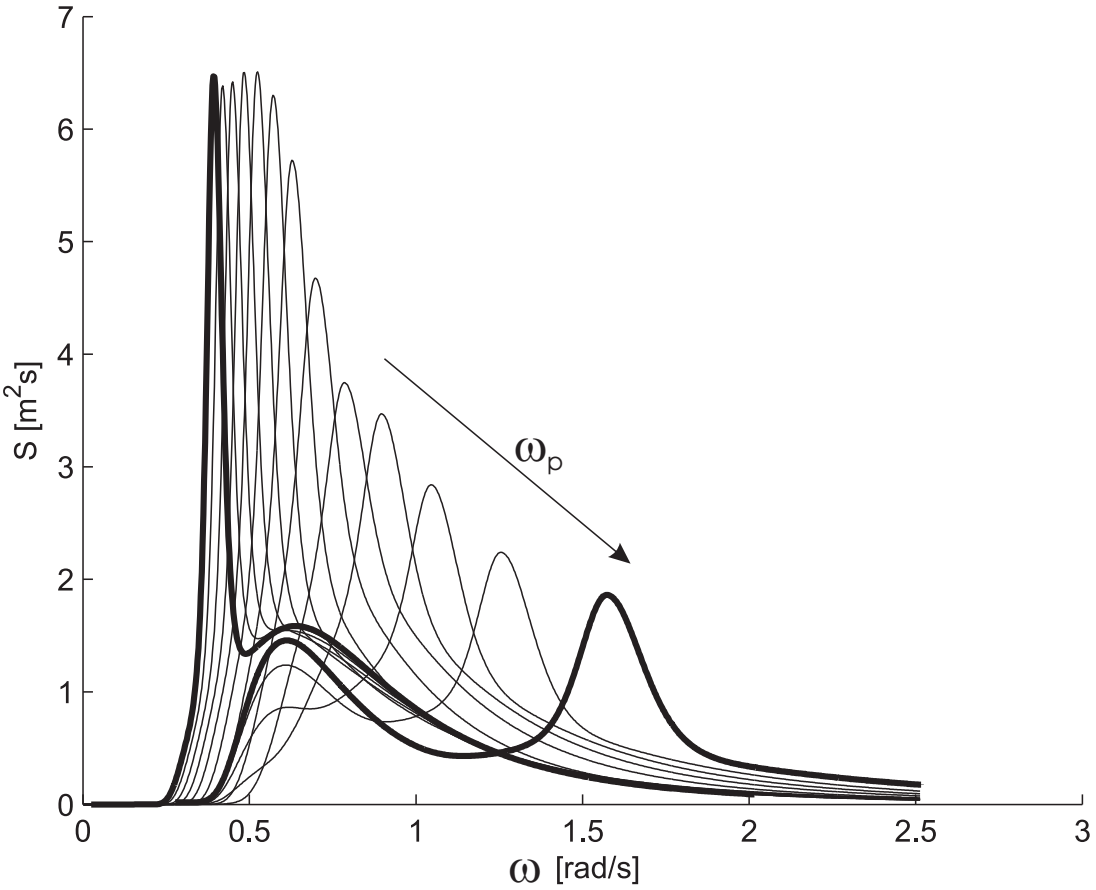

Figure 6.7: Double peaked wave spectrum for varying ω_p and constant H_s.

where ω is the wave frequency and g the acceleration of gravity. This gives

$$\omega = \sqrt{kg} = \sqrt{\frac{g}{\lambda}} \leq \sqrt{\frac{g}{7h}} \approx \sqrt{\frac{1.4}{h}}.$$

In terms of the wave amplitude $\zeta = h/2$, we get the maximum valid wave frequency from the wave amplitude

$$\omega \leq \sqrt{\frac{g}{14\zeta}} \approx \sqrt{\frac{0.7}{\zeta}},$$

or equivalently the maximum valid wave amplitude from the wave frequency

$$\zeta \leq \frac{g}{14\omega^2} \approx \frac{0.7}{\omega^2}.$$

Defining the wave length to height ratio as μ, the corresponding wave frequency can be calculated from h and κ

$$\begin{aligned} \mu &= \frac{\lambda}{h}, \\ \omega &= \sqrt{\frac{g}{\mu h}}. \end{aligned}$$

Common spreading functions

The most commonly used spreading function is according to Faltinsen (1993) formulated as

$$D(\psi-\psi_0)=\begin{cases}\frac{2^{2s-1}s!(s-1)!}{\pi(2s-1)!}\cos^{2s}(\psi-\psi_0) & \text{for } -\frac{\pi}{2}<(\psi-\psi_0)<\frac{\pi}{2}\\ 0 & \text{elsewhere}\end{cases}, \tag{6.22}$$

s is here an integer, with $s=1$ recommended by ITTC and $s=2$ recommended by ISSC. Figure 6.8 shows the spreading function for varying values of s. Increasing s centers the wave energy more about the mean direction ψ_0.

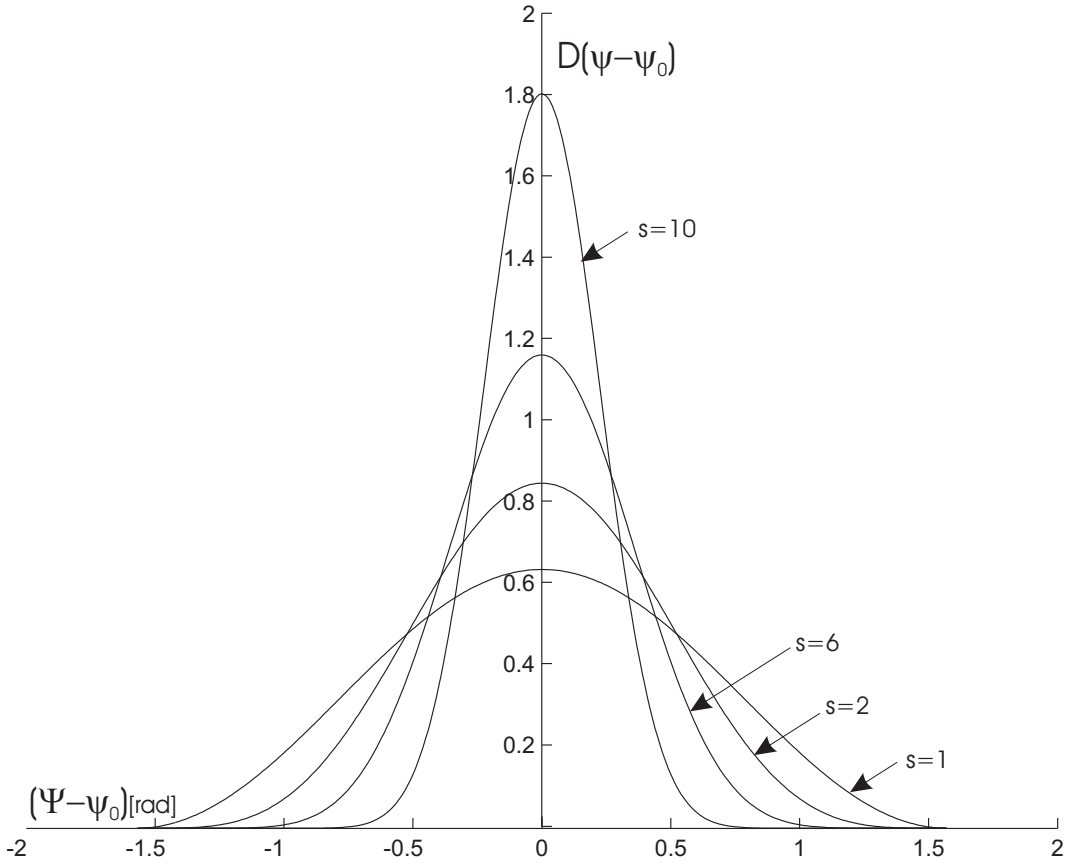

Figure 6.8: Example of spreading function realizations.

Implementation examples

The following figures show how the number of waves can be decreased by the methods described above. The wave spectrum is composed of a Torsethaugen frequency spectrum with significant wave height $H_s=4m$ and peak frequency $\omega_p=1rad/s$, and a spreading function with mean wave direction $\psi_0=-30^\circ$ and spreading factor $s=4$. The number of frequencies N and number of directions M were kept constant at $N=20$ and $M=10$ for all realizations. Figure 6.9 shows the wave spectrum for frequency cutoff factor $\xi=4$ and the direction limit $\psi_{\text{lim}}=0$. Clearly, a lot of insignificant components are included for high frequencies and far from the mean wave

direction. If instead choosing $\xi = 2.5$ and the direction limit $\psi_{\text{lim}} = 20°$, a much better resolution in the interesting area (i.e. about the peak frequency and mean direction) is obtained, as can be seen in Figure 6.10. The next step is to reduce the number of wave components. Figure 6.11 shows the chosen wave components as red stars when choosing the wave component energy limit $\kappa = 0.005$. A total of 96 wave components is included and 104 discarded. If in addition choosing the frequencies and directions at random within each interval the result is shown in Figure 6.12. To justify the exclusion of insignificant wave components, examples of surface realizations with varying number of wave components are shown in Figures 6.13 to 6.15. Figure 6.13 shows a realization of the spectrum defined above with all 200 wave components included, Figure 6.14 shows a realization of the same spectrum with the 100 most important wave components and Figure 6.15 shows a realization of the same spectrum with the 50 most important wave components. The difference between the realizations with 200 and 100 components is minimal, and yet the computational effort for the latter is only half. The difference is noticeable for the realization with 50 components, but the major waves are clearly unaltered; the difference lies in the smaller ripples in the surface due to the smaller wave components.

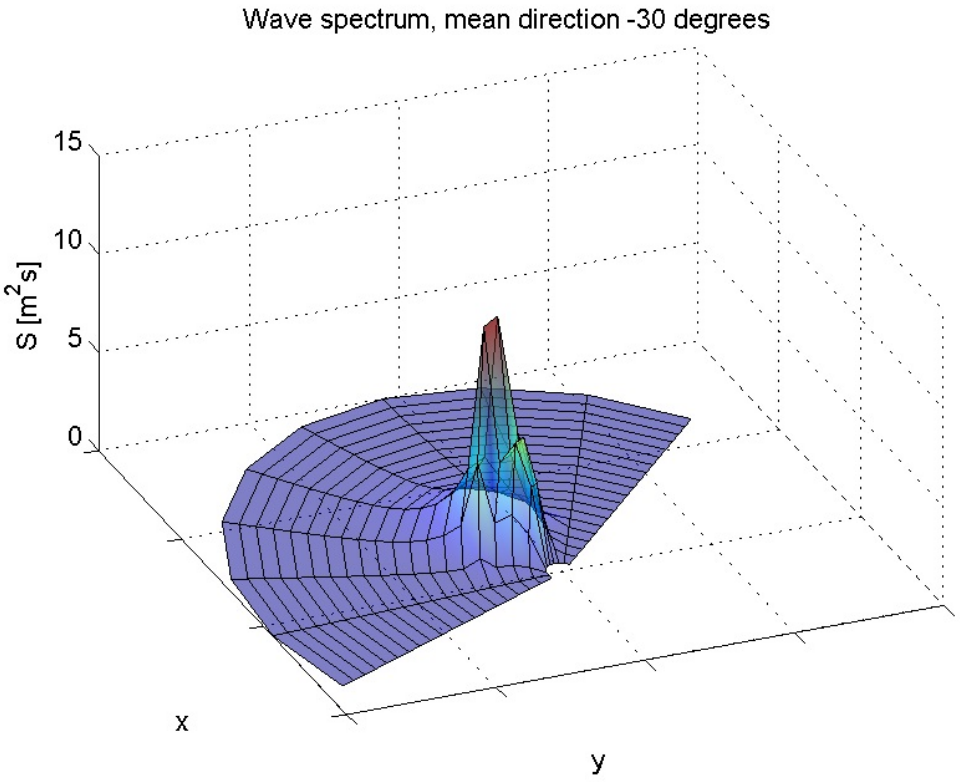

Figure 6.9: Torsethaugen frequency spectrum with $H_s = 4m$ and $\omega_p = 1rad/s$, spreading function with $\psi_0 = -30°$ and $s = 4$, number of frequencies and directions $N = 20$ and $M = 10$, frequency cutoff factor $\xi = 4$ and wave direction limit $\psi_{\text{lim}} = 0$.

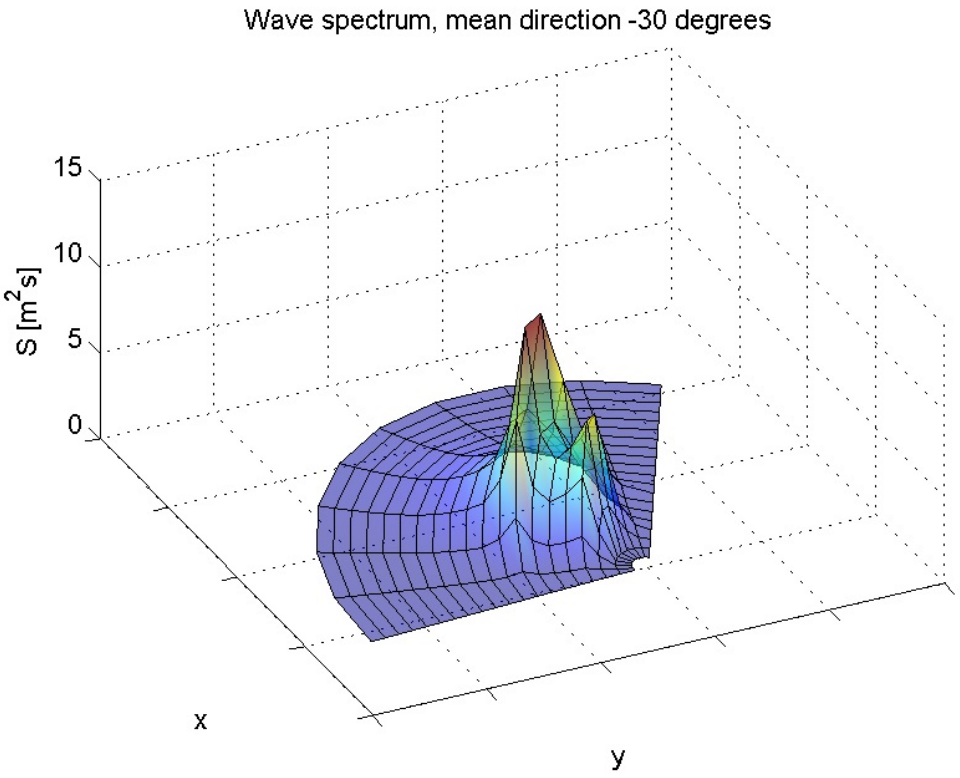

Figure 6.10: Torsethaugen frequency spectrum with $H_s = 4m$ and $\omega_p = 1rad/s$, spreading function with $\psi_0 = -30°$ and $s = 4$, number of frequencies and directions $N = 20$ and $M = 10$, frequency cutoff factor $\xi = 2.5$ and wave direction limit $\psi_{\text{lim}} = 20°$.

Joint distribution for wind and waves

The parameters describing the wind and wave state are interdependent. Johannessen et al. (2002) have developed a joint distribution for wind (described by the average wind speed 10 meters above sea level $\overline{U}_{10}$) and waves (described by significant wave height H_s and peak period $T_p = 2\pi/\omega_p$) in the northern North Sea, based on measurements in the 1973-99 period. Here we present only the mean peak period and mean wind speed as function of significant wave height, for use as a rule of thumb in modeling

$$E(T_p) = 4.883 + 2.680H_s^{0.54}, \tag{6.23}$$

$$E(\overline{U}_{10}) = 1.764 + 3.426H_s^{0.78}. \tag{6.24}$$

6.2.2 Wind

Wind is commonly divided in two components; a mean value and a fluctuating component, or gust. The mean component decreases with the distance to the ground, whereas the gust is approximately constant with the distance to the ground. Wind is in reality a three-dimensional phenomenon, but the descriptions commonly used are restricted to velocities in the horizontal plane, parameterized by the velocity U and the direction ψ.

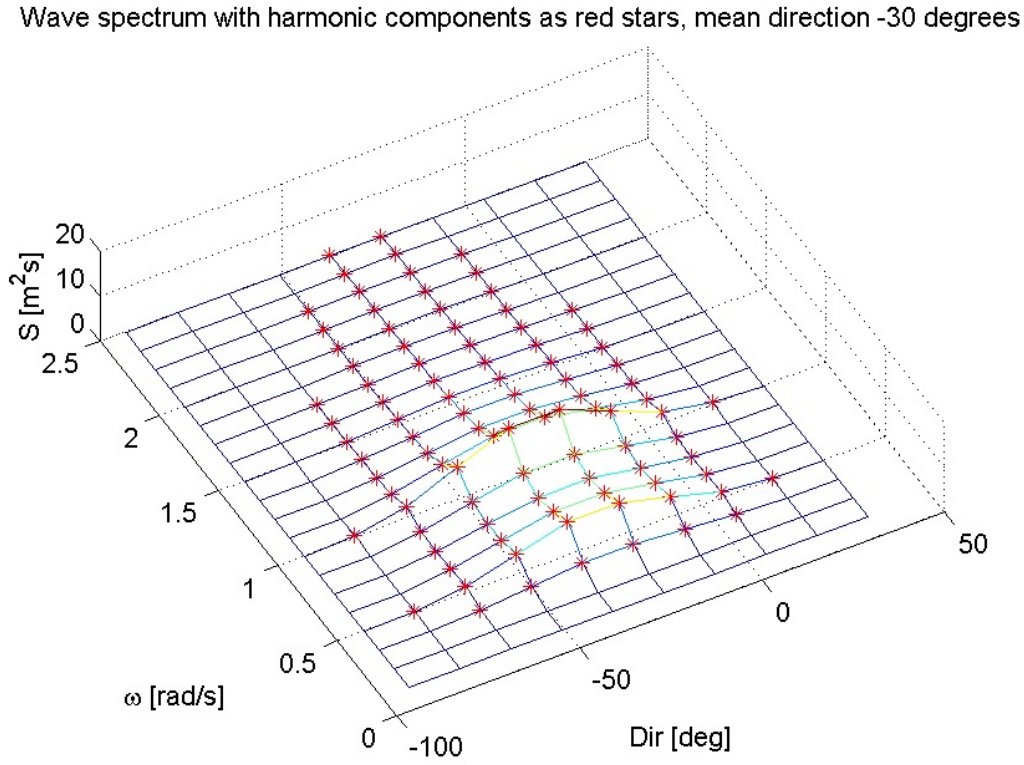

Figure 6.11: Wave spectrum with wave energy limit $\kappa = 0.005$. The frequencies and directions of the components, which are shown as red stars, are not chosen at random.

Mean wind component

The mean velocity $\bar{U}$ at elevation z may be written as

$$\frac{\bar{U}(z)}{\bar{U}_{10}} = \frac{5}{2}\sqrt{\kappa}\ln\frac{z}{z_0}; \quad z_0 = 10\exp(-\frac{2}{5\sqrt{\kappa}}). \tag{6.25}$$

$\bar{U}_{10}$ is the 1 hour mean wind speed at $10m$ elevation and κ is the sea surface drag coefficient Faltinsen (1993). Slowly-varying variations in the mean wind velocity may be implemented by a 1st order Gauss-Markov Process Fossen (2011)

$$\dot{\bar{U}} + \mu\bar{U} = w. \tag{6.26}$$

w is Gaussian white noise and $\mu \geq 0$ is a constant. For $\mu = 0$, this is a random walk process. The magnitude of the velocity should be restricted by saturation elements

$$0 \leq \bar{U}_{\min} \leq \bar{U} \leq \bar{U}_{\max}. \tag{6.27}$$

The variation in wind direction may be implemented in a similar way

$$\dot{\psi} + \mu_2\psi = w_2 \tag{6.28}$$

$$\psi_{\min} \leq \psi \leq \psi_{\max}, \tag{6.29}$$

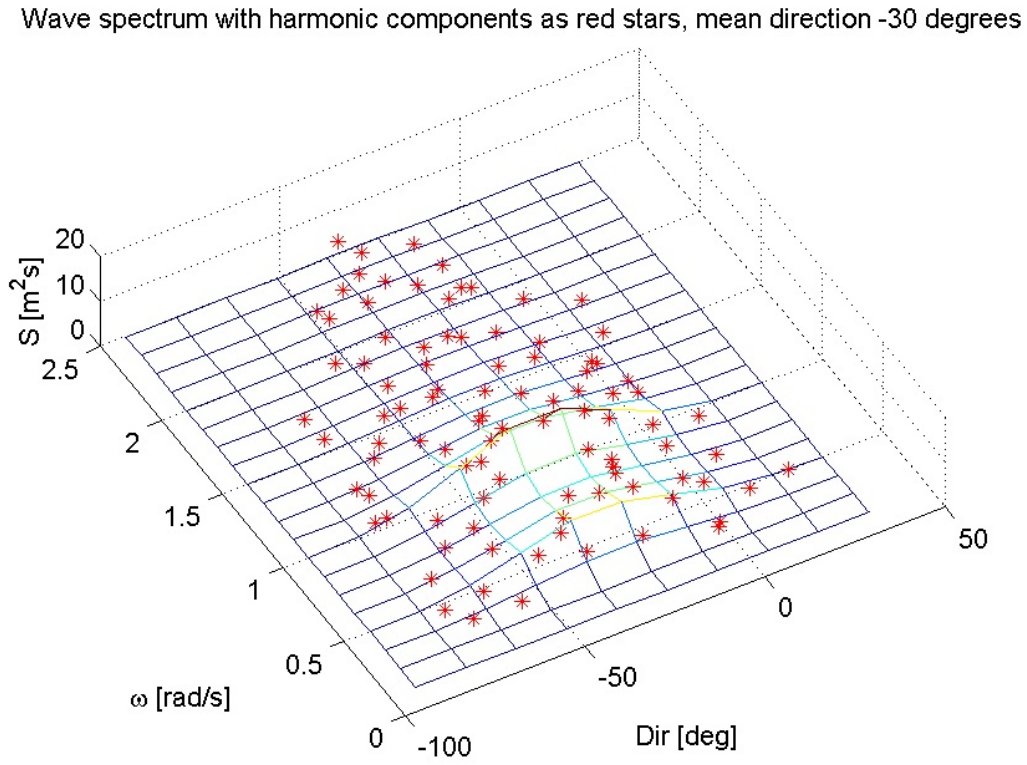

Figure 6.12: Wave spectrum with wave energy limit $\kappa = 0.005$. The frequencies and directions of the components, which are shown as red stars, are chosen at random.

where w_2 and μ_2 are white noise and a positive constant respectively. No saturation elements are necessary here, but may be implemented if wanted.

Wind gust

The wind gust is commonly described by a spectrum, in a similar way as for waves. A widely used formulation is the Harris wind spectrum

$$S(f) = \frac{4\kappa L\overline{U}_{10}}{(2+\widetilde{f^2})^{\frac{5}{6}}}, \quad \widetilde{f} = \frac{Lf}{\overline{U}_{10}}. \tag{6.30}$$

L is a scaling length, κ is the sea surface drag coefficient and f is the frequency in Hz. Example values for the parameters are $L = 1800m$ and $\kappa = 0.0026$. The Harris spectrum was based on measurements over land, and more resent studies have given alternative representations. Norsok (2018) recommends a wave spectrum which also varies with z

$$\begin{aligned} S(f) &= 320\frac{(\frac{U_{10}}{10})^2(\frac{z}{10})^{0.45}}{(1+x^n)^{\frac{5}{3n}}}, \quad n = 0.468; \\ x &= 172f(\frac{z}{10})^{2/3}(\frac{U_{10}}{10})^{-3/4}. \end{aligned} \tag{6.31}$$

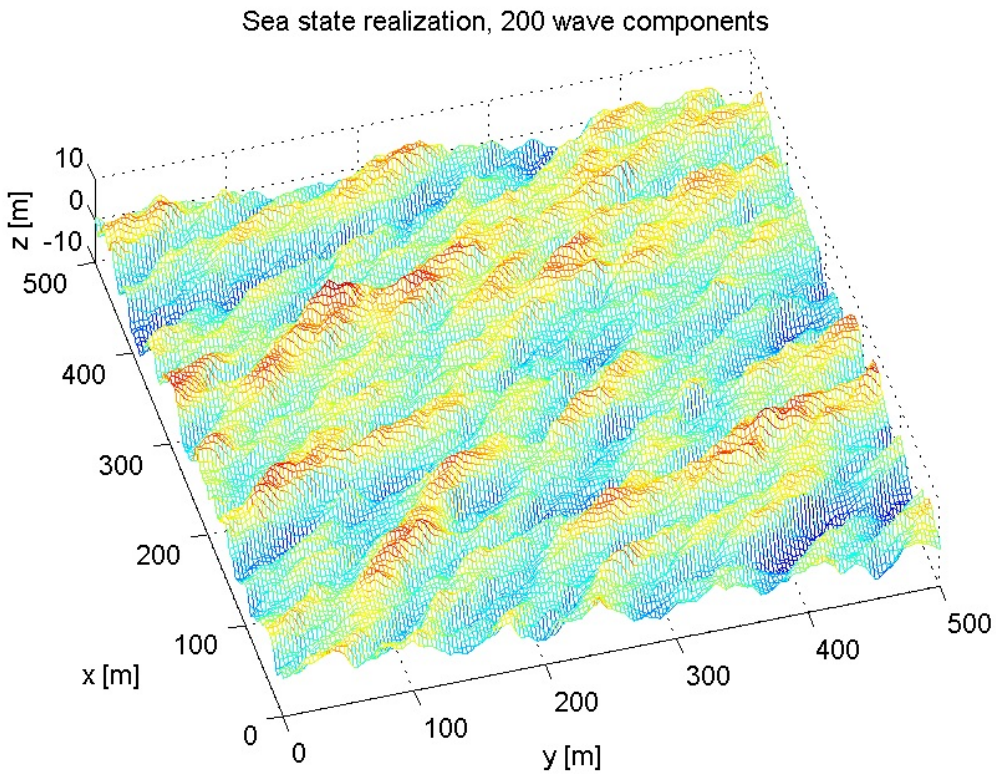

Figure 6.13: Realization of a Torsethaugen spectrum with 200 wave components.

Figures 6.16 shows the Harris and NORSOK wave spectra for $\overline{U}_{10} = 10m/s$. It is clear that the NORSOK spectrum contains more energy at lower frequencies.

A realization of the wind state may be done by superposing the gust realization and the mean wind at the desired elevation. The gust realization is done in the same manner as a the realization of a sea state from a wave spectrum. Harmonic component number i is defined as

$$U_{gi}(t) = \sqrt{2S(f_i)\Delta f_i}\cos(2\pi f_i t + \phi_i), \tag{6.32}$$

where f_i is the frequency, Δf_i the frequency interval and ϕ_i an evenly distributed phase angle. The total wind realization with N gust components is then written as

$$U(z,t) = \bar{U}(z) + \sum_{i=1}^{N} U_{gi}(t). \tag{6.33}$$

Implementation example Figure 6.17 shows a wind time series using the models defined above. The wind direction is slowly-varying with mean 0 degrees, the mean wind speed is 10 m/s and the wind gust is modelled by a NORSOK wind spectrum with 100 frequency components.

6.2.3 Water Current Model

We may divide current modeling in two levels of detail:

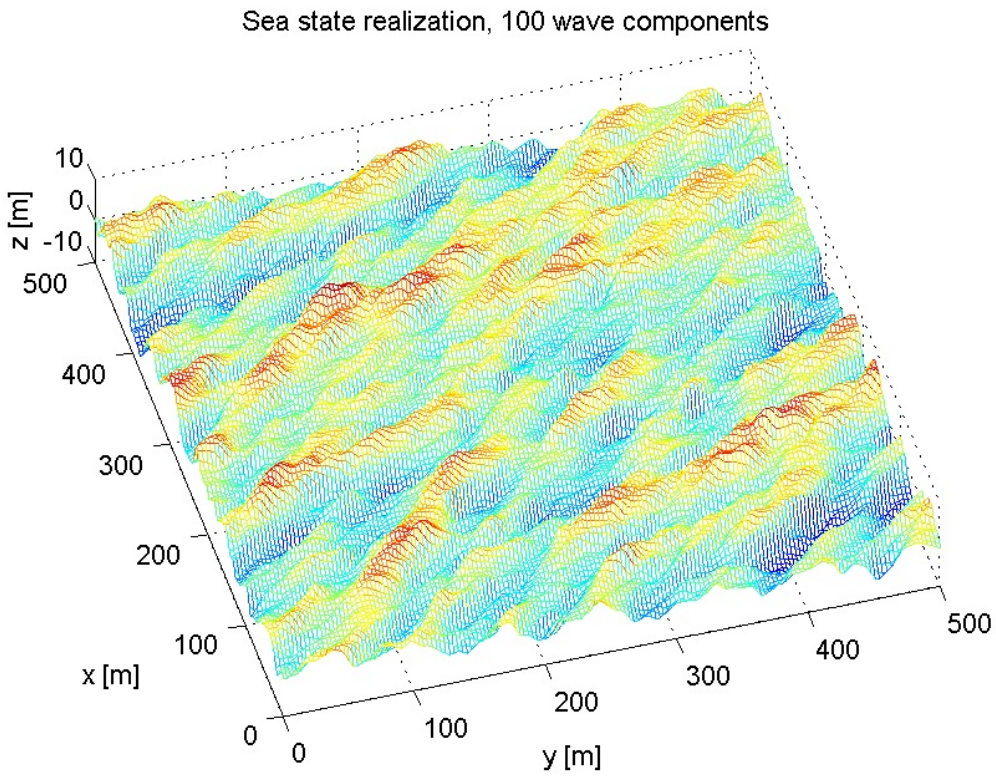

Figure 6.14: Realization of a Torsethaugen spectrum with 100 wave components.

- Surface current, for use in modeling of surface vessel response
- Full current profile, for use in modeling of risers, anchor lines etc.

Surface current

For modeling of surface vessels or other applications in the proximity of the surface, a 2-dimensional current model is sufficient. If the current is given by magnitude V_c and direction in the NED frame ψ_c, the current velocity vector ν_c may be written as

$$\nu_c = [V_c \cos(\psi_c), V_c \sin(\psi_c), 0]^T \tag{6.34}$$

The variation in current velocity may be implemented by a 1st order Gauss-Markov Process (Fossen, 2011)

$$\dot{V}_c + \mu V_c = w. \tag{6.35}$$

w is Gaussian white noise and $\mu \geq 0$ is a constant. For $\mu = 0$, this is a random walk process. The magnitude of the velocity should be restricted by saturation elements

$$V_{c,\min} \leq V_c \leq V_{c,\max}. \tag{6.36}$$

The variation in current direction may be implemented in a similar way

$$\dot{\psi}_c + \mu_2 \psi_c = w_2 \tag{6.37}$$

$$\psi_{c,\min} \leq \psi_c \leq \psi_{c,\max}. \tag{6.38}$$

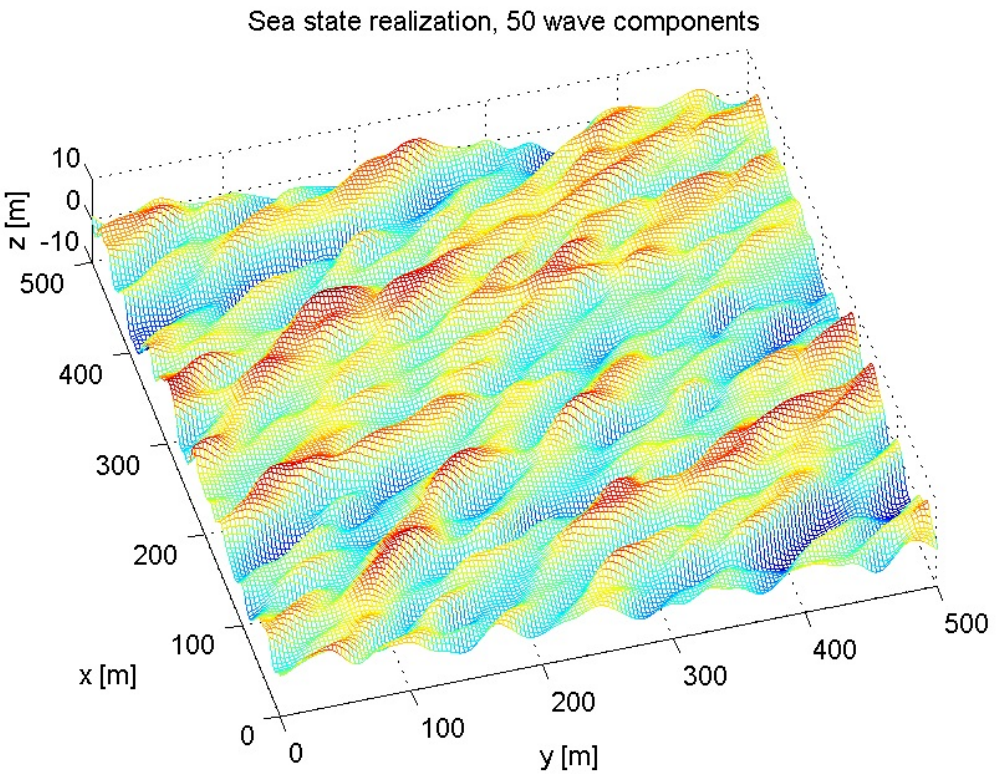

Figure 6.15: Realization of a Torsethaugen spectrum with 50 wave components.

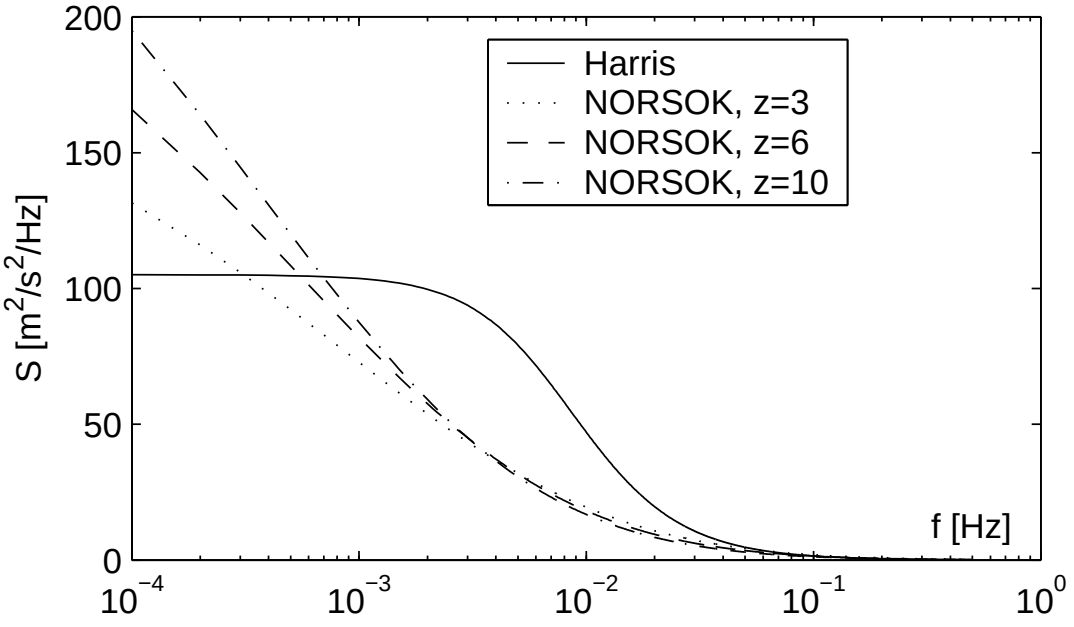

Figure 6.16: Harris and NORSOK wind spectra.

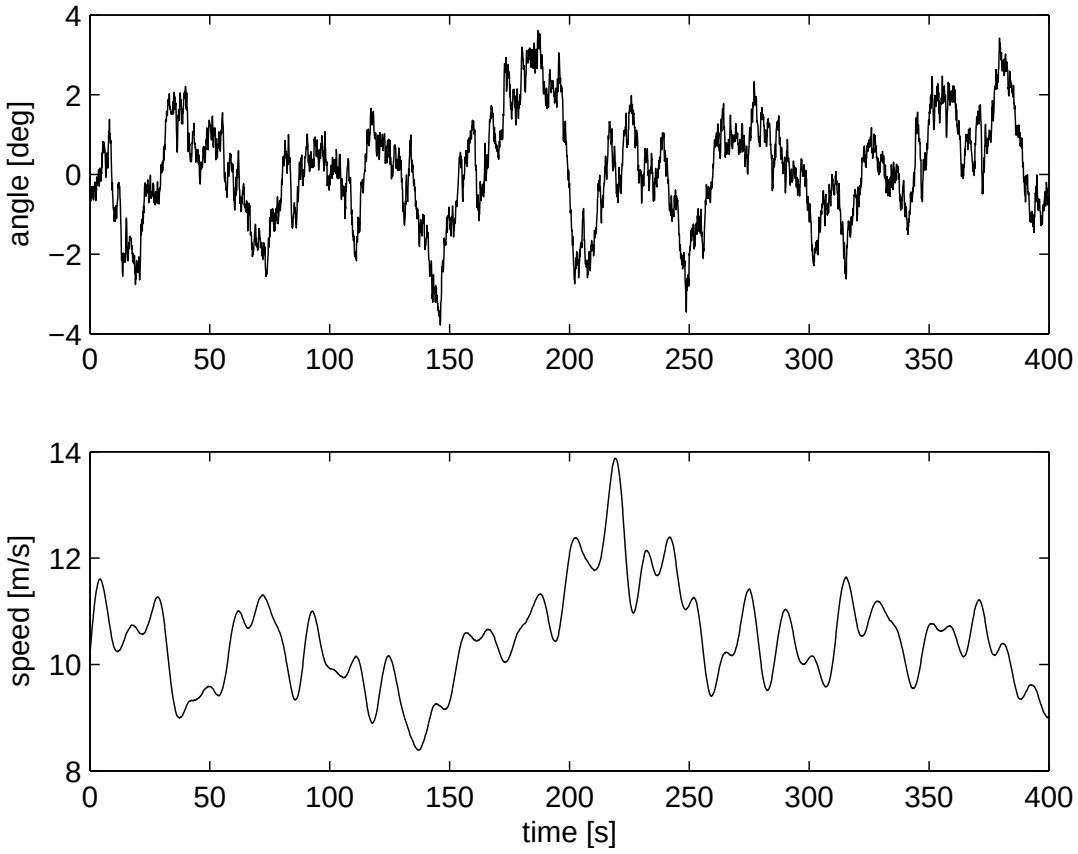

Figure 6.17: Wind realization of a slowly-varying direction with mean 0 degrees, mean speed of 10 m/s and gust components from the NORSOK wind spectrum.

In addition, the current is often divided in two components: Tidal and wind generated. If actual measurement data are available, these may be separated, but for most purposes they may be lumped into one component.

Current profile

In some applications, the actual current profile in which the current varies with the depth, is needed. If no actual field measurements are available, DNV GL recommends the following current profile $V_c(z)$, with z the depth (positive downwards)

$$V_c(z) = V_{c,tide}(z) + V_{c,wind}(z) \tag{6.39}$$

$$V_{c,tide}(z) = V_{c,tide}(\frac{h-z}{h})^{1/7} \quad \text{for } z \geq 0 \tag{6.40}$$

$$V_{c,wind}(z) = V_{c,wind}(\frac{h_0-z}{h_0})^{1/7} \quad \text{for } 0 \leq z \leq h_0 \tag{6.41}$$

$$V_{wind}(z) = 0 \quad \text{for } z \geq h_0, \tag{6.42}$$

where $V_{c,tide}$ is the tidal current velocity at surface level, $V_{c,wind}$ is the wind generated current velocity at surface level, h is the water depth, and h_0 is the reference depth for wind generated

current, example value $h_0 = 50m$.

The wind generated current may be taken as $V_{c,wind} = 0.015\overline{U}_{10}$, where $\overline{U}_{10}$ is the mean wind velocity 10 meters above sea level. In addition, the current profile should be stretched or compressed vertically to account for the change in water depth with the surface elevation due to waves. This may however be neglected at large water depths.

6.3 Kinematics

6.3.1 Reference Frames

The different reference frames used are illustrated in the Figures 6.18 - 6.19, and are described below:

- The Earth-fixed reference frame is denoted as the $X_{\mathrm{E}}Y_{\mathrm{E}}Z_{\mathrm{E}}$-frame. Measurement of the vessel's position and orientation coordinates are done in this frame relatively to a defined origin. One should notice that each position reference system has its own local coordinate system, which has to be transformed into the common Earth-fixed reference frame.
- In *sea keeping* analysis (vessel motions in waves) the hydrodynamic frame $X_{\mathrm{h}}Y_{\mathrm{h}}Z_{\mathrm{h}}$-frame is generally moving along the path of the vessel with the x-axis positive forwards, y-axis positive to the starboard, and z-axis positive downwards. The $X_{\mathrm{h}}Y_{\mathrm{h}}$-plane is assumed fixed and parallel to the mean water surface. The vessel is assumed to oscillate with small amplitudes about this frame such that linear theory may apply for modeling of the perturbations. Often in forward speed *sea keeping* analysis the hydrodynamic frame is moving forward with constant vessel speed U. In *station keeping* operations (dynamic positioning) about the coordinates x_{d}, y_{d}, and ψ_{d} the hydrodynamic frame is Earth-fixed and denoted as the *reference-parallel frame* $X_{\mathrm{R}}Y_{\mathrm{R}}Z_{\mathrm{R}}$. It is rotated to the desired heading angle ψ_{d}, and the origin is translated to the desired x_{d} and y_{d} position coordinates for the particular station keeping operation studied. Assuming small amplitudes of motion it is convenient to use this frame in the development of the control schemes.
- The body-fixed XYZ-frame is fixed to the vessel body with the x-axis positive forwards, y-axis positive to the starboard and z-axis positive downwards. For ships it is common to assume that the centre of gravity is located in the centre line of the vessel, and that the submerged part of the vessel is symmetric about the xz- plane (port/starboard). Here it is assumed that the origin is located in the mean oscillatory position (*flotation point*) in the average water plane. Hence, the centre of gravity is then located at $(x_{\mathrm{G}}, 0, z_{\mathrm{G}})$ in body coordinates. The motion and the loads acting on the vessel are calculated in this frame.

The vectors defining the generalized vessel's Earth-fixed position and orientation, and the body-fixed translation and rotation velocities are using SNAME (1950) notation given by

$$\begin{aligned} \eta_1 &= [x, y, z]^T, \quad \eta_2 = [\phi, \theta, \psi]^T, \\ \nu_1 &= [u, v, w]^T, \quad \nu_2 = [p, q, r]^T. \end{aligned} \tag{6.43}$$

Here, η_1 denotes the position vector in the Earth-fixed frame, and η_2 is a vector of Euler angles. ν_1 denotes the body-fixed linear surge, sway and heave velocity vector, and ν_2 denotes the body-fixed angular roll, pitch and yaw velocity vector. For surface vessels the orientation is normally represented in terms of Euler angles (Fossen, 2011).

Definition 6.1 *Degrees-of-Freedom - DOF. For a general body,the DOF is the set of independent displacements and rotations that completely specify the displaced position and orientation of the craft. A body that can move freely in the 3D space has maximum 6 DOFs with three translational and three rotational components.*

Definition 6.2 *Configuration Space. The n-dimensional configuration space is the space of possible positions and orientations that a body may attain subject to external constraints.*

Ships and rigs are often described in the horizontal plane only with surge sway and yaw (with $n = 3$ DOFs), while underwater vehicles may be described in $n = 6$ DOFs including both the horizontal (surge, sway, yaw) plane and vertical plane (heave, roll, pitch)

Definition 6.3 *Working Space The working space is a reduced space of dimension $m < n$ in which the control objective is defined.*

An underactuated vehicle has independent control forces and moments in only some DOFs such that $r < n$. For an underwater vehicle such as a Remotely Operated Vehicle (ROV) that is self-stabilized in roll and pitch, the working space may be $m = 4$ If the number of actuators r are less than m, the the control problem is referred to as underactuated control Stabilizing and tracking controllers for underactuated vehicles are usually designed by considering a working space of dimension $m < n$ satisfying $m = r$ (fully actuated in the working space but not in the configuration space). This may be the case for the ROV. Notice that many ships and underwater vehicles are overactuated with $r > m$ making the control allocation to an optimization problem with infinite many solutions.

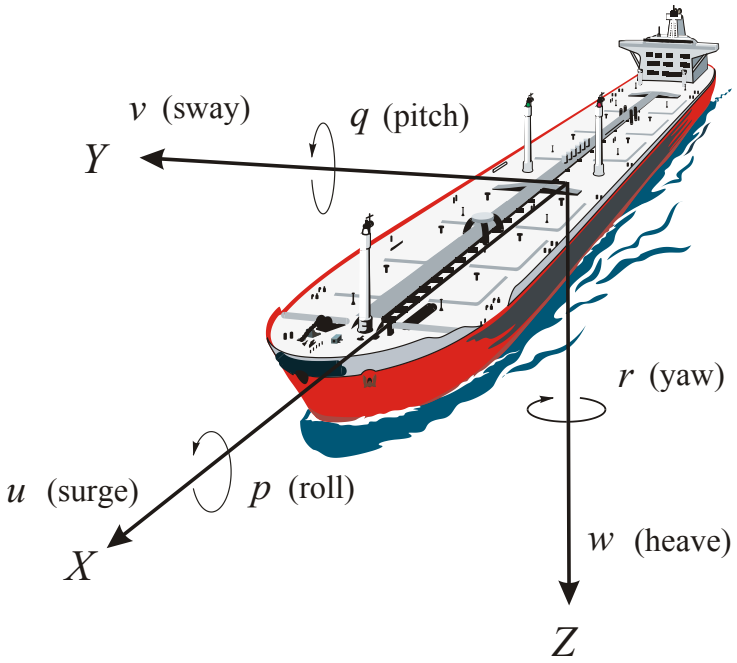

Figure 6.18: Definition of surge, sway, heave, roll, pitch and yaw modes of motion in body-fixed frame.

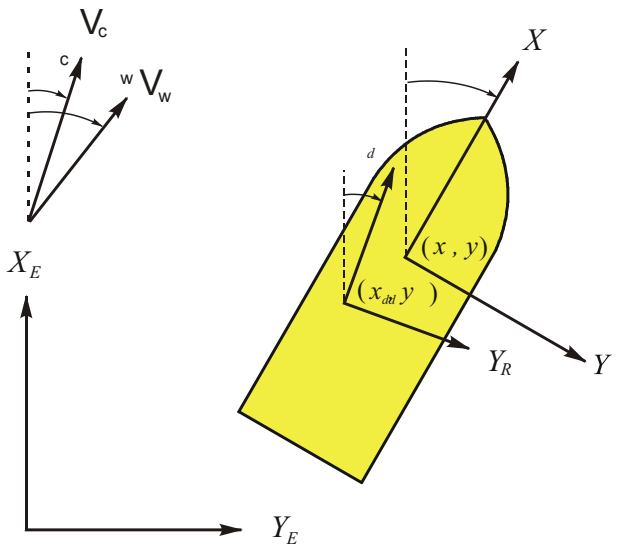

Figure 6.19: Definition of frames: Earth-fixed, reference-parallel and body-fixed.

6.3.2 The Euler Angle Transformation

Linear velocity

The Euler angles result from a sequence of rotations which is not arbitrary. The Euler angles appear from the following rotation sequence:

- Let $X_3Y_3Z_3$ be a Earth-fixed reference frame that is translated such that the origin is coinciding with the body-fixed XYZ-frame.
- Rotate $X_3Y_3Z_3$ a yaw angle ψ about the Z_3-axis such that a new reference frame denoted as $X_2Y_2Z_2$ appears.
- Rotate $X_2Y_2Z_2$ a pitch angle θ about the Y_2-axis such that a new reference frame denoted as $X_1Y_1Z_1$ appears.
- Rotate $X_1Y_1Z_1$ a roll angle ϕ about the X_1-axis such that the reference frame denoted as XYZ appears.

The rotation sequence is then given by

$$\mathbf{J}_1(\eta_2) = \mathbf{C}^T_{z,\psi}\mathbf{C}^T_{y,\theta}\mathbf{C}^T_{x,\phi}, \tag{6.44}$$

where

$$\mathbf{C}_{z,\psi} = \begin{bmatrix} c\psi & s\psi & 0 \\ -s\psi & c\psi & 0 \\ 0 & 0 & 1 \end{bmatrix}, \tag{6.45}$$

$$\mathbf{C}_{y,\theta} = \begin{bmatrix} c\theta & 0 & -s\theta \\ 0 & 1 & 0 \\ s\theta & 0 & c\theta \end{bmatrix}, \tag{6.46}$$

$$\mathbf{C}_{x,\phi} = \begin{bmatrix} 1 & 0 & 0 \\ 0 & c\phi & s\phi \\ 0 & -s\phi & c\phi \end{bmatrix}. \tag{6.47}$$

Hence, the rotation matrix $\mathbf{J}_1(\eta_2) \in \mathbf{SO}(3)$ can be defined as

$$\mathbf{J}_1(\eta_2) = \begin{bmatrix} c\psi c\theta & -s\psi c\phi + c\psi s\theta s\phi & s\psi s\phi + c\psi c\phi s\theta \\ s\psi c\theta & c\psi c\phi + s\phi s\theta s\psi & -c\psi s\phi + s\theta s\psi c\phi \\ -s\theta & c\theta s\phi & c\theta c\phi \end{bmatrix}, \tag{6.48}$$

where $c\cdot = \cos(\cdot)$, $s\cdot = \sin(\cdot)$ and $t\cdot = \tan(\cdot)$. The symbol $\mathbf{SO}(3)$ denotes *special orthogonal group* of order 3. Thus, the linear velocities of the vessel in the Earth-fixed frame is given by the transformation

$$\dot{\eta}_1 = \mathbf{J}_1(\eta_2)\nu_1. \tag{6.49}$$

Remark 6.2 *Two vectors $\mathbf{x}_1, \mathbf{x}_2 \in \times\mathbb{R}^{\mathrm{n}}$ are said to be orthogonal if $\mathbf{x}_1^T\mathbf{x}_2 = \mathbf{x}_2^T\mathbf{x}_1 = 0$. A set of vectors $\mathbf{x}_i \in \times\mathbb{R}^{\mathrm{n}}, i = 1, 2, ..., m$, is said to be orthonormal if*

$$\mathbf{x}_i^T\mathbf{x}_j = \begin{cases} 0 & if\ i \neq j, \\ 1, & if\ i = j. \end{cases} \tag{6.50}$$

Remark 6.3 *The reference frame matrix $\mathbf{C}_{i,\alpha} \in \mathbf{SO}(3)$ has the property (Fossen, 2011))*

$$\mathbf{C}_{i,\alpha}\mathbf{C}_{i,\alpha}^T = \mathbf{C}_{i,\alpha}^T\mathbf{C}_{i,\alpha} = \mathbf{I}, \tag{6.51}$$

where $\mathbf{C}_{i,\alpha}$ denotes a rotation angle α about the i-axis, and where

$$\det \mathbf{C}_{i,\alpha} = 1, \tag{6.52}$$

implies that $\mathbf{C}_{i,\alpha} = [\mathbf{c}_1, \mathbf{c}_2, \mathbf{c}_3]$ and $\mathbf{C}_{i,\alpha}^T = \left[\mathbf{c}_1^T, \mathbf{c}_2^T, \mathbf{c}_3^T\right]^T$ consist of orthonormal columns with the consequence that

$$\mathbf{C}_{i,\alpha}^{-1} = \mathbf{C}_{i,\alpha}^T. \tag{6.53}$$

Remark 6.4 *Based on (6.51) we can derive that*

$$\mathbf{J}_1^{-1}(\eta_2) = \mathbf{J}_1^T(\eta_2). \tag{6.54}$$

Hence,

$$\nu_1 = \mathbf{J}_1^{-1}(\eta_2)\dot{\eta}_1 = \mathbf{J}_1^T(\eta_2)\dot{\eta}_1. \tag{6.55}$$

Angular velocity rotation

The angular velocities of the vessel in the Earth-fixed frame is given by

$$\dot{\eta}_2 = \mathbf{J}_2(\eta_2)\nu_2. \tag{6.56}$$

The angular velocities in the body-fixed frame appear from the relation (Fossen, 2011)

$$\nu_2 = \begin{bmatrix} \dot{\phi} \\ 0 \\ 0 \end{bmatrix} + \mathbf{C}_{x,\phi} \begin{bmatrix} 0 \\ \dot{\theta} \\ 0 \end{bmatrix} + \mathbf{C}_{x,\phi}\mathbf{C}_{y,\theta} \begin{bmatrix} 0 \\ 0 \\ \dot{\psi} \end{bmatrix} = \mathbf{J}_2^{-1}(\eta_2)\,\dot{\eta}_2, \tag{6.57}$$

where we can expand (6.57) and derive that

$$\mathbf{J}_2^{-1}(\eta_2) = \begin{bmatrix} 1 & 0 & -s\theta \\ 0 & c\phi & c\theta s\phi \\ 0 & -s\phi & c\theta c\phi \end{bmatrix}. \tag{6.58}$$

Inverting (6.58) gives $\mathbf{J}_2(\eta_2) \in \mathbb{R}^{3\times 3}$ according to

$$\mathbf{J}_2(\eta_2) = \begin{bmatrix} 1 & s\phi t\theta & c\phi t\theta \\ 0 & c\phi & -s\phi \\ 0 & s\phi/c\theta & c\phi/c\theta \end{bmatrix}, \qquad c\theta \neq 0, \tag{6.59}$$

where $c\cdot = \cos(\cdot)$, $s\cdot = \sin(\cdot)$ and $t\cdot = \tan(\cdot)$.

6 DOF kinematics

The linear and angular velocities of the vessel in the Earth-fixed frame is given by

$$\dot{\eta} = \begin{bmatrix} \dot{\eta}_1 \\ \dot{\eta}_2 \end{bmatrix} = \begin{bmatrix} \mathbf{J}_1(\eta_2) & \mathbf{0}_{3\times 3} \\ \mathbf{0}_{3\times 3} & \mathbf{J}_2(\eta_2) \end{bmatrix} \begin{bmatrix} \nu_1 \\ \nu_2 \end{bmatrix} = \mathbf{J}(\eta_2)\nu. \tag{6.60}$$

6 DOF kinematics (small roll and pitch angle representation)

A frequently used kinematic approximation for metacentric stable vessels with small roll and pitch angles is

$$\begin{aligned} \dot{\eta} &= \mathbf{J}(\eta_2)\nu, && (6.61)\\ &\Downarrow \quad \eta_2 = [0,0,\psi]^T, \\ \dot{\eta} &= \mathbf{J}(\psi)\nu, && (6.62) \end{aligned}$$

where

$$\mathbf{J}(\psi) = \begin{bmatrix} \mathbf{C}_{z,\psi}^T & \mathbf{0}_{3\times 3} \\ \mathbf{0}_{3\times 3} & \mathbf{I}_{3\times 3} \end{bmatrix}. \tag{6.63}$$

Remark 6.5 *For small ϕ-roll and θ-pitch angles (less that 10°), we approximate* $\cos\phi \approx 1$ *and* $\cos\theta \approx 1$ *and* $\sin\phi \approx 0$ *and* $\sin\theta \approx 0$.

3 DOF kinematics (horizontal motion)

In many practical applications only the horizontal modes of motion are of interest. It is then convenient to find an appropriate kinematic representation only for the horizontal-plane motion. For surge, sway and yaw the 6 DOF kinematics reduces to

$$\dot{\eta} = \mathbf{R}(\psi)\nu, \qquad \mathbf{R}^{-1}(\psi) = \mathbf{R}^T(\psi) \tag{6.64}$$

where we have redefined the state vectors according to $\eta = [x \quad y \quad \psi]^T$ and $\nu = [u \quad v \quad r]^T$, and

$$\mathbf{R}(\psi) = \mathbf{C}_{z,\psi}^T = \begin{bmatrix} c\psi & -s\psi & 0 \\ s\psi & c\psi & 0 \\ 0 & 0 & 1 \end{bmatrix}.$$

In a reference-parallel formulation we can define

$$\dot{\eta}_R = \mathbf{R}(\psi - \psi_d)\nu. \tag{6.65}$$

Remark 6.6 *In hydrodynamic literature several conventions for hydrodynamic coefficients and reference frames are used. In Faltinsen (1993), added mass, wave radiation damping and restoring coefficients are denoted as A_{ij}, B_{ij}, C_{ji} with the x-axis positive backwards, y-axis positive to the starboard and z-axis positive upwards. In Newman (1997) a second convention is used with the x-axis positive forwards, y-axis positive upwards and z-axis positive to the starboard. Here, the notation of SNAME (1950) is used with the x-axis positive forwards, y-axis positive to the starboard and z-axis positive downwards. The SNAME notation is more established in hydrodynamic and control problems related to manoeuvring and positioning of ships.*

Remark 6.7 *Integration of the angular velocities $\int_o^t \nu_2(\tau)d\tau$ does not have any physical meaning. In order to have proper generalized coordinates $\dot{\eta}_2$ should be integrated.*

Remark 6.8 *$\mathbf{J}_2(\eta_2)$ is undefined for $\theta = \pm 90°$. Consequently $\mathbf{J}_2^{-1}(\eta_2) \neq \mathbf{J}_2^T(\eta_2)$ due to the singularity in $\theta = \pm 90°$. For surface vessels this is not of any problem. However, for underwater vehicles special precaution must be taken. Then a so-called quaternion (Euler parameters) could be used, see Fossen (2011) for details.*

Remark 6.9 *For low speed manoeuvring and change of setpoint in station keeping operations, the $X_{\mathrm{R}}Y_{\mathrm{R}}Z_{\mathrm{R}}$–frame will be time-varying following the trajectories for $x_{\mathrm{d}}(t), y_{\mathrm{d}}(t)$ and $\psi_{\mathrm{d}}(t)$.*

Remark 6.10 *In the reference-parallel frame $X_{\mathrm{R}}Y_{\mathrm{R}}Z_{\mathrm{R}}$ (and hydrodynamic frame as well) assuming small amplitudes of motion in yaw ($|\psi - \psi_d| \approx 0$), we have*

$$\dot{\eta}_R = \mathbf{R}(\psi - \psi_d)\nu \approx \mathbf{I}_{3\times 3}\nu, \tag{6.66}$$

where $\mathbf{I}_{3\times 3} \in \mathbb{R}^{3\times 3}$ is the identity matrix. Thus, the reference-parallel frame is convenient for design of linear controllers as we avoid the nonlinear kinematics.

Remark 6.11 *When considering moored structures, such as turret-moored tankers or moored semi-submersibles, it is common to locate the origin of the Earth-fixed frame in the natural equilibrium point for the mooring system. This position is often referred to as the* field zero point (FZP). *The body-fixed frame is located in the geometrical centre of the mooring system on the structure; for turret-moored ships this will be the centre of turret (COT).*

6.4 Vessel Dynamics

In mathematical modeling of the marine vessel dynamics it is common to separate the total model into a low-frequency (LF) model and a wave-frequency (WF) model by superposition. Hence, the total motion is a sum of the corresponding LF and the WF components, see Figure 6.20. The WF motions are assumed to be caused by first-order wave loads. Assuming small amplitudes these motions will be well represented by a linear model. The LF motions are assumed to be caused by second-order mean and slowly varying wave loads, current loads, wind loads, mooring and thrust forces. These motions are generally nonlinear, but linear approximations about certain operating points can be found.

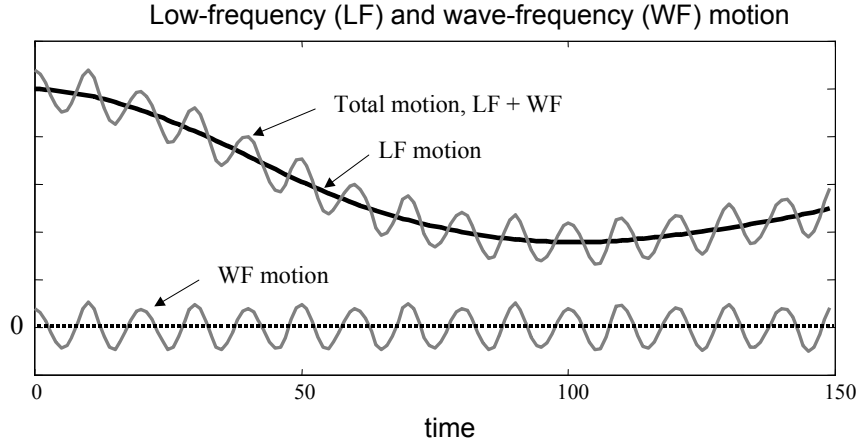

Figure 6.20: The total motion of a ship is modeled as a LF response with the WF response added as an output disturbance.

One should notice that for surface vessels, only the horizontal motions i.e. the surge, sway and yaw degrees-of-freedom (DOF), are subject for control. In the design of positioning control systems one should expect that it is sufficient to only consider the horizontal-plane dynamics in the LF model. This is normally an appropriate assumption, where the effect of vertical-plane dynamics i.e. the heave, roll and pitch DOF will be of minor practical interest for the control problem. However, according to Sørensen and Strand (2000) under certain circumstances this assumption may cause unacceptable reduction in the control performance. In their work it was suggested to characterize the control problem into two categories whether the natural periods in roll and pitch are within or outside the bandwidth of the positioning controller. Hence, the modeling problem can either be regarded as a three or a six DOF problem, where the following prerequisites can be made:

- **3 DOF:** For conventional ship and catamaran hulls in the low-frequency model only the three horizontal-plane surge, sway and yaw DOF are of practical interest for the controller design. For those vessels it can be assumed that the LF vertical-plane dynamics and the thruster action will not have any mutual influence on each other.
- **6 DOF**: For marine structures with a small-waterplane-area and low metacentric height, which results in relatively low hydrostatic restoring compared to the inertia forces, an unintentional coupling phenomenon between the vertical and the horizontal planes through the

thruster action can be invoked. Examples are found in semi-submersibles and SWATHs, which typically have natural periods in roll and pitch in the range of $35 - 65$ seconds. If the inherent vertical damping properties are small, the amplitudes of roll and pitch may be emphasized by the thruster's induction by up to 2°-5° in the resonance range. These oscillations have caused discomfort in the vessel's crew and have in some cases limited the operation. Hence, both the horizontal and vertical planes DOF should be considered.

Concerning the WF model it is normal to include all 6 DOF no matter how the LF model is formulated. The vertical-plane WF motions (heave, roll and pitch) must be used to adjust the acquired position measurements to some defined origin on the vessel. This could be in the plane of the undisturbed free surface with the z-axis through the centre of gravity (CG), the centre of buoyancy (CB) or the flotation point. Thus, the raw position reference system measurements will be strongly influenced by the vertical-plane motions depending on the locations of the installed GPS antennas, hydroacoustic position reference system transducers, Artemis receivers, Taut wire, etc. relative to the defined origin.

In the following, the mathematical model for marine vessels is presented. For an example of model parameters, see Appendix D, where a selection of parameters for the research vessel (R/V) Gunnerus are given.

6.4.1 Nonlinear Low-Frequency Vessel Model

The nonlinear 6 DOF body-fixed coupled equations of the LF motions in surge, sway, heave, roll, pitch and yaw are written as follows

$$\mathbf{M}\dot{\boldsymbol{\nu}} + \mathbf{C}_{\mathrm{RB}}(\nu)\nu + \mathbf{C}_{\mathrm{A}}(\nu_{\mathrm{r}})\nu_{\mathrm{r}} + \mathbf{D}(\kappa, \nu_{\mathrm{r}}) + \mathbf{G}(\eta) = \tau_{\mathrm{env}} + \tau_{\mathrm{moor}} + \tau_{\mathrm{ice}} + \tau_{\mathrm{thr}}. \tag{6.67}$$

The right-hand expression of (6.67) represents generalized external forces acting on the vessel and is treated later in this section. Forces in surge, sway and heave and moments in roll, pitch and yaw are referred to as generalized forces. $\tau_{\mathrm{env}} \in \mathbb{R}^6$ represents the slowly-varying environmental loads with the exception of current loads acting on the vessel. The effect of current is already included on the left hand side of (6.67) by the introduction of the relative velocity vector. $\tau_{\mathrm{thr}} \in \mathbb{R}^6$ represents the generalized forces generated by the propulsion system. Even if only the horizontal-plane surge, sway and yaw DOF are subject for control, geometrical coupling to the vertical-plane heave, roll and pitch DOF, will be invoked due to the actual locations of the thrusters. As discussed above the produced thrust components in the vertical-plane will be important to consider for marine structures with small-waterplane-area. If the vessel is attached to a mooring system, the effect of this is represented by $\tau_{\mathrm{moor}} \in \mathbb{R}^6$. For operation in ice the corresponding loads from level ice, ice floes and ice ridges are modeled by $\boldsymbol{\tau}_{\mathrm{ice}} \in \mathbb{R}^6$. In Nguyen and Sørensen (2009) models of level ice loads are presented.

Generalized inertial forces, $\mathbf{M}\dot{\nu}$:

The system inertia matrix $\mathbf{M} \in \mathbb{R}^{6\times 6}$ including added mass is defined as

$$\mathbf{M} = \begin{bmatrix} m - X_{\dot{u}} & 0 & -X_{\dot{w}} & 0 & mz_G - X_{\dot{q}} & 0 \\ 0 & m - Y_{\dot{v}} & 0 & -mz_G - Y_{\dot{p}} & 0 & mx_G - Y_{\dot{r}} \\ -Z_{\dot{u}} & 0 & m - Z_{\dot{w}} & 0 & -mx_G - Z_{\dot{q}} & 0 \\ 0 & -mz_G - K_{\dot{v}} & 0 & I_x - K_{\dot{p}} & 0 & -I_{xz} - K_{\dot{r}} \\ mz_G - M_{\dot{u}} & 0 & -mx_G - M_{\dot{w}} & 0 & I_y - M_{\dot{q}} & 0 \\ 0 & mx_G - N_{\dot{v}} & 0 & -I_{zx} - N_{\dot{p}} & 0 & I_z - N_{\dot{r}} \end{bmatrix}, \tag{6.68}$$

where m is the vessel mass, I_x, I_y and I_z are the moments of inertia about the x-, y- and z-axes and $I_{xz} = I_{zx}$ are the products of inertia. The zero-frequency added mass coefficients $X_{\dot{u}}, X_{\dot{w}}, X_{\dot{q}}, Y_{\dot{v}}$, and so on at low speed in surge, sway, heave, roll, pitch and yaw due to accelerations along the corresponding and the coupled axes are defined as in Faltinsen (1993). Hence, it can be shown that the system inertia matrix is symmetrical and positive definite (Appendix A), i.e. $\mathbf{M} = \mathbf{M}^T > 0$ and $\dot{\mathbf{M}} = \mathbf{0}$.

Generalized Coriolis and centripetal forces, $\mathbf{C}_{\mathrm{RB}}(\nu)\nu + \mathbf{C}_{\mathrm{A}}(\nu_{\mathrm{r}})\nu_{\mathrm{r}}$:

The matrix $\mathbf{C}_{\mathrm{RB}}(\nu) \in \mathbb{R}^{6\times 6}$ is the skew-symmetric Coriolis and centripetal matrix of the rigid body written (Fossen, 2011)

$$\mathbf{C}_{\mathrm{RB}}(\nu) = \begin{bmatrix} 0 & 0 & 0 & c_{41} & -c_{51} & -c_{61} \\ 0 & 0 & 0 & -c_{42} & c_{52} & -c_{62} \\ 0 & 0 & 0 & -c_{43} & -c_{53} & c_{63} \\ -c_{41} & c_{42} & c_{43} & 0 & -c_{54} & -c_{64} \\ c_{51} & -c_{52} & c_{53} & c_{54} & 0 & -c_{65} \\ c_{61} & c_{62} & -c_{63} & c_{64} & c_{65} & 0 \end{bmatrix}, \tag{6.69}$$

where

$$\begin{array}{llll} c_{41} = mz_G r & c_{42} = mw & c_{43} = m\left(z_G p - v\right) & \\ c_{51} = m\left(x_G q - w\right) & c_{52} = m(z_G r + x_G\, p) & c_{53} = m\left(z_G q + u\right) & c_{54} = I_{xz} p - I_z r \\ c_{61} = m\left(v + x_G r\right) & c_{62} = -mu & c_{63} = m x_G p & c_{64} = I_y q \\ c_{65} = I_x p + I_{xz} r. & & & \end{array} \tag{6.70}$$

We may divide the effect of current into two parts: the potential part and the viscous part. The Coriolis and centripetal matrix of the added mass including the potential part of the current load is formulated according to

$$\mathbf{C}_{\mathrm{A}}(\nu_{\mathrm{r}}) = \begin{bmatrix} 0 & 0 & 0 & 0 & -c_{a51} & -c_{a61} \\ 0 & 0 & 0 & -c_{a42} & 0 & -c_{a62} \\ 0 & 0 & 0 & -c_{a43} & -c_{a53} & 0 \\ 0 & c_{a42} & c_{a43} & 0 & -c_{a54} & -c_{a64} \\ c_{a51} & 0 & c_{a53} & c_{a54} & 0 & -c_{a65} \\ c_{a61} & c_{a62} & 0 & c_{a64} & c_{a65} & 0 \end{bmatrix}, \tag{6.71}$$

where

$$
\begin{array}{lll}
c_{a42} = -Z_{\dot{w}} w - X_{\dot{w}} u_r - Z_{\dot{q}} q & c_{a43} = Y_{\dot{p}} p + Y_{\dot{v}} v_r + Y_{\dot{r}} r & \\
c_{a51} = Z_{\dot{q}} q + Z_{\dot{w}} w + X_{\dot{w}} u_r & c_{a53} = -X_{\dot{q}} q - X_{\dot{u}} u_r - X_{\dot{w}} w & c_{a54} = Y_{\dot{r}} v_r + K_{\dot{r}} p + N_{\dot{r}} r \\
c_{a61} = -Y_{\dot{v}} v_r - Y_{\dot{p}} p - Y_{\dot{r}} r & c_{a62} = X_{\dot{u}} u_r + X_{\dot{w}} w + X_{\dot{q}} q & c_{a64} = X_{\dot{q}} u_r + Z_{\dot{q}} w + M_{\dot{q}} q \\
c_{a65} = Y_{\dot{p}} v_r + K_{\dot{p}} p + K_{\dot{r}} r &
\end{array}
\tag{6.72}
$$

Notice that the so-called Munk moments appear from the expression $\mathbf{C}_{\mathrm{A}}(\nu_{\mathrm{r}})\nu_{\mathrm{r}}$, see Faltinsen (1993) and Newman (1997).

Generalized damping and current forces, $\mathbf{D}(\kappa, \nu_{\mathrm{r}})$:

The damping vector may be divided into a nonlinear and a linear component according to

$$
\mathbf{D}(\kappa, \nu_{\mathrm{r}}) = \mathbf{D}_{\mathrm{L}}(\kappa, \nu_{\mathrm{r}})\nu_{\mathrm{r}} + \mathbf{d}_{\mathrm{NL}}(\nu_{\mathrm{r}}, \gamma_{\mathrm{r}}). \tag{6.73}
$$

The linear damping is assumed to vanish for increasing speed as the flow becomes turbulent. In order to incorporate this effect the linear damping is multiplied with an an exponential decaying functions according to:

$$
\mathbf{D}_{\mathrm{L}}(\kappa, \nu_{\mathrm{r}}) = \begin{bmatrix} X_{u_r} e^{-\kappa|u_r|} & .. & X_r e^{-\kappa|r|} \\ .. & .. & .. \\ N_{u_r} e^{-\kappa|u_r|} & .. & N_r e^{-\kappa|r|} \end{bmatrix},
$$

where κ is a positive constant such that $\kappa \in \mathbb{R}^+$.

Furthermore, the effect of current load is normally included in the nonlinear damping term by the definition of the relative velocity vector according to:

$$
\nu_{\mathrm{r}} = \begin{bmatrix} u - u_c & v - v_c & w & p & q & r \end{bmatrix}^T. \tag{6.74}
$$

The horizontal current components in surge and sway are defined as:

$$
u_c = V_c \cos(\beta_c - \psi), \quad v_c = V_c \sin(\beta_c - \psi), \tag{6.75}
$$

where V_c and β_c are the current velocity and direction respectively, see Figure 6.19. Notice that the current velocity components in heave, roll, pitch and yaw are not considered. The total relative current velocity is then defined as for $u_r = u - u_c$, and $v_r = v - v_c$ according to

$$
U_{cr} = \sqrt{u_r^2 + v_r^2}. \tag{6.76}
$$

The relative drag angle is found from the following relation:

$$
\gamma_{\mathrm{r}} = \mathrm{atan2}(-v_r, -u_r), \tag{6.77}
$$

where *atan*2 is the four quadrant arctangent function of the real parts of the elements of X and Y, such that $-\pi \leq \mathrm{atan2}(Y, X) \leq \pi$. The nonlinear damping is assumed to be caused by turbulent skin friction and viscous eddy-making, also denoted as vortex shedding, Faltinsen (1993).

Nonlinear damping and current forces Assuming small vertical motions, the 6-dimensional nonlinear damping vector is often formulated as:

$$\mathbf{d}_{\mathrm{NL}}(\nu_{\mathrm{r}},\gamma_{\mathrm{r}}) = 0.5\rho_w L_{pp} \begin{bmatrix} DC_{cx}(\gamma_{\mathrm{r}})|U_{cr}|U_{cr} \\ DC_{cy}(\gamma_{\mathrm{r}})|U_{cr}|U_{cr} \\ BC_{cz}(\gamma_{\mathrm{r}})|w|w \\ B^2C_{c\phi}(\gamma_{\mathrm{r}})|p|p + z_{py}DC_{cy}(\gamma_{\mathrm{r}})|U_{cr}|U_{cr} \\ L_{pp}BC_{c\theta}(\gamma_{\mathrm{r}})|q|q - z_{px}DC_{cx}(\gamma_{\mathrm{r}})|U_{cr}|U_{cr} \\ L_{pp}DC_{c\psi}(\gamma_{\mathrm{r}})|U_{cr}|U_{cr} \end{bmatrix}, \tag{6.78}$$

where $C_{cx}(\gamma_{\mathrm{r}})$, $C_{cy}(\gamma_{\mathrm{r}})$, $C_{cz}(\gamma_{\mathrm{r}})$, $C_{c\phi}(\gamma_{\mathrm{r}})$, $C_{c\theta}(\gamma_{\mathrm{r}})$ and $C_{c\psi}(\gamma_{\mathrm{r}})$ are the nondimensional drag coefficients found by model tests for the particular vessel with some defined location of the origin. B is the breadth, ρ_w is the density of water, L_{pp} is the length between the perpendiculars, and D is the draft. The second contributions to roll and pitch are the moments caused by the nonlinear damping and current forces in surge and sway, respectively, attacking in the corresponding centers of pressure located at z_{py} and z_{px}.

For relative current angles $|\beta_c - \psi| >> 0$ the cross flow principle (Faltinsen, 1993) may be applied to calculate the nonlinear current loads in sway d_2 and yaw d_6 in (6.78). In sway the cross flow formulation is written

$$d_2 = 0.5\rho_w \int_{L_{pp}} D(x)C_{cy}^{2D}(\gamma_{\mathrm{r}},x)\,(v_r + rx)\,|v_r + rx|dx, \tag{6.79}$$

where $D(x)$ is the longitudinal varying draft, and $C_{cy}^{2D}(\gamma_{\mathrm{r}},x)$ is the 2 dimensional drag coefficient. Similar as for sway, the cross flow expression in yaw is written

$$d_6 = 0.5\rho_w \int_{L_{pp}} D(x)C_{cy}^{2D}(\gamma_{\mathrm{r}},x)x\,(v_r + rx)\,|v_r + rx|dx. \tag{6.80}$$

For simplicity let us assume that $D(x) = D$, and that the drag coefficient is constant over the entire vessel length, that is $C_{cy}^{2D}(\gamma_{\mathrm{r}},x) = C_{cy}^{2D}$. Typical C_{cy}^{2D} values for ship (varying between $0.45 - 1.4$ dependent on Reynolds number), see Figure 6.16 in Faltinsen (1993). As shown in Figure 6.20 on page 197 in Faltinsen (1993) or slender bodies the drag coefficient may be adjusted for 3-dimensional effects due to the vertical vortex system at ship ends.

Let the origin be located in the middle of the ship, such that the distance to the bow is $L_{pp}/2$ and to the stern is $-L_{pp}/2$. Hence, a solution of (6.79) may be found to be

$$\begin{aligned} d_2 \;=\; & 0.5\rho_w DC_{cy}^{2D}\int_{L_{pp}} (v_r + rx)\,|v_r + rx|dx = \\ & 0.5\rho_w DC_{cy}^{2D}\begin{pmatrix} \int_0^{L_{pp}/2}\left(sgn(v_r)|v_r^2 + rv_rx| + sgn(rx)|rv_rx + r^2x^2|\right)dx + \\ \int_{-L_{pp}/2}^{0}\left(sgn(v_r)|v_r^2 + rv_rx| + sgn(rx)|rv_rx + r^2x^2|\right)dx \end{pmatrix} = \\ & 0.5\rho_w DC_{cy}^{2D}\begin{pmatrix} sgn(v_r)\left[\left|\frac{L_{pp}}{2}v_r^2 + \frac{L_{pp}^2}{8}v_rr\right| + \left|\frac{L_{pp}}{2}v_r^2 - \frac{L_{pp}^2}{8}v_rr\right|\right] + \\ sgn(r)\left[\left|\frac{L_{pp}^2}{8}v_rr + \frac{L_{pp}^3}{24}r^2\right| - \left|-\frac{L_{pp}^2}{8}v_rr + \frac{L_{pp}^3}{24}r^2\right|\right] \end{pmatrix}. \end{aligned} \tag{6.81}$$

sgn is the sign function defined such that $sgn(x) = 1$ for $x \geq 0$ and $sgn(x) = -1$ for $x < 0$. Notice that $sgn(rx) = sgn(r)sgn(x)$.

Similarly, (6.80) is rewritten

$$\begin{aligned} d_6 &= 0.5\rho_w D C_{cy}^{2D} \int_{L_{pp}} x\,(v_r + rx)\,|v_r + rx| dx = \\ & 0.5\rho_w D C_{cy}^{2D} \begin{pmatrix} \int_0^{L_{pp}/2} \left(sgn(v_r x)|v_r^2 x + r v_r x^2| + sgn(rx^2)|r v_r x^2 + r^2 x^3|\right) dx + \\ \int_{-L_{pp}/2}^{0} \left(sgn(v_r x)|x v_r^2 + r v_r x^2| + sgn(rx^2)|r v_r x^2 + r^2 x^3|\right) dx \end{pmatrix} = \\ & 0.5\rho_w D C_{cy}^{2D} \begin{pmatrix} sgn(v_r)\left[\left|\frac{L_{pp}^2}{8} v_r^2 + \frac{L_{pp}^3}{24} v_r r\right| - \left|-\frac{L_{pp}^2}{8} v_r^2 + \frac{L_{pp}^3}{24} v_r r\right|\right] + \\ sgn(r)\left[\left|\frac{L_{pp}^3}{24} v_r r + \frac{L_{pp}^4}{64} r^2\right| + \left|\frac{L_{pp}^3}{24} v_r r - \frac{L_{pp}^4}{64} r^2\right|\right] \end{pmatrix}. \end{aligned} \tag{6.82}$$

Notice that $sgn(rx^2) = sgn(r)sgn(x^2) = sgn(r)$.

Remark 6.12 *One should notice that for sway and yaw in (6.78), it is assumed that*

$$0.5\rho_w \int_{L_{pp}} D(x) C_{cy}^{2D}(\gamma_{\mathrm{r}}, x)\,(v_r + rx)\,|v_r + rx| dx \approx 0.5\rho_w L_{pp} D C_{cy}(\gamma_{\mathrm{r}})|U_{cr}|U_{cr},$$

and

$$0.5\rho_w \int_{L_{pp}} D(x) C_{cy}^{2D}(\gamma_{\mathrm{r}}, x) x\,(v_r + rx)\,|v_r + rx| dx \approx 0.5\rho_w L_{pp}^2 D C_{c\psi}(\gamma_{\mathrm{r}})|U_{cr}|U_{cr},$$

implying that the effect of yaw angular velocity, r, is small relative to the effect of v_r.

Remark 6.13 *Furthermore, if the drag coefficient in sway is given by model tests, an alternative expression for the 2-dimensional drag coefficient applied in (6.79) and (6.80) may be found to be*

$$C_{cy}^{2D} = C_{cy}(\pi/2). \tag{6.83}$$

Linear damping It is important to notice that for velocities close to zero, linear damping becomes more significant than the nonlinear damping. The strictly positive linear damping matrix $\mathbf{D}_{\mathrm{L}} \in \mathbb{R}^{6\times 6}$ caused by linear wave drift damping and the laminar skin friction is written as

$$\mathbf{D}_{\mathrm{L}} = -\begin{bmatrix} X_u & 0 & X_w & 0 & X_q & 0 \\ 0 & Y_v & 0 & Y_p & 0 & Y_r \\ Z_u & 0 & Z_w & 0 & Z_q & 0 \\ 0 & K_v & 0 & K_p & 0 & K_r \\ M_u & 0 & M_w & 0 & M_q & 0 \\ 0 & N_v & 0 & N_p & 0 & N_r \end{bmatrix}. \tag{6.84}$$

This kind of damping must not be confused with the frequency-dependent wave radiation damping used in the wave-frequency model. In general, the effect of wave radiation damping can be neglected in the LF model due to the low frequency of oscillation, especially for the horizontal modes of motions. For the vertical-plane modes (heave, roll and pitch), potential damping may be of interest in the frequency range of interest for control, and should therefore be considered to be included in the LF model. Wave drift damping in surge can be interpreted as added resistance for the vessel advancing in waves and is proportional to the square of the significant wave height.

It is for most bodies hard to calculate the damping coefficients. A combination of empirical formulas, model tests and computational fluid dynamics (CFD) are normally used to find

Dominating damping	High sea state	Low sea state
Surge	Linear wave drift. Nonlinear turbulent skin friction.	Nonlinear turbulent skin friction, when $\|u_r\| > 0$. Linear laminar skin friction, for low KC number and $u_r \to 0$.
Sway	Nonlinear eddy-making. Linear wave drift.	Nonlinear eddy-making, when $\|v_r\| > 0$. Linear laminar skin friction, for low KC number and $v_r \to 0$.
Yaw	Nonlinear eddy-making. Linear wave drift.	Nonlinear eddy-making, when $\|v_r, r\| > 0$. Linear laminar skin friction, for low KC number and $v_r, r \to 0$.

Table 6.1: Dominating damping effects.

the damping coefficients. In Table 6.1 the dominating damping effects are described for the horizontal-plane DOF. The heave, roll and pitch will normally follow the same tendency as the sway and yaw.

The Keulegan-Carpenter number in Table 6.1 is defined as $KC = UT/D$, where U is the free stream velocity, T is the oscillation period and D is the characteristic length of the body. For sway and yaw the nonlinear damping due to eddy-making will dominate the damping until very low velocity, where the damping behavior is seen to be linear, suggesting that laminar skin friction is present. In the literature some authors do not include any linear damping terms in the models. Instead they let the drag coefficients increase to large values for small velocities $u_r, v_r, r \to 0$. However, from a control point of view it is appropriate to include both linear and nonlinear damping, as this seems to be more in agreement with the physics.

The coefficients can be calculated by special software or found by model tests. In the last years the importance of wave-drift damping has been more appreciated, and some effort has been made to include wave-drift damping predictions in hydrodynamic software programs. The cross-flow principle and strip theory can be used to calculate viscous damping in sway and yaw. The cross-flow principle assumes that the flow separates due to the cross-flow past the ship, and that the transverse forces on a cross section is mainly due to separated flow effects on the pressure distribution around the ship. The method is semi-empirical in the sense that empirical drag coefficients are employed. For conventional ships data on nonlinear drag coefficients for the horizontal-plane modes are available. Instead of applying semi-empirical methods, model tests are often used. When using model tests it should be kept in mind that scale effects may be important for the viscous forces. The transition from laminar to turbulent boundary layer is dependent on the Reynolds number, which is different in model and in full scale. This may also affect the separation point and thus the eddy-making damping. In cases with a clearly defined separation point, such as a bilge keel, scale effects are not supposed to be significant for the eddy-making damping. Wave drift damping is considered to be unaffected by scale effects.

If there already exists data from other ships, based on model tests or numerical calculations, experience has shown that using proper scaling techniques, these coefficients may represent a reasonable good estimate for ships with similar geometrical hull shapes. For further details

about damping the reader is referred to Faltinsen (1993) and Newman (1997).

Remark 6.14 *In implementation of the linear damping terms for ships due to linear skin friction, it is suggested to ramp down these damping contributions when the relative speed exceeds* $0.25\ m/s$. *Notice that the linear damping due to wave drift should be maintained.*

Generalized restoring forces, $\mathbf{G}(\eta)$:

Here it is assumed small roll and pitch angles, such that the restoring vector can be linearized to $\mathbf{G}\eta$, where $\mathbf{G} \in \mathbb{R}^{6\times 6}$ is a matrix of linear generalized gravitation and buoyancy force coefficients and is for xz-plane symmetry written

$$\mathbf{G} = -\begin{bmatrix} 0 & 0 & 0 & 0 & 0 & 0 \\ 0 & 0 & 0 & 0 & 0 & 0 \\ 0 & 0 & Z_z & 0 & Z_\theta & 0 \\ 0 & 0 & 0 & K_\phi & 0 & 0 \\ 0 & 0 & M_z & 0 & M_\theta & 0 \\ 0 & 0 & 0 & 0 & 0 & 0 \end{bmatrix}, \tag{6.85}$$

where the coefficients are defined as

$$Z_z \triangleq -\rho_w g A_{WP}, \tag{6.86}$$

$$Z_\theta = M_z \triangleq \rho_w g \iint\limits_{A_{WP}} x dA, \tag{6.87}$$

$$K_\phi \triangleq -\rho_w g \nabla (z_G - z_B) - \rho_w g \iint\limits_{A_{WP}} y^2 dA = -\rho_w g V \overline{GM_T}, \tag{6.88}$$

$$M_\theta \triangleq -\rho_w g \nabla (z_G - z_B) - \rho_w g \iint\limits_{A_{WP}} x^2 dA = -\rho_w g V \overline{GM_L}. \tag{6.89}$$

Here, g is the acceleration of gravity, A_{WP} is the waterplane area, $dA = dxdy$, ∇ is the displaced volume of water, and $\overline{GM_T}$ and $\overline{GM_L}$ are the transverse and longitudinal metacentric heights, respectively.

6.4.2 Environmental Loads

The slowly-varying environmental loads acting on the vessel are composed of

$$\tau_{\text{env}} = \tau_{\text{wind}} + \tau_{\text{wave2}}. \tag{6.90}$$

Remember that the current load vector already is included by the relative velocity vector in the nonlinear damping term.

Wind load model

The effect of wind may be divided into mean, slowly-varying and rapidly-varying wind loads. The relative wind velocity vector is defined as

$$\nu_{\mathrm{rw}} = \left[\begin{array}{cccccc} u - u_w & v - v_w & w & p & q & r \end{array} \right]^T. \tag{6.91}$$

The components of the wind velocities are defined according to

$$u_w = V_w \cos\left(\beta_w - \psi\right), \;\; v_w = V_w \sin\left(\beta_w - \psi\right), \tag{6.92}$$

where V_w and β_w are the wind velocity and direction respectively, see Figure 6.19. The total relative wind velocity is then defined as for $u_{rw} = u - u_w$, and $v_{rw} = v - v_w$ according to

$$U_{wr} = \sqrt{u_{rw}^2 + v_{rw}^2}. \tag{6.93}$$

The relative wind angle is found from the following relation:

$$\gamma_{\mathrm{w}} = \mathrm{atan2}(-v_{rw}, -u_{rw}). \tag{6.94}$$

The wind load vector is then formulated

$$\tau_{\mathrm{wind}} = 0.5\rho_a \left[\begin{array}{l} A_x C_{wx}(\gamma_w) \left|U_{wr}\right| U_{wr} \\ A_y C_{wy}(\gamma_w) \left|U_{wr}\right| U_{wr} \\ 0 \\ A_y L_{yz} C_{wy}(\gamma_w) \left|U_{wr}\right| U_{wr} \\ -A_x L_{xz} C_{wx}(\gamma_w) \left|U_{wr}\right| U_{wr} \\ A_y L_{oa} C_{w\psi}(\gamma_w) \left|U_{wr}\right| U_{wr} \end{array} \right]. \tag{6.95}$$

Here, ρ_a is the density of air, L_{oa} is the overall length of the vessel, L_{xz} and L_{yz} are the vertical distances between transverse and longitudinal origin and the wind load point of attack, A_x and A_y are the lateral and longitudinal areas of the non-submerged part of the ship projected on the xz-plane and yz-plane. $C_{wx}(\gamma_w), C_{wy}(\gamma_w)$,and $C_{w\psi}(\gamma_w)$ are the non-dimensional wind coefficients in surge, sway and yaw respectively. These coefficients are often found by model testing or by employing semi-empirical formulas as presented in Isherwood (1972) and Blendermann (1986).

Remark 6.15 *In station keeping operations the wind velocity is often assumed to be much larger than the vessel velocity, such that the relative wind angle may be simplified to* $\gamma_w = \beta_w - \psi$, *and* $U_{wr} = \sqrt{u_w^2 + v_w^2}$.

Wave load model

The wave drift loads contribute to a significant part of the total excitation force in the low-frequency model. The second-order wave effects are divided into mean, slowly varying (difference frequencies) and rapidly varying (sum frequencies) wave loads. For the applications considered here the effect of the rapidly varying second order wave loads can be neglected. The determination of the second-order wave effects can be done by means of quadratic transfer functions as given in Newman (1997) and Faltinsen (1993))

$$\begin{aligned} \tau_{wave2}^i &= \bar{\tau}_{wm}^i + \tau_{wsv}^i, \quad i = 1..6 \\ &= \sum_{j=1}^{N} \sum_{k=1}^{N} A_j A_k \left[T_{jk}^{ic} \cos\left(\left(\omega_k - \omega_j\right) t + \varepsilon_k - \varepsilon_j\right) + T_{jk}^{is} \sin\left(\left(\omega_k - \omega_j\right) t + \varepsilon_k - \varepsilon_j\right) \right], \end{aligned} \tag{6.96}$$

where ω_j is the wave frequency, A_j is the wave amplitude and ε_j is a random phase angle. The superscript c and s denote cos and sin, respectively. The quadratic transfer functions T_{jk} are dependent on both the first and second order velocity potentials, which require a nonlinear panel methodology. In addition, it is time-consuming to calculate the T_{jk} for all combinations of ω_k and ω_j. This motivates to derive some simplifications. One should notice that the transfer functions when $k = j$, T_{jj}, represents the mean wave loads, and can be calculated from the first order velocity potential only. The most interesting slowly-varying wave loads are those where $\omega_k - \omega_j$ is small and the loads are truly slowly-varying. Normally, T_{jk} will not vary significantly with the frequency. Then, the following approximation byNewman (1997) will give satisfactory results

$$T_{jk}^{ic} = T_{kj}^{ic} = \frac{1}{2}\left(T_{jj}^{ic} + T_{kk}^{ic}\right) \tag{6.97}$$

$$T_{jk}^{is} = T_{kj}^{is} = 0 \tag{6.98}$$

The slowly-varying loads are approximated by the mean drift loads, and hence, the computation becomes much simpler and less time consuming. This approximation based on frequency dependent wave drift coefficients will then further be applied. By dividing the sea wave spectrum (usually of Pierson-Moskowitz type) into N equal frequency intervals with corresponding wave frequency, ω_j, and amplitude, A_j, the wave drift loads are found to be

$$\begin{aligned} \tau_{wave2}^{i} &= \bar{\tau}_{wm}^{i} + \tau_{wsv}^{i} \\ &= 2\left(\sum_{j=1}^{N} A_j \left(T_{jj}^{i}\left(\omega_j, \beta_{wave} - \psi\right)\right)^{1/2} \cos\left(\omega_j t + \varepsilon_j\right)\right)^2, \end{aligned} \tag{6.99}$$

where $T_{jj}^{i} > 0$ is the frequency-dependent wave drift function and β_{wave} is the mean wave direction (assumed to follow the same sign convention as wind and current). A disadvantage with this approximation is the numerical generation of high-frequency components of no physical meaning. By numerical filtering this can be avoided. Eq. (6.99) can also be extended to include wave spreading. In general, the second-order wave loads are much smaller than the first-order wave loads. The second-order wave loads are proportional to the square of the wave amplitude, whereas the first-order wave loads are proportional to the wave amplitude. This means that the second-order wave loads have an increased importance for increasing sea states.

6.4.3 Linear Wave-Frequency Model

In linear theory small waves and amplitudes of motion are assumed. The WF motion is in the literature calculated in the hydrodynamic frame. The hydrodynamic problem of a vessel in regular waves is solved as two sub-problems *wave reaction* and *wave excitation*, which are added together Faltinsen (1993). Potential theory is assumed, neglecting viscous effects.

- *Wave Reaction*: Forces and moments on the vessel when the vessel is forced to oscillate with the wave excitation frequency. The hydrodynamic loads are identified as added mass and wave radiation damping terms.
- *Wave Excitation*: Forces and moments on the vessel when the vessel is restrained from oscillating and there are incident waves. This gives the wave excitation loads which are

composed of so-called Froude-Kriloff (forces and moments due to the undisturbed pressure field as if the vessel was not present) and diffraction forces and moments (forces and moments because the presence of the vessel changes the pressure field).

In *station keeping* operations assuming small motions about the coordinates x_{d}, y_{d}, and ψ_{d}, the coupled equations of WF motions can in the hydrodynamic frame be formulated according to

$$\begin{aligned} \mathbf{M}(\omega)\ddot{\eta}_{Rw} + \mathbf{D}_p(\omega)\dot{\eta}_{Rw} + \mathbf{G}\eta_{Rw} &= \tau_{\mathrm{wave1}} \\ \dot{\eta}_w &= \mathbf{J}(\bar{\eta}_{\mathbf{2}})\dot{\eta}_{Rw}, \end{aligned} \tag{6.100}$$

where $\eta_{Rw} \in \mathbb{R}^6$ is the WF motion vector in the hydrodynamic frame, $\eta_w \in \mathbb{R}^6$ is the WF motion vector in the Earth-fixed frame, and $\bar{\eta}_2 = [0 \quad 0 \quad \psi_d]^T$. $\tau_{\mathrm{wave1}} \in \mathbb{R}^6$ is the first order wave excitation vector, which is dependent on the vessel heading relative to the incident wave direction. $\mathbf{M}(\omega) \in \mathbb{R}^{6\times6}$ is the system inertia matrix containing frequency dependent added mass coefficients in addition to the vessel's mass and moment of inertia. $\mathbf{D}_p(\omega) \in \mathbb{R}^{6\times6}$ is the wave radiation (potential) damping matrix. $\mathbf{G} \in \mathbb{R}^{6\times6}$ is the linearized restoring coefficient matrix due to the gravity and buoyancy affecting heave, roll and pitch only. It is assumed that the mooring lines will not affect the WF motion (Triantafyllou, 1994).

Generally, a time domain equation cannot be expressed with frequency domain coefficient. However, this is a common used formulation denoted as a *pseudo-differential equation.* .An important feature of the added mass terms and the wave radiation damping terms is the memory effects, which in particular are important to consider for non-stationary cases, e.g. rapid changes of heading angle. Memory effects can be taken into account by introducing a convolution integral or a so-called retardation function, see Newman (1997) or state space models as presented in Fossen (2011).

Results from model tests and computer programs for vessel response analysis often come in the form of transfer functions or tables of coefficients. This applies to linear wave-induced motions, 2^{nd} -order wave drift and slowly varying motions. To a large extent, linear theory is sufficient for describing wave-induced motions and loads on vessels. This is especially true for moderate sea states. In irregular seas, the response of the vessel may be calculated by adding results for regular waves of different amplitudes, frequencies and directions. Nonlinear effects become increasingly important in severe sea states, and is still a subject for further research.

6.4.4 Thrust Servo Model

Usually, perfect control action without imposing the thruster dynamics are assumed. Unfortunately, this will not be true in a real system. The thrust response is affected by the dynamics in the actuators and the drive system. This will cause reduced command following capabilities such as phase lag and amplitude reduction when the frequency increases. There will also be a loss of thrust efficiency due to disturbances in the water inflow to the thruster blades, caused by thrust-to-thrust and thrust-to-hull interactions, current and vessel velocities. In addition the influence from the free surface will affect the thrust efficiency. Reduced thruster efficiency caused by disturbances in the water inflow is compensated for in the controller. This will be addressed in detail in Chapter 8. However, experience obtained from full-scale experiments indicates that a first-order model is well suited as a first approximation. Hence, the thruster dynamics is represented by the following simplified model:

$$\dot{\tau}_{\mathrm{thr}} = -\mathbf{A}_{\mathrm{thr}} \left(\tau_{\mathrm{thr}} + \tau_{\mathrm{c}} \right), \tag{6.101}$$

where $\tau_c \in \mathbb{R}^3$ is the commanded thrust vector in surge, sway and yaw produced by the controller. $\mathbf{A}_{\text{thr}} = \text{diag}\{1/T_1, 1/T_2, 1/T_3\}$ is the diagonal thruster dynamics matrix. Determination of the commanded thrust vector will be treated more in detail in Section 7.3.

6.5 Static Analysis of Cable Segments

6.5.1 Basic Assumptions

A basic assumption when working with cables is that we have no bending stiffness and no torsional stiffness. This means that only axial stiffness will be considered, and this simplifies the analysis of cables considerable compared to for instance beams.

Another assumption is that the axial tension in the cable is small enough to allow us to operate in the linear range of stress/strain relationship. This is reasonable for metallic cables and synthetic cables under normal tension.

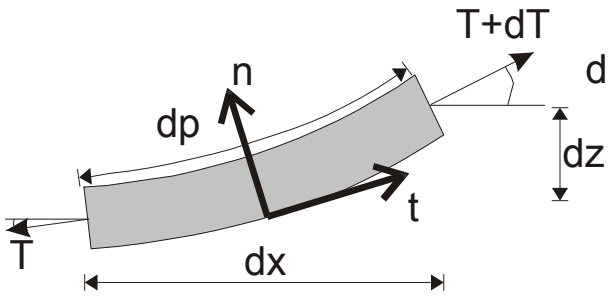

Figure 6.21: An infinitesimal cable segment.

Consider Figure 6.21 which shows a cable segment. The cable's weight per unit length in air is denoted $w_a = mg$, where g is the earth's gravity and m is the mass per length unit. When the cable is submerged a hydrostatic force will appear according to

$$B = \rho_w g A. \tag{6.102}$$

ρ_w is the density of water and A is the cross-sectional area. Given a cable tension, T_c, Triantafyllou (1990) shows that the effective tension, T, may be written as

$$T = T_c + p_e A, \tag{6.103}$$

where p_e is the hydrostatic pressure at the specific point of the cable. This leads to the following definition of the stretched cable's weight in water, w_1:

$$w_1 = w_a - B. \tag{6.104}$$

When working with cables we assume that the material is *isotropic*. *Isotropic* materials' properties are by definition independent of direction. Such materials have only 2 independent variables (i.e. elastic constants) in their stiffness and compliance matrices. The generalized Hooke's law for axial strain may be written as

$$\sigma = E\varepsilon = \frac{T}{A}, \tag{6.105}$$

where σ is strain, E is Young's modulus, ε is axial strain and ν is Poisson's ratio. Applies this law on the submerged cable and find

$$\varepsilon = \frac{1}{E}\left(\frac{T_c}{A} + 2\nu p_e\right). \tag{6.106}$$

Notice that a Posisson's ration of $\frac{1}{2}$ results in a incompressible material. Poisson's ratio for synthetic cables are close to $\frac{1}{2}$, while metallic materials have a ratio approximately $\frac{1}{3}$ (Triantafyllou, 1990). A substantial simplification of the forthcoming analysis is achieved if we assume that Poisson's ratio is close to $\frac{1}{2}$. Using (6.103) in (6.106) a simplified expression for the axial strain is found to be

$$\varepsilon = \frac{1}{EA}(T_c + p_e A) = \frac{T}{EA}. \tag{6.107}$$

This leads to the last assumption; the cross-sectional area of the cable, A, will not undergo significant changes due to the axial deformation of the cable.

6.5.2 Catenary Equations

Catenary equations are widely used in mooring analysis of anchored bodies. In mooring analysis the effect of each mooring line is first analyzed separately and thereafter summarized to constitute the complete mooring system, often consisting of several deployed mooring lines.

For anchored floating vessels it is assumed that each mooring line is fastened in the seabed and in the vessel. Vertical and horizontal forces caused by the mooring system will act on the vessel at the terminal points. However, often only the horizontal forces are important for the vessel response in the horizontal plane. Along the mooring line gravity and buoyancy forces are assumed to be most important. For this purpose a two-dimensional approach is often considered to be sufficient. If varying current in space is considered, a three-dimensional approach may be needed.

Two-dimensional approach

An infinite small element of a cable is shown in Figure 6.21. The tangential and normal forces to this element may be written as

$$\mathbf{F} = \begin{bmatrix} F_t \\ F_n \end{bmatrix} = \begin{bmatrix} -T - w_1 \sin\varphi \; dp + (T + dT)\cos(d\varphi) \\ -w_1 \cos\varphi \; dp + (T + dT)\sin(d\varphi) \end{bmatrix} = \begin{bmatrix} 0 \\ 0 \end{bmatrix}. \tag{6.108}$$

Taking the limit

$$\lim_{dp\to 0} \mathbf{F} \Rightarrow \begin{bmatrix} \frac{dT}{dp} \\ T\frac{d\varphi}{dp} \end{bmatrix} = \begin{bmatrix} w_1 \sin\varphi \\ w_1 \cos\varphi \end{bmatrix}, \tag{6.109}$$

because

$$\lim_{d\varphi\to 0} \begin{bmatrix} \sin(d\varphi) \\ \cos(\varphi) \end{bmatrix} = \begin{bmatrix} d\varphi \\ 1 \end{bmatrix}. \tag{6.110}$$

From the Figure 6.21 we also find that

$$\begin{bmatrix} dx \\ dz \end{bmatrix} = \begin{bmatrix} dp\cos\varphi \\ dp\sin\varphi \end{bmatrix}. \tag{6.111}$$

It is appropriate to formulate the equations for the tension as a function of the cable's Lagrangian coordinate, denoted as s, along the unstretched length. The cable's strain is given in (6.107), but may also be written as

$$\varepsilon = \frac{dp - ds}{ds} = \frac{dp}{ds} - 1, \tag{6.112}$$

where p is the cable's stretched length. Triantafyllou Triantafyllou (1990) shows the relation between mass, buoyancy and specific weight of the stretched and unstretched cable are

$$\begin{aligned} m_0\, ds &= m\, dp, && (6.113a)\\ B_0\, ds &= B\, dp, && (6.113b)\\ w_z\, ds &= w_1\, dp. && (6.113c) \end{aligned}$$

Combining (6.109) and (6.111) with (6.112) and (6.113) leads to the following two-dimensional *catenary equations*

$$\begin{aligned} \frac{dT}{ds} &= w_z \sin\varphi, && (6.114a)\\ T\frac{d\varphi}{ds} &= w_z \cos\varphi, && (6.114b)\\ \frac{dx}{ds} &= (1+\varepsilon)\cos\varphi, && (6.114c)\\ \frac{dz}{ds} &= (1+\varepsilon)\sin\varphi. && (6.114d) \end{aligned}$$

Notice that (6.114) is a set of ODEs which may be written in the form (10.1) described in Section 10.2.1. If we know that an axial force is acting at the end of the cable, this is an initial value problem where s is the independent variable. Numerical routines like MATLAB's `ode45` could be utilized, but in the next section we will show that there exists an analytical solution.

Solution of the two-dimensional equations

Consider the cable in Figure 6.22. An axial force T_B acts in point B, and no vertical force is present in point A. This is decomposed into a vertical and a horizontal force

$$\begin{aligned} V_B &= T_B \sin\varphi, && (6.115a)\\ H_B &= T_B \cos\varphi, && (6.115b)\\ \tan\varphi &= \frac{V_B}{H_B}. && (6.115c) \end{aligned}$$

Combining (6.114a) and (6.114b) gives

$$\frac{dT}{T} = \tan\varphi\, d\varphi. \tag{6.116}$$

Integrating and applying the boundary condition in (6.115b) leads to

$$T = \frac{H_B}{\cos\varphi}. \tag{6.117}$$

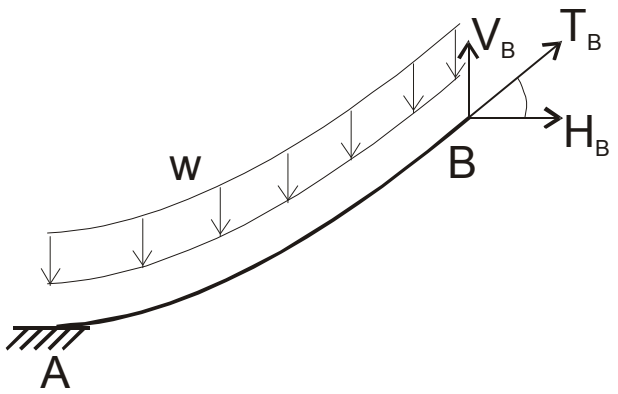

Figure 6.22: A marine mooring cable.

Introducing (6.117) into (6.114b)

$$\frac{d\varphi}{ds} = \frac{w}{H_B}\cos^2\varphi. \tag{6.118}$$

Integration and use of (6.115c) leads to

$$\tan\varphi = \frac{V_B}{H_B} - \frac{w}{H_B}(L-s), \tag{6.119}$$

where L is the cable's unstretched length.

φ may now easily be calculated as a function of s in (6.119). First, notice the following relations

$$\cos x = \frac{1}{\pm\sqrt{1+\tan^2 x}}, \tag{6.120}$$

$$\sinh^{-1}(x) = \ln(x+\sqrt{1+x^2}), \tag{6.121}$$

$$\sin x = \frac{\tan x}{\pm\sqrt{1+\tan^2 x}}. \tag{6.122}$$

Use of (6.120) leads to an expression for the tension along the Lagrangian variable s

$$\begin{aligned} T(s) &= \frac{H_B}{\cos\varphi} = H_B\sqrt{1+\tan^2\varphi}, \qquad (6.123)\\ &= H_B\sqrt{1+\frac{(V_B - w_z(L-s))^2}{H_B^2}} = \sqrt{H_B^2 + (V_B - w_z(L-s))^2}. \end{aligned}$$

Notice that for $s = L$ this gives the relation $T_B^2 = H_B^2 + V_B^2$.

Sometimes it may be valuable to calculate the Cartesian coordinates of the line. Eqs. (6.114c) and (6.114d) can be rewritten to:

$$\frac{dx}{ds} = (1+\varepsilon)\cos\varphi = \left(1+\frac{T(s)}{EA}\right)\cos\varphi, \tag{6.124a}$$

$$\frac{dz}{ds} = (1+\varepsilon)\sin\varphi = \left(1+\frac{T(s)}{EA}\right)\sin\varphi. \tag{6.124b}$$

Still assuming constant H_B we find that

$$\frac{dx}{ds} = \left(1+\frac{T(s)}{EA}\right)\cos\varphi = \cos\varphi + \frac{H_B}{EA}, \tag{6.125}$$

$$\frac{dz}{ds} = \left(1+\frac{T(s)}{EA}\right)\sin\varphi = \sin\varphi + \frac{V(s)}{EA} = \sin\varphi + \frac{V_B - w_z(L-s)}{EA}. \tag{6.126}$$

Use of (6.120) and (6.122) yields

$$\int_0^s dx = \int_0^s \cos\varphi + \frac{H_B}{EA}ds = \int_0^s \frac{1}{\sqrt{1+\frac{(V_B-w_z(L-s))^2}{H_B^2}}} + \frac{H_B}{EA}ds, \tag{6.127}$$

$$\int_0^s dz = \int_0^s \sin\varphi + \frac{V_B - w_z(L-s)}{EA}ds, \tag{6.128}$$

$$= \int_0^s \frac{\frac{V_B-w_z(L-s)}{H_B}}{\sqrt{1+\frac{(V_B-w_z(L-s))^2}{H_B^2}}} + \frac{V_B - w_z(L-s)}{EA}ds,$$

$$\Downarrow$$

$$\int_0^s dx = \int_0^s \frac{H_B}{\sqrt{H_B^2+(V_B-w_z(L-s))^2}} + \frac{H_B}{EA}ds, \tag{6.129}$$

$$\int_0^s dz = \int_0^s \frac{V_B - w_z(L-s)}{\sqrt{H_B^2+(V_B-w_z(L-s))^2}} + \frac{V_B - w_z(L-s)}{EA}ds. \tag{6.130}$$

Integration of this expression along the variable s leads to

$$x(s) = \frac{H_B}{w_z}\ln\left[V_B - w_z(L-s) + \sqrt{H_B^2+[V_B-w_z(L-s)]^2}\right]$$
$$-\frac{H_B}{w_z}\ln\left[V_B - w_zL + \sqrt{H_B^2+(V_B-w_zL)^2}\right] + \frac{H_Bs}{EA} + C_x, \tag{6.131}$$

$$z(s) = \frac{1}{w_z}\left(\sqrt{H_B^2+[V_B-w_z(L-s)]^2} - \sqrt{H_B^2+(V_B-w_zL)^2}\right)$$
$$+\frac{1}{EA}\left(V_Bs + \frac{w_z}{2}(L-s)^2\right) + C_z. \tag{6.132}$$

We may want our coordinates for the start point $s = 0$ to be $(0,0)$. Applies this boundary condition to find C_x and C_z. This gives

$$C_x = 0, \tag{6.133}$$

$$C_z = -\frac{1}{2EA}w_zL^2. \tag{6.134}$$

In some literature, e.g. Triantafyllou (1990), it is common to write $x(s)$ as a hyperbolic sine. If we make use of (6.121) we may write

$$\begin{aligned} x(s) &= \frac{H_B}{w_z}\ln\left[\frac{V_B - w_z(L-s)}{H_B} + \sqrt{1+\frac{\left[V_B - w_z(L-s)\right]^2}{H_B^2}}\right] \\ &\quad -\frac{H_B}{w_z}\ln\left[\frac{V_B - w_z L}{H_B} + \sqrt{1+\frac{(V_B - w_z L)^2}{H_B^2}}\right] + \frac{H_B s}{EA}, \end{aligned} \tag{6.135}$$

$$x(s) = \frac{H_B}{w_z}\left[\sinh^{-1}\left(\frac{V_B - w_z(L-s)}{H_B}\right) - \sinh^{-1}\left(\frac{V_B - w_z L}{H_B}\right)\right] + \frac{H_B s}{EA}. \tag{6.136}$$

Sometimes it may be useful to express the z- and x-coordinates as a function of each other. Remember that $V(0) = 0$. Eq. (6.123) may be written as

$$T(s) = \sqrt{H_B^2 + (w_z s)^2}\,. \tag{6.137}$$

Eq. (6.119) may be rewritten to

$$\tan\varphi = \frac{V(s)}{H_B} = \frac{dz}{dx} = \frac{w_z s}{H_B}. \tag{6.138}$$

Combining the equations above leads to

$$T = \sqrt{H_B^2 + H_B^2\left(\frac{dz}{dx}\right)^2} = H_B\sqrt{1+\left(\frac{dz}{dx}\right)^2}. \tag{6.139}$$

From Figure 6.21

$$dp^2 = dx^2 + dz^2, \tag{6.140}$$

and by use of the relation $dp = ds(1+\varepsilon)$, we find

$$\frac{ds}{dx} = \frac{1}{1+\varepsilon}\sqrt{1+\left(\frac{dz}{dx}\right)^2}, \tag{6.141}$$

$$\Rightarrow \quad s(x) = \int_0^x \frac{1}{1+\varepsilon}\sqrt{1+\left(\frac{dz}{dx}\right)^2}\,dx. \tag{6.142}$$

Combining with (6.138) the following relation appears

$$\frac{dz}{dx} = \frac{w_z}{H_B}\int_0^x \frac{1}{1+\varepsilon}\sqrt{1+\left(\frac{dz}{dx}\right)^2}\,dx. \tag{6.143}$$

If we assume *inelastic* material and substitute

$$\sinh u = \frac{dz}{dx}, \tag{6.144}$$

which leads to

$$\sinh u = \frac{w_z}{H_B}\int_0^x \sqrt{1+\sinh^2 u}\,dx, \tag{6.145}$$

$$\sinh u = \frac{w_z}{H_B}\int_0^x \cosh u\,dx. \tag{6.146}$$

Derivation on both sides

$$\frac{du}{dx}\cosh u = \frac{w_z}{H_B}\cosh u, \tag{6.147}$$

$$du = \frac{w_z}{H_B}dx, \tag{6.148}$$

$$u = \frac{w_z}{H_B}x + C_1. \tag{6.149}$$

Considering the boundary condition $\sinh u|_{x=0} = 0$, we find that $C_1 = 0$. Integration of (6.144)

$$z = \frac{w_z}{H_B}\cosh\frac{w_z}{H_B}x + C_2. \tag{6.150}$$

Boundary condition $z|_{x=0} = 0 \Rightarrow C_2 = -\frac{w_z}{H_B}$. Finally we have for the inelastic case:

$$z(x) = \frac{w}{H_B}\cosh\frac{w}{H_B}x - \frac{w}{H_B}. \tag{6.151}$$

For the elastic case the substitution in (6.144) does not solve the problem, and the final expression for $z(x)$ becomes very unhandy.

Catenary in the three-dimensional case

This section is mainly based on Sagatun (2001). Remember the assumption of no significant reduction of the cable's cross-sectional area when it is stretched. Considering the cable with one-dimensional strain along the Lagrangian variable s, Hooke's law is

$$\sigma = \frac{T}{A} = E\varepsilon, \tag{6.152}$$

$$\Rightarrow T = \sigma A = EA\varepsilon, \tag{6.153}$$

where ε is given in (6.112). Combining the equations we find that

$$T = EA\left(\frac{dp}{ds} - 1\right). \tag{6.154}$$

Seeking a solution in Cartesian coordinates of the cable as a function of s, the identity $\frac{d\mathbf{r}}{ds} = \frac{d\mathbf{r}}{dp}\frac{dp}{ds}$ will be useful. $\mathbf{r} = [x\ y\ z]^T$ contains the Cartesian coordinates as a function of s or p. This leads to the relation

$$\frac{d\mathbf{r}}{ds} = \frac{d\mathbf{r}}{dp}\left(\frac{T}{EA} + 1\right). \tag{6.155}$$

Consider the first segment of a cable with distributed vertical force, w_z, a vertical concentrated force, $f_{1,z}$ and axial tension T, in the end point. Inspection of Figure 6.23 gives

$$f_{0,z} = T\frac{dz}{dp}\bigg|_{s=s_1} + \bar{f}_{1,z} + w_z(s_1 - s_0), \tag{6.156}$$

for static equilibrium. s_i indicates the value of s in node i, and $\bar{f}_{i,k}$ indicates the value of concentrated force in node i and Cartesian direction k.

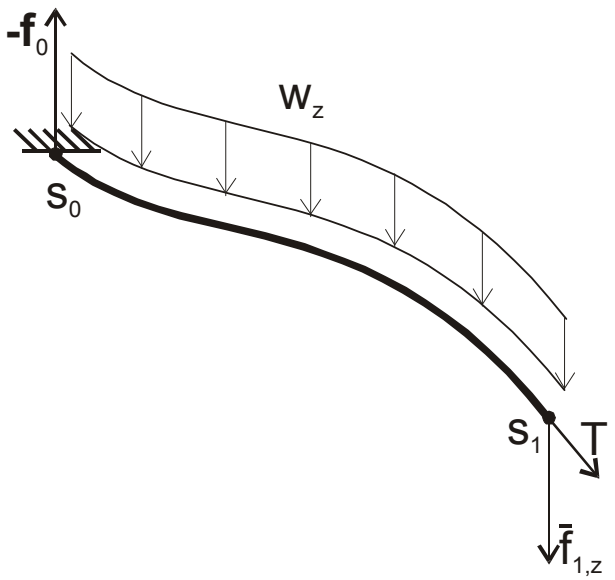

Figure 6.23: A cable segment with concentrated and distributed loads (Sagatun (2001)).

Assume that the cable is terminated in point 0, and that concentrated forces, $\bar{\mathbf{f}}_i$, may act in discrete points (cable nodes). Combination of this assumption and (6.156) written in vectorial form gives the following equation for the forces acting in the cable's terminating point:

$$\mathbf{f}_0 = T\frac{d\mathbf{r}}{dp}\bigg|_{s=L} + \sum_{i=1}^{n} \bar{\mathbf{f}}_i + \sum_{i=1}^{n} \mathbf{w}_i(s_i - s_{i-1}), \tag{6.157}$$

where $\{s \in [0, L] \to \mathbb{R},\ k \in [1, n] \to \mathbb{N} \mid s \in [s_{k-1}, s_k]\}$. n is the number of cable segments and L is the cable's unstretched length. $\mathbf{w}_i = [w_{ix}\ w_{iy}\ w_{iz}]^T$ indicates the constant distributed force vector in segment i.

An investigation of Figure 6.24 may make it easier to keep the indexes of the variables right.

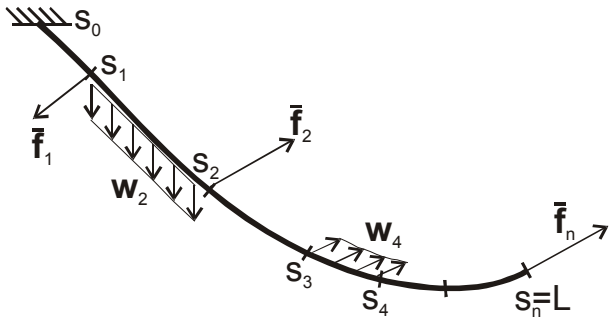

Figure 6.24: A cable of several segments with concentrated forces, $\bar{\mathbf{f}}_i$, and distributed forces, $\mathbf{w}_i$. Notice the indexes.

The cable must be divided into a new segment when one of the following conditions are fulfilled:

1. A concentrated force occurs

2. A change in distributed force occurs

3. A change in cross-sectional area occurs

4. A change in the cable's Young's modulus occurs

A constant distributed force along the cable leads to a simplification of (6.157)

$$\mathbf{f}_0 = T\frac{d\mathbf{r}}{dp}\bigg|_{p(s=L)} + \sum_{i=1}^{n} \overline{\mathbf{f}}_i + \mathbf{w}L, \tag{6.158}$$

where $\mathbf{w}$ is the constant distributed force along the cable.

Sagatun (2001) gives the following derivation of a differential equation for the cable. It is assumed that (6.158) holds. Reordering of (6.158) leads to

$$T\frac{d\mathbf{r}}{dp}\bigg|_{p(s=L)} = \mathbf{f}_0 - \sum_{i=1}^{n} \overline{\mathbf{f}}_i - \mathbf{w}L. \tag{6.159}$$

We want to find the tension vector as a function of s. Assume that $s(p)$ may be found from (6.155). Then the following relation must hold

$$T\frac{d\mathbf{r}}{dp}(s) = \mathbf{f}_0 - \sum_{i=1}^{k} \overline{\mathbf{f}}_i - \mathbf{w}s, \tag{6.160}$$

where $\{s \in [0, L] \to \mathbb{R},\ k \in [1, n] \to \mathbb{N} \mid s \in [s_{k-1}, s_k]\}$. We define

$$\mathbf{T}(p) = T\begin{bmatrix} \frac{dx}{dp} \\ \frac{dy}{dp} \\ \frac{dz}{dp} \end{bmatrix} = T\frac{d\mathbf{r}}{dp}, \tag{6.161}$$

$$\mathbf{T}^T\mathbf{T} = T^2\frac{d\mathbf{r}}{dp}^T\frac{d\mathbf{r}}{dp}, \tag{6.162}$$

where $\mathbf{T} \in \mathbb{R}^3$. The substitution

$$\mathbf{f}_k = \mathbf{f}_0 - \sum_{i=1}^{k} \overline{\mathbf{f}}_i, \tag{6.163}$$

where $\{k \in [1, n] \to \mathbb{N}, s \in [0, L] \to \mathbb{R} \mid s \in [s_{k-1}, s_k]\}$, gives

$$T(s) = \sqrt{(\mathbf{f}_k - \mathbf{w}s)^T(\mathbf{f}_k - \mathbf{w}s)}. \tag{6.164}$$

Combining (6.163) and (6.160) gives

$$T\frac{d\mathbf{r}}{dp}(s) = \mathbf{f}_0 - \sum_{i=1}^{k} \overline{\mathbf{f}}_i - \mathbf{w}s = \mathbf{f}_k - \mathbf{w}s. \tag{6.165}$$

Use of (6.155)

$$T\frac{d\mathbf{r}}{dp} = \left(\frac{1}{EA} + \frac{1}{T}\right)^{-1}\frac{d\mathbf{r}}{ds} = \mathbf{f}_k - \mathbf{w}s. \tag{6.166}$$

Reordering leads to

$$\frac{d\mathbf{r}}{ds} = (\mathbf{f}_k - \mathbf{w}s)\left(\frac{1}{EA} + \frac{1}{T}\right). \tag{6.167}$$

Compare this equation to (6.124) found in the previous section. Remember that $\mathbf{T} = (\mathbf{f}_k - \mathbf{w}s)$ represents the tension in vectorial form. The trigonometric terms in (6.124) is a way of decomposing $\mathbf{T}$ into the xz-plane. This shows the relation between the two-dimensional case solved by Triantafyllou (1990) and the three-dimensional case solved by Sagatun (2001).

Substituting (6.164) gives the final differential equation

$$\frac{d\mathbf{r}}{ds} = (\mathbf{f}_k - \mathbf{w}s)\left(\frac{1}{EA} + \frac{1}{\sqrt{(\mathbf{f}_k - \mathbf{w}s)^T(\mathbf{f}_k - \mathbf{w}s)}}\right). \tag{6.168}$$

This is an ODE with s as the independent variable. This may be solved directly from the rewritten form

$$\mathbf{r}_k = \int_{s_{k-1}}^{s_k} (\mathbf{f}_k - \mathbf{w}s)\left(\frac{1}{EA} + \frac{1}{\sqrt{(\mathbf{f}_k - \mathbf{w}s)^T(\mathbf{f}_k - \mathbf{w}s)}}\right) ds, \tag{6.169}$$

where k is the actual cable segment. $\mathbf{r}_k$ is an expression for the local solution within segment k.

Numerical methods could have been utilized to solve the ODE/IVP, but Sagatun Sagatun (2001) gives the following solution to the integral

$$\begin{aligned}\mathbf{r}_k(s) &= \frac{\alpha(s)}{\beta^3}\left(\mathbf{f}_k\beta^2 - \mathbf{f}_k \otimes \mathbf{w} \otimes \mathbf{w} - \mathbf{f}_k \otimes (\mathbf{P}(\mathbf{f}_k \otimes \mathbf{w}))\right) - \mathbf{w}\frac{1}{\beta^2}\sqrt{(\mathbf{f}_k - \mathbf{w}s)^T(\mathbf{f}_k - \mathbf{w}s)} \\ &\quad + \frac{1}{EA}\left(\mathbf{f}_k s - \frac{1}{2}\mathbf{w}s^2\right) + \mathbf{C}_i,\end{aligned} \tag{6.170}$$

where $\otimes$ denotes component wise multiplication and

$$\beta = \sqrt{\mathbf{w}^T\mathbf{w}} = \|\mathbf{w}\|_2, \tag{6.171}$$

$$\alpha = \ln\left[\left(\beta s - \frac{1}{\beta}\mathbf{f}_k^T\mathbf{w}\right) + \sqrt{(\mathbf{f}_k - \mathbf{w}s)^T(\mathbf{f}_k - \mathbf{w}s)}\right], \tag{6.172}$$

$$\mathbf{P} = \begin{bmatrix} 0 & 1 & 1 \\ 1 & 0 & 1 \\ 1 & 1 & 0 \end{bmatrix}. \tag{6.173}$$

Assume that we want segment no. 1 of the global solution $\mathbf{r}(s)$ to start in the origin. We also want to ensure continuity between the segments. The following conditions should be fulfilled

$$\mathbf{r}(0) = \mathbf{0}, \tag{6.174}$$

$$\mathbf{r}(s_i)^- = \mathbf{r}(s_i)^+, \quad \{i \in [1, n-1] \to \mathbb{N}\}. \tag{6.175}$$

The integration constants, $\mathbf{C}_i,\ i \in [0, n-1]$, may be calculated from

$$\mathbf{C}_{k-1} = \begin{cases} -\mathbf{r}_1(0), \ for\ k = 1 \\ \mathbf{r}_{k-1}(s_{k-1}) - \mathbf{r}_k(s_{k-1}), \quad for\ k \in [2, n] \to \mathbb{N},\ for\ n \geq 2 \end{cases}. \tag{6.176}$$

If s belongs to a segment with index higher than 1, $\mathbf{C}_{k-1}$ must be calculated iteratively before the solution of $\mathbf{r}(s)$ can be found. The final global solution may now be calculated from

$$\begin{aligned}\mathbf{r}(s) &= \frac{\alpha(s)}{\beta^3}\left(\mathbf{f}_k\beta^2 - \mathbf{f}_k\otimes\mathbf{w}\otimes\mathbf{w} - \mathbf{f}_k\otimes\left(\mathbf{P}\left(\mathbf{f}_k\otimes\mathbf{w}\right)\right)\right) - \mathbf{w}\frac{1}{\beta^2}\sqrt{\left(\mathbf{f}_k-\mathbf{w}s\right)^T\left(\mathbf{f}_k-\mathbf{w}s\right)} \\ &\quad + \frac{1}{EA}\left(\mathbf{f}_k s - \frac{1}{2}\mathbf{w}s^2\right) + \mathbf{C}_{k-1}, \end{aligned} \tag{6.177}$$

where $\left\{s\in[0,L]\to\mathbb{R},\ k\in[1,n]\to\mathbb{N}\mid s\in[s_{k-1},s_k]\right\}$.

Spatial variation in the distributed load

The solution given above is only valid for constant distributed load along the entire cable. However, an extension to different distributed loads for each segment may be found. Instead of using (6.158), we will assume that the distributed load is constant only within each segment. This means that $\mathbf{f}_0$ must be calculated from (6.157). Eq. (6.165) must be rewritten to

$$T\frac{d\mathbf{r}}{dp}(s) = \mathbf{f}_0 - \sum_{i=1}^{k}\overline{\mathbf{f}}_i - \sum_{i=1}^{k-1}\mathbf{w}_i(s_i-s_{i-1}) - \mathbf{w}_k(s-s_{k-1}), \tag{6.178}$$

where $\left\{s\in[0,L]\to\mathbb{R},\ k\in[1,n]\to\mathbb{N}\mid s\in[s_{k-1},s_k]\right\}$. We modify (6.163) to

$$\mathbf{f}_k = \mathbf{f}_0 - \sum_{i=1}^{k}\overline{\mathbf{f}}_i - \sum_{i=1}^{k-1}\mathbf{w}_i(s_i-s_{i-1}) + \mathbf{w}_k s_{k-1}. \tag{6.179}$$

Now the derivation goes just like in the previous section, and we end up with

$$\mathbf{r}_k = \int_{s_{k-1}}^{s_k}\left(\mathbf{f}_k-\mathbf{w}_k s\right)\left(\frac{1}{EA} + \frac{1}{\sqrt{\left(\mathbf{f}_k-\mathbf{w}_k s\right)^T\left(\mathbf{f}_k-\mathbf{w}_k s\right)}}\right)ds. \tag{6.180}$$

Continuing on the boundary condition and claiming continuity between segments, the integration constants may be calculated as before. The new solution for spatially varying distributed loads with the assumptions made above, are given from

$$\begin{aligned}\mathbf{r}(s) &= \frac{\alpha(s)}{\beta^3}\left(\mathbf{f}_k\beta^2 - \mathbf{f}_k\otimes\mathbf{w}_k\otimes\mathbf{w}_k - \mathbf{f}_k\otimes\left(\mathbf{P}\left(\mathbf{f}_k\otimes\mathbf{w}_k\right)\right)\right) - \mathbf{w}_k\frac{1}{\beta^2}\sqrt{\left(\mathbf{f}_k-\mathbf{w}_k s\right)^T\left(\mathbf{f}_k-\mathbf{w}_k s\right)} \\ &\quad + \frac{1}{EA}\left(\mathbf{f}_k s - \frac{1}{2}\mathbf{w}_k s^2\right) + \mathbf{C}_{k-1}, \end{aligned} \tag{6.181}$$

$$\beta = \sqrt{\mathbf{w}_k^T\mathbf{w}_k} = \left\|\mathbf{w}_k\right\|_2, \tag{6.182}$$

$$\alpha = \ln\left[\left(\beta s - \frac{1}{\beta}\mathbf{f}_k^T\mathbf{w}_k\right) + \sqrt{\left(\mathbf{f}_k-\mathbf{w}_k s\right)^T\left(\mathbf{f}_k-\mathbf{w}_k s\right)}\right], \tag{6.183}$$

$$\mathbf{P} = \begin{bmatrix} 0 & 1 & 1 \\ 1 & 0 & 1 \\ 1 & 1 & 0 \end{bmatrix}. \tag{6.184}$$

6.5.3 Catenaries as Boundary Value Problems (BVP)

To this point we have considered catenaries as a cable with known properties and known loads. The goal has been to achieve a solution for the end point. Let us revert this and try to find the force components when the two end points are known. In this section we will assume that the cable consists of only one segment. The governing differential equations are still known, see (6.168). The problem has now changed from a ODE/IVP to a ODE/BVP (see Section 10.2.1). An analytical solution to this problem could be found if $\mathbf{f}_k$ was solved from (6.168). Nobody has published such analytical solution, and we will have to deal with numerical solutions of the problem. Both MATLAB's function `bvp4c` or e.g. a finite element solution will do if the cable's geometry is of particular interest.

Sometimes other problems arises when we are dealing with boundary value problems. We may for instance know the boundary coordinates, but want to find the end force to yield this solution. The ODE/BVP has now increased to include an estimation of the parameter $\overline{\mathbf{f}}_1$. A shooting method based on the accurate analytical solution might be applied. We will now given an example where we use MATLAB's routine to estimate this force.

Example 6.1 *3D catenary BVP with end force estimation.*

A cable of length 10 meters is fastened in (0,0,0). The cable's weight is 1N/m, and $EA = 7.854 \cdot 10^4$. *The end force is* $\overline{\mathbf{f}}_1 = [10\ 0\ 10]^T$ *N. Eq. (6.177) gives the end point (8.8137,0,4.1421). MATLAB's routine* `bvp4c` *was applied to these parameters, and an estimate of the end force was found. The results are shown in Figure 6.25.*

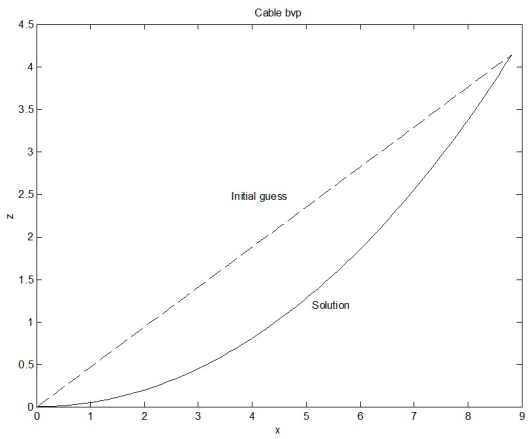

Figure 6.25: Solution of the boundary value problem for a hanging cable. MATLAB's routine `bvp4c` was applied. The dashed line shows the initial guess for a solution.

Even if the initial guess for the estimated force deviated from the correct value, the routine managed to find very good estimates. The results were dependent on the numerical option and the mesh in the variable s. The MATLAB code for this solution is shown below.

```
function cable3dbvp
W=[0 0 -1]'; %Constant distributed force
```

```
Fguess=[5 0 8]'; %Guess for end force (We know this guess is wrong)
E=1e9; %Modulus of elasticity
D=0.1; %Cable's diameter
A=pi*(D/2)^2; %Cable's cross-sectional area
L=10; %Cable's length
EndP=[8.8137 0 4.1421]'; %Boundary point for second end.

s=0:.1:L; %Initial mesh

%Calculates an initial guess for the cable's geometry (a straight line)
n=length(s);
Xguess=linspace(0,EndP(1),n);
Yguess=linspace(0,EndP(2),n);
Zguess=linspace(0,EndP(3),n);
sol.x=s;
sol.y=[Xguess; Yguess; Zguess];
sol.parameters=Fguess;

%Plots the initial guess
figure(1)
clf
plot(sol.y(1,:),sol.y(3,:),'k--')
xlabel('x')
ylabel('z')
title('Cable bvp')

sol = bvp4c(@cableODE,@cableBC,sol,[],W,E,A,L,EndP); %Solves the BVP

%Plots the result
hold on
plot(sol.y(1,:),sol.y(3,:),'k-')
hold off

disp(sprintf('Calculated end force is ...
[%1.2f %1.2f %1.2f] N \n',sol.parameters(1),sol.parameters(2),sol.parameters(3)))


%System's ODEs
function drds = cableODE(s,r,F,W,E,A,L,EndP)
Fk=F+W*L;
drds = (Fk-W*s)*(1/sqrt((Fk-W*s)'*(Fk-W*s))+1/(E*A));

%System's boundary values
function res = cableBC(ya,yb,F,W,E,A,L,EndP)
res = [ ya(1)
 ya(2)
```

```
ya(3)
yb(1)-EndP(1)
yb(2)-EndP(2)
yb(3)-EndP(3)];
```

6.5.4 Hydrodynamic Drag Loads

Consider the current acting on a small cable element dp in Figure 6.26.

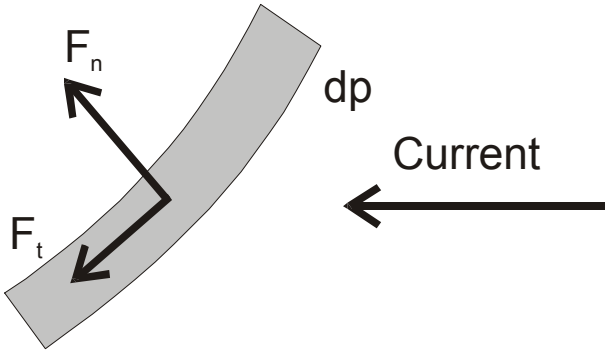

Figure 6.26: Static hydrodynamic forces acting on an infinitesimal cable element dp.

Hydrodynamic loading on mooring lines are usually modelled with the so-called cross-flow principle. This principle assumes that the flow separates due to cross-flow past the cable, that the longitudinal current components do not influence on the transverse forces on a cross-section, and that the transverse forces on a cross-section is mainly due to separated flow effects on the pressure distribution around the body (Faltinsen, 1993). From *Morison's equation* we get

$$d\mathbf{f}_{dt} = -\frac{1}{2}C_{DT}\rho_w d\,(dp)\,|\mathbf{v}\cdot\mathbf{t}|\,(\mathbf{v}\cdot\mathbf{t})\,\mathbf{t} = -\frac{1}{2}C_{DT}\rho_w d\,(dp)\,|\mathbf{v}_t|\,\mathbf{v}_t, \tag{6.185}$$

$$d\mathbf{f}_{dn} = -\frac{1}{2}C_{DN}\rho_w d\,(dp)\,|\mathbf{v}-(\mathbf{v}\cdot\mathbf{t})\,\mathbf{t}|\,(\mathbf{v}-(\mathbf{v}\cdot\mathbf{t})\,\mathbf{t}) = -\frac{1}{2}C_{DN}\rho_w d\,(dp)\,|\mathbf{v}_n|\,\mathbf{v}_n, \tag{6.186}$$

where ρ_w is the density of water, d is the cable's diameter, C_{DT} and C_{DN} are tangential and normal drag coefficients, $\mathbf{t}$ is tangential vector of the cable, $\mathbf{v}, \mathbf{v}_t$, and $\mathbf{v}_n$ are velocity, normal velocity and tangential velocity on the cable on vectorial form. Notice that it is common to normalize to the projected area $d\cdot(dp)$, in this kind of hydrodynamic forces. Some refer to $\mathbf{f}_{dn}$ as the normal friction force, but this is inaccurate. Friction forces are usually normalized to wet surface of the body. For a cable in the normal direction this leads to

$$d\mathbf{f}_{df} = -\frac{1}{2}C_{DF}\rho d\pi(dp)\,|\mathbf{v}-(\mathbf{v}\cdot\mathbf{t})\,\mathbf{t}|\,(\mathbf{v}-(\mathbf{v}\cdot\mathbf{t})\,\mathbf{t}) = -\frac{1}{2}C_{DF}\rho d\pi\,(dp)\,|\mathbf{v}_n|\,\mathbf{v}_n, \tag{6.187}$$

where $C_{DF} = \frac{1}{\pi}C_{DN}$.

Hydrodynamic forces may not be handled in the same way as gravity in the catenary equations. Gravity acts on each cable segment independently of it's orientation. This means that the shape and tension may be solved explicitly. Calculation of current forces requires information on

the cable segment's orientation, and calculation of orientation requires knowledge of the current forces. Consequently, an iteration procedure is needed.

The calculation of hydrodynamic forces (6.185) and (6.186) assumes that the water's velocity is constant over the actual segment. For analytical solutions the hydrodynamic forces have to be constant over each segment. This means that the density of segments should be higher is areas with high curvature, and lower in areas with low curvature. For the calculation, it is natural to apply the vector between the segment boundaries as the vector $\mathbf{t}$.

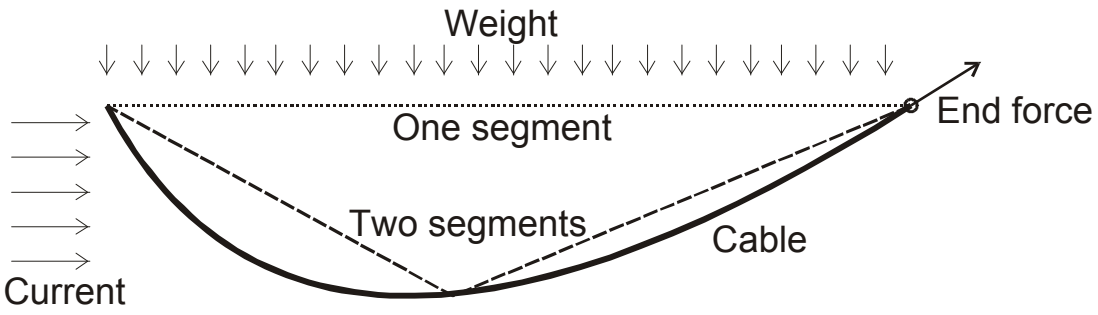

Figure 6.27: Division of the cable into one segment shows that the current will in this case have no effect when the straight line between the nodal points are used as the tangential vector, $\mathbf{t}$, in the expression for hydrodynamic forces. Two segments yields a slightly better result.

When the analytical solution is applied to a problem which involves high curvature on the cable, the effect of current forces should be iterated to obtain a good result. First, a geometry should be calculated with no influence from the current. In the next step the current forces should be turned on, and a new geometry will be obtained. This will again make the basis for the next solution, and so on. The iteration can be stopped when the difference between two consecutive solutions is low.

6.6 Mooring System for FPSOs

Generally, a mooring system consists of n_m lines connected to the structure and horizontally spread out in a certain pattern. The anchor lines are composed of chain, wire lines or synthetic material, often partitioned into several segments of different types and properties. For turret-moored ships, when the turret is rotatable, the relative angle between the turret and the body-fixed frame is given by the *turret angle* α_{tu}. The length of each anchor line is adjusted by winches and determines the pre-tension and thus the stiffness of the mooring system. The anchor lines enter the turret through fairleads below the hull and the coordinates are defined as *terminal points* (TP). Mooring lines are subjected to three types of excitation (Triantafyllou, 1994): Large amplitude LF motions, medium amplitude WF motions and small amplitude, very high frequency vortex-induced vibrations. For the purpose of PM control system design it is appropriate to consider the mooring lines' influence on the low-frequency vessel model.

A horizontal-plane spread mooring model can be formulated as

$$\tau_{\text{moor}} = -\mathbf{R}^{\text{T}}(\psi)\mathbf{g}_{\text{mo}}(\eta) - \mathbf{d}_{\text{mo}}(\nu), \tag{6.188}$$

where $\tau_{\text{mo}} \in \mathbb{R}^3$ is the vector of generalized mooring forces, $\mathbf{d}_{\text{mo}} \in \mathbb{R}^3$ represents the additional damping in the system due to the mooring system, and $\mathbf{g}_{\text{mo}} \in \mathbb{R}^3$ is the Earth-fixed *restoring*

term

$$\mathbf{g}_{\rm mo} = \sum_{i=1}^{\rm n_m} \begin{bmatrix} H_i \cos\beta_i \\ H_i \sin\beta_i \\ H_i \bar{x}_i \sin\beta_i - H_i \bar{y}_i \cos\beta_i \end{bmatrix}, \tag{6.189}$$

which is the vectorial sum of the force contribution from each line. H_i is the horizontal force at the attachment point of the ship along the direction of line i, and β_i is the earth-fixed direction of the line. $\bar{x}_i$ and $\bar{y}_i$ are the corresponding moment arms. In a *quasi-static* approach, by disregarding the dynamic effects in the mooring lines, the restoring forces $\mathbf{g}_{\rm mo}$ are treated as function of the low-frequency ship position and heading η only according to

$$\mathbf{g}_{\rm mo} \overset{q.s.}{\approx} \bar{\mathbf{g}}_{\rm mo}(\eta; \alpha_{\rm tu}), \tag{6.190}$$

where the horizontal force contributions H_i in (6.189) are replaced by the *static line characteristics* (distance/force relationships) for each line i by

$$\bar{H}_i = f_{Hi}(h_i), \tag{6.191}$$

which is a function of the horizontal distance h_i between TP and the anchor of each line. About a working point the line characteristics (6.191) can be linearized by

$$\bar{H}_i = \bar{H}_{oi} + \left.\frac{df_{Hi}}{dh_i}\right|_{h_i=h_{io}} \Delta h_i, \tag{6.192}$$

where $\bar{H}_{oi}$ is the average horizontal force in the working point h_{io}, and $\left.\frac{df_{Hi}}{dh_i}\right|_{h_i=h_{io}}$ is the slope of the line characteristics (6.191) at h_{io}. By assuming fixed anchor line length and neglecting the influence of the current field along the line profile, the generalized mooring forces (6.188) in a working point can be approximated by a 1st-order Taylor expansion of the static restoring mooring forces and the mooring damping about the working points $\eta = \eta_{\rm o}$ and $\nu = \mathbf{0}$ according to

$$\bar{\mathbf{g}}_{\rm mo}(\eta) = \bar{\mathbf{g}}_{\rm mo}(\eta_{\rm o}) + \mathbf{G}_{\rm mo}(\eta - \eta_{\rm o}) + h.o.t. \tag{6.193}$$

$$\mathbf{d}_{\rm mo}(\nu) = \mathbf{D}_{\rm mo}\nu + h.o.t., \tag{6.194}$$

where h.o.t. denotes higher order terms and

$$\mathbf{G}_{\rm mo} = \left.\frac{\partial \bar{\mathbf{g}}_{\rm mo}}{\partial \eta}\right|_{\eta=\eta_o}, \quad \mathbf{D}_{\rm mo} = \left.\frac{\partial \mathbf{d}_{\rm mo}}{\partial \nu}\right|_{\nu=\mathbf{0}}. \tag{6.195}$$

For simplicity, the Earth-fixed frame is often placed in the natural equilibrium point of the mooring system, i.e. $\bar{\mathbf{g}}_{\rm mo}(\eta_{\rm o} = 0) = \mathbf{0}$. $\mathbf{D}_{mo}$ and $\mathbf{G}_{mo}$ are the linearized mooring damping and stiffness matrices assumed to only contribute in the horizontal-plane. They can, for symmetrical mooring patterns about the xz- and yz- planes be formulated as

$$\mathbf{G}_{\rm mo} = \text{diag}\left\{ \begin{array}{cccccc} g_{m11} & g_{m22} & 0 & 0 & 0 & g_{m66} \end{array} \right\}, \tag{6.196}$$

$$\mathbf{D}_{\rm mo} = \text{diag}\left\{ \begin{array}{cccccc} d_{m11} & d_{m22} & 0 & 0 & 0 & d_{m66} \end{array} \right\}. \tag{6.197}$$

Hence, the *quasi-static* mooring model can be written

$$\tau_{\rm moor} = -\mathbf{R}^{\rm T}(\psi)\mathbf{G}_{\rm mo}\eta - \mathbf{D}_{\rm mo}\nu. \tag{6.198}$$

For further details in modeling, see Faltinsen (1993) and the references therein. For fully dynamically positioned vessels with no anchor system, $\tau_{\rm moor}$ is equal to zero.

Chapter 7

Dynamic Positioning Control System

This chapter contains a comprehensive introduction to dynamic positioning (DP) and thruster assisted position mooring (PM) including design of observers and controllers.

Learning outcome of the chapter: The reader shall understand:

- The principles of dynamic positioning (DP) of ships and offshore structures.
- The control objective on how and why to compensate for low-frequency (LF) motions while accepting to follow the wave-frequency (WF) motion.
- The concept of filtering the wave-induced motion components in the control input signal also called wave filtering.
- How to design an observer and controller for DP.
- The principles for thrust allocation.

7.1 Introduction

The real-time control hierarchy, or the *control structure,* of a marine control system (Sørensen, 2005) may be divided into three levels: the *guidance system*, the *high-level plant control* (e.g. DP controller including thrust allocation), and the *low-level thruster control*. Description of DP systems including the early history can be found in Fay (1989), Sørensen et al. (1996), Sørensen (2011) and Fossen (2011). In the 1960s the first DP system was introduced for horizontal modes of motion (surge, sway and yaw) using single-input single-output PID control algorithms in combination with low-pass and/or notch filter. In the 1970s more advanced output control methods based on multivariable optimal control and Kalman filter theory was proposed by Balchen et al. (1980) and Grimble and Johnsen (1988).

The introduction of observers with wave filtering techniques based on Kalman filter theory (Fossen and Perez, 2009) by Balchen, Jenssen and Sælid is regarded as a breakthrough in marine control systems in general, and has indeed been an inspiration for many other marine control applications as well.

In the 1990s nonlinear DP controller designs were proposed by several research groups. In the work of Fossen and Strand (1999) the important contribution of passive nonlinear observer with adaptive wave filtering is presented. One of the motivations using nonlinear passivity theory

was to reduce the complexity in the control software getting rid of cumbersome linearizations and the corresponding logic's.

As the DP technology became more mature research efforts were put into the integration of vessel control systems and the refinement of performance for the various vessel types and missions by including operational requirements into the design of both the guidance systems and the controllers. Sørensen and Strand (2000) proposed a DP control law for small-waterplane-area marine vessels like semisubmersibles with the inclusion of roll and pitch damping. Sørensen et al. (2001) recommended the concept of optimal setpoint chasing for deep-water drilling and intervention vessels. Fossen and Strand (2001) presented the nonlinear passive weather optimal positioning control system for ships and rigs increasing the operational window and reducing the fuel consumption.

Most of the current DP systems have been designed to operate up to a certain limit of weather condition limited by the thrust and power capacity. Due to the accuracy and availability of the inertia measurement units (IMU), Lindegaard (2003) proposed acceleration feedback (AFB) to increase the performance of DP systems in severe seas. AFB denotes here output acceleration feedback in addition to output PID controller. Sørensen (2005) proposed passive nonlinear observer without wave frequency (WF) filtering for output PID-controller in extreme seas, especially where swell becomes dominant.

Use of hybrid control theory as proposed by Hespanha (2002) and Hespanha et al. (2003) and fault-tolerant control by Blanke et al. (2003) enabled the design of proper control architecture and formalism for the integration of multi-functional controllers combining discrete events and continuous control. Nguyen et al. (2007), Nguyen et al. (2008) and Nguyen and Sørensen (2009) proposed the design of supervisory-switched controllers for DP from calm to extreme sea conditions and from transit to station keeping operations. The main objective of the supervisory-switched control is to integrate an appropriate bank of controllers and models at the plant control level into a hybrid DP system being able to operate in varying environmental and operational conditions. Implementing the hybrid control concept will increase the so-called weather window making it possible to conduct all-year marine operations, such as subsea installation and intervention, drilling, and pipe laying in harsh environment. Concerning large changes in environmental conditions, in particular, when conducting marine operations in deep-water, the feature of hybrid control is important as the operations are more time consuming, and hence more sensitive to changes in sea states. Lately, with increasing interest for hydrocarbons in the arctic DP operations in various ice conditions like level ice, managed ice and ice ridges have been studied. For DP vessels operating partly in ice and open water, see Figure 7.1, switching between controllers and control settings on both the plant-level and low-level will be necessary. More on hybrid control systems including recent research results are found in Chapter 9.

The number of the safety critical and demanding DP operations is increasing. As a consequence of this the system integrity and requirements to further physical and functional integration between the DP system, marine automation system, thruster and propulsion system and power plant will follow accordingly. It is believed that more research efforts will be directed into diagnostics and fault-tolerant control as presented in Blanke et al. (2003). As a part of this proper testing and verification of the DP system software are crucial for the safety and profitability, see Johansen and Sørensen (2009) and Smogeli (2010)).

Thruster assisted position mooring (PM) systems have been commercially available since the 1980s and provide a flexible solution for floating structures for drilling and oil&gas exploitation on the smaller and marginal fields. Modeling and control of turret-moored ships are treated

Figure 7.1: DP operations in Arctic hydrocarbon exploration.

in Strand et al. (1998) and Nguyen and Sørensen (2009). Important areas of guidance and navigation are not covered here. For further references on these topics the reader is referred to Fossen (2011).

7.2 Observer Design for Dynamic Positioning

This section is a extension and modification of the observer design presented in Fossen and Strand (1999). Filtering and state estimation are important features for all kind of control systems. A measured signal very often content noise which may have negative impact on the controller performance if no precaution is taken in the dynamic positioning (DP) and position mooring (PM) systems. The main purposes of the state estimators (observers) in the positioning systems are:

- *Reconstruction of non-measured data.* For many applications important process states are not measured. Typical reasons for this could be that no convenient sensors exist, or simply that cost reasons motivate to not to install the sensor. In such cases sophisticated model based filtering techniques - state estimation - can be applied. The main purpose of the state estimator (observer) is to reconstruct unmeasured signals and perform filtering before the signals are used in a feedback control system, see Figure 4.4. The input to the state estimator is sensor data e.g. from inertial measurement units (IMU/VRS/MRU), gyro compasses and positioning reference systems (DGPS, HPR, Artemis, Taut wire, Fanbeam, etc.), see Section 2.2.

- *Dead reckoning.* All kind of equipment will fail according to some failure rate. Experience from industrial applications has shown that the one of the most frequent control system failure are caused by sensor failures. In safety critical marine applications a sudden drop-out of the control system may lead to dangerous situations, if not an adequate signal substitution will take place. Applying model based filters, the signal may, at least for some period of time, replace by model prediction the measured signal.

- *Wave filtering.* Motions of marine vessels can often be divided into a low-frequency (LF) part and a wave-frequency (WF) part. For most positioning applications the WF motion is not subject for control. The reason for this could be that the WF motion does not matter for the particular operation, or that the vessel does not have enough power and thrust capacity for doing any noticeable compensation at all. The latter is the most usual reason. Hence, there is no point to waist fuel and cause additional wear and tear of the propulsion equipment. In order to avoid this wave filters are designed filtering out the WF motions, see Figure 6.20.

We will in this section discuss three different methods for position and velocity state estimation:

- *Extended Kalman filter design (1976-present):* The traditional Kalman filter based estimators are linearized about a set of pre-defined constant yaw angles, typically 36 operating points in steps of 10 degrees, to cover the whole heading envelope between 0 and 360 degrees Balchen et al. (1980) and Sørensen et al. (1996). When this estimator is used in conjunction with a linear quadratic Gaussian (LQG), PID or H_∞ controller in conjuncture with a separation principle, there is no guarantee for global stability of the total nonlinear system. However, these systems have been used by several DP producers since the 1970s. The price for using linear theory is that linearization of the kinematic equations may degrade the performance of the system. Besides, the number of filter gains and switching transitions between the various sectors are large.

- *Nonlinear observer design (1998-present):* The nonlinear observer is motivated from passivity arguments (Fossen and Strand, 1999) and (Fossen, 2011). Also the nonlinear observer includes wave filtering, velocity and bias state estimation. In addition it is proven to be global asymptotic stable (GES), through a passivation design. Compared to the Kalman filter, the number of tuning parameters is significantly reduced, and the tuning parameters are coupled more directly to the physics of the system. By using a nonlinear formulation, the software algorithms are simplified.

- *Adaptive and nonlinear observer design (1999-present):* The nonlinear and passive observer is further extended to adaptive wave filtering by an augmentation design technique, see Strand and Fossen (1999). This implies that the wave frequency model can be estimated recursively *on-line* such that accurate filtering is obtained for different sea states. However, conducting DP operations in extreme seas, as proposed in Sørensen et al. (2002), Nguyen et al. (2007) and Sørensen (2011) has shown that adaptive wave filtering may degrade the performance significantly using the same controller strategy as in normal DP operation in calm and moderate seas.

7.2.1 Objectives

The objective of this section is to present the state-of-the-art and most recent observer designs for conventional surface ships and rigs operating about *zero (station keeping)* and *low speed tracking*. The vessels can either be both free-floating or anchored. In the latter case we assume a symmetrical, spread mooring system, with linear response of the mooring system. It is assumed that the vessels are *metacentric stable*, which implies that there exist restoring forces in heave, roll and pitch, such that these motions can be modeled as damped oscillators with zero mean and limited amplitude. Hence, the horizontal motions (surge, sway and yaw) are considered in the modeling and observer design. The objectives for the observer are:

- *Position and velocity estimation.* It is assumed that only position and heading measurements are available. Hence, one objective is to produce velocity estimates for feedback control. In addition, the observer should remove measurement noise from the position and heading measurements.

- *Bias estimation.* By estimating a bias term, accounting for slowly-varying environmental loads and unmodeled effects, there will be no steady-state offsets in the velocity estimates. Moreover, the bias estimates may be used as a feedforward term in the positioning controller. However, this should be done with care as the bias estimate under certain circumstances may be rather fluctuating.

- *Wave filtering.* The position and heading signals used in the feedback controller should *not* contain the WF part of the motion. By including a synthetic wave-induced motion model in the observer, wave filtering is obtained, see below:

Definition 7.1 (Wave filtering) *Wave filtering can be defined as the reconstruction of the LF motion components from noisy measurements of position and heading by means of analog or digital filters. In addition to this, if an observer (state estimator) is used, noise-free estimates of the non-measured LF velocities can be produced. This is crucial in ship motion control systems since the WF part of the motion should* ***not*** *be compensated for by the positioning system. If*

the WF part of the motion enters the feedback loop, this will cause unnecessary wear and tear of the actuators and increase the fuel consumption.

7.2.2 Control Plant Model: Vessel Model

As shown in Chapter 6, it is common to separate the modeling of marine vessels into a LF model and WF model. The nonlinear LF equations of motion are driven by $2nd$-order mean and slowly-varying wave, current and wind loads as well as thruster forces. The WF motion of the ship is due to 1st-order wave-induced loads, see Figure 6.20. For the purpose of model-based observer and controller design it is sufficient to derive a simplified mathematical model, *control plant model*, which nevertheless is detailed enough to describe the main physical characteristics of the dynamic system.

Low-frequency control plant model

For the purpose of controller design and analysis, it is convenient to simplify (6.67) and derive a nonlinear LF control plant model in surge, sway and yaw about zero vessel velocity according to

$$\dot{\eta} = \mathbf{R}(\psi)\nu, \tag{7.1}$$

$$\mathbf{M}\dot{\nu} + \mathbf{D}\nu + \mathbf{R}^T(\psi)\mathbf{G}\eta = \tau + \mathbf{R}^T(\psi)\mathbf{b}, \tag{7.2}$$

where $\nu = [u, v, r]^T$, $\eta = [x, y, \psi]^T$, $\mathbf{b} \in \mathbb{R}^3$ is the bias vector, and $\tau = [\tau_x, \tau_y, \tau_\psi]^T$ is the control input vector. Notice the control plant model is nonlinear because of the rotation matrix

$$\mathbf{R}(\psi) = \begin{bmatrix} c\psi & -s\psi & 0 \\ s\psi & c\psi & 0 \\ 0 & 0 & 1 \end{bmatrix}.$$

For low-speed applications, the different matrices are defined according to

$$\mathbf{M} = \begin{bmatrix} m - X_{\dot{u}} & 0 & 0 \\ 0 & m - Y_{\dot{v}} & mx_G - Y_{\dot{r}} \\ 0 & mx_G - N_{\dot{v}} & I_z - N_{\dot{r}} \end{bmatrix},$$

$$\mathbf{D} = \begin{bmatrix} -X_u & 0 & 0 \\ 0 & -Y_v & -Y_r \\ 0 & -N_v & -N_r \end{bmatrix}, \quad \mathbf{G} = \begin{bmatrix} -X_x & 0 & 0 \\ 0 & -Y_y & 0 \\ 0 & 0 & -N_\psi \end{bmatrix}.$$

Remark 7.1 *We have here assumed that* $\mathbf{G}$ *is a constant, diagonal matrix. One should notice that for DP operations (no mooring system present) there is no stiffness such that* $\mathbf{G} = \mathbf{0}_{3\times 3}$. *However, for anchored structures there will be restoring terms due to the mooring lines.*

Remark 7.2 *For later use in the observer and controller design we may assume that (7.1) and (7.2) are a linear model about a desired position and heading vector. In this case we replace with* ψ *with the desired heading* ψ_d.

Wave-frequency control plant model

In the controller design synthetic white-noise-driven processes consisting of uncoupled harmonic oscillators with damping will be used to model the WF motions. The synthetic WF model can be written in state-space form according to

$$\begin{aligned} \dot{\xi}_w &= \mathbf{A}_w \xi_w + \mathbf{E}_w \mathbf{w}_w, \\ \eta_w &= \mathbf{C}_w \xi_w. \end{aligned} \tag{7.3}$$

$\eta_w \in \mathbb{R}^3$ is the position and orientation measurement vector, $\mathbf{w}_w \in \mathbb{R}^3$ is a zero-mean Gaussian white noise vector, and $\xi_w \in \mathbb{R}^6$. A linear 2nd-order WF model is considered to be sufficient for representing the WF-induced motions, although higher order models may also be used, see Grimble and Johnsen (1988). The system matrix $\mathbf{A}_w \in \mathbb{R}^{6\times 6}$, the disturbance matrix $\mathbf{E}_w \in \mathbb{R}^{6\times 3}$ and the measurement matrix $\mathbf{C}_w \in \mathbb{R}^{3\times 6}$ may formulated as

$$\mathbf{A}_w = \begin{bmatrix} \mathbf{0}_{3\times 3} & \mathbf{I}_{3\times 3} \\ -\mathbf{\Omega}^2 & -2\mathbf{\Lambda}\mathbf{\Omega} \end{bmatrix}, \tag{7.4a}$$

$$\mathbf{C}_w = \begin{bmatrix} \mathbf{0}_{3\times 3} & \mathbf{I}_{3\times 3} \end{bmatrix}, \quad \mathbf{E}_w = \begin{bmatrix} \mathbf{0}_{3\times 3} \\ \mathbf{K}_w \end{bmatrix}, \tag{7.4b}$$

where $\mathbf{\Omega} = \mathrm{diag}\{\omega_1, \omega_2, \omega_3\}$, $\mathbf{\Lambda} = \mathrm{diag}\{\zeta_1, \zeta_2, \zeta_3\}$ and $\mathbf{K}_w = \mathrm{diag}\{K_{w1}, K_{w2}, K_{w3}\}$. This model corresponds to

$$\frac{\eta_{w_i}}{w_{w_i}}(s) = \frac{K_{w_i} s}{s^2 + 2\zeta_i \omega_i s + \omega_i^2}. \tag{7.5}$$

From a practical point of view, the WF model parameters are slowly-varying quantities depending on the prevailing sea state. Typically, the wave periods T_i, corresponding to wave frequency $\omega_i = 2\pi/T_i$, are in the range of 5 to 20 seconds in the North Sea for wind generated seas. The periods of swell components may be even longer than 20 seconds. The relative damping ratio ζ_i will typically be in the range $0.05 - 0.10$. As suggested by Strand and Fossen (1999) adaptive schemes may be used to update ω_i for the varying sea states. However, this should be done with care in heavy sea states with long wave lengths.

Bias model

A frequently used bias model $\mathbf{b} \in \mathbb{R}^3$ for marine control applications is the first order *Markov* model

$$\dot{\mathbf{b}} = -\mathbf{T}_b^{-1}\mathbf{b} + \mathbf{E}_b \mathbf{w}_b, \tag{7.6}$$

where $\mathbf{w}_b \in \mathbb{R}^3$ is a zero-mean Gaussian white noise vector, $\mathbf{T}_b \in \mathbb{R}^{3\times 3}$ is a diagonal matrix of bias time constants, and $\mathbf{E}_b \in \mathbb{R}^{3\times 3}$ is a diagonal scaling matrix. The bias model accounts for slowly-varying forces and moment due to 2nd-order wave loads, ocean currents and wind. In addition, the bias model will account for errors in the modeling.

Alternatively, the bias model may also be modelled as random walk, i.e. *Wiener* process

$$\dot{\mathbf{b}} = \mathbf{E}_b \mathbf{w}_b. \tag{7.7}$$

Measurements

The measurement equation is written

$$\mathbf{y} = \eta + \eta_w + \mathbf{v}, \tag{7.8}$$

where $\mathbf{v} \in \mathbb{R}^3$ is the zero-mean Gaussian measurement noise vector.

Resulting control plant model

The resulting control plant model is written

$$\begin{aligned}
\dot{\xi} &= \mathbf{A}_w \xi + \mathbf{E}_w \mathbf{w}_w, && (7.9a)\\
\dot{\eta} &= \mathbf{R}(\psi)\nu, && (7.9b)\\
\dot{\mathbf{b}} &= \mathbf{E}_b \mathbf{w}_b, && (7.9c)\\
\mathbf{M}\dot{\nu} &= -\mathbf{D}\nu - \mathbf{R}^T(\psi)\mathbf{G}\eta + \mathbf{R}^T(\psi)\mathbf{b} + \tau, && (7.9d)\\
\mathbf{y} &= \eta + \mathbf{C}_w \xi + \mathbf{v}. && (7.9e)
\end{aligned}$$

Here, the Wiener bias model is used. The state-space model is of dimension $\mathbf{x} \in \mathbb{R}^{15}, \tau \in \mathbb{R}^3$ and $\mathbf{y} \in \mathbb{R}^3$. In addition, it is common to augment two additional states to the state-space model if wind speed and direction are available as measurements. If not, these are treated as slowly-varying disturbances to be included in the bias term $\mathbf{b}$. In the next section, we will show how all these states can be estimated by using only 3 measurements.

Control plant model for extreme seas

As suggested in Sørensen et al. (2002) the wave filtering should be avoided for long wave lengths (low wave frequencies) appearing in extreme seas or in swell dominated seas. For such conditions the following control plant model is proposed

$$\begin{aligned}
\dot{\mathbf{b}} &= \mathbf{E}_b \mathbf{w}_b, && (7.10a)\\
\mathbf{M}\dot{\nu} &= -\mathbf{D}\nu - \mathbf{R}^T(\psi)\mathbf{G}\eta + \mathbf{R}^T(\psi)\mathbf{b} + \tau, && (7.10b)\\
\dot{\eta} &= \mathbf{R}(\psi)\nu, && (7.10c)\\
\mathbf{y} &= \eta + \mathbf{v}. && (7.10d)
\end{aligned}$$

7.2.3 Extended Kalman Filter Design

The extended Kalman (EKF) filter design is based on the nonlinear model

$$\begin{aligned}
\dot{\mathbf{x}} &= \mathbf{f}(\mathbf{x}) + \mathbf{B}\mathbf{u} + \mathbf{E}\mathbf{w}, && (7.11a)\\
\mathbf{y} &= \mathbf{H}\mathbf{x} + \mathbf{v}, && (7.11b)
\end{aligned}$$

where $\mathbf{f}(\mathbf{x}), \mathbf{B}, \mathbf{E}$ and $\mathbf{H}$ are given by (7.9a)–(7.9e). Moreover,

$$\mathbf{f}(\mathbf{x}) = \begin{bmatrix} \mathbf{A}_w\xi \\ \mathbf{R}(\psi)\nu \\ -\mathbf{T}_b^{-1}\mathbf{b} \\ -\mathbf{M}^{-1}\mathbf{D}\nu - \mathbf{M}^{-1}\mathbf{R}^T(\psi)\mathbf{G}\eta + \mathbf{M}^{-1}\mathbf{R}^T(\psi)\mathbf{b} \end{bmatrix}, \quad \mathbf{B} = \begin{bmatrix} \mathbf{0}_{6\times3} \\ \mathbf{0}_{3\times3} \\ \mathbf{0}_{3\times3} \\ \mathbf{M}^{-1} \end{bmatrix}, \tag{7.12}$$

$$\mathbf{E} = \begin{bmatrix} \mathbf{E}_w & \mathbf{0}_{6\times3} \\ \mathbf{0}_{3\times3} & \mathbf{0}_{3\times3} \\ \mathbf{0}_{3\times3} & \mathbf{E}_b \\ \mathbf{0}_{3\times3} & \mathbf{0}_{3\times3} \end{bmatrix}, \quad \mathbf{H} = \begin{bmatrix} \mathbf{C}_w & \mathbf{I}_{3\times3} & \mathbf{0}_{3\times3} & \mathbf{0}_{3\times3} \end{bmatrix}, \tag{7.13}$$

where $\mathbf{x} = [\xi^T, \eta^T, \mathbf{b}^T, \nu^T]^T, \mathbf{w} = [\mathbf{w}_w^T, \mathbf{w}_b^T]^T$ and $\mathbf{u} = \tau$. Hence, for a commercial system with $n = 15$ states the covariance weight matrices $\mathbf{Q} = E(\mathbf{w}^T\mathbf{w}) \in \mathbb{R}^{6\times6}$ (process noise covariance matrix) and $\mathbf{R} = E(\mathbf{v}^T\mathbf{v}) \in \mathbb{R}^{3\times3}$ (position and heading measurement noise covariance matrix). This again implies that $n + n(n+1)/2 = 135$ ODEs must be integrated on-line. In order to simplify the tuning procedure these two matrices are usually treated as two diagonal design matrices which can be chosen by applying *Bryson's inverse square method,* Anderson and Moore (1989), for instance.

Discrete-time EKF equations

The discrete-time EKF equations are given by:

Initial values:

$$\bar{\mathbf{x}}_{k=0} = \mathbf{x}_0, \tag{7.14a}$$

$$\bar{\mathbf{P}}_{k=0} = E\left[(\mathbf{x}(0) - \hat{\mathbf{x}}(0))\left(\mathbf{x}(0) - \hat{\mathbf{x}}(0)^T\right)\right] = \mathbf{P}_0. \tag{7.14b}$$

Corrector:

$$\mathbf{K}_k = \bar{\mathbf{P}}_k\mathbf{H}^T\left[\mathbf{H}\bar{\mathbf{P}}_k\mathbf{H}^T + \mathbf{R}\right]^{-1}, \tag{7.15a}$$

$$\hat{\mathbf{P}}_k = (\mathbf{I} - \mathbf{K}_k\mathbf{H})\bar{\mathbf{P}}_k(\mathbf{I} - \mathbf{K}_k\mathbf{H})^T + \mathbf{K}_k\mathbf{R}\mathbf{K}_k^T, \tag{7.15b}$$

$$\hat{\mathbf{x}}_k = \bar{\mathbf{x}}_k + \mathbf{K}_k(\mathbf{y}_k - \mathbf{H}\bar{\mathbf{x}}_k). \tag{7.15c}$$

Predictor:

$$\bar{\mathbf{P}}_{k+1} = \mathbf{\Phi}_k\hat{\mathbf{P}}_k\mathbf{\Phi}_k^T + \mathbf{\Gamma}_k\mathbf{Q}\mathbf{\Gamma}_k^T, \tag{7.16a}$$

$$\bar{\mathbf{x}}_{k+1} = \mathbf{f}_k(\hat{\mathbf{x}}_k, \mathbf{u}_k), \tag{7.16b}$$

where $\hat{\mathbf{x}}_k = [\hat{\xi}_k^T, \hat{\eta}_k^T, \hat{\mathbf{b}}_k^T, \hat{\nu}_k^T]^T$, $\mathbf{f}_k(\hat{\mathbf{x}}_k, \mathbf{u}_k), \mathbf{\Phi}_k$ and $\mathbf{\Gamma}_k$ can be found by using *forward Euler* for instance. Moreover

$$\mathbf{f}_k(\hat{\mathbf{x}}_k, \mathbf{u}_k) = \hat{\mathbf{x}}_k + T[\mathbf{f}(\hat{\mathbf{x}}_k) + \mathbf{B}\mathbf{u}_k], \tag{7.17a}$$

$$\mathbf{\Phi}_k = \mathbf{I}_{n\times n} + T\left.\frac{\partial\mathbf{f}_k(\mathbf{x}_k, \mathbf{u}_k)}{\partial\mathbf{x}_k}\right|_{\mathbf{x}_k=\hat{\mathbf{x}}_k}, \tag{7.17b}$$

$$\mathbf{\Gamma}_k = T\mathbf{E}, \tag{7.17c}$$

where $T > 0$ is the sampling period and $n = 15$. The EKF has been used in most industrial ship control systems. It should, however, be noted that there are no prove of global asymptotic stability when the system is linearized. In particular, it is difficult to obtain asymptotic convergence of the bias estimates $\hat{\mathbf{b}}$ when using the EKF algorithm in DP and PM. In the next section, we will demonstrate how a nonlinear observer can be designed to meet the requirement of global exponential stability (GES) through a passivation design. The nonlinear observer has excellent convergence properties, and it is easy to tune since the covariance equations are not needed.

7.2.4 Nonlinear Observer Design

Two different nonlinear observers will be presented. The first one is similar to the observer of Fossen and Strand (1999) for dynamically positioned (free-floating) ships with extension to spread mooring-vessel systems (Strand et al., 1998). The second representation of the nonlinear observer is an augmented design where the filtered state of the innovation signals are used to obtain better filtering, see Strand and Fossen (1999). By using feedback from the high-pass filtered innovation in the WF part of the observer there will be no steady-state offsets in the WF estimates. Another advantage is that by using the low-pass filtered innovation for bias estimation, these estimates will be less noisy and, thus, may be used directly as a feedforward term in the control law. However, this should be done with care.

The adaptive observer proposed in Section 7.2.5 is an extension of the augmented observer. SPR-Lyapunov analysis is used to prove passivity and stability of the nonlinear observers.

Observer equations in the Earth-fixed frame

When designing the observer, the following assumptions are made in the Lyapunov analysis:

A1 Position and heading sensor noise are neglected, that is $\mathbf{v} = \mathbf{0}$, since this term is negligible compared to the wave-induced motion.

A2 The amplitude of the wave-induced yaw motion ψ_w is assumed to be small, that is less than 1 degree during normal operation of the vessel and less than 5 degrees in extreme weather conditions. Hence, $\mathbf{R}(\psi) \approx \mathbf{R}(\psi + \psi_w)$. From **A1** this implies that $\mathbf{R}(\psi) \approx \mathbf{R}(\psi_y)$, where $\psi_y \triangleq \psi + \psi_w$ denotes the measured heading.

This assumptions are only for a matter of convenience such that Lyapunov stability theory can be used to derive the structure of the observer updating mechanism. It turns out the SPR-Lyapunov based observer equations are robust for white Gaussian white noise so these assumptions can be relaxed when implementing the observer. Similar for nonlinear systems, as also pointed out for linear systems in the Remark in Section 7.2.2, it is recommended to replace with ψ_y with the desired heading ψ_d.

We will also exploit the following model properties of the inertia and damping matrices in the passive design

$$\mathbf{M} = \mathbf{M}^T > 0, \quad \dot{\mathbf{M}} = \mathbf{0}, \quad \mathbf{D} > 0.$$

Observer equations (representation 1)

A nonlinear observer copying the vessel and environmental models (7.9a)–(7.9e) is

$$\dot{\hat{\xi}} = \mathbf{A}_w\hat{\xi} + \mathbf{K}_1\tilde{\mathbf{y}}, \tag{7.18a}$$
$$\dot{\hat{\eta}} = \mathbf{R}(\psi_d)\hat{\nu} + \mathbf{K}_2\tilde{\mathbf{y}}, \tag{7.18b}$$
$$\dot{\hat{\mathbf{b}}} = -\mathbf{T}_b^{-1}\hat{\mathbf{b}} + \mathbf{K}_3\tilde{\mathbf{y}}, \tag{7.18c}$$
$$\mathbf{M}\dot{\hat{\nu}} = -\mathbf{D}\hat{\nu} - \mathbf{R}^T(\psi_d)\mathbf{G}\hat{\eta} + \mathbf{R}^T(\psi_d)\hat{\mathbf{b}} + \tau + \mathbf{R}^T(\psi_d)\mathbf{K}_4\tilde{\mathbf{y}}\ , \tag{7.18d}$$
$$\hat{\mathbf{y}} = \hat{\eta} + \mathbf{C}_w\hat{\xi}, \tag{7.18e}$$

where $\tilde{\mathbf{y}} = \mathbf{y} - \hat{\mathbf{y}} \in \mathbb{R}^3$ is the estimation error (in the literature also denoted as the innovation or injection term), $\mathbf{K}_1 \in \mathbb{R}^{6\times 3}$, and $\mathbf{K}_2, \mathbf{K}_3, \mathbf{K}_4 \in \mathbb{R}^{3\times 3}$ are observer gain matrices to be determined later. The nonlinear observer is implemented as 15 ODEs with no covariance updates. Using Wiener bias model (7.18a) is simply replaced with

$$\dot{\hat{\mathbf{b}}} = \mathbf{K}_3\tilde{\mathbf{y}}. \tag{7.19}$$

Vik and Fossen (2001) has shown that using the Wiener bias model the estimation error will converge asymptotically (asymptotic stable), while exponential stability are proven using the Markov model.

Observer estimation errors

The observer estimation errors are defined as $\tilde{\xi} = \xi - \hat{\xi}$, $\tilde{\eta} = \eta - \hat{\eta}$, $\tilde{\mathbf{b}} = \mathbf{b} - \hat{\mathbf{b}}$ and $\tilde{\nu} = \nu - \hat{\nu}$. Hence, from (7.9a)–(7.9e) and (7.18a)–(7.18e) the observer error dynamics is

$$\dot{\tilde{\xi}} = \mathbf{A}_w\tilde{\xi} - \mathbf{K}_1\tilde{\mathbf{y}} + \mathbf{E}_w\mathbf{w}_w, \tag{7.20a}$$
$$\dot{\tilde{\eta}} = \mathbf{R}(\psi_d)\tilde{\nu} - \mathbf{K}_2\tilde{\mathbf{y}}, \tag{7.20b}$$
$$\dot{\tilde{\mathbf{b}}} = -\mathbf{T}_b^{-1}\tilde{\mathbf{b}} - \mathbf{K}_3\tilde{\mathbf{y}} + \mathbf{E}_b\mathbf{w}_b, \tag{7.20c}$$
$$\mathbf{M}\dot{\tilde{\nu}} = -\mathbf{D}\tilde{\nu} - \mathbf{R}^T(\psi_d)\mathbf{G}\tilde{\eta} + \mathbf{R}^T(\psi_d)\tilde{\mathbf{b}} - \mathbf{R}^T(\psi_d)\mathbf{K}_4\tilde{\mathbf{y}}, \tag{7.20d}$$
$$\tilde{\mathbf{y}} = \tilde{\eta} + \mathbf{C}_w\tilde{\xi}. \tag{7.20e}$$

By defining a new output

$$\tilde{\mathbf{z}}_o \triangleq \mathbf{K}_4\tilde{\mathbf{y}} + \mathbf{G}\tilde{\eta} - \tilde{\mathbf{b}} \triangleq \mathbf{C}_o\tilde{\mathbf{x}}_o, \tag{7.21}$$

and the vectors

$$\tilde{\mathbf{x}}_o \triangleq \begin{bmatrix} \tilde{\xi} \\ \tilde{\eta} \\ \tilde{\mathbf{b}} \end{bmatrix}, \quad \mathbf{w} \triangleq \begin{bmatrix} \mathbf{w}_w \\ \mathbf{w}_b \end{bmatrix}, \tag{7.22}$$

the *error dynamics* (7.20a)–(7.20d) can be written in compact form as

$$\mathbf{M}\dot{\tilde{\nu}} = -\mathbf{D}\tilde{\nu} - \mathbf{R}^T(\psi_d)\mathbf{C}_o\tilde{\mathbf{x}}_o, \tag{7.23a}$$
$$\dot{\tilde{\mathbf{x}}}_o = \mathbf{A}_o\tilde{\mathbf{x}}_o + \mathbf{B}_o\mathbf{R}(\psi_d)\tilde{\nu} + \mathbf{E}_o\mathbf{w}, \tag{7.23b}$$

where

$$\begin{aligned}
\mathbf{A}_o &= \begin{bmatrix} \mathbf{A}_w - \mathbf{K}_1\mathbf{C}_w & -\mathbf{K}_1 & \mathbf{0}_{6\times 3} \\ -\mathbf{K}_2\mathbf{C}_w & -\mathbf{K}_2 & \mathbf{0}_{3\times 3} \\ -\mathbf{K}_3\mathbf{C}_w & -\mathbf{K}_3 & -\mathbf{T}_b^{-1} \end{bmatrix}, \\
\mathbf{C}_o &= \begin{bmatrix} \mathbf{K}_4\mathbf{C}_w & \mathbf{K}_4+\mathbf{G} & -\mathbf{I}_{3\times 3} \end{bmatrix}, \\
\mathbf{B}_o &= \begin{bmatrix} \mathbf{0}_{6\times 3} \\ \mathbf{I}_{3\times 3} \\ \mathbf{0}_{3\times 3} \end{bmatrix}, \ \mathbf{E}_o = \begin{bmatrix} \mathbf{E}_w & \mathbf{0}_{6\times 3} \\ \mathbf{0}_{3\times 3} & \mathbf{0}_{3\times 3} \\ \mathbf{0}_{3\times 3} & \mathbf{E}_b \end{bmatrix}.
\end{aligned}$$

The observer gain matrices can be chosen such that the error dynamics is passive and GES.

It is convenient to prove passivity and stability by using an SPR-Lyapunov approach. In the error dynamics in Figure 7.2 two new error terms ε_z and ε_ν are defined according to

$$\varepsilon_z \triangleq -\mathbf{R}^T(\psi_d)\tilde{\mathbf{z}}_o, \quad \varepsilon_\nu \triangleq \mathbf{R}(\psi_d)\tilde{\nu}. \tag{7.24}$$

Thus, the observer error system can be viewed as two linear blocks $\mathcal{H}_1$ and $\mathcal{H}_2$, interconnected through the bounded transformation matrix $\mathbf{R}(\psi_d)$.

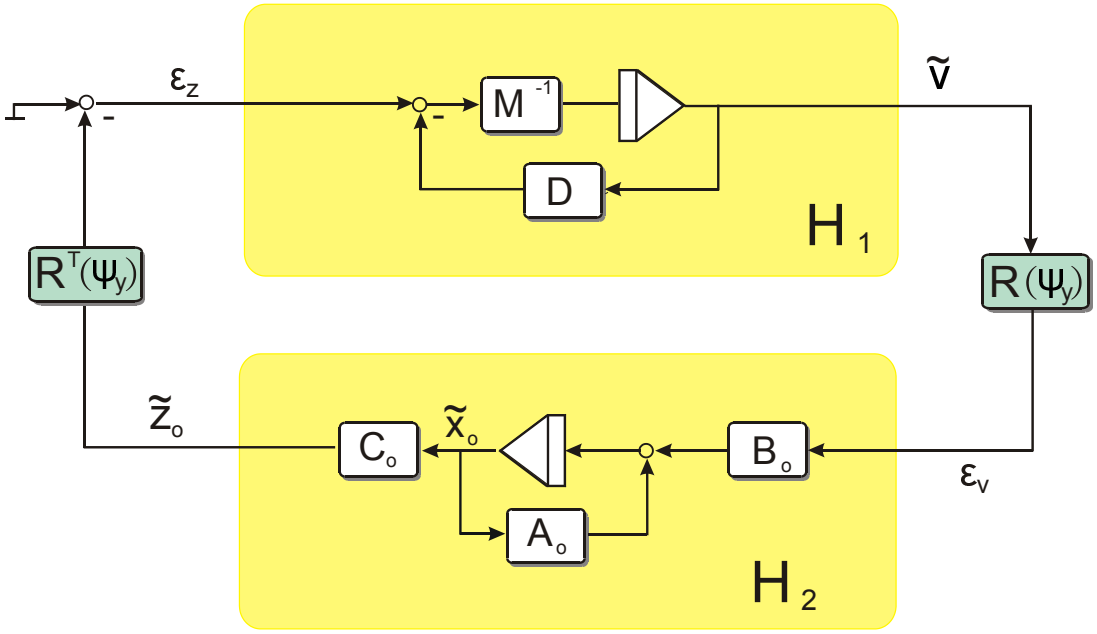

Figure 7.2: Block diagram of the observer error dynamics.

Based on the physical properties of the ship dynamics, we can make the following statement:

Proposition 7.1 *The mapping $\varepsilon_z \mapsto \tilde{\nu}$ is* state strictly passive *(system $\mathcal{H}_1$ in Figure 7.2).*
Proof. *Let*

$$S_1 = \frac{1}{2}\tilde{\nu}^T\mathbf{M}\tilde{\nu} > 0 \tag{7.25}$$

be a positive definite storage function. From (7.23a) we have:

$$\dot{S}_1 = -\frac{1}{2}\tilde{\nu}^T(\mathbf{D}+\mathbf{D}^T)\tilde{\nu} + \tilde{\nu}^T\varepsilon_z \tag{7.26}$$

$$\Downarrow$$

$$\tilde{\nu}^T\varepsilon_z \geq \dot{S}_1 + \beta\tilde{\nu}^T\tilde{\nu}, \tag{7.27}$$

where $\beta = \frac{1}{2}\lambda_{\min}(\mathbf{D}+\mathbf{D}^T) > 0$ *and* $\lambda_{\min}(\cdot)$ *denotes the minimum eigenvalue. Thus, (7.27) proves that* $\varepsilon_z \mapsto \tilde{\nu}$ *is state strictly passive, see e.g. Khalil (2002). Moreover, since this mapping is strictly passive, post-multiplication with the bounded transformation matrix* $\mathbf{R}(\psi_y)$ *and pre-multiplication by it's transpose will not affect the passivity properties. Hence the block* $\mathcal{H}_1$ *is strictly passive.* □

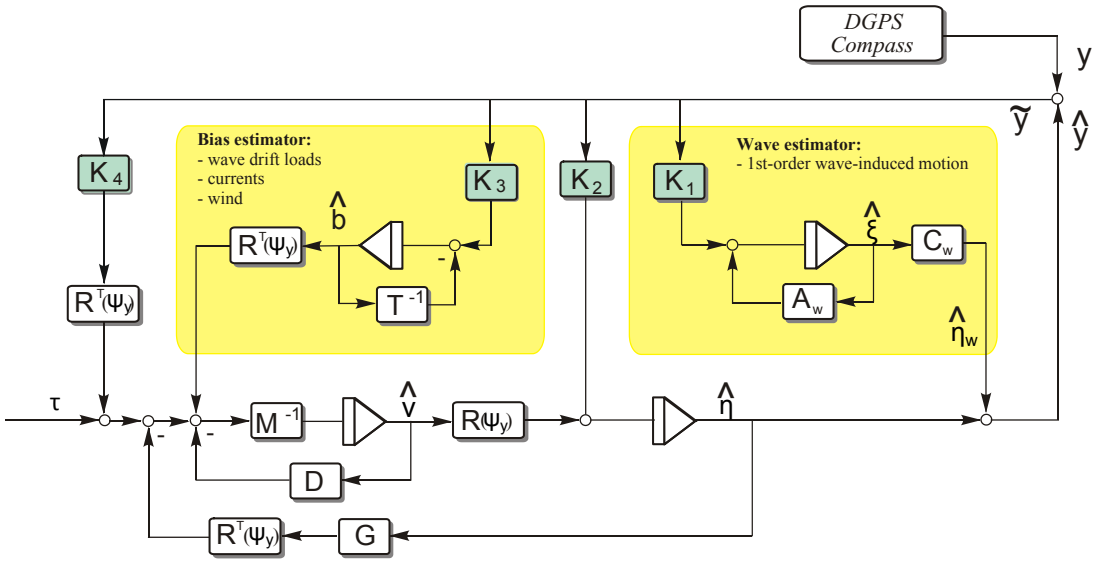

Figure 7.3: Block description of the observer.

Passivity and stability of the total system will be provided if the observer gain matrices $\mathbf{K}_1, ..., \mathbf{K}_4$ can be chosen such that the mapping $\varepsilon_\nu \mapsto \tilde{\mathbf{z}}_o$ is strictly positive real (SPR). This is obtained if the matrices $\mathbf{A}_o$, $\mathbf{B}_o$, $\mathbf{C}_o$ in (7.23a)–(7.23b) satisfy the *Kalman-Yakubovich-Popov (KYP) Lemma*:

Lemma 7.1 (Kalman-Yakubovich-Popov) *Let* $\mathbf{Z}(s) = \mathbf{C}(s\mathbf{I}-\mathbf{A})^{-1}\mathbf{B}$ *be an* $m \times m$ *transfer function matrix, where* $\mathbf{A}$ *is Hurwitz,* $(\mathbf{A}, \mathbf{B})$ *is controllable, and* $(\mathbf{A}, \mathbf{C})$ *is observable. Then* $\mathbf{Z}(s)$ *is strictly positive real (SPR) if and only if there exist positive definite matrices* $\mathbf{P} = \mathbf{P}^T > 0$ *and* $\mathbf{Q} = \mathbf{Q}^T > 0$ *such that*

$$\mathbf{P}\mathbf{A} + \mathbf{A}^T\mathbf{P} = -\mathbf{Q}, \tag{7.28}$$

$$\mathbf{B}^T\mathbf{P} = \mathbf{C}. \tag{7.29}$$

Proof. *See Khalil (2002).*

Theorem 7.1 (Main result: passive observer error dynamics) *The nonlinear observer error dynamics (7.18a)–(7.18d) is passive if the observer gain matrices* $\mathbf{K}_i$ *(*$i = 1, .., 4$*) are chosen such that (7.23b) satisfies the KYP-Lemma.*

Proof. *Since it is established that* $\mathcal{H}_1$ *is strictly passive and* $\mathcal{H}_2$ *, which is given by* $\mathbf{A} = \mathbf{A}_o$*,* $\mathbf{B} = \mathbf{B}_o$ *and* $\mathbf{C} = \mathbf{C}_o$*, can be made SPR by choosing the gain matrices* $\mathbf{K}_i$ *(*$i = 1, .., 4$*) according to the KYP lemma, the nonlinear observer error (7.18a)–(7.18d) is passive. In addition the observer error dynamics is GES (Figure 7.2), see Fossen and Strand (1999).*□

In practice it is easy to find a set of gain matrices $\mathbf{K}_i$ $(i = 1, .., 4)$ satisfying the KYP lemma. Since the mooring stiffness matrix $\mathbf{G}$ is assumed to be diagonal, the mapping $\varepsilon_\nu \mapsto \tilde{\mathbf{z}}_o$ will, by choosing a diagonal structure of the observer gain matrices

$$\mathbf{K}_1 = \begin{bmatrix} \text{diag}\{k_1, k_2, k_3\} \\ \text{diag}\{k_4, k_5, k_6\} \end{bmatrix}, \tag{7.30a}$$

$$\mathbf{K}_2 = \text{diag}\{k_7, k_8, k_9\}, \tag{7.30b}$$

$$\mathbf{K}_3 = \text{diag}\{k_{10}, k_{11}, k_{12}\}, \tag{7.30c}$$

$$\mathbf{K}_4 = \text{diag}\{k_{13}, k_{14}, k_{15}\}, \tag{7.30d}$$

be described by three decoupled transfer functions

$$\frac{\tilde{\mathbf{z}}_o}{\varepsilon_\nu}(s) = \text{diag}\{h_{z1}(s), h_{z2}(s), h_{z3}(s)\}, \tag{7.31}$$

where a typical transfer function $h_{zi}(s)$ is presented in Figure 7.4. The wave filtering properties is clearly seen by the notch effect in the frequency range of the wave motion. In order to meet the SPR requirement, one necessary condition is that the transfer functions $h_{zi}(s)$, $(i = 1, 2, 3)$ have phase greater than $-90°$ and less than $+90°$. Regarding the choice of observer gain matrices, the tuning procedure can be similar as for the observer for free-floating ships in Fossen and Strand (1999), where loop shaping techniques are used.

Tuning rules

In order to ensure passivity and to relate the observer gains of (7.30a) and (7.30b) to the dominating wave response frequencies, it is proposed that

$$k_i = -2\left(\zeta_{ni} - \zeta_i\right)\frac{\omega_{ci}}{\omega_i} \quad , \; i = 1,\, 2 \text{ and } 3 \tag{7.32}$$

$$k_i = 2\omega_i\left(\zeta_{ni} - \zeta_i\right) \quad , \; i = 4,\, 5 \text{ and } 6 \tag{7.33}$$

$$k_i = \omega_{ci} \quad , \; i = 7,\, 8 \text{ and } 9, \tag{7.34}$$

where $\omega_{ci} > \omega_i$ is the filter cut-off frequency. $\zeta_{ni} > \zeta_i$ are tuning parameters to be set between $0.1 - 1.0$, (typic values: $\zeta_{ni} = 1.0$ and $\zeta_n = 0.1$). $k_{10} - k_{12}$ should be sufficient high to ensure proper bias estimation. One should notice that $\mathbf{A}_w$ is also dependent on the actual sea state through the parameter ω_i. Notice that ω_i is often set equal to the wave peak frequency, that is $\omega_i \approx 2pi/T_{pi}$. This assumption may be appropriate for most cases. However, it is a common misunderstanding in the literature to mix the wave response estimation with the wave amplitude estimation. The wave response is the result of a series of signals transformations from the wave amplitude to the wave load and finally to the wave response.

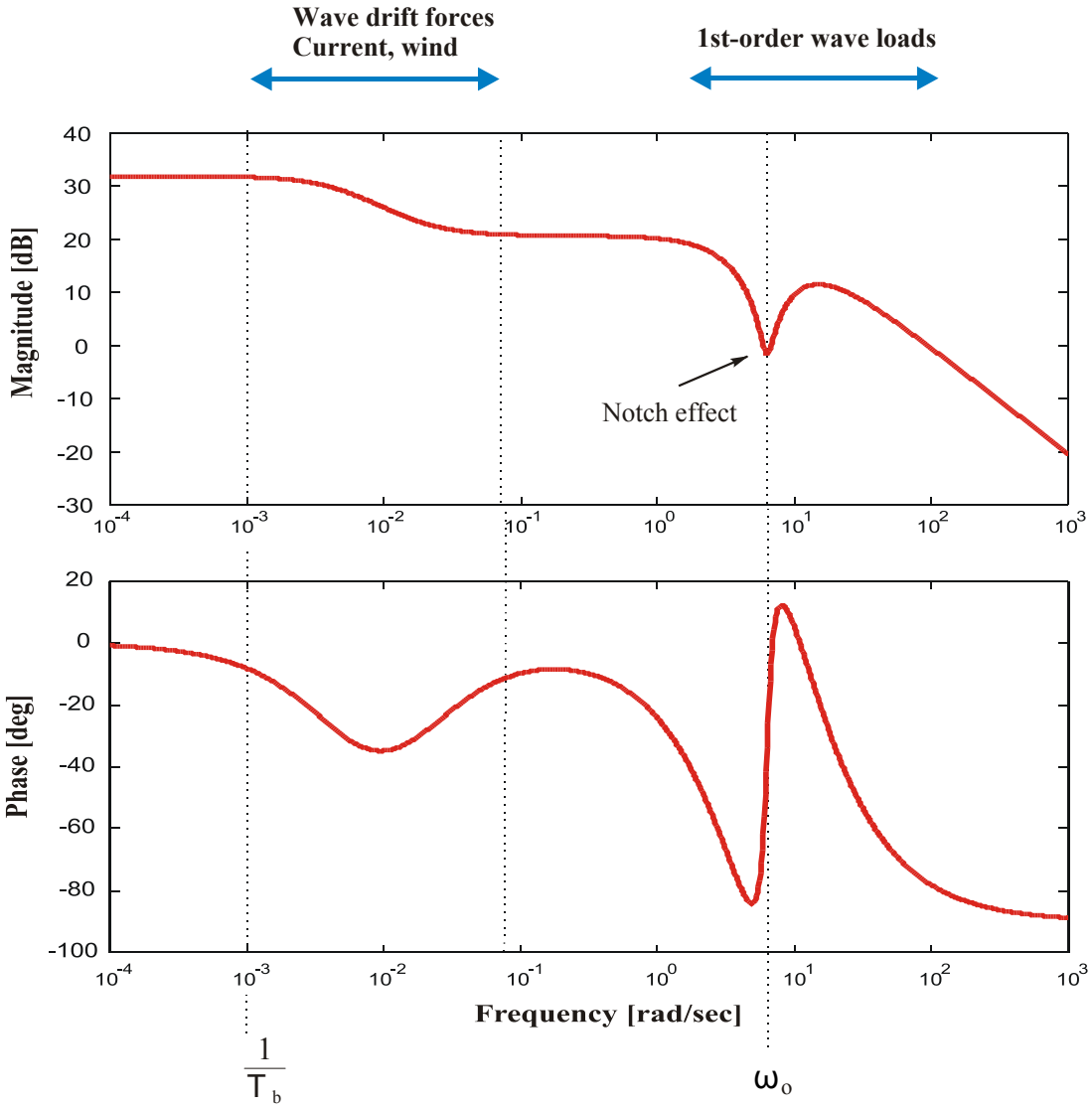

Figure 7.4: A typical bode plot of the transfer function $h_{zi}(s)$.

Augmented observer (representation 2)

The proposed observer can be further refined by augmenting a new state. The augmented design provides more flexibility, better filtering and it is the basis for the adaptive observer in Section 7.2.5. We start by adding a new state, $\mathbf{x}_f$, in the observer, which is the low-pass filtered innovation $\tilde{\mathbf{y}}$. Moreover

$$\dot{\mathbf{x}}_f = -\mathbf{T}_f^{-1}\mathbf{x}_f + \tilde{\mathbf{y}} = -\mathbf{T}_f^{-1}\mathbf{x}_f + \tilde{\eta} + \mathbf{C}_w\tilde{\xi}, \tag{7.35}$$

where $\mathbf{x}_f \in \mathbb{R}^3$, and $\mathbf{T}_f$ =diag$\{T_{f1}, T_{f2}, T_{f3}\}$ contains positive filter constants. Highpass filtered innovation signals can be derived from $\mathbf{x}_f$ by

$$\tilde{\mathbf{y}}_f = -\mathbf{T}_f^{-1}\mathbf{x}_f + \tilde{\mathbf{y}} = -\mathbf{T}_f^{-1}\mathbf{x}_f + \tilde{\eta} + \mathbf{C}_w\tilde{\xi}. \tag{7.36}$$

Thus, both the low-pass and high-pass filtered innovation are available for feedback. Moreover,

$$\left.\begin{array}{l} \mathbf{x}_f^{\{i\}}(s) = \frac{T_{fi}}{1+T_{fi}s}\tilde{\mathbf{y}}^{\{i\}}(s) \\ \tilde{\mathbf{y}}_f^{\{i\}}(s) = \frac{T_{fi}s}{1+T_{fi}s}\tilde{\mathbf{y}}^{\{i\}}(s) \end{array}\right\}, \quad (i=1,2,3). \tag{7.37}$$

The cut-off frequency in the filters should be below the frequencies of the dominating waves in the WF model (7.3). The augmented observer equations are

$$\begin{aligned} \dot{\hat{\xi}} &= \mathbf{A}_w\hat{\xi} + \mathbf{K}_{1\mathrm{h}}\tilde{\mathbf{y}}_f, && (7.38a)\\ \dot{\hat{\eta}} &= \mathbf{R}(\psi_d)\hat{\nu} + \mathbf{K}_2\tilde{\mathbf{y}} + \mathbf{K}_{2\mathrm{l}}\mathbf{x}_f + \mathbf{K}_{2\mathrm{h}}\tilde{\mathbf{y}}_f, && (7.38b)\\ \dot{\hat{\mathbf{b}}} &= -\mathbf{T}_b^{-1}\hat{\mathbf{b}} + \mathbf{K}_3\tilde{\mathbf{y}} + \mathbf{K}_{3\mathrm{l}}\mathbf{x}_f, && (7.38c)\\ \mathbf{M}\dot{\hat{\nu}} &= -\mathbf{D}\hat{\nu} - \mathbf{R}^T(\psi_d)\mathbf{G}\hat{\eta} + \mathbf{R}^T(\psi_d)\hat{\mathbf{b}} + \tau, \\ &\quad +\mathbf{R}^T(\psi_d)\left(\mathbf{K}_4\tilde{\mathbf{y}} + \mathbf{K}_{4\mathrm{l}}\mathbf{x}_f + \mathbf{K}_{4\mathrm{h}}\tilde{\mathbf{y}}_f\right), && (7.38d)\\ \hat{\mathbf{y}} &= \hat{\eta} + \mathbf{C}_w\hat{\xi}, && (7.38e) \end{aligned}$$

where $\mathbf{x}_f$ is the low-pass filtered innovation vector, and $\tilde{\mathbf{y}}_f$ is the high-pass filtered innovation given by (7.35) and (7.36), respectively. Here $\mathbf{K}_{1\mathrm{h}} \in \mathbb{R}^{6x3}$ and $\mathbf{K}_{2\mathrm{l}}$, $\mathbf{K}_{2\mathrm{h}}$, $\mathbf{K}_{3\mathrm{l}}$, $\mathbf{K}_{4\mathrm{l}}$, $\mathbf{K}_{4\mathrm{h}} \in \mathbb{R}^{3x3}$ are new observer gain matrices to be determined.

Augmented observer error equations

The augmented observer error dynamics can be written compactly as

$$\begin{aligned} \mathbf{M}\dot{\tilde{\nu}} &= -\mathbf{D}\tilde{\nu} - \mathbf{R}^T(\psi_d)\mathbf{C}_a\tilde{\mathbf{x}}_a, && (7.39a)\\ \dot{\tilde{\mathbf{x}}}_a &= \mathbf{A}_a\tilde{\mathbf{x}}_a + \mathbf{B}_a\mathbf{R}(\psi_d)\tilde{\nu} + \mathbf{E}_a\mathbf{w}, && (7.39b) \end{aligned}$$

where

$$\begin{aligned} \tilde{\mathbf{x}}_a &\triangleq \begin{bmatrix} \tilde{\xi}^T & \tilde{\eta}^T & \mathbf{x}_f^T & \tilde{\mathbf{b}}^T \end{bmatrix}^T, && (7.40)\\ \tilde{\mathbf{z}}_a &\triangleq \mathbf{K}_4\tilde{\mathbf{y}} + \mathbf{K}_{4\mathrm{l}}\mathbf{x}_f + \mathbf{K}_{4\mathrm{h}}\tilde{\mathbf{y}}_f + \mathbf{G}\tilde{\eta} - \tilde{\mathbf{b}} \triangleq \mathbf{C}_a\tilde{\mathbf{x}}_a, && (7.41) \end{aligned}$$

and

$$\begin{aligned} \mathbf{A}_a &= \begin{bmatrix} \mathbf{A}_w - \mathbf{K}_{1\mathrm{h}}\mathbf{C}_w & -\mathbf{K}_{1\mathrm{h}} & \mathbf{K}_{1\mathrm{h}}\mathbf{T}_f^{-1} & \mathbf{0}_{6\times3} \\ -(\mathbf{K}_2+\mathbf{K}_{2\mathrm{h}})\mathbf{C}_w & -(\mathbf{K}_2+\mathbf{K}_{2\mathrm{h}}) & \mathbf{K}_{2\mathrm{l}}\mathbf{T}_f^{-1} - \mathbf{K}_{2\mathrm{l}} & \mathbf{0}_{3\times3} \\ \mathbf{C}_w & \mathbf{I}_{3\times3} & -\mathbf{T}_f^{-1} & \mathbf{0}_{3\times3} \\ -\mathbf{K}_3\mathbf{C}_w & -\mathbf{K}_3 & -\mathbf{K}_{3\mathrm{l}} & -\mathbf{T}_b^{-1} \end{bmatrix}, \\ \mathbf{B}_a &= \begin{bmatrix} \mathbf{0}_{6\times3} \\ \mathbf{I}_{3\times3} \\ \mathbf{0}_{3\times3} \\ \mathbf{0}_{3\times3} \end{bmatrix}, \qquad \mathbf{E}_a = \begin{bmatrix} \mathbf{E}_w & \mathbf{0}_{6\times3} \\ \mathbf{0}_{3\times3} & \mathbf{0}_{3\times3} \\ \mathbf{0}_{3\times3} & \mathbf{0}_{3\times3} \\ \mathbf{0}_{3\times3} & \mathbf{E}_b \end{bmatrix}, \\ \mathbf{C}_a &= \begin{bmatrix} (\mathbf{K}_4+\mathbf{K}_{4\mathrm{h}})\mathbf{C}_w & (\mathbf{K}_4+\mathbf{K}_{4\mathrm{h}}) + \mathbf{G} & -\mathbf{K}_{4\mathrm{h}}\mathbf{T}_f^{-1} + \mathbf{K}_{4\mathrm{l}} & -\mathbf{I}_{3\times3} \end{bmatrix}. \end{aligned}$$

The signals $\tilde{\mathbf{y}}_f$ and $\mathbf{x}_f$ are extracted from $\tilde{\mathbf{x}}_a$ by $\tilde{\mathbf{y}}_f = \mathbf{C}_h\tilde{\mathbf{x}}_a$ and $\mathbf{x}_f = \mathbf{C}_l\tilde{\mathbf{x}}_a$ where

$$\mathbf{C}_h = \begin{bmatrix} \mathbf{C}_w & \mathbf{I}_{3\times3} & -\mathbf{T}_f^{-1} & \mathbf{0}_{3\times3} \end{bmatrix}, \quad \mathbf{C}_l = \begin{bmatrix} \mathbf{0}_{6\times3} & \mathbf{0}_{3\times3} & \mathbf{I}_{3\times3} & \mathbf{0}_{3\times3} \end{bmatrix}. \tag{7.42}$$

Again, the gain matrices should be chosen such that $(\mathbf{A}_a, \mathbf{B}_a, \mathbf{C}_a)$ satisfies the KYP lemma in order to obtain passivity and GES, see Strand and Fossen (1999) for more details.

7.2.5 Adaptive Observer Design

In this section we treat the problem when the parameters of $\mathbf{A}_w$ in the WF model (7.9a) are *not* known (Strand and Fossen, 1999). The parameters vary with the different sea-states in which the ship is operating. Gain-scheduling techniques, using off-line batch processing frequency trackers and external sensors such as wind velocity, wave radars and roll, pitch angle measurements can also be used to adjust the WF model parameters to varying sea states (Fossen, 2011). Additional sensors units can, however, be avoided by using an adaptive observer design. Since the wave models are assumed to be decoupled in surge, sway and yaw, $\mathbf{\Lambda}$ and $\mathbf{\Omega}$ in $\mathbf{A}_w$ are diagonal matrices given by

$$\mathbf{A}_w(\theta) = \begin{bmatrix} \mathbf{0}_{3\times 3} & \mathbf{I}_{3\times 3} \\ -\mathbf{\Omega}^2 & -2\mathbf{\Lambda}\mathbf{\Omega} \end{bmatrix} \triangleq \begin{bmatrix} \mathbf{0}_{3\times 3} & \mathbf{I}_{3\times 3} \\ -\mathrm{diag}(\theta_1) & -\mathrm{diag}(\theta_2) \end{bmatrix}, \tag{7.43}$$

where $\theta = [\theta_1^T,\ \theta_2^T]^T$, and $\theta_1, \theta_2 \in \mathbb{R}^3$ contain the unknown wave model parameters to be estimated. We start with the following assumption:

A3 **Constant environmental parameters.** It is assumed that the unknown parameters Ω and Λ in $\mathbf{A}_w$ are constant or at least slowly-varying compared to the states of the system. In addition, the wave spectrum parameters are limited by

$$\left.\begin{array}{c} 0 < \omega_{o,\min} < \omega_{oi} < \omega_{o,\max} \\ 0 < \zeta_{\min} < \zeta_i < \zeta_{\max} \end{array}\right\}, \quad i = 1,2,3 \tag{7.44}$$

such that $\mathbf{A}_w$ is Hurwitz. Hence, the unknown wave model parameters are treated as constants in the analysis, such that:

$$\dot{\theta} = \mathbf{0}. \tag{7.45}$$

Adaptive observer equations

The adaptive version of the observer is based on the augmented observer equations (7.38a)–(7.38e), except from the WF part where we now propose to use the estimated WF parameters, $\hat{\theta}$, such that

$$\dot{\hat{\xi}} = \mathbf{A}_w(\hat{\theta})\hat{\xi} + \mathbf{K}_{1\mathrm{h}}\tilde{\mathbf{y}}_f. \tag{7.46a}$$

The parameter update law is

$$\begin{aligned} \dot{\hat{\theta}} &= -\mathbf{\Gamma}_w \mathbf{\Phi}(\hat{\xi})\mathbf{C}_h\tilde{\mathbf{x}}_a \\ &= -\mathbf{\Gamma}_w \mathbf{\Phi}(\hat{\xi})\tilde{\mathbf{y}}_f, \qquad \mathbf{\Gamma}_w > 0 \end{aligned} \tag{7.47}$$

where $\mathbf{\Phi}(\hat{\xi}) \in \mathbb{R}^{6\times 3}$ is the regressor matrix. The regressor matrix is further investigated by considering the error dynamics.

Adaptive observer error dynamics

The adaptive WF observer error dynamics is

$$\dot{\tilde{\xi}} = \mathbf{A}_w\xi - \mathbf{A}_w(\hat{\theta})\hat{\xi} - \mathbf{K}_{1\mathrm{h}}\tilde{\mathbf{y}}_f + \mathbf{E}_w\mathbf{w}_w. \tag{7.48}$$

By adding and subtracting $\mathbf{A}_w\hat{\xi}$, defining

$$\mathbf{B}_w\mathbf{\Phi}^T(\hat{\xi})\tilde{\theta} \triangleq (\mathbf{A}_w - \mathbf{A}_w(\hat{\theta}))\hat{\xi}, \tag{7.49}$$

where $\tilde{\theta} = \hat{\theta} - \theta$ denotes the estimation error,

$$\mathbf{\Phi}^T(\hat{\xi}) \triangleq \begin{bmatrix} \text{diag}(\hat{\xi}_1) & \text{diag}(\hat{\xi}_2) \end{bmatrix}, \tag{7.50}$$

$$\mathbf{B}_w \triangleq \begin{bmatrix} \mathbf{0}_{3\times3} & \mathbf{I}_{3\times3} \end{bmatrix}^T, \tag{7.51}$$

where $\hat{\xi} = [\hat{\xi}_1^T, \hat{\xi}_2^T]^T$, $\hat{\xi}_1, \hat{\xi}_2 \in \mathbb{R}^3$, and by using (7.36), then (7.48) can be rewritten as

$$\begin{aligned} \dot{\tilde{\xi}} &= (\mathbf{A}_w - \mathbf{K}_{1\text{f}}\mathbf{C}_w)\tilde{\xi} - \mathbf{K}_{1\text{f}}\tilde{\eta} + \mathbf{B}_w\mathbf{\Phi}^T(\hat{\xi})\tilde{\theta} \\ &\quad + \mathbf{K}_{1\text{f}}\mathbf{T}_f^{-1}\mathbf{x}_f + \mathbf{E}_w\mathbf{w}_w. \end{aligned} \tag{7.52}$$

The observer error dynamics can be written compactly as

$$\mathbf{M}\dot{\tilde{\nu}} = -\mathbf{D}\tilde{\nu} - \mathbf{R}^T(\psi_y)\mathbf{C}_a\tilde{\mathbf{x}}_a, \tag{7.53a}$$

$$\dot{\tilde{\mathbf{x}}}_a = \mathbf{A}_a\tilde{\mathbf{x}}_a + \mathbf{B}_a\mathbf{R}(\psi_y)\tilde{\nu} + \mathbf{H}_a\mathbf{\Phi}^T(\hat{\xi})\tilde{\theta} + \mathbf{E}_a\mathbf{w}, \tag{7.53b}$$

where

$$\mathbf{H}_a = \begin{bmatrix} \mathbf{B}_w^T & \mathbf{0}_{3\times3} & \mathbf{0}_{3\times3} & \mathbf{0}_{3\times3} \end{bmatrix}^T. \tag{7.54}$$

In the adaptive case, we want the WF adaptive law to be updated by the high-pass filtered innovations signals. Hence, it is required that the observer gain matrices are chosen such that

$$\mathbf{A}_a^T\mathbf{P}_a + \mathbf{P}_a\mathbf{A}_a = -\mathbf{Q}_a, \tag{7.55a}$$

$$\mathbf{B}_a^T\mathbf{P}_a = \mathbf{C}_a, \tag{7.55b}$$

$$\mathbf{H}_a^T\mathbf{P}_a = \mathbf{C}_h. \tag{7.55c}$$

in order to obtain passivity, see Strand and Fossen (1999). It should be noted that GES cannot be guaranteed for this case since this requires persistency of excitation. However, global convergence of all state estimation errors to zero can be guaranteed at the same time as the parameter estimation error is bounded. We will, however, see from the experimental results that also the parameters converge to their true values when considering a ship rest but exposed to waves.

7.2.6 Nonlinear Observer Design for Extreme Seas

Frequency domain analysis

In order to analyze the effect of the nonlinear observer assume that the rotation matrix $\mathbf{R}$ is equal to the identity matrix $\mathbf{I}_{3\times3}$. Let us define $\hat{\mathbf{x}} = [\hat{\xi}^T, \hat{\eta}^T, \hat{\mathbf{b}}^T, \hat{\nu}^T]^T$, then a state space formulation for the linearized observer can be written

$$\begin{aligned} \dot{\hat{\mathbf{x}}} &= \mathbf{A}\hat{\mathbf{x}} + \mathbf{K}\left(\mathbf{y} - \hat{\mathbf{y}}\right), \\ &= \left(\mathbf{A} - \mathbf{K}\mathbf{H}\right)\hat{\mathbf{x}} + \mathbf{K}\mathbf{y}, \\ &= \mathbf{A}_{cl}\hat{\mathbf{x}} + \mathbf{K}\mathbf{y}, \end{aligned} \tag{7.56}$$

where $\hat{\mathbf{y}} = \mathbf{H}\hat{\mathbf{x}}$ and

$$\mathbf{A} = \begin{bmatrix} \mathbf{A}_w & \mathbf{0}_{6\times9} \\ \mathbf{0}_{9\times6} & \mathbf{A}_{LF} \end{bmatrix}, \tag{7.57}$$

where $\mathbf{A}_w$ is as defined in (7.4a), $\mathbf{H}$ is as defined in (7.13), and

$$\mathbf{A}_{LF} = \begin{bmatrix} \mathbf{0}_{3\times3} & \mathbf{0}_{3\times3} & \mathbf{I}_{3\times3} \\ \mathbf{0}_{3\times3} & -\mathbf{T}_b^{-1} & \mathbf{0}_{3\times3} \\ -\mathbf{M}^{-1}\mathbf{G} & \mathbf{M}^{-1} & -\mathbf{M}^{-1}\mathbf{D} \end{bmatrix}, \tag{7.58}$$

$$\mathbf{K} = \begin{bmatrix} \mathbf{K}_1^T & \mathbf{K}_2^T & \mathbf{K}_3^T & (\mathbf{M}^{-1}\mathbf{K}_4)^T \end{bmatrix}^T. \tag{7.59}$$

When performing adaptive wave filtering subject to very high wave periods, the LF feedback signals supposed to be controlled are filtered away (Sørensen et al., 2002). This happens because notch effect with $\omega_i = 2pi/T_{pi}$ will be within the bandwidth of the controller for large wave peak periods T_{pi}. This is illustrated in Figure 7.5, that shows the transfer functions between the estimated and measured surge position using (7.56) for a DP operated shuttle tanker (Figure 7.6) with significant wave height $H_{mo} = 6m$ and T_p equal to $15s$ (right), $20s$ (middle) and $40s$ (left). The length between perpendiculars is $256m$, and mass is $143.000\,tons$. The passivity property of the linearized observer is also shown by studying the phase that is within $\pm 90^o$. Notice that in this example there is no mooring system such that $\mathbf{G} = \mathbf{0}$.

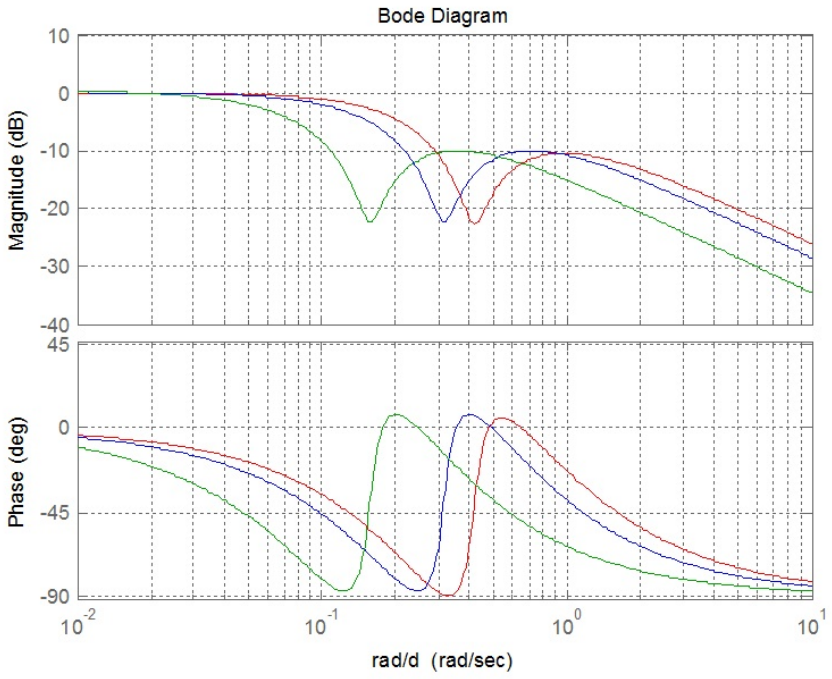

Figure 7.5: Transfer functions between measured and estimated LF surge position (left $T_p = 40s$, middle $T_p = 20s$ and right $T_p = 15s$).

Figure 7.6: Shuttle tanker.

Observer equations extreme seas (representation 3)

Operating in extreme seas we will propose to reformulate the observer given in (7.18a)–(7.18e) as

$$\begin{aligned}
\dot{\hat{\eta}} &= \mathbf{R}(\psi_d)\hat{\nu} + \mathbf{K}_2\tilde{\mathbf{y}}, && \text{(7.60a)}\\
\dot{\hat{\mathbf{b}}} &= \mathbf{K}_3\tilde{\mathbf{y}}, && \text{(7.60b)}\\
\mathbf{M}\dot{\hat{\nu}} &= -\mathbf{D}\hat{\nu} - \mathbf{R}^T(\psi_d)\mathbf{G}\hat{\eta} + \mathbf{R}^T(\psi_d)\hat{\mathbf{b}} + && \text{(7.60c)}\\
&\quad \tau + \mathbf{R}^T(\psi_d)\mathbf{K}_4\tilde{\mathbf{y}}\ , &&\\
\hat{\mathbf{y}} &= \hat{\eta}. && \text{(7.60d)}
\end{aligned}$$

The notch effect is removed. In order to ensure bumpless transition between the two observers, proper smooth switching schemes subject to the prevailing sea state must be introduced.

7.2.7 Experimental Results

Both the augmented and the adaptive observer have been implemented and tested at the Guidance, Navigation and Control (GNC) Laboratory at the Department of Engineering Cybernetics, NTNU. A detailed description of the laboratory is found in Strand (1999). In the experiments Cybership I was used, see Figure 7.7.

A nonlinear PID controller is used for maintaining the ship at the desired position (x_d, y_d) and heading ψ_d.

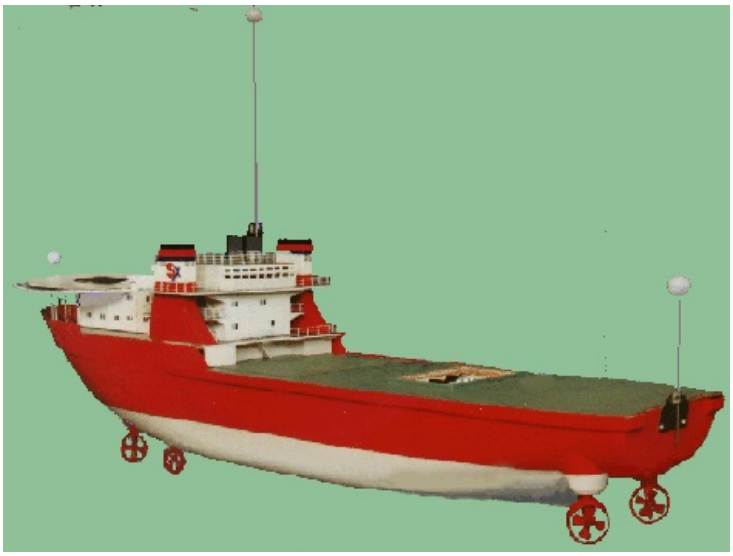

Figure 7.7: CyberShip I: Model ship scale 1:70.

position:	L_s/L_m
linear velocity:	$\sqrt{L_s/L_m}$
angular velocity:	$\sqrt{L_m/L_s}$
linear acceleration:	1
angular acceleration:	L_m/L_s
force:	m_s/m_m
moment:	$\frac{m_s L_s}{m_m L_m}$
time:	$\sqrt{L_s/L_m}$

Table 7.1: Scaling factors used in the experiments (Bis scaling).

An illustration of the experimental setup is given in Figure 7.8. The experimental results are transformed to full scale by requiring that the *Froude number* $F_n = U/\sqrt{Lg}$ =constant. Here U is the vessel speed, L is the length of the ship and g is the acceleration of gravity.

The scaling factors are given in Table 7.1 where m is the mass and the subscripts m and s denote the model and the full-scale ship, respectively. The length of the model ship is $L_m = 1.19$ meters and the mass is $m_m = 17.6$ kg. A full scale ship similar to Cybership I has typically a length of $70 - 90$ meters and mass of $4000 - 5000$ tones.

The experiment can be divided in three phases:

- *Phase I (No waves).* Initially the ship is maintaining the desired position and heading with no environmental loads acting on the ship (calm water). The reference heading is -140 degrees. When the data acquisition starts, a wind fan is switched on. There is no adaptive wave filtering and the observer is identical to the augmented design (Representation 2). The effect of the wind loads are reflected in the bias estimates in Figure 7.10.

- *Phase II (Waves, adaptive wave filter is off).* After 1700 seconds the wave generator is started. In this phase we can see the performance of the observer without adaptive wave

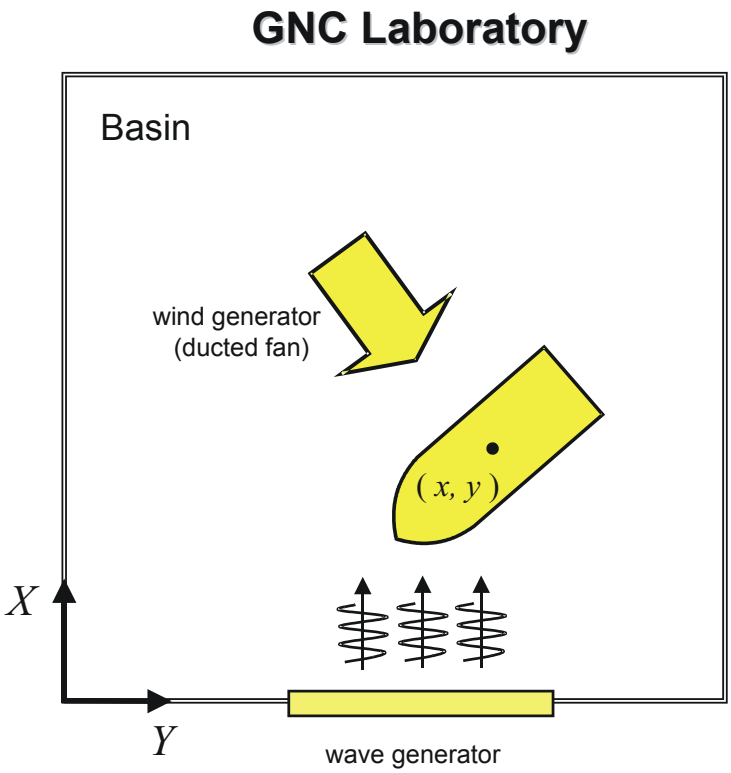

Figure 7.8: Experimental setup in model basin.

filter. In the wave model we are assuming that the dominating wave period is 9.2 seconds and the relative damping ratio is 0.1, see Figure 7.9.

- *Phase III (Waves, adaptive wave filter is on).* After 2800 seconds the adaptive wave filter is activated. The estimates of dominating wave period and relative damping are plotted in Figure 7.9 for surge, sway and yaw.

A spectrum analysis of the position and heading measurements shows that the estimated wave periods converge to their true values, that is wave periods of approximately 7.8 seconds and relative damping ratios of 0.07, see Figure 7.9. In Figure 7.10 the measured position deviation and heading are plotted together with the corresponding LF estimates. The effect of the adaptive wave filtering is clearly seen in Figure 7.12, where the innovation signals are significantly reduced during Phase III, when the adaptation is active and the wave model parameters start converging to their true values. The effect of *bad* wave filtering is reflected by noisy control action by the thrusters during phase II, see Figure 7.12. A zoom-in of the heading measurement together with the LF estimate is given is Figure 7.11 both for phase II and III. Here we see that the LF estimates have a significant WF contribution when the adaptive wave filter is off. This is the reason for the noisy control action in phase II. The other zoom-in shows excellent LF estimation when the adaptive wave filter is active and the wave model parameters have converged to their true values. Hence, it can be concluded that adaptive wave filtering yields a significant improvement in performance compared to filters with fixed WF model parameters operating in varying sea states.

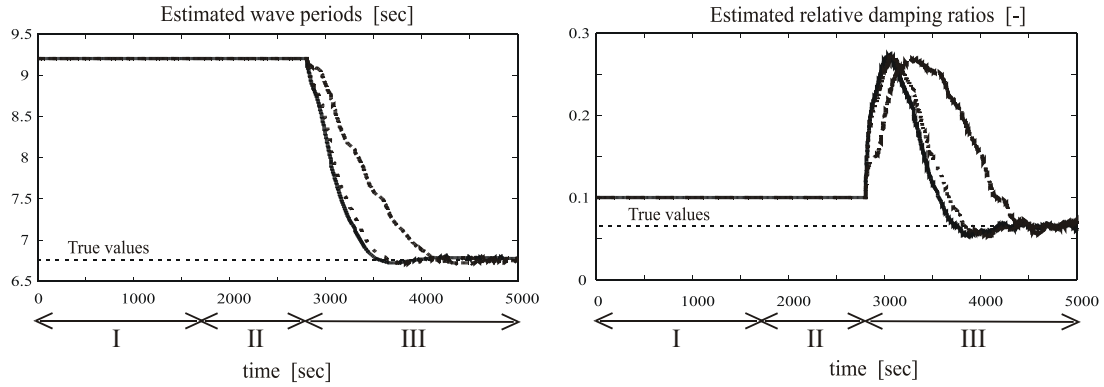

Figure 7.9: Estimated wave periods (left) and estimated relative damping ratios (right) for surge (solid), sway (dashed) and yaw (dotted). The adaptive wave-filter is activated after 2800 seconds.

7.3 Controller Design for Dynamic Positioning

In the design of dynamic positioning (DP) systems and thruster assisted position mooring (PM) systems it has been adequate to regard the control objective as a three degrees-of-freedom (DOF) problem in the horizontal-plane in surge, sway and yaw respectively However as mentioned in Section 6, for semi-submersibles an unintentional coupling phenomena between the vertical and the horizontal planes through the thruster action can be invoked. The natural periods in roll and pitch are in the range of 35-65 seconds and are within the bandwidth of the positioning controller. In Sørensen and Strand (2000) it was shown that roll and pitch may be unintentionally excited by the thruster system, which is only supposed to act in the horizontal-plane. If the inherent vertical damping properties are small, the amplitudes of roll and pitch may be emphasized by the thruster's induction by up to 2°-5° in the resonance range.

In this section different model-based multivariable control strategies accounting for both horizontal and vertical motions, with the exception of heave, is described. Since it is undesirable to counteract the wave-frequency (WF) motions caused by first-order wave loads, the control action of the propulsion system is produced by the low-frequency (LF) part of the vessel's motion, which is caused by current, wind and second-order mean and slowly varying wave loads. The computation of feedback signals to be used in the controller are based on nonlinear observer theory as presented in the Section 7.2.

7.3.1 Control Plant Model

The control plan model is as in Section 7.2.2.

Linear low-frequency model

For the purpose of controller design and analysis, it is convenient to derive a linear LF control plant model about zero vessel velocity. By assuming small roll and pitch amplitudes, and that the yaw angle is defined with respect to the desired heading angle, the rotation matrix $\mathbf{J}(\eta_2)$ can be approximated by the identity matrix, see Section 6.3. The measured position and heading signals are transformed into the reference-parallel frame before the estimator and the controller

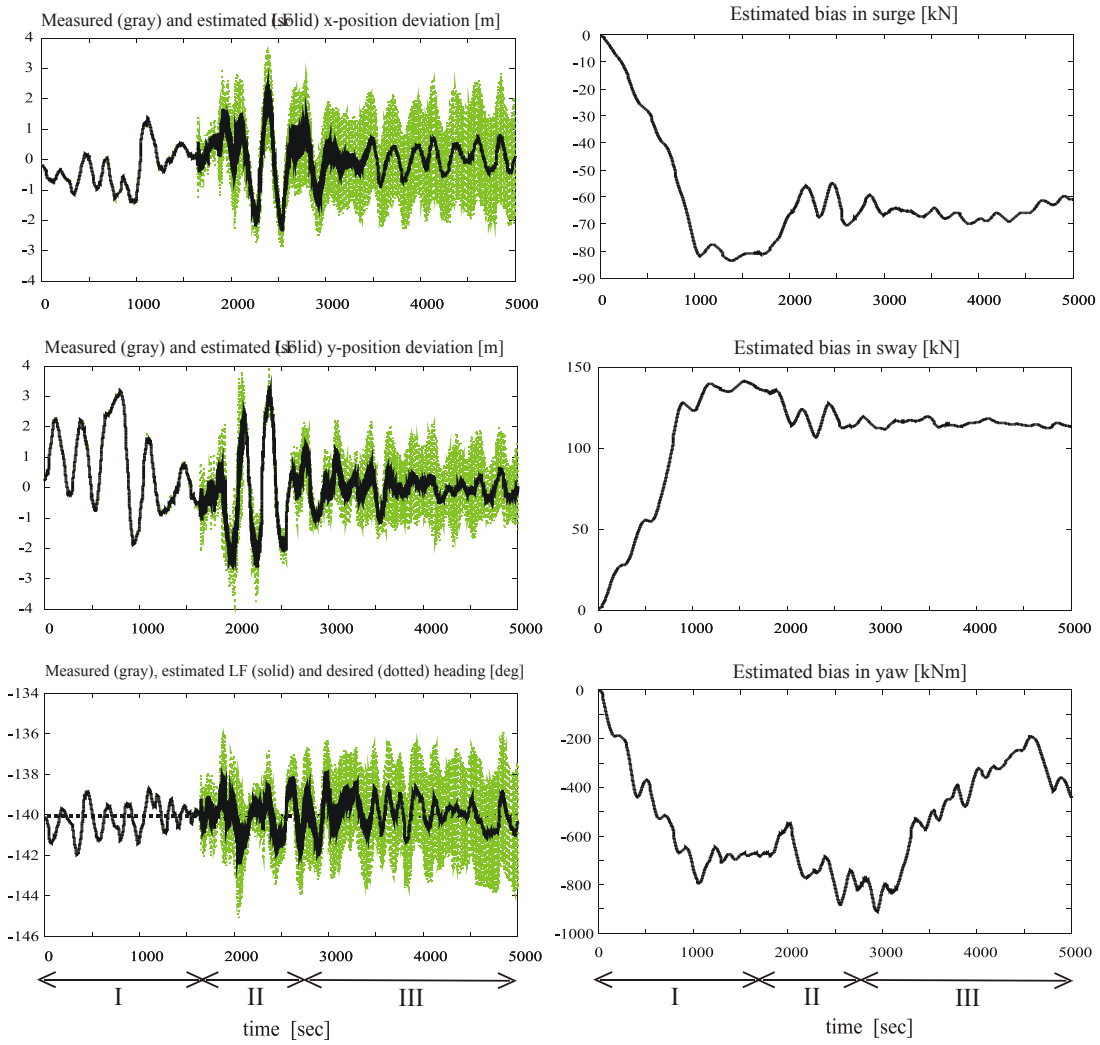

Figure 7.10: Left column: Measured position and heading (gray) together with corresponding LF estimates (solid). Right column: Estimated bias in surge, sway and yaw.

process them.

In the new control strategy for small-waterplane-area marine constructions the conventional 3 DOF multivariable controller in surge, sway and yaw will be extended to account for couplings to roll and pitch. In order to derive the new controller it is appropriate to define the model

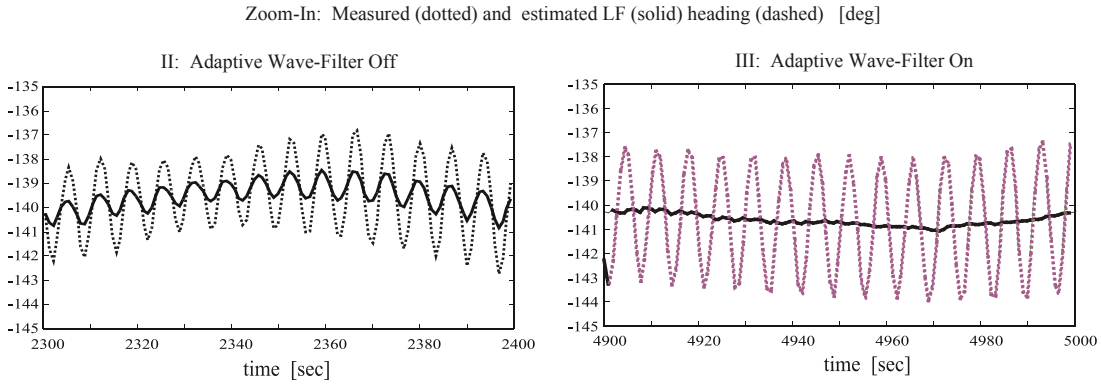

Figure 7.11: Zoom-in of measured and estimated LF heading. Left: Observer without adaptive wave-filtering. Right: Observer with adaptive wave-filtering.

reduction matrices

$$\mathbf{H}_{5\times 6} = \begin{bmatrix} 1 & 0 & 0 & 0 & 0 & 0 \\ 0 & 1 & 0 & 0 & 0 & 0 \\ 0 & 0 & 0 & 1 & 0 & 0 \\ 0 & 0 & 0 & 0 & 1 & 0 \\ 0 & 0 & 0 & 0 & 0 & 1 \end{bmatrix},$$

$$\mathbf{H}_{5\times 3} = \begin{bmatrix} 1 & 0 & 0 \\ 0 & 1 & 0 \\ 0 & 0 & 0 \\ 0 & 0 & 0 \\ 0 & 0 & 1 \end{bmatrix}, \tag{7.61}$$

$$\mathbf{H}_{3\times 6} = \begin{bmatrix} 1 & 0 & 0 & 0 & 0 & 0 \\ 0 & 1 & 0 & 0 & 0 & 0 \\ 0 & 0 & 0 & 0 & 0 & 1 \end{bmatrix},$$

$$\mathbf{H}_{3\times 3} = \mathbf{I}_{3\times 3}, \ \mathbf{H}_{6\times 6} = \mathbf{I}_{6\times 6}.$$

Hence, the $i \times i$ dimensional mass, damping and restoring matrices can be written in reduced order form according to

$$\begin{aligned} \mathbf{M}_i &= \mathbf{H}_{i\times 6}\mathbf{M}\mathbf{H}_{i\times 6}^T, \\ \mathbf{D}_i &= \mathbf{H}_{i\times 6}(\mathbf{D}_L + \mathbf{D}_m)\mathbf{H}_{i\times 6}^T, \\ \mathbf{G}_i &= \mathbf{H}_{i\times 6}(\mathbf{G}_B + \mathbf{G}_m)\mathbf{H}_{i\times 6}^T, \end{aligned} \tag{7.62}$$

where $i = 3$ describes the conventional horizontal model matrices in surge, sway and yaw, and $i = 5$ will represent the 5 DOF model of surge, sway, roll, pitch and yaw. $\mathbf{D}_L$, $\mathbf{D}_m$, $\mathbf{G}_B$ and $\mathbf{G}_m$ are as specified in Section 6.4. In reference parallel frame the linearized control plant model can be written

$$\mathbf{M}_i\dot{\boldsymbol{\nu}}_i + \mathbf{D}_i\boldsymbol{\nu}_i + \mathbf{G}_i\boldsymbol{\eta}_i = \boldsymbol{\tau}_{ic} + \mathbf{w}_i, \tag{7.63}$$

The corresponding linear LF state-space model can be formulated as

$$\begin{aligned} \dot{\mathbf{x}}_i &= \mathbf{A}_i\mathbf{x}_i + \mathbf{B}_i\boldsymbol{\tau}_{ic} + \mathbf{E}_i\mathbf{w}_i \\ \mathbf{y}_i &= \mathbf{C}_i\mathbf{x}_i + \mathbf{v}_i. \end{aligned} \tag{7.64}$$

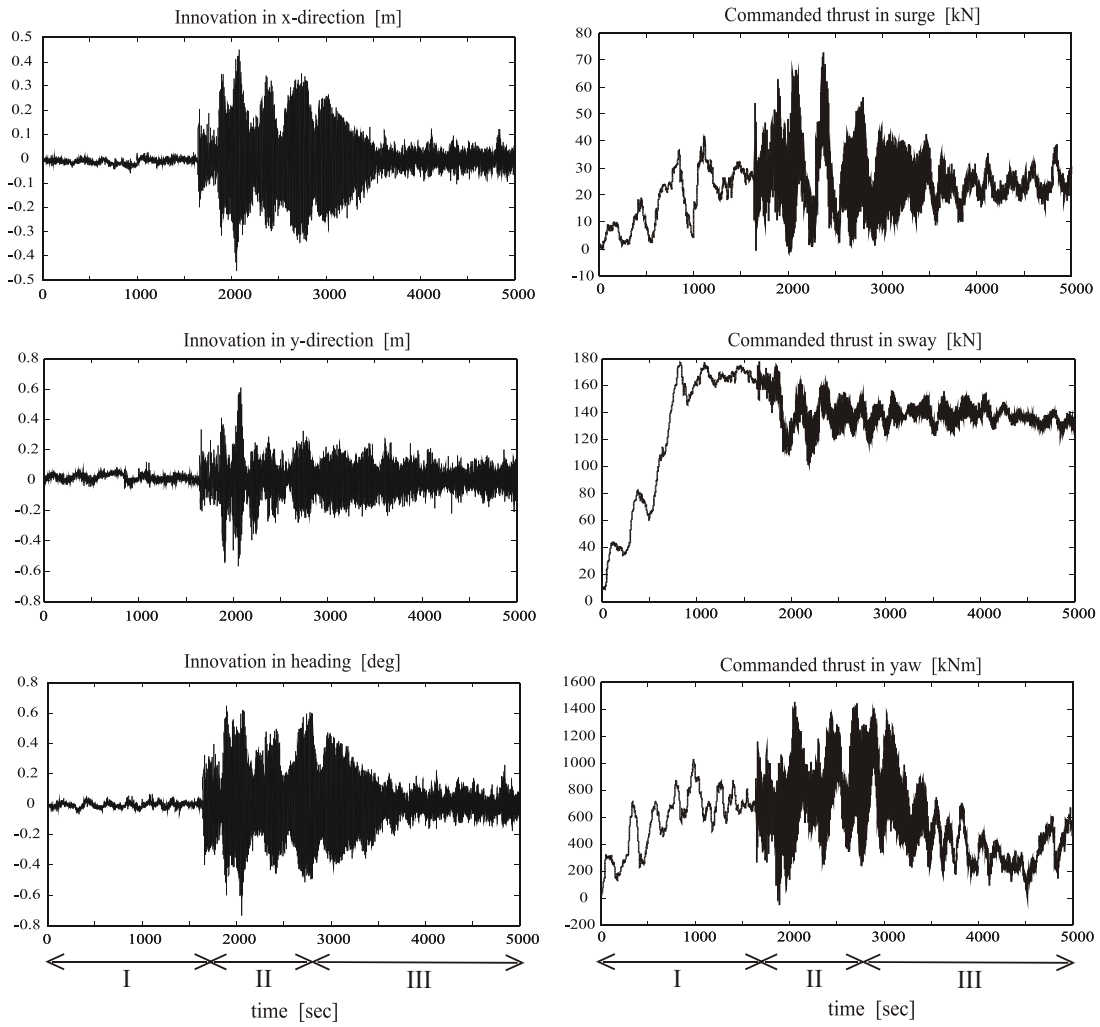

Figure 7.12: Left column: Innovation in position and heading. Right column: Commanded thrust in surge, sway and yaw.

For $i = 3$ and $i = 5$ the state-space vectors become

$$\mathbf{x}_3 = [u, v, r, x, y, \psi]^T, \tag{7.65}$$

$$\mathbf{x}_5 = [u, v, q, p, r, x, y, \phi, \theta, \psi]^T. \tag{7.66}$$

$\tau_{ic} \in \mathbb{R}^3$ is the commanded control vector. $\mathbf{w}_i$, $\mathbf{y}_i$, $\mathbf{v}_i \in \mathbb{R}^{\mathrm{i}}$ are the disturbance, measurement and noise vectors respectively. The system matrix $\mathbf{A}_i \in \mathbb{R}^{2\mathrm{i}\times 2\mathrm{i}}$ is then written

$$\mathbf{A}_i = \begin{bmatrix} -\mathbf{M}_i^{-1}\mathbf{D}_i & -\mathbf{M}_i^{-1}\mathbf{G}_i \\ \mathbf{I}_{i\times i} & \mathbf{0}_{i\times i} \end{bmatrix}, \tag{7.67}$$

where $\mathbf{I}_{i\times i} \in \mathbb{R}^{\mathrm{i}\times\mathrm{i}}$ is the identity matrix and $\mathbf{0}_{i\times i} \in \mathbb{R}^{\mathrm{i}\times\mathrm{i}}$ is the zero matrix. The control input matrix $\mathbf{B}_i \in \mathbb{R}^{2\mathrm{i}\times 3}$ is defined to be

$$\mathbf{B}_i = \begin{bmatrix} \mathbf{M}_i^{-1}\mathbf{H}_{i\times 3} \\ \mathbf{0}_{i\times i}\mathbf{H}_{i\times 3} \end{bmatrix}. \tag{7.68}$$

The disturbance matrix $\mathbf{E}_i \in \mathbb{R}^{2\mathrm{i}\times\mathrm{i}}$ becomes

$$\mathbf{E}_i = \begin{bmatrix} \mathbf{M}_i^{-1} \\ \mathbf{0}_{i\times i} \end{bmatrix}. \tag{7.69}$$

In this text it is assumed that only the position and the orientation are measured. Converting the position and heading measurements to the reference-parallel frame, the LF measurement matrix $\mathbf{C}_i \in \mathbb{R}^{\mathrm{i}\times 2\mathrm{i}}$ becomes

$$\mathbf{C}_i = \begin{bmatrix} \mathbf{0}_{i\times i} & \mathbf{I}_{i\times i} \end{bmatrix}. \tag{7.70}$$

Linear wave-frequency model

In the controller design synthetic white-noise-driven processes consisting of uncoupled harmonic oscillators with damping will be used to model the WF motions. Applying model reduction as for the LF model, the synthetic WF model can be written in state-space form for $i = 3$ and $i = 5$ according to

$$\begin{aligned} \dot{\xi}_{iw} &= \mathbf{A}_{iw}\xi_{iw} + \mathbf{E}_{iw}\mathbf{w}_{iw}, \\ \eta_{iw} &= \mathbf{C}_{iw}\xi_{iw}. \end{aligned} \tag{7.71}$$

$\eta_{iw} \in \mathbb{R}^{\mathrm{i}}$ is the measurement vector of the wave-frequency motion, $\mathbf{w}_{iw} \in \mathbb{R}^i$ is a zero-mean Gaussian white noise vector, and $\xi_{iw} \in \mathbb{R}^{2i}$. The system matrix $\mathbf{A}_{iw} \in \mathbb{R}^{2\mathrm{i}\times 2\mathrm{i}}$, the disturbance matrix $\mathbf{E}_{iw} \in \mathbb{R}^{2\mathrm{i}\times\mathrm{i}}$ and the measurement matrix $\mathbf{C}_{iw} \in \mathbb{R}^{\mathrm{i}\times 2\mathrm{i}}$ are formulated as in Section 7.2.2.

7.3.2 Horizontal-plane Controller

The horizontal-plane positioning controller consists of feedback and feedforward controller terms, which may be linear or nonlinear. Usually, linear controllers have been used. However, extensive research in this field has contributed to the introduction of nonlinear control theory, see Strand (1999) and the references therein.

Linear horizontal-plane PD control law based on LQG synthesis

A conventional linear multivariable proportional and derivative (PD) type controller based on the horizontal-plane surge, sway and yaw DOF can be written

$$\tau_{\mathrm{pd}} = -\mathbf{G}\mathbf{e} = -\mathbf{G}_p\mathbf{e}_2 - \mathbf{G}_d\mathbf{e}_1, \tag{7.72}$$

where the the error vector is decomposed in the reference-parallel frame according to

$$\mathbf{e}_2 = \mathbf{R}^T(\psi_d)\left[\hat{\eta} - \eta_d\right]^T, \tag{7.73}$$

$$\mathbf{e}_1 = \dot{\mathbf{e}}_2 \tag{7.74}$$

with $\hat{\eta} = \left[\hat{x},\ \hat{y},\ \hat{\psi}\right]^T, \hat{\eta}_d = [x_d,\ y_d,\ \psi_d]^T$ and $\mathbf{G}_p, \mathbf{G}_d \in \mathbb{R}^{3\times 3}$ are the non-negative controller gain matrices found by appropriate control synthesis methods. If we only consider the proportional and derivative terms for the horizontal-plane modes of motion in the control objective for (7.64) and assume that the pair $(\mathbf{A}_3, \mathbf{B}_3)$ is reachable, we can formulate a linear quadratic performance index according to

$$J = E\left\{\lim_{T\to\infty}\frac{1}{T}\int_0^T \mathbf{e}^T\mathbf{Q}\mathbf{e} + \tau_{\mathrm{pd}}^T\mathbf{P}\tau_{\mathrm{pd}}dt\right\}, \tag{7.75}$$

where error vector $\mathbf{e} \in \mathbb{R}^6$ is defined as $\mathbf{e} = \left[\mathbf{e}_1^T, \mathbf{e}_2^T\right]^T$ and $\mathbf{Q}, \mathbf{P} \in \mathbb{R}^{3\times3}$.The following properties hold for the error weighting matrix $\mathbf{Q} = \mathbf{Q}^T \geq 0$ and the control weighting matrix $\mathbf{P} = \mathbf{P}^T > 0$. By minimizing the control index J, the Linear Quadratic Gaussian - LQG method returns the control gain matrix $\mathbf{G} \in \mathbb{R}^{3\times6}$. For LTI systems, stationary solutions of the Ricatti equation can be found. Hence, the Ricatti equation computations reduce to solving

$$\begin{aligned} \dot{\mathbf{R}} &= -\mathbf{A}_3\mathbf{R} - \mathbf{A}_3^T\mathbf{R} + \mathbf{R}\mathbf{B_3}\mathbf{P}^{-1}\mathbf{B}_3^T\mathbf{R} - \mathbf{Q}, && (7.76)\\ &\Downarrow \quad \dot{\mathbf{R}} \to \mathbf{0} \text{ and } \mathbf{R} \to \mathbf{R}_\infty && (7.77)\\ \mathbf{0} &= -\mathbf{A_3}\mathbf{R}_\infty - \mathbf{A}_3^T\mathbf{R}_\infty + \mathbf{R}_\infty\mathbf{B_3}\mathbf{P}^{-1}\mathbf{B}_3^T\mathbf{R}_\infty - \mathbf{Q}, && (7.78) \end{aligned}$$

where $\mathbf{R}_\infty$ is a 6×6 dimensional non-negative symmetric matrix. The stationary LQG gain matrix is then

$$\mathbf{G} = \mathbf{P}^{-1}\mathbf{B}_3^T\mathbf{R}_\infty = \left[\begin{array}{cc} \mathbf{G}_d & \mathbf{G}_p \end{array}\right]. \tag{7.79}$$

Remark 7.3 *We have here utilized the so-called* Separation theorem or the Certainty equivalence principle *(Section 4.3.2). expressing that control of a linear system is conducted with stochastic excitation and the measurement vector derived by the estimated state vector provided by an observer. Thus, the controller consists of two separate functions: state estimation and feedback control from the estimated state vector.*

Integral action

In order to meet the special command-following and disturbance-rejection performance specifications, it is necessary to append three free integrators to the control model. It is then desirable to define a property space $\mathbf{z}$ which expresses the variables to be controlled towards certain setpoints. The dimension of the property space is the same as the control vector space, that is $\tau_i \in \mathbb{R}^3$ implies that $\mathbf{z} \in \mathbb{R}^3$. The variables to be controlled to the setpoints are fewer than those constituting the full state space $\mathbf{e} \in \mathbb{R}^6$. The relation between these variables and the state space is given through the transformation

$$\mathbf{z} = \mathbf{g}(\mathbf{e}) = \mathbf{e}_2. \tag{7.80}$$

A multivariable PI algorithm is then achieved by means of an integral loop, controlling the property $\mathbf{z}$ in parallel with the proportional LQ control loop. Inspired by classical SISO PI controller tuning, one can specify the eigenvalues of the integral loop in a diagonal matrix $\mathbf{\Lambda}_G$. Since the integral loop will be slower than the proportional LQ loop, the following approximation for the integral loop can be found

$$\dot{\mathbf{z}} = \mathbf{G}_i\mathbf{G}_z\left(\mathbf{A}_3 - \mathbf{B}_3\mathbf{G}\right)^{-1}\mathbf{B}_3\mathbf{z} = \mathbf{\Lambda}_G\mathbf{z}, \tag{7.81}$$

where $\mathbf{G}_z \in \mathbb{R}^{3\times6}$ is a property matrix given by

$$\mathbf{G}_z = \frac{\partial\mathbf{g}(\mathbf{e})}{\partial\mathbf{e}} = \left[\mathbf{0}_{3\times3}, \mathbf{I}_{3\times3}\right]. \tag{7.82}$$

This leads to the integral loop-gain matrix

$$\mathbf{G}_i = \mathbf{\Lambda}_G\left(\mathbf{G}_z\left(\mathbf{A}_3 - \mathbf{B}_3\mathbf{G}\right)^{-1}\mathbf{B}_3\right)^{-1}, \tag{7.83}$$

where the matrix $\mathbf{G}_z \left(\mathbf{A}_3 - \mathbf{B}_3\mathbf{G}\right)^{-1}\mathbf{B}_3$ must be non-singular. Open integrators, as they appear both in the control loop and the estimator, should be equipped with anti-windup precautions in case their outputs reach amplitude restrictions such as saturation in the physical control devices. The resulting integral control law is written

$$\dot{\tau}_i = \mathbf{A}_{\mathrm{wi}}\tau_i + \mathbf{G}_i\mathbf{z}, \tag{7.84}$$

where $\mathbf{A}_{\mathrm{wi}} \in \mathbb{R}^{3\times3}$ is the anti-windup precaution matrix, and $-\mathbf{G}_i \in \mathbb{R}^{3\times3}$ is the non-negative integrator gain matrix. Integrator anti-windup should be implemented in order to avoid that the integrator integrates up beyond the saturation limits of the actuators. A simple method to avoid this is to stop integrating when the integral term tends to a given percentage of the actuator saturation limit. More sophisticated algorithms are found in e.g. Åstrøm and Wittenmark (1997).

Wind feedforward control action

Wind loads have an important impact on the vessel's response. Especially for semisubmersibles the wind loads are dominating. In order to obtain fast disturbance rejection with respect to varying wind loads, it is desirable to introduce a wind feedforward controller. The wind forces and moment in surge, sway and yaw may be estimated by a Kalman filter and a Luenberger observer, where the wind velocity and wind direction are measured. The estimates are multiplied by a feedforward gain matrix. The wind feedforward control law is taken to be

$$\tau_{\mathrm{w}} = -\mathbf{G}_w\hat{\tau}_{\mathrm{wind}}, \tag{7.85}$$

where $\hat{\tau}_{\mathrm{wind}} \in \mathbb{R}^3$ is the vector of estimated wind forces and moment in surge, sway and yaw respectively. It is assumed that the coupling in wind loads is covered by the wind coefficients, so that the gain matrix $\mathbf{G}_w \in \mathbb{R}^{3\times3}$ is a non-negative diagonal matrix.

Model reference feedforward control action

In order to improve the performance of the controller during tracking operations a feedforward control action based on input from the reference model is included. The feedforward control action is written

$$\tau_{\mathrm{t}} = \mathbf{M}_3\mathbf{a}_d + \mathbf{D}_3\mathbf{v}_d + \mathbf{d}_3(\mathbf{v}_d) + \mathbf{C}(\mathbf{v}_d)\mathbf{v}_d, \tag{7.86}$$

where $\mathbf{a}_d$ and $\mathbf{v}_d \in \mathbb{R}^3$ are the desired generalized reference acceleration and velocity vectors respectively computed by appropriate reference models.

Reference model

For DP operations close to other offshore structures or ships, it is crucial to be capable to perform controlled movements and rotations of the vessel. The automatic guidance function which takes the vessel from the prevailing setpoint coordinates to the new setpoint is defined as the "marked position", and can be specified either in the reference-parallel frame or in the Earth-fixed frame. The movement and rotation can be done for each degree of freedom (DOF) separately, or as a fully 3 DOF coupled motion. In order to provide high-performance DP operations with bumbles transfer between station-keeping and marked position operations, a reference model must be introduced for the calculation of feasible trajectories of the desired vessel motion for each degree

of freedom. Experience achieved from full-scale experiments has demonstrated that the following reference model in the Earth-fixed frame is appropriate

$$\mathbf{a}_d^e + \mathbf{\Omega}\mathbf{v}_d^e + \mathbf{\Gamma}\mathbf{x}_d^e = \mathbf{\Gamma}\mathbf{x}_{ref}. \tag{7.87}$$

$$\dot{\mathbf{x}}_{ref} = -\mathbf{A}_f\mathbf{x}_{ref} + \mathbf{A}_f\eta_r. \tag{7.88}$$

where $\mathbf{a}_d^e, \mathbf{v}_d^e$ and $\mathbf{x}_d^e \in \mathbb{R}^3$ define the desired vessel acceleration, velocity and position trajectories in the Earth-fixed frame. The vector $\eta_r \in \mathbb{R}^3$ defines the new reference coordinates, either relative to the previous setpoint, or as global Earth-fixed coordinates. The vector $\mathbf{x}_{ref} \in \mathbb{R}^3$ defines the filtered reference coordinates. The design parameters in the reference model consist of a non-negative diagonal damping matrix $\mathbf{\Omega} \in \mathbb{R}^{3\times3}$ and a diagonal stiffness matrix $\mathbf{\Gamma} \in \mathbb{R}^{3\times3}$ written as

$$\mathbf{\Omega} = \quad diag\{2\zeta_i\omega_i\}, \quad i = 1\,,2\,,\,3 \tag{7.89}$$

$$\mathbf{\Gamma} = \quad diag\{\omega_i^2\}, \quad i = 1\,,2\,,\,3. \tag{7.90}$$

The first order diagonal and non-negative setpoint filter gain matrix $\mathbf{A}_f \in \mathbb{R}^3$ is written

$$\mathbf{A}_f = diag\{1/t_i\}, \quad i = 1\,,2\,,\,3. \tag{7.91}$$

The Earth-fixed desired vessel acceleration, velocity and position trajectories are transformed into a moving reference-parallel frame which follows the desired Earth-fixed position and heading trajectory. Hence,

$$\mathbf{a}_d = \mathbf{R}^T(\psi_d)\mathbf{a}_d^e, \tag{7.92}$$

$$\mathbf{v}_d = \mathbf{R}^T(\psi_d)\mathbf{v}_d^e, \tag{7.93}$$

$$\mathbf{x}_d = \mathbf{R}^T(\psi_d)\mathbf{x}_d^e. \tag{7.94}$$

The reference model may also run in station-keeping operations, but then with the desired velocity and acceleration equal to zero. This provides a smooth transfer between the operational modes.

Resulting control law

The resulting horizontal-plane station keeping control law, including both feedback and feedforward terms is written

$$\tau_{3c} = \tau_{\mathrm{w}} + \tau_{\mathrm{t}} + \tau_i + \tau_{\mathrm{pd}}, \tag{7.95}$$

where the different terms are defined below. A graphical illustration of the controller is shown in Figure 7.13.

7.3.3 Horizontal-plane Controller with Roll-Pitch Damping

The horizontal-plane positioning control law (7.95) can be extended to also include roll and pitch damping. This is motivated by the fact the hydrodynamic couplings the surge and sway feedback loops will be extended to incorporate feedback from the low frequency estimated pitch and roll angular velocities, denoted as $\hat{p}$ and $\hat{q}$ respectively.

Roll-pitch control law

By using a linear formulation the roll-pitch control law is formulated according to

$$\tau_{\text{rpd}} = -\mathbf{G}_{\text{rpd}} \begin{bmatrix} \hat{p} \\ \hat{q} \end{bmatrix}, \tag{7.96}$$

where the roll-pitch controller gain matrix $\mathbf{G}_{\text{rpd}} \in \mathbb{R}^{3\times 2}$ is defined as

$$\mathbf{G}_{\text{rpd}} = \begin{bmatrix} 0 & g_{xq} \\ g_{yp} & 0 \\ g_{\psi p} & 0 \end{bmatrix}, \tag{7.97}$$

and g_{xq}, g_{yp} and $g_{\psi p}$ are the corresponding non-negative roll-pitch controller gains.

Resulting control law

The resulting positioning control law including roll-pitch damping becomes

$$\tau_{5c} = \tau_{3c} + \tau_{\text{rpd}}. \tag{7.98}$$

7.3.4 Controller Analysis

The effect of the roll-pitch damping controller can be shown by analyzing the impact of the extended control law given by (7.98) on the linearized model given in (7.64). The coupled linearized low-frequency surge-pitch and sway-roll-yaw models will be considered. In the analysis it is assumed that the wind feedforward controller and the integral control action will compensate for the wind load, the current load and the mean second-order wave drift loads. Hence, the linearized coupled surge-pitch model can be written

$$m_{11}\dot{u} + m_{15}\dot{q} + d_{11}u + d_{15}q + g_{11}x = \tau_{5\text{surge}}, \tag{7.99}$$

$$m_{51}\dot{u} + m_{55}\dot{q} + d_{51}u + d_{55}q + g_{55}\theta = 0, \tag{7.100}$$

where subscript ij reflects the element of the matrices (7.62) for the case $i = 6$, that is all six DOFs are included. By inserting (7.99) in (7.100), the pitch dynamics can be reformulated to

$$(m_{55} - \frac{m_{51}m_{15}}{m_{11}})\dot{q} + (d_{55} - \frac{m_{51}d_{15}}{m_{11}})q + g_{55}\theta + (d_{51} - \frac{m_{51}d_{11}}{m_{11}})u - \frac{m_{51}g_{11}}{m_{11}}x = -\frac{m_{51}}{m_{11}}\tau_{5\text{surge}}. \tag{7.101}$$

The pure surge part of the multivariable control law in (7.98), assuming only PD and the roll-pitch control actions is written as

$$\tau_{5\text{surge}} = -g_x x - g_u u + \frac{m_{11}}{m_{51}} g_{xq} q, \tag{7.102}$$

where g_x, $g_u \geq 0$ are the PD controller gains. Substituting (7.102) in (7.101) gives the following closed-loop pitch dynamics

$$\begin{aligned} &(m_{55} - \tfrac{m_{51}m_{15}}{m_{11}})\dot{q} + (d_{55} - \tfrac{m_{51}d_{15}}{m_{11}} + g_{xq})q + g_{55}\theta + \\ &(d_{51} - \tfrac{m_{51}d_{11}}{m_{11}} - g_u\tfrac{m_{51}}{m_{11}})u - (g_{11} + g_x)\tfrac{m_{51}}{m_{11}}x = 0. \end{aligned} \tag{7.103}$$

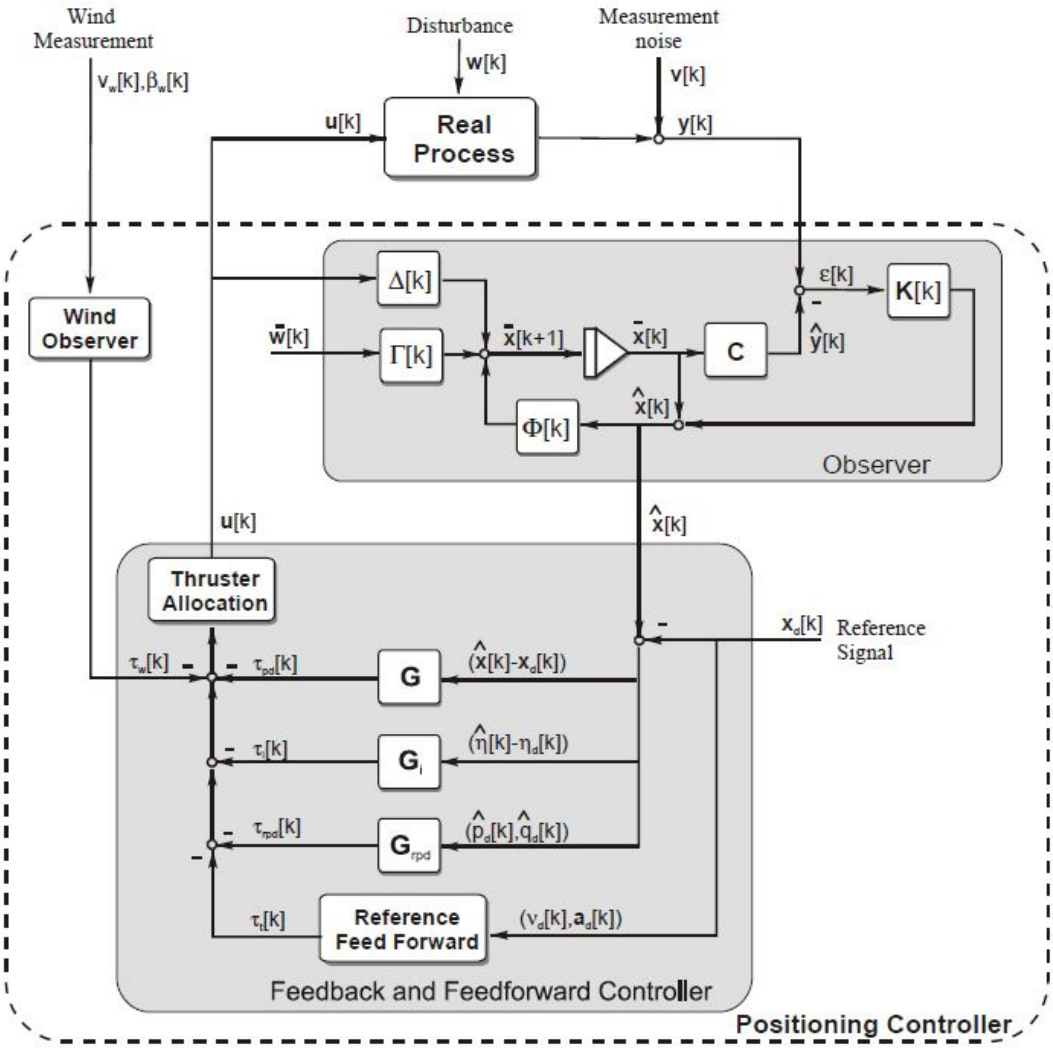

Figure 7.13: Illustration of the DP controller.

Assume that the horizontal-plane controller will force the surge velocity u and position deviation x to zero. Hence, the closed-loop pitch dynamics in (7.103) can be simplified to

$$(m_{55} - \frac{m_{51}m_{15}}{m_{11}})\dot{q} + (d_{55} - \frac{m_{51}d_{15}}{m_{11}} + g_{xq})q + g_{55}\theta = 0. \tag{7.104}$$

(7.104) can be recognized as a second-order mass-damper-spring system, where it is clearly shown that the effect of the new control law increases the damping in pitch.

A similar formulation can be found for the coupled sway-roll-yaw model. The coupled equations of motion in sway, roll and yaw are

$$m_{22}\dot{v} + m_{24}\dot{p} + m_{26}\dot{r} + d_{22}v + d_{24}p + d_{26}r + g_{22}y = \tau_{5\text{sway}}, \tag{7.105}$$
$$m_{42}\dot{v} + m_{44}\dot{p} + m_{46}\dot{r} + d_{42}v + d_{44}p + d_{46}r + g_{44}\phi = 0, \tag{7.106}$$
$$m_{62}\dot{v} + m_{64}\dot{p} + m_{66}\dot{r} + d_{62}v + d_{64}p + d_{66}r + g_{66}\psi = \tau_{5\text{yaw}}, \tag{7.107}$$

where τ^5_{sway} and τ^5_{yaw} are the control actions in sway and yaw, respectively. Thus, by including feedback from angular roll velocity in the sway and yaw control laws

$$\tau_{5\text{sway}} = -g_y y - g_{y\psi}\psi - g_v v - g_{vr} r - \frac{g_{yp}}{b_y} p, \tag{7.108}$$

$$\tau_{5\text{yaw}} = -g_{\psi y} y - g_{\psi}\psi - g_{rv} v - g_r r - \frac{g_{\psi p}}{b_{\psi}} p, \tag{7.109}$$

a similar damping effect as in the pitch case can be obtained. Here, g_y, g_ψ, g_v, $g_r \geq 0$ are the diagonal gains of the PD part of the control law. Moreover, $g_{y\psi}$, $g_{\psi y}$, g_{vr} and g_{rv} are the off-diagonal controller gains with appropriate signs reflecting the hydrodynamic coupling between sway and yaw. As for surge, assume that the sway and yaw velocities, v and r, position and angle, y and ψ are forced to zero by the horizontal-plane controller. Thus, the closed-loop roll dynamics becomes

$$m_p \dot{p} + (d_p + g_{yp} + g_{\psi p})\, p + g_{44}\phi = 0, \tag{7.110}$$

where

$$m_p = m_{44} - \frac{m_{42}m_{24}}{m_{22}} + \frac{m_{46} - \frac{m_{42}m_{26}}{m_{22}}}{1 - \frac{m_{62}}{m_{66}}\frac{m_{26}}{m_{22}}} \left(\frac{m_{62}}{m_{66}}\frac{m_{24}}{m_{22}} - \frac{m_{64}}{m_{66}} \right), \tag{7.111}$$

$$d_p = d_{44} - \frac{m_{42}d_{24}}{m_{22}} + \frac{m_{46} - \frac{m_{42}m_{26}}{m_{22}}}{1 - \frac{m_{62}}{m_{66}}\frac{m_{26}}{m_{22}}} \left(\frac{m_{62}}{m_{66}}\frac{d_{24}}{m_{22}} - \frac{d_{64}}{m_{66}} \right), \tag{7.112}$$

$$b_y = \frac{m_{42}}{m_{22}} + \frac{m_{62}}{m_{22}m_{66}} \frac{\frac{m_{42}m_{26}}{m_{22}} - m_{46}}{(1 - \frac{m_{62}}{m_{66}}\frac{m_{26}}{m_{22}})}\ , \tag{7.113}$$

$$b_\psi = \frac{1}{m_{66}} \frac{m_{46} - \frac{m_{42}m_{26}}{m_{22}}}{(1 - \frac{m_{62}}{m_{66}}\frac{m_{26}}{m_{22}})}\ . \tag{7.114}$$

It is clearly shown here how the damping is increased in roll by applying the extended control law.

7.3.5 Thrust Allocation

Optimal thrust allocation

The relation between the control vector $\tau_c \in \mathbb{R}^3$ and the produced thrust from the r thrusters $\mathbf{T}_d \in \mathbb{R}^{\text{r}}$ is defined by

$$\tau_c = \mathbf{T}_{3\times r}(\alpha)\mathbf{T}_d, \tag{7.115}$$

where $\mathbf{T}_{3\times r}(\alpha) \in \mathbb{R}^{3\times \text{r}}$ is the thrust configuration matrix, and $\alpha \in \mathbb{R}^{\text{r}}$ is the thruster orientation vector. Let $\mathbf{T}_d = \mathbf{K}\mathbf{u}_d$, where $\mathbf{K} \in \mathbb{R}^{\text{r}\times\text{r}}$ is the diagonal matrix of thrust force coefficients written $\mathbf{K} = diag\{k_i\}$. $\mathbf{u}_d \in \mathbb{R}^{\text{r}}$ is the control vector of either pitch-controlled, revolution-controlled or torque- and power-controlled propeller inputs as treated in Chapter 8. The thrust provided by the thruster unit i, disregarding the thrust losses, is calculated to be

$$T_{di} = k_i u_{di}. \tag{7.116}$$

For a fixed mounted propeller or thruster the corresponding orientation angle is set to a fixed value reflecting the actual orientation of the device itself. In case of an azimuthing thruster,

α_i is an additional control input to be determined by the thrust allocation algorithm. The commanded control action provided by the thrusters becomes

$$\mathbf{u}_d = \mathbf{K}^{-1}\mathbf{T}^{+}_{3\times r}(\alpha)\tau_c, \tag{7.117}$$

where $\mathbf{T}^{+}_{3\times r}(\alpha) \in \mathbb{R}^{\mathrm{r}\times 3}$ is the pseudo-inverse thrust configuration matrix.

Geometrical thrust induction

The effect of the commanded thruster action provided by the thrusters in (7.117) on the six degrees-of-freedom vessel model (6.67) defined in the mathematical modeling Section 6.4 can be calculated to be

$$\tau_{\mathrm{thr}} = \mathbf{T}_{6\times r}(\alpha)\mathbf{K}\mathbf{u}_d, \tag{7.118}$$

where $\tau_{\mathrm{thr}} \in \mathbb{R}^6$ is the corresponding actual control vector acting the vessel as shown in Section 6.4, and $\mathbf{T}_{6\times r}(\alpha) \in \mathbb{R}^{6\times \mathrm{r}}$ is the thrust configuration matrix accounting for the six DOF contribution of the produced thruster actions. The reader should notice that (7.118) will introduce roll and pitch moments, that may be important to consider for rigs as they may introduce unintentional roll and pitch motions.

Example 7.1 *Consider the thrust configuration as shown in Figure 7.14. The ship is in the bow equipped with one azimuthing thruster and one tunnel thruster located the distance l_{ba} and l_{bt} from the origin, respectively. One tunnel thruster is located stern the distance l_{st} from the origin. Finally, two podded units are located stern at the longitudinal distance l_p and transverse distance b_s and b_p from the origin, respectively. The thrusters are numbered according to: 1. Bow azimuthing thruster, 2. Bow tunnel thruster, 3. Stern tunnel thruster, 4. Starboard pod, and 5. Port pod. The thrust configuration matrix becomes accordingly*

$$T_{3\times 5} = \begin{bmatrix} \cos\alpha_1 & 0 & 0 & \cos\alpha_4 & \cos\alpha_5 \\ \sin\alpha_1 & 1 & 1 & \sin\alpha_4 & \sin\alpha_5 \\ l_{ba}\sin\alpha_1 & l_{bt} & -l_{st} & -l_p\sin\alpha_4 - b_s\cos\alpha_4 & l_p\sin\alpha_5 - b_s\cos\alpha_5 \end{bmatrix},$$

where the azimuthing angle α_i is defined such that $\alpha_i = 0^o$ gives maximum positive surge thrust and $\alpha_i = 90^o$ gives maximum positive sway thrust.

7.3.6 Case Study

A simulation study of a dynamically positioned semi-submersible is carried out to demonstrate the effect of the thruster induced roll and pitch motions. The performance of the new control strategy, denoted as τ_{5c}, and the conventional horizontal control law, denoted as τ_{3c}, is compared. A semi-submersible, see Figure 7.15, equipped with 4 azimuthing thrusters, each able to produce a force of 1000 kN located at the four corners at the two pontoons, is used in the simulations. The operational draft is equal to 24 m, vessel mass at operational draft is 45000 $tons$, the length is 110 m, and the breadth is 75 m. Radius of gyration in roll is 30 m, in pitch equal to 33 m and in yaw 38 m. The undamped resonance periods in roll and pitch are found to be 55 s and 60 s, respectively.

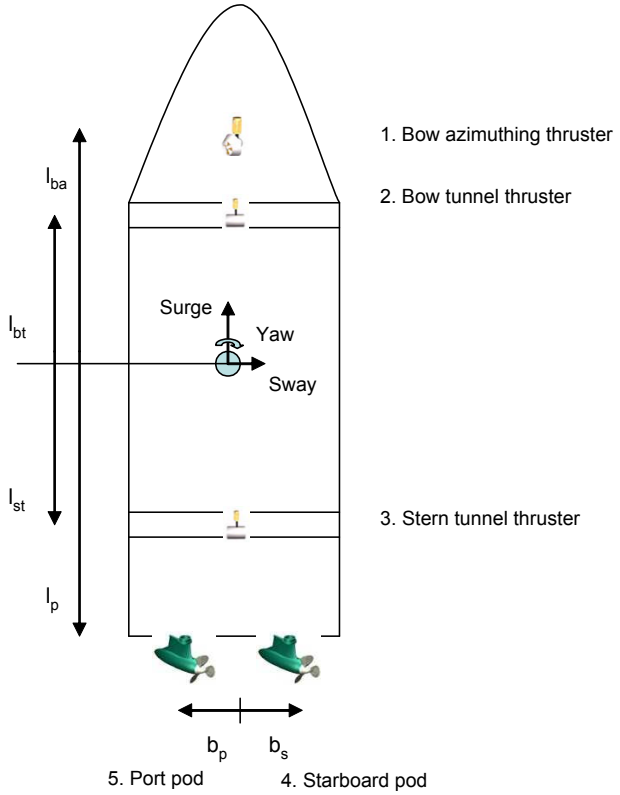

Figure 7.14: Example of a thruster configuration.

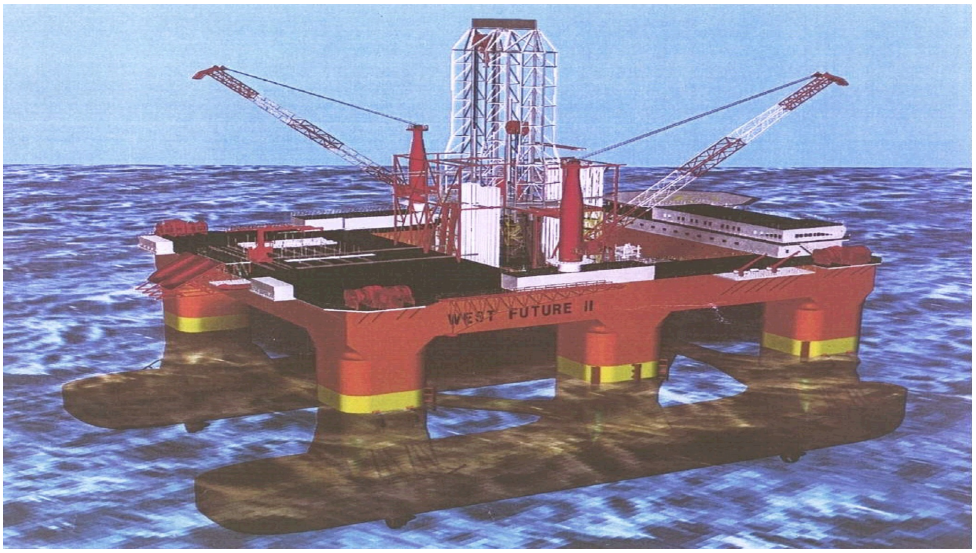

Figure 7.15: Semi-submersible.

Frequency domain analysis

The linearized system given in (7.64) is analyzed in the frequency domain. The transfer functions of the coupled surge-pitch model subjected to disturbances are shown for the open-loop system,

closed loop system with the conventional horizontal-plane (3 DOF) controller and the new extended roll-pitch (5 DOF) controller. In Figure 7.16 it can be seen that a significant notch-effect is achieved about the pitch resonance frequency with the new control law. Figures 7.17 and 7.18 show how the damping in pitch is amplified about the resonance frequency applying the new control law. Similar progress for the coupled sway-roll-yaw model can also be shown.

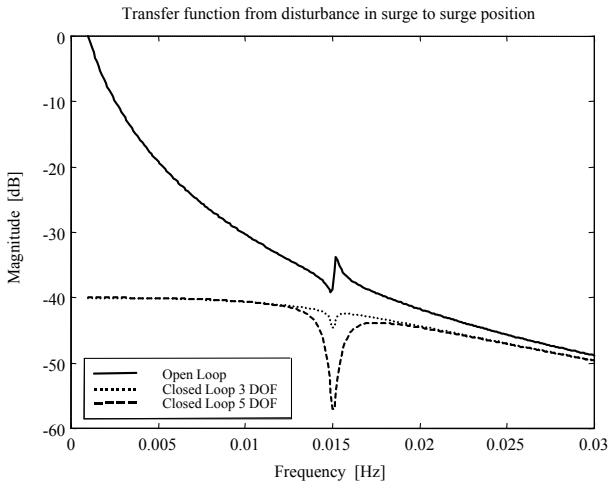

Figure 7.16: Normalized transfer function from disturbance in surge to surge position for the open-loop system (solid), applying conventional controller τ_{3c} (dotted) and new controller τ_{5c} (dashed).

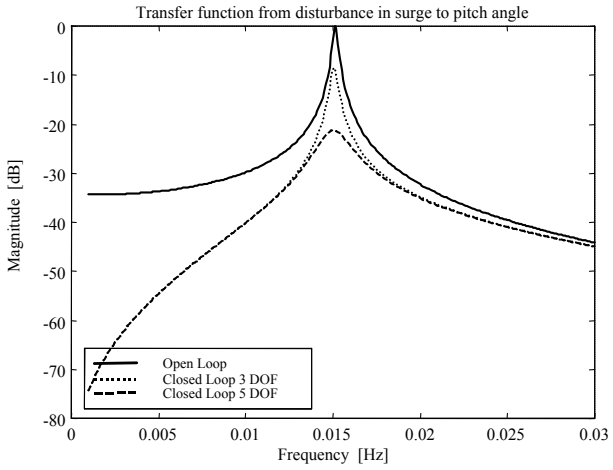

Figure 7.17: Normalized transfer function from disturbance in surge to pitch angle for the open-loop system (solid), applying conventional controller τ_{3c} (dotted) and new controller τ_{5c} (dashed).

Time domain numerical simulations

The time domain numerical simulations are performed with a significant wave height of $6\,m$, wave peak period $10\,s$, current velocity $0.5\,m/s$ and wind velocity $10\,m/s$. The Earth-fixed directions

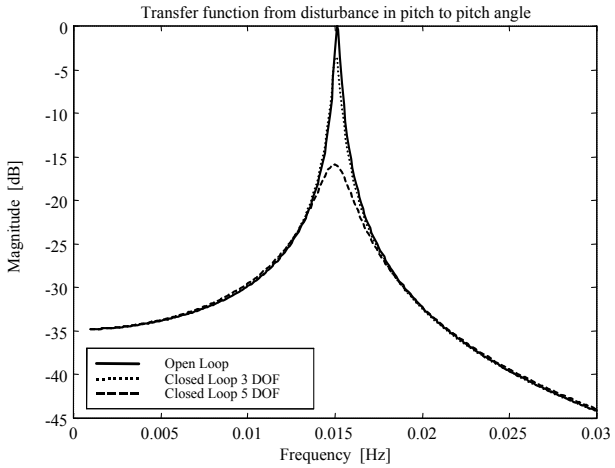

Figure 7.18: Normalized transfer function from disturbance in pitch to pitch angle for the open-loop system (solid), applying conventional controller τ_{3c} (dotted) and new controller τ_{5c} (dashed).

of waves, wind and current are colinear and equal to 225° in this simulation. The induced thrust components in roll and pitch are clearly shown in Figures 7.21 and 7.22. Accordingly, it is the important to control these components by the roll-pitch control law to ensure a safe and optimal operation.

By applying the proposed new control strategy the roll and pitch amplitudes are significantly reduced as shown in the time series of Figures 7.19 and 7.20. It is also evident that the new controller does not reduce the horizontal positioning accuracy (Figures 7.19 and 7.20).

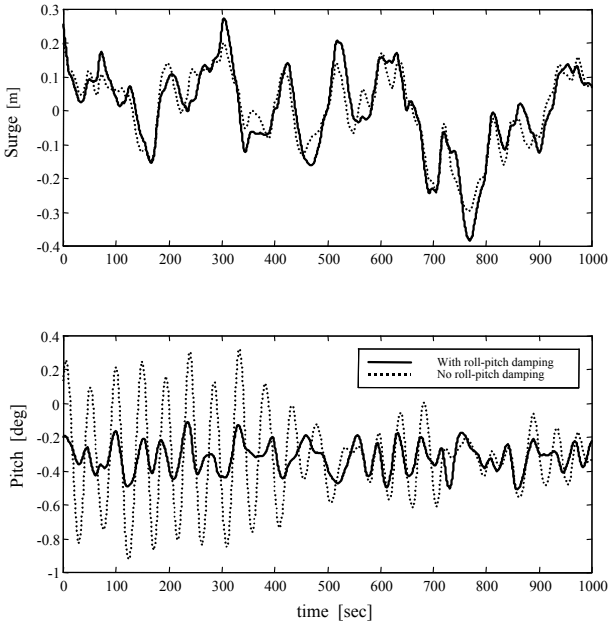

Figure 7.19: Surge position and pitch angle applying conventional controller τ_{3c} (dotted) and new controller τ_{5c} (solid).

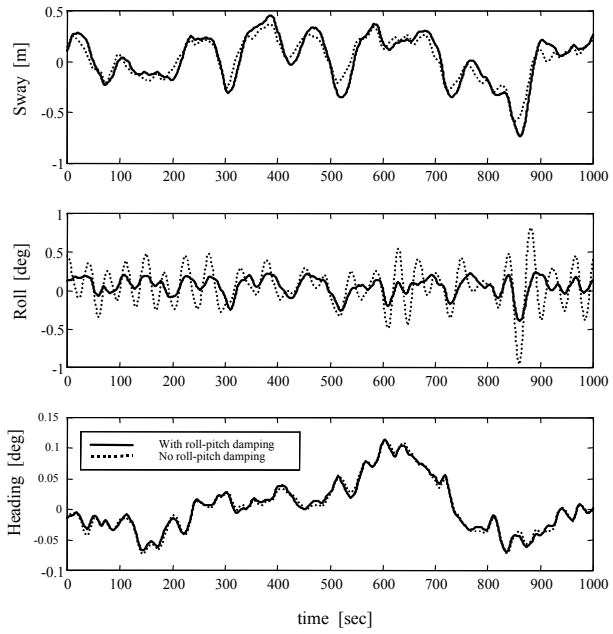

Figure 7.20: Sway position, roll and yaw angles applying conventional controller τ_{3c} (dotted) and new controller τ_{5c} (solid).

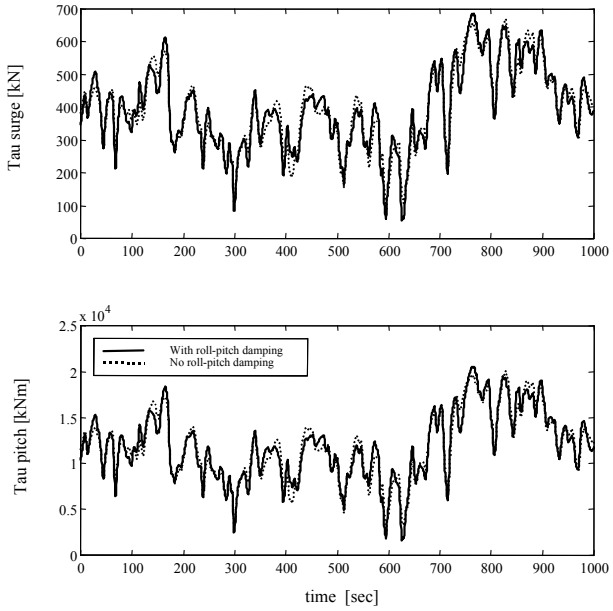

Figure 7.21: Produced thrust components in surge and pitch applying conventional controller τ_{3c} (dotted) and new controller τ_{5c} (solid).

The effect of the suppressed roll and pitch motions is, as expected, most effective about the resonance frequencies, as shown in the power spectra of Figure 7.23. The simulations further indicate that by maintaining the same level of positioning accuracy, the total energy consumption when applying the new controller will be lower than using the conventional design philosophy.

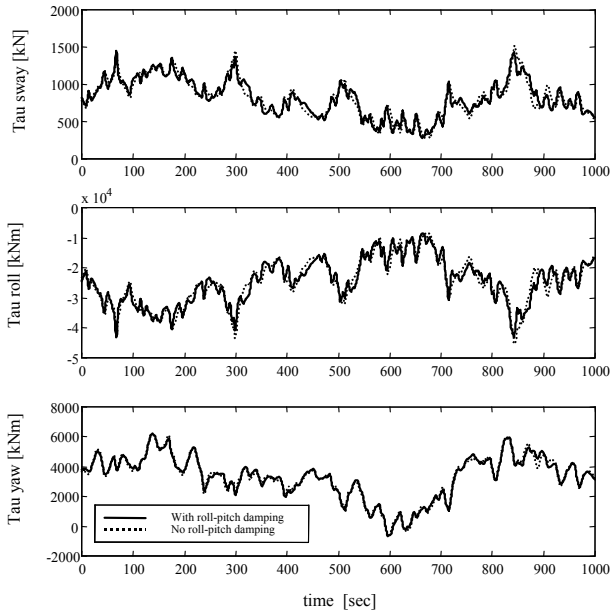

Figure 7.22: Produced thrust components in sway, roll and yaw applying conventional controller τ_{3c} (dotted) and new controller τ_{5c} (solid).

Oscillations in roll and pitch will, through the hydrodynamic coupling, induce motions in surge, sway and yaw, which have to be compensated for by the controller anyhow. In the roll-pitch control strategy these coupling effects are exploited in an optimal manner to damp the oscillations, and thereby also avoiding unintentional roll and pitch induced surge, sway and yaw motions.

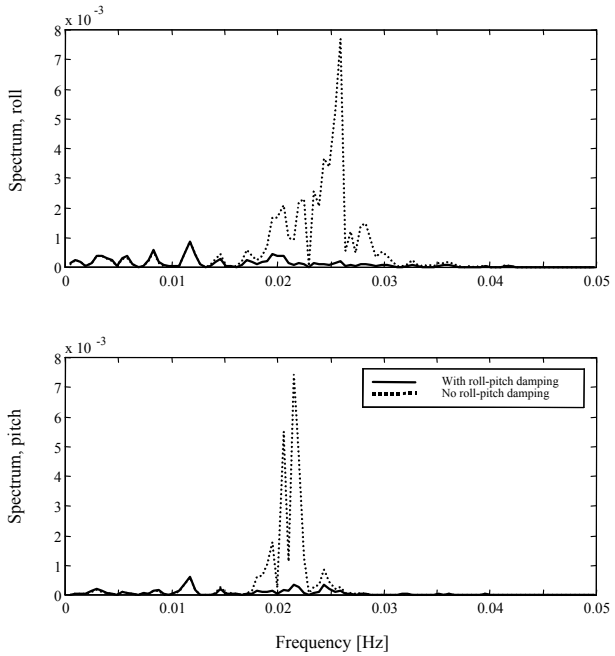

Figure 7.23: Power spectra of roll and pitch applying conventional controller τ_{3c} (dotted) and new controller τ_{5c} (solid).

Chapter 8

Propulsion Control

This chapter shows the importance on propulsion and thruster controls considering low-level control designs of the actuators ensuring that the high-level control demands are fulfilled according to the control objective.

Learning outcome of the chapter: The reader shall understand:

- The various types of propellers.
- The control objective for low-level control in order to fulfill high-level control commands.
- The propeller characteristics, propulsion efficiency and thrust losses.
- How to design low-level controllers based on propeller speed, torque and power.
- How to deal with extreme situations such as ventilation and how avoid it using ant-spin control.

8.1 Introduction

The motivation to develop improved methods for propulsion and local thruster control was initiated by former colleagues in ABB in the middle of 1990s. The idea was to better utilize the nice properties of electrical drives and motors to the benefit of improved control and power plant performance as well as reduced mechanical wear and tear of the propulsion components. The first initial publication on this topic was Sørensen et al. (1997). Later on this work has been addressed more extensively by several MSc theses and PhD scholarships at NTNU in joint cooperation with industry partners. In particular, thruster control in extreme conditions has been studied. Here, robust thruster control in extreme seas accounting for severe thrust losses due to *ventilation* and *in-and-out-of-water effects* is developed, and an *anti-spin thruster controller,* motivated by similar effects in wheel slip control on cars, is developed for thrusters on marine vessels.

Several sections of this chapter are based on research results containing both theoretical and experimental contributions published in papers by Smogeli and Ruth as a part of their PhD study. In particular, material from the following publications are used: Sørensen et al. (1997), Smogeli (2006), Smogeli and Sørensen (2009), Ruth (2008), Sørensen and Smogeli (2009).

Installed power capacity on marine vessels and offshore installations is normally limited. Besides there is an increased focus on environmental aspects motivating technical solutions that reduce the total energy consumption and emission of exhaust gases. The different subsystems/equipment installed on a vessel or offshore installation can be categorized into two parts, *producers* and *consumers* of energy. For dynamically positioned vessels the thruster system normally represents one of the main consumers of energy, and is regarded as a critical system with respect to safety. On the contrary, the dynamic positioning system is only an auxiliary system for the vessel to do a profitable operation of one kind or another, such as drilling, oil production, loading, and so on. Hence, the thruster usage should not cause a load shedding of those productive consumers, or in worst case cause a total power *black-out* because of unintended power consumption. The strong requirements to vessel performance, operational availability and overall safety have therefore resulted in increased focus on the total vessel concept and the interactions between the different equipment and systems installed. Flexibility in operation has enabled electrical power generation and distribution systems for propulsion, positioning, oil production, drilling, and loading, where all equipment and control systems are integrated into a common power plant network and automation network. In fully integrated systems, functional in addition to physical integration of power and automation systems combined with thorough marine process knowledge introduces new and far better opportunities to optimize the overall vessel mission objective at lower life cycle costs. In order to accomplish this it is essential to properly address the energy control of the consumers and producers of electrical power onboard the vessel. If the various consumers (thrusters, pumps, compressors etc.) of power act separately and uncoordinated from each other, the power generation system must be dimensioned and operated with larger safety margins to account for the corresponding larger mean power demands and unintentional power peaks.

This chapter will illustrate the importance of focusing on low level actuator control exemplified on thruster control in order to achieve a thorough successful control result, which does not have negative impact on the other systems on the ship.

8.2 Propellers and Thrusters

8.2.1 Shaft Propulsion

In a diesel-electric power and propulsion system, the shaft propellers are normally driven by variable-speed electric motors. The horizontal motors may be directly connected to the shaft, which results in a simple and mechanically robust solution, or via a gear coupling, which allows for increased rotational speed of the motor and results in a more compact unit.

Shaft propellers are used mainly in shuttle tankers and other vessels in which the propulsion power required is too high for conventional azimuth thrusters. By use of high-lift rudders, shaft propellers may also be used to provide a certain degree of transverse thrust.

8.2.2 Thrusters

Tunnel thrusters produce fixed-direction transverse thrust and are often used in vessels in which shaft propellers are amply dimensioned for the longitudinal thrust needed in DP operation. The motors are normally vertically mounted with an L-shaped gear or horizontally mounted with a Z-shaped gear where the geared transmission allows for higher rotational speed and smaller motor constructions.

Tunnel thrusters may be of the variable-speed fixed-pitch (FPP) type or equipped with constant-speed controllable-pitch propellers (CPP). The FPP solution has a simpler mechanical construction since the pitch transmission can be omitted. Furthermore, low-thrust losses will be reduced from levels typically 15% of rated power to essentially zero. This is the main reason for why FPP has become so popular for DP operated vessels. The FPP thruster must be driven by a variable-speed thruster drive.

Azimuth thrusters are rotatable devices for production of thrust in any direction. Although it is optimized for positive-thrust direction, it should have a certain degree of negative thrust capability as well, to maintain dynamic thrust capacity without performing continuous azimuth rotation. The electric motor is normally vertically mounted and drives an L-shaped gear transmission. With regard to azimuth thrusters, a variable-speed thruster motor drive and FPP simplify the underwater mechanical construction and reduce low-thrust losses significantly.

Conventional azimuth thrusters are used with power ratings up to $6 - 7MW$.

8.2.3 Podded Propulsion

In podded propulsion units (Figure 8.1), a variable-speed electric motor is located in a compact pod. The fixed-pitch propeller is mounted directly on the motor shaft. Since a mechanical gear is avoided, the transmission efficiency is higher than in an azimuth thruster. Like the conventional azimuth thruster, the podded propulsor is freely rotatable and may produce thrust in both forward and aft directions if the thrust bearings are designed for it. The electrical power is transferred to the motor via flexible cabling or slip rings for 360-degree operation. Since the propeller pitch is fixed and there is no gear transmission, the mechanical construction is simple and robust.

The pod can be designed for pushing or pulling operation. Especially the pulling type pod gives the propeller a near optimum and uniform wake field, which increases the hydrodynamic efficiency of the propeller and reduces the risk for cavitation, and hence give reduced noise and vibrations.

Podded propulsion units have been in operation for more than eight years in cruise vessels, ice breakers, service vessels and tankers. Recent new-built semi-submersible drilling units are now also utilizing podded propulsion as station keeping/transit propulsion thrusters.

Podded propulsion units are today available in power ranges up to at least $25MW$. The larger units provide access into the pod for visual inspection.

8.2.4 Mechanical Pod

The conventional azimuth thruster is normally used for station keeping and maneuvering. In order to improve the hydrodynamics and steering capability that is required for propulsion, the shape of the thruster is adapted.

A mechanical pod is a mechanical drive designed for propulsion at higher ship velocities. It is powered from an in-board motor, and the mechanical power is transferred to the propeller with an L-shaped gear. The shape is optimized for low hydrodynamic resistance and high propulsion efficiency.

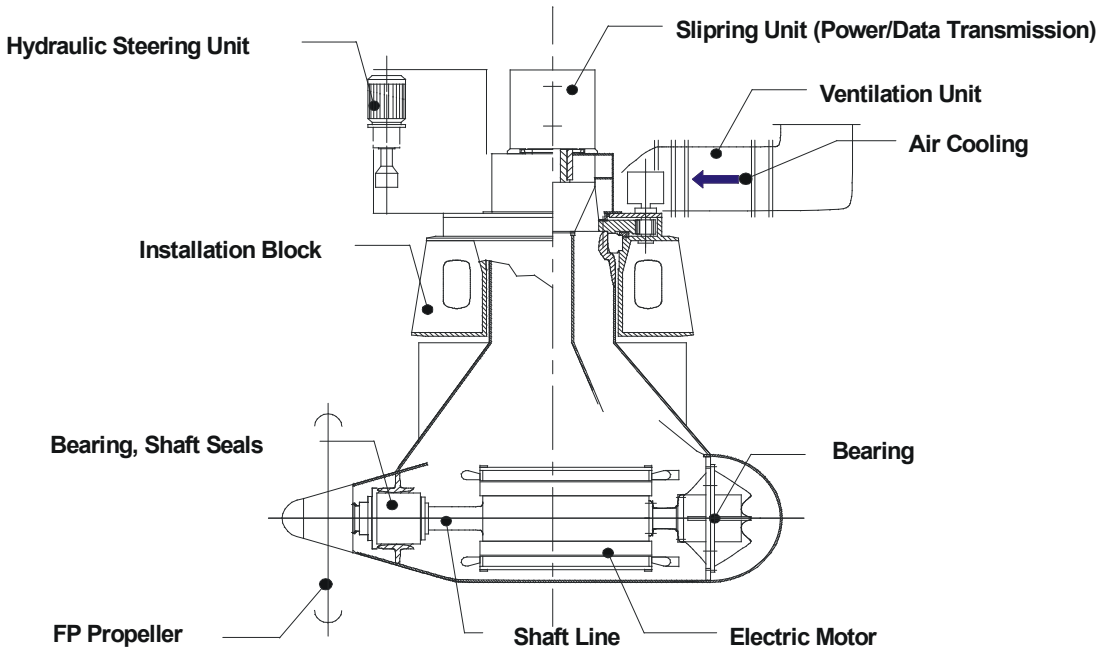

Figure 8.1: Podded propulsion.

8.2.5 Water Jets

Water jets are used mainly in high vessel speed operations. There has been presented concepts where the water jet is driven by electrical motors, but the number of applications are limited.

8.3 Control Problem Formulation

As seen in the previous sections the positioning systems include different control functions for automatic positioning and guidance. The high-level positioning controller produces a commanded thrust vector $\tau_c \in \mathbb{R}^3$ in surge, sway and yaw. The problem of finding the corresponding force and direction of the thrusters that meets the high-level thrust commands is called *thrust allocation*. By using the singular value decomposition and geometrical filtering techniques the optimal force and direction for each thrust device can be found avoiding singular thrust behavior with reduced wear and tear and energy consumption for any thrust configuration and type of thruster, see Sørdalen (1997).

The propeller and thruster devices can be controllable pitch propeller (CPP) with fixed speed, controllable speed with fixed pitch propeller (FPP), or controllable pitch and speed in combination. The propeller pitch is measured at a radius $0.7R$ of the propeller blade, and is defined as the travelled distance per revolution when advancing the propeller as a screw with screw angle equal to the blade angle at $0.7R$. The pitch ratio P/D is defined as the ratio of pitch at $0.7R$.D is the propeller diameter. Traditionally, the propeller pitch ratio or the shaft speed is used to indirectly control the propeller force towards the reference setpoint T_d specified by the thrust allocation. In the thrust devices, a local pitch or speed controller is present. A static mapping, see Figure 8.2, from the reference force to the actual control input (speed), n_{d},

which can be either pitch or propeller speed is used according to

$$n_{\mathrm{d}} = g(T_{\mathrm{d}}). \tag{8.1}$$

Since normally no sensors are available for measuring the actual force developed by the propeller, there is no guarantee for fulfilling the high-level thrust commands, and the mapping from commanded thruster force to actual propeller force can be viewed as an open-loop system. Thus, sophisticated control designs will be significantly degraded with respect to performance and stability margins if the high-level control inputs are not produced by the local controllers.

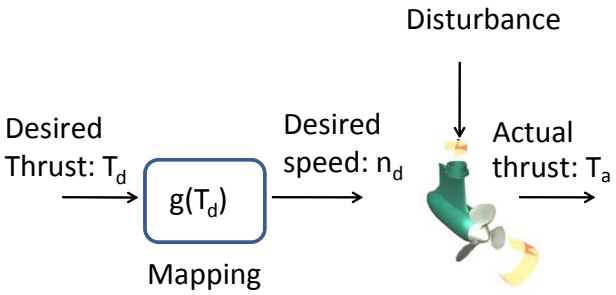

Figure 8.2: Relationship between commanded thruster force, T_{d}, and actual developed propeller force, T_a.

Conventionally, the resulting pitch or speed set-point signals are determined from stationary propeller force-to-speed/pitch relations based on information about thruster characteristics found from model tests and bollard pull tests provided by the thruster manufacturer. These relations may later be modified during sea trials. However, as shown later they are strongly influenced by the local water flow around the propeller blades, hull design, operational philosophy, vessel motion, waves and water current. Hence, the developed thrust T_a may differ substantially from the commanded thrust setpoint T_d. In conventional positioning systems, variations in these relations are not accounted for in the control system, resulting in reduced positioning performance with respect to accuracy and response time. In addition, the variations may lead to deterioration of performance and stability in the electrical power plant network due to unintentional power peaks or drops caused by load fluctuations on the propeller shafts, as shown in Figure 8.3. The unpredictable load variations force the operator to have more available power than necessary. This implies that the diesel generators will get more running hours at lower loads in average, which in terms gives more wear, tear and increased maintenance costs. This motivates finding improved methods for local thruster control.

In this section, the method of torque and power control is described using forces-to-torque/power mappings, Sørensen et al. (1997). Hence, the force-to-pitch/speed (*rpm*) mappings, see (8.1), are replaced by force-to-torque/power mappings. This approach will give more stable power loads, and the method is less sensitive to disturbances. *rpm* denotes *revolutions-per-minute*.

Modeling of propellers is complicated by the fact that it is impossible to develop a finite-dimensional plant model from first principles. A combination of simplified analytical and empirical models is therefore the commonly used solution. This section treats modeling of propellers from a control point of view. This means that the models are required to be accurate enough to capture the main physical effects, and such facilitate control system design and testing.

The actual propeller thrust T_a and torque Q_a are influenced by many parameters, the most important being propeller geometry, submergence, and propeller loading – which depends on the

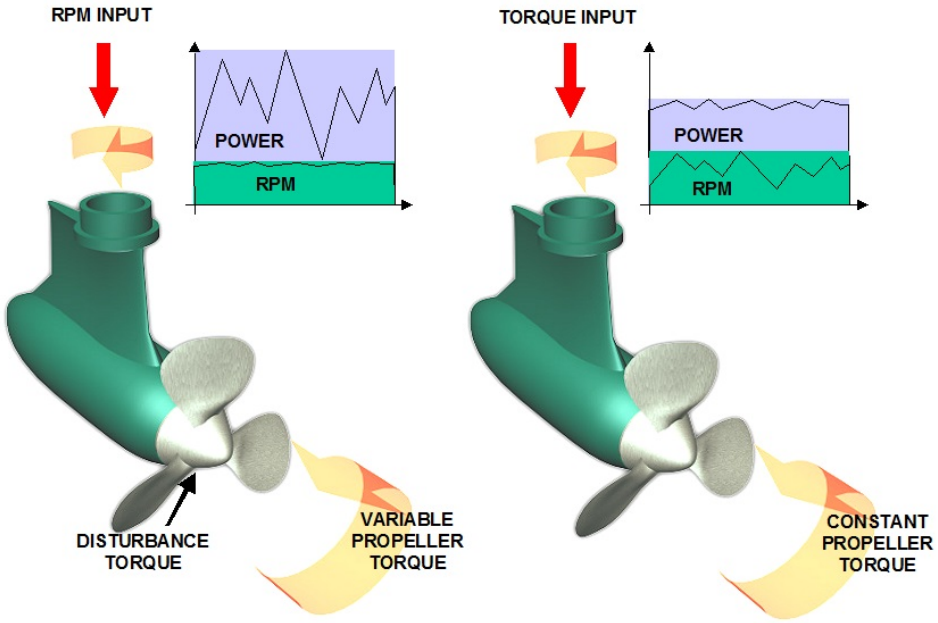

Figure 8.3: Torque and power control reduce the dynamic load variations and allows for lower spinning reserves.

propeller pitch ratio and shaft speed. T_a and Q_a can in general be formulated as functions of fixed thruster parameters θ_p (i.e. propeller diameter, geometry, position, etc.), the shaft speed n, and variables $\mathbf{x}_p$ (i.e. pitch ratio, advance velocity, submergence, etc.)

$$T_a = f_T(n, \mathbf{x}_p, \theta_p), \tag{8.2a}$$
$$Q_a = f_Q(n, \mathbf{x}_p, \theta_p). \tag{8.2b}$$

In the following, only speed controlled FPP at low advance speed will be considered. The models are, however, easily extendable to both controllable pitch propellers (CPP) and higher inflow velocities, as experienced on vessels in transit, see Smogeli (2006) and Ruth (2008). The pitch ratio will in this case be a fixed parameter. The functions $f_Q(\cdot)$ and $f_T(\cdot)$ may include loss effects due to e.g. in-line and transverse velocity fluctuations, ventilation, in-and-out-of water effects, and thruster-thruster interaction, as well as dynamic flow effects. In addition, the dynamics of the motor and shaft must be considered. In the following sections basic propeller characteristics, some quasi-static loss effects, and dynamic effects due to the water inflow, motor, and shaft are considered.

8.4 Propeller Characteristics

The relationships between the propeller thrust T_a, torque Q_a, shaft speed n (in revolutions-per-

	1^{st}	2^{nd}	3^{rd}	4^{th}
n	≥ 0	< 0	< 0	≥ 0
V_a	≥ 0	≥ 0	< 0	< 0

Table 8.1: The 4 quadrants of operation for a propeller, with advance velocity V_a and shaft speed n.

second – rps), diameter D, and density of water ρ are commonly given by Carlton (1994)

$$T_a = f_T(\cdot) = sign(n) K_T \rho D^4 n^2, \tag{8.3}$$
$$Q_a = f_Q(\cdot) = sign(n) K_Q \rho D^5 n^2. \tag{8.4}$$

K_T and K_Q are strictly positive thrust and torque coefficients, where the effects of thrust and torque losses have been accounted for. The inclusion of loss effects in K_T and K_Q is not conventional, but is convenient for consistency in the description of the propeller characteristics. The propeller power consumption P_a is written as

$$P_a = 2\pi n Q_a = sign(n) 2\pi K_Q \rho D^5 n^3. \tag{8.5}$$

The expressions for K_T and K_Q for deeply submerged propellers are found by so-called open water tests, usually performed in a cavitation tunnel or a towing tank. This relationship is commonly referred to as an *open-water propeller characteristics*. The so-called advance ratio is defined as

$$J_a = \frac{V_a}{nD}, \tag{8.6}$$

where V_a is the inflow velocity to the propeller. The corresponding open-water efficiency η_0 is defined as the ratio of produced to consumed power for the propeller

$$\eta_0 = \frac{V_a T_a}{2\pi n Q_a} = \frac{V_a K_T}{2\pi n K_Q D} = \frac{J_a K_T}{2\pi K_Q}. \tag{8.7}$$

The expressions for K_T and K_Q for deeply submerged thrusters are described by the following parameters (Oosterveld and Oossanen, 1975)

$$K_T = f_1\left(J_a, \frac{P}{D}, \frac{A_E}{A_o}, Z\right), \tag{8.8}$$
$$K_Q = f_2\left(J_a, \frac{P}{D}, \frac{A_E}{A_o}, Z, R_n, \frac{t}{c}\right), \tag{8.9}$$

where P/D is the pitch ratio, A_E/A_O is the expanded-area ratio, Z is the number of blades, R_n is the Reynolds number, t is the maximum thickness of the blade section, and c is the chord length of the blade section. The curves for K_T, K_Q, and η_o are shown in Figure 8.5 for different pitch ratios for a Wageningen B-screw series based on Table 5 in Oosterveld and Oossanen (1975), with $R_n = 2 \cdot 10^6$, $Z = 4$, $D = 3.1$ m, and $A_E/A_o = 0.52$.

Propellers are, with the exception of tunnel thrusters, usually asymmetric and optimized for producing thrust in one direction. The propeller characteristics will therefore depend on both the rotational direction of the propeller and the inflow direction. The 4 quadrants of operation of a propeller are defined in Table 8.1. The typical open-water characteristics is a *1-*

quadrant model, covering positive shaft speeds and positive advance velocities. The open-water characteristics is extended into the 2nd quadrant, i.e. negative V_a. If reversing the propeller operating direction, this can be modeled by a similar open-water characteristics for negative shaft speeds and negative advance velocities. In a complete *4-quadrant* model both positive and negative shaft speeds and positive and negative advance velocities are covered. This is typically done by modeling the propeller lift and drag coefficients as a function of propeller blade angle of attack. In van Lammeren and van Manen (1969) the 4-quadrant characteristics of some of the Wageningen B-series propellers are given by a Fourier series representation. It is also possible to tabulate the lift and drag coefficients as functions of propeller blade angle of attack (Bachmayer et al., 2000). A simplification of the 1-quadrant propeller characteristics often seen in literature is to approximate the K_T and K_Q curves to be linear in J_a, see Fossen and Blanke (2000):

$$\begin{aligned} K_T &= K_{T0} - \alpha_{T1} J_a, && (8.10a)\\ K_Q &= K_{Q0} - \alpha_{Q1} J_a, && (8.10b)\\ &\Downarrow \\ T_a &= T_{nn} n\,|n| - T_{nv}\,|n|\, V_a, && (8.10c)\\ Q_a &= Q_{nn} n\,|n| - Q_{nv}\,|n|\, V_a, && (8.10d) \end{aligned}$$

where K_{T0}, K_{Q0}, α_{T1}, and α_{Q1} are constant coefficients for $V_a = 0$ and:

$$\begin{aligned} T_{nn} = \rho D^4 K_{T0}, \quad T_{nv} = \rho D^3 \alpha_{T1}, \\ Q_{nn} = \rho D^5 K_{Q0}, \quad Q_{nv} = \rho D^4 \alpha_{Q1}. \end{aligned}$$

This approximation is in reality only valid in the 1st quadrant. (8.10c) and (8.10d) clearly show the dependence of the thrust and torque on V_a. K_{T0} and K_{Q0} are the *nominal* thrust and torque coefficients for a deeply submerged propeller with $V_a = 0$ and no thrust losses. The corresponding nominal thrust T_n, torque Q_n, and power P_n are expressed by:

$$\begin{aligned} T_n &= sign(n) K_{T0} \rho D^4 n^2, && (8.11a)\\ Q_n &= sign(n) K_{Q0} \rho D^5 n^2, && (8.11b)\\ P_n &= 2\pi n Q_n = sign(n) 2\pi K_{Q0} \rho D^5 n^3. && (8.11c) \end{aligned}$$

The nominal thrust, torque, and power of a reversed propeller are expressed as above , but with K_{T0} and K_{Q0} replaced with their reverse counterparts, K_{T0r} and K_{Q0r}. Note that K_{T0r} and K_{Q0r} are positive, since the thrust direction is accounted for in the expression.

Remark 8.1 *Notice that with reference to the thrust allocation we here have assumed a speed controlled propeller with* $k = \rho_w D^4 K_{T0}$, $u_d = |n_d|\, n_d$, $T_d = k u_d$. *In this case* $T_n = T_d$, $n = n_d$, *and subsequently* $Q_n = Q_d$

Remark 8.2 *As we will see later in this section the actual propeller thrust* T_a *and moment* Q_a *are the real produced thrust and moment, while* T_d *and* Q_d *are the corresponding desired values that are input to the local thruster controllers. Ideally, they should be equal. However, this is hard or almost impossible to achieve.*

In Figure 8.4 the relation between the output $\tau_c \in \mathbb{R}^3$ from the DP controller and the propeller speed setpoint n_d is shown.

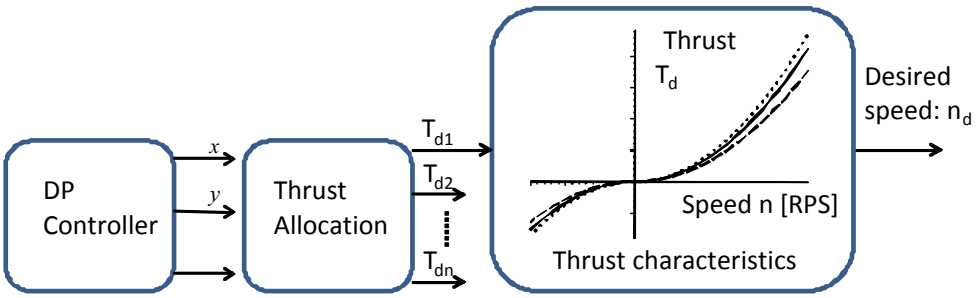

Figure 8.4: Relation between the DP controller and the thrust setpoint for a speed controller thruster.

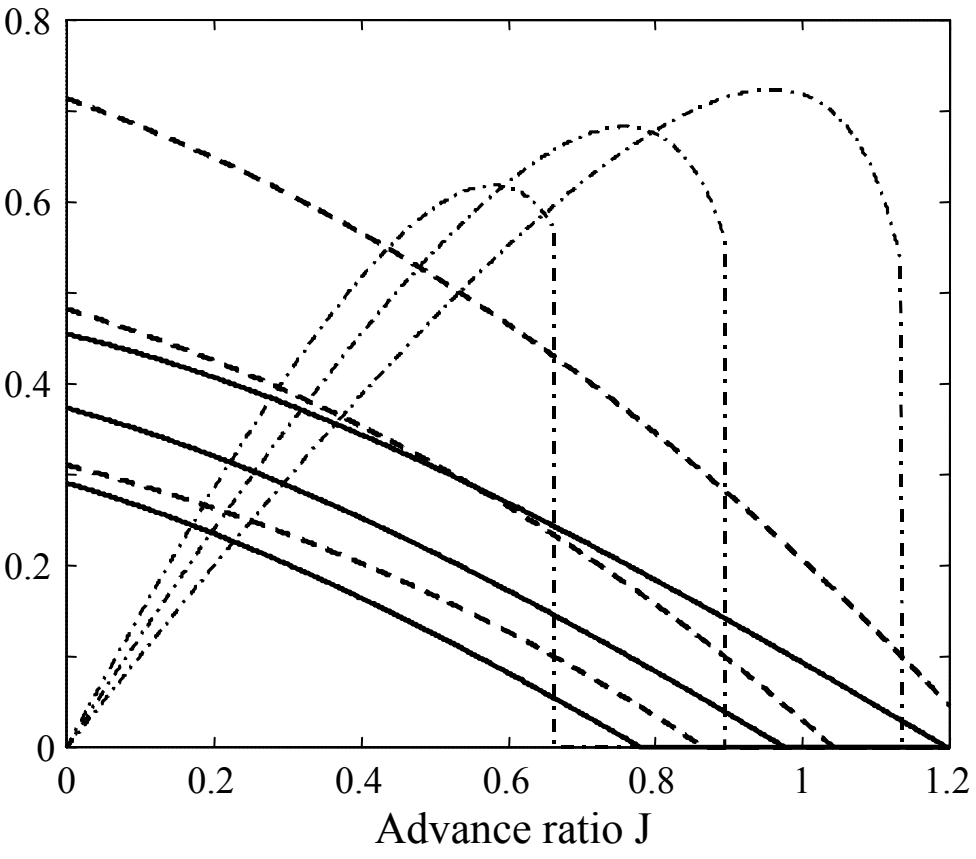

Figure 8.5: Open water K_T (solid), $10 \cdot K_Q$ (dash) and η_o (dash-dot) as a function of advance ratio J for $P/D = 0.7$, 0.89 and 1.1.

8.4.1 Example

Consider the following speed controlled thruster given by $P/D = 0.89$, $Z = 4$, $D = 3.1\ m$, $\rho_w = 1025\, kg/m^3$ and $A_E/A_o = 0.52$. The maximum and minimum rpm for the thruster are set to be $300\, rpm$ and $-100\, rpm$, respectively. This is transferred to revolutions-per-second (rps)

according to

$$\begin{aligned} n_{\max} &= 300\,rpm = 300\frac{1}{60}rps = 5\,rps, \\ n_{\min} &= -100\,rpm = -100\frac{1}{60}rps = -1.67\,rps. \end{aligned}$$

First, assume bollard pull condition, that is $J_a = 0$. From Figure 8.5 we find that $K_{T0} = 0.36$. The thrust characteristics is then in $[kN]$ given by (8.11a) according to

$$\begin{aligned} T_{\text{d\_0}} &= \rho_w D^4 K_{T0}\,|n_d|\,n_d, \\ &= 1.025(3.1)^4 0.36\,|n_d|\,n_d, \\ &= 34.078\,|n_d|\,n_d. \end{aligned}$$

Next, assume that incoming current or vessel speed increase J_a such that $K_{T1} = 0.30$

$$\begin{aligned} T_{\text{d\_1}} &= \rho_w D^4 K_{T1}\,|n_d|\,n_d, \\ &= 1.025(3.1)^4 0.30\,|n_d|\,n_d, \\ &= 28.398\,|n_d|\,n_d. \end{aligned}$$

Finally we assume an increase in K_T due to negative advance speed such that $K_{T2} = 0.4$ and

$$\begin{aligned} T_{\text{d\_2}} &= \rho_w D^4 K_{T2}\,|n_d|\,n_d, \\ &= 1.025(3.1)^4 0.4\,|n_d|\,n_d, \\ &= 37.864\,|n_d|\,n_d. \end{aligned}$$

In Figure 8.6 the different thrust characteristics $(T_{\text{d\_0}}, T_{\text{d\_1}}, T_{\text{d\_2}})$ are plotted for the defined speed range $[n_{min}, n_{max}]$.

We observe from Figure 8.6 that a change in the propeller thrust coefficient K_T will have large impact on the thrust characteristics. This may cause problems in the dynamic positioning system and in the electrical propulsion system as they usually only operate with one set of thrust characteristics, e.g. $T_{\text{d\_0}} = \rho_w D^4 K_{T0}\,|n_d|\,n_d$. In the real situation the thruster characteristics will vary as shown in Figure 8.6, resulting in large moment and power fluctuations as shown later in the chapter.

8.5 Propulsion Efficiency

The difference between the ship speed U and the inflow velocity to the propeller V_a is called the *wake*. For a ship moving forward, V_a is less than U since the after-body flow changes its magnitude between ship speed near the vessel and zero far from the vessel. The stationary relationship for axial water inflow can be modeled as (Carlton, 1994)

$$V_a = U(1 - (w_w + w_p + w_v)) = U(1 - w), \tag{8.12}$$

where w is the *wake fraction number*, typically in the range of $0 < w < 0.4$. w_w is the wake fraction caused by the wave motion of the water particles. w_p is the wake fraction caused by so-called potential effects for a hull advancing forward in an ideal fluid, and w_v is the wake fraction caused by viscous effects due to the effect of boundary layers. One should notice that (8.12)

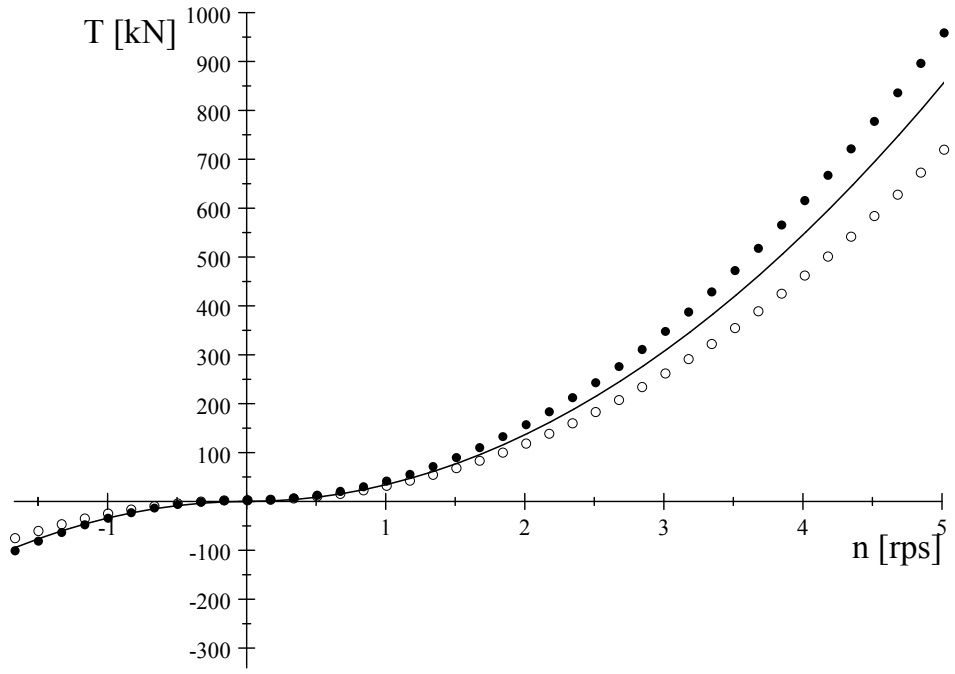

Figure 8.6: Thruster characteristics for $K_{T0} = 0.36$ (solid), $K_{T1} = 0.3$ (circle), and $K_{T2} = 0.4$ (dotted).

only must serve as a rough estimate, since it does not account for the interactions between the vessel motion and the actual wave particle flow. By applying a moment equation to a control volume surrounding the inlet flow, the thrust can be related to the rate of change of moment of the control volume. This will give a dynamic equation for the advance speed.

Consider a towed ship without any propeller installed, then a pressure field is set up given the hull shape and the towing speed. If the same ship is self-propelled with a propeller at the same speed, the pressure field experienced for the towed ship will be changed due to the propeller action (thrust). At the aft part of the hull the propeller will increase the flow velocity, and thereby according to Bernoulli reduce the local pressure. Hence, the suction of the propeller generally reduces the pressure at the stern resulting in increased resistance or drag d_s according to

$$d_s = T_{\mathrm{a}} t_d, \tag{8.13}$$

where t_d is the thrust-deduction coefficient, typically in the range of $0 < t_d < 0.2$ caused by pressure reduction due to potential effects, viscous effects, waves, and appendices. In some extreme cases t_d may become negative. In steady state the effective thrust is equal to the total resistance R according to

$$R = T_{\mathrm{a}}(1 - t_d). \tag{8.14}$$

The thrust coefficient behind the hull is normally assumed to be unchanged compared to open water, while the torque coefficient will be affected by the change in inflow at the stern,

K_{QB}. This is accounted for by the relative rotative efficiency

$$\eta_r = \frac{\eta_B}{\eta_o} = \frac{\frac{J}{2\pi}\frac{K_T}{K_{QB}}}{\eta_o} = \frac{K_Q}{K_{QB}}. \tag{8.15}$$

The overall propulsion efficiency can now be found as the ratio between the useful work done by the product of drag and ship speed divided by the work required to overcome the shaft torque

$$\eta_p = \frac{RU}{2\pi n Q_{\mathrm{a}}} = \eta_h \eta_o \eta_r \eta_m, \tag{8.16}$$

where $\eta_h = \frac{1-t_d}{1-w}$ is defined as the hull efficiency and is according to Newman (1997) in the range of 1.0–1.2. η_m is the mechanical efficiency typically in the range of 0.8–0.9.

8.6 Propeller and Thruster Losses

Modeling of thrust losses, which are constituted of complex physical phenomena, is most commonly solved by empirical methods in conjunction with analytical models. The following loss effects may be considered:

- In-line velocity fluctuations (only for open and ducted propellers).
- Water inflow perpendicular to the propeller axis caused by current, vessel speed or jets from other thrusters will introduce a force in the direction of the inflow due to deflection of the propeller race. This is often referred to as *cross-coupling drag.*
- For heavily loaded propellers *ventilation* (air suction) caused by decreasing pressure on the propeller blades may occur, especially when the submergence of the propeller becomes small due to vessel's wave frequency motion.
- For extreme conditions with large vessel motions the *in-and-out-of-water effects* will result in sudden drop of thrust and torque following a hysteresis pattern.
- Both thrust reduction and change of thrust direction may occur due to thruster-hull interaction caused by frictional losses and pressure effects when the thruster race sweeps along the hull. The last is referred to as the *Coanda effect.*
- Thruster-thruster interaction caused by influence from the propeller race from one thruster on neighboring thrusters may lead to significant thrust reduction, if not appropriate precautions are taken in the thrust allocation algorithm.

The sensitivity to the different types of losses depends on the type of propeller and thruster used, application of skegs and fins, hull design and operational philosophy. Main propellers are subject to large thrust losses due to air ventilation and in-and-out-of-water effects. Rotatable azimuth thrusters are subject to losses caused by hull friction and interaction with other thrusters. Tunnel thrusters are subject to losses caused by non-axial inflow due to current and vessel speed and ventilation phenomenon in heavy seas.

The effects of the above mentioned losses are modeled by the thrust and the torque reduction functions h_T and h_Q based on a combination of analytical and empirical data. Hence, the actual thrust T_a and torque Q_a experienced by the propeller can be expressed as

$$T_a = h_T(n, \mathbf{x}_p, \theta_p)(1 - t_d)T_n \triangleq f_T(n, \mathbf{x}_p, \theta_p), \tag{8.17}$$
$$Q_a = h_Q(n, \mathbf{x}_p, \theta_p)Q_n \triangleq f_Q(n, \mathbf{x}_p, \theta_p), \tag{8.18}$$

where $\mathbf{x}_p$ represents dynamic states, such as vessel motion, propeller submergence and environmental conditions. Propeller dependent parameters are represented by the vector θ_p. In the following, only speed controlled fixed pitch propellers will be considered. The pitch ratio will in this case be a fixed parameter. Research results on thrust losses may be found in for example Minsaas et al. (1987), Smogeli (2006) and Ruth (2008). Unfortunately, no general mathematical model is outlined for describing the thruster performance in time-varying conditions, including transient effects. Especially for a dynamically positioned vessel, with advance numbers close to zero, few results are available.

Thrust losses as shown in (8.17) and (8.18) may be expressed by the thrust and torque reduction coefficients β_T and β_Q, which express the ratio of actual to nominal thrust and torque Minsaas et al. (1987)

$$\frac{T_a}{T_n} = h_T(n, \mathbf{x}_p, \theta_p)(1 - t_d) = \beta_T = \frac{K_T}{K_{T0}}, \tag{8.19}$$
$$\frac{Q_{a.}}{Q_n} = h_Q(n, \mathbf{x}_p, \theta_p) = \beta_Q = \frac{K_Q}{K_{Q0}}. \tag{8.20}$$

In Figure 8.21 thrust reduction functions from accounting for in-and-out-of-water effects are illustrated. To investigate the effect of ventilation and loss of effective disc area in a DP situation, two sets of model tests as presented in Smogeli (2006) will be shown: 1) Stationary tests of a ducted propeller in a cavitation tunnel. 2) Dynamic tests of the same ducted propeller subject to waves and varying submergence in open water.

8.6.1 In-line Velocity Fluctuations

Waves, currents and vessel motion induce a varying velocity field around the propeller. This may be composed in an in-line component due to waves, current and vessel surge, sway and yaw motion, and a transverse component due to waves and vessel heave, roll and pitch motion. The in-line, or axial, component gives rise to changes in the advance velocity V_a, and hence advance number J_a as shown in (8.12). As the thruster operating point is moving on the thrust and torque curves, fluctuations in thrust, torque, power, and shaft speed are induced. Let the advance number including only the hull wake be denoted J_h, then the thrust and torque loss factors $\beta_{T,ax}$ and $\beta_{Q,ax}$ due to axial flow are written

$$\beta_{T,ax} = \frac{K_T(J_a)}{K_T(J_h)}, \tag{8.21}$$
$$\beta_{Q,ax} = \frac{K_Q(J_a)}{K_Q(J_h)}. \tag{8.22}$$

Figures 8.7 and 8.6 show thrust curves for varying advance speeds V_a, and clearly illustrates that the resulting thrust loss is significant. The thrust and torque loss factors for in-line velocity

fluctuations will take on values both larger than and smaller than unity, since the variations in advance speed may lead to both higher and lower propeller load than the nominal value for $V_a = 0$. Note that this loss effect is not applicable to a tunnel thruster, since the thrust then is independent of the in-line velocity.

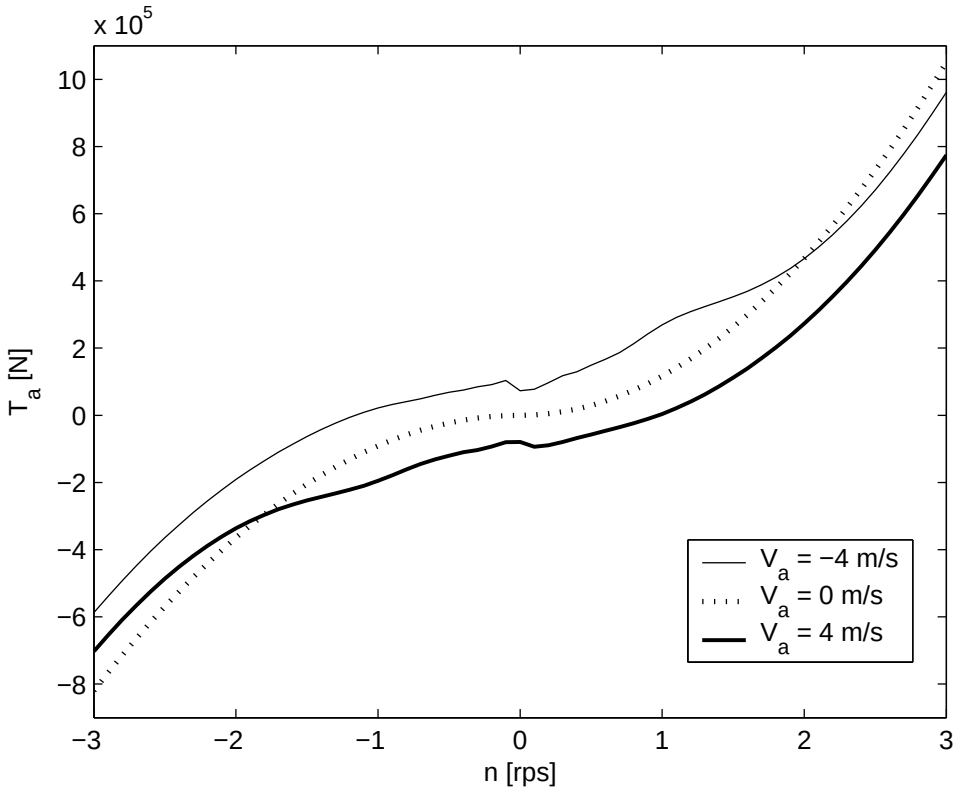

Figure 8.7: Example thrust curves for varying advance speed V_a.

8.6.2 Transverse Velocity Fluctuations

The transverse velocity fluctuations have different effects on tunnel thrusters compared to conventional open and ducted propellers.

Open and ducted propellers

The transverse velocity component will give rise to a bending of the propeller race, and thus a force perpendicular to the propeller axis. This force is given by

$$F_t = K_{cc} D \sqrt{\rho_w T_a} V_{tr}, \tag{8.23}$$

with K_{cc} a cross-coupling drag factor and V_{tr} the transverse velocity component. V_{tr} consists of components from the vessel motion, current and wave induced velocities. K_{cc} is commonly set to 0.25 for ducted propellers and 0.31 for open propellers. From momentum considerations, the

thrust loss factor $\beta_{T,tr}$ is given by

$$\begin{aligned}\beta_{T,tr} &= 1 - \left(\frac{F_t}{T_a}\right)^2 = 1 - \left(\frac{K_{cc} D \sqrt{\rho_w T_a} V_{tr}}{T_a}\right)^2 \\ &= 1 - \rho_w {K_{cc}}^2 D^2 \frac{{V_{tr}}^2}{T_a}. \end{aligned} \tag{8.24}$$

Notice that this loss effect does not affect the thruster torque directly, so that the torque loss function $\beta_{Q,tr}$ will be unity. Figure 8.8 shows an example of $\beta_{T,tr}$ as function of transverse velocity for varying thrusts.

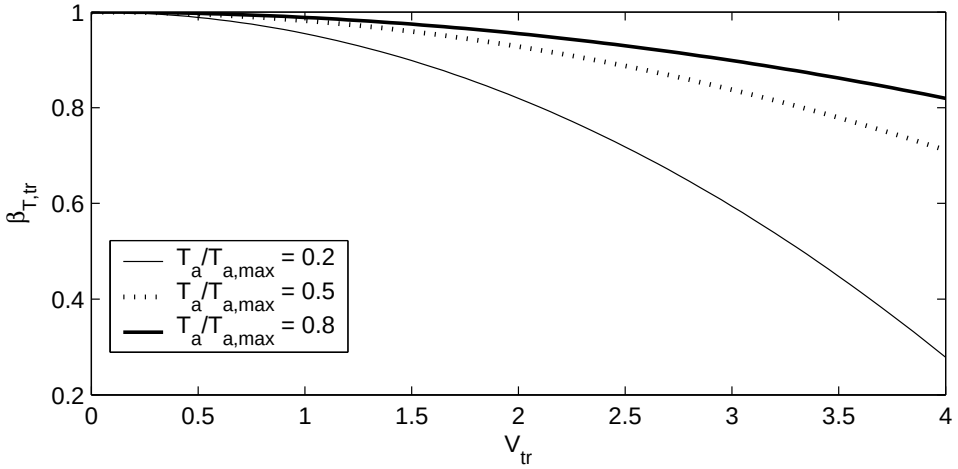

Figure 8.8: Example thrust loss factor due to cross-coupling drag $\beta_{T,tr}$ versus transverse velocity V_{tr} for varying nondimensional thrust $T_a/T_{a,\max}$.

Tunnel thrusters

A tunnel thruster will experience large thrust losses caused by relative motion between the vessel and water. Using the transverse velocity component V_{tr}, the relative velocity V_{rel} is expressed as

$$V_{rel} = \frac{V_{tr}}{V_w}, \tag{8.25}$$

where V_w is the jet velocity in the wake of the thruster

$$V_w = \sqrt{\frac{2T_a}{\rho_w A_p}}. \tag{8.26}$$

A_p is the propeller disc area. Figure 8.9 shows a typical plot of the thrust loss factor $\beta_{T,tr}$ as function of V_{rel}. Again, this effect does not affect the thruster torque, so that $\beta_{Q,tr} = 1$.

8.6.3 Ventilation and In-and-out-of Water Effects

Ventilation, cavitation, loss of effective disc area, and the Wagner effect are all closely related physical phenomena. A generic thrust loss model due to ventilation and loss of effective disc

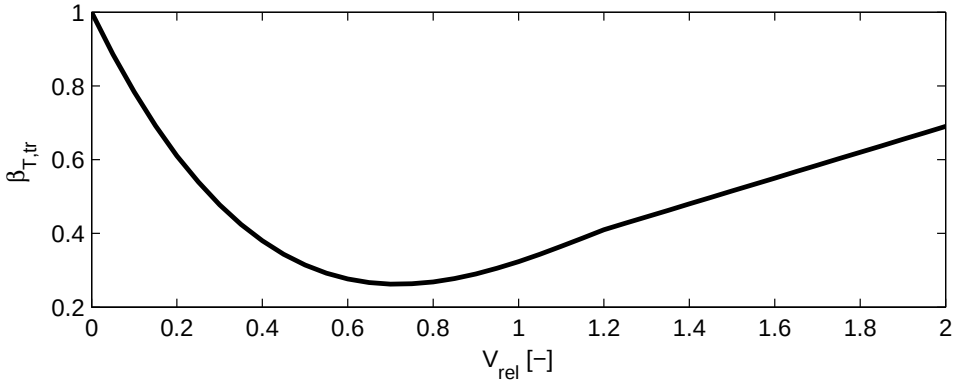

Figure 8.9: Example tunnel thruster speed loss factor as function of relative velocity V_{rel}.

area has been implemented based on the experimental results presented later in this section. An extension capturing the hysteresis introduced by the Wagner effect is under development. The loss factor $\beta_{T,vent}$ is given as a two-dimensional function of the relative immersion h/R and relative shaft speed $n/n_{\max}$. h is the propeller shaft submergence, R is the propeller radius and $n_{\max}$ the maximum shaft speed of the propeller. The loss function captures the main characteristics of the ventilation and the loss of effective disc area, see Figure 8.10. For large submergence $\beta_{T,vent} = 1$, which means zero loss and full thrust. For low propeller loading, decreasing submergence leads to gradually decreasing $\beta_{T,vent}$ – and hence thrust. This corresponds to a loss of effective disc area. For high propeller loading, decreasing submergence leads to an abrupt loss of thrust due to ventilation. Note that the loss model will be propeller specific, and the critical values of h/R and $n/n_{\max}$ where ventilation starts will vary.

The torque loss factor for ventilation will usually be larger than the thrust loss factor, and may be related to the thrust reduction factor by:

$$\beta_{Q,vent} = (\beta_{T,vent})^m, \tag{8.27}$$

where $m = 0.65$ for a ducted propeller, $m = 0.843$ for an open propeller, and $m = 0.575$ for a tunnel thruster (Minsaas et al., 1987).

Experimental results from the cavitation tunnel tests

Systematic tests with a ducted propeller were carried out at the cavitation tunnel at NTNU. The advance number was kept at approximately 0.2, and the thruster shaft speed and submergence varied while measuring propeller and duct thrust and propeller torque. Figure 8.11 shows K_T as function of relative submergence h/R and propeller shaft speed. h is the propeller shaft submergence, and R the propeller radius. The torque coefficient has a similar form. Nondimensionalized total thrust is presented in Figure 8.12. These results agree with previous research on the subject, but contain additional information for the DP case; at low speeds, with J close to zero, the advance number is no longer a sufficient parameter for describing the losses. For large submergence, the thruster exhibits the expected behavior, yielding the normal thrust characteristics with K_T constant and thrust proportional to n^2. For low shaft speeds, and hence low propeller load, the thrust is constant for $h/R = 1.5$ to $h/R = 1$, and then decays almost linearly from $h/R = 1$ to $h/R = 0$. This can be seen in Figure 8.12, and corresponds to lost

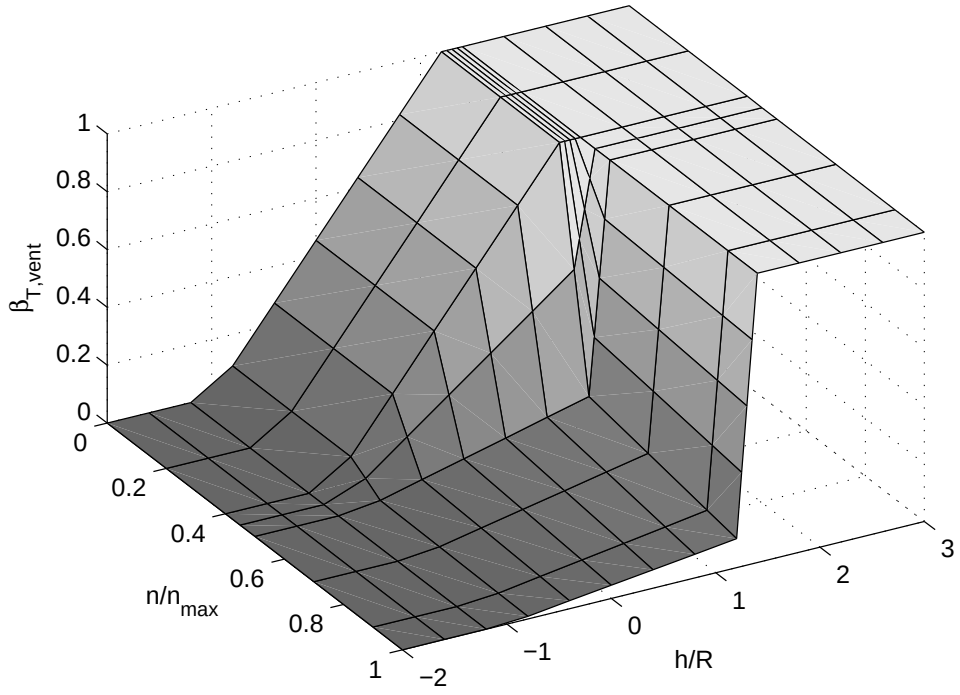

Figure 8.10: Ventilation thrust loss model as function of relative shaft speed $n/n_{\max}$ and relative submergence h/R.

thrust due to loss of effective disc area, as given by Minsaas et al. Minsaas et al. (1987). For higher propeller loads, the thrust (and load torque) drops rapidly with decreasing submergence. It is evident that for a heavily loaded propeller, proximity to the surface may lead to an abrupt loss of thrust. As can be seen in Figure 8.12, the results indicate that a reduction of shaft speed in such a case will increase the thrust. This was the key observation from the experiments, motivating the design of an anti-spin thruster controller, shown later in the section.

Open water experimental results from MCLab

The results from the cavitation tunnel were all obtained at steady state, and are such stationary results. A thruster will in reality be operating in more dynamic conditions where transient effects are important. To investigate dynamic effects, tests in the Marine Cybernetics Laboratory (MCLab) at NTNU were carried out with the same propeller unit. The results here were less clear than the stationary results, but confirmed that it is advantageous to reduce the shaft speed when the thruster is subject to ventilation. Figure 8.13 shows a time series of the propeller thrust and shaft speed for $h/R = 1.5$ in moderate waves. The thrust increases for increasing n, but suddenly drops sharply when the propeller load becomes too high. The time series from these tests showed that ventilation caused the thrust to drop sharply by as much as 85 % in a time span of only 1.5 seconds. This illustrates the fast dynamics that the thruster control system has to deal with.

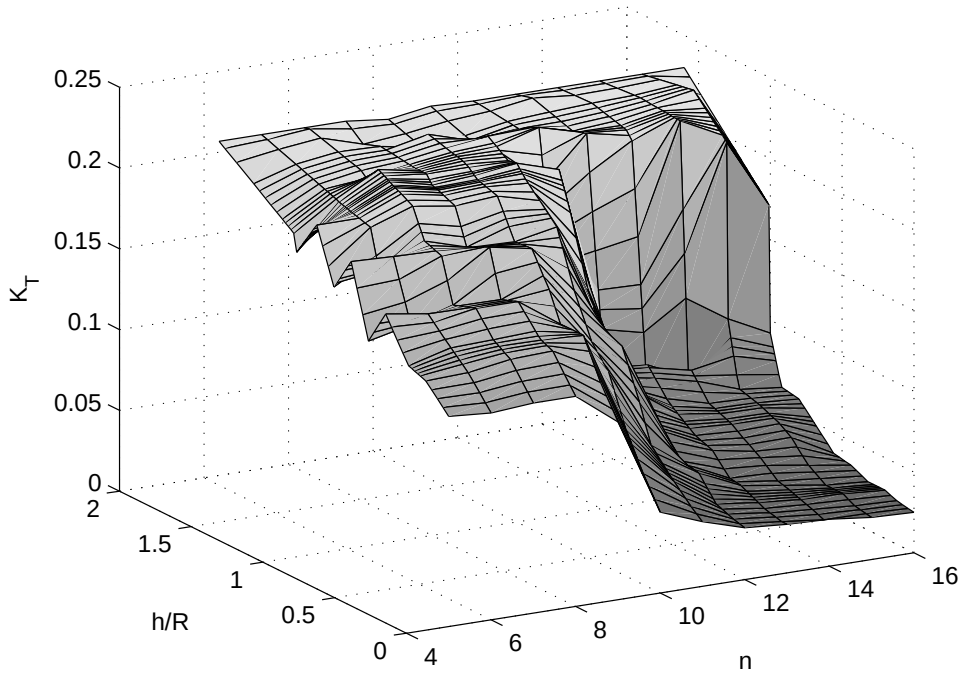

Figure 8.11: Thrust coefficient K_T vs. relative submergence h/R and propeller shaft speed n for $J_a = 0.2$.

8.7 Propeller Shaft Model

Let Q_m denote the torque generated by the propeller motor. A torque balance for the propeller shaft is written

$$I_s\dot{\omega} = Q_m - Q_a - Q_f(\omega), \tag{8.28}$$

where I_s is the moment of inertia for the shaft, propeller, and motor, $\omega = 2\pi n$ is the angular shaft speed, and $Q_f(\omega)$ is the shaft friction. The friction may for most applications be viewed as a sum of a static friction (or starting torque) Q_s and a linear component:

$$Q_f(\omega) = \tanh(\omega/\varepsilon)Q_s + K_\omega\omega, \tag{8.29}$$

where $\varepsilon > 0$ is an appropriately chosen small constant, and K_ω is a linear friction coefficient. If desired, more sophisticated friction models may be used, including e.g. nonlinear elements, Stribeck friction, and hysteresis effects. This has not been considered in the current work; even though the experimental facility exhibited some nonlinear friction characteristics, the model in (8.29) proved sufficient for control and control design purposes. If we disregard the static friction, the torque balance (Figure 8.14) for the propeller shaft is written

$$I_s\dot{\omega} = Q_m - Q_a - K_\omega\omega. \tag{8.30}$$

The power delivered by the motor and the actual propeller shaft power accounting for the

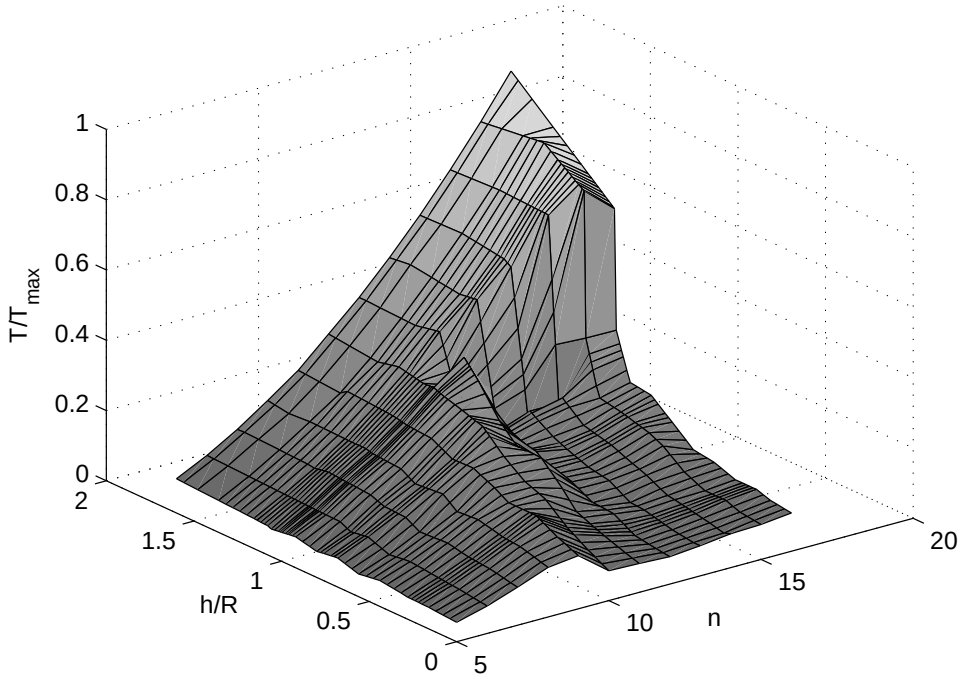

Figure 8.12: Nondimensionalized thrust vs. relative submergence h/R and propeller shaft speed n for $J_a = 0.2$.

effect of thrust losses are given by

$$P_m = \omega Q_m = 2\pi n Q_m, \tag{8.31}$$
$$P_a = \omega Q_a = 2\pi n Q_a. \tag{8.32}$$

By combining (8.11a), (8.11b) and (8.32) and let $T_n = T_d$ and $n = n_d$, it is possible to express the actual thrust produced as function of propeller power and torque according to

$$\begin{aligned} T_a &= h_T(n, \mathbf{x}_p, \theta_p)(1-t_d)T_d, \\ &= h_T(\cdot)(1-t_d)\rho_w D^4 K_T \left|n_d\right| n_d, \\ &= h_T(\cdot)(1-t_d)\frac{K_T}{K_Q D}\rho_w D^5 K_Q \left|n_d\right| n_d, \\ &= \frac{h_T(\cdot)(1-t_d)}{h_Q(\cdot)}\frac{K_T}{K_Q D}\cdot Q_a. \end{aligned} \tag{8.33}$$

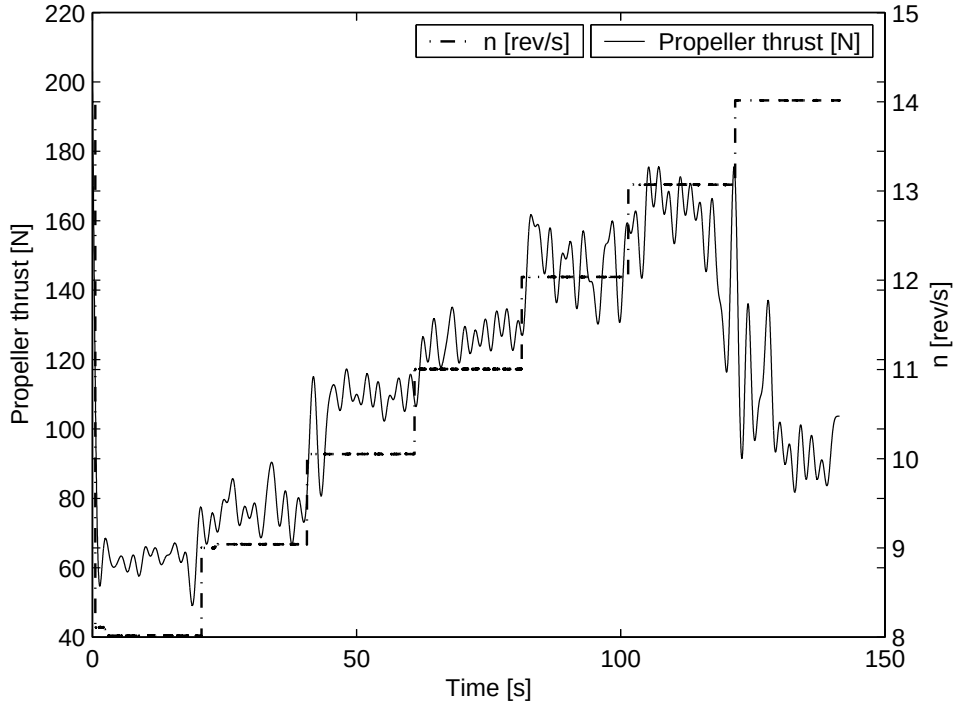

Figure 8.13: Time series of propeller thrust T_a and shaft speed n in moderate waves, with ventilation at high propeller loading (high n).

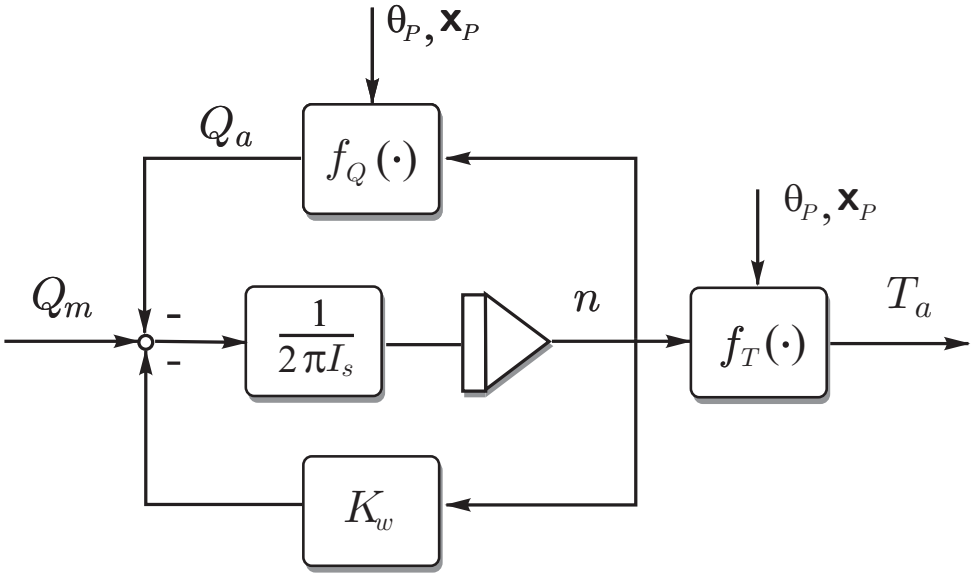

Figure 8.14: Propeller shaft model with linear friction.

Let $n_d = \text{sgn}(n_d)\sqrt{\frac{T_d}{\rho_w D^4 K_T}}$, then the actual consumed power may be rewritten as

$$\begin{aligned} P_a &= \omega Q_a = 2\pi n Q_a, \\ &= 2\pi n_d D \frac{K_Q}{K_T} h_Q(\cdot) T_d, \\ &= 2\pi D \frac{K_Q}{K_T} h_Q(\cdot) T_d \text{sgn}(n_d) \sqrt{\frac{T_d}{\rho_w D^4 K_T}}, \\ &= \text{sgn}(n_d) 2\pi K_Q h_Q(\cdot) \frac{D}{(K_T)^{3/2} D^2 \sqrt{\rho_w}} T_d^{3/2}, \\ &= \text{sgn}(n_d) 2\pi K_Q h_Q(\cdot) \frac{1}{D\sqrt{\rho_w}} \frac{1}{(K_T h_T(\cdot)(1-w_t))^{3/2}} T_a^{3/2}. \end{aligned} \tag{8.34}$$

The actual thrust is

$$T_a = \text{sgn}(n_d)\frac{\rho_w^{1/3} D^{2/3} K_T h_T (1-t_d)}{(2\pi \cdot K_Q \cdot h_Q)^{2/3}} \cdot P_a^{2/3}. \tag{8.35}$$

8.7.1 Torque Loop in an Electrical Motor Drive

The torque control is inherent in the design of most applied control schemes for variable speed drive systems. The torque is controlled by means of motor currents and motor fluxes with high accuracy and bandwidth, see Figure 8.15. Theoretically the rise time of the torque in PWM (Pulse Width Modulated) drives is limited by the motor's inductance (in load commutated inverters, LCI's, also by the DC choke). However, in practice the controller limits the rate of change of torque in order to prevent damages on the mechanics. The closed loop of motor and torque controller may for practical reasons be assumed to be equivalent with the 1st order model, where T_m is the time constant in the range of $20 - 200$ *milliseconds* (ms) and Q_c the commanded torque

$$\dot{Q}_m = \frac{1}{T_m}(Q_c - Q_m), \tag{8.36}$$

or written by Laplace transform as

$$Q_m(s) = \frac{1}{1 + T_m s} Q_c(s). \tag{8.37}$$

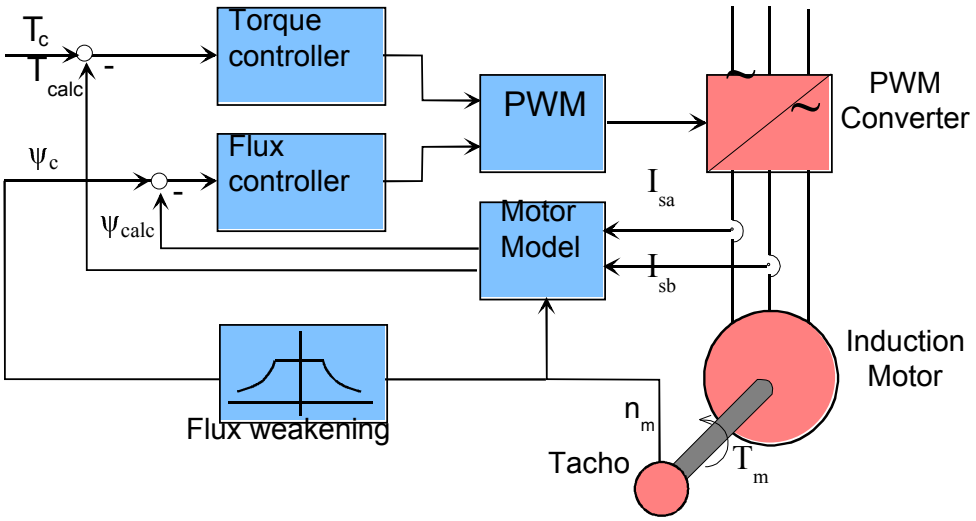

Figure 8.15: Torque loop in electrical motor drive.

8.7.2 Resulting Thruster Dynamics

Combining the hydrodynamic thruster model, the shaft model, the motor model and the local thruster controller yields the total thruster dynamics for one thruster unit. This is shown in Figure 8.16, where the position of the thruster dynamics in the total vessel dynamics also is shown.

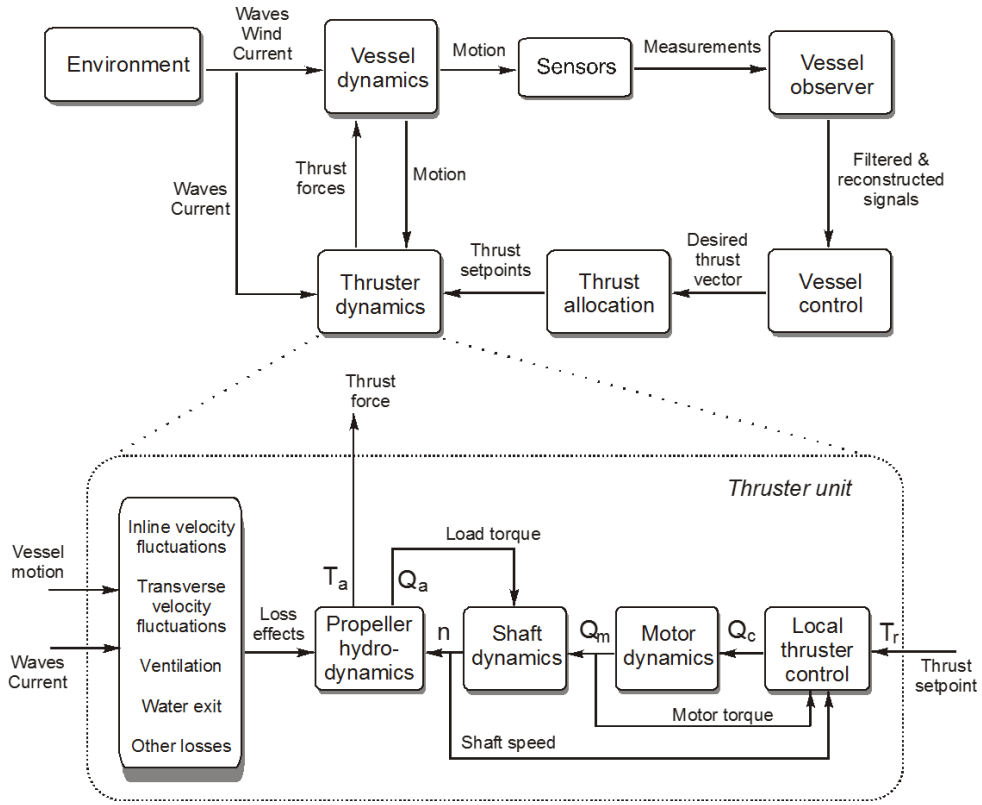

Figure 8.16: Total thruster dynamics and its position in the total vessel dynamics.

8.7.3 Thrust, Torque, Power, and Shaft Speed Relations

The shaft speed n can be expressed in terms of the thrust T_a or the torque Q_a by inverting (8.3) and (8.4):

$$n = sign(T_a)\sqrt{\frac{|T_a|}{\rho D^4 K_T}}, \tag{8.38}$$

$$n = sign(Q_a)\sqrt{\frac{|Q_a|}{\rho D^5 K_Q}}. \tag{8.39}$$

From (8.5), the magnitude of the shaft speed is expressed in terms of P_a by:

$$|n| = \frac{P_a^{1/3}}{(2\pi K_Q \rho)^{1/3} D^{5/3}}. \tag{8.40}$$

The thrust T_a can be expressed in terms of the torque Q_a by eliminating $sign(n)\rho n^2 D^4$ between (8.3) and (8.4):

$$T_a = \frac{K_T}{K_Q D} Q_a. \tag{8.41}$$

Similarly, T_a can be expressed in terms of P_a by eliminating $sign(n)\rho n^2 D^4$ between (8.3) and (8.5) and inserting (8.38):

$$|T_a| = \frac{\rho^{1/3} D^{2/3} K_T}{(2\pi)^{2/3} K_Q^{2/3}} P_a^{2/3}. \tag{8.42}$$

Finally, Q_a can be expressed in terms of P_a by inserting (8.39) in (8.5):

$$|Q_a| = \frac{\rho^{1/3} D^{5/3} K_Q^{1/3}}{(2\pi)^{2/3}} P_a^{2/3}. \tag{8.43}$$

8.8 Low-Level Thruster Controllers

The purpose of the low-level thruster controller is to relate the desired thrust T_d, given by the thrust allocation routine, to the commanded motor torque Q_c. The thruster controllers may be divided in two control regimes, depending on the operational conditions:

(a) Thruster control in normal conditions, when experiencing low to moderate thrust losses.

(b) Thruster control in extreme conditions, when experiencing large and abrupt thrust losses due to ventilation and in-and-out-of-water effects.

For surface vessels with FPP, shaft speed control is the industry standard, whereas torque and power control was introduced by Sørensen et al. (1997), and a combined torque and power controller was presented in Sørensen and Smogeli (2009).

8.8.1 Control Objectives

Shaft speed feedback control is the conventional way to control a FPP. However, as will be shown later, this may not be the best design choice. The ultimate goal of any thruster controller is to make the actual thrust track the desired thrust. Since no feedback from the actual thrust is available, different ways of trying to achieve this for a FPP are:

- Shaft speed feedback control.
- Torque feedforward control.
- Power feedback control.
- Combinations of the above.

In dynamic operating conditions, other goals may be more important than tracking the desired thrust, e.g. reducing mechanical wear and tear, and limiting power oscillations and peak values. Predictable power consumption is of major concern to the power management system in order to avoid blackouts and improving the performance and the stability of the electrical power plant network. Other performance criteria than thrust production should therefore also be taken into account. In this work, the following performance criteria are considered:

1. Thrust production in presence of disturbances, i.e. ability to locally counteract thrust losses.

2. Mechanical wear and tear caused by transients and oscillations in motor and propeller torque.

3. Predictable power consumption.

8.9 Thruster Control in Normal Conditions

8.9.1 Controller Structure

The low-level thruster controller is proposed to be composed of five main building blocks: reference generator, core controller, inertia compensation, friction compensation, and torque limiting. This is shown in Figure 8.17, where a block diagram of a thruster with low-level thruster controller is presented. The commanded torque from the core controller is termed Q_{ci}, where $i = n$ for shaft speed control, $i = q$ for torque control, $i = p$ for power control, and $i = c$ for combined torque/power control. The commanded torque from the friction and inertia compensation schemes are termed Q_{ff} and Q_{if}, respectively, and the total commanded torque before torque and power limiting Q_{c0} is given by:

$$Q_{c0} = Q_{ci} + Q_{ff} + Q_{if}. \tag{8.44}$$

Q_{c0} is then limited by a torque and power limiting function to yield the commanded torque to the motor Q_c.

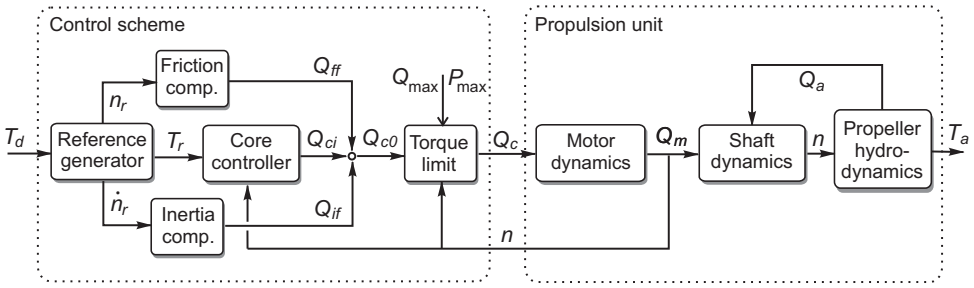

Figure 8.17: Block diagram of a thruster with reference generator, core controller, inertia and friction compensation, and torque limiting.

8.9.2 Control Plant Model Parameters

Since the propeller diameter D and density of water ρ are known and constant, the only remaining parameters are the thrust and torque coefficients K_T and K_Q. The thrust and torque coefficients used in the controllers are termed K_{TC} and K_{QC}, and denoted *control coefficients*.

Choosing K_{TC} and K_{QC}

In thruster control for station-keeping operations, estimates of the nominal thrust and torque coefficients K_{T0} and K_{Q0} are usually chosen as control coefficients, because the actual advance velocity is unknown to the controller. Doppler logs, GPS, or similar may be used to give estimates of the advance velocity, but these measurements are usually not of sufficient accuracy for inclusion in the low-level thruster controllers.

For thruster control in transit, only the main propellers of the vessel are used. If the propeller characteristics are known, improved controller performance may be achieved by estimating the propeller advance velocity V_a using the known vessel surge speed U and an estimated hull wake factor, or a low-pass filtered measurement from a Doppler log or GPS. K_{TC} and K_{QC} could then be estimated from the propeller characteristics. Similar reasoning may be applied to an underwater vehicle, where the propeller normally is deeply submerged and not subject to wave effects, ventilation and water exits. Such an output feedback shaft speed controller with advance speed compensation for AUVs can be found in Fossen and Blanke (2000). In the following, station-keeping and low-speed maneuvering operations of surface vessels are of main concern, such that the control coefficients are taken as K_{T0} and K_{Q0}.

Reverse thrust

With the exception of tunnel thrusters, most propellers are asymmetric. To achieve good performance for both positive and negative thrust references, it may therefore be necessary to use two sets of control parameters. For low-speed operations, this means that K_{T0} and K_{Q0} should be used for positive T_r, and the reverse thrust coefficients K_{T0r} and K_{Q0r} for negative T_r. The following control coefficients are therefore proposed:

$$K_{TC} = K_{T0}\lambda_c + (1-\lambda_c)K_{T0r}, \tag{8.45a}$$

$$K_{QC} = K_{Q0}\lambda_c + (1-\lambda_c)K_{Q0r}, \tag{8.45b}$$

where λ_c is a smooth switching function given by:

$$\lambda_c = \lambda_c(n_r) = \frac{1}{2} + \frac{1}{2}\tanh(\varepsilon_c \frac{n_r}{n_c}), \tag{8.46}$$

where $\varepsilon_c > 0$ is a constant. The shaft speed reference n_r is given from T_r by:

$$n_r = g_n(T_r) = sign(T_r)\sqrt{\frac{|T_r|}{\rho D^4 K_{TC}}}, \tag{8.47}$$

which is the inverse function of the nominal shaft speed-to-force characteristics given in (8.11a) with K_{T0} replaced by K_{TC}. The switch between the coefficients occurs smoothly in the interval $n_r \in [-n_c, n_c]$, such that $\lambda_c \approx 0$ for $n_r < -n_c$ and $\lambda_c \approx 1$ for $n_r > n_c$. The switch "width" n_c may be chosen freely. Equation (8.45) does not affect the stability properties of the controllers when compared to using constant control coefficients, since K_{T0}, K_{Q0}, K_{T0r}, and K_{Q0r} are strictly positive, and the values of K_{TC} and K_{QC} only affect the mappings from thrust reference to shaft speed, torque, and power reference. Using n_r as the switching variable instead of e.g. the measured shaft speed n means that no measurement noise is entered into the control law through (8.45).

8.9.3 Reference Generator

An appropriate reference generator for this system is a second-order filter with rate limiting. The reference generator is imposed on the desired shaft speed n_d, where n_d is given from T_d by g_n in (8.47), and T_d is given from n_d by the inverse $g_n^{-1}(n_d)$, which is equal to (8.11a) with K_{T0}

replaced by K_{TC}. The second-order filter has damping ratio ζ_r and natural frequency ω_{r0}, and the shaft speed rate limit is set to $\dot{n}_{slew}$, such that the reference generator is given by:

$$\begin{aligned} n_d &= g_n(T_d), \\ \dot{n}_{d2} &= \min(\max(\dot{n}_d, -\dot{n}_{slew}), \dot{n}_{slew}), \\ n_r(s) &= n_{d2}(s)\frac{\omega_{r0}^2}{s^2 + 2\zeta_r\omega_{r0}s + \omega_{r0}^2}, \\ T_r &= g_n^{-1}(n_r). \end{aligned} \tag{8.48}$$

Notice that the reference generator gives a continuous acceleration reference $\dot{n}_r$, which is available directly from the implementation of the second-order filter.

8.9.4 Inertia Compensation

For a large thruster, the rotational inertia may be a dominating dynamic term. In order to achieve the desired closed loop properties with respect to response and tracking, it may therefore be beneficial to include an inertia compensation term. The inertial term in the rotational dynamics (8.28) is $I_s\dot{\omega}$. Since differentiation of the measured shaft speed is undesirable, and the inertia compensation is wanted only when the thrust reference is changed, the following feedforward compensation is proposed:

$$Q_{if}(n_r) = I_c 2\pi\dot{n}_r, \tag{8.49}$$

where I_c is an estimate of the rotational inertia I_s, and $\dot{n}_r$ is given by the reference generator in (8.48).

8.9.5 Friction Compensation

In the torque and power controllers, the friction term $Q_f(\omega)$ will be compensated by a feedforward controller. If this is not the case, and the friction is significant, the controllers will be inaccurate, since at steady state $Q_m \approx Q_a$ no longer holds, see (8.28). If the shaft friction becomes significant, a feedforward friction term Q_{ff} should therefore be included in the control law. Note that the inclusion of Q_{ff} in the shaft speed controller is unnecessary, since this controller automatically compensates for the friction.

Q_{ff} should be designed to compensate for the friction term $Q_f(\omega)$, i.e. $Q_{ff} \approx Q_f(\omega)$, without destabilizing the system. Therefore a feedforward compensation based on the *reference* shaft speed n_r from (8.47) is chosen instead of a destabilizing feedback compensation based on n. Motivated by (8.29) the friction is assumed to consist of a static and a linear term, and the friction compensation scheme is proposed as:

$$Q_{ff}(n_r) = Q_{ff0}(n_r) + Q_{ff1}(n_r). \tag{8.50}$$

$Q_{ff0}(n_r)$ is proposed as:

$$Q_{ff0}(n_r) = Q_{f0}\tanh(\varepsilon_f\frac{n_r}{n_s}), \tag{8.51}$$

where Q_{f0}, $\varepsilon_s > 0$, and n_s are constants. The switch between $-Q_{f0}$ and Q_{f0} occurs smoothly in the interval $n_r \in [-n_s, n_s]$ such that $|n_r| > n_s \Rightarrow Q_{ff0}(n_r) = sign(n_r)Q_{f0}$, and $n_r = 0 \Rightarrow$

$Q_{ff0}(n_r) = 0$. Note that the switching function is of similar form as the one used in (8.46). Q_{ff1} is proposed as:

$$Q_{ff1}(n_r) = 2\pi Q_{f1} n_r, \tag{8.52}$$

where the linear friction coefficient Q_{f1} should be chosen such that $Q_{f1} \approx K_\omega$. In nominal conditions, $n = n_r \Rightarrow Q_{ff1}(n_r) \approx K_\omega \omega$. For $n \neq n_r$, $Q_{ff1}(n_r) \neq K_\omega \omega$, but this only affects the performance about the equilibrium point.

8.9.6 Torque and Power Limiting

The rated (nominal) torque and power for continuous operation of the motor are denoted Q_N and P_N. The maximum torque and power for the motor are usually set to

$$Q_{\max} = kQ_N, \quad P_{\max} = kP_N, \tag{8.53}$$

where k typically is in the range of $1.1 - 1.2$. The input to the motor should be limited by a torque limiting function given by:

$$|Q_c| = \min\{|Q_{c0}|, Q_{\max}, P_{\max}/|2\pi n|\},$$

where Q_{c0} is the commanded torque from the controller (8.44). The maximum power limit yields hyperbolic limit curves for the torque as a function of speed. Since the maximum power is not limited by the converter and motor ratings only, but also by the available power in the generators, this limit should vary accordingly. By this method the power limitation will become fast and accurate, allowing to utilize the power system power capability with a built-in blackout prevention.

8.9.7 Shaft Speed Feedback Control

For conventional FPP a speed controller is used to achieve the commanded propeller force. Given a specified force command T_r the corresponding reference (commanded) speed of the propeller n_r is found by the shaft speed mapping in (8.47). The shaft speed PI controller utilizes shaft speed feedback from the thruster, and sets the commanded motor torque Q_{cn} according to

$$Q_{cn} = K_p e + K_i \int_0^t e(\tau) d\tau, \tag{8.54}$$

where the shaft speed error is $e = n_r - n$, and K_p and K_i are the nonnegative PI gains. The motor torque is controlled by the inner torque control loop. K_i is often given as $K_i = K_p/T_i$, where T_i is the integral time constant. The integral term in the PI controller should be limited according to $Q_{\max}$ to avoid integral windup.

8.9.8 Torque Feedforward Control

In the torque control strategy the outer speed control loop is removed, and the thruster is controlled by its inner torque control loop with a commanded torque Q_{cq} as set-point. A mapping from the reference thrust T_r to the reference torque Q_r can be found from (8.11a) and (8.11b) with K_{T0} and K_{Q0} replaced by K_{TC} and K_{QC}. The commanded motor torque Q_{cq} is set equal to the reference torque:

$$Q_{cq} = Q_r = \frac{K_{QC}}{K_{TC}} D T_r. \tag{8.55}$$

If the response of the thruster is slow, e.g. due to high rotational inertia, the inertia compensation scheme in (8.49) may be needed to speed up the response. This replaces the "inner torque algorithm" (Figure 8.15).

8.9.9 Power Feedback Control

Power control is based on controlling the power consumption of the thruster motor. The inner torque control loop is maintained, and the reference power P_r is found by inserting Q_r from (8.55) and n_r from (8.47) in (8.11c) such that

$$P_r = Q_r 2\pi n_r = |T_r|^{3/2} \frac{2\pi K_{QC}}{\sqrt{\rho} D K_{TC}^{3/2}}. \tag{8.56}$$

To determine the torque direction, the signed reference power P_{rs} is defined as

$$P_{rs} = sign(T_r) P_r = sign(T_r)|T_r|^{3/2} \frac{2\pi K_{QC}}{\sqrt{\rho} D K_{TC}^{3/2}}. \tag{8.57}$$

The commanded motor torque Q_{cp} is calculated from P_{rs} using feedback from the measured shaft speed $n \neq 0$ according to

$$Q_{cp} = \frac{P_{rs}}{2\pi|n|} = \frac{K_{QC}}{\sqrt{\rho} D K_{TC}^{3/2}} \frac{sign(T_r)|T_r|^{3/2}}{|n|}. \tag{8.58}$$

Note that the power controller is singular for zero shaft speed. As in torque control the inertia compensation scheme in (8.49) may be added if the response of the thruster is slow, replacing the "inner power algorithm".

8.9.10 Combined Torque and Power Control

A significant shortcoming of the power control scheme in (8.58) is the fact that it is singular for zero shaft speed. This means that power control should not be used close to the singular point, for example when commanding low thrust or changing the thrust direction. For low thrust commands, torque control shows better performance in terms of constant thrust production, since the mapping from thrust to torque is more directly related to the propeller loading than the mapping from thrust to power. For high thrust commands, it is essential to avoid power transients, as these lead to higher fuel consumption and possible danger of power blackout and harmonic distortion of the power plant network. Power control is hence a natural choice for high thrust commands. This motivates the construction of a combined torque/power control scheme, utilizing the best properties of both controllers.

Combining the reference torque from the torque controller Q_{cq} given by (8.55) and the reference torque from the power controller Q_{cp} given by (8.58), the commanded motor torque Q_{cc} from the combined torque/power controller is defined as:

$$Q_{cc} = \alpha_c(n) Q_{cq} + (1 - \alpha_c(n)) Q_{cp}. \tag{8.59}$$

$\alpha_c(n)$ is a weighting function:

$$\alpha_c(n) = e^{-k|pn|^r}, \text{ for } n \in \mathbb{Z}, \tag{8.60}$$

where k, p and r are positive constants. It satisfies:

$$\lim_{n\to 0} \alpha_c(n) = 1, \quad \lim_{n\to\infty} \alpha_c(n) = 0,$$

and shows smooth behavior for all n. Particularly, $d\alpha_c/dn = 0$ for $n = 0$ and $n \to \pm\infty$. The shape of $\alpha_c(n)$ defines the dominant regimes of the two control schemes, and can be used to tune the controller according to user specifications. The parameter p will act as a scaling factor for n. A small p will widen the weighting function, giving a wider transition between 0 and 1. Increasing the parameter k sharpens the peak about $n = 0$, whereas r widens it and makes the transition from 0 to 1 more steep. The shaft speed is physically limited to some max value $n_{\max}$, such that $\alpha_c(n_{\max})$ should be close to zero. It is easily shown that Q_{cc} is non-singular if $r > 1$. Hence, the power control singularity for $n = 0$ is removed.

Remark 8.3 *The torque and power controllers aim at controlling the motor torque or power, respectively. There is no need for integral action in these controllers, since the motor torque is controlled by its inner torque control loop. Consequently, the torque and power controllers allow the shaft speed of the propeller to vary with the propeller loading, in order to keep the torque or power constant.*

Figure 8.18 shows $\alpha_c(n)$ for varying k, p and r. The parameter p will act as a scaling factor for the weighting variable n. A small p will widen the weighting function, giving a wider transition between 0 and 1. Increasing the parameter k sharpens the peak about $n = 0$, whereas r widens it and makes the transition from 0 to 1 more steep.

The weight function must show smooth behavior for all x. The derivative of α with respect to x is

$$\begin{aligned}\frac{d\alpha_c(n)}{dn} &= -k\,|pn|^r\, e^{-k|pn|^r}(-kpr\,|pn|^{r-1}) \\ &= k^2 pr\,|pn|^{2r-1}\, e^{-k|pn|^r} \\ &= k^2 p^{2r} r\,|n|^{2r-1}\,\alpha_c(n), \end{aligned} \tag{8.61}$$

which is smooth in x. Particularly, $d\alpha_c/dn = 0$ for $n = 0$ and $n \to \pm\infty$.

8.10 Thruster Control in Extreme Conditions

8.10.1 Loss Estimation and Ventilation Detection

In the development of the anti-spin thruster controller, a scheme for thruster performance monitoring and ventilation detection will be essential. This section presents a *load torque observer* based on the thruster rotational dynamics in (8.28), as presented in Smogeli (2006). The load torque estimate can be used to calculate the *estimated torque loss* factor $\hat{\beta}_Q$. Finally, a *ventilation detection* scheme based on $\hat{\beta}_Q$ and the measured motor torque Q_m will be developed.

Load Torque Observer

From (8.28), the following control plant model of the thruster dynamics is proposed:

$$\begin{aligned} I_s\dot{\omega} &= Q_m - Q_a - Q_{ff0}(n_r) - Q_{f1}\omega + \delta_f, \\ \dot{Q}_a &= w_q, \end{aligned} \tag{8.62}$$

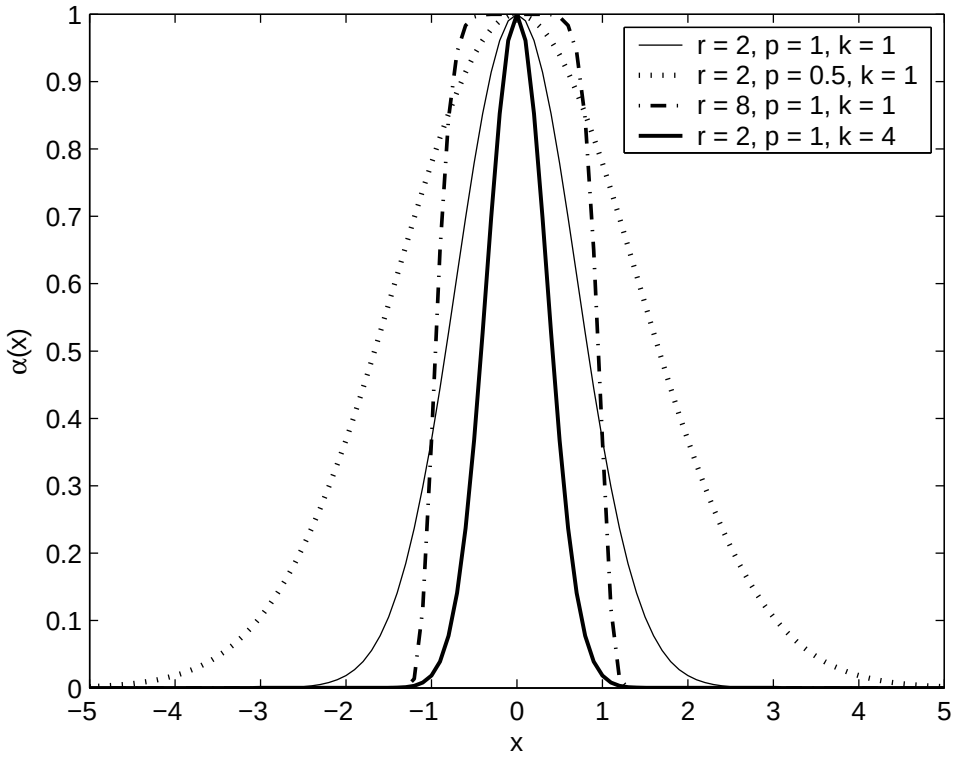

Figure 8.18: Weight function $\alpha_c(x)$ for varying r, p and k.

where the measured Q_m has been used instead of Q_c. Since $K_Q(n, \mathbf{x}_p, \theta_p)$ in (8.4) is unknown and may exhibit highly nonlinear behavior, Q_a is here assumed to be a bias term driven by an exogenous bounded disturbance w_q. This is necessary in order to capture the fast transients during ventilation. The static friction compensation term $Q_{ff0}(n_r)$ from (8.50) is used instead of a static friction model based on ω in order to avoid oscillations in this term about $\omega \approx 0$. Errors in the friction model are accounted for by δ_f. With the measurement $y = \omega + v$ contaminated with a bounded disturbance v, and $\hat{y} = \hat{\omega}$, a propeller load torque observer copying the control plant model (8.62) is:

$$\begin{aligned} \dot{\hat{\omega}} &= 1/I_s[Q_m - \hat{Q}_a - Q_{ff0}(n_r) - Q_{f1}\hat{\omega}] + k_a(y - \hat{y}), \\ \dot{\hat{Q}}_a &= k_b(y - \hat{y}), \end{aligned} \tag{8.63}$$

where k_a and k_b are the observer gains. In Smogeli and Sørensen (2009) it is shown that with a constant load torque Q_a implied by $w_q = 0$, zero measurement disturbance $v = 0$, and perfect friction knowledge such that $\delta_f = 0$, the equilibrium point of the observer estimation error is globally exponentially stable (GES) if the observer gains are chosen as $k_a > -Q_{f1}/I_s$ and $k_b < 0$.

Torque loss estimation

For DP operation the *expected* nominal propeller load torque $\hat{Q}_n$ may be calculated from (8.11b) by feedback from the propeller shaft speed n. Based on (8.20), the estimated torque loss factor

$\hat{\beta}_Q$ is calculated from $\hat{Q}_a$ in (8.63) and $\hat{Q}_n$ as:

$$\hat{\beta}_Q = \frac{\hat{Q}_a}{\hat{Q}_n} = \frac{\hat{Q}_a}{K_{QC}\rho D^5 n\,|n|}, \quad n \neq 0, \tag{8.64}$$

where the control coefficient K_{QC} (usually equal to K_{Q0}) is used to calculate $\hat{Q}_n$.

Remark 8.4 *There are no thrust losses for $n = 0$. Hence, the singularity for $n = 0$ is easily avoided by redefining (8.64) as $\hat{\beta}_Q = \alpha_b(n) + (1 - \alpha_b(n))\hat{Q}_a/\hat{Q}_n$, where $\alpha_b(n)$ is a function of the type (8.60).*

Ventilation detection

In this work, the ventilation detection algorithm is implemented by defining limits for the onset and termination of ventilation, $\beta_{v,on}$ and $\beta_{v,off}$, and generating a detection signal by monitoring the thrust loss factor $\hat{\beta}_Q$. An additional criterion for detection is that the magnitude of the motor torque Q_m is non-increasing. A ventilation incident will then give the following evolution of the detection signal ζ, with time instants $t_1 < t_2 < t_3$:

$$\begin{array}{lcl} t_1: & \hat{\beta}_Q > \beta_{v,on} & \Rightarrow \zeta = 0, \\ t_2: & \hat{\beta}_Q \leq \beta_{v,on} \cap sign(Q_m)\dot{Q}_m \leq 0 & \Rightarrow \zeta = 1, \\ t_3: & \hat{\beta}_Q \geq \beta_{v,off} & \Rightarrow \zeta = 0. \end{array} \tag{8.65}$$

To avoid switching and chattering of the detection signal due to measurement noise and transients, an algorithm implementing a detection delay is added, such that once ventilation has been detected, it cannot be reset until after a given time interval T_{vent}. The detection delay can be seen as an implementation of the switching dwell-time proposed in Hespanha (2002). This ventilation detection scheme has shown good performance in both simulations and experiments. Note that $\beta_{v,on}$ should be chosen significantly lower than 1 in order to allow for natural oscillations about the nominal propeller loading due to time-varying inflow to the propeller.

8.10.2 Anti-spin Thruster Control

The torque and power controllers, although advantageous for normal operating conditions, will show unacceptable behavior when subject to large thrust losses. The nature of this problem is in many ways similar to that of a car wheel losing traction on a slippery surface during acceleration or braking. The work on anti-spin thruster control has therefore been motivated by similar control strategies in car anti-spin and ABS braking systems. With any of the core controllers from Section 8.9 in use for normal operating conditions, the proposed anti-spin control scheme is divided in two:

1. Primary anti-spin action: override the core controller and take control of the shaft speed.
2. Secondary anti-spin action: lower the setpoint of the controller to reduce the shaft speed.

Similarities to car anti-spin/ABS

Since both the structures of the physical systems and the control objectives are similar, the development of the thruster anti-spin control system has been motivated by similar hybrid control strategies in car anti-spin and ABS systems. In car anti-spin/ABS, a commonly used model is the "quarter car".

$$\begin{aligned} I_w\dot{\omega}_w &= -rF_x + Q_w, \\ \frac{F_x}{F_z} &= \mu(\lambda), \\ m\dot{v} &= F_x, \end{aligned} \tag{8.66}$$

where I_w is the wheel rotational inertia, ω_w is the wheel angular velocity, r is the wheel radius, F_x is the tire friction force, Q_w is the breaking or accelerating input torque to the wheel from brakes and motor, F_z is the vertical force between tire and road, μ is the tire friction coefficient, λ is the wheel slip, m is the mass of a quarter car, and v is the car speed. The actuator dynamics have been neglected.

$$\lambda = \begin{cases} 1 - \frac{r\omega_w}{v} & \text{if} \quad v > r\omega_w, \quad v \neq 0, \qquad \text{(braking)}, \\ 1 - \frac{v}{r\omega_w} & \text{if} \quad v < r\omega_w, \quad \omega_w \neq 0, \quad \text{(accelerating)}. \end{cases} \tag{8.67}$$

When $\lambda = 1$ there is no sliding (pure rolling), and when $\lambda = 0$ there is full sliding. The shape of the friction coefficient $\mu(\lambda)$ depends on many parameters, which can be summed up in the tire characteristics, the road conditions, and the vehicle operational conditions. The aim of the anti-spin/ABS control systems is commonly to keep the wheel slip at a specified set-point or to maintain a specified wheel acceleration.

When comparing the two models for propulsion and car anti-spin, many similarities may be noticed. The rotational dynamics of the propeller and the wheel are identical, with inertial terms $I_s\dot{\omega}$ and $I_w\dot{\omega}_w$, motor input terms Q_m and Q_w, and load torque terms $Q_a = f_Q(\theta, \xi)$ and $rF_x = rF_z\mu(\lambda)$ respectively. In both cases, the aim of the anti-spin control is to optimize the load torque through control of the motor input. For car anti-spin, a too high input torque will lead to loss of friction through spin (acceleration) or wheel lock (braking), and hence reduced acceleration or stopping force. For thruster anti-spin, a too high load on a propeller operating close to the free surface will lead to loss of torque through ventilation, and hence loss of thrust. In addition, the propeller load torque and tire friction force depend on many other parameters, most of which are unknown to the controller.

However, some differences should also be noticed. The tire friction force can be directly related to the vehicle dynamics, and the wheel slip can be estimated from the vehicle speed and wheel angular velocity. This leaves only the friction coefficient $\mu(\lambda)$ unknown. However, for most conditions, the shape of the friction coefficient will be known, making it possible to develop a general anti-spin scheme. The propeller load torque Q_a is composed of several complex physical phenomena, and must be considered as an exogenous disturbance from a control point of view. In addition, no general mapping between the load torque and the propeller thrust T_a exists. And even if this mapping could be established, the relationship between the propeller thrust and the vessel dynamics is more complex than the car dynamics, especially for a vessel equipped with multiple propellers. Finally, the operating conditions of the propeller will probably be changing faster than for the wheel; the propeller could be constantly moving in and out of water, whereas the wheel may experience less rapidly changing road conditions.

Primary anti-spin action

If a ventilation incident is detected by the detection algorithm in (8.65), the desired primary anti-spin control action is to take control of the shaft speed until the ventilation has terminated. This is done by modifying the core controller output Q_{ci} in (8.44) with a torque scaling factor γ:

$$Q_{cas} = \gamma Q_{ci}, \tag{8.68}$$

where Q_{cas} is the anti-spin commanded torque, and γ is proposed as:

$$\gamma = \begin{cases} 1 & \text{for} \quad \zeta = 0 \quad \text{(not ventilated)}, \\ \hat{\beta}_Q & \text{for} \quad \zeta = 1 \quad \text{(ventilated)}. \end{cases} \tag{8.69}$$

In Smogeli and Sørensen (2009) it is shown that the anti-spin control law will give a bounded shaft speed during ventilation.

Secondary anti-spin action: setpoint mapping

For optimization of thrust production and reduction of wear and tear due to dynamic propeller loading during ventilation, it may desirable to reduce the propeller shaft speed. This can be done by modifying the thrust reference during ventilation, since the primary anti-spin control action assures that the shaft speed is kept close to its reference. The desired shaft speed during ventilation, n_{as}, will be a thruster specific parameter, and must be chosen as a trade-off between thrust production, wear and tear, and response time. The nominal shaft speed reference n_r from (8.47) should not be changed to n_{as} instantaneously, as this will lead to undesired transients. It is therefore proposed to add a low-pass filter with time constant τ_n and a rate limiting algorithm to the change from n_r to n_{as} at ventilation detection, and from n_{as} to n_r at ventilation termination. The filtered and rate limited shaft speed reference is termed n_{ras}, i.e. $\dot{n}_{fall} < \dot{n}_{ras} < \dot{n}_{rise}$, where $\dot{n}_{fall}$ and $\dot{n}_{rise}$ are the rate limits. The thrust reference corresponding to n_{ras} is termed T_{ras}, and is given by (8.11a) with K_{T0} replaced by K_{TC}:

$$T_{ras} = sign(n_{ras}) K_{TC} \rho D^4 n_{ras}^2. \tag{8.70}$$

Since (8.70) is the inverse of (8.47), $T_{ras} \equiv T_r$ when ventilation is not detected.

8.10.3 Implementation Aspects

Perfect shaft speed control during ventilation would be possible if the ventilation incident could be foreseen, and $\beta_Q(t, \omega)$ was known. However, since the propeller torque is not available as a measurement, and the ventilation incidents are random processes caused by wave elevation and vessel motion, this is not possible. An implementable solution is to use the torque loss estimation and ventilation detection schemes. The deviation of the shaft speed from the steady-state solution will then depend on the deviation of the torque modification factor γ from the actual torque loss factor $\beta_Q(t, \omega)$ during ventilation.

To achieve the best possible control over the shaft speed during ventilation, γ should be switched from 1 to $\hat{\beta}_Q$ immediately when ventilation is detected. However, in order to avoid transients in the control input, the transition of γ from 1 to $\hat{\beta}_Q$ at ventilation detection, and from $\hat{\beta}_Q$ to 1 at ventilation termination, should be rate limited, i.e. $\dot{\gamma}_{fall} < \dot{\gamma} < \dot{\gamma}_{rise}$. The rate limits $\dot{\gamma}_{rise}$ and $\dot{\gamma}_{fall}$ would typically be of magnitude 1. Furthermore, to avoid using the

potentially noisy estimate $\hat{\beta}_Q$ directly in the control law, it may be beneficial to filter γ by a properly chosen low-pass filter with time constant τ_γ.

A block diagram of the resulting thruster controller with anti-spin is shown in Figure 8.19. Note that the proposed anti-spin controller may be used with all the core controllers from Section 8.9.

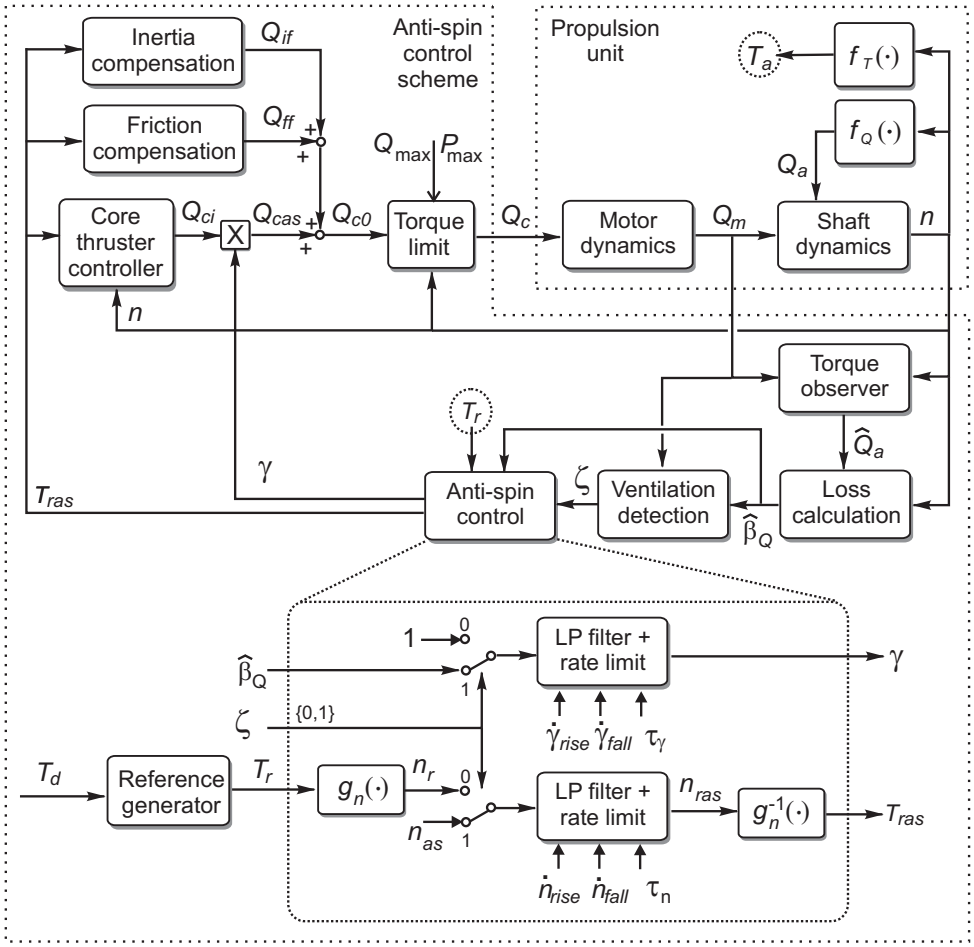

Figure 8.19: The anti-spin control scheme, including core controller, torque observer, loss calculation, ventilation detection, and anti-spin control actions.

Remark 8.5 *The deviation of γ from $\beta_Q(t,\omega)$ during ventilation will be affected by the ventilation detection scheme, the accuracy of the estimated torque loss factor $\hat{\beta}_Q$, and the chosen rate limits and low-pass filter for γ. The proposed rate limits and filter on γ will lead to a larger perturbation bound, and hence also a larger shaft speed bound. However, with reference to the control objectives, this may be a necessary trade-off to avoid unnecessary wear and tear and power transients.*

Remark 8.6 *A well-tuned shaft speed controller will produce a controller output similar to the proposed anti-spin controller in (8.68) during ventilation, since the objective of the shaft speed controller is to keep the shaft speed constant, regardless of the load disturbance. However, since*

it is desired to use torque and power control in normal conditions, using a shaft speed controller during ventilation would require switching between the two controllers. This approach is further discussed in Smogeli (2006). If shaft speed control is chosen for normal conditions, anti-spin control may not be necessary. However, performance improvements may still be achievable.

Remark 8.7 *From a practical point of view, the proposed torque/power controller with anti-spin requires more system knowledge than a conventional shaft speed controller. However, the most important parameters are all readily available from the propeller and motor characteristics. In addition, all industrial installations of thruster controllers require some manual tuning. Hence, the remaining parameters, like the various rate limits and filter time constants, may be tuned on site. The experience so far has been that the performance is acceptable within a large parameter range.*

8.11 Sensitivity to Thrust Losses

In order to analyze the performance and the robustness of the control laws given above we will demonstrate the sensitivity subject to thrust losses. In order to compare the different control schemes a simplified sensitivity analysis is carried out to address the most significant properties of speed control, torque control and power control. Pitch control is not studied, but is expected in general to have the same behavior as speed control.

8.11.1 Shaft Speed Feedback Control

Assume that the shaft speed equals the speed reference at steady state. Using (8.11a), (8.17) and $n = \text{sgn}(n)\sqrt{\frac{T_n}{\rho_w D^4 K_T}}$, the relationship between actual propeller thrust and the reference thrust becomes

$$T_a = h_T(\cdot)(1-t_d)\frac{K_T}{K_{T0}}T_{\text{n}} \triangleq s_n(\cdot)T_{\text{n}}. \tag{8.71}$$

Using (8.19) we can show that $s_n(\cdot) = \beta_T$.

8.11.2 Torque Feedforward Control

From a similar consideration of the torque control scheme, it is assumed that the motor torque and the propeller torque equal the torque reference $Q_n = sign(n)K_{Q0}\rho D^5 n^2$ at steady state. Hence, combining (8.11a), (8.4), (8.17), and (8.18) yields

$$T_a = \frac{h_T(\cdot)(1-t_d)}{h_Q(\cdot)}\frac{K_{Q0}}{K_Q}\frac{K_T}{K_{T0}}T_{\text{n}} \triangleq s_Q(\cdot)T_{\text{n}}. \tag{8.72}$$

Using (8.20) we can show that $s_Q(\cdot) = \frac{\beta_T}{\beta_Q}$.

8.11.3 Power Feedback Control

For the power control scheme the propeller and motor power tend to the power reference P_{d} at steady state. Hence, combining (8.11a), (8.4), (8.18), and (8.56) yields

$$T_a = \frac{h_T(\cdot)(1-t_d)}{h_Q^{2/3}(\cdot)}\left(\frac{K_{Q0}}{K_Q}\right)^{2/3}\frac{K_T}{K_{T0}}T_{\text{n}} \triangleq s_P(\cdot)T_{\text{n}}. \tag{8.73}$$

We can show that $s_P(\cdot) = \frac{\beta_T}{\beta_Q^{2/3}}$.

8.11.4 Combined Power and Torque Control

The analysis of the sensitivity of the combined power/torque controller is not as straightforward as in the preceding cases. However, since the combined controller is a linear combination of the power and torque controllers, it is a reasonable assumption that the sensitivity function for combined power/torque control $s_c(\cdot)$ may be expressed as

$$s_c(\cdot) = \frac{\beta_T}{\beta_Q{}^{\kappa}} \quad \text{for} \quad \kappa \in [\tfrac{2}{3}, 1], \tag{8.74}$$

such that for high n, $s_c(\cdot) \approx s_P(\cdot)$ and for low n, $s_c(\cdot) \approx s_Q(\cdot)$. It can be shown that κ then may be approximated by the linear function $\kappa = 2/3 + 1/3\alpha_c(n)$, where $\alpha(n)$ is the weighting function used in the combined controller (8.59).

8.11.5 Positioning Performance

The effect of positioning performance for the different control schemes is clearly seen from the two examples illustrated in Figures 8.20 and 8.22.

Example 8.1 *Let $t_d = 0$ and $h_T = h_Q = 1$. By using (8.8), (8.9), $K_{T0} = K_T(J_a = 0)$ and $K_{Q0} = K_Q(J_a = 0)$ with the same parameters as used in Figure 8.5 for $P/D = 0.89$, the sensitivity functions s_n , s_Q , and s_P (8.71)–(8.73) can be computed as a function of advance ratio J_a, see Figure 8.20. As expected all three sensitivity functions decrease, resulting in increased thrust losses, for increasing J. The speed control scheme is less robust for variations in J_a, while the torque control scheme shows the best robustness.*

Example 8.2 *Thrust losses (Figure 8.21) caused by in-and-out-of-water effects can be modelled by the thrust and the torque reduction functions h_F and h_T (8.17)- (8.18) as a function of the submergence of the propeller shaft h divided by the propeller radius R. The reduced disc area due to the reduced submergence is accounted for in the computation of (8.8) and (8.9) according to Lehn (1992). Let $t_d = 0$, $K_{T0} = K_T(J_a = 0)$ and $K_{Q0} = K_Q(J_a = 0)$ with the same parameters as used in Figure 8.5 for $P/D = 0.89$, then the sensitivity functions s_n , s_T, and s_P (8.71)–(8.73) can be computed as a function of h/R, see Figure 8.22. As expected all three sensitivity functions decrease, resulting in increased thrust losses, for decreasing h/R. The speed control scheme appears to be less robust for reduced submergence, while the torque control scheme appears to show the best robustness. However, care should be taken concerning these observations. In order to achieve the reduced sensitivity, the torque controller will increase the thruster speed significantly, resulting in propeller racing. This is an undesired effect. As shown here, this will be solved by the anti-spin controller.*

8.11.6 Sensitivity Functions Summary

Based on the controller formulations, the relations in the previous section, and assuming that all controllers perform ideally, the steady-state sensitivity functions for speed control, torque control and power control are shown in Table 8.2. For details in the derivation of the sensitivity functions, see Sørensen et al. (1997) and Smogeli Smogeli (2006).

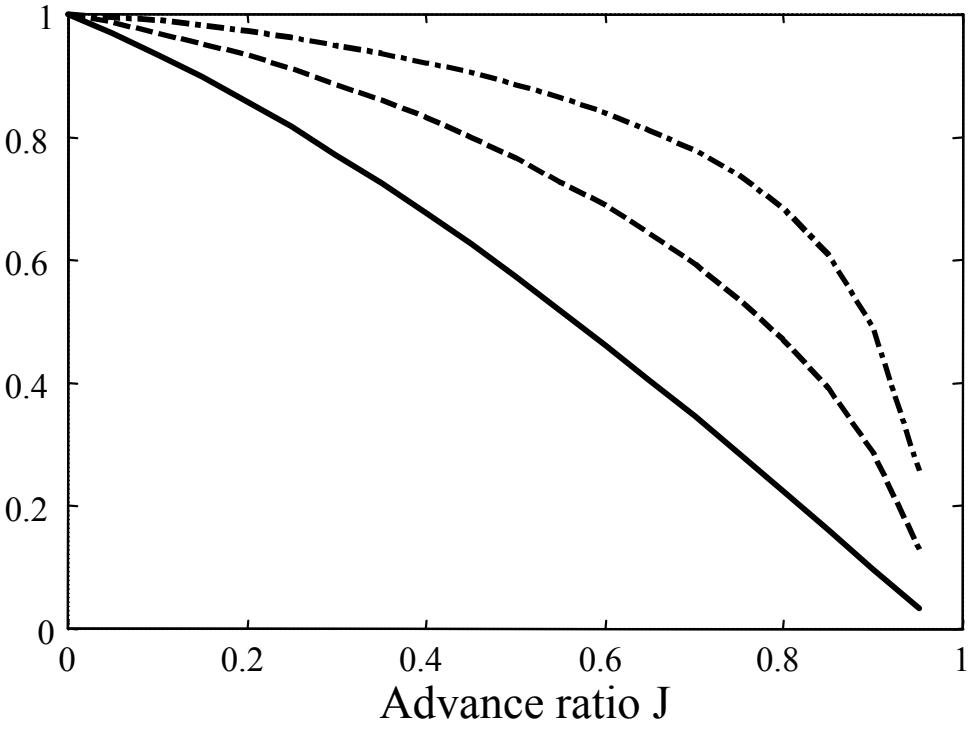

Figure 8.20: Sensitivity functions for the different control schemes: s_n (solid), s_Q (dash-dot) and s_P (dash) as function of advance ratio J_a for $P/D = 0.89$.

The analysis of the sensitivity of the combined torque/power controller is not as straightforward as in the preceding cases. In Smogeli (2006) it is shown that for the combined controller the sensitivity function $st_c(\cdot)$ may be expressed as

$$st_c(\cdot) \approx \frac{K_T}{K_{TC}} \left(\frac{K_{QC}}{K_Q}\right)^{2/3+1/3\alpha_c}, \tag{8.75}$$

such that for high n, $st_c(\cdot) \approx st_p(\cdot)$ and for low n, $st_c(\cdot) \approx st_q(\cdot)$. For $K_{QC}/K_Q > 0.02$ this gives an error of less than 5%, and has the correct limiting values for $\alpha_c = 0$ and $\alpha_c = 1$. Through α_c the combined controller thrust sensitivity is dependent on the shaft speed n, which makes it less convenient for analysis. However, it is clear that $st_c(\cdot)$ will lie between $st_q(\cdot)$ and $st_p(\cdot)$ for all n. It is interesting to note that if the controllers have knowledge of the instantaneous values of K_T and K_Q, such that $K_{TC} = K_T$ and $K_{QC} = K_Q$ at all times, all sensitivity functions reduce to unity, since n_r from (8.47), Q_r from (8.55), and P_r from (8.57) will be equal to the true values n, Q_a, and P_a. This means that all controllers perform identically. Also notice that $sn_i(\cdot)sq_i(\cdot) \equiv sp_i(\cdot)$ for all controllers, as should be expected.

8.12 Experiments

This section presents experimental results with the controllers designed above. The importance of the friction compensation scheme is investigated, and the dynamic performance of the controllers in various operating conditions tested.

The majority of the experiments were conducted for shaft speed control, torque control, and power control, since the main purpose of this work was to test the properties of the basic

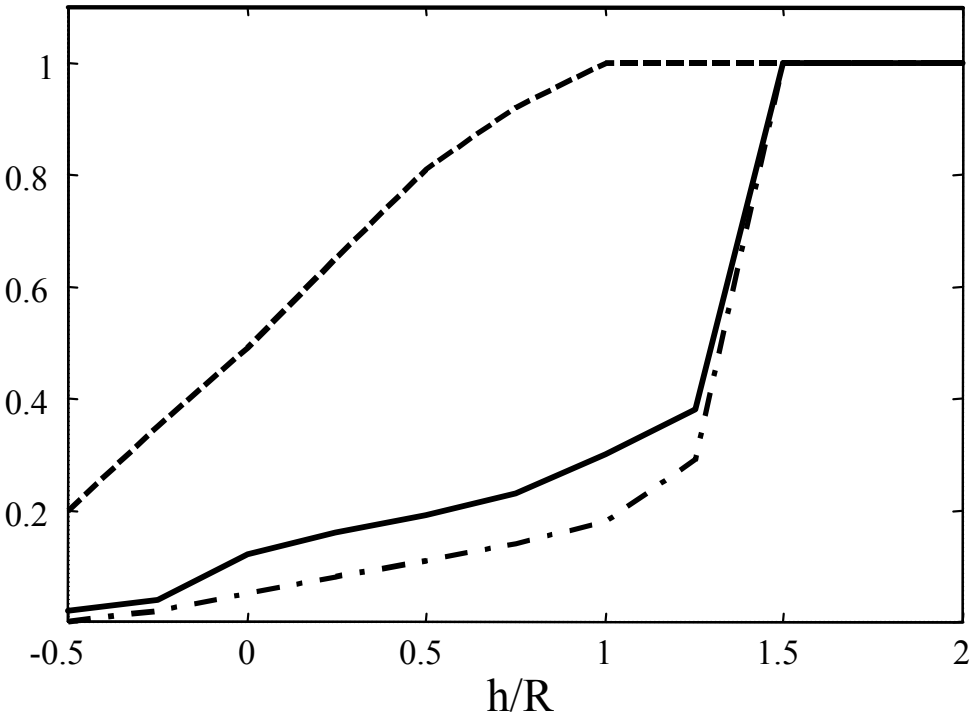

Figure 8.21: Mean thrust losses h_T (dash-dot), h_Q (solid) and reduced disk area (dash) due to reduced submergence in calm water of a heavily loaded propeller as a function h/R for $P/D = 0.89$, based on Fig. 4.1 in Lehn.

thruster control methods. The combined torque/power controller was also tested, and behaved exactly as expected. Its performance can be inferred from the performance of the torque and power controllers.

8.12.1 Experimental Setup

The experiments were conducted in the Marine Cybernetics Laboratory (MCLab) at NTNU. The MCLab basin is 40m long, 6.45m wide, and 1.5m deep, and is equipped with a towing carriage and a wave-maker system. Two types of setups were used during the various tests. The tested propeller was of conventional design with 4 blades, pitch ratio at 70% of the propeller radius $P/D = 1.0$, and expanded blade area ratio $EAR = 0.55$. The propeller was tested both with and without duct. For the results presented here a duct was used for the anti-spin tests only. The propeller was attached to a shaft equipped with thrust and torque sensors inside an underwater housing, and driven by an electric motor via shafts and gears with gear ratio 1:1. The rig with motor, gears, underwater housing, shaft and propeller was fixed to the towing carriage on a vertical slide, which was used to control the submergence of the propeller relative to the free surface. Ventilation incidents could hence be generated by moving the propeller vertically with a calm free surface. The motor torque was controlled from a PC onboard the carriage, using feedback from the propeller shaft speed and the motor torque. The control code was generated by rapid prototyping using Opal RT-Lab and source code in Matlab/Simulink. A sketch of the experimental setup is given in Figure 8.23.

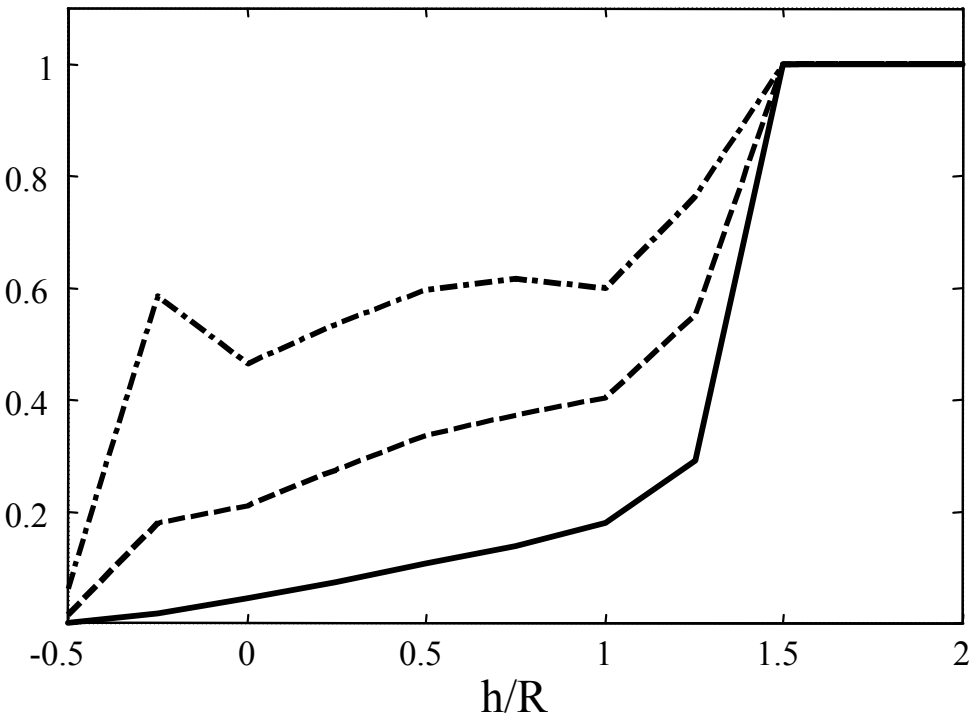

Figure 8.22: Sensitivity functions for the different control schemes: s_n (solid), s_Q (dash-dot) and s_P (dash) as function of h/R, h_T and h_Q.

The main characteristics of the ducted propeller and drive system are summarized in Table 8.3. The nominal thrust and torque coefficients for the propeller without duct were found to be $K_{T0} = 0.570$ and $K_{Q0} = 0.0750$. The nominal thrust and torque coefficients for reversed thrust were found to be $K_{T0r} = 0.393$ and $K_{Q0r} = 0.0655$.

Friction

In the experiments presented here, the shaft friction turned out to affect the performance of the torque and power controllers. A feedforward friction compensation scheme as proposed in Section 8.9.5 was therefore implemented. Over the course of the experiments, the friction compensation coefficients were found to be in the range $Q_{f0} \in [0.8, 1.0]$ and $Q_{f1} \in [0.009, 0.011]$.

Control parameters

The control coefficients K_{TC} and K_{QC} used in the experiments were as given by (8.45), with the half "width" of the transition region $n_c = 3$. The rotational inertia of the model-scale propeller was not found to be a dominating term. Hence, the inertia compensation scheme in (8.49) was not needed. Therefore, and since only feasible thrust reference trajectories were used, no reference generator as in (8.48) was used. The constant plus linear friction compensation scheme (8.50) was used, with Q_{f0} and Q_{f1} appropriately chosen in the range specified above. The switching "width" of the smooth switching function in (8.51) was chosen as $n_s = 0.5$. The shaft speed PI controller parameters (8.54) were chosen as $K_p = 0.2$ and $T_i = 0.05$ s, which gave adequate tracking properties. For the combined controller (8.59), the weighting function

Sensitivity	Speed control	Torque control	Power control
Thrust: $st_i(\cdot) \triangleq \frac{T_a}{T_r}$	$st_n(\cdot) = \frac{K_T}{K_{TC}}$	$st_q(\cdot) = \frac{K_T}{K_{TC}} \frac{K_{QC}}{K_Q}$	$st_p(\cdot) = \frac{K_T}{K_{TC}} (\frac{K_{QC}}{K_Q})^{2/3}$
Speed: $sn_i(\cdot) \triangleq \frac{n}{n_r}$	$sn_n(\cdot) = 1$	$sn_q(\cdot) = \sqrt{\frac{K_{QC}}{K_Q}}$	$sn_p(\cdot) = \frac{K_{QC}^{1/3}}{K_Q^{1/3}}$
Torque: $sq_i(\cdot) \triangleq \frac{Q_a}{Q_r}$	$sq_n(\cdot) = \frac{K_Q}{K_{QC}}$	$sq_q(\cdot) = 1$	$sq_p(\cdot) = \frac{K_Q^{1/3}}{K_{QC}^{1/3}}$
Power: $sp_i(\cdot) \triangleq \frac{P_a}{P_r}$	$sp_n(\cdot) = \frac{K_Q}{K_{QC}}$	$sp_q(\cdot) = \frac{K_{QC}^{1/2}}{K_Q^{1/2}}$	$sp_p(\cdot) = 1$

Table 8.2: Sensitivity functions, where i=n for shaft speed control, i=q for torque control, i=p for power control, and i=c for combined torque/power control

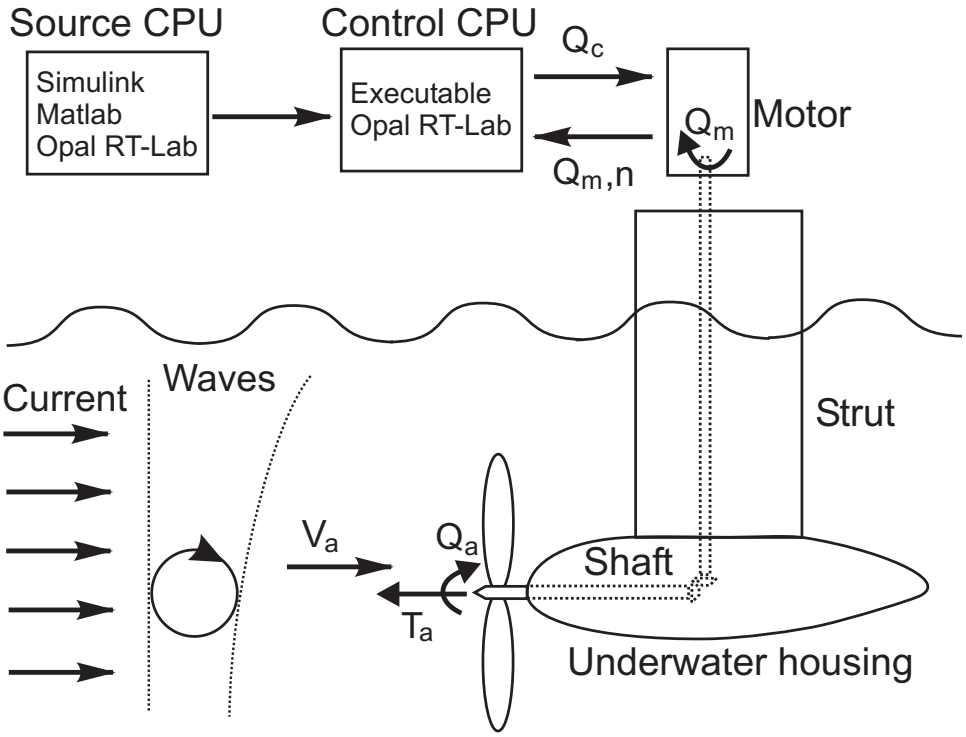

Figure 8.23: Sketch of the experimental setup.

parameters (8.60) were chosen as $[r, p, k] = [4, 0.5, 1]$. This gave a pure torque controller for $n < 0.5$ and a pure power controller for $n > 3$.

The friction compensation was chosen with $Q_{f0s} = 1.0$Nm and $Q_{f1} = 0.01$Nms. The inertia compensation was not needed for the small model-scale propeller. The control coefficients were chosen as $K_{TC} = K_{T0} = 0.513$ and $K_{QC} = K_{Q0} = 0.0444$. For the combined controller (8.59), the weighting function parameters (8.60) were chosen as $[r, p, k] = [4, 0.5, 1]$. This gave a pure torque controller for $n < 0.5$rps and a pure power controller for $n > 3$rps. The shaft speed PI controller parameters (8.54) were chosen as $K_p = 0.2$ and $T_i = 0.05$s.

In the load torque observer, the gains were chosen as $k_a = 15$ and $k_b = -25$. In the ventilation detection scheme, the parameters were chosen as $\beta_{v,on} = 0.6$ and $\beta_{v,off} = 0.9$, and the detection delay was set to $T_{vent} = 1$s. For the proposed anti-spin controller, the settings for the primary

D [m]	K_{T0}	K_{Q0}	I_s [kgm^2]	Q_s[Nm]	K_ω[Nms]
0.25	0.513	0.0444	0.05	1.0	0.01

Table 8.3: Main propeller data.

anti-spin action were $\dot{\gamma}_{rise} = 1\text{s}^{-1}$, $\dot{\gamma}_{fall} = -1\text{s}^{-1}$, and unless otherwise stated $\tau_\gamma = 0.3$s. For the secondary anti-spin action, the filter time constant was chosen as $\tau_n = 0.05$s, and the rate limits were chosen as $\dot{n}_{rise} = 3\text{s}^{-2}$ and $\dot{n}_{fall} = -3\text{s}^{-2}$. The desired shaft speed during ventilation was set to $n_{as} = 9$rps. The latter choice was motivated from observations during the tests, where it seemed that the most violent dynamic loading disappeared below 10rps. A maximum shaft speed of $n_{\max} = 25$rps was enforced.

The anti-spin control scheme appears to be robust to parameter tuning. In order to avoid detection chattering, however, it is important not to choose $\beta_{v,on}$ too large. In addition, if the rate limits are chosen too low or the filter time constants too large, the anti-spin controller response will become slow, and the shaft speed will be allowed to increase more during ventilation. A further discussion and guidelines on tuning are given in Smogeli (2006).

Figure 8.24 shows time series for the proposed anti-spin controller with varying filter time constants τ_γ at a thrust reference of 200N. Only the primary anti-spin action was used, such that the goal of the anti-spin controller here was to keep the shaft speed constant. $\tau_\gamma = 0.3$s was found to be a good trade-off between response time and noise in the control law, and used in the remainder of the tests presented below.

8.12.2 Nominal Tests

A total of 36 tests were run with zero advance velocity and varying motor setpoints. Each setpoint was run for approximately 60 seconds in order to get good statistical values. The nominal thrust and torque coefficients K_{T0} and K_{Q0} for varying propeller shaft speed n and $V_a = 0$ are shown in Figure 8.25, where also the mean values used in the rest of the work are shown. The resulting mean values were $K_{T0} = 0.5359$ and $K_{Q0} = 0.0832$. The shaft friction for the tested propeller was found as the steady-state difference between the motor torque Q_m and the propeller torque Q_a, and is plotted versus n in Figure 8.26. A second-order model was fitted to the data and used in the rest of the work. The model is only valid in the tested shaft speed range, i.e. $n \in [0, 10]$ rps.

8.12.3 Sensitivity Tests

In the sensitivity tests the thrust reference was kept constant at $T_{ref} = 100N$, the advance velocities were $V_a = \{-1, -0.5, 0, 0.5, 1, 1.5\}$ m/s and the speed, torque and power controllers were used. Each combination was run 3 times, giving a total of 54 runs. The length of the test series were limited by the length of the basin, but gave adequate statistical values. The thrust characteristics of the tested propeller is shown in Figure 8.27, where data points from all the sensitivity tests with positive advance velocities are compiled together with 3^{rd} order polynomial curve fits. The thrust and torque coefficients K_T and K_Q and the open-water efficiency η_0 were calculated using the mean values of T_a, Q_a and n from each run.

The performance of the three controllers are summed up in Figure 8.28, where the propeller thrust T_a, propeller torque Q_a, shaft speed n, motor torque Q_m and motor power P_m are shown for varying advance speeds. The friction compensation is not included in the plots of motor

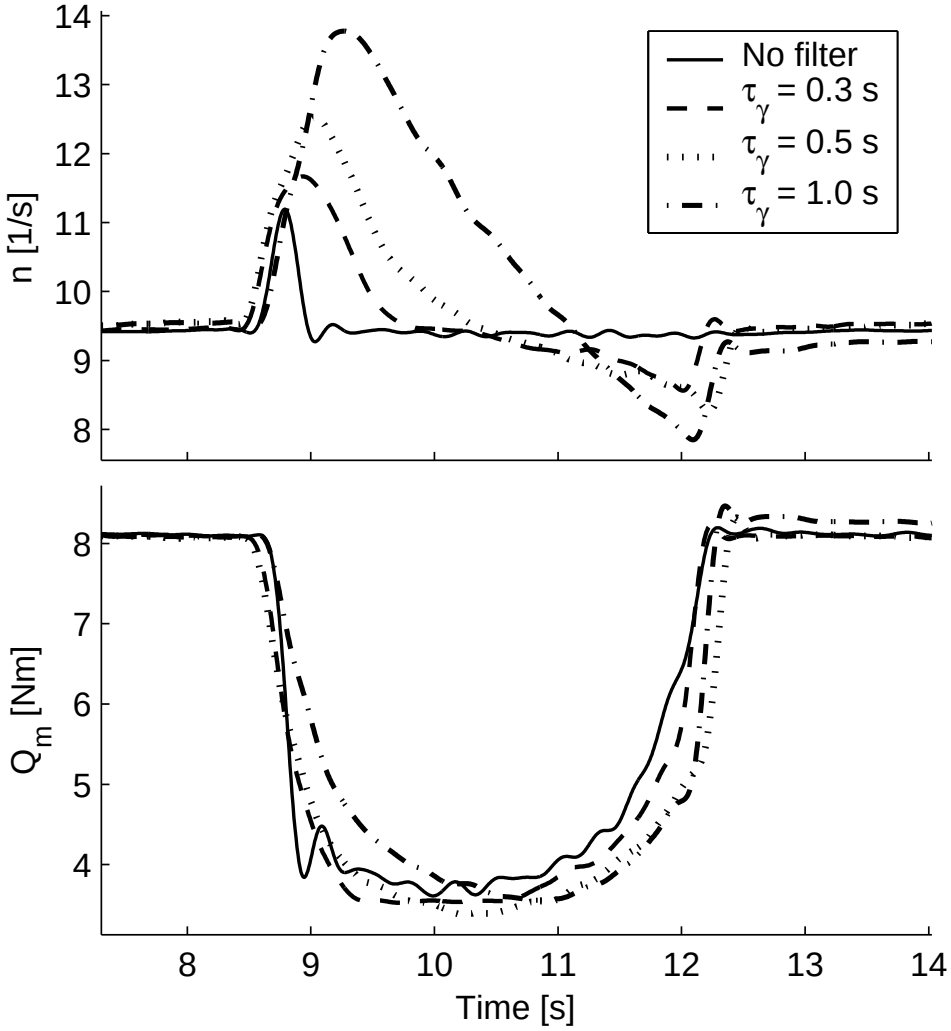

Figure 8.24: Comparison of shaft speed and motor torque during a ventilation incident for the combined controller with primary antispin action, using varying γ filter time constants at $T_r = 200$ N.

torque and power. It is clear that the three controllers obtain their objectives: The shaft speed controller keeps the shaft speed constant, the torque controller keeps the motor torque constant, and the power controller keeps the motor power constant. As the advance speed increases, the effective angle of attack of the propeller blades is decreased, and the propeller loading decreases for a constant shaft speed. This can be seen in terms of reduced propeller thrust and torque at increasing advance velocities for the shaft speed controller: At $V_a = 1.5m/s$, the propeller thrust is reduced from $100N$ to $18N$. The torque and power controllers have much better performance, since they will increase the shaft speed as the propeller loading decreases: At $V_a = 1.5m/s$, the propeller thrust is reduced from $100N$ to $65N$ and $50N$ respectively. The reason for the propeller torque not remaining constant for increasing advance velocities are inaccuracies in the

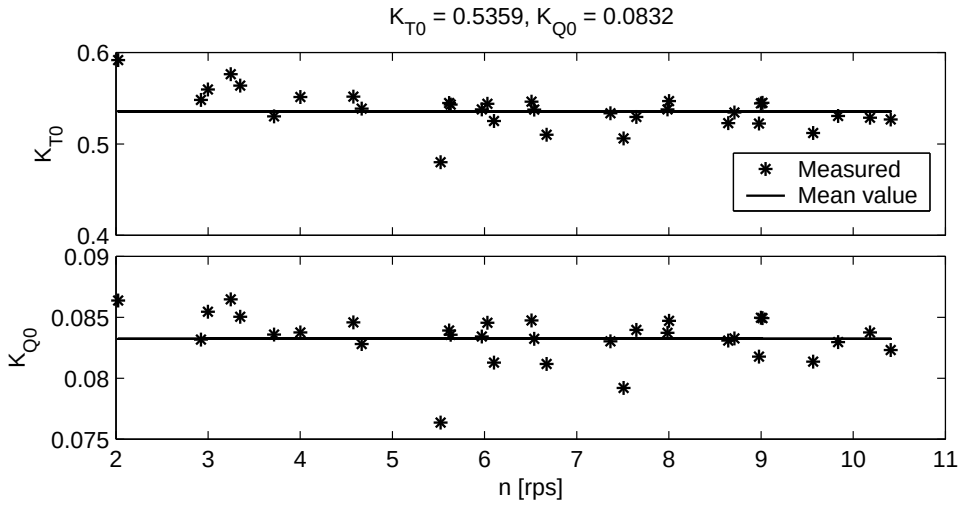

Figure 8.25: Nominal thrust coefficient K_{T0} and nominal torque coefficient K_{Q0} measurements for varying shaft speed n, and the mean values used in the rest of the work.

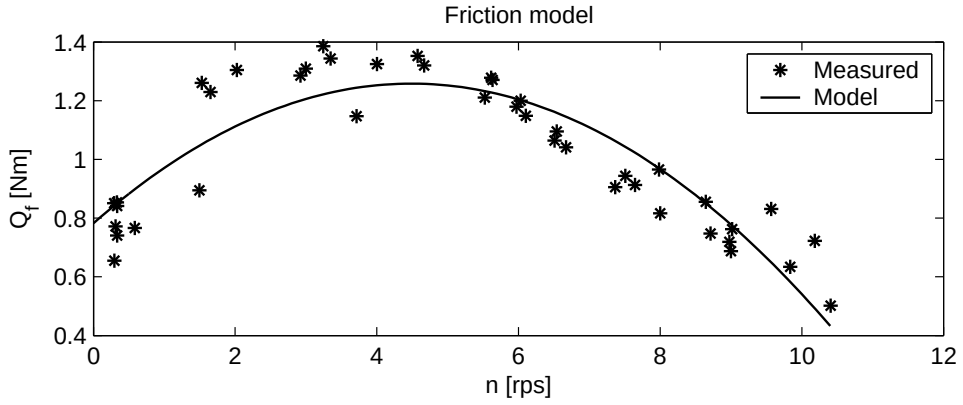

Figure 8.26: Shaft friction Q_f measurements for varying shaft speed n and the second order model used in the rest of the work.

friction model.

The sensitivity to variations in advance velocity V_a can be studied by representing K_T and K_Q as functions of J or V_a and ignoring all other loss effects, such that $K_T = K_T(J)$ and $K_Q = K_Q(J)$. The experimentally determined sensitivity functions for varying advance velocity are shown in Figure 8.29. This confirms that the shaft speed controller is the most sensitive and the torque controller the least sensitive to variations in advance velocity.

In all the results presented in this section, the data points for negative advance speeds are in general less accurate than for positive advance speeds due to inhomogeneous inflow to the propeller.

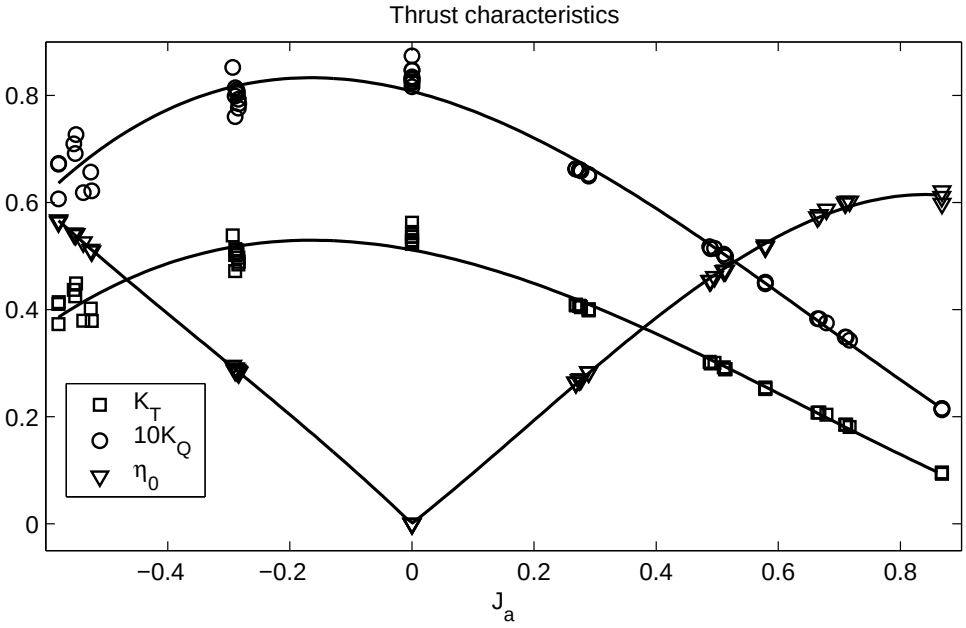

Figure 8.27: Thrust characteristics from experiments. The continuous lines are found from 3rd order polynominal fits to the data points.

8.12.4 Dynamic Tests in Waves

To validate the dynamic performance of the controllers when subject to rapidly changing inflow to the propeller a total of 34 tests in regular and irregular waves were performed. The thrust reference was $T_d = 100N$ and the carriage was kept stationary. A comparison of the controller performance in regular waves with wave height $8cm$ and period $1s$ is shown in Figure 8.30. DP functionality has been simulated, such that all controllers gave the same mean thrust. The results are summarized in the following:

- The shaft speed controller keeps the shaft speed constant, and has to vary the motor torque and power in order to achieve this. The resulting propeller thrust and torque have the largest variance.
- The torque controller keeps the motor torque constant, and as a result the shaft speed varies with the loading. The resulting propeller thrust and torque have the smallest variance.
- The power controller keeps the motor power constant, and as a result both the shaft speed and motor torque varies with the loading. The resulting propeller thrust and torque lie between the shaft speed and torque controller values.

8.12.5 Anti-spin Tests

The anti-spin control scheme was tested in a variety of operating conditions: for constant and time-varying thrust references, in waves, with a calm free surface and forced vertical motion of varying amplitude A_v, period T_v, and mean submergence h_0, and in combinations of waves

and vertical motion. In the results presented here, the thrust reference was kept constant during forced vertical motion with a calm free surface. This improved repeatability and enabled comparison of the various controllers, since the time series could be synchronized by comparing the relative vertical motion of the propeller. Because of the chaotic nature of ventilation, the actual operational conditions for the propeller vary from one test run to another. However, the repeatability is in general good. The results presented below are for $h_0 = 15$cm, $A_v = 15$cm, and $T_v = 5$s. Performance comparisons in other conditions, further validating the robust performance of the anti-spin controller, are presented in Smogeli (2006).

Figure 8.31 shows comparisons of the thrust T_a, propeller torque Q_a, shaft speed n, motor torque Q_m, and motor power P_m for four different thruster controllers during a ventilation incident with $T_r = 200$N. The ventilation incident starts at $t \approx 11.2$s, and terminates at $t \approx 14.5$s. The compared controllers are shaft speed PI control (8.54), torque control (8.55), power control (8.58), and the proposed anti-spin controller based on combined torque/power control (8.59). With anti-spin activated, both the primary (8.68) and the secondary (8.70) anti-spin actions were used. The time series show that the torque controller and the power controller both lead to propeller racing. The shaft speed controller and the anti-spin controller limit the shaft speed as intended, with the secondary anti-spin action giving a slightly reduced shaft speed during ventilation. The resulting thrust during ventilation is about the same for all controllers. That is, the anti-spin controller, which reduces the shaft speed to 9rps during ventilation, produces the same thrust as the torque controller, which races to the imposed limit of 25rps. This corresponds well to the experimental results shown in Figure 8.12. The power consumption of the torque controller is unacceptably high, whereas the power controller keeps the power consumption limited. The shaft speed and anti-spin controllers give a lower power consumption during ventilation, but this is not considered to be a problem.

Figure 8.32 shows comparisons of T_a, Q_a, n, Q_m, and P_m for four controllers during a ventilation incident with $T_r = 300$N: power control, combined control with primary anti-spin action only (marked P), combined control with primary and secondary anti-spin action (marked P+S), and shaft speed control. The torque controller could not be tested for this thrust reference, since the propeller racing was too severe to give sensible results. The ventilation incident starts at $t \approx 16.2$s, and terminates at $t \approx 19.5$s. Again, the thrust levels during ventilation are almost identical for all the controllers. It can be noted that the primary anti-spin controller and the shaft speed controller behave almost identically, confirming that the proposed anti-spin controller has a similar performance as a well-tuned shaft speed PI controller during ventilation. The secondary anti-spin action lowers the shaft speed as intended during ventilation. Figure 8.33 shows details from the anti-spin controller during a ventilation incident: propeller torque Q_a versus estimated propeller torque $\hat{Q}_a$, estimated torque loss factor $\hat{\beta}_Q$ and ventilation detection signal ζ, torque modification factor γ, deviation of γ from the measured β_Q, and the desired shaft speed n_{ras}. The time series show that the anti-spin controller, including torque observer and ventilation detection, performs as intended.

8.12.6 Discussion

The power plant on ships consists of several gas turbines or diesel engines driving electrical generators. For safe operation there must in all load conditions be enough spinning reserves providing sufficient available power for unpredictable variations in load in order to prevent black-out. The black-out prevention by means of reducing load on heavy consumers must typically respond faster than $500\,ms$ to be effective. With torque and power control, the propeller load

is less sensitive to variations in the surroundings, giving less power disturbances on the network and improved voltage and frequency quality. Additionally, the maximum power consumption may easily be limited to the available power in both schemes, since the power limitation is explicit in the torque and power control algorithm. This in contrast to speed controlled and pitch controlled propellers, where the actual power load must be measured as a feedback signal with an inherent time lag which deteriorates the black-out prevention response time. The accurate and fast control of power and power limitation in torque and power control gives less unpredictable load changes, and less need for available power. Hence, there will be a reduced probability of blackout due to overload, since unintentional power peaks will be suppressed. In traditional speed controlled drives there can be an overshoot in the commanded torque/power of up to 5%. If this occurs for several thrusters simultaneously, significantly more power than requested by the positioning system is consumed. With torque and power control this transient overshoot problem is removed. The number of running generators can be reduced, such that the average loading can be higher. This reduces wear and tear and gives less maintenance of the prime movers. In addition torque and power control will lead to reduced mechanical wear and tear of the propulsion components.

Low-level controllers based on shaft speed, torque, and power control for electrically driven thrusters on vessels in normal operating conditions have been investigated, and evaluated according to three main performance criteria. The conventional shaft speed controller gave the thrust, torque, and power with the largest variance, and it was the least robust to disturbances in the in-line flow velocity. The torque controller produced the thrust and torque with the smallest variance, and was superior with respect to compensating for thrust losses due to disturbances in the inflow. The power controller gave the least oscillations in the power, with the resulting propeller thrust and torque in-between the shaft speed and torque controller values. The combined torque and power controller gave the overall best improvement in the performance from low to high loadings. Steady-state sensitivity functions describing the performance of the various controllers in terms of resulting thrust, shaft speed, torque, and power when subject to thrust losses were presented. Experiments illustrated the difference in performance and robustness of the different controllers.

It has been shown that torque and power control is a feasible solution for high-performance thruster control only if special precautions are taken during extreme environmental conditions, when the propeller may be subject to ventilation and in-and-out-of water effects. To solve this problem, an anti-spin thruster controller has been designed. The thruster performance was monitored by a load torque observer, and the anti-spin controller was triggered by a ventilation detection scheme. The anti-spin controller took control of and lowered the shaft speed. Experiments with a model scale propeller were presented. The results showed that the torque and power controllers with anti-spin had comparable performance to that of a well-tuned shaft speed PI controller during ventilation, without compromising the superior performance of torque and power control in normal conditions.

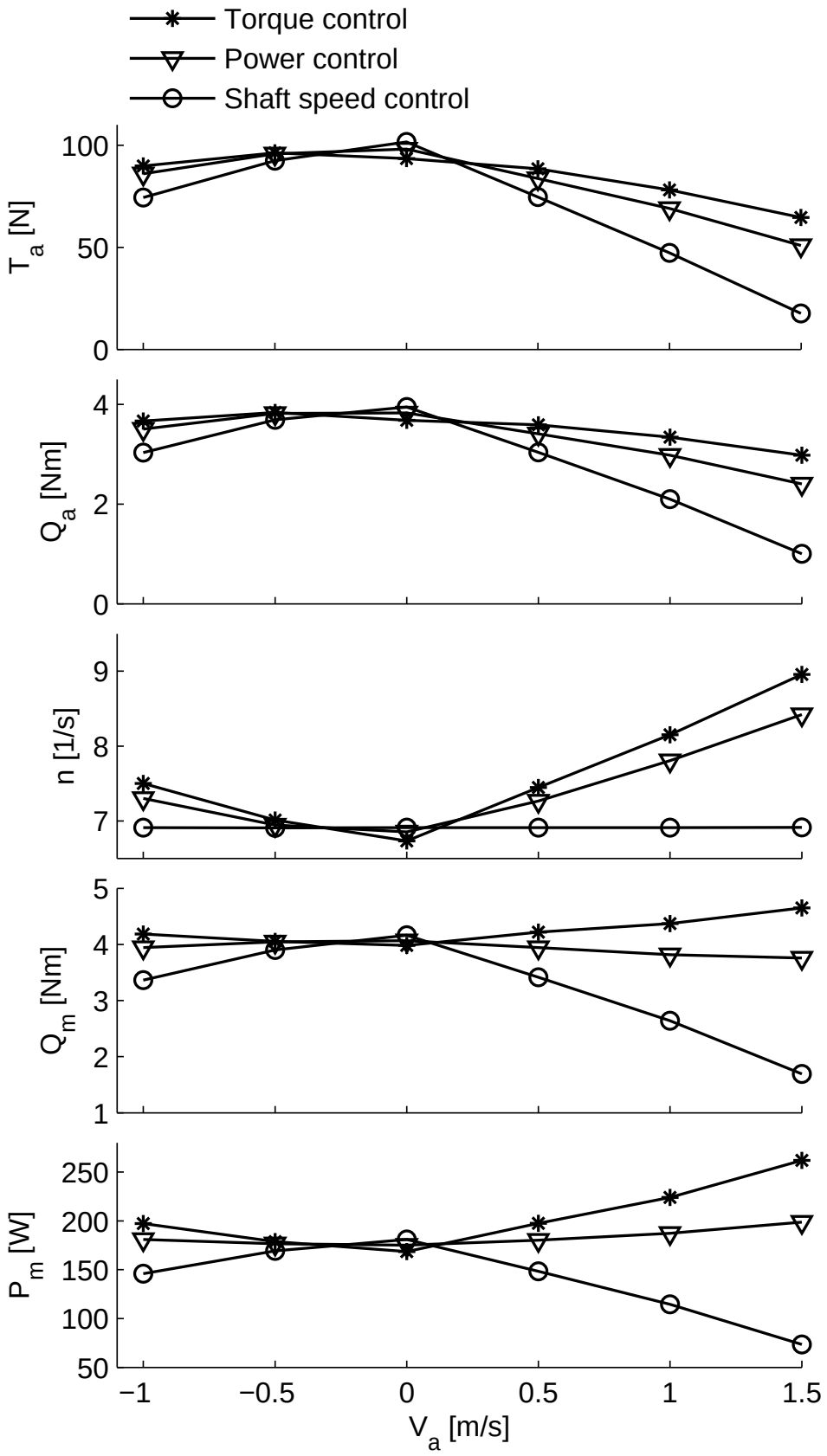

Figure 8.28: Comparison of propeller thrust T_a, torque Q_a, shaft speed n, motor torque Q_m and power P_m for the shaft speed, torque and power controllers in varying advance velocities V_a.

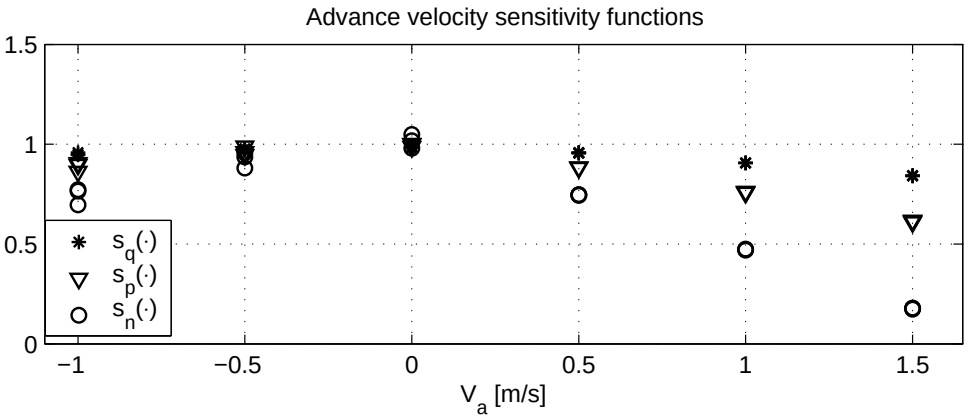

Figure 8.29: Advance velocity sensitivity functions $s_n(\cdot)$ (shaft speed control), $s_Q(\cdot)$ (torque control) and $s_P(\cdot)$ (power control) for the tested propeller.

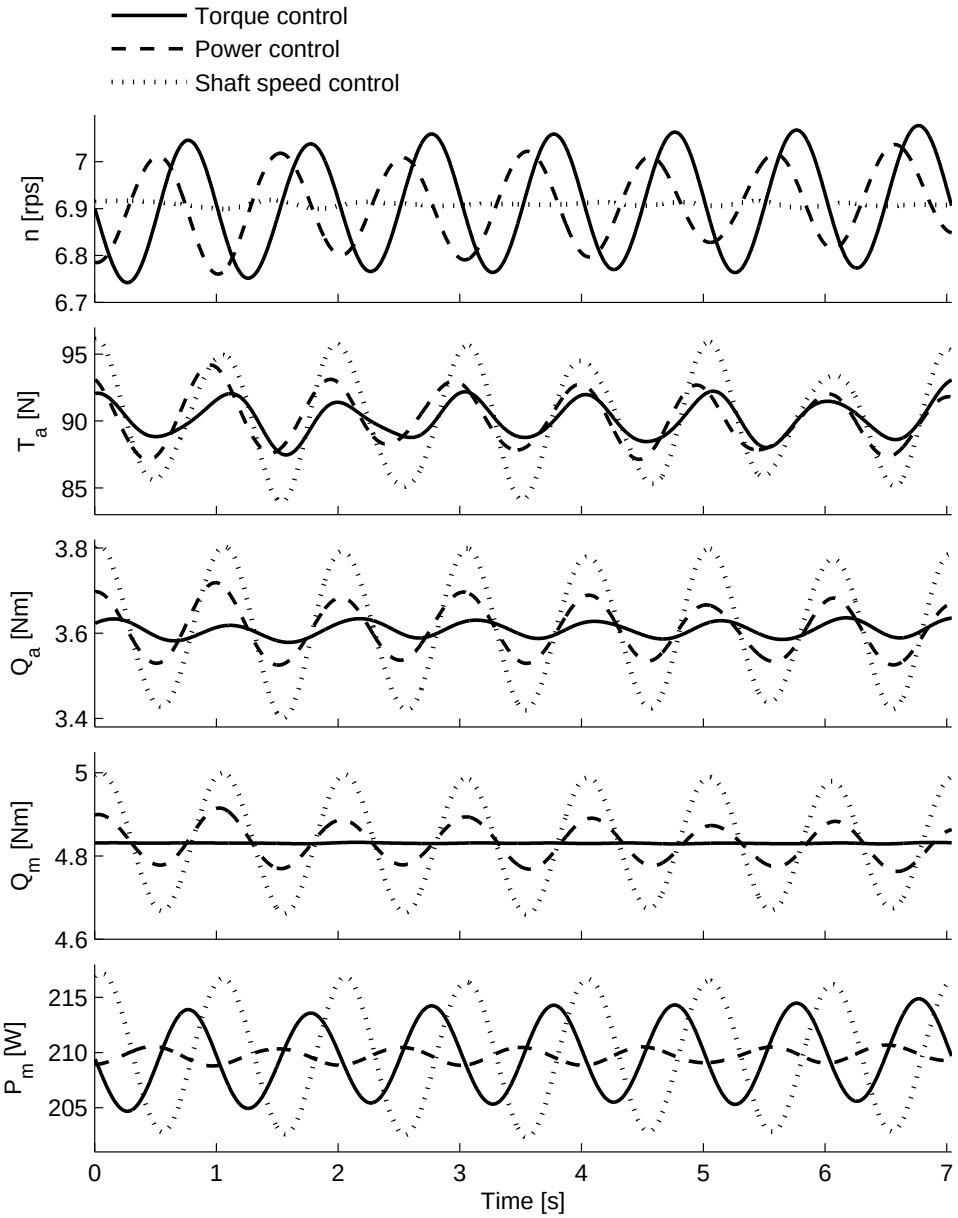

Figure 8.30: Controller comparison in regular waves. DP functionality has been simulated, such that all controllers give the same mean thrust.

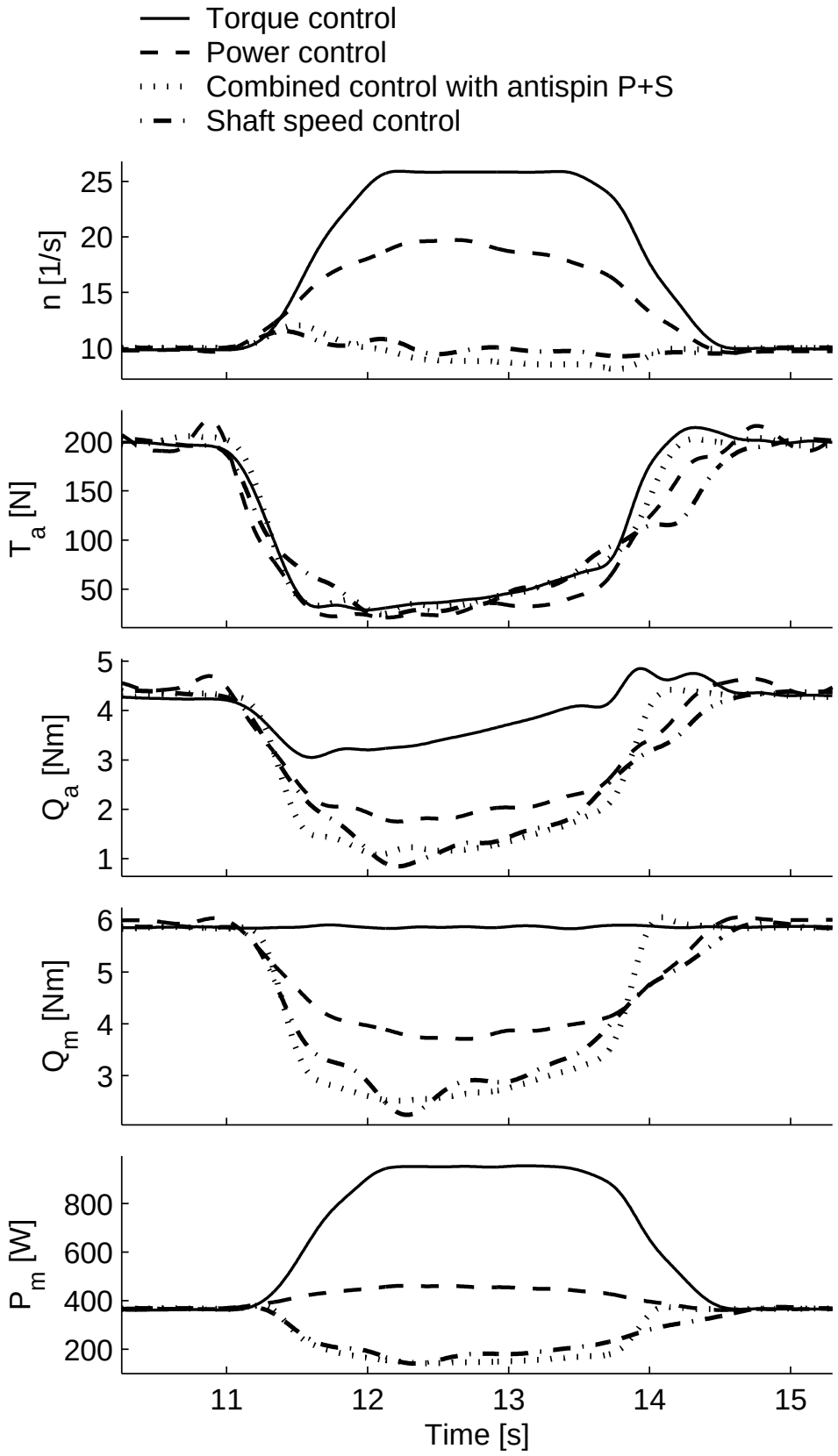

Figure 8.31: Comparison of four controllers during a ventilation incident at $T_r = 200$N.

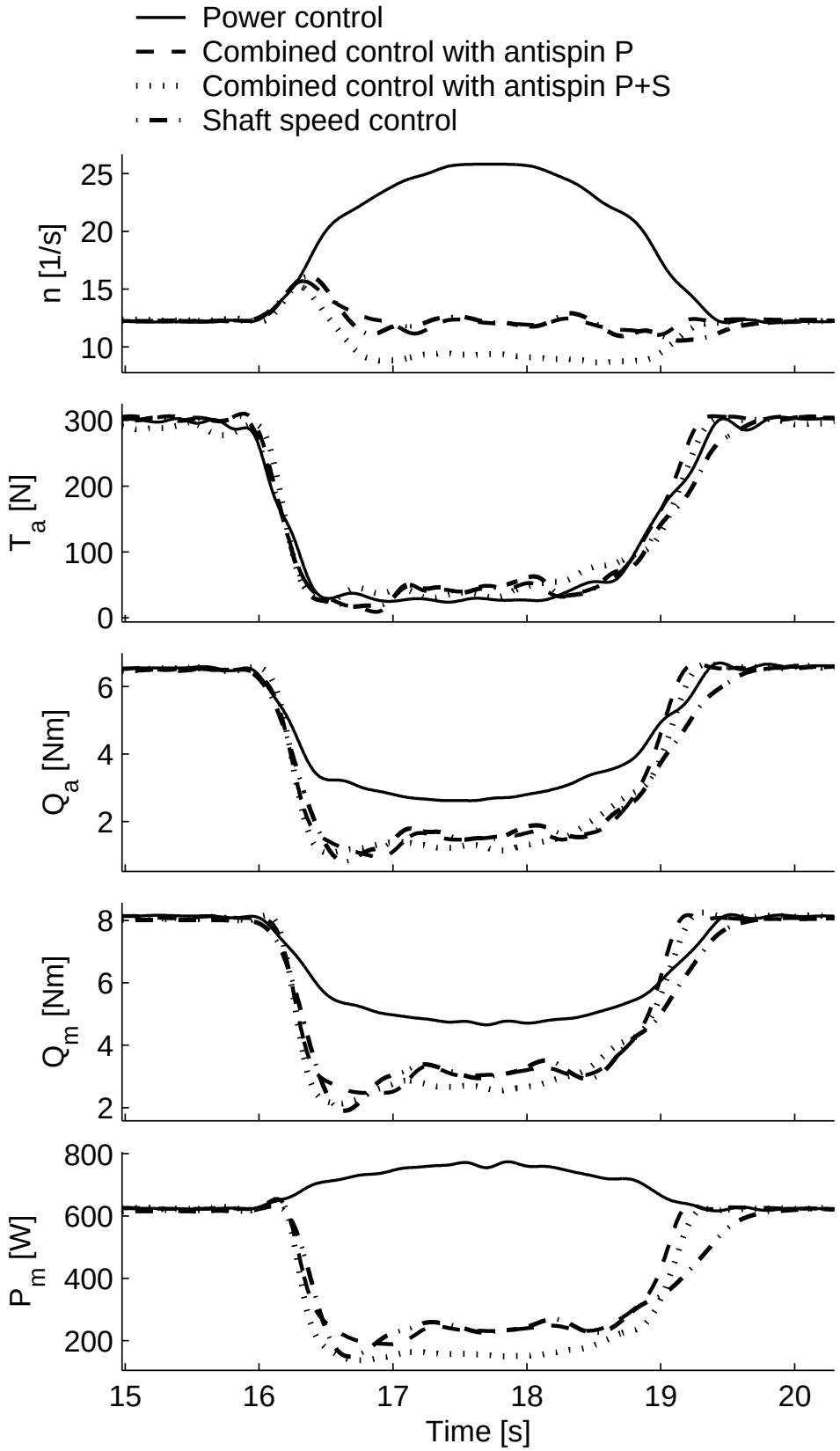

Figure 8.32: Comparison of four controllers during a ventilation incident at $T_r = 300$N.

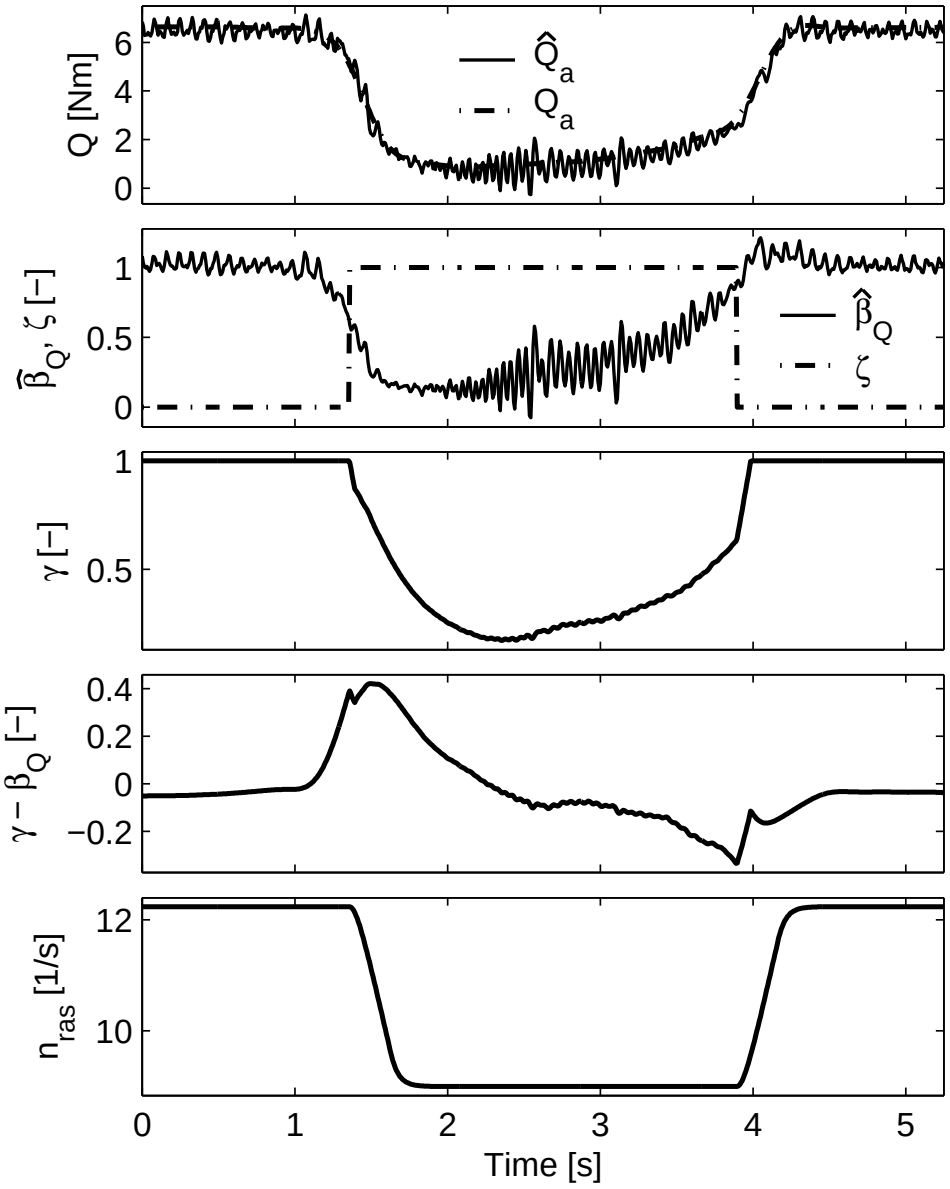

Figure 8.33: Time series of the main parameters in the anti-spin control law with primary and secondary control action during a ventilation incident at $T_r = 300$N.

Chapter 9

Hybrid Control of Marine Vessels

Author: Astrid H. Brodtkorb, NTNU

This chapter gives an introduction to hybrid control systems, with performance monitoring and switching logic, and gives examples of applications of hybrid theory to marine control systems. Hybrid systems theory provides a formalism for the integration of multi-functional controllers combining discrete events and continuous control.

Learning outcome of the chapter: The reader shall:

- Understand some basic modeling principles for hybrid systems.
- Be familiar with a common control structure for hybrid marine control systems, and the importance of designing appropriate performance monitoring and switching logic.

9.1 Motivation and Literature Review

The demand for increased levels of autonomy and system integration for marine vessels have forced control engineers to deal with increasingly larger and more complex systems. Higher levels of autonomy may lead to performance improvement in terms of increased precision, larger operational windows, lower fuel consumption and increased safety for passengers, crew and equipment.

Generally, several dimensions of vessel operation conditions may be defined. For illustration purposes (Figure 9.1) a 3-dimensional illustration is shown. The vessel operational conditions with *use mode, speed*, *environment* and (although not shown explicitly in the figure) *loading condition* indicates how the vessel performs different tasks with varying speed in an unknown and changing environment. The use mode includes algorithms that satisfy different control objectives such as stationkeeping, maneuvering, and target tracking, which is closely linked with the vessel speed. Environment refers to the state of the environment consisting of wind, waves and current, and loading condition is the mass distribution and draught of the vessel. Naturally, certain operations can only be performed in calm conditions. Because different physical effects matter for the various vessel operational conditions, there are distinct models and control strategies which are designed specifically for each operational condition. Some examples were introduced in the previous chapters. When the controllers for each condition are combined into one control system by using performance monitoring and switching logic, dynamics arise that differential

equations on their own cannot describe. Systems that include both continuous- and discrete-time dynamics are called *hybrid dynamical systems*, or just hybrid systems, and the interaction between the different types of dynamics leads to challenging modeling and control problems. In essence, the hybrid system can be thought of as a sequential patching together of dynamical systems with initial and final states, the jumps performing a reset to a (generally different) initial state of a (generally different) dynamical system whenever a final state is reached.

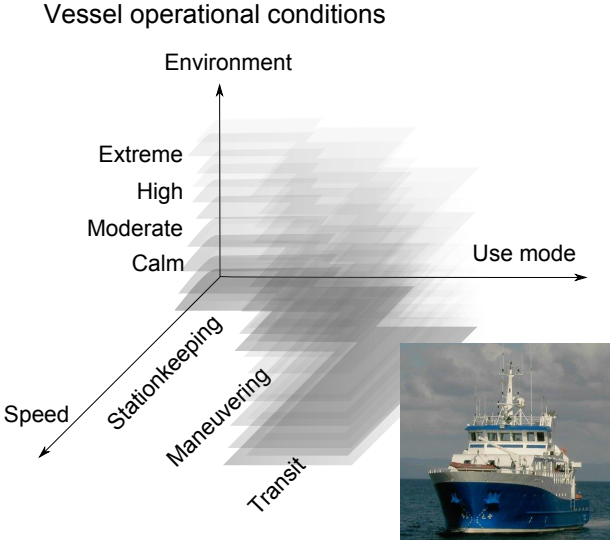

Figure 9.1: Vessel operational conditions: environment, use mode and speed.

In the industry, switching using different ad-hoc methods for phasing in and out controllers have been used with success for many years. However, when increasing the number of system functions that switch *automatically*, it is of increasing importance to know that the dynamics triggered by a switch are well behaved. Mathematical modeling and analysis tools in hybrid systems frameworks can combine continuous-time dynamics with discrete-time logics into one system, and are able to describe marine vessel dynamics over all operational regimes with the related control algorithms. A hybrid control system that can evaluate different control strategies, and choose the best one on its own, will improve system reactivity, safety, and performance relative to having an operator change the use mode and vessel speed.

Developing theory for hybrid systems is not a new area. As early as in the 1960's (Witsenhausen, 1966) systems with continuous and discrete dynamics were modeled and analyzed, and during the last 20 years, formal mathematical tools for modeling, stability and robustness analysis of hybrid systems have been developed. Examples of systems that can be modeled using hybrid frameworks include impulsive differential equations, systems with distinct logical states (also called hybrid automata), switching control systems, resetting control algorithms, synchronized behaviour that occurs in biological systems, and systems in networks. Examples of systems that can be modeled using hybrid frameworks include impulsive differential equations like a bouncing ball, Newton's cradle, and collisions, systems with distinct logical states (also called hybrid automata), switching control systems, resetting control algorithms, synchronized behaviour that occurs in biological systems like the flashing of fireflies and singing of crickets, and systems in networks. Since there are so many types of hybrid systems, naturally there are also a number of mathematical frameworks for modeling and stability analysis, see for instance;

Branicky (1995), Lygeros (1996), Henzinger (2000), Hespanha and Morse (2002), Goebel et al. (2012), and Arcak et al. (2016), to name a few. Hybrid systems frameworks are especially suited for describing marine vessel dynamics because the large diversity in dynamical behaviour for various vessel operational conditions can be captured using different sub-models merged into one hybrid system. Control system design based on hybrid vessel models that involve logic may be analyzed using diverse tools, and stability criteria may be obtained, ensuring safer, smarter and greener marine operations.

The interest for applying hybrid systems theory to the marine area began about 10-15 years ago (Nguyen, 2006; Nguyen et al., 2004; Sørensen et al., 2004, 2002). In the three latter, the hybrid framework of Hespanha and Morse (2002) was used to design hybrid controllers for changing environmental conditions (Nguyen et al., 2007), and for switching automatically between controllers for different speed ranges (Nguyen et al., 2008). In a similar manner as Nguyen et al. (2007), Brodtkorb et al. (2014) proposes a controller for changing environmental conditions, by using the hybrid framework in Goebel et al. (2012) for modeling and analyzing stability. The framework in Goebel et al. (2012) is introduced in this chapter.

Some hybrid control algorithms that quickly can detect and correct for a disturbance after it is encountered, include resetting strategies (Kjerstad, 2016; Tutturen and Skjetne, 2015), jumping between estimates from different observer types based on performance (Brodtkorb et al., 2016b, 2018b), and hybrid signal-based observers (Brodtkorb et al., 2015b, 2016a). Supervisory control for thrust allocation was investigated by Ruth (2008), and a slightly different application area for hybrid systems is control of top-tensioned risers (Rustad, 2007).

A reactive control system requires that the power system can deliver a lot of power over a short time frame, and that the thruster system dynamics are fast. Batteries are one type of responsive power source that can support reactive control strategies, by combining them with conventional diesel engines connected to a generator, like presented in Miyazaki et al. (2016). This makes the power generation and thruster system more decoupled, giving better working conditions for both systems. This strategy is also in line with the International Maritime Organization (IMO) emission regulations (IMO, 2011), which encourages the design of new power system solutions.

9.2 Hybrid Control System Structure for Marine Vessels

The hybrid motion control system in Figure 9.2 shows observer, controller, control allocation and thruster control candidates that are switched between automatically. The vessel is equipped with instrumentation, providing measurements, with different sampling rates, required for operation. The position reference system, for instance GNSS, hydroacoustic, laser, tautwire or riser angle measurement system, provides measurements of the vessel's position. Other common sensor systems include IMUs with gyros and accelerometers, for measuring angular rate and specific force, gyrocompass and/or magnetic compass for measuring heading, wind sensors, draft sensors, and sensors that are specific to the marine operation, like tension sensors for pipelay operations, or thruster-assisted position mooring. Actuators include propellers, rudders, stabilizing fins, and rotatable thrusters. Each component of the motion control system in Figure 9.2 is described in detail in previous chapters, and is summarized below.

- The signal processing software checks the measurement signals for errors and rejects bad signals. It usually includes wildpoint, signal freeze and high variance detection. In most

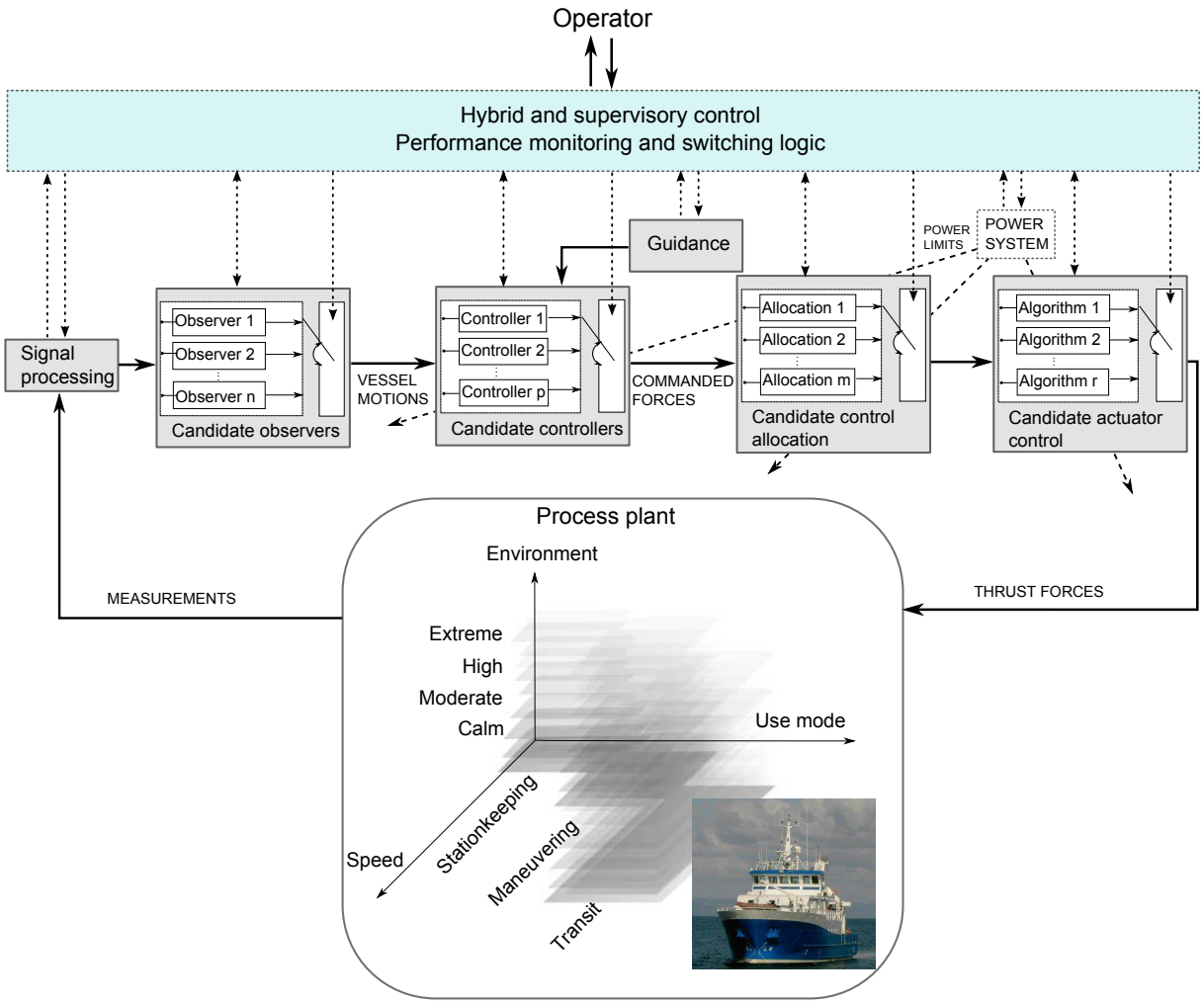

Figure 9.2: Hybrid control system for a marine vessel in a changing environment in different speed ranges and for various operational use modes. The ship is R/V Gunnerus.

marine motion control systems redundant sensor measurements are weighted or voted. See Chapter 5.

- Observers, also called state estimators, estimate unmeasured system states, filter out noise and wave-frequency motion, and in the case of signal loss, predict the vessel states, often referred to as dead reckoning. There are different observers amongst the *candidate observers* that have their areas of expertise. See Chapter 4 and Section 7.2.

- The guidance system provides smooth references to the controller based on the position of the vessel, waypoints and weather data provided by the operator.

- The controller commands desired generalized forces in surge, sway, and yaw in order to satisfy the control objective, for instance stationkeeping, path following, or maneuvering. The control law usually consists of a feedback part using position and velocity estimates from the observer, and a feedforward part consisting of mean wind forces and reference.

There are different controllers amongst the *candidate controllers* for different speed ranges and that satisfy different control objectives. See Chapter 7.3 for examples on DP control algorithms.

- The control allocation system takes the commanded forces and moment from the controller, and calculates the desired force and direction for each actuator. Thrusters that can be rotated, called azimuthing thrusters, are commonly used on DP vessels, and the thrust allocation needs to take into account forbidden directional sectors. Optimization based on fuel consumption is also common. See Section 7.3.5.

- Local actuator control algorithms control the actuators according to the setpoints from the thrust allocation system. See Chapter 8.

- The power system is not a direct part of the motion control system, however power limits are sent to the controllers, thrust allocation system, and local actuator control in order to prevent a system blackout, as this is one of the most severe failure modes for marine vessels.

- The performance monitoring monitors the performance of the different blocks, and the switching logic chooses which algorithms to use in closed-loop control from the candidates. When necessary the parameters in the different algorithms are altered according to the vessel operational conditions. Relevant information and alarms are sent to the operator, and input from the operator is inserted where needed. Transitions between the different use modes and speed ranges are handled automatically in this block. Performance monitoring and switching logic are descussed in detail below.

- The operator has screens monitoring the system performance, either onboard or remotely. Performance monitoring functions alert the operator by raising alarms and warnings, and provide decision support.

9.2.1 Performance Monitoring and Switching Logic

In order for a hybrid control system to be reliable, good switching criteria that are robust to measurement noise and system errors need to be established for the vessel speed, use modes, and environmental conditions. Figure 9.3 illustrates parts of the functionality that can be found within the performance monitoring and switching block in a hybrid control system. Firstly, the performance monitoring detects and diagnoses, and secondly the switching logic reconfigures the blocks in the hybrid control system, in a similar way to fault-tolerant control (Blanke et al., 2003).

The main tasks of the performance monitoring functions are to decide which of the candidate algorithms to use in closed loop, detect faults (and alert the operator of these) and provide decision support for the operator, when the system needs human interaction. The performance monitoring takes input from the operator, references, operating conditions, measured position, estimated position, control input, line tension, risk management system, measured wind speed, and more, depending on the operation taking place. Different norms of the inputs can be used as performance measures, for instance the Euclidean norm, p-norm and infinity norm (Desoer and Vidyasager, 1975).

Often, several different parameters need to be considered in order to get a good picture of the overall performance, and here the norms of different inputs may be combined in cost functions.

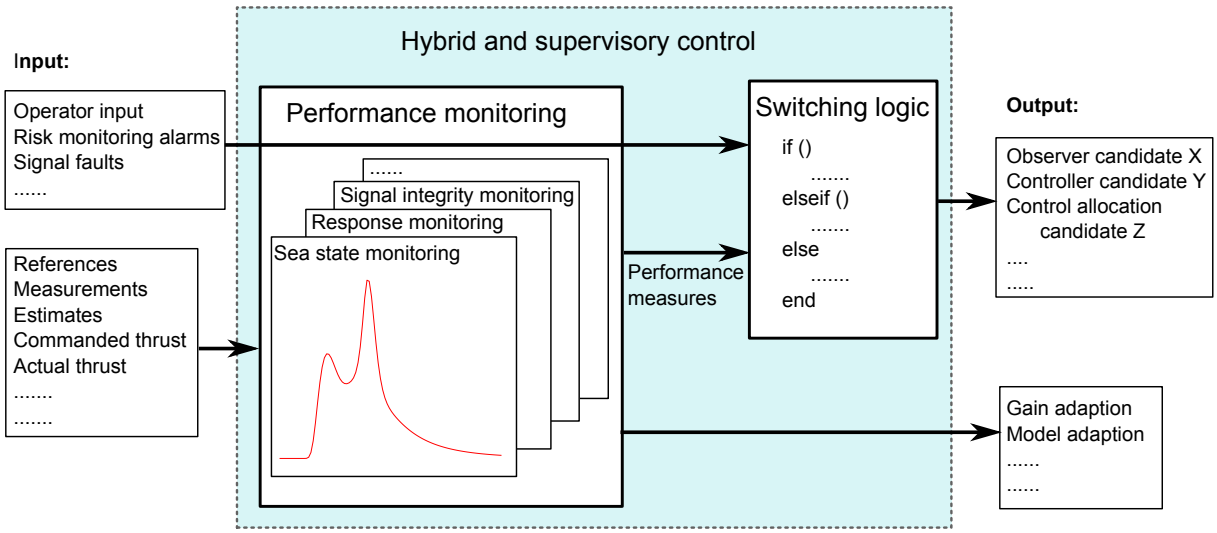

Figure 9.3: Illustration of performance monitoring and switching logic setup. As indicated by the layers in the performance monitoring, there are various functions that monitor different aspects of the vessel performance. Certain inputs, like signal faults, some operator inputs and risk management alarms, will override performance monitoring functions. Based on performance measures, the switching logic chooses algorithms from the candidates to use in closed-loop control.

An example of a performance measure that takes positioning error $\boldsymbol{\eta}(t) - \boldsymbol{\eta}_d(t)$, estimation error $\boldsymbol{\eta}(t) - \hat{\boldsymbol{\eta}}_i(t)$ for observer i, and thrust usage $\boldsymbol{\tau}_j$ for controller j into account could for instance look like,

$$\boldsymbol{J}(\boldsymbol{\eta}, \hat{\boldsymbol{\eta}}_i, \boldsymbol{\tau}_j) = \boldsymbol{W}_\eta \int_{t_0}^{T} |\boldsymbol{\eta}(t) - \boldsymbol{\eta}_d(t)| dt + \boldsymbol{W}_{\hat{\eta}} \int_{t_0}^{T} |\boldsymbol{\eta}(t) - \hat{\boldsymbol{\eta}}_i(t)| dt + \boldsymbol{W}_\tau \int_{t_0}^{T} |\boldsymbol{\tau}_j(t)| dt, \tag{9.1}$$

where $\boldsymbol{J}(\boldsymbol{\eta}, \hat{\boldsymbol{\eta}}_i, \boldsymbol{\tau}_j)$ is the total *cost* over a time interval (t_0, T) for a certain combination of observer and controller algorithms, and $\boldsymbol{W}_\eta$, $\boldsymbol{W}_{\hat{\eta}}$ and $\boldsymbol{W}_\tau$ are weight matrices. This type of performance measure could be used to compare the performance of multiple observer $\hat{\boldsymbol{\eta}}_i$, $i = \{1, ..., n\}$ and controller $\boldsymbol{\tau}_j$, $j = \{1, ..., p\}$ algorithms in order to decide which to use in closed-loop control. In some cases the inputs to the performance monitoring functions have large oscillations, due to wave-induced motion or noise. In these cases, averaging the cost functions over a short time may be useful in order to prevent unnecessary switching. Which variables to include, and how to weight them depends on the operational condition, and as the layers in Figure 9.3 indicate, there are various functions for monitoring different operational aspects. Sea state estimation algorithms (Brodtkorb et al., 2015a, 2018a) are examples of environmental monitoring functions, and response prediction (Nielsen et al., 2018) may be another useful monitoring function. Some inputs, like alarms from the risk management software, certain operator inputs, and signal faults, will override performance monitoring.

Fault handling of measurement signals is taken care of by the signal processing software. The performance monitoring can further detect faults due to modeling, implementation, and software/hardware integration errors, by comparing outputs from multiple sources that have different inputs and/or structures in a signal integrity monitoring function. Knowing that mea-

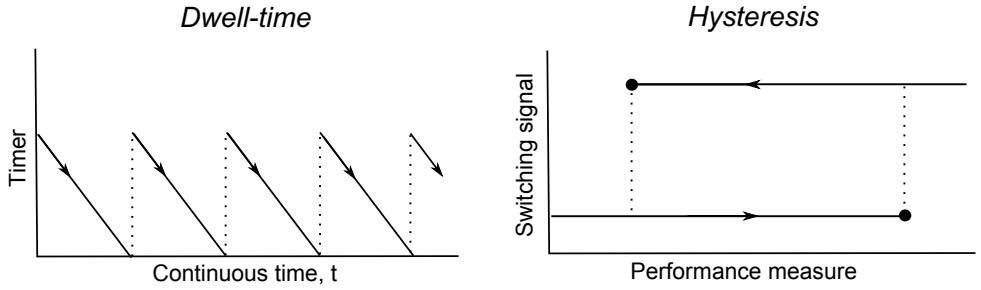

Figure 9.4: Illustration of dwell-time and hysteresis switching constraints, which commonly are included in switching logic. The timer dynamics to the left only allows periodic switches each time the timer reaches zero. The hysteresis on the right switches based on the history of the system state, or performance measure. A jump is indicated by the dotted lines.

surement signals may fail and this may remain undetected, it is important to have redundancy in performance measures, and have safe-modes available.

The task of the switching logic is to ensure safe switching to the candidate algorithms indicated by the performance measures. A switch, here also referred to as a *jump*, induces a transient in the continuous-time system, which introduces additional dynamics that are not encountered in purely continuous-time systems. Therefore analyzing the hybrid system behavior is important in order to avoid instability. Two challenges related to automatic switching are:

1. Switching during transients
2. Chattering

In the first case, the hybrid system is not allowed enough time to come to steady state, so that jumps are triggered based on the transient system behavior. This may lead to instability induced by switching. The transient could be due to initialization, a change of heading or setpoint, or it could be due to a previous jump.

Another common phenomenon that may occur in systems that switch automatically, is rapid switching back and forth, called chattering. In order to avoid such scenarios, explicit constraints on switching may be achieved through hybrid stability analysis. Constraining switches can be done though switching logic based on time, such as dwell-time or average dwell-time dynamics, or based on the system variables, such as hysteresis (Hespanha et al., 2003; Hespanha and Morse, 2002). Figure 9.4 shows examples of both dwell-time and hysteresis switching constraints. During dwell-time or average dwell-time switching a timer keeps track of the time from the last switch, and does not allow a new switch until a certain time has passed. Hysteresis switching is based on the history of the variables, allowing switching only if the variable crosses a boundary with a certain direction of change. In many cases it is possible to implement both types of switching logic, however the choice should complement the system dynamics as much as possible.

9.2.2 Hybrid Systems and Autonomy

Higher levels of autonomy in the next generation marine control systems may lead to smarter and more efficient operations in the future. Control systems today have certain functionality that can be characterized as autonomous, from low-level performance switching control, to automatic navigation with collision avoidance schemes, and online risk monitoring. Collision avoidance

algorithms identify objects, and plan a new route in order to avoid collision in accordance with marine traffic rules (COLREG, 1972). Generally the components, or modules, of a fully autonomous control system already exist, thus it is the combination of these modules into a safe and reliable system that is the challenge. The risk of a certain module may be known, but the interactions between these risks and other types of risk, could cause unexpected nonlinear and stochastic behavior. Since there is little operational experience from autonomous operations, it is difficult to model risk for these types of operations, and this poses challenges related to verification of safe performance (Utne et al., 2017).

The autonomous system must be able to determine if it can continue with possible degraded performance by detecting, isolating and handling failures and faults. Performance monitoring and switching logic is an integral part of this, and therefore, hybrid systems theory may become a core design and stability analysis tool for marine control systems with higher levels of autonomy.

9.3 Mathematical Framework for Hybrid Systems

As mentioned, there are many mathematical frameworks for modeling hybrid dynamical system. Here we informally introduce the hybrid framework that is presented in the book *Hybrid Dynamical Systems* by Goebel, Sanfelice, and Teel (2012). The book unifies some of the key developments for hybrid dynamical systems, and introduces the necessary tools for understanding the stability of these systems. The modeling, stability and robustness results are extensions of nonlinear systems theory (Khalil, 2002) to include discrete dynamics and the interconnection of discrete and continuous dynamics into one system. The following section is based on the first few chapters of Goebel et al. (2012), focusing on the data structure, mathematical modeling illustrated by simple examples, and some mathematical properties. The interested reader is referred to the book for more details. The theory presented in this section is illustrated through a case study improving the transient performance of a marine vessel during a DP operation, see Section 9.4. Table 9.1 contains a list of some of the symbols used in this section.

Table 9.1: List of symbols.

$\dot{\boldsymbol{x}}$	Time derivative of the state of a hybrid system $\boldsymbol{x}$
$\boldsymbol{x}^+$	Value of the state of a hybrid system $\boldsymbol{x}$ after a jump
$\mathbb{R}$	The set of real numbers
$\mathbb{R}_{\geq 0}$	The set of nonnegative real numbers
$\mathbb{R}^n$	n-dimensional Euclidean space
$\mathbb{N}$	The set of nonnegative integers
$\in$	Element of
$\subset$	Subset of
$\Sigma_1 \times \Sigma_2$	The ordered pairs (σ_1, σ_2) with $\sigma_1 \in \Sigma_1$ and $\sigma_2 \in \Sigma_2$
:	Such that
:=	Defined as

9.3.1 The Modeling Framework

The hybrid system $\mathcal{H} = (\boldsymbol{C}, \boldsymbol{f}, \boldsymbol{D}, \boldsymbol{g})$ can be modeled as

$$\boldsymbol{x} \in \boldsymbol{C} \quad \dot{\boldsymbol{x}} = \boldsymbol{f}(\boldsymbol{x}) \tag{9.2a}$$

$$\boldsymbol{x} \in \boldsymbol{D} \quad \boldsymbol{x}^+ = \boldsymbol{g}(\boldsymbol{x}), \tag{9.2b}$$

where the hybrid state $\boldsymbol{x}$ evolves in continuous time according to the differential equation $\dot{\boldsymbol{x}} = \boldsymbol{f}(\boldsymbol{x})$ when $\boldsymbol{x} \in \boldsymbol{C}$, and when $\boldsymbol{x} \in \boldsymbol{D}$ the state is allowed to change instantaneously according to the difference equation $\boldsymbol{x}^+ = \boldsymbol{g}(\boldsymbol{x})$. $\boldsymbol{x}^+$ represents the value of $\boldsymbol{x}$ after an instantaneous change. Changes that occur according to the differential equation are called *flows*, and changes that occur according to the difference equation are called *jumps*. A more general representation of a hybrid system $\mathcal{H} = (\boldsymbol{C}, \boldsymbol{F}, \boldsymbol{D}, \boldsymbol{G})$ can be written in terms of set-valued mappings,

$$\boldsymbol{x} \in \boldsymbol{C} \quad \dot{\boldsymbol{x}} \in \boldsymbol{F}(\boldsymbol{x}) \tag{9.3a}$$

$$\boldsymbol{x} \in \boldsymbol{D} \quad \boldsymbol{x}^+ \in \boldsymbol{G}(\boldsymbol{x}), \tag{9.3b}$$

where the differential and difference inclusions $\dot{\boldsymbol{x}} \in \boldsymbol{F}(\boldsymbol{x})$ and $\boldsymbol{x}^+ \in \boldsymbol{G}(\boldsymbol{x})$ are generalizations of the differential and difference equations $\dot{\boldsymbol{x}} = \boldsymbol{f}(\boldsymbol{x})$ and $\boldsymbol{x}^+ = \boldsymbol{g}(\boldsymbol{x})$. The *set-valued mappings* $\boldsymbol{F} : \mathbb{R}^n \rightrightarrows \mathbb{R}^n$ and $\boldsymbol{G} : \mathbb{R}^n \rightrightarrows \mathbb{R}^n$ relate the input $\boldsymbol{x}$ to one, *or more*, outputs (hence the double arrow), see Figure 9.5 for an illustration. This implies that $\boldsymbol{F}(\boldsymbol{x})$ and $\boldsymbol{G}(\boldsymbol{x})$ are *sets* rather than single points. See Rockafellar and Wets (1998) for more on set analysis.

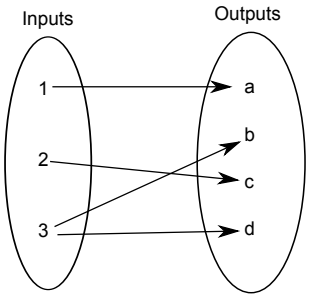

Figure 9.5: Example of a set-valued mapping. Notice that one input can be mapped to multiple outputs.

Summarizing the hybrid system data, we have that

- $\boldsymbol{C}$ is the flow set,
- $\boldsymbol{D}$ is the jump set,
- $\boldsymbol{F}$ (or $\boldsymbol{f}$) is the flow map, and
- $\boldsymbol{G}$ (or $\boldsymbol{g}$) is the jump map.

The hybrid state $\boldsymbol{x}$ can contain a mix of states that change only during continuous time, logic variables, timers, and variables that change both during continuous and discrete time.

To illustrate the modeling framework, let's look at two different examples. The first is of a bouncing ball, which is a simple mechanical system with impacts. The second is of a switching controller, which is a common control structure for marine control systems.

Example 9.1 ***Hybrid model for a bouncing ball***
A ball is dropped from some height above the floor, and as it hits the floor it bounces, see Figure 9.6 for an illustration. A simplified model of the ball's vertical motion is to assume that while the ball is in the air, it is only affected by gravity, and when the ball hits the floor, the vertical velocity changes sign instantaneously and is reduced due to dissipation of energy. The ball system has the state

$$\boldsymbol{x} = \begin{bmatrix} x_1 \\ x_2 \end{bmatrix} \in \mathbb{R}^2,$$

where x_1 represents the ball's height above the floor, and x_2 represents the vertical velocity. We want our model to flow when the ball is in the air, and when it is in touch with the floor on the way upwards. This gives the following flow set:

$$\boldsymbol{C} = \{\boldsymbol{x} \in \mathbb{R}^2 : x_1 > 0 \text{ or } x_1 = 0, x_2 \geq 0\}$$

Since the ball is only influenced by gravity when it is in the air, a flow map describing these dynamics is:

$$\boldsymbol{f}(\boldsymbol{x}) = \begin{bmatrix} x_2 \\ -\mu \end{bmatrix} \text{ when } x_1 > 0 \text{ or } x_1 = 0, x_2 \geq 0,$$

and μ is the acceleration due to gravity. We should also specify that when the ball is at rest on the floor, the flow map is zero, $\boldsymbol{f}(\mathbf{0}_{2\times 1}) = \mathbf{0}_{2\times 1}$. We want our model to jump when the ball hits the floor on the way downwards, so the jump set is:

$$\boldsymbol{D} = \{\boldsymbol{x} \in \mathbb{R}^2 : x_1 = 0, x_2 < 0\}$$

Finally, the jump map can be written as:

$$\boldsymbol{g}(\boldsymbol{x}) = \begin{bmatrix} 0 \\ -\lambda x_2 \end{bmatrix}$$

The coefficient $\lambda \in (0, 1)$ models the dissipation of energy that occurs when the ball hits the floor. Our model for a bouncing ball is

$$\boldsymbol{C} = \{\boldsymbol{x} \in \mathbb{R}^2 : x_1 > 0 \text{ or } x_1 = 0, x_2 \geq 0\}, \qquad \dot{\boldsymbol{x}} = \begin{bmatrix} x_2 \\ -\mu \end{bmatrix}$$
$$\boldsymbol{D} = \{\boldsymbol{x} \in \mathbb{R}^2 : x_1 = 0, x_2 < 0\}, \qquad \boldsymbol{x}^+ = \begin{bmatrix} 0 \\ -\lambda x_2 \end{bmatrix}.$$

The right side of Figure 9.6 illustrates the data for the hybrid bouncing ball model.

Example 9.2 ***Switching controller with hysteresis***

A marine vessel is performing a dynamic position operation, where the positioning accuracy constraint is relaxed, and we want the vessel to stay within a certain distance to the setpoint. When we are close to the setpoint, the vessel should minimize energy consumption in order to be more environmentally friendly and reduce costs. Far away from the setpoint, we would like the control system to get the vessel back to the setpoint as quickly as possible. This requires a

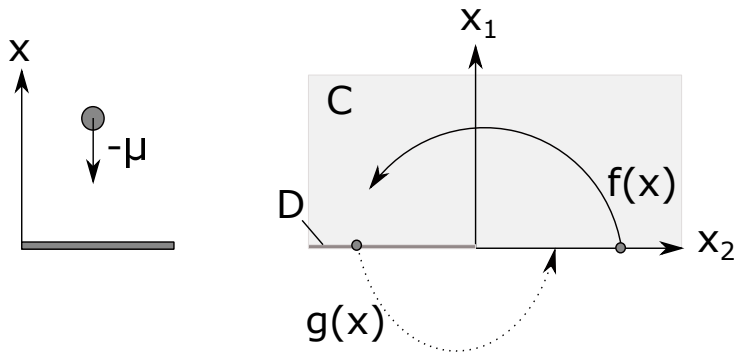

Figure 9.6: Example of a hybrid model for a bouncing ball. To the left the ball is in free fall towards the floor with the acceleration of gravity μ affecting it. To the right, the data of the hybrid model are illustrated.

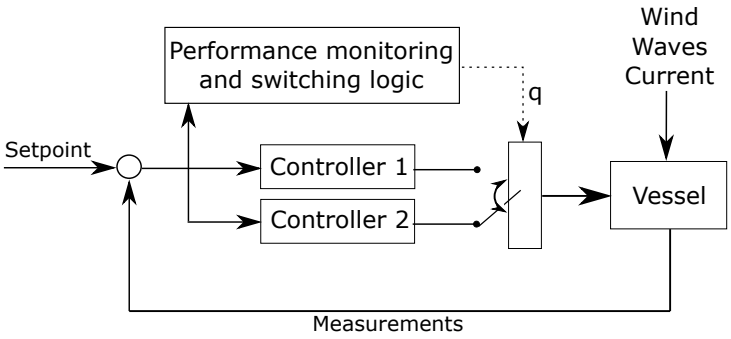

Figure 9.7: Block diagram for a switching controller.

more aggressive control strategy, which increases the power consumption. Figure 9.7 shows the block diagram for a switching control system with two candidate controllers, and performance monitoring. We want to use controller 1 close to the setpoint, and controller 2 far away from the setpoint.

Figure 9.8 illustrates the flow and jump sets for the two controllers, which we will model in the following. Our hybrid state $\boldsymbol{x} = [\boldsymbol{z}, q]^\top$ *contains the position and velocity of the vessel in* $\boldsymbol{z}$*, and a logic variable* q *that indicates which controller to use in closed loop. When we are close to the setpoint, controller 1 is used in closed loop, and the vessel dynamics can be written as*

$$\boldsymbol{z} \in \boldsymbol{C}_1, \quad \dot{\boldsymbol{z}} = \boldsymbol{f}(\boldsymbol{z}, \boldsymbol{\tau}_1(\boldsymbol{z})),$$

where $\boldsymbol{\tau}_1(\boldsymbol{z})$ *is the feedback control law of controller 1. Similarily, far away from the setpoint, controller 2 is used in closed loop, and the vessel dynamics take the form*

$$\boldsymbol{z} \in \boldsymbol{C}_2, \quad \dot{\boldsymbol{z}} = \boldsymbol{f}(\boldsymbol{z}, \boldsymbol{\tau}_2(\boldsymbol{z})).$$

The logic variable q *does not change during flows,* $\dot{q} = 0$*.*

When we are using controller 1, and enter the set $\boldsymbol{D}_1$*, a switch to controller 2 is triggered, and when we are using controller 2, and enter the set* $\boldsymbol{D}_2$*, a switch to controller 1 is triggered. The position and velocity states of the system remain the same after a switch is triggered,* $\boldsymbol{z}^+ = \boldsymbol{z}$*.*

Then, our hybrid model can be written as

$$\boldsymbol{x} \in \boldsymbol{C} := (\boldsymbol{C}_1 \times \{1\}) \text{ and } (\boldsymbol{C}_2 \times \{2\}), \qquad \begin{bmatrix} \dot{\boldsymbol{z}} \\ \dot{q} \end{bmatrix} = \begin{bmatrix} \boldsymbol{f}(\boldsymbol{z}, \boldsymbol{\tau}_q(\boldsymbol{z})) \\ 0 \end{bmatrix},$$

$$\boldsymbol{x} \in \boldsymbol{D} := (\boldsymbol{D}_1 \times \{1\}) \text{ and } (\boldsymbol{D}_2 \times \{2\}), \qquad \begin{bmatrix} \boldsymbol{z}^+ \\ q^+ \end{bmatrix} = \begin{bmatrix} \boldsymbol{z} \\ 3 - q \end{bmatrix}.$$

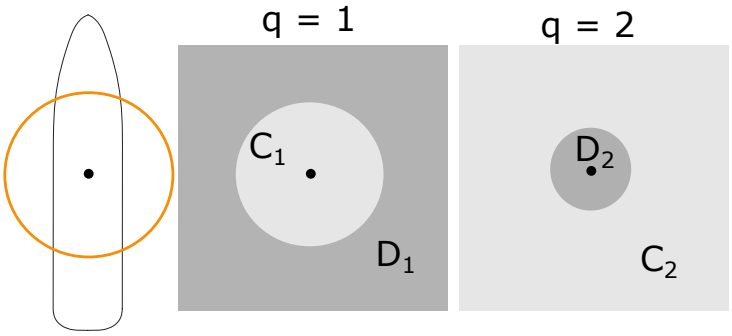

Figure 9.8: Illustration of flow and jump sets for switching controller with hysteresis.

The hysteresis mechanism is achieved in the construction of the sets $\boldsymbol{C}_1$ and $\boldsymbol{D}_2$, where $\boldsymbol{D}_2$ is strictly contained than $\boldsymbol{C}_1$. This makes sure there is no unnecessary switching back and forth between the control laws. The relationship between $\boldsymbol{C}_1$, $\boldsymbol{D}_1$, and the behavior of the controlled vessel needs to be appropriately designed in order for the hybrid control law to work as intended.

The structure of the hybrid system in Example 9.2, is a common control structure for various marine control applications. Notice that Figure 9.7 is a simplified version of the block diagram in Figure 9.2. Some examples of different marine applications with a similar structure as the system in Example 9.2 include:

- Hybrid observer and controller for changing environmental conditions (Brodtkorb et al., 2014; Nguyen et al., 2007).
- Switching automatically between controllers for different speed ranges (Nguyen et al., 2008).
- Switching control for thruster-assisted position mooring (Nguyen and Sørensen, 2009).
- Hybrid algorithms that quickly can detect and correct for a disturbance after it is encountered, including resetting strategies (Kjerstad, 2016; Tutturen and Skjetne, 2015).
- Jumping between estimates from different observer types based on performance (Brodtkorb et al., 2016b, 2018b), see the case study in Section 9.4.
- Adding batteries to conventional marine power grids consisting of diesel-engines coupled with generators in order to give better working conditions for the diesel-engines when the load variations are large Miyazaki et al. (2016).
- Supervisory control of top-tensioned risers (Rustad, 2007).

9.3.2 The Solution Concept

Solutions to hybrid systems are called *hybrid arcs*, which are functions that evolve in continuous time $t \in \mathbb{R}_{\geq 0}$ and in discrete time $j \in \mathbb{N}$, where j denotes the number of jumps. Only certain subsets of $\mathbb{R}_{\geq 0} \times \mathbb{N}$ can correspond to evolutions of hybrid systems, and these subsets are called *hybrid time domains*.

Definition 9.1 *Hybrid time domain (Goebel et al., 2012, Def. 2.3)*
A subset $\boldsymbol{E} \subset \mathbb{R}_{\geq 0} \times \mathbb{N}$ is a compact hybrid time domain if

$$\boldsymbol{E} = \bigcup_{j=0}^{J-1} ([t_j, t_{j+1}], j)$$

for some finite sequence of times $0 = t_0 \leq t_1 \leq t_2 \leq ... \leq t_J$. It is a hybrid time domain if for all $(T, J) \in \boldsymbol{E}$, $\boldsymbol{E} \cap ([0, T] \times \{0, 1, ..., J\})$ is a compact hybrid domain.

An example of a hybrid time domain $\boldsymbol{E}$ is shown to the left in Figure 9.9, with $0 = t_0 < t_1 < t_2 = t_3 < t_4$. For all $(T, J) \in \boldsymbol{E}$ in Figure 9.9, the domain $\boldsymbol{E} \cap ([0, T] \times \{0, 1, ..., J\})$ is a compact hybrid time domain. It follows from Definition 9.1 that the points $(0, 1)$ and $(1, 0)$ cannot belong to the same hybrid time domain.

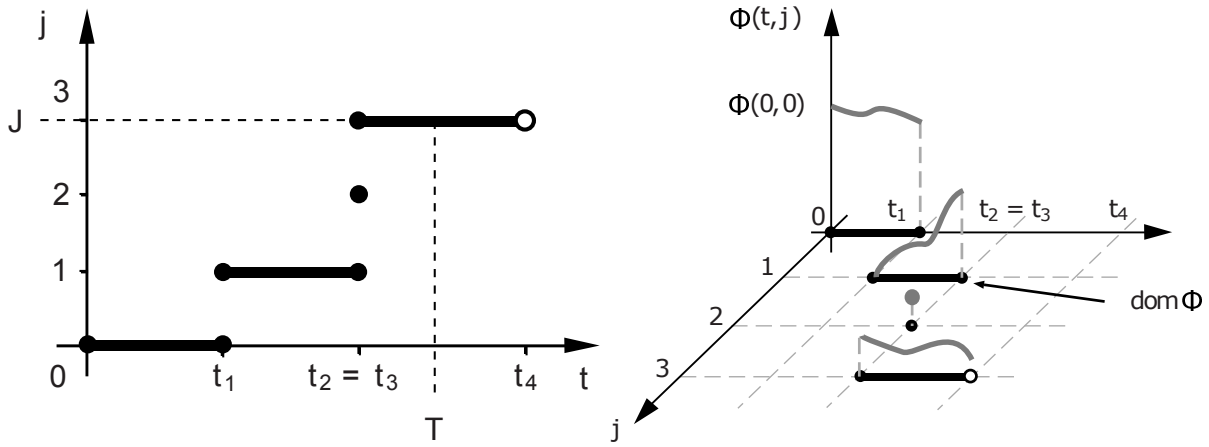

Figure 9.9: Example of a hybrid time domain $\boldsymbol{E}$ (left), and example of a hybrid arc $\boldsymbol{\phi}(t, j)$ (right). Source: Goebel et al. (2012).

Definition 9.2 *Hybrid arc (Goebel et al., 2012, Def. 2.4)*
A function $\boldsymbol{\phi} : \boldsymbol{E} \to \mathbb{R}^n$ is a hybrid arc if $\boldsymbol{E}$ is a hybrid time domain and if for each $j \in \mathbb{N}$, the function $t \mapsto \boldsymbol{\phi}(t, j)$ is locally absolutely continuous on the interval $I^j := \{t : (t, j) \in \boldsymbol{E}\}$.

A function is locally absolutely continuous if the derivative is continuous for almost all time, and the function can be recovered by integrating the derivative. Absolute continuity is a smoothness property of functions that is stronger than continuity and uniform continuity. An example of a hybrid arc is shown to the right in Figure 9.9.

Definition 9.3 *Solution to a hybrid system (Goebel et al., 2012, Def. 2.6)*
A hybrid arc $\boldsymbol{\phi}$ is a solution to a hybrid system $\mathcal{H} = (\boldsymbol{C}, \boldsymbol{F}, \boldsymbol{D}, \boldsymbol{G})$ if $\boldsymbol{\phi}(0, 0) \in \bar{\boldsymbol{C}} \cup \boldsymbol{D}$, and

(i) for all $j \in \mathbb{N}$ such that $I^j := \{t : (t, j) \in \text{dom } \boldsymbol{\phi}\}$ has nonempty interior

$$\begin{aligned} \boldsymbol{\phi}(t, j) &\in \boldsymbol{C} && \text{for all} && t \in \text{int} I^j, \\ \dot{\boldsymbol{\phi}}(t, j) &\in \boldsymbol{F}(\boldsymbol{\phi}(t, j)) && \text{for almost all} && t \in I^j; \end{aligned} \tag{9.4}$$

(ii) for all $t, j \in \text{dom } \boldsymbol{\phi}$ such that $(t, j + 1) \in \text{dom } \boldsymbol{\phi}$,

$$\begin{aligned} \boldsymbol{\phi}(t, j) &\in \boldsymbol{D}, \\ \boldsymbol{\phi}(t, j + 1) &\in \boldsymbol{G}(\boldsymbol{\phi}(t, j)). \end{aligned} \tag{9.5}$$

$\bar{\boldsymbol{C}}$ denotes the closure of $\boldsymbol{C}$, and $\text{int} I^j$ denotes the interior of the interval I^j. This is a broad definition that admits solutions of many forms. A solution is said to be complete if the domain of the solution dom $\boldsymbol{\phi}$ is unbounded, i.e., if length(dom $\boldsymbol{\phi}$) $= \infty$. A solution can be classified based on the structure of its domain, for instance if dom $\boldsymbol{\phi} \subset \{0\} \times \mathbb{N}$, the solution is *discrete*, and if dom $\boldsymbol{\phi} \subset \mathbb{R}_{\geq 0} \times \{0\}$, the solution is *continuous*. For more on the solution concept, see Goebel et al. (2012), Chapter 2.

Let's summarize the definitions of a solution with the example of the bouncing ball. The figures are generated using the MATLAB Hybrid equations toolbox (Sanfelice et al., 2013).

Example 9.3 ***Solutions to the bouncing ball system***
Recall our bouncing ball model,

$$\boldsymbol{C} = \{\boldsymbol{x} \in \mathbb{R}^2 : x_1 > 0 \text{ or } x_1 = 0, x_2 \geq 0\}, \qquad \dot{\boldsymbol{x}} = \boldsymbol{f}(\boldsymbol{x}) = \begin{bmatrix} x_2 \\ -\mu \end{bmatrix}$$
$$\boldsymbol{D} = \{\boldsymbol{x} \in \mathbb{R}^2 : x_1 = 0, x_2 < 0\}, \qquad \boldsymbol{x}^+ = \boldsymbol{g}(\boldsymbol{x}) = \begin{bmatrix} 0 \\ -\lambda x_2 \end{bmatrix}.$$

Figure 9.10 shows the position of the ball over the floor in terms of (t, j). The blue lines show the solution, which is a hybrid arc, and the red lines show the corresponding hybrid time domain. Notice that when the ball comes to rest on the floor, the hybrid model continues with consecutive jumping. This solution can be classified as eventually discrete. The simulation is stopped after $j = 20$ jumps.

Figure 9.11 shows the states of the bouncing ball system in terms of flows and jumps, position to the left and velocity to the right. The position flows from 5 m above the floor, and bounces up to a slightly lower height. After 9 seconds, the ball comes to rest on the ground, indicated by the blue asterisk. The position jumps are indicated by the red dots in the lower left plot, and the blue dashed line indicates the height above the floor the ball reaches in between jumps. The first jump occurs at 1 second, the second jump occurs at around 2.6 seconds, and so on. The velocity of the ball flows linearly with time, and when the ball hits the floor, the velocity changes direction instantaneously and the magnitude is reduced by the factor λ. After 9 seconds, the velocity stops flowing. In the velocity jumps, it can be seen that many jumps are needed before the ball comes to a complete rest on the floor.

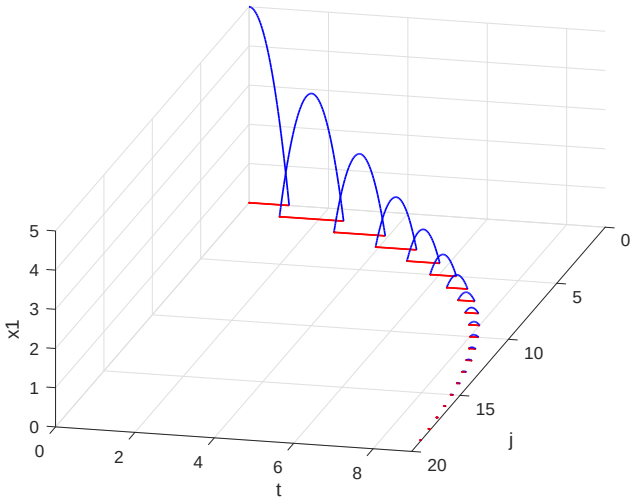

Figure 9.10: A solution (hybrid arc) to the bouncing ball system for initial condition $\boldsymbol{\phi}(0,0) = [5,0]^\top$, $\mu = 9.81$ and $\lambda = 0.8$.

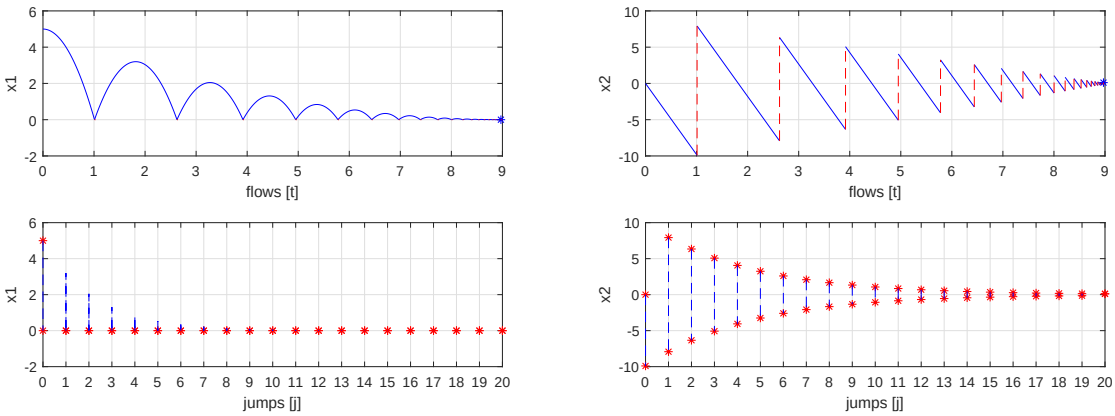

Figure 9.11: States for the bouncing ball system for initial condition $\boldsymbol{\phi}(0,0) = [5,0]^\top$, $\mu = 9.81$ and $\lambda = 0.8$. Position to the left, and velocity to the right.

9.3.3 Stability Analysis

For control purposes, analyzing the stability properties of the equilibrium point(s) of a system is desired. For a hybrid system the equilibrium is a set of points, usually denoted $\mathcal{A}$. Stability analysis provides qualitative information about the solutions to the system, and their long term trends. A useful mathematical property of systems is *well-posedness*, which usually implies that a solution exits, is unique, and that the solution has a reasonable dependence on the initial condition (Hadamard, 1902). A well-posed hybrid system has good robustness properties, and numerous stability tools may be applied[1]. Formally, a hybrid system $\mathcal{H} = (\boldsymbol{C}, \boldsymbol{F}, \boldsymbol{D}, \boldsymbol{G})$ is

[1]In some cases, there are reasons to consider hybrid systems that are not well-posed, i.e., systems that do not have solutions from some initial conditions, or systems with non-unique solutions (Goebel et al., 2009, pp.

well-posed if the system satisfies the hybrid basic assumptions.

Assumption 9.1 *Hybrid basic assumptions (Goebel et al., 2012, Assumption 6.5)*

(A1) $\boldsymbol{C}$ *and* $\boldsymbol{D}$ *are closed subsets of* $\mathbb{R}^n$*;*

(A2) The set-valued mapping $\boldsymbol{F} : \mathbb{R}^n \rightrightarrows \mathbb{R}^n$ *is outer semi-continuous (OSC) and locally bounded relative to* $\boldsymbol{C}$*,* $\boldsymbol{C} \subset$ *dom* $\boldsymbol{F}$*, and* $\boldsymbol{F}(\boldsymbol{x})$ *is convex for every* $\boldsymbol{x} \in \boldsymbol{C}$*;*

(A3) The set-valued mapping $\boldsymbol{G} : \mathbb{R}^n \rightrightarrows \mathbb{R}^n$ *is OSC and locally bounded relative to* $\boldsymbol{D}$*, and* $\boldsymbol{D} \subset$ *dom* $\boldsymbol{G}$*.*

A set-valued mapping $\boldsymbol{H} : \mathbb{R}^n \rightrightarrows \mathbb{R}^n$ is OSC if for each convergent sequence $\{(\boldsymbol{x}_i, \boldsymbol{y}_i)\}_{i=1}^{\infty}$ that satisfies $\boldsymbol{y}_i \in \boldsymbol{H}(\boldsymbol{x}_i), \forall i \geq 1$ and the limit denoted $(\boldsymbol{x}, \boldsymbol{y})$ satisfies $\boldsymbol{y} \in \boldsymbol{H}(\boldsymbol{x})$ (Goebel et al., 2012, Def. 5.9). If $\boldsymbol{F} : \boldsymbol{C} \to \mathbb{R}^n$ is continuous and $\boldsymbol{C}$ is closed, then $\boldsymbol{F}$ is OSC, or more generally if the graph of a mapping is closed, then the mapping is also OSC.

If a system can be written as in (9.3) and is nominally well-posed, the stability and robustness results from Goebel et al. (2012), Chapter 7, can be applied to check the stability properties of the hybrid system.

9.4 Case Study: Hybrid Observer for Improving the Transient Response of a Marine Vessel in Dynamic Positioning

During marine operations, both variations in stationary dynamics and transient behavior are important to account for in an all-year operation philosophy subject to changing weather, sea loads, and modes of operation (Perez, Sørensen, and Blanke, 2006). There are many unknown factors that may cause transients in the vessel response, both from the environment (e.g., wave trains and wind gusts) and triggered by the operation taking place (e.g., heading changes or crane operations of heavy goods). In this section, a case study modeling a hybrid system for a marine vessel including two observers, a controller and a switching mechanism is presented, see Figure 9.12. The goal is to improve the transient response of a vessel during a DP operation, while maintaining good stationary behavior.

The first observer is here referred to as a *model-based observer*, and is the same observer presented in Section 7.2 of the compendium (Fossen and Strand, 1999). The observer is based on the control plant model, includes wave filtering and bias force estimation, and is especially well suited during steady state operation. The other observer is here referred to as a *signal-based observer*, and has a different structure than the model-based observer. It is based on the kinematic model, which is introduced below. The signal-based observer is more reactive during transients, even though it is more sensitive to signal noise. The main idea of this work is therefore to use the model-based observer during steady state, and when a transient is detected, switch to the signal-based observer in order to secure better positioning performance. Performance of the proposed concept is demonstrated experimentally through model-scale experiments with the hybrid observer estimates used in closed-loop output feedback control, and through estimation

44-47). For instance, for certain classes of switching systems where the flow dynamics are described by set-valued mappings, or systems where the flow and jump sets overlap, the solutions may be non-unique. Stability analysis tools that do not require the hybrid system to be well-posed can be found in Goebel et al. (2012), Chapter 3.

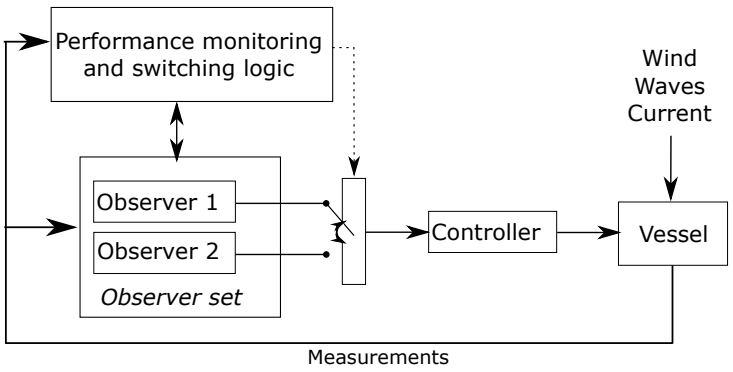

Figure 9.12: Hybrid observer for transient performance improvement.

on full-scale field data. Although not shown here, stability analysis of the hybrid system applies results from Goebel, Sanfelice, and Teel (2009). For details see Brodtkorb et al. (2018b).

This section starts by introducing the kinematic model, and assumptions on the measurements that are available for the observers to use. The two observers and control algorithm are presented before the hybrid system is assembled. The section is wrapped up with a discussion of performance model-scale experiments and estimation on full-scale field data.

9.4.1 Kinematic Model

In Sections 6.4 and 7.2, the process plant model and the control plant model were introduced. A different type of model that is not based on the process plant model, is the kinematic model. It is a 6 DOF model relating the angular rates of the vessel to angles, and the acceleration of the vessel to velocity and position, see Figure 9.13 for an illustration. The kinematic model splits

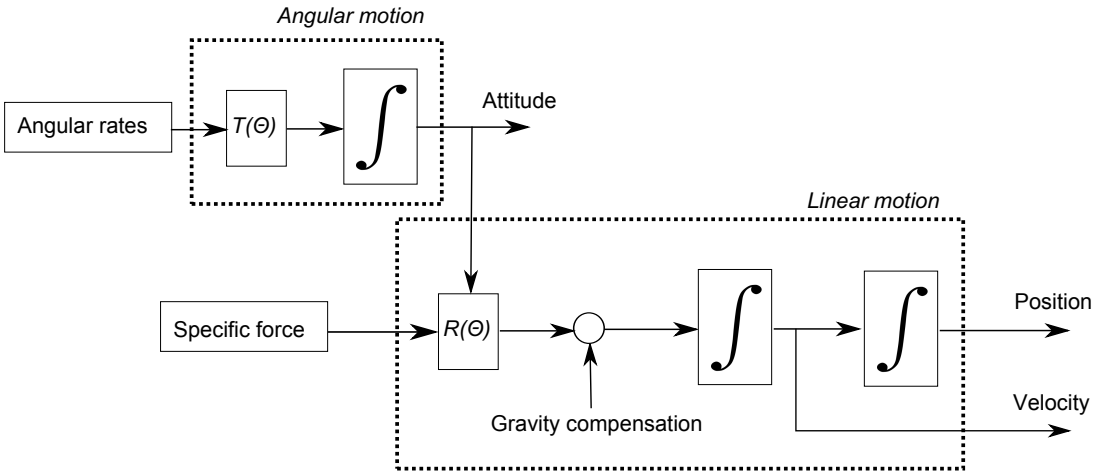

Figure 9.13: Kinematic model consisting of an angular part and a linear part. Angular rates are integrated to obtain the attitude, which are used to rotate the *specific force*, consisting of the linear acceleration of the vessel and acceleration due to gravity, into the Earth-fixed frame. The acceleration due to gravity is constant in the Earth-fixed frame, and therefore efficiently eliminated. The linear acceleration of the vessel is integrated to get velocity and position.

the vessel motion into an angular part and a translational part, and is essentially an expansion of the kinematic relation given by:

$$\begin{aligned} \dot{\boldsymbol{\eta}} &= \boldsymbol{J}(\boldsymbol{\Theta})\boldsymbol{\nu}, \\ &\Updownarrow \\ \begin{bmatrix} \dot{\boldsymbol{p}}^n \\ \dot{\boldsymbol{\Theta}} \end{bmatrix} &= \begin{bmatrix} \boldsymbol{R}(\boldsymbol{\Theta}) & \boldsymbol{0}_{3\times 3} \\ \boldsymbol{0}_{3\times 3} & \boldsymbol{T}(\boldsymbol{\Theta}) \end{bmatrix} \begin{bmatrix} \boldsymbol{v}^b \\ \boldsymbol{\omega}^b \end{bmatrix}. \end{aligned} \tag{9.6}$$

The generalized position $\boldsymbol{\eta}$ and velocity $\boldsymbol{\nu}$ of a marine vessel in 6 DOFs are defined as

$$\begin{aligned} \boldsymbol{\eta} &:= [\boldsymbol{p}^{n\top}, \boldsymbol{\Theta}^\top]^\top, \qquad & \boldsymbol{\nu} &:= [\boldsymbol{v}^{b\top}, \boldsymbol{\omega}^{b\top}]^\top \\ \boldsymbol{p}^n &:= [x, y, z]^\top, & \boldsymbol{v}^b &:= [u, v, w]^\top \\ \boldsymbol{\Theta} &:= [\phi, \theta, \psi]^\top, & \boldsymbol{\omega}^b &:= [p, q, r]^\top \end{aligned} \tag{9.7}$$

$\boldsymbol{\eta}$ is given in the NED frame, and $\boldsymbol{\nu}$ is in the body frame. $\boldsymbol{p}^n$ is the North, East, Down position, $\boldsymbol{v}^b$ is the linear velocity in surge, sway, heave, $\boldsymbol{\Theta}$ are the Euler angles roll, pitch, yaw, and $\boldsymbol{\omega}^b$ are the angular rates in roll, pitch and yaw. $\boldsymbol{R}(\boldsymbol{\Theta})$ is the rotation matrix, and $\boldsymbol{T}(\boldsymbol{\Theta})$ is the transformation of angular velocity from the body to the NED frame,

$$\boldsymbol{R}(\boldsymbol{\Theta}) := \begin{bmatrix} c\psi c\theta & -s\psi c\phi + c\psi s\theta s\phi & s\psi s\phi + c\psi c\phi s\theta \\ s\psi c\theta & c\psi c\phi + s\phi s\theta s\psi & -c\psi s\phi + s\theta s\psi c\phi \\ -s\theta & c\theta s\phi & c\theta c\phi \end{bmatrix}, \tag{9.8}$$

$$\boldsymbol{T}(\boldsymbol{\Theta}) := \begin{bmatrix} 1 & s\phi t\theta & c\phi t\theta \\ 0 & c\phi & -s\phi \\ 0 & s\phi/c\theta & c\phi/c\theta \end{bmatrix}, \tag{9.9}$$

with $s\cdot$ denoting $\sin(\cdot)$, $c\cdot$ denoting $\cos(\cdot)$, and $t\cdot$ denoting $\tan(\cdot)$.

The kinematic model is usually formulated in the Earth-fixed frame, but for marine vessels with relatively low speed, the rotation of the Earth can be neglected, and the kinematic model can be expressed in the NED frame. The equations may be written as

$$\dot{\boldsymbol{\Theta}} = \boldsymbol{T}(\boldsymbol{\Theta})\boldsymbol{\omega}^b \tag{9.10a}$$

$$\dot{\boldsymbol{p}}^n = \boldsymbol{v}^n \tag{9.10b}$$

$$\dot{\boldsymbol{v}}^n = \boldsymbol{R}(\boldsymbol{\Theta})\boldsymbol{f}^b + \boldsymbol{g}^n, \tag{9.10c}$$

where the states are the Euler angles $\boldsymbol{\Theta}$, and the NED position and velocity $(\boldsymbol{p}^n, \boldsymbol{v}^n)$ from (9.7), with the NED velocity vector $\boldsymbol{v}^n := \boldsymbol{R}(\boldsymbol{\Theta})\boldsymbol{v}^b$. $\boldsymbol{\omega}^b$ is the angular rate, and $\boldsymbol{f}^b$ is the specific force, i.e., the *measurable* acceleration including the linear acceleration of the vessel $\dot{\boldsymbol{v}}^b$ and the acceleration due to gravity $\boldsymbol{g}^n$, with units $[m/s^2]$. An alternative formulation of the attitude dynamics (9.10a) is

$$\dot{\boldsymbol{R}}(\boldsymbol{\Theta}) = \boldsymbol{R}(\boldsymbol{\Theta})\boldsymbol{S}(\boldsymbol{\omega}^b), \tag{9.11}$$

where the rotation matrix $\boldsymbol{R}(\boldsymbol{\Theta})$ given in (9.8) is the state, with

$$\boldsymbol{S}(\boldsymbol{\omega}^b) := \begin{bmatrix} 0 & -r & q \\ r & 0 & -p \\ -q & p & 0 \end{bmatrix}. \tag{9.12}$$

For more details on the kinematic model, see for instance Fossen (2011) or Bryne et al. (2017).

9.4.2 Measurements

Common instrumentation in DP vessels includes position reference systems, typically Global Navigation Satellite System (GNSS), compass, and inertial measurement units (IMU). The available measurements, denoted with subscript m, are here assumed to be of the form

$$\boldsymbol{p}_m^n = [x, y]^\top \tag{9.13a}$$
$$\psi_m^n = \psi \tag{9.13b}$$
$$\boldsymbol{\omega}_m^b = \boldsymbol{\omega}^b + \boldsymbol{b}_g \tag{9.13c}$$
$$\boldsymbol{f}_m^b = \boldsymbol{R}(\boldsymbol{\Theta})^\top(\dot{\boldsymbol{v}}^n - \boldsymbol{g}^n), \tag{9.13d}$$

where the measurements in the North-East-Down (NED) frame (an Earth-fixed local reference frame assumed to be inertial) have superscript n, and measurements in the body-fixed frame have superscript b. The vector $\boldsymbol{p}_m^n \in \mathbb{R}^2$ is the measured position in North and East. A vertical measurement may also be obtained through GNSS, but it is typically of low quality, and is not used here; see Section 9.4.3. The measured angle $\psi_m^n \in \mathbb{R}$ includes the low frequency yaw angle ψ and the wave-induced heading oscillations ψ_w, which are assumed to be small (Fossen and Strand, 1999). The angular velocity measurement $\boldsymbol{\omega}_m^b$ contains constant gyro bias $\boldsymbol{b}_g$, which needs to be compensated for in the signal-based observer. The vector $\boldsymbol{f}_m^b \in \mathbb{R}^3$ is the measured specific force (measurable acceleration), including the acceleration of the vessel $\dot{\boldsymbol{v}}^n$ and the acceleration due to gravity $\boldsymbol{g}^n \in \mathbb{R}^3$. $\boldsymbol{R}(\boldsymbol{\Theta}) \in \mathbb{R}^{3\times3}$ is the rotation matrix about the (z, y, x)-axes given in (9.8). We assume $\boldsymbol{f}_m^b$ is non-biased.

9.4.3 Candidate Observers and Controller

Two observers based on two philosophically different models of the same vessel are presented in the next sections. The relationship between the models are as follows:

$$\boldsymbol{\eta} + \boldsymbol{\eta}_w \equiv [\boldsymbol{p}_{(1,1)}^n, \boldsymbol{p}_{(2,1)}^n, \boldsymbol{\Theta}_{(3,1)}]^\top \tag{9.14a}$$
$$\boldsymbol{\nu} + \boldsymbol{\nu}_w \equiv [\boldsymbol{v}_{(1,1)}^b, \boldsymbol{v}_{(2,1)}^b, \boldsymbol{\omega}_{(3,1)}^b]^\top, \tag{9.14b}$$

with the subscript (i, j) denoting the elements of the corresponding vectors. On the left-hand side we have the generalized position vector $\boldsymbol{\eta} + \boldsymbol{\eta}_w \in \mathbb{R}^3$ (North, East, yaw) and generalized velocity vector $\boldsymbol{\nu} + \boldsymbol{\nu}_w \in \mathbb{R}^3$ (surge, sway, yaw) split into low-frequency and wave-frequency components. $\boldsymbol{\eta}$ and $\boldsymbol{\nu}$ will later be estimated in the model-based observer and marked with a hat. On the right-hand side we have the low-frequency and wave-frequency position $\boldsymbol{p}_{(1:2)}^n \in \mathbb{R}^2$ (North, East) and yaw $\boldsymbol{\Theta}_{(3,1)}$, and velocity $\boldsymbol{v}_{(1:2)}^b \in \mathbb{R}^2$ (surge, sway) and yaw $\boldsymbol{\omega}_{(3,1)}^b$. Two consecutive elements of a vector are denoted with subscript $(1:2)$. $\boldsymbol{p}^n$ and $\boldsymbol{v}^n := \boldsymbol{R}(\boldsymbol{\Theta})\boldsymbol{v}^b$ are estimated in the signal-based observer and marked with a hat. Note that $\boldsymbol{\Theta}_{(3,1)} \equiv \psi + \psi_w \approx \psi$, as the wave-frequency motion in yaw is assumed to be small.

Model-based observer

We have chosen to work with the nonlinear passive observer (Fossen and Strand, 1999), also presented in Chapter 7.2, since it is an intuitive observer to tune, and it has global stability properties. This observer is based on the DP control plant model, which is a simplification of the real vessel dynamics. The inputs to the observer are the measurement $\boldsymbol{y} = [\boldsymbol{p}_m^{n\top}, \psi_m^n]^\top \in \mathbb{R}^3$

and the control input $\boldsymbol{\tau} \in \mathbb{R}^3$. The 3 DOF model-based observer algorithm for a ship-shaped vessel in DP can be written as (Fossen and Strand, 1999)

$$\dot{\hat{\boldsymbol{\xi}}} = \boldsymbol{A}_\omega \hat{\boldsymbol{\xi}} + \boldsymbol{K}_{1,\omega} \tilde{\boldsymbol{y}} \tag{9.15a}$$

$$\dot{\hat{\boldsymbol{\eta}}} = \boldsymbol{R}(\psi_m^n) \hat{\boldsymbol{\nu}} + \boldsymbol{K}_2 \tilde{\boldsymbol{y}} \tag{9.15b}$$

$$\dot{\hat{\boldsymbol{b}}} = -\boldsymbol{T}_b^{-1} \hat{\boldsymbol{b}} + \boldsymbol{K}_3 \tilde{y} \tag{9.15c}$$

$$\boldsymbol{M} \dot{\hat{\boldsymbol{\nu}}} = -\boldsymbol{D}_L \hat{\boldsymbol{\nu}} + \boldsymbol{R}^\top(\psi_m^n) \hat{\boldsymbol{b}} + \boldsymbol{\tau} + \boldsymbol{R}^\top(\psi_m^n) \boldsymbol{K}_4 \tilde{\boldsymbol{y}} \tag{9.15d}$$

$$\hat{\boldsymbol{y}} = \hat{\boldsymbol{\eta}} + \boldsymbol{W} \hat{\boldsymbol{\xi}}, \tag{9.15e}$$

where $\hat{\boldsymbol{\xi}} \in \mathbb{R}^6, \hat{\boldsymbol{\eta}}, \hat{\boldsymbol{\nu}}, \hat{\boldsymbol{b}} \in \mathbb{R}^3$ are the state estimates. $\tilde{\boldsymbol{y}} := \boldsymbol{y} - \hat{\boldsymbol{y}}$ is the measurement estimation error, and $\boldsymbol{K}_{1,\omega} \in \mathbb{R}^{6\times3}, \boldsymbol{K}_2, \boldsymbol{K}_3, \boldsymbol{K}_4 \in \mathbb{R}^{3\times3}_{>0}$ are the observer gain-matrices. $\boldsymbol{A}_\omega \in \mathbb{R}^{6\times6}$ is a Hurwitz matrix containing wave parameters, $\boldsymbol{R}(\psi) \in \mathbb{R}^{3\times3}$ is the rotation matrix about the z-axis

$$\boldsymbol{R}(\psi) = \begin{bmatrix} \cos(\psi) & -\sin(\psi) & 0 \\ \sin(\psi) & \cos(\psi) & 0 \\ 0 & 0 & 1 \end{bmatrix}, \tag{9.16}$$

$\boldsymbol{M} = \boldsymbol{M}^\top \in \mathbb{R}^{3\times3}$ is the inertia matrix including added mass, $\boldsymbol{D}_L \in \mathbb{R}^{3\times3}$ is the linear damping coefficient matrix including second-order wave-induced damping, and $\boldsymbol{T}_b \in \mathbb{R}^{3\times3}$ is a diagonal matrix of bias time constants. The first-order model (9.15c) accounts for *slowly-varying* environmental disturbances from mean wind, current, and second-order wave loads, as well as unmodeled vessel dynamics.

(A1) The bias force dynamics (9.15c) are assumed to account for only slowly-varying loads (Fossen and Strand, 1999).

Having slow bias force estimation dynamics is beneficial for the steady state observer performance, in order to not interfere with the wave filtering. However, if the bias forces on the vessel changes fast, for instance when the vessel changes heading (unless the heading change is forced to be very slow), then the bias force estimate will lag behind during the transient and for some time after, propagating to the velocity and position estimates as well.

Wave filtering is achieved by separating the wave-frequency motion estimate $\hat{\boldsymbol{\eta}}_w = \boldsymbol{W}\hat{\boldsymbol{\xi}}$, $\boldsymbol{W} = [\boldsymbol{0}_{3\times3}, \boldsymbol{I}_{3\times3}]$ from the low frequency estimate $\hat{\boldsymbol{\eta}}$, giving the output from the model-based observer $\hat{\boldsymbol{\eta}}_1 := \hat{\boldsymbol{\eta}}$ and $\hat{\boldsymbol{\nu}}_1 := \hat{\boldsymbol{\nu}}$. For later use, the model-based observer dynamics, are written compactly as

$$\dot{\hat{\boldsymbol{x}}}_1 = \boldsymbol{F}_1(\hat{\boldsymbol{x}}_1, \boldsymbol{p}_m^n, \psi_m^n), \tag{9.17}$$

with state vector

$$\hat{\boldsymbol{x}}_1 = [\hat{\boldsymbol{\xi}}^\top, \hat{\boldsymbol{b}}^\top, \hat{\boldsymbol{\eta}}^\top, \hat{\boldsymbol{\nu}}^\top]^\top \in \mathbb{R}^{15}.$$

Signal-based observer

Grip et al. (2015) propose a nonlinear observer, for GNSS-aided inertial navigation with biased gyro measurements. It is based on the kinematic model introduced above, with an angular and a translational part, relating the position, velocity, and acceleration of the vessel in 6 DOFs.

The inputs to the signal-based observer are $\boldsymbol{p}_m^n$, ψ_m^n, $\boldsymbol{\omega}_m^b$, and $\boldsymbol{f}_m^b$ from (9.13). The rotation matrix $\boldsymbol{R}(\boldsymbol{\Theta})$ given in (9.8) is estimated directly and the gyro bias is compensated for, giving

$$\dot{\hat{\boldsymbol{R}}}(\boldsymbol{\Theta}) = \hat{\boldsymbol{R}}(\boldsymbol{\Theta})\boldsymbol{S}(\boldsymbol{\omega}_m^b - \hat{\boldsymbol{b}}_g) + \sigma \boldsymbol{L}_p \hat{\boldsymbol{J}} \tag{9.18a}$$

$$\dot{\hat{\boldsymbol{b}}}_g = \mathrm{Proj}_{M_b}(\hat{\boldsymbol{b}}_g, -\boldsymbol{L}_I \mathrm{vex}(\mathbb{P}_a(\hat{\boldsymbol{R}}_s(\boldsymbol{\Theta})^\top \boldsymbol{L}_P \hat{\boldsymbol{J}}))). \tag{9.18b}$$

$\hat{\boldsymbol{R}}(\boldsymbol{\Theta})$ is the rotation matrix estimate, $\hat{\boldsymbol{b}}_g$ is the gyro bias estimate, and the angular rate estimate is $\hat{\boldsymbol{\omega}}^b := \boldsymbol{\omega}_m^b - \hat{\boldsymbol{b}}_g$. The projection function $\mathrm{Proj}_{M_b}(\cdot,\cdot)$ (Grip et al., 2015, Appendix) ensures that $\hat{\boldsymbol{b}}_g$ is bounded, and the $\boldsymbol{S}(\cdot)$, $\mathrm{vex}(\cdot)$, and $\mathbb{P}_a(\cdot)$ operators are defined in the footnote[2]. $\hat{\boldsymbol{R}}_s(\boldsymbol{\Theta})$, appearing in (9.18b), is saturated elementwise with bound 1; $\hat{\boldsymbol{R}}_s(\boldsymbol{\Theta}) := \mathrm{sat}_1(\hat{\boldsymbol{R}}(\boldsymbol{\Theta}))$. The gain-matrices are $\boldsymbol{L}_P \in \mathbb{R}^{3\times3}_{>0}, \boldsymbol{L}_I \in \mathbb{R}^{3\times3}_{>0}$, and $\sigma \geq 1$ is a scaling factor that is tuned to achieve stability. $\hat{\boldsymbol{J}}$ is a stabilizing term (Grip et al., 2015, (3) and (5)) that takes ψ_m^n measured by the compass, and the specific force measurement $\boldsymbol{f}_m^b$ as input. The translational observer algorithm is

$$\dot{\hat{p}}_I = \hat{\boldsymbol{p}}_{(3,1)}^n + k_{pipi}\tilde{p}_I \tag{9.19a}$$

$$\dot{\hat{\boldsymbol{p}}}^n = \hat{\boldsymbol{v}}^n + \boldsymbol{C}_p \boldsymbol{e} \tag{9.19b}$$

$$\dot{\hat{\boldsymbol{v}}}^n = \hat{\boldsymbol{f}}^n + \boldsymbol{g}^n + \boldsymbol{C}_v \boldsymbol{e} \tag{9.19c}$$

$$\dot{\boldsymbol{\xi}}_f = -\sigma \boldsymbol{L}_p \hat{\boldsymbol{J}} \boldsymbol{f}_m^b + \boldsymbol{C}_\xi \boldsymbol{e} \tag{9.19d}$$

$$\hat{\boldsymbol{f}}^n = \hat{\boldsymbol{R}}(\boldsymbol{\Theta})\boldsymbol{f}_m^b + \boldsymbol{\xi}_f, \tag{9.19e}$$

with estimates $\hat{p}_I, \hat{\boldsymbol{p}}^n, \hat{\boldsymbol{v}}^n$ and $\hat{\boldsymbol{f}}^n$, $\hat{\boldsymbol{R}}(\boldsymbol{\Theta})$ is from (9.18), and $\boldsymbol{\xi}_f$ is a correction term on the specific force estimate. (9.19b-e) are standard kinematic observer equations, and (9.19a) is an addition from Bryne, Fossen, and Johansen (2015) that comes instead of using the vertical GNSS position measurement height. The augmentation is motivated by the fact that a marine vessel in normal operation oscillates in heave about the mean sea surface. It may be assumed that:

(A2) The mean vertical position of the vessel over time is zero (Godhaven, 1998), $p_I = 0$.

p_I is called the *virtual vertical reference*. In (9.19a) the vertical position estimate $\hat{\boldsymbol{p}}_{(3,1)}^n$ is integrated to give $\hat{p}_I$, which is compared with p_I and used as the driving error for the vertical dynamics. For more details, see Bryne et al. (2015). The driving error is $\boldsymbol{e} := [\tilde{p}_I, \tilde{\boldsymbol{p}}^\top]^\top \in \mathbb{R}^3$ with $\tilde{\boldsymbol{p}} := \boldsymbol{p}_m^n - \hat{\boldsymbol{p}}_{(1:2)}^n \in \mathbb{R}^2$, $\tilde{p}_I := p_I - \hat{p}_I = 0 - \hat{p}_I \in \mathbb{R}$. The correction gain-matrices are

$$\boldsymbol{C}_p = \begin{bmatrix} \boldsymbol{0}_{2\times1} & \boldsymbol{K}_{pp} \\ k_{ppi} & \boldsymbol{0}_{1\times2} \end{bmatrix} \quad \boldsymbol{C}_v = \begin{bmatrix} \boldsymbol{0}_{2\times1} & \boldsymbol{K}_{vp} \\ k_{vpi} & \boldsymbol{0}_{1\times2} \end{bmatrix} \quad \boldsymbol{C}_\xi = \begin{bmatrix} \boldsymbol{0}_{2\times1} & \boldsymbol{K}_{\xi p} \\ k_{\xi pi} & \boldsymbol{0}_{1\times2} \end{bmatrix}.$$

The North and East gain components are $\boldsymbol{K}_{pp}, \boldsymbol{K}_{vp}, \boldsymbol{K}_{\xi p} \in \mathbb{R}^{2\times2}_{>0}$, and the down gains are $k_{pipi}, k_{ppi}, k_{vpi}, k_{\xi pi} \in \mathbb{R}_{>0}$. The signal-based estimation error dynamics are written compactly as

$$\dot{\hat{\boldsymbol{x}}}_2 = \boldsymbol{F}_2(\hat{\boldsymbol{x}}_2, \boldsymbol{p}_m^n, \psi_m^n, \boldsymbol{\omega}_m^b, \boldsymbol{f}_m^b), \tag{9.20}$$

with state vector

$$\hat{\boldsymbol{x}}_2 = [\hat{\boldsymbol{r}}^\top, \hat{\boldsymbol{b}}_g^\top, \hat{p}_I, \hat{\boldsymbol{p}}^{n\top}, \hat{\boldsymbol{v}}^{n\top}, \hat{\boldsymbol{f}}^{n\top}]^\top \in \mathbb{R}^{22},$$

[2]For a vector $\boldsymbol{x} \in \mathbb{R}^3$, $\boldsymbol{S}(\boldsymbol{x})$ denotes a skew-symmetric matrix so that for any $\boldsymbol{y} \in \mathbb{R}^3$, $\boldsymbol{S}(\boldsymbol{x})\boldsymbol{y} = \boldsymbol{x} \times \boldsymbol{y}$, where $\times$ denotes the cross product. The skew-symmetric part of a matrix $\boldsymbol{X}$ is denoted by $\mathbb{P}_a(\boldsymbol{X}) = \frac{1}{2}(\boldsymbol{X} - \boldsymbol{X}^\top)$. The linear function $\mathrm{vex}(\boldsymbol{X})$, with $\boldsymbol{X}$ skew symmetric is defined so that $\boldsymbol{S}(\mathrm{vex}(\boldsymbol{X})) = \boldsymbol{X}$ and $\mathrm{vex}(\boldsymbol{S}(\boldsymbol{x})) = \boldsymbol{x}$.

with $\hat{\boldsymbol{r}} := [\boldsymbol{R}_{(1,:)}(\boldsymbol{\Theta}), \boldsymbol{R}_{(2,:)}(\boldsymbol{\Theta}), \boldsymbol{R}_{(3,:)}(\boldsymbol{\Theta})]^\top \in \mathbb{R}^9$. ':' denotes all elements of the row/column.

The output from the signal-based observer is in the same way as for the model-based observer, so that $\hat{\boldsymbol{\eta}}_2 := [\hat{\boldsymbol{p}}^n_{(1,1)}, \hat{\boldsymbol{p}}^n_{(2,1)}, \hat{\boldsymbol{\Theta}}_{(3,1)}]^\top$, $\hat{\boldsymbol{\nu}}_2 := [\hat{\boldsymbol{v}}^b_{(1,1)}, \hat{\boldsymbol{v}}^b_{(2,1)}, \hat{\boldsymbol{\omega}}^b_{(3,1)}]^\top$, where the heading angle estimate $\hat{\boldsymbol{\Theta}}_{(3,1)}$ is extracted from $\hat{\boldsymbol{R}}(\boldsymbol{\Theta})$, and $\hat{\boldsymbol{v}}^b = \hat{\boldsymbol{R}}^\top(\boldsymbol{\Theta})\hat{\boldsymbol{v}}^n$. Because this observer relies on the specific force measurements instead of estimating the bias force, it reacts fast and accurately to transients. Here, no wave filter is included so $\hat{\boldsymbol{\eta}}_2$ and $\hat{\boldsymbol{\nu}}_2$ capture the combined low-frequency and wave-frequency motion. For shorter periods of time this may be acceptable, which is the case during transients.

Controller

The control objective is to control the vessel to the desired time-varying trajectory $\boldsymbol{\eta}_d(t)$ with the desired velocity trajectory $\boldsymbol{\nu}_d(t)$. The proposed control law is a PID control law with reference feedforward.

$$\begin{aligned}
\dot{\boldsymbol{\zeta}}_s &= \hat{\boldsymbol{\eta}}_s - \boldsymbol{\eta}_d \\
\boldsymbol{\tau} &= -\boldsymbol{K}_p \boldsymbol{R}^\top(\psi^n_m)(\hat{\boldsymbol{\eta}}_s - \boldsymbol{\eta}_d) - \boldsymbol{K}_d(\hat{\boldsymbol{\nu}}_s - \boldsymbol{\nu}_d) \\
&\quad - \boldsymbol{K}_i \boldsymbol{R}^\top(\psi^n_m)\boldsymbol{\zeta}_s + \boldsymbol{M}\dot{\boldsymbol{\nu}}_d + \boldsymbol{D}_L\boldsymbol{\nu}_d,
\end{aligned} \tag{9.21}$$

where $\boldsymbol{\tau} \in \mathbb{R}^3$ is the commanded thrust vector, $\boldsymbol{K}_p, \boldsymbol{K}_d, \boldsymbol{K}_i \in \mathbb{R}^{3\times 3}_{\geq 0}$ are gain-matrices, and $\hat{\boldsymbol{\eta}}_s$ and $\hat{\boldsymbol{\nu}}_s$ are the estimates from the model-based observer when $s = 1$, and from the signal-based observer when $s = 2$. $\boldsymbol{\zeta}_s$ compensates for the unknown bias force vector $\boldsymbol{b}$ with dynamics $\dot{\boldsymbol{b}} = -\boldsymbol{T}_b^{-1}\boldsymbol{b}$, see Section 7.2.2. The last two terms in (9.21) are feedforward terms of the desired acceleration and desired velocity.

9.4.4 Hybrid System

In this section the hybrid observer is assembled. The observers flow in parallel in the hybrid observer design, and the position and velocity in surge, sway, and yaw from the observer that performs best is used in output feedback with (9.21). The estimation errors are monitored, and switching is limited by hysteresis. We start by designing the performance monitoring for transient detection and switching logic.

Performance monitoring

We want to use the model-based observer in steady state, due to good wave filtering capabilities, and want to use the signal-based observer in transients because the response is faster. In transients, the bias force on the vessel change rapidly, and the bias estimate in the model-based observer is not able to keep up. This deviation will propagate to the model-based observer estimates of velocity and position. Therefore, we choose to compute the difference in estimation error in North and East $(\boldsymbol{p}^n_m - \hat{\boldsymbol{\eta}}_{2(1:2)}) - (\boldsymbol{p}^n_m - \hat{\boldsymbol{\eta}}_{1(1:2)}) = (\hat{\boldsymbol{\eta}}_{1(1:2)} - \hat{\boldsymbol{\eta}}_{2(1:2)})$ in order to evaluate the performance of the observers. We also take the Euclidean norm on this difference. Because the vessel is subject to wave loads, $||\hat{\boldsymbol{\eta}}_{1(1:2)} - \hat{\boldsymbol{\eta}}_{2(1:2)}||$ may oscillate a lot. To get a smoother signal to base the switching upon, we save n past differences in a shift register of size n with state $\boldsymbol{m} \in \mathbb{R}^n$, see (9.22c), so that siwtching can be based upon the average of the states $\boldsymbol{m}$. The position measurement has sample time T, and a timer t_m keeps track of when to save a

new estimation difference into state m_1 of the shift register. The dynamics for the performance monitoring is as follows:

$$\dot{m}_i = 0, \qquad i = \{1, ..., n\} \tag{9.22a}$$

$$t_m = -1 \tag{9.22b}$$

$$m_i^+ = \begin{cases} ||\hat{\boldsymbol{\eta}}_{1(1:2)} - \hat{\boldsymbol{\eta}}_{2(1:2)}||, & \text{for } i = 1 \\ m_{i-1}, & \text{for } i = \{2, ..., n\} \end{cases} \tag{9.22c}$$

$$t_m^+ = T \tag{9.22d}$$

$\boldsymbol{m}$ does not change during flows. The *performance monitoring signal* $\bar{m}$ is the average of the shift register states

$$\bar{m} = \tfrac{1}{n} \sum_{i=1}^{n} m_i. \tag{9.23}$$

We send $\bar{m}$ to the switching logic, and choose which observer to use in closed loop based upon this quantity.

Switching logic

During steady state, the observer estimates will agree, since the estimates all converge to the vessel motion. Then we can choose a threshold $\varepsilon_{ss} \geq 0$ so that the performance monitoring signal $\bar{m}$ will be smaller than this when the vessel is in steady state. During transients the bias force from the environment on the vessel change rapidly, and the bias estimate in the model-based observer is not able to keep up. This deviation propagates to the model-based observer estimates of velocity and position. This does not occur for the signal-based observer estimates, which uses the measured acceleration of the vessel instead of a bias estimate. Then we can choose a threshold $\varepsilon_{tr} \geq 0$ so that the performance monitoring signal increases above this threshold during transients. Choose $\epsilon_{tr} > \epsilon_{ss}$ with some margin to provide hysteresis that suppresses unnecessary switching back and forth.

Switching based upon the estimation difference of the observers is a *reactive* switching strategy. In the case where a heading change is commanded, we can also switch *proactively*, as we know the forces on the hull will change rapidly in this situation. Therefore we choose to use the signal-based observer in closed loop when the desired yaw rate $\boldsymbol{\nu}_{d(3,1)}$ is larger than some threshold δ. The switching logic dynamics can be written as:

$$\dot{s} = 0 \tag{9.24a}$$

$$s^+ = \begin{cases} 1, & \text{if } \bar{m} \leq \epsilon_{ss} \\ 2, & \text{if } \bar{m} \geq \epsilon_{tr} \\ 2, & \text{if } \boldsymbol{\nu}_{d(3,1)} \geq \delta \\ s, & \text{otherwise,} \end{cases} \tag{9.24b}$$

When applying Assumption (A1) we assume that the control plant model is an exact deterministic model of the real vessel dynamics. Then there may only be switching due to reference changes and due to transients during initialization. However, as shown through experiments in Section 9.4.5, switching based on performance is triggered because Assumption (A1) of slowly-varying bias loads does not hold during transients.

Assembling the hybrid system

The control plant model and the kinematic model represent, with some overlap, the same underlying dynamics being the motion of the vessel. Therefore the kinematic model with state $\boldsymbol{x}_2$ is not included in the hybrid analysis. We define the state vector of the hybrid system as

$$\begin{aligned}\boldsymbol{x} &:= (\boldsymbol{x}_1, \boldsymbol{\zeta}_s, \hat{\boldsymbol{x}}_1, \hat{\boldsymbol{x}}_2, \boldsymbol{m}, t_m, s) \\ &\in \mathbb{R}^{15} \times \mathbb{R}^3 \times \mathbb{R}^{15} \times \mathbb{R}^{22} \times \mathbb{R}^n \times [0, T] \times \{1, 2\},\end{aligned} \tag{9.25}$$

consisting of the control plant model state $\boldsymbol{x}_1$, the integral state in the control law $\boldsymbol{\zeta}_s$, the model-based observer estimates $\hat{\boldsymbol{x}}_1$, the signal-based observer estimates $\hat{\boldsymbol{x}}_2$, the performance monitoring states $\boldsymbol{m}$, the timer t_m, and the switching signal s.

The flow dynamics of the hybrid system constitutes the vessel described by the control plant model, controller, observer, and timer dynamics:

$$\dot{\boldsymbol{x}}_1 = \boldsymbol{F}_0(\boldsymbol{x}_1, \boldsymbol{\tau}) \tag{9.26a}$$

$$\dot{\boldsymbol{\zeta}}_s = \hat{\boldsymbol{\eta}}_s - \boldsymbol{\eta}_d \tag{9.26b}$$

$$\dot{\hat{\boldsymbol{x}}}_1 = \boldsymbol{F}_1(\hat{\boldsymbol{x}}_1, \boldsymbol{p}_m^n, \psi_m^n) \tag{9.26c}$$

$$\dot{\hat{\boldsymbol{x}}}_2 = \boldsymbol{F}_2(\hat{\boldsymbol{x}}_2, \boldsymbol{p}_m^n, \psi_m^n, \boldsymbol{\omega}_m^b, \boldsymbol{f}_m^b) \tag{9.26d}$$

$$\dot{\boldsymbol{m}} = \boldsymbol{0}, \tag{9.26e}$$

$$\dot{t}_m = -1 \tag{9.26f}$$

$$\dot{s} = 0 \tag{9.26g}$$

(9.26a) are the control plant model of the vessel dynamics, with the feedback control law (9.21) as input, (9.26b) is the integrator in the controller, (9.26c) is the model-based observer (9.15), and (9.26d) is the signal-based observer from (9.18) and (9.19). $s \in \{1, 2\}$ is a logic variable that indicates if the model-based or signal-based estimates are used in closed-loop control. $s = 1$ is model-based and $s = 2$ is the signal-based estimates, as decided by the performance monitoring and switching logic. Flows are allowed when $\boldsymbol{x} \in \boldsymbol{C}$,

$$\boldsymbol{C} := \mathbb{R}^{55+n} \times [0, T] \times \{1, 2\}. \tag{9.27}$$

The jump dynamics for the hybrid system constitutes the performance monitoring and switching logic:

$$\boldsymbol{x}_1^+ = \boldsymbol{x}_1,\ \boldsymbol{\zeta}_s^+ = \boldsymbol{\zeta}_s,\ \hat{\boldsymbol{x}}_1^+ = \hat{\boldsymbol{x}}_1,\ \hat{\boldsymbol{x}}_2^+ = \hat{\boldsymbol{x}}_2 \tag{9.28a}$$

$$m_i^+ = \begin{cases} ||\hat{\boldsymbol{\eta}}_{1(1:2)} - \hat{\boldsymbol{\eta}}_{2(1:2)}||, & \text{for } i = 1 \\ m_{i-1}, & \text{for } i = \{2, ..., n\} \end{cases} \tag{9.28b}$$

$$t_m^+ = T \tag{9.28c}$$

$$s^+ = \begin{cases} 1, & \text{if } \bar{m} \leq \epsilon_{ss} \\ 2, & \text{if } \bar{m} \geq \epsilon_{tr} \\ 2, & \text{if } \boldsymbol{\nu}_{d(3,1)} \geq \delta \\ s, & \text{otherwise,} \end{cases} \tag{9.28d}$$

The states $\boldsymbol{x}_1, \boldsymbol{\zeta}_s, \hat{\boldsymbol{x}}_1$, and $\hat{\boldsymbol{x}}_2$ do not change during jumps (9.28a). The performance monitoring and switching dynamics for $\boldsymbol{m}$, t_m, and s are explained in the previous section. Jumps are allowed when $\boldsymbol{x} \in \boldsymbol{D}$,

$$\boldsymbol{D} := \mathbb{R}^{55+n} \times \{0\} \times \{1, 2\}. \tag{9.29}$$

9.4.5 Experimental Setup, Results and Discussion

The model-scale experiments were conducted with C/S Inocean Cat I Drillship, a 1:90 scale model with dimensions (length, beam) = (2.578 m, 0.44 m) in the Marine Cybernetics Laboratory (MCLab) at NTNU. The full-scale DP data was collected during the AMOS DP Research Cruise 2016 (ADPRC'16) onboard R/V Gunnerus, see Skjetne et al. (2017) for details. The model-based observer was in both cases tuned using tuning rules in Fossen (2011), Ch. 11, for good steady state, and adequate transient performance. The same IMUs were used to provide input to the signal-based observer both in model-scale and full-scale, showing that the proposed hybrid observer setup is robust to large variations in signal-to-noise ratio. In full-scale, the signal-based observer tuning from Bryne et al. (2015) was tweaked to work better for R/V Gunnerus, but in the MCLab the tuning was found from scratch. Tuning of the controller in the MCLab was found using standard PID tuning rules (Fossen, 2011, Ch. 12), which were tweaked to work well with both observer estimates in feedback. The algorithms were coded in Matlab/Simulink and run in NI Veristand[3] software.

Model-scale experiments

The Froude-scaled sea state in the MCLab had significant wave height $H_s = 0.04$ m and peak period $T_p = 1.1$ s, which in full-scale corresponds to a rough sea state with $H_s = 3.6$ m and $T_p = 10.4$ s. In a rough sea state the expected mean wind velocity is 11.3-13.9 m/s (Fossen, 2011, Ch.8), which constitutes a lot of the mean forces on the hull. Since wind is not available in the MCLab, the directional dependence of the bias force that is seen in full-scale applications was less prominent in the lab. Hence, switching based on observer performance was triggered by pushing the model off setpoint using a boat-hook, inducing an unknown, rapid transient, see Figure 9.14. The model is pushed off setpoint twice; at time 170 s and 520 s. In the first transient, the observer is fixed with the model-based observer in closed loop. The vessel spends a long time coming back to the setpoint, since the estimates from the model-based observer (especially the velocity estimate) is off during the transient. In the second transient the observer is allowed to switch based on performance, and chooses the signal-based observer in closed loop for most of the transient, although there is some switching back and forth. The reason is that the hysteresis from choosing $\varepsilon_{tr} > \varepsilon_{ss}$ is small, $\epsilon_{tr} = 0.02, \epsilon_{ss} = 0.005, \delta = 0.05$.

The heading reaches steady state somewhat faster when the signal-based observer is in closed loop, *although comparison of the two pushes can be seen only as indications of performance since the conditions were not identical.* Brodtkorb et al. (2016b) and the section below compares the model-based observer, signal-based observer and hybrid approach in closed loop in simulations, and estimation performance on full-scale data, respectively.

Switching during heading changes, based on desired yaw rate, worked well in the MCLab. The transients during heading changes were amplified both by waves and by moving the global

[3]The Bogacki-Shampine solver (Matlab ode23) was used with fixed step 0.01 s, www.ni.com/veristand/.

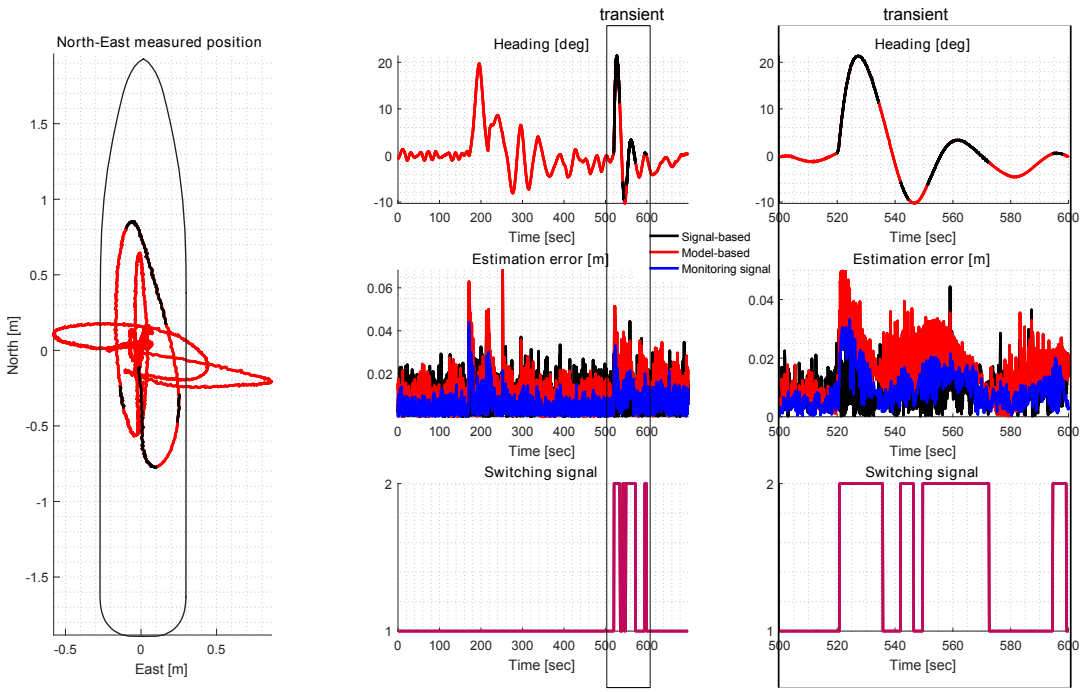

Figure 9.14: Closed-loop control: C/S Inocean Cat I Drillship is pushed off position using a boat-hook at time 170 s and 520 s. North-East position track (left), heading, estimation error, monitoring signal and switching signal (middle), details of the second transient (right). Position and heading trajectories are red when model-based estimates are used in closed loop, and black when signal-based estimates are used. Environmental conditions corresponding to rough full-scale sea state with significant wave height $H_s = 3.6$ m, peak period $T_p = 10.4$ s, head sea, no wind nor current, $\epsilon_{tr} = 0.02, \epsilon_{ss} = 0.005, \delta = 0.05$.

reference frame, which can be seen as a current from the model's perspective. How large δ is chosen should be dependent on the vessel size and the maximum desired yaw rate.

During the experiments it was observed that the thrusters changed thrust direction more frequently when the signal-based estimates were used in closed loop, since the states were not wave filtered. The thrust usage when the model-based or the signal-based observer estimates were used in closed loop was not significantly different.

Estimation based on full-scale measurements

Figure 9.15 shows estimation results on full-scale R/V Gunnerus data from a DP 4 corner maneuver. The vessel moves along the sides of a square of length 40 m, triggering couplings between the different DOFs in five maneuvers. The current velocity was 0.3 m/s from 290°, and the wind velocity was 7 m/s from 260°. The wave buoy recorded waves with $H_s = 0.2$ m and $T_p = 13.6$ s. Even though the waves were not large the day of the tests, the bias forces from the environment on the hull of R/V Gunnerus were sufficiently large, so it was easy to find values of ϵ_{ss} and ϵ_{tr} that gave a sufficient hysteresis effect: $\epsilon_{tr} = 0.5, \epsilon_{ss} = 0.03, \delta = 0.2$. The maneuver and observer behavior is explained in the following.

1. *Pure sway:* The maneuver starts at 17 s with a setpoint change to -40 m East while

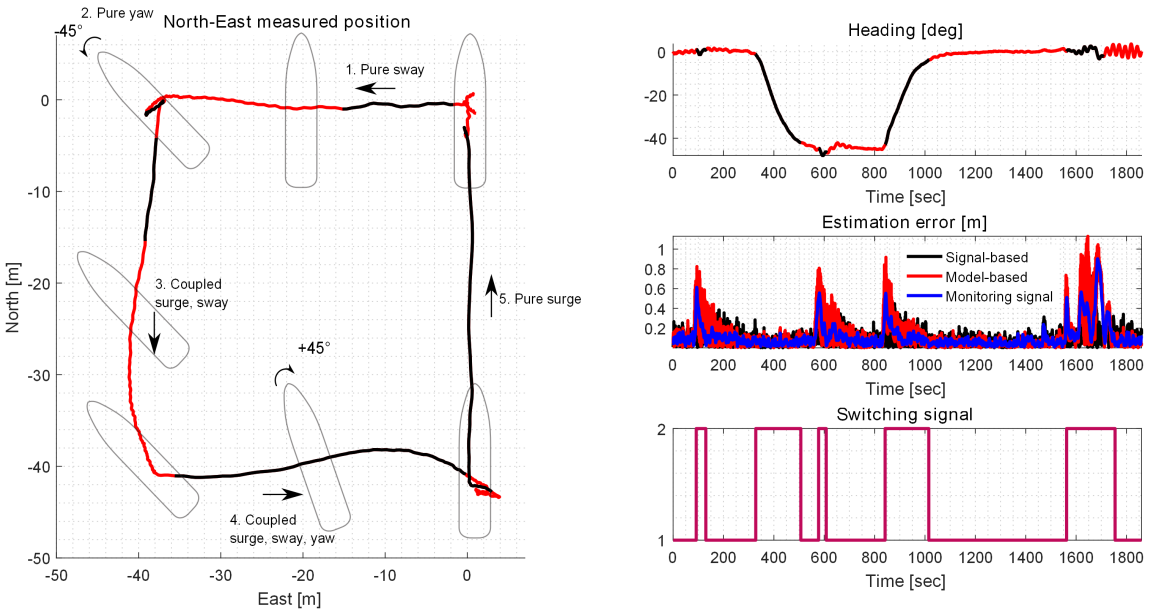

Figure 9.15: Estimation: R/V Gunnerus is doing a DP 4 corner maneuver, staring at (0,0) and moving as indicated by the arrows. North-East position track (left), heading, observer estimation error and monitoring signal, and switching signal (right). The position and heading trajectories are red when the model-based estimates should be used in closed loop, and black when the signal-based estimates should be used in closed loop. Environmental conditions: current 0.3 m/s, 290°, wind 7 m/s, 260°, and waves with significant wave height $H_s = 0.2$ m, peak period $T_p = 13.6$ s, and direction 260°. $\epsilon_{tr} = 0.5, \epsilon_{ss} = 0.03, \delta = 0.2$.

maintaining heading 0° (North) giving pure sway motion. As the vessel accelerates, the forces on the hull change, and the model-based estimation error suddenly increases. This is caught by the monitoring function, which triggers a switch to the signal-based observer for a short time, while the model-based bias estimate converges to the new value.

2. *Pure yaw:* The heading is changed to -45° at around 170 s while keeping the position, and since the desired yaw rate is nonzero, the signal-based observer is chosen for most of the maneuver.

3. *Coupled surge and sway:* At time 519 s the setpoint is changed -40 m South while maintaining -45° heading. This gives a coupled surge and sway motion, and makes it more challenging for the vessel to stay on the desired track. The signal-based observer is chosen for the first fourth of the leg, and the model-based observer is chosen for the rest.

4. *Coupled surge, sway and yaw:* The setpoint is changed from (-40,-40) to (0,-40) while changing the heading from -45° to 0° at time 783 s. This is a coupled maneuver in surge, sway, and yaw, and the signal-based observer is chosen for almost the entire leg.

5. *Pure surge:* The last leg of the DP 4 corner test is a pure surge motion 40 m North back to (0,0). A pure surge motion should not induce much transients, however during this

maneuver the heading oscillates ±3°. The signal-based observer is chosen for most of the leg.

If the third and fourth parts of the maneuver were to be done close to other offshore infrastructure, R/V Gunnerus may have been required to either reduce the speed, or choose another control strategy in order to stay on the desired straight-line segments of the square. Depending on the vessel size, propulsion system, and instrumentation, a smarter choice of controller could make the vessel stay on the desired path with a higher speed, reducing the vessel operation time. This DP 4-corner maneuver took around 30 minutes to complete. See Skjetne et al. (2017) for more on the tests.

Figure 9.16 and Table 9.2 show the cumulative estimation errors over time when the model-based, signal-based and hybrid observer (switching between the model-based and signal-based) are used for estimation on full-scale data. The hybrid observer has the lowest estimation error at the end of the time series in surge and sway, a bit lower than the signal-based observer, and much lower than the model-based observer, which accumulates estimation error fast during transients. The signal-based observer has the smallest estimation error in yaw; 34% lower than the model-based observer, and 28% lower than the hybrid observer. A reason may be that the signal-based observer uses more information about the yaw angle through the yaw rate to construct the estimate. Keep in mind that the maneuver R/V Gunnerus performs in this case includes a lot of transients, and therefore favors the signal-based observer over the model-based observer. In the case where there are more periods of steady state, the model-based observer and hybrid approach are more beneficial.

Table 9.2: Cumulative estimation errors for the model-based, signal-based and hybrid observers at the end of R/V Gunnerus' DP 4 corner maneuver.

Observer	Surge [m]	Sway [m]	Yaw [deg]
Model-based	1368.3	998.0	1372.7
Signal-based	964.3	949.9	902.9
Hybrid	945.1	901.3	1247.3

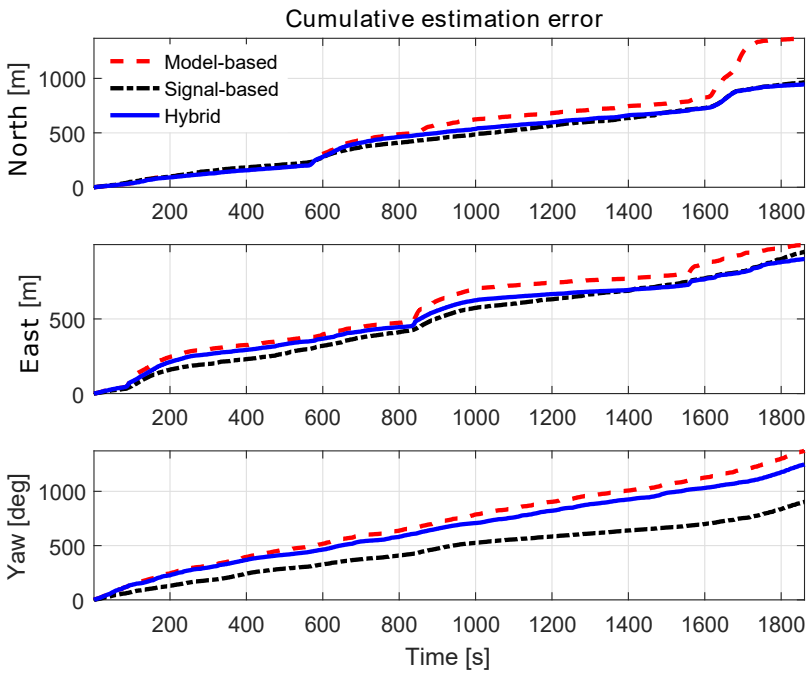

Figure 9.16: Cumulative estimation error when the model-based, signal-based and hybrid observers are used for estimation on full scale field data from R/V Gunnerus doing a DP 4-corner maneuver.

9.5 Chapter Summary

In this chapter an introduction to mathematical modeling of hybrid systems for the purpose of marine applications was given.

- The control structure for a general hybrid marine control system was presented, and the importance of designing appropriate performance monitoring and switching logic was discussed.
- The general structure for a mathematical model of a hybrid system was introduced, focusing on the data structure and solutions.
- A case study of a hybrid observer for transient performance improvement for a vessel in DP was presented in detail.

Chapter 10

Modeling and Control of Ocean Structures

This chapter presents research concerning marine control systems applied on ocean structures. In particular, various marine operations involving slender flexible structures and marine vessels are studied.

Learning outcome of the chapter: The reader shall understand:

- Mathematical modeling of flexible slender marine structures described by partial differential equations (PDE).
- The main principles of numerical solution of the PDE describing slender flexible structures using finite element method (FEM).
- How to model and control top tensioned risers on tensioned leg platforms (TLP).
- How to improve the dynamically positioned (DP) system on a drilling unit to automatically incorporate the behavior of the drilling riser in optimizing the setpoint to the DP controller. This one example towards autonomous marine operations and systems.

10.1 Introduction

A flexible system is here defined as a dynamic system, which includes discernible *elastic* or *flexible* motions in addition to the *rigid body* motion dynamics. When designing a control system for a flexible system it is essential to account for the flexibility in the development of the controller algorithm and in the location of sensors and actuators. In this chapter two different examples of control of flexible ocean structures are shown.

The first example is about modeling and control of tensioned risers installed on so-called tensioned leg platforms (TLPs). We will in this section investigate the possibility to reduce the riser interference by use of automatic control of the riser top tension. In addition, the aim of this section is to give an introduction to the concept of tension legged platforms, the finite element method (FEM) and usage, the differences between a control plant model (CPM) and process plant model (PPM), how to verify a mathematical model, control of slender ocean structures and how to combine advanced modeling and control for real applications.

The second example considers dynamic positioning of a surface vessel connected to a riser conducting a drilling or work-over operation. As the surface vessel is one of the boundary conditions to the riser, coupling phenomena between the surface vessel motion and the riser may cause troubles, unless precautions are taken in the dynamic positioning system. By proper control of the vessel position, an d thereby the boundary condition, the riser is controlled. Conventional controller designs for dynamic positioning of ships and floating marine structures have so far been based on the principle on automatic positioning in the horizontal-plane about desired position and heading coordinates defined by the operator. A three degrees of freedom multivariable controller either of linear or nonlinear type, normally with feedback signals from surge, sway and yaw position and velocities, has been regarded as adequate for the control objective. For floating structures with small waterplane area such as semi-submersibles, feedback from roll and pitch angular rotation velocity may also be included to avoid thrust induced roll and pitch motions that are caused by the hydrodynamic and the geometrical couplings between the horizontal and vertical planes. However, for certain marine operations this control philosophy may not be the most appropriate approach ensuring safety and cost-effectiveness. For drilling and work-over operations the main positioning objective is to minimize the bending stresses along the riser and the riser angle magnitudes at the well head on the subsea structure, and at the top joint as well. A positioning control strategy solely based on manual setting of the desired position coordinates may not be the most optimal solution for these applications. Here a hybrid dynamic positioning controller, that also accounts for riser angle offsets and bending stresses is proposed. It is shown that a significant reduction in riser angle magnitude can be achieved.

10.2 Mathematical Background

Flexible systems are described by *partial differential equations* (PDEs) involving two and several independent variables (often time and spatial coordinates) in contrast to *ordinary differential equations* (ODEs) that are dependent on a single independent variable only (often the time). If we have spatial independent variables, then, by specifying the values of the dependent variable on some boundary denoted as *boundary conditions*, arbitrary functions in the general solution can be evaluated and a particular solution can be obtained. If one of the independent variables is the time, then we must also specify the *initial conditions* in order to obtain a particular solution. Problems involving boundary and initial conditions are called *boundary-value problems*. ODE together with an initial condition is called an *initial-value problem.*

In the present study, a focus will be set on implementation of the solutions. The software package MATLAB will be used, and predefined functions within this software will be accessed in the solutions.

10.2.1 Ordinary Differential Equations (ODE)

An ordinary differential equation (ODE) is an equation that contains one or several derivatives, in one variable, of an unknown function $\mathbf{f}(t, \mathbf{r})$. In general form, ODEs are often written as

$$\mathbf{M}(t, \mathbf{r}) \frac{d\mathbf{r}}{dt} = \mathbf{f}(t, \mathbf{r}), \tag{10.1}$$

where $\mathbf{M}$ is a matrix, $\mathbf{r}$ is state vector and $\mathbf{f}$ is a vector of functions. If $\mathbf{M}$ is invertible, it may be incorporated in $\mathbf{f}$. Otherwise, the system is said to be a differential-algebraic problem (DAE),

but this class of systems will not be a topic in cable mechanics. Notice that the equation is written in vector notation. If the equation contains higher order derivatives, reordering may bring it over to the general form.

Example 10.1 *Conversion of higher order ODEs.*
Given the following system

$$\frac{d^2y}{dt^2} + 4y = 0. \tag{10.2}$$

We want the system to fit into the general form, and want to have only first derivatives. The following substitution may solve this:

$$y_1 = y, \tag{10.3}$$
$$y_2 = \frac{dy}{dt}. \tag{10.4}$$

Rewriting the equation we find the following system of ODEs

$$\frac{dy_1}{dt} = y_2, \tag{10.5}$$
$$\frac{dy_2}{dt} = -4y_1. \tag{10.6}$$

this fits into the general form where $\mathbf{M} = \mathbf{I}_{2\times 2}$ *and* $\mathbf{f} = \begin{bmatrix} y_2 \\ -4y_1 \end{bmatrix}$.

The solution to an ODE is a specific function $\mathbf{r}(t)$ which satisfies (10.1) in the domain of interest, $\mathbf{\Omega}(t)$, where $\{t \in [t_0, t] \to \mathbb{R},\ \mathbf{\Omega} \to \mathbb{C}^n \mid n = \dim(\mathbf{r})\}$. The derivative of ODEs is often time, but we will see that also spatial variables may be taken as arguments. ODEs may be further classified on linearity and the order of derivatives. Dependent on this classification analytical solutions may be found, and various techniques are available, see for instance Kreyszig (1993).

Initial value problems (IVP) and boundary value problems (BVP)

A problem described by ODEs may be classified as an Initial Value Problem (IVP) or a Boundary Value Problem (BVP). If an analytical solution to a problem can be found, both IVPs and BVPs may be solved directly by introducing the known parameters in the expression. If no analytical solution can be found, several numerical methods are available. However, these do often demand that a classification of the problem as IVP or BVP is done in advance.

IVPs requires that the initial values of the states are known. The solution is the states for different values of the independent variable, e.g. time. The probably most common use of IVPs described by ODEs is time simulation of a given system. In control problems, the systems are often described by ODEs, and the effect of the controller may be verified by a simulation in time. The general features of IVPs/ODEs are described in detail in Hoffman (2001). Numerical solution of ODE/IVPs are almost solely based on *finite difference methods* . The Runge-Kutta methods are widely used for ODE/IVPs, but other methods may be better for specific systems Egeland and Gravdahl (2002).

Example 10.2 *Initial value problem: Mass-spring-damper system.*

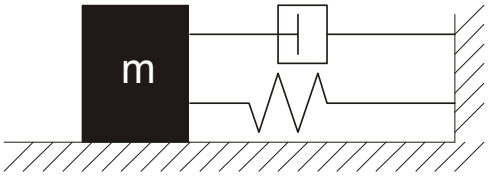

Figure 10.1: Mass-spring-damper system.

A mass-spring-damper system may be described by the following equation

$$m\ddot{x} + d\dot{x} + kx = 0, \tag{10.7}$$

where m is the mass, d is the damping, k is the spring stiffness and x is the mass' position. We substitute $x_1 = x$ and $x_2 = \dot{x}$. This gives the following set of ODEs:

$$\begin{bmatrix} \dot{x}_1 \\ \dot{x}_2 \end{bmatrix} = \begin{bmatrix} 0 & 1 \\ -\frac{k}{m} & -\frac{d}{m} \end{bmatrix} \begin{bmatrix} x_1 \\ x_2 \end{bmatrix}. \tag{10.8}$$

Given a set of initial values for x_1 and x_2, the system's states (position and velocity of the mass) as a function of time may be solved directly from the ODEs. This is a typical initial value problem.

If the present problem described by ODEs has specified boundary values, it is classified as a BVP. ODE/BVPs are often steady-state problems where the boundary values are given in space. Typical examples are heat-transfer problems and beams with lateral loading.

Example 10.3 *Boundary value problem: Deflection of a beam.*

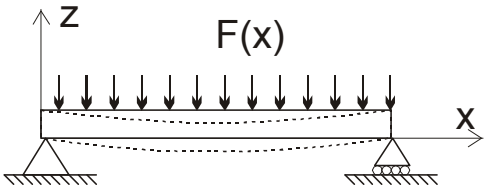

Figure 10.2: Uniform beam with lateral load, $F(x)$.

The deflection of a homogeneous beam may be described by the following equation:

$$EI\frac{d^4z}{dx^4} = F(x), \tag{10.9}$$

where E is the modulus of elasticity, I is the moment of inertia of the beam cross section and $F(x)$ is a lateral distributed force acting on the beam. This equation is sometimes written as

$$\frac{d^2M(x)}{dx^2} = F(x), \tag{10.10}$$

where $M(x) = EI\frac{d^2z}{dx^2}$. The system may be rewritten in the following form

$$\begin{bmatrix} \frac{dz_1}{dx} \\ \frac{dz_2}{dx} \\ \frac{dz_3}{dx} \\ \frac{dz_4}{dx} \end{bmatrix} = \begin{bmatrix} z_2 \\ z_3 \\ z_4 \\ \frac{F(x)}{EI(x)} \end{bmatrix}, \tag{10.11}$$

where the first substitution is $z_1 = z$. This is a problem where the boundary values are known, and the dependent variable, x, is spatial. If we assume that $F(x)$ is constant (or symmetric around the middle of the beam), we realize that the deflection will be symmetric. It is now possible to apply boundary conditions to the ODEs: $z_1(0) = z_1(L) = 0$ and $\frac{d^2z(0)}{dx^2} = \frac{d^2z(L)}{dx^2} = 0$, or $z_3(0) = z_3(L) = 0$ gives four boundary conditions for the system of four equations. Notice that the two last boundary conditions gives a pinned beam. If these were replaced by $z_2(0) = z_2(L) = 0$, it would represent a clamped beam. The problem of finding a $z(x)$ which fulfills the boundary conditions is a boundary value problem.

For ODE/BVPs and PDEs (see Section 10.2.2), three types of boundary conditions may be specified. Assume that the equation is written on standard form and that f is the solution of the equation (for PDEs, u is often the solution). Then the following boundary condition may be specified:

1. *Dirichlet boundary condition.* The value of the function is specified.

   f is specified on the boundary.

2. *Neumann boundary condition.* The value of the derivative normal to the boundary is specified.

   $\frac{\partial f}{\partial n}$ is specified on the boundary.

3. *Mixed boundary condition.* A combination of the function and its normal derivative is specified on the boundary, i.e.

   $af + b\frac{\partial f}{\partial n}$ is specified on the boundary.

In Example 10.3, *Dirichlet boundary conditions* were applied for the rewritten problem.

Hoffman (2001) shows two main classes of methods for BVPs: Finite difference methods and methods based on trial functions which have to satisfy conditions on the boundaries. The finite difference approach is divided into the *shooting methods* and the *equilibrium methods*.

The shooting method takes the boundary values at one end as initial values and solves the problem as an IVP. If the solution does not satisfy the boundary values at the other end, a tuning of the initial values or some other parameters of the system must be done before another "shot" from the first end is performed. In this way an iterative approach may solve the problem.

The equilibrium method constructs a finite difference approximation of the exact ODE at every point of the finite difference grid, including the boundaries. A system of coupled finite difference equations results, which must be solved simultaneously, thus relaxing the entire solution, including the boundary conditions, simultaneously.

The second class of solving ODE/BVPs is based on approximating the solution by a linear combination of trial functions, and determining the coefficients in the trial functions so as to satisfy the boundary-value ODE in some optimum manner. The most common examples of this type of methods are:

1. The Rayleigh-Ritz method.
2. The Galerkin method.
3. The finite element method.

An overview of these methods are important in cable mechanics, and will be described further at the end of this section.

Implementation of ODE problems in MATLAB

The MATLAB computer package provides several routines which are suited to solve ODE/IVP. The routines are based on the system's characteristics, e.g. stiffness. The most general routine is `ode45`, and should be used as a first attempt.

Implementation of Example 10.2 requires two functions stored at the same location on the computer. One main program and one function returning the derivatives of the states. Each fixed parameter is given a value, and a time dependant solution to the system is found. Before we proceed to the code, please recognize the system in the example to be of the form $\dot{\mathbf{x}} = \mathbf{A}\mathbf{x}$. This expression may be found in the code below:

```
function msd
m=2;    % Mass
d=1.5;  % Damping
k=6;    % Spring constant
x0=[3 5]'; %Initial values

[t,y]=ode45('xdot',[0 20], x0,[],m,d,k);

figure(1)
clf
subplot(211)
plot(t,y(:,1))
grid
xlabel('Time')
ylabel('Position')

subplot(212)
plot(t,y(:,2))
grid
xlabel('time')
ylabel('Velocity')

function xd=xdot(t,x,flag,m,d,k)
A=[    0    1;
    -k/m -d/m];
xd=A*x;
```

The code above results in the plot found in Figure 10.3.

Implementation of ODE/BVPs are slightly more difficult than IVPs. MATLAB provides a routine for two-point boundary-value problems. A good solution is dependent on the system's properties and a good initial guess. If analytical expressions for the partial derivatives can be given, the solution will be more accurate and speed up.

Let's solve the beam deflection problem in Example 10.3. Some reasonable parameters are given, and the resulting code is given below:

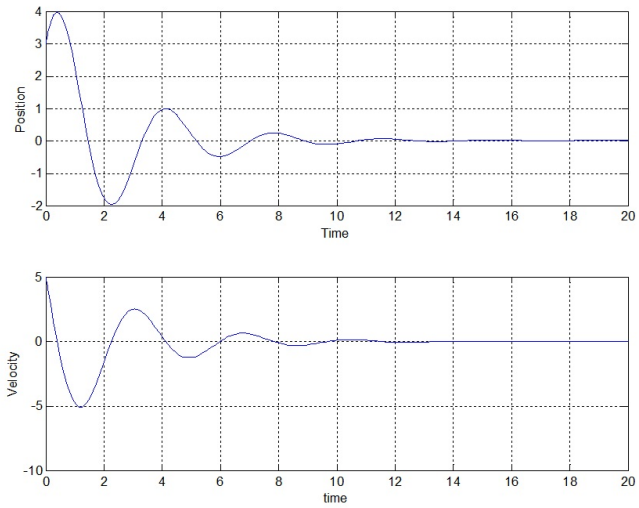

Figure 10.3: Time simulation of mass-spring-damper system.

```
function beam
w=0.05;     %Width of beam
h=0.1;      %Height of beam
L=5;        %Length of beam
I=w*h^3/12; %Moment of inertia
E=90e9;     %Modulus of elasticity
F=-2000;    %Constant distributed force
x0=0:0.1:L; %Initial mesh
sol = bvpinit(x0,[0 0 0 0]); %Creates initial guess for all states
sol = bvp4c(@beamODE,@beamBC,sol,[],E,I,F,L); %Solves the BVP
%Plots the result
figure(1)
clf
plot(sol.x,sol.y(1,:))
xlabel('x-axis')
ylabel('Deflection (z-value)')
title('Geometry of the beam')
%System's ODEs
function dzdx = beamODE(x,z,E,I,F,L)
dzdx = [  z(2)
          z(3)
          z(4)
          F/(E*I) ];
%System's boundary values
function res = beamBC(ya,yb,E,I,F,L)
res = [ ya(1)   %Pos. 1st end=0 :z(0)=0
        yb(1)   %Pos. 2nd end=0 :z(L)=0
        ya(3)   %2. derivative 1st end=0 :z''(0)=0
```

```
yb(3)]; %2. derivative 2nd end=0 :z''(L)=0
```

The code above will produce the plot shown in Figure 10.4.

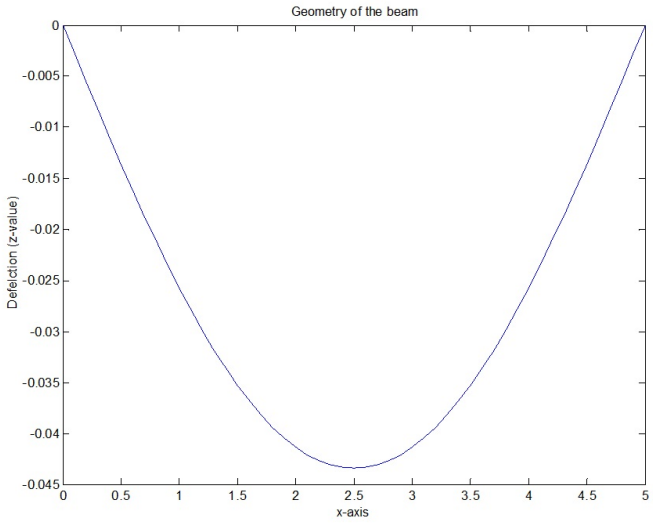

Figure 10.4: Deflection of a beam with transversal load.

10.2.2 Partial Differential Equations (PDE)

A partial differential equation (PDE) is an equation which contains one or more partial derivatives of an (unknown) function of two or more independent variables. The order of the highest derivative is called the order of the equation. PDEs may be linear, quasi-linear or nonlinear. A further classification in elliptic, parabolic and hyperbolic equations may be carried out, but this will not be discussed in the present text. A few classes of PDEs have analytical solutions. The others have to rely on numerical solutions. Computer packages like MATLAB may solve some easy and common classes of PDEs, but the user will some times have to write his own algorithms to solve a specific problem.

For the current topics the PDEs considered is of the class nonlinear hyperbolic equations. Equations in this class is among others suited to solve continuum mechanics as cable mechanics problems, vibrating strings, membranes and the motion of compressible fluids.

In Section 10.2.1 we divided problems described by ODEs into initial value problems and boundary value problems. For the problems involving PDEs, we will in the present text only consider initial-boundary value problems, IBVPs. The current problems will have both spatial and time dependent terms. This may be considered as two incorporated ODEs of time and spatial problems. In the previous section it was mentioned that time dependent problems were associated with IVPs and spatial equilibrium problems usually were associated with BVPs. When it comes to PDE/IBVPs, a direct relation to ODEs can be found: The time dependence is solved as an initial value problem and the spatial dependence is solved as a boundary value problem.

Example 10.4 *PDE for a vibrating string - the wave equation.*

It can be shown that a vibrating string (with small amplitudes) may be modelled as

$$\frac{\partial^2 z(x,t)}{\partial t^2} = c^2 \frac{\partial^2 z(x,t)}{\partial x^2}, \tag{10.12}$$

where z is deflection, x is longitudinal axis and $c = \sqrt{\frac{T}{m_0}}$. T is axial tension in the string and m_0 is mass per unit length. Notice that the solution u depends on both time and space, and that the partial derivatives of time and space are constituted in the equation. With that, this equation qualifies to the definition of a PDE. This particular equation is called the wave equation.

Example 10.5 *Bernoulli beam.*

We will now extend the static formulation for a homogenous beam with transversal load in Example 10.3. It can be shown that time dependent response from a specified load may be written

$$m_0 \frac{\partial^2 z}{\partial t^2} + EI \frac{\partial^4 z}{\partial x^4} = F(t,x). \tag{10.13}$$

The boundary conditions are similar to the static case. Because the equation contains derivatives of both space and time, it fulfills the criterion to be a PDE.

MATLAB basic version has one built-in routine for solving PDEs. It may only solve a limited class of equations, and only in one spatial variable. To apply this routine, the equation should be written in the following form

$$\mathbf{c}(x,t,u,\frac{\partial u}{\partial x})\frac{\partial u}{\partial t} = x^{-m}\frac{\partial}{\partial x}\left(x^m \mathbf{f}(x,t,u,\frac{\partial u}{\partial x})\right) + \mathbf{g}(x,t,u,\frac{\partial u}{\partial x}), \tag{10.14}$$

where x is the spatial vector, t is time, $\mathbf{c}$ is a diagonal matrix and $\mathbf{g}$ and $\mathbf{f}$ are vectors. u is the solution. It turns out that this is not suitable for our hyperbolic systems, and an additional toolbox is needed. MATLAB's PDE toolbox can only solve problems in a 2-dimensional region, have to be hacked in order to solve this 1-dimensional problem. The 3rd-party software FEMLAB is able to solve problems in 1D, 2D and 3D and time, and would be an appropriate supplement to the MATLAB family if a commercial solver is chosen.

A more direct option is to make an implementation on your own. This will be discussed in the next section.

10.2.3 Methods for Numerical Solution of the Relevant Systems

In this section we will focus on the numerical solution of selected ODEs and PDEs. We will formulate the spatial terms as a boundary value problem. Insertion of the solution will lead to a time dependent ODE which may be solved with common methods described in e.g. Egeland and Gravdahl (2002). The basis for the subsequent discussion will be the equation for an Euler Bernoulli beam

$$m_0 \frac{\partial^2 z}{\partial t^2} + EI \frac{\partial^4 z}{\partial x^4} = F(t,x). \tag{10.15}$$

The Rayleigh-Ritz method

This section is mainly based on Hoffman (2001), Larsen (2000) and a variety of other sources which are not referred here.

The Rayleigh-Ritz method belongs to a class called *variational* methods. The objective of these is to determine a minimum or maximum of a functional which depends on other functions such as

$$J\left[u\right] = \int_{t_1}^{t_2} \int_{x_1}^{x_2} G(x, t, u, u', u'', \dot{u})\, dx\, dt, \tag{10.16}$$

where J is the *functional* and G is the *fundamental function*. The goal is now to determine the particular function $u(x)$ which extremalizes $J[u]$.We then define

$$\begin{aligned} \delta J &= \int_{t_1}^{t_2} \int_{x_1}^{x_2} \left(\frac{\partial G}{\partial u} + \frac{\partial G}{\partial u'} \delta u' + \frac{\partial G}{\partial u''} \delta u'' + \frac{\partial G}{\partial t} \delta \dot{u} \right) dx\, dt, \\ &= \int_{t_1}^{t_2} \int_{x_1}^{x_2} \left(\frac{\partial G}{\partial u} + \frac{\partial G}{\partial u'} \frac{d\left(\delta u\right)}{dx} + \frac{\partial G}{\partial u''} \frac{d^2\left(\delta u\right)}{dx^2} + \frac{\partial G}{\partial t} \frac{d(\delta u)}{dt} \right) dx\, dt, \end{aligned} \tag{10.17}$$

where δ is the *variational operator*. In order to find an extremum, J is set equal to zero. We apply integration by parts on the last three terms inside the integral, and because we demand $\delta u = 0$ at the boundaries (according to fixed end points) we obtain

$$\delta J = \int_{t_1}^{t_2} \int_{x_1}^{x_2} \left[\frac{\partial G}{\partial u} - \frac{d}{dx}\left(\frac{\partial G}{\partial u'} \right) + \frac{d^2}{dx^2}\left(\frac{\partial G}{\partial u''} \right) - \frac{d}{dt}\left(\frac{\partial G}{\partial \dot{u}} \right) \right] dx\, dt = 0. \tag{10.18}$$

This equation must be satisfied for arbitrary distributions of δu, and this requires that the expression inside the brackets to be equal to zero. We now receives the general *Euler equation* for a time dependent system with one-dimensional deflection

$$\frac{\partial G}{\partial u} - \frac{d}{dx}\left(\frac{\partial G}{\partial u'} \right) + \frac{d^2}{dx^2}\left(\frac{\partial G}{\partial u''} \right) - \frac{d}{dt}\left(\frac{\partial G}{\partial \dot{u}} \right) = 0. \tag{10.19}$$

Now, it may not be obvious how this relates to the solution of an ODE/BVP or PDE. Let us consider the static beam problem in Example 10.3, written on the following form

$$\frac{d^2 M(x)}{dx^2} = M''(x) = F(x). \tag{10.20}$$

This equation contains no terms in time or u or u' (M is the solution, as u was the solution in the beginning of the section). The method requires that a fundamental function, G, is found, and this should yield the system equation when the Euler equation is applied (10.19). In this particular case, the functional will be given by

$$G = \left(M'\right)^2 + 2FM. \tag{10.21}$$

Applying the Euler equation (10.19) gives

$$\frac{\partial G}{\partial M} = \frac{d}{dx}\left(\frac{\partial G}{\partial M'} \right), \tag{10.22a}$$

$$2F = \frac{d}{dx}\left(2M'\right), \tag{10.22b}$$

$$M'' = F, \tag{10.22c}$$

which (fortunately) resulted in the original equation.

We assume that the solution may be written in the form

$$u(t,x) = \sum_{i=1}^{i=n} \phi_i(x)\, q_i(t). \tag{10.23}$$

This equation is often written as the product of vectors

$$u(t,x) = \phi^T(x)\, \mathbf{q}(t). \tag{10.24}$$

Because our system is time independent, $q_i(t) = C_i$, where C_i is a constant. The Rayleigh-Ritz method now asks for suggestions for what the solution looks like. These suggestions should be placed in the $\phi_i$which are called trial functions. It is very important that these functions are linearly independent, i.e. $\phi_i = c\phi_j \Rightarrow c = 0 \forall i \neq j$,and that they satisfy the boundary conditions. For the current problem $\phi_1(x) = x$, $\phi_2(x) = x(x-1)$ and $\phi_3(x) = x^2(x-1)$ should be suitable.

The next step is to substitute the trial functions into the functional to obtain $J[C_i]$. Our suggestion is from (10.23) that the beam's bending moment can be found from

$$u(x) = M(x) = C_1 x + C_2 x(x-1) + C_3 x^2(x-1). \tag{10.25}$$

Use of (10.21) then gives a function on the form $J[u(x, C_1, C_2, C_3)]$ .Taking the variation of this, we find that $\delta J[u(x, C_1, C_2, C_3)] = \frac{\partial J}{\partial C_1}\delta C_1 + \frac{\partial J}{\partial C_2}\delta C_2 + \frac{\partial J}{\partial C_2}\delta C_3$, which is only satisfied when

$$\frac{\partial J}{\partial C_i} = 0. \tag{10.26}$$

When a solution to (10.26) is found with respect to C_i, the values should be inserted into (10.23). This will now be the final solution to the problem according to the Rayleigh-Ritz method.

In our case this gives the following equations when the beam has length 1

$$J = \int_0^1 \left(M'\right)^2 + 2FM\, dx, \tag{10.27}$$

$$\frac{\partial J}{\partial C_2} = \int_0^1 \frac{\partial}{\partial C_2}\left(M'\right)^2 + \frac{\partial}{\partial C_2} 2FM\, dx, \tag{10.28}$$

$$\frac{\partial J}{\partial C_3} = \int_0^1 \frac{\partial}{\partial C_3}\left(M'\right)^2 + \frac{\partial}{\partial C_3} 2FM\, dx. \tag{10.29}$$

$C_1 = 0$ is determined from the boundary conditions. Assuming that $F(x)$ =constant, some algebra leads to the following relation:

$$\frac{1}{3}C_2 + \frac{1}{6}C_3 = \frac{F}{6}, \tag{10.30}$$

$$\frac{1}{6}C_2 + \frac{2}{15}C_3 = \frac{F}{12}, \tag{10.31}$$

which has solution $C_2 = \frac{F}{2}$, $C_3 = 0$. Inserting into (10.25) gives the solution indicated in Figure 10.5. $z(x)$ may be found from integration of the relation $M(x) = EI\frac{d^2z}{dx^2}$.

Until this stage we have only considered time independent systems. When time dependence must be considered, the $q_i(t)$ in (10.23) will no longer be constant. The first extended challenge

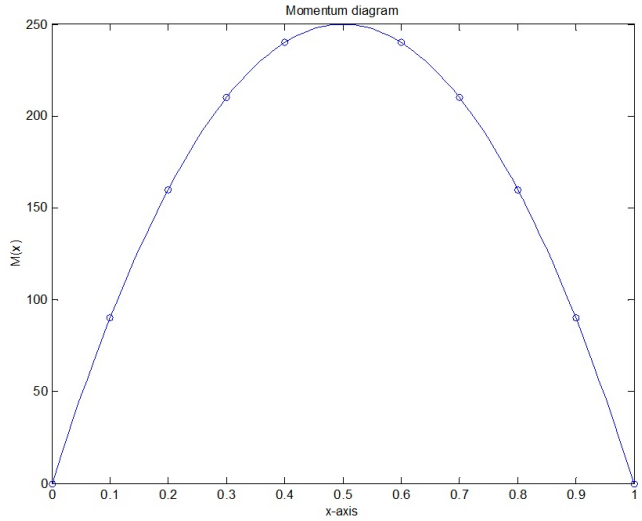

Figure 10.5: Bending moment diagram for the transversally loaded beam. 'o' is the solution found from the Rayleigh-Ritz method, and the solid line is an exact solution for some special parameters.

will now be to find a suitable fundamental function which fits into the Euler equation (10.19). *Hamilton's principle* states that the integral of the difference between kinetic and potential energy is stationary (attains a minimum value) for the real path of motion when the initial and final values are given Larsen (2000). When we are working on energy, it is natural to consider the Lagrange functional which is defined by:

$$L = T - U - A, \tag{10.32}$$

where T is the kinetic energy, U is the potential (strain) energy and A is the potential energy for the external load. The Lagrangian for the beam example will then be given by

$$L = \int_0^L (T - U - A)\, dx = \int_0^L \left[\frac{1}{2} m_0 \dot{z}^2 - \frac{1}{2} EI(z'')^2 - F(t,x)z\right] dx = \int_0^L G\, dx. \tag{10.33}$$

Hamilton's principle states that

$$\delta \int_{t_1}^{t_2} L dt = \delta \int_{t_1}^{t_2} \int_0^L G\, dx\, dt. \tag{10.34}$$

Insertion into the Euler equation (10.19) gives

$$m_0 \frac{\partial^2 z}{\partial t^2} + EI \frac{\partial^4 z}{\partial x^4} = F(t,x), \tag{10.35}$$

which is the equation which we want to solve. This energy-based approach is a common way of finding the functional which has to be utilized in the Rayleigh-Ritz method.

The next step is to find appropriate functions for $q_i(t)$. It is usual to assume that the system exhibits harmonic vibrations., i.e. $\mathbf{q}(t) = \mathbf{q}_0 \sin \omega t$. It can be shown that the fundamental

frequency ω may be found as the Rayleigh quotient, which is expressed by

$$\omega^2 = \frac{\mathbf{q}_0^T \mathbf{K} \mathbf{q}_0}{\mathbf{q}_0^T \mathbf{M} \mathbf{q}_0}, \tag{10.36}$$

where the stiffness matrix is given from

$$\mathbf{K} = \int_0^L EI\phi'' \left(\phi''\right)^T dx, \tag{10.37}$$

and the mass matrix is given from

$$\mathbf{M} = \int_0^L m_0 \phi \phi^T dx. \tag{10.38}$$

This eigenvalue problem in n degrees of freedom will give n eigenfrequencies. Notice that the eigenfrequencies depends on the shape functions (via $\mathbf{K}$ and $\mathbf{M}$**).** The shape functions should therefore be chosen from physical insight of the particular problem. With this method restrictions on the mode of vibration are introduced. The system may be too stiff, and the method gives an upper bound solution to the eigenfrequency ω. If the external load force, $F(t, x)$, cannot be described by a linear combination of the elements in $\mathbf{q}(t)$, the solution is not likely to reflect this force's influence on the vibration in a very good manner.

This closes the discussion on the Rayleigh-Ritz method. Although this method is widely used within structural mechanics, it will not be applied to any of the problems related to cable mechanics which is discussed in this report. The Rayleigh-Ritz approach requires that a fundamental function like (10.21) is found for the system. In the current issues of cable mechanics only the governing differential equations are known, and this favours another solution technique - The Galerkin method.

The Galerkin method

The Galerkin method belongs to a class of methods called *residual methods*. The Rayleigh-Ritz method were based on trial functions, and the minimization of the residual (error) by the calculus of variations. As opposed to this approach, the Galerkin method is based on minimizing the residual over the spatial variable. This is done by the use of weighting functions.

Consider the ODE/BVP problem in Example 10.3. The residual is given by

$$R = \frac{d^2 u(x)}{dx^2} - F(x), \tag{10.39}$$

where u is another notation for the bending moment, $M(x)$. We assume that the solution is given by

$$u(t, x) = \sum_{i=1}^{i=n} \phi_i(x)\, q_i(t). \tag{10.40}$$

$\phi_i(x)$ must be linearly independent and satisfy the boundary conditions. Because the system is not time dependent, $q_i(t) = C_i$ where C_i is constant. Next step is to choose weighting functions, $W_j(x)$, for the integral of the residual. The unknown parameters C_i may now be solved from

$$\int_{x_1}^{x_2} W_j(x) R(x)\, dx = 0. \tag{10.41}$$

Insertion of the parameters into (10.40) will lead to a solution of the problem.

Let's see how this relates to the beam problem. The residual is given from (10.39). We choose $\phi_1(x) = x$, $\phi_2(x) = x(x-1)$ and $\phi_3(x) = x^2(x-1)$.These functions are linearly independent and satisfy the boundary conditions for beam length $L = 1$. This leads to the following approximation of the solution for the beam's bending moment (10.40)

$$M(x) = u(x) = C_1 x + C_2 x(x-1) + C_3 x^2(x-1). \tag{10.42}$$

C_1 is chosen to be 0 (see page 284).The next step is to choose the weighting functions, $W_i(x)$. These are often chosen to be equal to the shape functions: $W_i(x) = \phi_i(x)$. For the beam, this leads to the following integrated residual (10.41)

$$\int_0^1 x(x-1)\left[2C_2 + C_3(6x-2) - F\right]\, dx \;=\; 0, \tag{10.43}$$

$$\int_0^1 x^2(x-1)\left[2C_2 + C_3(6x-2) - F\right]\, dx \;=\; 0. \tag{10.44}$$

For $F = constant$ the final result is $C_2 = \frac{F}{2}$, $C_3 = 0$, which is the same as for the similar case with the Rayleigh-Ritz method. This will always occur when the trial functions in the Rayleigh-Ritz method is chosen to be the same as the weighting functions in the Galerkin method (Hoffman, 2001).

Now it is time to look at time dependent systems. Much of this material is taken from Egeland and Gravdahl (2002). Again, a beam with time dependence will be considered. The system is given by the equation

$$m_0 \frac{\partial^2 z(t,x)}{\partial t^2} + EI \frac{\partial^4 z(t,x)}{\partial x^4} = b(x)\, u_c(t). \tag{10.45}$$

Notice that the traditional forcing term is replaced by $F(t,x) = b(x)\, u_c(t)$ in this particular case. We define the residual

$$R = m_0 \frac{\partial^2 z}{\partial t^2} + EI \frac{\partial^4 z}{\partial x^4} - b(x)\, u_c(t). \tag{10.46}$$

Use of (10.40) and (10.41) and a choice of $W_i(x) = \phi_i(x)$ leads to

$$\int_0^L \phi_j(x) \sum_{i=1}^{N} \left[EI\; q_i(t)\, \phi_i''''(x) + m_0\, \ddot{q}_i(t)\, \phi_i(x)\right]\, dx = \int_0^L \phi_j(x)\, b(x)\, u_c(t)\, dx. \tag{10.47}$$

In the Galerkin method it is standard procedure to apply partial integration to reduce the order of derivatives in this expression. Egeland and Gravdahl (2002) show that

$$\int_0^L \phi_j(x)\phi_i''''(x)\, dx = \int_0^L \phi_j''(x)\phi_i''(x)\, dx, \tag{10.48}$$

when the condition

$$\phi_j'''(x)\phi_i(x)\big|_0^L = \phi_j'(x)\phi_i'''(x)\big|_0^L = 0, \tag{10.49}$$

is fulfilled. Insertion into (10.47) and reordering of terms gives

$$\sum_{i=1}^{N} \int_0^L \left[m_0\; \phi_i(x)\phi_j(x)\right]\, dx\, \ddot{q}_i(t) + \int_0^L \left[EI\;\; \phi_j''(x)\phi_i''(x)\right]\, dx\, q_i(t) = \int_0^L \left[\phi_j(x)\, b(x)\right]\, dx\, u_c(t). \tag{10.50}$$

This may be written in matrix form as:

$$\mathbf{M}\ddot{\mathbf{q}} + \mathbf{K}\mathbf{q} = \mathbf{b}u_c(t), \tag{10.51}$$

where

$$m_{ij} = \int_0^L [m_0\ \phi_i(x)\phi_j(x)]\ dx, \tag{10.52}$$

$$k_{ij} = \int_0^L \left[EI\ \ \phi_j''(x)\phi_i''(x)\right]\ dx, \tag{10.53}$$

$$b_i = \int_0^L [\phi_j(x)\, b(x)]\ dx. \tag{10.54}$$

Eq. (10.51) may be recognized as an ODE/IVP which may be solved by standard methods (see Section 10.2.1). Usually the shape functions are chosen to be Hermitian polynomials of third order, and this leads to a consistent mass- and stiffness matrix.

In the present example the external force were separated into a product of spatial and time dependent functions. This may not always be possible. Instead we may use the fact that the operator $\frac{\partial^4}{\partial x^4}$ on a finite interval $x \in [0, L]$ has eigenvalues β_i and corresponding eigenfunctions $\phi_i, i \in \{1, 2, 3, ...\}$, so that

$$\frac{\partial^4 \phi(x)}{\partial x^4} = \beta_i^4 \phi_i(x), i \in \{1, 2, 3, ...\}. \tag{10.55}$$

The solutions for β_i and $\phi_i(x)$ depend on the boundary conditions.

Sometimes the weighting functions, $W_i(x)$ are chosen to be Dirac's delta function. The method is then called the *collocation method*. This reduced complexity also leads to reduced accuracy of the results, and the method is therefore seldom used.

The Galerkin method will be applied to some of the problems in cable mechanics, and a deeper insight will hopefully be achieved with further examples.

The Finite Element Method

Up to this stage we have only described the problems with solutions based on shape functions and one single element. In order to increase the accuracy, let's divide the spatial domain, $D(x)$, into several smaller domains, $D_i(x)$.Now we can solve the spatial problem for each of the smaller subdomains and collect the results in the end, see Figure 10.6.

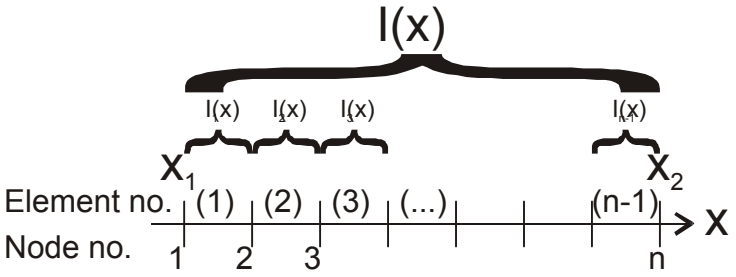

Figure 10.6: Division of the spatial domain, and discretization of the weighted integral $I(x)$.

The elements may be solved by the Rayleigh-Ritz method, the Galerkin method or other methods which are found suitable. In the following we will only focus on the Galerkin method. For a time independent system the weighted residual integral may be written as

$$I[u(x)] = \int_0^L W_j(x)R(x)\,dx. \tag{10.56}$$

When the solution domain is divided into several subdomains, the global integral may be written as a sum of all subintegrals. Let superscript (i) denote element number and subscript j denote the node number.

$$I[u(x)] = \sum_{i=1}^{n-1} I^{(i)}[u^{(i)}(x)], \tag{10.57}$$

where

$$I^{(i)}[u^{(i)}(x)] = \int_{x_i}^{x_{i+1}} W_j^{(i)}(x)R(x)\,dx, \tag{10.58}$$

is the integral for subdomain $D_i(x)$, i.e. interval number i. Here we assume that the global exact solution $u(x)$ may be approximated by the series

$$u(x) = u^{(1)}(x) + u^{(2)}(x) + ... + u^{(n-1)}(x), \tag{10.59}$$

where $u^{(i)}(x)$ is a local solution for each element, n is the number of nodes and $n-1$ is the number of elements. In the Galerkin weighted residual approach, the weighting factors $W_j(x)$ are chosen to be the shape functions, φ, for the solution. When it comes to the Finite Element Method, we will limit the discussion of static boundary value problems to linear interpolation functions. Two approaches are dominating: The *element formulation* and the *nodal formulation*. In the element formulation the local solution is given by two shape functions (Figure 10.7)

$$u^{(i)}(x) = u_i\varphi_i^{(i)}(x) + u_{i+1}\varphi_{i+1}^{(i)}(x),\ x_i \le x \le x_{i+1}, \tag{10.60}$$

where

$$\varphi_i^{(i)}(x) = \begin{cases} 0 & x < x_i \\ -\frac{x-x_{i+1}}{x_{i+1}-x_i} = -\frac{x-x_{i+1}}{\Delta x^{(i)}} & x_i \le x < x_{i+1} \\ 0 & x_{i+1} \le x \end{cases}, \tag{10.61}$$

$$\varphi_{i+1}^{(i)}(x) = \begin{cases} 0 & x < x_i \\ \frac{x-x_i}{x_{i+1}-x_i} = \frac{x-x_i}{\Delta x^{(i)}} & x_i \le x < x_{i+1} \\ 0 & x_{i+1} \le x \end{cases}. \tag{10.62}$$

The nodal formulation is given by

$$u(x) = u_1\varphi_1(x) + u_2\varphi_2(x) + ... + u_n\varphi_n(x), \tag{10.63}$$

where

$$\varphi_i(x) = \varphi_i^{(i.-1)}(x) + \varphi_i^{(i)}(x), \tag{10.64}$$

and

$$\varphi_i^{(i-1)}(x) = \begin{cases} 0 \\ \frac{x-x_{i-1}}{x_i-x_{i-1}} \\ 0 \end{cases} = \begin{cases} 0 & x < x_{i-1} \\ \frac{x-x_{i-1}}{\Delta x^{(i-1)}} & x_{i-1} \le x < x_i \\ 0 & x_i \le x \end{cases}, \tag{10.65}$$

$$\varphi_i^{(i)}(x) = \begin{cases} 0 \\ -\frac{x-x_{i+1}}{x_{i+1}-x_i} \\ 0 \end{cases} = \begin{cases} 0 & x < x_i \\ -\frac{x-x_{i+1}}{\Delta x^{(i)}} & x_i \le x < x_{i+1} \\ 0 & x_{i+1} \le x \end{cases}. \tag{10.66}$$

The element formulation is often considered to be easier to handle in higher dimensions.

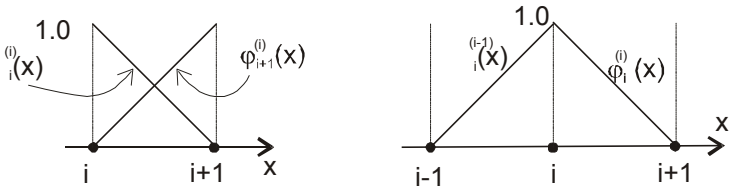

Figure 10.7: Shape functions for element formulation (left) and nodal formulation (right).

Let's return to the static beam problem from Example 10.3. The residual may be expressed as

$$R = M''(x) - F(x). \tag{10.67}$$

We apply the weighting functions and integrate over the whole solution domain

$$I = \int_0^L W_j(x) \left[M''(x) - F(x) \right] dx = 0. \tag{10.68}$$

A standard procedure is to reduce the order of the derivative in (10.68). Integration of the first term by parts yields

$$\begin{aligned} \int_0^L W_j M'' \, dx &= M' W_j \big|_0^L - \int_0^L W_j' M'' \, dx, \\ &= -\int_0^L W_j' M' \, dx + M'(L) W_j(L) - M'(0) W_j(0). \end{aligned} \tag{10.69}$$

The last two terms in this equation involve derivative boundary conditions. For Dirichlet boundary conditions these terms are not needed, but for Neumann boundary conditions they introduce the derivative condition on the global solution domain. Combination of (10.68) and (10.69) gives

$$I = \int_0^L \left(-W_j' M' - W_j F \right) dx + M'(L) W_j(L) - M'(0) W_j(0). \tag{10.70}$$

Our goal is to find a procedure or algorithm for the solution at each nodal point. Eq. (10.66) and discretization yields

$$I = \int_{x_{i-1}}^{x_i} \left(-\frac{d\varphi_i^{(i-1)}(x)}{dx} M' - \varphi_i^{(i-1)}(x) F \right) dx + \int_{x_i}^{x_{i+1}} \left(-\frac{d\varphi_i^{(i)}(x)}{dx} M' - \varphi_i^{(i)}(x) F \right) dx = 0. \tag{10.71}$$

Because

$$\frac{d\varphi_i^{(i-1)}(x)}{dx} = \frac{1}{\Delta x^{(i-1)}}, \tag{10.72}$$

$$\frac{d\varphi_i^{(i)}(x)}{dx} = -\frac{1}{\Delta x^{(i)}}, \tag{10.73}$$

we find the following integral for the system

$$I = \int_{x_{i-1}}^{x_i} \left(-\frac{1}{\Delta x^{(i-1)}} M' - \varphi_i^{(i-1)}(x) F \right) dx + \int_{x_i}^{x_{i+1}} \left(\frac{1}{\Delta x^{(i)}} M' - \varphi_i^{(i)}(x) F \right) dx = 0. \tag{10.74}$$

The integral of the shape functions alone is simply the area of a triangle. We may for simplicity approximate the external force to be constant over an element. This constant force can be written

$$\bar{F}^{(i)} = \frac{F_{i+1} + F_i}{2}. \tag{10.75}$$

This leads to the following integral

$$\begin{array}{c} I = -\frac{1}{\Delta x^{(i-1)}} \int_{x_{i-1}}^{x_i} M' dx - \bar{F}^{(i-1)} \int_{x_{i-1}}^{x_i} \varphi_i^{(i-1)}(x) dx + \\ \frac{1}{\Delta x^{(i)}} \int_{x_i}^{x_{i+1}} M' dx - \bar{F}^{(i)} \int_{x_i}^{x_{i+1}} \varphi_i^{(i)}(x) dx = 0. \end{array} \tag{10.76}$$

We know that

$$\begin{aligned} \int_{x_{i-1}}^{x_i} M' dx &= \int_{x_{i-1}}^{x_i} \left(M_{i-1} \frac{d\varphi_{i-1}^{(i-1)}(x)}{dx} + \frac{d\varphi_i^{(i-1)}}{dx} M_i \right) dx, \\ &= \int_{x_{i-1}}^{x_i} \frac{M_i}{\Delta x^{(i-1)}} - \frac{M_{i-1}}{\Delta x^{(i-1)}} dx = M_i - M_{i-1}, \end{aligned} \tag{10.77}$$

and that

$$\int_{x_{i-1}}^{x_i} \varphi_i^{(i-1)} dx = \frac{\Delta x^{(i-1)}}{2}, \tag{10.78}$$

$$\int_{x_i}^{x_{i+1}} \varphi_i^{(i)} dx = \frac{\Delta x^{(i)}}{2}, \tag{10.79}$$

which yields

$$I = -\frac{1}{\Delta x^{(i-1)}} (M_i - M_{i-1}) - \bar{F}^{(i-1)} \frac{\Delta x^{(i-1)}}{2} + \frac{1}{\Delta x^{(i)}} (M_{i+1} - M_i) - \bar{F}^{(i)} \frac{\Delta x^{(i)}}{2} = 0. \tag{10.80}$$

Eq. (10.80) is valid for nonuniform grid. If we assume that the grid is uniform, and (10.80) is multiplied by Δx, the nodal equation for node i will be

$$M_{i+1} - 2M_i + M_{i-1} = \left(\frac{\bar{F}^{(i-1)} + \bar{F}^{(i)}}{2} \right) \Delta x^2. \tag{10.81}$$

This equation holds for all nodes in the grid except for the boundary nodes if Neumann boundary conditions are provided. Eq. (10.70) shows that the derivative conditions have to be included in

the integral at the boundaries. Notice that $W_1(0) = \varphi_1^{(1)}(0) = 1$, and $W_n(L) = \varphi_n^{(n-1)}(L) = 1$. The solution for end nodes may then be calculated from

$$-M_1 + M_2 = \frac{\bar{F}^{(1)}}{2}\Delta x^2 + \Delta x\, M_1', \tag{10.82}$$

$$M_{n-1} - M_n = \frac{\bar{F}^{(n-1)}}{2}\Delta x^2 - \Delta x\, M_n'. \tag{10.83}$$

Example 10.6 *Calculation for static beam problem based on a finite element model.*
The static beam problem is given by

$$M'' = F. \tag{10.84}$$

A nodal solution involving linear shape functions is given in (10.81). Assume that this is discretized into five nodes and four elements. The boundary conditions are given from $M_1 = C_1$, *and* $M_5 = C_5$, *where* C_i *is a constant. The unknown moments,* M_2, M_3 *and* M_4 *are given from (10.81), and may be calculated from the solution of the following equation:*

$$\begin{bmatrix} -2 & 1 & 0 \\ 1 & -2 & 1 \\ 0 & 1 & -2 \end{bmatrix} \begin{bmatrix} M_2 \\ M_3 \\ M_4 \end{bmatrix} = \frac{\Delta x^2}{2} \begin{bmatrix} 1 & 1 & 0 & 0 \\ 0 & 1 & 1 & 0 \\ 0 & 0 & 1 & 1 \end{bmatrix} \begin{bmatrix} \bar{F}^{(1)} \\ \bar{F}^{(2)} \\ \bar{F}^{(3)} \\ \bar{F}^{(4)} \end{bmatrix} + \begin{bmatrix} -C_1 \\ 0 \\ -C_5 \end{bmatrix}. \tag{10.85}$$

Notice that solution of this equation may involve calculation of the inverse of the first left-hand matrix. This matrix grows in size when the number of elements are increased, and calculation of inverse may require high computation time. Other solutions are possible, but those will not be discussed in this text.

A simple implementation of the static beam problem is shown in the code below.

```
function fem_beam
n=30; %Number of nodes
L=1; %Length of beam
Dx=L/(n-1); %Deltax
M1=0; %Boundary condition
Mn=0; %Boundary condition
Fc =-2000; %Constant distributed force.

%Boundary condition matrix
Mb=zeros(n-2,1);
Mb(1)=M1;
Mb(length(Mb))=Mn;

%Left hand matrix
A=diag(-2*ones(n-2,1),0)+diag(ones(n-3,1),1)+diag(ones(n-3,1),-1);
Fselect=diag(ones(n-2,1),0)+diag(ones(n-3,1),1);
```

```
%Force matrix
F=ones(n-2,1)*Fc;

%Calculation of solution
M=inv(A)*Dx^2/2*Fselect*F+Mb;

%Adds the boundary solutions to the solution vector
Msol=[M1; M; Mn];
xsol=0:Dx:L;

%Plots the results
figure(1)
plot(xsol,Msol)
```

The code produces the plot shown in Figure 10.8. Notice how the FEM solution converges to the exact solution as the number of elements is increased.

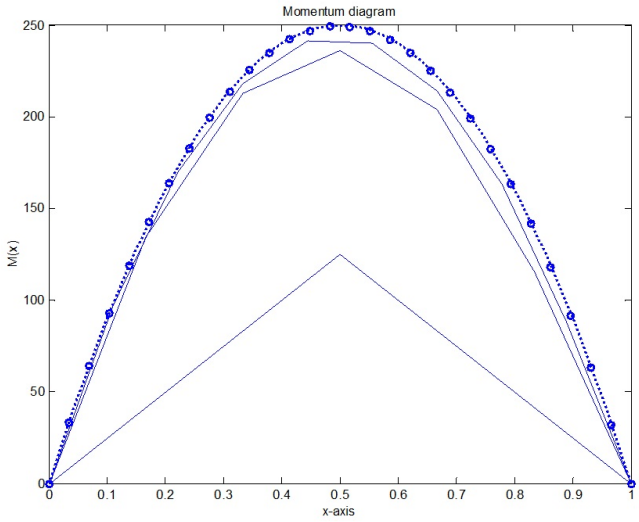

Figure 10.8: Solution of the static beam problem with the Finite element method and linear interpolation functions. The exact solution is shown with a thick solid line. FEM solutions is shown with 3, 7 and 10 nodes (thin solid lines), and for 30 nodes ('o').

The last step of our discussion of the Finite Element Method will include equations with time dependence - PDEs. This material is mostly found in Egeland and Gravdahl (2002). Again, our system is

$$m_0 \frac{\partial^2 z}{\partial t^2} + EI \frac{\partial^4 z}{\partial x^4} = F(t,x), \tag{10.86}$$

where $F(t,x)$ is assumed to be written $F(t,x) = b(x)\, u_c(t)$. The procedure described for ODE/BVP will not apply. Instead, we write the solution as

$$z(t,x) = \sum_{i=1}^{n} \left[\varphi_{i,1}(x)\, q_{i,1}(t) + \varphi_{i,2}(x)\, q_{i,2}(t) \right], \tag{10.87}$$

where $\varphi_{i,1}$and $\varphi_{i,2}$ are linearly independent and zero in every node apart from node i. The condition $\varphi_{i,1}(x) = \varphi_{i,2}(x) = 0, x \notin \langle x_{i-1}, x_{i+1} \rangle$ is also fulfilled. The physical interpretation of the physical coordinates is

$$q_{i,1}(t) = z(t, x_i), \tag{10.88}$$

$$q_{i,2(t)} = \frac{\partial z(t, x_i)}{\partial x}. \tag{10.89}$$

We may now define

$$\varphi = \left[\varphi_{1,1}, \varphi_{2,1}, \varphi_{2,1}, \varphi_{2,2}, ..., \varphi_{n,1}, \varphi_{n,2}\right]^T, \tag{10.90}$$

$$\mathbf{q} = \left[q_{1,1}, q_{2,1}, q_{2,1}, q_{2,2}, ..., q_{n,1}, q_{n,2}\right]^T. \tag{10.91}$$

The system may now be written as

$$\mathbf{M}\ddot{\mathbf{q}} + \mathbf{K}\mathbf{q} = \mathbf{b}u, \tag{10.92}$$

where

$$\mathbf{M} = \int_0^L m_0 \varphi \, \varphi^T dx, \tag{10.93}$$

$$\mathbf{K} = \int_0^L m_0 \varphi'' \left(\varphi''\right)^T dx, \tag{10.94}$$

$$\mathbf{b} = \int_0^L \varphi b(x) \, dx. \tag{10.95}$$

Eq. (10.92) may now be solved by traditional methods for ODE/IVPs.

An example of typical shape functions which holds for beams is

$$\varphi_{i,1} = \begin{cases} 3\frac{(x-x_{i-1})^2}{\Delta x_{i-1}^2} - 2\frac{(x-x_{i-1})^3}{\Delta x_{i-1}^3} & x_{i-1} \leq x \leq x_i \\ 1 - 3\frac{(x-x_i)^2}{\Delta x_i^2} + 2\frac{(x-x_i)^3}{\Delta x_i^3}, & x_i \leq x \leq x_{i+1} \\ 0 & \text{otherwise} \end{cases}, \tag{10.96}$$

$$\varphi_{i,2} = \begin{cases} -\frac{(x-x_{i-1})^2}{\Delta x_{i-1}} + \frac{(x-x_{i-1})^3}{\Delta x_{i-1}^2} & x_{i-1} \leq x \leq x_i \\ x - 2\frac{(x-x_i)^2}{\Delta x_i} + \frac{(x-x_i)^3}{\Delta x_i^2}, & x_i \leq x \leq x_{i+1} \\ 0 & \text{otherwise} \end{cases}. \tag{10.97}$$

These are the Hermite polynomials, and they satisfy the conditions which are set to shape functions in the Finite Element Method.

Notice that the solution of (10.92) is a solution of the spatial variable as a boundary value problem, and a solution in time as an initial value problem. Problems like this are often called initial-boundary value problems, IBVPs as seen Section 10.2.2.

10.3 Modeling and Control Top Tensioned Risers

Anne Marthine Rustad
Department of Marine Technology, NTNU

We will in this section investigate the possibility to reduce the riser interference by use of automatic control of the riser top tension. A control strategy based on equal payout for all risers in an array was proposed by Huse and Kleiven (2000). Results from the model tests showed that the equal payout by connecting all the risers to one common frame at the top end gave a significant reduction of the probability of collision in steady current. This section is motivated by their work, but instead of keeping the risers fixed to a plate, the top tension of each riser is controlled individually using the payout of the heave compensator as the measured input. A comprehensive model of the dual riser system with TLP and current forces is presented. The riser model is verified by use of the computer program RIFLEX (2018). The top tensioned riser control system includes both the physical structure with identification of the limitations and the software implementation with controller objective and algorithm. This section is based on work published in Rustad (2007) and Rustad et al. (2007). For details in references, please see Rustad (2007).

This section is organized as follows: Section 10.3.1 describes the problem statement in more detail, while Section 10.3.2 gives and introduction to the TLP concept. Section 10.3.3 deduces the modeling of the system, including the current forces acting as a disturbance. In Section 10.3.4 this model is verified by use of the existing software RIFLEX. Section 10.3.5 compares the different control plant models. The controller design is presented in Section 10.3.6, while simulations and results are found in Section 10.3.7. Section 10.3.8 summarises the section.

10.3.1 Motivation and Problem Description

Offshore petroleum production started in the most shallow waters. As these reservoirs are exploited, combined with an increasing demand for oil and gas, the petroleum industry has been moving to ever deeper waters. Riser technology is an important issue both when considering field development costs and technological feasibility. In deeper waters, interference between adjacent top tensioned risers in an array is an issue of considerable concern. Collision may lead to dents in the riser pipe and also damage in the coating, with fatigue and corrosion as possible consequences. Even a single collision event may be damaging if the collision takes place with sufficiently high impact.

If the riser spacing and properties are kept constant, the risk of collision will increase with increasing water depth, since the static deflection due to the uniform current drag is proportional to the square of the length. In deep waters this means that even a relatively small difference in static forces may lead to mechanical contact. In addition flow separation and shielding effects between risers in an array can change the local flow velocity. This difference in current forces may cause large relative motions and lead to contact between neighboring risers. There are mainly two design parameters that will prevent interference between risers:

1. Increasing the riser spacing.

2. Increasing the top tension.

Both may result in significant cost penalties. Increasing the riser spacing means increasing the size of the wellbay (Figure 10.9). This has influence on the global platform parameters like deck space and load carrying capacity. The other option is increasing the top tension to a high and constant level, which will increase the wear and tear on the cylinders in a heave compensation system. The aim of this section is to show how the number of collisions can be reduced by applying dynamically varying feedback control of the riser top tension.

Figure 10.9: The wellbay on the Snorre TLP (www.statoil.com).

For deep water production systems, riser solutions are traditionally divided into two main groups; (1) subsea wellheads (wet trees) with flexible risers up to a floater like a semi-submersible or a production ship (floating production storage offloading - FPSO), and (2) tensioned risers with wellhead on a compliant platform, like tension leg platform (TLP), spar[1] or deep draft floater (DDF). These are the most common dry tree solutions for floating production systems. Dry tree systems are often the preferred solution for production as they provide easy access to the well for maintenance, intervention and workover.

Top tensioned risers operated from spars and TLPs are arranged in clusters of (near) vertical riser arrays. The number of individual risers in an array may be 20 or more, and may consist of different risers applied for production, drilling, workover, export, etc.

A TLP is chosen as the platform concept in the example presented here. The main reason is that tensioned risers can be applied at a TLP with a relatively small requirement for stroke capacity even at large TLP offsets. This is due to the geometric restrictions for heave motions caused by the axially rigid tendons. For other floaters like spars, FPSOs and semi-submersibles, the demand for stroke capacity will be much higher, which means that other riser solutions like

[1] A spar is a vertical, cylindrical buoyant platform, usually manned.

steel catenary risers (SCR) or other types of flexible risers are preferred. Note however, that most of the mathematical modeling of the TLP in Sec. 10.3.3 is independent of vessel type, and is also applicable for a semi-submersible or similar.

10.3.2 Tension Leg Platform

The main purpose of the TLP model in this example is to represent the platform motions at the wellhead area where the risers are connected to the platform. The surge motions will act as a prescribed dynamic boundary condition in the riser analysis, while heave relative to vertical motions of the upper riser end is subjected to active control. Heave motions of a TLP have two components. One is caused by dynamic elastic strain and deflections of the tendons, which will influence the true distance between its ends. The other component is referred to as *surge induced heave*, and is easily understood by realizing that the inclined tendon will have another vertical distance from the seafloor than its true length. The motions caused by local tendon dynamics are significantly smaller than the surge induced component - in particular in extreme wave conditions - and is neglected in this work. This was done for the case of simplicity, but could have been included without any conceptual changes in the approach. Conclusions from this study are hence valid even if this simplification was made. This section is mainly based on Faltinsen (1993).

Background for the TLP solution

Offshore platform concepts are usually classified into two major categories; *fixed* and *compliant*.

Fixed platforms stand at the sea bed and remain in place by a combination of their weight and/or piles driven into the soil. Little or no motions are observed for such structures. The fixed platforms resist the environmental forces like wind, wave and current by generating large internal reaction forces. The first offshore oil and gas fields were found in shallow water, and mainly fixed structures were build in the first decades of offshore oil production. Fixed platforms will normally have natural periods shorter than 5s and their responses that are caused by extreme waves will therefore be quasi-static since such waves typically will have periods above 10s. As offshore development moved towards deeper waters, the application of conventional fixed jackets approached its limits principally imposed by the dynamic behavior of the structures. With increasing water depths, fixed platforms become more flexible, and their natural periods started to enter the high energy levels of the ocean waves. To keep the eigenperiods away from this damaging range, fixed structures had to be designed to be stiffer, requiring more steel and exponentially increasing costs. The obvious alternative to fixed platforms in deep water is to use compliant platforms. The basic idea is to allow for rigid body motions with eigenperiods longer than wave periods ($T > 30$s). Compliant platforms may be divided into three types; floaters, towers and TLPs.

A **floating platform** will have all its structural eigenperiods well below 5s, which means that ordinary wave loads will not give any structural dynamic response. However, dynamics of rigid body motions for floaters are of concern. Eigenperiods are controlled by the geometry of the water-plane (heave, pitch and roll) and design of the anchor system (surge, sway and yaw). These eigenperiods are normally above wave periods, but resonance may still occur due to wind and higher order wave forces. Hydrodynamic damping is the key to reduce these types of response. Any anchored vessel, semi-submersible, spar and FPSO belong to this category.

Towers are fixed to the sea floor by an arrangement that eliminates, or at least reduces, the bending moment at the bottom end. Horizontal motions of the deck are compliant, but vertical motion components are equivalent to a fixed platform.

A **TLP** acts like a floater with regard to in-plane motion components (surge, sway and yaw), but like a fixed platform for the out-of-plane components (heave, roll and pitch). The governing parameters for the in-plane stiffness are the tension and length of the tendons, while the cross section area, modulus of elasticity and length of the tendons decides out-of-plane stiffness. The design premises for the tendon system are hence to determine these parameters so that desired values of the eigenfrequencies can be obtained. In addition to considering the sensitivity of the platform to external environmental forces, the choice of platform system also depends upon other considerations. Amongst these are the technical and economic factors, including water depth, production rate, reservoir size, service life and removal requirements. However, in deep water the major factor in selecting the platform for a field development plan is the cost which is correlated to its weight. The cost of the floating system, especially that of the TLP, are relatively insensitive to changes in the water depths compared to the cost of the compliant towers and fixed structures. Hence, economic factors make the compliant platforms and the TLPs in particular one of the leading candidates for major deep water developments, especially when a dry tree solution is preferred.

The TLP concept

The main idea behind the TLP concept was to make a platform that is partly compliant and partly rigid. In order to maintain a steel riser connection between the sea floor and the production equipment aboard the platform, heave, roll and pitch motions had to be minimized and considered as rigid degrees of freedom. The horizontal forces due to waves on the vertical cylinders will always be larger in the horizontal plane than in the vertical direction. Hence, by making in-plane motions compliant, the largest environmental forces can be balanced by inertia forces instead of by forces in rigid structural members. This idea can be realized by a pendulum using buoyancy to reverse gravity forces.

The TLP is defined as a compliant structure, but might also be classified as a moored structure. In general, the TLP is similar to other column stabilized moored platforms with one exception; the buoyancy of a TLP exceeds its weight, and thus the vertical equilibrium of the platforms requires taut moorings connecting the upper structure to a foundation at the sea bed. These taut mooring are called tension legs, tethers or tendons. Drilling and production risers connecting the platform to the wellhead template on the seafloor are in general not a part of the TLP mooring system. The different parts of the TLP are illustrated in Figure 10.10, and defined as follows:

- **The hull** consists of the buoyant columns, pontoons and the intermediate structure bracings.
- **The deck structure** supports operational loads. It is a multilevel facility consisting of trusses, deep girders and deck beams.
- **The platform** consists of the hull and deck structure.
- **The foundation** is found at the sea bed and consists of templates and piles, or even a gravity system.

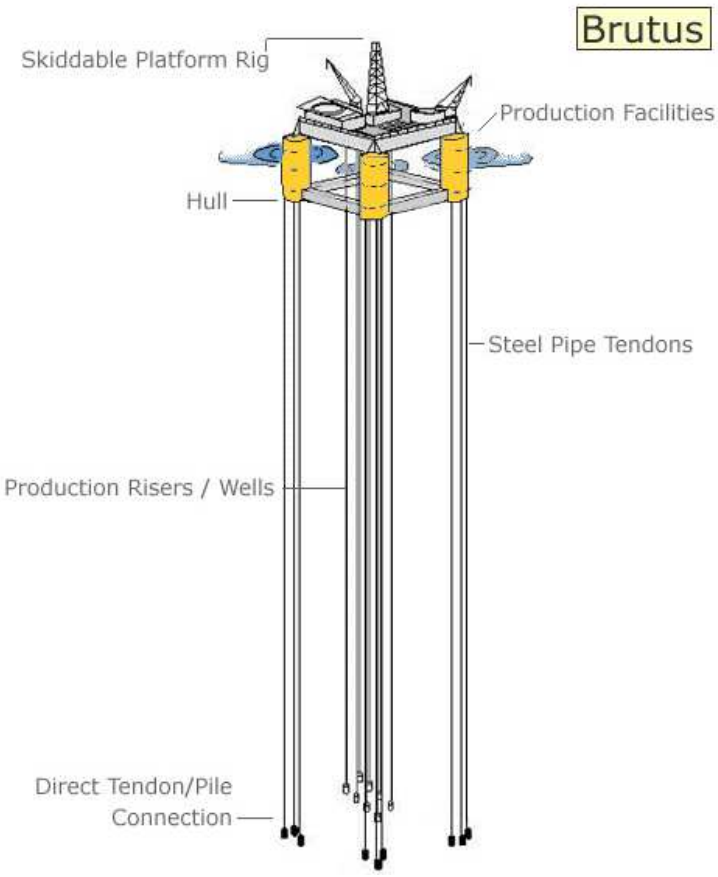

Figure 10.10: The layout of the Brutus TLP in the GoM (www.offshore-technology.com).

- **The tendons** connects the platform to the foundation at the sea bed.
- **The mooring system** consists of the tendons and the foundation.
- **The risers** include drilling, production and export risers.
- **The well system** includes flowlines, risers, riser tensioners, wellhead and the subsea well templates.
- **The tension leg platform** includes all the above, in addition to all deck equipment and the hull system.

Interest in TLPs dates back to 1960. During the following two decades, and especially after the installation of the Hutton TLP in 1984, the TLP concept began attracting more attention from the offshore industry as an appropriate structure for deep water applications.

There are at the moment installed approximately fifteen TLPs, of which three are found in the North Sea. Deepwater TLPs are mainly found in the Gulf of Mexico, but there are also some West of Africa and off the coast of Brazil. The increase in water depth for TLP is shown in Figure 10.11

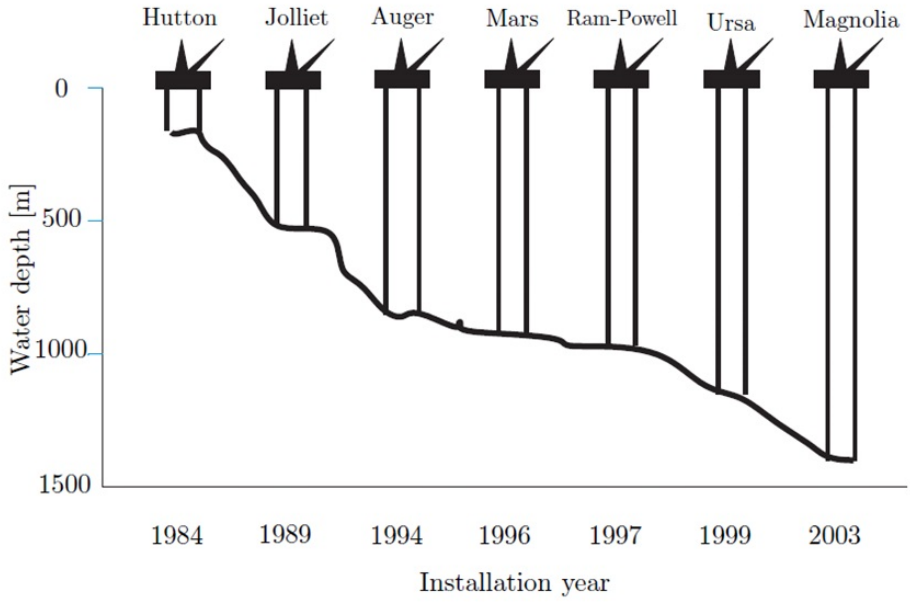

Figure 10.11: Development of TLPs and riser depths.

10.3.3 Mathematical Modeling

Mathematical models may be formulated in various levels of complexity. We usually distinguish between *process plant models* and *control plant models*. The process plant model (PPM) is a comprehensive model of the actual physical process. The main purpose of this model is to simulate the real plant dynamics, including environmental disturbances, control inputs and sensor outputs. A successful numerical simulation for design and verification of our control system require a sufficiently detailed mathematical model of the actual process. The control plant model (CPM) is simplified from the process plant model containing only the main physical properties. It may be a part of the model-based controller. The CPM is often formulated such that the analytical stability analysis becomes feasible.

This section will focus on mathematical model of the process plant. The system modeled here consists of two risers connected to a TLP through the top nodes, forcing the top nodes to follow the prescribed motion from the TLP in the horizontal direction. The top nodes are free in the vertical direction, only affected by the top tension acting as a vertical force. In addition the risers are exposed to current forces that are found by considering hydrodynamic interactions between the risers. The current is modeled as an in-plane profile with varying velocity through the water column. The TLP is exposed to surface current, wind and waves.

Hydrodynamic interaction

Interaction between two cylinders are often classified into two categories according to the space between them; the *proximity interference* when the two cylinders are close to each other, and *wake interference* when one cylinder is in the wake of an upstream cylinder. Top tensioned marine riser systems normally falls into the latter category, although proximity interference also can take place. It is also found that the in-line motion are much larger than the transverse motion. Hence, in this paper we will focus on two risers in a tandem arrangement, were the centers

of the two cylinders are aligned parallel to the free stream (Figure 10.12). A two dimensional model will capture the most important dynamics of the riser array system.

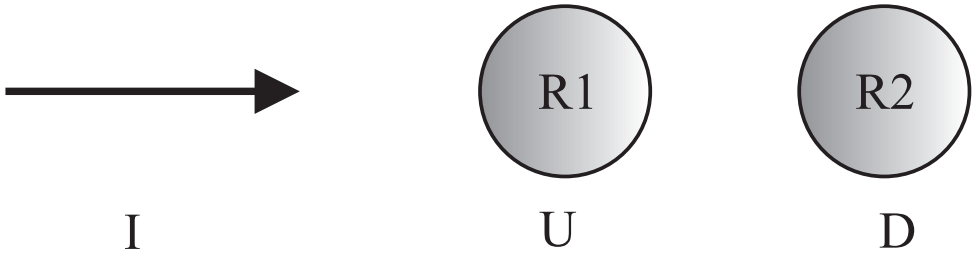

Figure 10.12: The risers in a tandem arrangement. I: Incoming flow, U: Upstream riser, D: Downstream riser.

Kalleklev et al. (2003) stated that interaction between two neighboring risers will not have any hydrodynamic influence on the upstream riser (R1) beyond a certain point. Hence, R1 can be treated as an isolated riser. The attention will therefore be given to the hydrodynamic influence on the downstream riser (R2).

In the literature it is distinguished between three different kinds of excitation forces and physical mechanisms on a pair of adjacent risers. The most important effects for assessment of riser interaction are found in DNV-RP-F203 DNVGL (2018):

1. Mean force and shielding effects, tending to bring the risers closer.
2. WIO on the downstream riser.
3. VIV leading to amplified drag coefficients for both risers.

Here, focus will be on shielding effects, which is of main importance when calculating the mean current force, and hence the position of the second riser in the wake. The two latter effects will not be treated any further. So far we do not have a reliable model for prediction of the WIO type of response. Inclusion of these effects may have an influence on the presented results.

R2 experiences reduced mean drag force due to shielding effects, depending on the location in the wake. A semi-empirical static wake formulation to account for the hydrodynamic interaction between individual risers in steady current was proposed by Huse (1993). The reduced velocity field in the wake of the upstream cylinder, see Figure 10.13, is given by

$$V_r(x,y) = k_2 V_c \sqrt{\frac{C_D D_e}{x_s}} e^{-0.693\left(\frac{y}{b}\right)^2}, \tag{10.98}$$

where V_c is the incoming current velocity on R1, C_D is the drag coefficient, D_e is the diameter, and y is the distance away from the centerline of incoming velocity profile. x_s and b are defined as

$$x_s = x + \frac{4D_e}{C_D}, \quad b = k_1\sqrt{C_D D_e x_s}, \tag{10.99}$$

where $k_1 = 0.25$ and $k_2 = 1.0$ for a smooth cylinder. x is the distance behind the upstream riser R1, and x_s is the distance between the downstream riser R2 and a virtual wake source upstream of R1. The mean inflow on the downstream riser is hence given by

$$V_{mean} = V_c - V_r. \tag{10.100}$$

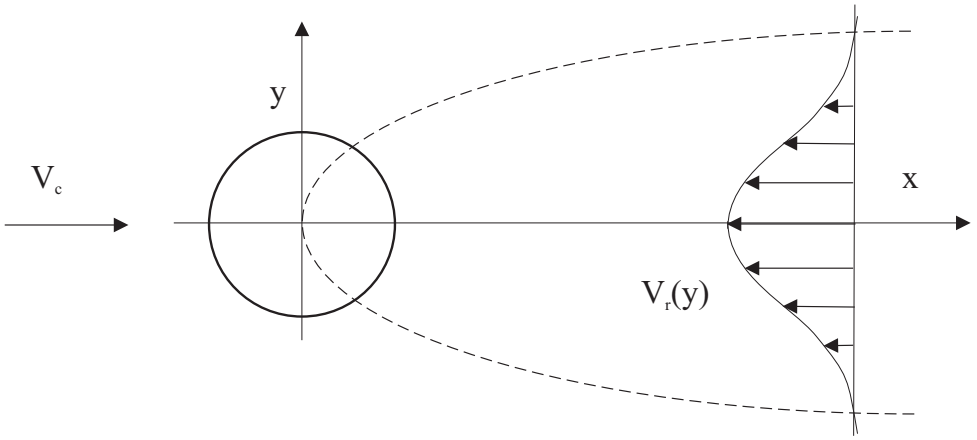

Figure 10.13: The decrease in the in-line water particle velocity in the wake region, from Huse, Huse (1993).

It is assumed that mechanical contact occurs when the distance between the riser centers is equal to one riser diameter (1D). The parametric wake model is only applicable for the far wake region larger than two diameters (2D) behind R1. The behaviour of the flow in the near region is not adequately described as this is a highly nonlinear phenomenon, where R2 might experience negative drag forces. The center to center distance should therefore preferably be kept larger than 2D.

Kinematics and the coordinate systems

Four orthogonal coordinate systems are used to describe the riser and TLP motions, see Figure 10.14. A bold letter with subscript $i = \{1, 2, 3\}$ denotes the unit vector along the x, y and z axes in the frame respectively, i.e. $\mathbf{f}_1$ denotes the unit vector along the x-axis for the sea floor fixed frame.

- The f-frame (o_f $\mathbf{f}_1$ $\mathbf{f}_2$ $\mathbf{f}_3$) is considered inertial and is fixed to the sea floor. The positions of all the riser nodes in the global system are described relative to this frame.
- The b-frame (o_b $\mathbf{b}_1$ $\mathbf{b}_2$ $\mathbf{b}_3$) is fixed to the body of the TLP with axes chosen to coincide with the principal axes of inertia for the body.
- The global g-frame (o_g $\mathbf{g}_1$ $\mathbf{g}_2$ $\mathbf{g}_3$) is fixed to the sea surface right above the f-frame with a distance in heave direction equal to the water depth and is also considered inertial.
- The i-frames (o_i $\mathbf{i}_1$ $\mathbf{i}_2$ $\mathbf{i}_3$) are located in the i-th node of the riser and is a local frame for each element i. $\mathbf{i}_1$ is to the right of the element, $\mathbf{i}_2$ is pointing into the plane, and $\mathbf{i}_3$ is along the axial direction of the element pointing upwards.

Riser modeling with the Finite Element Method

The partial differential equation (PDE) governing the static and dynamic behaviour of a riser can not be solved exactly for arbitrary riser problems and load patterns. Hence, a numerical

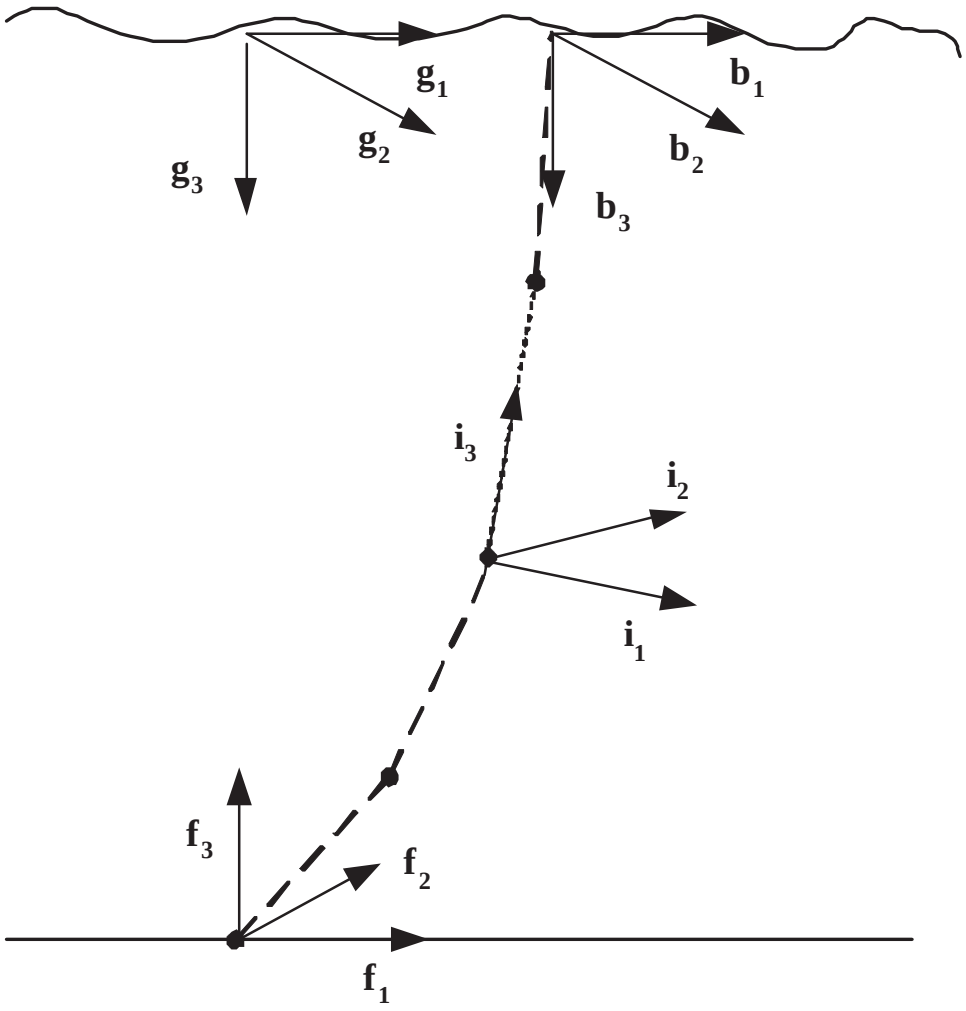

Figure 10.14: The coordinate systems: f -fixed frame for first riser, g - global frame at the surface, b - body frame of TLP, i - element frames.

method is required, such as the finite element method (FEM). The stiffness matrix in the FE model will have an elastic and a geometric component. The elastic stiffness matrix accounts for the axial and bending stiffness as present in any beam, while the geometric stiffness matrix will take into account the changes of the global geometry and the stiffening effect from the tension. As the depth is increasing, the riser will behave more and more like a cable, and the geometric stiffness will become more important than the elastic stiffness. Hence, the geometric stiffness gives the main contribution to lateral resistance against the static and dynamic forces acting perpendicular to the longitudinal riser axis.

At larger water depths a simplification of the riser model can be made by neglecting the bending stiffness and assuming free rotations at the ends. In cases where the global geometry are of major importance this will only introduce a small error. Hence, a model consisting of bar elements is sufficient. Each bar element can be described with four degrees of freedom (DOFs), that is two translational DOFs in both ends of the element. x is transverse of the element, positive to the right along $\mathbf{i}_1$, and z is along the element, positive upwards along $\mathbf{i}_3$, see Figure

10.15.

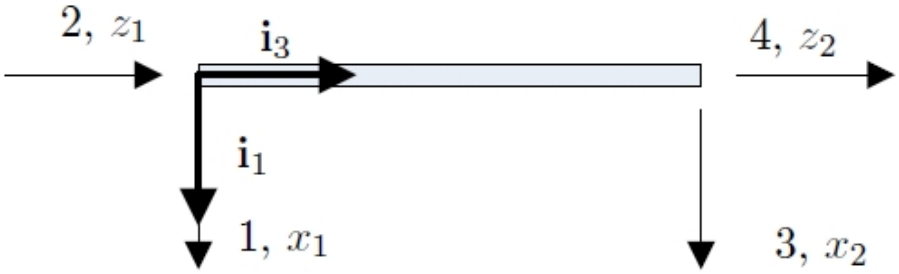

Figure 10.15: The bar element with four DOFs. Node 1 to the left with the two first DOFs. Node 2 to the right with the third and fourth DOFs.

The riser is fixed to the sea bed, and the top node displacement is prescribed in the horizontal direction, whereas it is free to move vertically. Note, however, that the top tension, P_{top}, is introduced at the upper end, which prevents the riser from collapsing. The tension vector, $\mathbf{f}_{top}$, is an external force and will be found on the right hand side of the equation of motion according to

$$\mathbf{f}_{top} = \begin{bmatrix} \mathbf{0}_{1\times(2n+1)} & P_{top} \end{bmatrix}^T. \tag{10.101}$$

Transformation of the riser elements There are n elements and $n+1$ nodes, with node number 1 at the sea bed and node $n+1$ at the sea surface. θ_i is the inclination of element i relative to the global coordinate system f-frame, which is situated at the sea bed in the first node of the upstream riser. The numbering of elements, nodes and the angle of each local element are illustrated in Figure 10.16. $\mathbf{v}_i^f$ is the current in node i expressed in the inertial f-frame. Note that i is used as the numbering of the elements, nodes and the corresponding inclination.

The positions x_i and z_i of the nodes along the riser are found through equilibrium iterations, and are used to calculate the sine and cosine of the inclination θ_i of each element, needed for use in the transformations between the global and local coordinate systems. The length of each element i is found by use of the Pythagorean theorem.

$$\Delta x_i = x_{i+1} - x_i, \quad \Delta z_i = z_{i+1} - z_i, \quad l_i = \sqrt{\Delta x_i^2 + \Delta z_i^2}, \tag{10.102}$$

$$\cos\theta_i = \frac{\Delta z_i}{l_i}, \quad \sin\theta_i = \frac{\Delta x_i}{l_i}. \tag{10.103}$$

Since we are only considering a two dimensional system with two dofs in each node, the transformation matrix from i to f is written as

$$\mathbf{T}_{0,i}^f(\mathbf{r}) = \begin{bmatrix} \cos\theta_i & \sin\theta_i \\ -\sin\theta_i & \cos\theta_i \end{bmatrix}, \tag{10.104}$$

where $\mathbf{r}$ is the displacement vector, as the inclination in each element is given as a function of the positions, given in the sea floor fixed f-frame. For notational simplicity the superscript f is omitted as $\mathbf{r}$ is always given in the f-frame. The full displacement vector is given as

$$\mathbf{r} = \begin{bmatrix} x_1 & z_1 & x_2 & z_2 & \cdots & x_i & z_i & \cdots & x_n & z_n & x_{TLP} & z_{n+1} \end{bmatrix}^T. \tag{10.105}$$

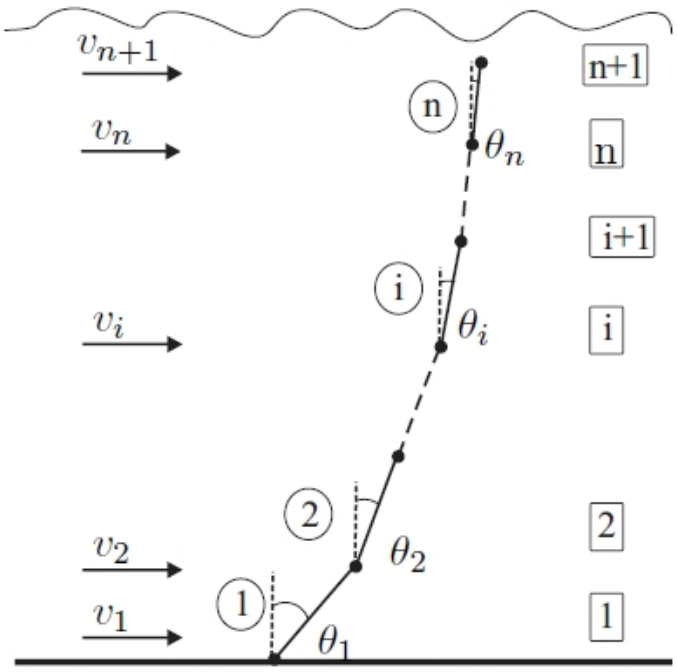

Figure 10.16: Numbering of the elements encircled, nodes in boxes, current v_i in each node i and the attitude θ_i of each local element i, relative to the global frame.

For all four dofs related to an element we have

$$\mathbf{T}_i^f(\mathbf{r}) = \begin{bmatrix} \mathbf{T}_{0,i}^f(\mathbf{r}) & \mathbf{0}_{2\times 2} \\ \mathbf{0}_{2\times 2} & \mathbf{T}_{0,i}^f(\mathbf{r}) \end{bmatrix}, \tag{10.106}$$

as the inclination of each element is a function of the positions of its end nodes.

Riser system stiffness matrix For each element a stiffness matrix is defined based on the local coordinate system. The local stiffness matrix consists of two terms; the elastic stiffness, $\mathbf{k}_E$, and the geometric stiffness, $\mathbf{k}_G$. The geometric stiffness matrix includes the axial tension P_i acting on the particular element i. The elastic stiffness matrix works in the axial direction, whereas the geometric stiffness in the lateral direction. The resulting stiffness matrix $\mathbf{k}_i$ for the element i in its own frame becomes

$$\mathbf{k}_i = \mathbf{k}_{E_i} + \mathbf{k}_{G_i} = \frac{1}{l_i}\left(EA \begin{bmatrix} 0 & 0 & 0 & 0 \\ 0 & 1 & 0 & -1 \\ 0 & 0 & 0 & 0 \\ 0 & -1 & 0 & 1 \end{bmatrix} + P_i \begin{bmatrix} 1 & 0 & -1 & 0 \\ 0 & 0 & 0 & 0 \\ -1 & 0 & 1 & 0 \\ 0 & 0 & 0 & 0 \end{bmatrix} \right), \tag{10.107}$$

where E is Young's modulus of elasticity, A is the cross sectional area of of the riser material, here steel, and l_i is the length of element i found in (10.102). The axial tension P_i in each element is found as a function of the elongation of the element i;

$$P_i = \frac{EA}{l_0}\Delta l_i, \quad \Delta l_i = l_i - l_0, \tag{10.108}$$

where l_0 is the initial length of an element in an untensioned riser.

Each local matrix $\mathbf{k}_i$ is transformed to the global f-frame fixed to the seabed, and all the local stiffness matrices are assembled to form the global stiffness matrix $\mathbf{K}$ for the riser. The local stiffness matrix is transformed to f-frame by

$$\bar{\mathbf{k}}_i = \mathbf{T}_i^f \mathbf{k}_i \mathbf{T}_i^{fT} = \begin{bmatrix} \bar{\mathbf{k}}_{11}^i & \bar{\mathbf{k}}_{12}^i \\ \bar{\mathbf{k}}_{21}^i & \bar{\mathbf{k}}_{22}^i \end{bmatrix}, \tag{10.109}$$

where $\bar{\mathbf{k}}_i$ is the stiffness matrix for element i in the global f-frame. For $\bar{\mathbf{k}}_{11}^i$ the superscript is used to recognize the element number, and the subscript is used to identify the different parts of the stiffness matrix, needed for the concatenation to the global matrix. $\mathbf{T}_f^i$ is the transformation matrix from the f-frame to the i-frame. The full, global stiffness matrix in the f-frame for n elements is then

$$\mathbf{K} = \begin{bmatrix} \bar{\mathbf{k}}_{11}^1 & \bar{\mathbf{k}}_{12}^1 & & & & \\ \bar{\mathbf{k}}_{21}^1 & \bar{\mathbf{k}}_{22}^1 + \bar{\mathbf{k}}_{11}^2 & \bar{\mathbf{k}}_{12}^2 & & & \\ & \bar{\mathbf{k}}_{21}^2 & \bar{\mathbf{k}}_{22}^2 + \bar{\mathbf{k}}_{11}^3 & & & \\ & & & \ddots & & \\ & & & & \bar{\mathbf{k}}_{22}^{n-1} + \bar{\mathbf{k}}_{11}^n & \bar{\mathbf{k}}_{12}^n \\ & & & & \bar{\mathbf{k}}_{21}^n & \bar{\mathbf{k}}_{22}^n \end{bmatrix}.$$

The global stiffness matrix $\mathbf{K}$ is always given in the f-frame, and the superscript f is hence omitted.

Riser system mass matrix The local mass matrix consists of three terms; the structural mass of the riser $\mathbf{m}_s$, the internal fluid $\mathbf{m}_f$, and the hydrodynamic added mass $\mathbf{m}_a$. The structural mass is given by

$$\mathbf{m}_{si} = \frac{\rho_s A l_i}{6} \begin{bmatrix} 2 & 0 & 1 & 0 \\ 0 & 2 & 0 & 1 \\ 1 & 0 & 2 & 0 \\ 0 & 1 & 0 & 2 \end{bmatrix}, \tag{10.110}$$

where ρ_s is the density of the riser material steel. The internal fluid is included as well

$$\mathbf{m}_{fi} = \frac{\rho_f A_{int} l_i}{6} \begin{bmatrix} 2 & 0 & 1 & 0 \\ 0 & 2 & 0 & 1 \\ 1 & 0 & 2 & 0 \\ 0 & 1 & 0 & 2 \end{bmatrix}, \tag{10.111}$$

where A_{int} is the internal area of the riser, and ρ_f is the density of the internal fluid.

The local added mass in the axial z-direction is assumed to be zero, while the added mass for a circular cylinder in the lateral x-direction is equal to the displaced water volume. The matrix for the added mass is then given as

$$\mathbf{m}_{ai} = \frac{\rho_w C_m A_e l_i}{6} \begin{bmatrix} 2 & 0 & 1 & 0 \\ 0 & 0 & 0 & 0 \\ 1 & 0 & 2 & 0 \\ 0 & 0 & 0 & 0 \end{bmatrix}, \tag{10.112}$$

where A_e is the area found from the exterior diameter D_e, and ρ_w is the density of water. The coefficient C_m is called the hydrodynamic added mass coefficient. For a circular cylinder $C_m = 1$. The total local mass matrix $\mathbf{m}_i$ for each element i in its own frame is then the sum of the three terms written as

$$\mathbf{m}_i = \mathbf{m}_{si} + \mathbf{m}_{fi} + \mathbf{m}_{ai}. \tag{10.113}$$

To calculate the global mass matrix for the riser, we transform each local mass matrix from its local i-frame to the global f-frame, similar to what was done with the stiffness matrix. These are assembled to the global mass matrix $\mathbf{M}$ in the same way as the stiffness matrix.

Structural damping The damping experienced by a riser is a combination of the structural damping and hydrodynamic damping, resulting from both radiation and viscous dissipation of energy, see Faltinsen (1993). The structural damping is due to the strain and elasticity properties of steel. The damping matrix for a tensioned steel riser is based on proportional Rayleigh damping and assumed proportional to the global stiffness matrix

$$\mathbf{C} = \alpha_2 \mathbf{K}. \tag{10.114}$$

The coefficient α_2 can be found from simple equations if the total damping level is known. The term proportional to mass is neglected, see Berge et al. (1992). Here we have assumed that the structural damping is 1.5% of the critical damping at the eigenperiod of $T = 10$s. Frequencies lower than this will have smaller damping, and the damping is assumed linearly increasing with logarithmic increasing ω, such that $\lambda = 0.15\%$ for $T = 100$s. Thus, the material damping is small relative to the hydrodynamic damping.

Hydrodynamic forces

The hydrodynamic forces on the risers are calculated using Morison's equation modified for a moving circular cylinder. The horizontal hydrodynamic force on a strip of the cylinder can be written

$$df_{hyd} = \rho_w C_M \frac{\pi D_e^2}{4} a dz - \rho_w C_m \frac{\pi D_e^2}{4} \ddot{r} dz + \frac{1}{2} \rho_w C_D D_e \left(v - \dot{r}\right) \left|v - \dot{r}\right| dz, \tag{10.115}$$

where v and a are the undisturbed water velocity and acceleration, $\dot{r}$ is the response velocity, and $\ddot{r}$ is the structure's acceleration. $C_M = C_m + 1$ is the inertia force coefficient. The acceleration of the water has a material derivative, $a = \frac{Dv}{Dt}$, as the water velocity field is varying in space due to shielding effects, but this is assumed to be small. This and the fact that the wave induced water motion is assumed negligible for a riser in deep waters, means that the first term of (10.115) can be neglected. The added mass term is already included in the mass term on the left hand side of the equation of motion. Hence, the only hydrodynamic force included on the right hand side is the drag force df_{drag}, which is the last term of (10.115). This drag force is calculated for each element and summarized as concentrated forces in each node. The force vector $\mathbf{f}_{drag}$ is found at the right hand side in the equation of motion given in (10.120) later in the text.

The added mass C_m for a circular cylinder is known to be 1.0. However, this value may for the downstream cylinder be influenced by the wake. VIV for both risers may also cause some variations of C_m. For this application such effects are considered to be insignificant, and a constant value is therefore applied in this study. The drag coefficient is influenced by similar effects as added mass, and C_D is known to depend on the flow velocity for a specific cross

section. However, it is not easy to describe such variations, and it is therefore common practice for engineering purposes to assume a constant value. This approach is taken in the present study, and a value of $C_D = 1.0$ for both risers is applied. It is also important to note that variations of C_D will not alter any conclusions regarding the control system design for this study since the estimates of drag forces are not needed for control purposes.

Equilibrium iteration and numerical integration method

The modeled system contains nonlinearities in the mass, stiffness and damping matrices, in addition to the nonlinearities due to drag and hydrodynamic damping. In addition, the top tension is varying in time as it is the control input. The tension variation is linearly decreasing along the riser. The forces acting on each element, such as tension, effective weight and current due to drag are computed in the i-frame for each element and thereafter transformed to the f-frame.

As in traditional FEM, the nonlinearities are solved numerically by incremental formulation with the Newmark-β time integration method and Newton-Raphson equilibrium iteration. The force equilibrium between the internal force $\mathbf{F}_{int}$, due to tension, and the external force $\mathbf{F}_{ext}$, due to drag and effective weight (illustrated in Figure 10.17) is found for each time step. Iteration with the Newton-Raphson method continues until an equilibrium solution is found with desired accuracy.

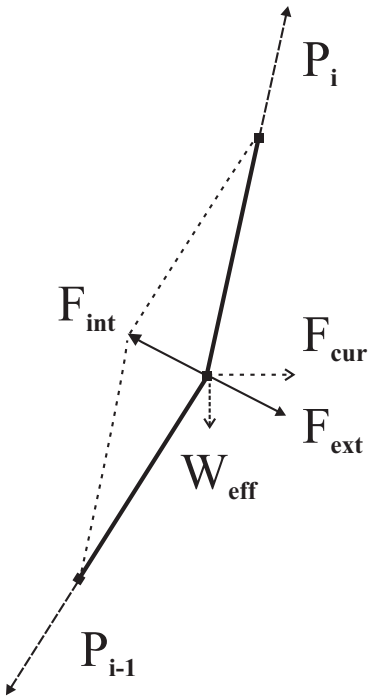

Figure 10.17: Balanced internal and external force.

The Newmark-β method for numeric integration uses the assumption of constant acceleration in each time step. This integration method is unconditionally stable for linear systems. However, for nonlinear systems the step length the simulations most be small enough to capture system dynamics also for the stiff vertical DOFs. A step length of 0.1s is seen to be stable in all DOFs

for all simulations.

TLP modeling

Recall that the TLP is a partly rigid and partly compliant structure. The eigenfrequencies for in-plane motions must be below frequencies for wave energy and the frequencies for the out-of-plane motions must be above. With respect to the horizontal degrees of freedom, the TLP is compliant and behaves similar to other floating structures. The horizontal degrees of freedom surge, sway and yaw are inertia dominated with eigenperiods around 1-2 minutes, well above the range of first order waves with periods of 5-20s. With respect to the vertical degrees of freedom, it is stiff and resembles a fixed structure. The vertical degrees of freedom heave, roll and pitch are stiffness dominated with eigenperiods in the order 2-4s, and well below the period of the first order waves.

The eigenfrequencies in all six degrees of freedom (DOFs) are tuned relative to the first order wave loads. Thus, loads at the wave frequencies do not excite the TLP at its natural frequencies. On the other hand, second or higher order loads at the sum and difference frequencies can produce significant resonant excitations at the TLP natural frequencies because of the small amount of damping available at these frequencies, see Faltinsen (1993).

- Higher order components and sum frequencies ($2\omega_i$, $2\omega_j$, $\omega_i + \omega_j$) in waves may give significant resonance oscillations for the TLP in heave, roll and pitch known as *ringing* and *springing*. The restoring forces are due to the tendons and the mass forces due to the TLP, and they are excited by the nonlinear wave effects. Ringing is associated with transients effects, while springing is steady-state oscillations.

- Loads on difference frequencies ($\omega_i - \omega_j$) will give slowly varying wave loads that may give rise to resonant in-plane motions. Excitation from wind gusts may appear in the same frequency range and contribute significantly to such motions.

Both these nonlinear phenomena should be considered when designing a TLP. The ringing and springing phenomena have impact on the upper and lower limits of the tendon force. The mean wave drift and current loads on the hull will induce a *mean offset force*. Assuming linear analysis as the water depth increases, the eigenperiod of the riser system increases as well. The first eigenperiod for a riser at 1200m water depth is approximately 30-40s depending of the top tension and cross section properties. As the riser eigenperiod is approaching the eigenperiods in surge and sway for the TLP, induced motions from these components may have more influence on the riser dynamics than in more shallow waters.

Riser stroke calculations Marine risers made of steel have very low structural strength against lateral loading unless they are tensioned. It is therefore important to maintain the upper end tensioned under all realistic conditions, irrespective of the platform motions, dynamic riser response and internal flow parameters. The tensioner system will therefore act as a heave compensating system with an adequate stroke capacity and ability to maintain a near constant tension.

If the relative platform/riser motion exceeds the stroke capacity, unwanted loss of tension or tension increase will occur. Such situations may result in excessive bending stress in the riser, excessive rotation of the ball joint, or end loads may cause damage to the well template or the

riser tensioning system. Other unwanted effects might be mechanical contact between adjacent risers or between the riser and the platform. Consequences of such incidents must be taken into considerations, when designing the riser tensioner system.

The platform vertical motion is the most important parameter that defines the stroke. For a TLP with vertical and parallel tendons in the initial zero offset position, motions in surge direction will not induce any pitch motion, but will be coupled to the vertical motion referred to as *surge induced heave* or *setdown*. Using the Pythagorean theorem and assuming both risers and tendons to be straightlined, the relative setdown between the riser and the platform can be found. The setdown of the platform is controlled by the tendons. The offset in surge, x_{TLP}, is equal for the risers and the tendons, but as the risers are longer and have larger radius, their setdowns are smaller. The relative setdown, Δs, is found as

$$\Delta s = \Delta s_T - \Delta s_R = \left(l_T - \sqrt{l_T^2 - x_{TLP}^2} \right) - \left(l_R - \sqrt{l_R^2 - x_{TLP}^2} \right), \tag{10.116}$$

where Δs_T and Δs_R are the tendon and riser setdown respectively, and l_T and l_R are the tendon and riser lengths. This is illustrated in Figure 10.18. For d being the water depth, we can calculate the setdown with known offset, riser and tendon lengths. The relative setdown is small, even for large water depths and offsets, due to the tendon riser geometry. Hence, the requirement for heave compensation due to offset is also small. This makes TLP favorable to other floaters which do not have surge induced setdown, such that their relative difference between the platforms and the risers is larger.

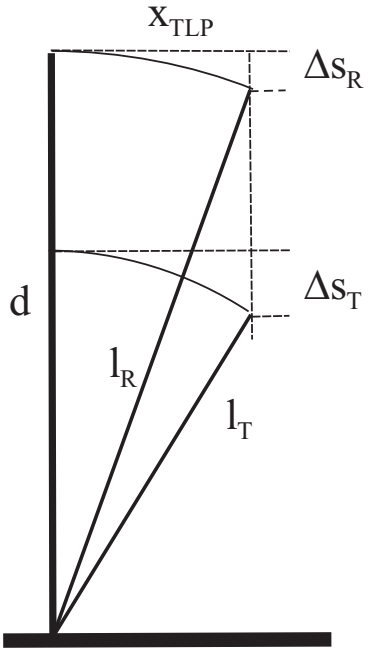

Figure 10.18: Setdown due to tendon/riser geometry.

Other effects having an influence on the stroke are the effect of temperature, tension, pressure, production tolerances and riser deflections. Note that this calculations on set-down is specific for the TLP solution and not applicable for other type of vessels.

Transformation of the TLP The motions of the TLP is given as the motion of the b-frame relative to the g-frame in the g-frame with the position vector position vector $\mathbf{r}_{TLP,ob}^{\ g} = [x_{bg}^g, y_{bg}^g, z_{bg}^g]^T$. As the riser motions are expressed in the f-frame, the rotation matrix between the f- and the g-frames is needed. The transformation from g- to f-frame is given by the diagonal matrix

$$\mathbf{R}_g^f = diag\,(1,\ -1,\ -1)\,. \tag{10.117}$$

Since both frames are considered inertial and fixed with a translation in heave direction only, all axis are parallel, and the x-axis are always pointing in the same direction. In a two dimensional system, only the surge motion of the TLP is of interest as the prescribed motion of the riser. Hence, the motion in x-direction for the TLP described in the g-frame is equal to the x-position given in the f-frame. Thus the frames are omitted for the surge position of the TLP, x_{TLP}.

TLP surge modeling Analysis of floater models are usually divided into two groups; *separated or de-coupled analysis* and *coupled analysis*. For separated analysis the vessel motions are found first. The effects from moorings and risers are included as nonlinear positions dependent forces or stiffness. The damping or velocity dependent forces, which are important for estimation of the LF motion may be neglected. In the second step, the dynamic response on the risers and moorings are analyzed, using the vessel response from step one as a forced displacement on the top node. The main problem with this method is that inertia and drag forces on the risers and tendons are not accounted for. These effects could be large in deep waters. The term coupled analysis means simultaneous analysis of vessel motions, mooring systems and riser dynamics where the full interaction is taken into account. The main drawback with this method is that it is very time consuming since a nonlinear time domain simulation is required.

In this study we assume that the TLP motions influence the riser behavior, but that the risers do not affect the TLP motion. Hence, a de-coupled analysis model is applied. The main purpose of the modeled TLP is to represent the prescribed motion in surge for the top node of the risers. Since the system model is two-dimensional, only the surge motion for the TLP is needed. It is modeled as a low frequency harmonic motions

$$x_{TLP} = A_{TLP} \sin\left(\frac{2\pi}{T_{TLP}} t\right) + x_{off}, \tag{10.118}$$

where x_{off} is the static TLP offset, A_{TLP} is the amplitude, and T_{TLP} is the period of the TLP motion.

TLP prescribed forces The complete stiffness, damping and mass matrices found for the riser can be divided into submatrices that contain the free and prescribed (fixed or with specified motion) dofs respectively. The columns and rows corresponding to the prescribed dofs are removed from the original system matrices, meaning that only the free dofs are present in the dynamic equation of motion. The fixed dofs are the displacement at the bottom (both $x_{i=1}$ and $z_{i=1}$), whereas $x_{n+1} = x_{TLP}$ at the top node is the only node with specified motion. The specified motion will give contribution to the vector with dynamic loads found on the right hand side of the equation of motion. These contributions are found from elements in the original riser system matrices that links the free DOFs to the DOFs with specified motions (spe). For the present case this contribution will be given by

$$\mathbf{f}_{TLP} = \mathbf{m}_{spe}\ddot{x}_{TLP} + \mathbf{c}_{spe}\dot{x}_{TLP} + \mathbf{k}_{spe}x_{TLP,} \tag{10.119}$$

where $\mathbf{f}_{TLP}$ is the force vector that originates from the TLP motions. $\mathbf{m}_{spe}$, $\mathbf{c}_{spe}$ and $\mathbf{k}_{spe}$ are columns in the original riser system matrices that correspond to x_{TLP}, and hence are removed from the riser system matrices used in the dynamic equation of motion.

Dynamic equation of motion

In the dynamic equation of motion, the mass-damper-spring system for the free DOFs in the riser system are found on the left hand side. On the right hand side the external forces from top tension, current and drag forces, and the specified motion from the TLP is included.

$$\mathbf{M}(\mathbf{r})\,\ddot{\mathbf{r}} + \mathbf{C}(\mathbf{r})\,\dot{\mathbf{r}} + \mathbf{K}(\mathbf{r})\,\mathbf{r} = \mathbf{f}_{top} + \mathbf{f}_{cur} - \mathbf{f}_{TLP}, \tag{10.120}$$

where $\mathbf{r}$ is the riser position vector, $\mathbf{f}_{top}$ is the top tension, and $\mathbf{f}_{cur}$ is the drag forces from current and riser motions. The superscript f is omitted as the equation of motion is given in the f-frame. In this equation the fixed and prescribed DOFs are removed from the equation, and the influence from specified DOFs is included on the right hand side as a force acting on the system. The riser position vector is then

$$\mathbf{r} = \begin{bmatrix} x_2 & z_2 & \cdots & x_i & z_i & \cdots & x_n & z_n & z_{n+1} \end{bmatrix}^T. \tag{10.121}$$

Remark that this vector correspond to the entire position vector found in Eq. (10.105), but the prescribed DOFs are left out.

Actuator and constraints

The riser tensioner system or heave compensator can be implemented as a hydraulic cylinder with a piston. Today this setup strive to keep the tension close to constant, compensating for the stroke parameters listed in Sec. 10.3.3. This is obtained by using a compressed air volume as a soft spring in the hydraulic system. Hence, no active control is needed. Designing the heave compensator such that the payout is controlled, will still give the same physical constraints. These could be divided into two groups; (1) constraints due to stroke and (2) constraints due to tension. The stroke parameters are based on the the definitions by Larsen in Larsen (1993), slightly modified, and illustrated in Figure 10.19. The *initial position* refers to a riser and platform condition without offset or environmental forces, and a desired level of top tension. The *static position* is a particular case with defined environmental and operational conditions. *Payout* is the distance between the bottom of the cylinder and the top of the riser, positive downwards. The *stroke variation* is the maximum length variation the tensioner system can provide. The *dynamic stroke* is the length variation needed to tension the riser in a particular condition. The dynamic stroke must compensate for the relative motion between the platform and the riser subjected to all environmental conditions.

In addition to the boundaries given by the limitations for payout and stroke, the top tension forced on the riser is physically constrained with upper and lower boundaries. If this tension is too low, i.e. less than the effective weight of the riser, the riser will experience buckling. Hence, the lower limit for tension should be the effective weight plus a safety margin. The upper tension limit is restricted by the yield stress for the riser material and chosen such that the stress is less than 40% of the yield stress for steel. A given tensioning system will also have limitations regarding maximum tension due to limitations of pressure in the hydraulic system.

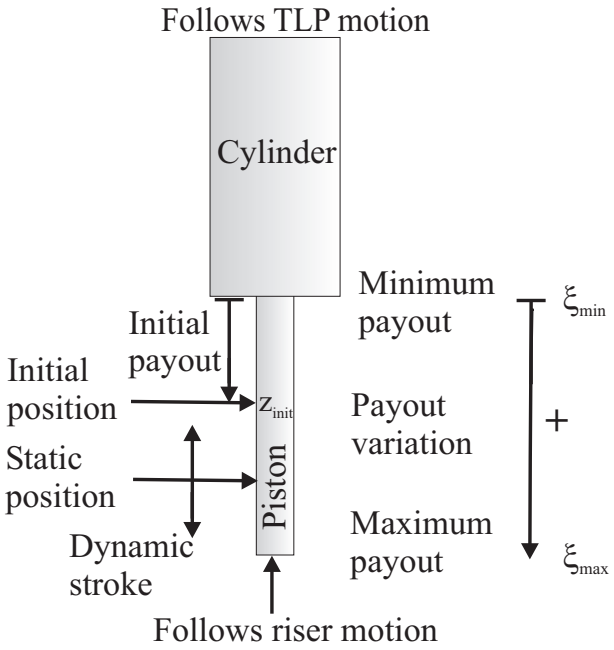

Figure 10.19: Stroke parameters of one individual cylinder.

Measurements

The non-compensated initial position, z_0, is defined with the design tension and no environmental forces or offsets, and it will be equal for all risers in the present study. When the TLP is in an offset position, the setdown of the initial position can be found from the tendon geometry, such that the initial position compensated for setdown, Δs_T is found from

$$z_{init}(t) = z_0 - \Delta s_T(t). \tag{10.122}$$

Recall that this compensation for set-down is typical for a TLP and noe applicable for vessels in general. The measured parameter used in the control loop is the payout for each piston, denoted ξ_j. Payout is defined positive when it adds elongation to the riser and negative in the opposite direction. *Minimum payout*, $\xi_{\min}$, means that the piston is as far into the cylinder as possible, for simplicity assumed zero here. *Maximum payout*, $\xi_{\max}$, refers to the position with maximum free piston length. The *initial payout*, ξ_0, is the distance between the lower end of the cylinder and the initial position. The total *dynamic payout* is given as

$$\xi_j(t) = \xi_0 + z_{init}(t) - z_{j,n+1}(t),\ j = 1, 2. \tag{10.123}$$

where $z_{j,n+1}$ is the vertical top position of riser j. An example of dynamic payout with TLP motions is illustrated in Figure 10.20.

10.3.4 Model Verification

RIFLEX RIFLEX (2018) is a commercial FEM program for static and dynamic analysis of slender marine structures. For the purpose of control system design, a more convenient numerical procedure and software code has been implemented in Matlab/Simulink. The algorithm implemented is equivalent to what is found in RIFLEX. The motivation behind this section is to

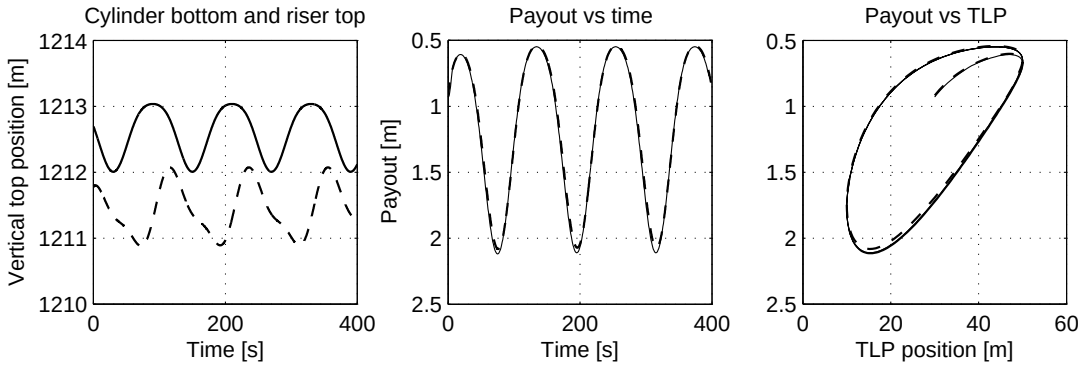

Figure 10.20: From left: a) The cylinder bottom (–) and the riser top (- -), b) the distance between them; payout for RIFLEX(–) and Simulink (- -), and c) payout vs TLP position, RIFLEX(–) and Simulink(- -).

validate the riser model from Section 10.3.3 implemented in Matlab/Simulink and verify that it is appropriate as a model of the real world used in the simulations (i.e. prosess plant model) and for the purpose of control system design (i.e. control plant model), despite the simplifications made in the modeling. In this case, the model should give a good picture of the global geometry of the riser, with focus on the maximum horizontal displacement and the vertical position of the riser top, exposed to varying TLP positions and tensions. Features often included in riser analysis, which are of less importance in this case are:

- Bending stiffness EI in the riser model.
- End conditions, i.e. bending stiffeners in the top and bottom end points.
- Stress.

Hence, in the presented Simulink model, the simplifications can be summarized as:

- No bending stiffness included.
- Free rotations in the ends.
- Few elements compared to typical structural analysis, 2-20 versus 400.

The first two of these items are assumed to be insignificant at large water depths (large length to diameter ratio), as long as the global geometry is of main importance. Note that for structural analysis where stress and fatigue is of importance the simplifications listed above can not be made and more refined models are needed. Note that it is crucial to have a clear understanding of the purpose of the analysis before simplifications in the model is made.

The bending stiffness has been included in the RIFLEX model in all analyses presented herein. In the verification of the code, a relatively large number of elements ($N = 20$) are chosen to increase the resolution and accuracy. Four tests are run:

1. Quasi-static verification with increasing TLP offset.

2. Quasi-static verification with increasing top tension.

3. Dynamic verification with harmonic TLP motions.

4. Dynamic verification with harmonic top tension variations.

Set-up and current profiles

The TLP/riser system is simulated at 1200m water depth. For simplicity, the riser top is assumed to be at the level of the free surface, i.e. 1200m above the sea floor. The model run in RIFLEX consists of 400 elements, each of length 3m. The model implemented in Simulink is run with 20 elements which gives an element length of 60m. In order to limit the computation time for real-time control applications, it is of interest to minimize the number of elements applied in the riser model, while still maintaining a sufficient level of accuracy, such that the implemented model can represent the geometry of the real world. In Section 10.3.5, this model with the number of elements varying between 2 and 20 are analyzed and compared to investigate the size of the error introduced.

Three different geographic areas are chosen to compare the behavior of the risers with various profiles. Among these are design profiles representing the Ormen Lange field in the North Sea, loop eddies in the Golf of Mexico (GoM), and a bidirectional shear current, see Figure 10.21. The Ormen Lange current profile is close to a shelf edge. This gives often strong and variable current, and might potentially cause operational challenges. The velocities are strong all the way down to the sea bed, but even stronger close to the sea surface due to wind generated current. The data from the Ormen Lange field is extended from 850m to 1200m water depth and the current between these depths are considered constant at 0.5m/s. In the current from the GoM a loop eddy is seen to reduce the current at 200-400m water depth, whereas the velocity increase again for even larger water depths. The bidirectional shear current is due to typically residual warm flow northeastward usually in the upper layer, and a southwestern cold flow in the lower layer. In addition to the residual flow there are tidal current, that do not vary with depth.

A selection of the verification tests are given in the following sections. The physical riser data are found in Table 10.1 below. The TLP data is from the ASM 1200, see Rustad et al. (2007). The estimated surge eigenperiod is 136s.

Quasi-Static verification with increasing TLP offset

The quasi-static riser model was verified first. The TLP offset was increased in steps of 5m from 0m to 70m, corresponding to 0 to 5.8% of the water depth. The static equilibrium solution is found for each TLP position for both the RIFLEX and the Simulink models. The models were run for all the different current profiles and with various current velocity amplitudes. Deflections of the riser with the design current from the Ormen Lange field with surface velocity 1.15m/s are seen in Figure 10.22a).

x and o mark the position along the riser with the maximum horizontal displacement for RIFLEX and Simulink, respectively. The riser models match close to perfect. The deviation in the vertical position of the node with max displacement is due to the relatively low number of elements in the Simulink model. The deviation for the riser configuration is seen to be small. 20 elements as seen in the Figure 10.22, gave as expected a better correspondence between the RIFLEX and Simulink calculations than fewer elements, like 5 or 10, see Section 10.3.5.

Parameter	Description	Value	Dimension
α_2	Damping coefficient	0.0477	[-]
D_e	Diameter	0.3	[m]
d	Water depth	1200	[m]
t_h	Wall thickness	0.015	[m]
C_D	Drag coefficient	1.0	-
C_M	Mass coefficient	2.0	-
E	Modulus of elasticity	206	[GPa]
f_u	Yield stress steel	500	[MPa]
l_r	Riser length	1200	[m]
l_t	Tendon length	1166	[m]
T_{max}	Upper tension limit	2700	[kN]
T_{min}	Lower tension limit	1200	[kN]
ξ_0	Initial payout	0.5	[m]
ρ_s	Specific weight for steel	7850	[kg/m^3]
ρ_f	Specific weight for filling	800	[kg/m^3]
ρ_w	Specific weight for sea water	1026	[kg/m^3]
Δx_d	Initial riser distance	15	[D]

Table 10.1: Riser data for 1200m water depth.

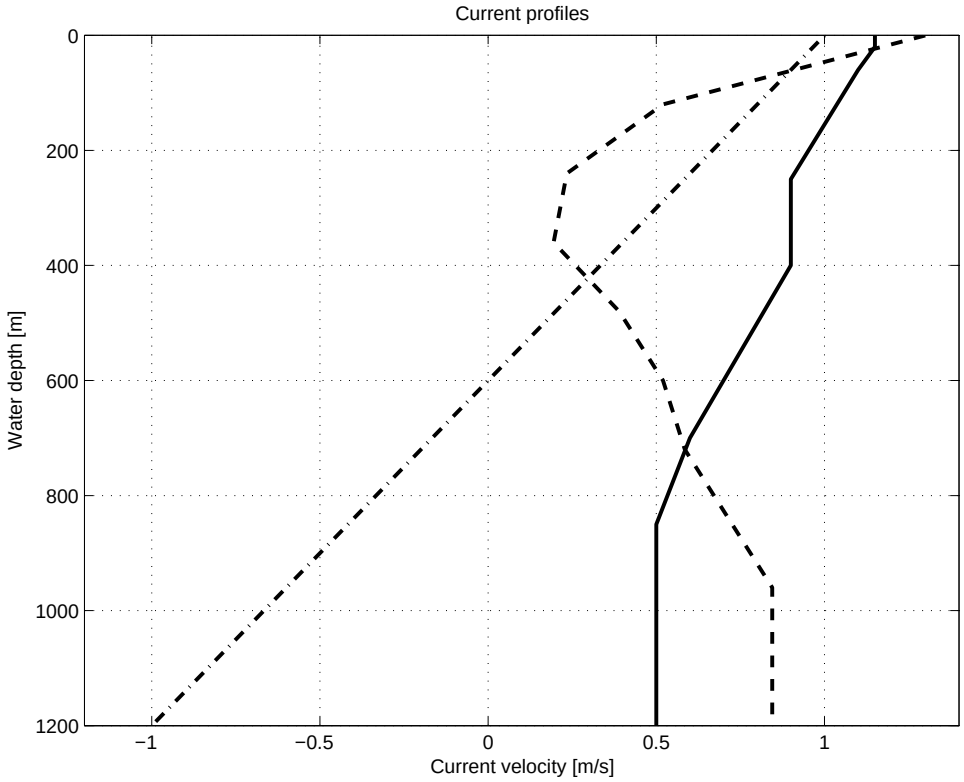

Figure 10.21: Simulated current profiles from the Ormen Lange field (–), Golf of Mexico (- -) and a bidirectional shear current (-.).

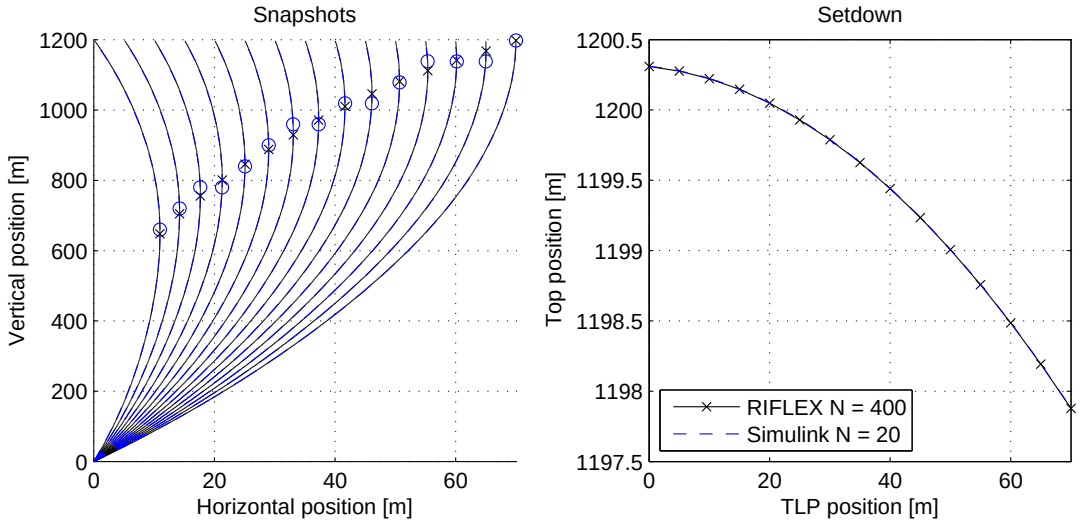

Figure 10.22: Deflections (a) and setdown (b) for the quasi-static riser model with TLP offset 0-70m and Ormen Lange design current. RIFLEX(– x) and Simulink (- -o).

The setdown is given in Figure 10.22b). It is seen to correspond nicely for the two models.

The setdown curve reflects the setdown due to surge, which also is used to describe the TLPs motion on a sphere surface. We achieved similar correspondence in snapshots and setdown for the other current profiles.

Quasi-Static verification with increasing top tension

In the second verification of the quasi-static riser model, the tension was increased from 1200kN to 2700kN in steps of 50kN. All current profiles were tested with TLP positioned in zero and 30m offset, $x_{off} = \{0, 30\}$m. The lower tension limit was the effective weight plus a safety margin for the structure connection at the sea bed. The upper tension limit was given by a percentage of the yield stress for steel.

Figure 10.23 shows the relations between top tension, vertical top position and maximum horizontal displacement for the Ormen Lange design current. The verification showed good agreement between the models within the tension limits. For lower tensions, nonlinear effects like buckling may appear. These effects are not implemented in the Simulink model. Top tension less than the lower saturation limit is therefore not simulated.

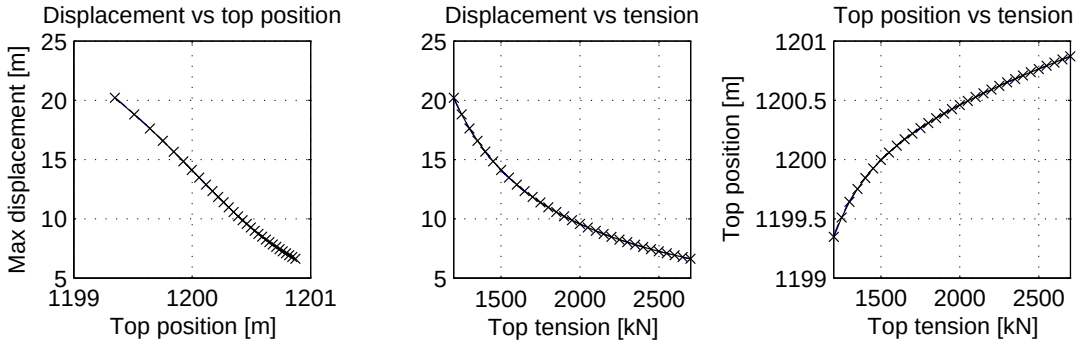

Figure 10.23: From left: a) Maximum horizontal displacement vs vertical top position, $x_{max}(z_{max})$, b) Maximum horizontal displacement vs top tension, $x_{max}(T)$, c) Vertical top position vs top tension, $z_{max}(T)$. All plots are for the quasi-static riser model exposed to the Ormen Lange profile. RIFLEX(– x) and Simulink (- -).

Verification with dynamically moving TLP

The dynamics of the system and the influence from the current and drag forces were tested by dynamic surge motions of the TLP with amplitude $A_{TLP} = 20$m and periods in the range $T_{TLP} = 60 - 300$s. The static offset was $x_{off} = 30$m, and the riser tension was kept constant. Figure 10.24 shows snapshots of the dynamic riser motion at the Ormen Lange field simulated in Simulink with $T_{TLP} = 120$s. The static configuration and the dynamic enveloping curves are found from RIFLEX.

Top position versus time is plotted in Figure 10.25a), while Figure 10.25b) shows the correspondence between the top position and the TLP surge position. The deviation in top position is bigger for larger curvature of the riser. This was best seen when the TLP was moving from its maximum to its minimum offset, with the smallest surge period, $T_{TLP} = 60$s, not shown here.

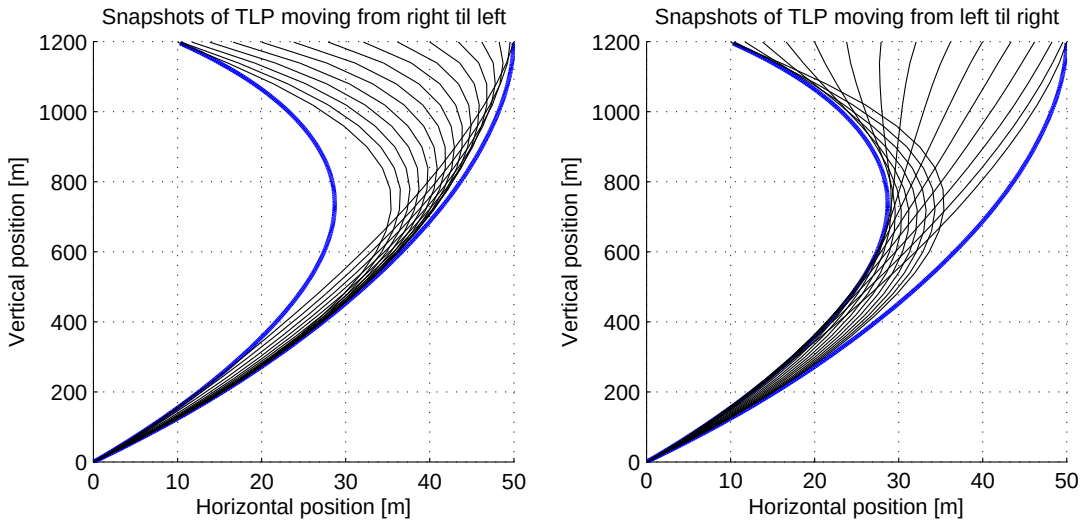

Figure 10.24: Snapshots of the TLP moving from right to left (a), and from left to right (b) for the Ormen Lange design current. The snapshots are from Simulink and the thick, blue lines are envelope displacement curves from RIFLEX.

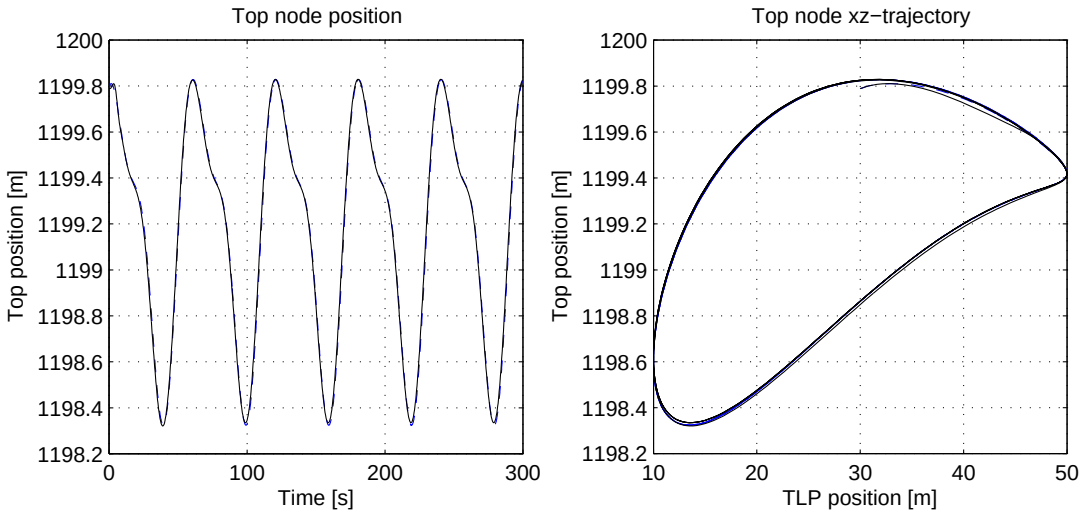

Figure 10.25: Top position as a function of time (a) and TLP motion (b) with period of 60s. RIFLEX(–) and Simulink (- -) for the Ormen Lange design current.

Verification with dynamically varying tension

The fourth and last of the riser model verification tests included harmonic tension variations. The initial tension was 1950kN, with an amplitude of 750kN and periods of 60s and 120s. This gives maximum tension rates of 75kN/s and 37.5kN/s, respectively. This is far more than the limit of a conventional tension system. Hence, if the riser model is valid for these large and fast changes in tension, it will also be valid for slower limit rates. Simulations were run with currents corresponding to the Ormen Lange field, GoM2 and the bidirectional current profile.

Figure 10.26 shows the dynamic variation of the top tension (a) and the top position (b) with period of 120s. The motion trajectory for vertical position versus tension is seen in Figure 10.26 c). A transient period from the static initial condition is seen. The results from simulations with 60s are similar.

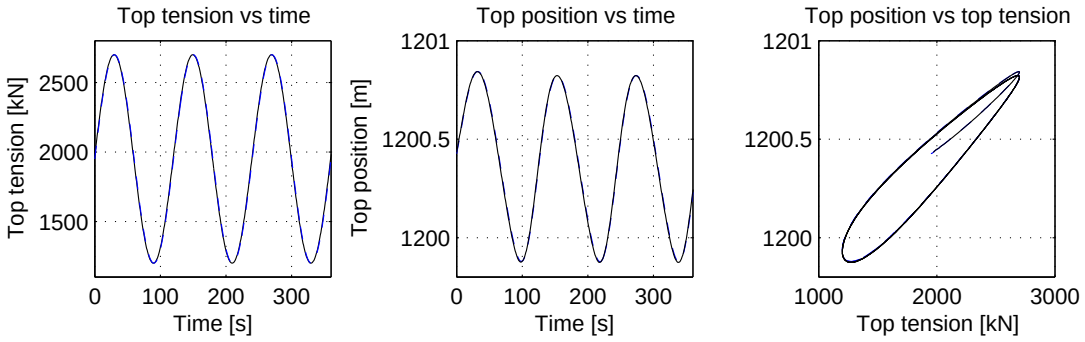

Figure 10.26: Top tension (a) and position (b) as functions of time, and top position vs top tension (c). RIFLEX(–) and Simulink (- -) for Ormen Lange design current.

There were also run tests where the motion of the top node in RIFLEX was a prescribed vertical sinusoidal. In the corresponding simulations in Simulink, sinusoidal tension was used. The correlation between tension and vertical top position is nonlinear and asymmetric, meaning that more tension is needed to lift the riser 0.5m than the reduction in tension when lowering the top with 0.5m. This is caused by hydrodynamic drag forces that will increase needed tension for an upwards motion, but decrease the tension reduction for a downwards motion. However, the results presented in this section are better suited for the purpose of verification. The results with prescribed motions are not presented here, but can be found in Rustad (2007).

10.3.5 Control Plant Model Analysis

In Section 10.3.3, a mathematical model for a riser is derived. This model was implemented in Simulink and verified by comparing it to the commercial FEM software RIFLEX RIFLEX (2018) in Section 10.3.4. The model had the same physical behavior as RIFLEX in all deep water cases, and could be said to be close to the real world and an adequate model of the riser process. The model used in the verifications had 20 elements, and satisfied the desired level of accuracy. As defined in Section 10.3.3, the purpose of the PPM is to describe the actual physical process as accurately as possible. For the purpose of control applications, the CPM should be computationally fast, however, still describe the main physics. This is motivated by the realtime requirements for control systems. A low order model gives small system matrices and keeps the number of numerical operations down. A simple processor could then be able to run the model online. Small, simple computers help to keep the costs to a minimum, while large and fast computers cost more.

In this section we will investigate how many elements are needed to keep a desired level of accuracy, both for the PPM and for the CPM. Different means to measure the performance of a model are considered. Generally, better performance is expected for more elements. How many elements are good enough? And which cases might need more elements to keep the desired level of accuracy?

Analysis input data and set-up

Recall that the riser top is assumed to be at the level of free sea surface, i.e. 1200m above the sea bed. The RIFLEX model has 400 elements, each of length 3m. The number of elements for the Simulink riser models are common multiples of 400, ranging from 2 to 20, i.e. $N = \{2, 4, 5, 8, 10, 16, 20\}$. This is done to get the nodes at the same height above the sea bed, and hence more easily compare the horizontal displacements, especially of interest in the quasi-static analyses. With a water depth of 1200m, the element lengths were respectively $l_0 = \{600, 400, 240, 150, 120, 75, 60\}$m for the different models and increasing number of elements. The Simulink models are hereafter called CPMs. These 7 versions of the model are identical except for the number of elements, and are compared under the same environmental conditions. Two current profiles were run in all tests. These are:

- Uniform current with velocity 0.7m/s.
- One year return period Ormen Lange current profile, with surface velocity 1.15m/s and velocity close to the sea bed 0.5m/s, illustrated in Figure 10.21.

The test set-up and the simulation results for the RIFLEX model are the same as in Section 10.3.4 and are used in the analysis to illustrate the anticipated correct solution.

Figure 10.27 shows the static riser configuration with the Ormen Lange current, but without TLP offsets for all CPMs. The models with 2, 4, and 5 elements are all seen to give rather rough estimates of the riser configuration. The 10 elements model give a good impression of the riser curve. For more elements, the deviation is even smaller. The same color code as in Figure 10.27 is used throughout this section, unless otherwise specified.

Only the dynamic results are included in this section. The quasi-static analysis can be found in Rustad Rustad (2007).

Dynamically moving TLP

The CPMs were exposed to harmonic TLP motions using the same setup as in Section 10.3.4. Figures 10.28 a) and b) show the payout versus time and TLP position, respectively, for TLP periods 60s and the Ormen Lange current profile. All CPMs are close to the RIFLEX solution at large offsets where the risers are straight. When the TLP is moving from right to left (see Figure10.24a)) the deflection is increasing, and also the payout. The two element model does not capture the large deflection, and their change in payout is only half as much as for the RIFLEX solution. The other few element CPMs ($N = \{4, 5\}$) capture the main deflection. The medium order CPMs ($N = \{8, 10\}$) follow the solution nicely, while the highest order CPMs ($N = \{16, 20\}$) are hardly seen as they are on the curve for the RIFLEX solution.

The payout in Figure 10.28 a) shows that the first mode corresponding to the TLP motion is dominating. The TLP motion and setdown is seen in Figure 10.29 as the bottom of the cylinder in the tension system (blue, thick line).

The riser tops are plotted in the same graph, such that the distance between them are the payouts. The second order riser mode shape is clearly seen in the riser tops and corresponds to the second order mode shape in Figure 10.24b) where the TLP moves from left to right. The payout error

$$|e_\xi| = |\xi_R - \xi_{N=i}|, \tag{10.124}$$

is plotted in Figure 10.30.

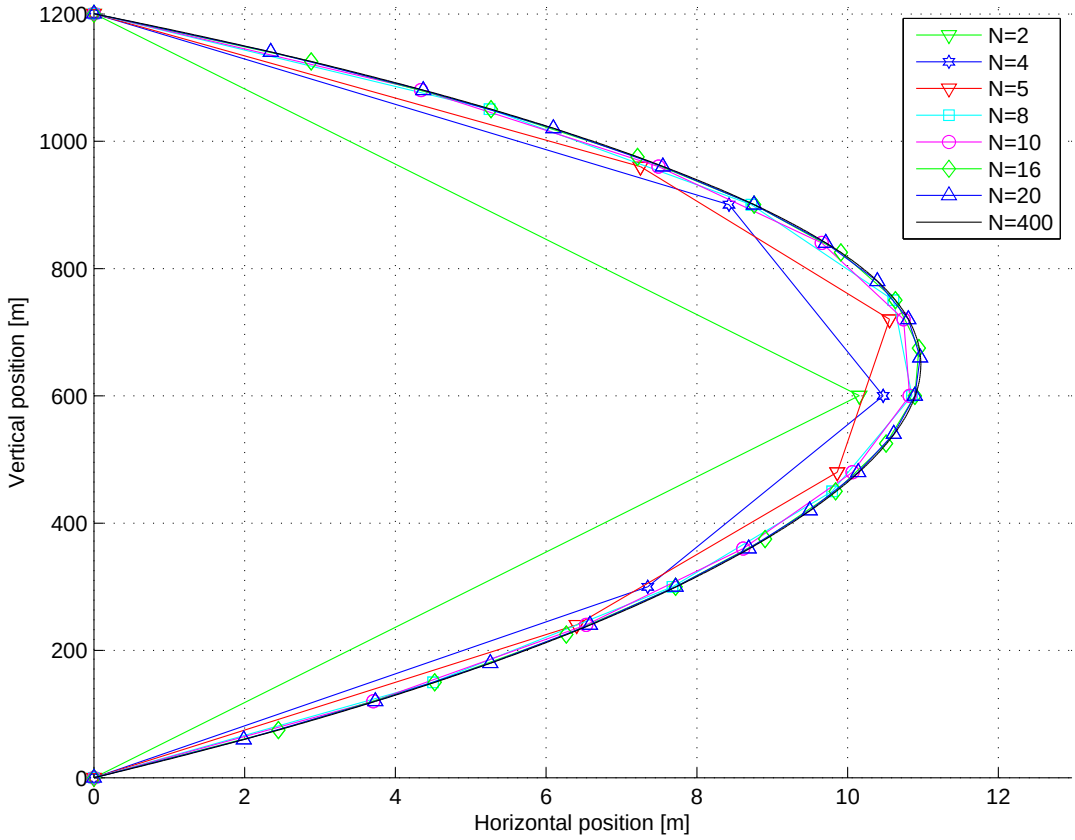

Figure 10.27: Riser configuration without TLP offset for an increasing number of elements exposed to the Ormen Lange design current.

For the low order CPMs, the first mode dominates. The error for $N = 2$ is up to 45% for the smallest TLP offset with the largest deflection. Such a large error on the first mode shape dominates the second mode shape seen in Figure 10.29. The error from first mode shape is also dominating for $N = \{4, 5\}$, with errors of approximately 20% and 15%, respectively. For the medium and high order CPMs, the total errors are less than 8% and 5%, respectively. The first mode shape errors are small such the second mode shape errors are observed. Note that these results presented here are those with largest relative error. At larger TLP periods, like 120s, the errors were smaller, especially for the low order models. At 300s, the risers were close to quasi-static and only the first mode shape was seen. Smaller current velocities gave also smaller errors.

Analysis of dynamic variation in top tension

Finally, the dynamical CPMs were analyzed with harmonically varying tension. The set-up was the same as for similar analysis in Section 10.3.4. The simulations shown here are with a tension period of 120s and a riser exposed to the Ormen Lange current. Figure 10.31 shows the top position as a function of time (a) and top tension (b). The top position versus top tension is seen to be a hysteresis function due to relative velocity and drag. Hence, a given tension does not

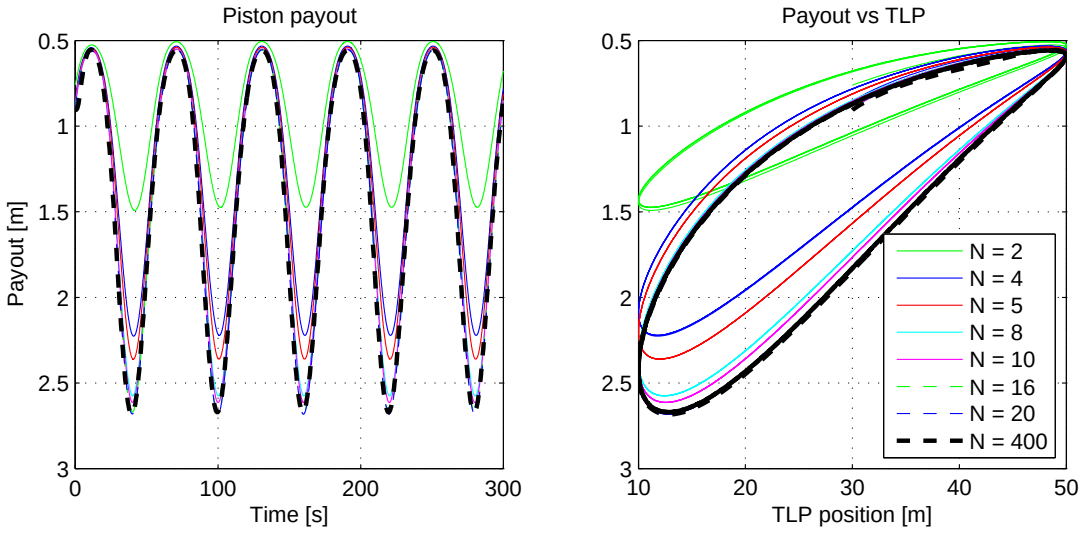

Figure 10.28: Payout as a function of time (a) and TLP offset(b) exposed to the Ormen Lange current.

correspond to one top position, but depends on whether the tension is increasing or decreasing as well. The deviations in top position between the models are largest for low tensions and low top positions. For higher tensions, the deviations are smaller. This is expected based on the results from the recent paragraphs. Figure 10.31 b) illustrates how an increasing number of elements result in a better match between the CPM model and RIFLEX.

Figure 10.32 shows the relative payout error. Maximum errors are seen for the low order CPMs, with approximately 0.22m for $N = 2$, and 0.09m for $N = 4$. For the medium and high order CPMs, the maximum error is $\pm$ 0.02m. A small second order nonlinearity and phase shifts are seen. This due to the nonlinear viscous forces, i.e. the drag forces and difference in relative velocity when the tension is decreased and increased.

Discussion of the control plant models

In Section 10.3.4, we verified the mathematical model. In this section, we investigated what happens if the number of elements is decreased. From a control point of view, the possibility of realtime operations are of great importance. We therefore seek the smallest and least complex model which still afford the desired level of accuracy for the current operation. The analysis in this section could be divided into three levels of accuracy. These correspond to the fast control plant model (FCPM), the accurate control plant model (ACPM) and the process plant model (PPM).

Recall that the size of the system matrices are $2(n+1) \times 2(n+1)$ giving $4(n+1)^2$ matrix elements, where n is the number of riser segments. Hence, doubling the number of riser nodes increases the number of matrix elements by a multiple of four. This slows down the computation speed considerably for the time consuming matrix operations and iterations. The low order CPMs, with $N = \{4, 5\}$, follow the main configuration. A small number of elements gives small system matrices. The matrix operations are fewer, which gives shorter simulation times. The main dynamic properties are still kept in this model. The medium order CPMs, with

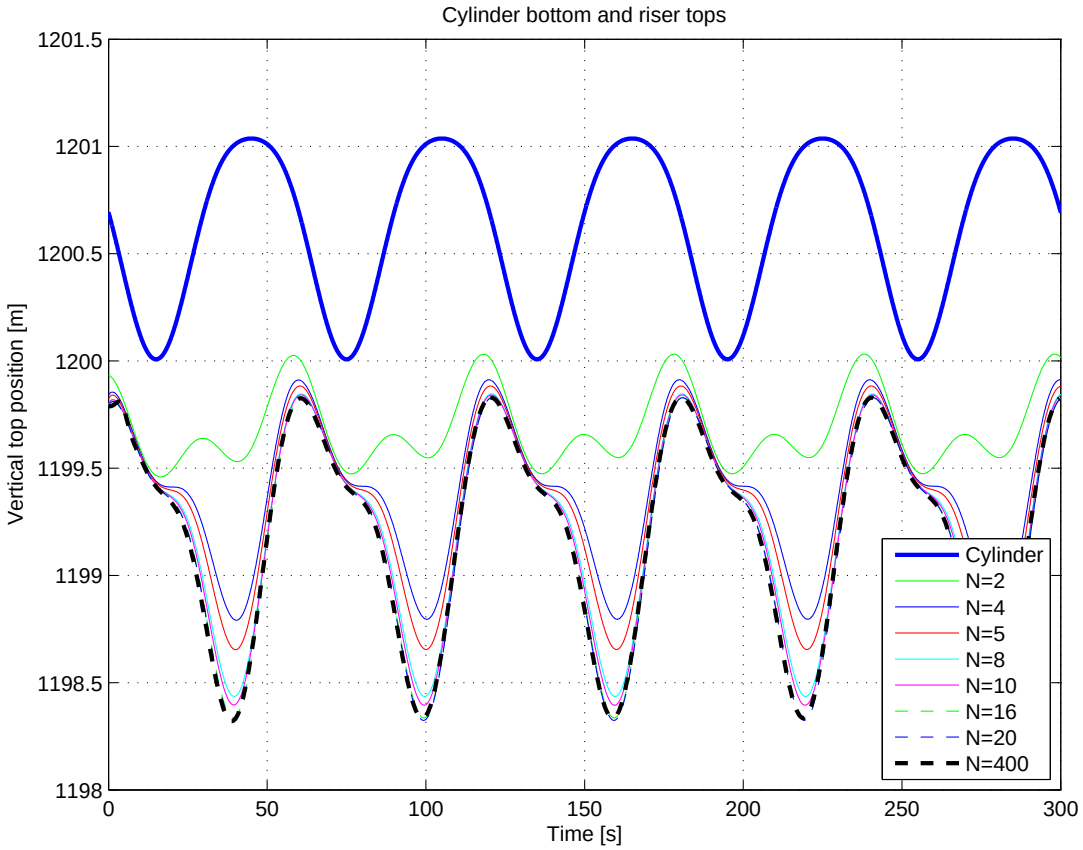

Figure 10.29: Cylinder bottom (blue line) and riser top positions for TLP motions and Ormen Lange current.

$N = \{8, 10\}$, have small quasi-static deviations, and follow the dynamics with errors less than 8%. The high order CPMs with $N = \{16, 20\}$, have very small static deviations and follow the dynamics of the specified motion of the TLP and tension with errors less than 5%. These results are categorized in Table 10.2.

The proposed limits and relative errors are based on the worst simulated case. For slower TLP dynamics and smaller current velocities, the results are better with smaller relative errors. Hence, the limit for the different model classifications could be set differently, such that the needed number of elements N are chosen to correspond to the physics of the environment.

Note that the number of elements for the FCPMs and ACPMs does not need to be a common multiple of the PPM, but can be chosen freely within the given limits. Increasing the number of elements gives a more accurate model at the expense of slower simulations due to larger system matrices.

10.3.6 Control System Design

In Chapter 1, the typical various levels of control used in marine control systems was addressed. The real-time control structure is suggested being divided into *low level actuator control*, *high*

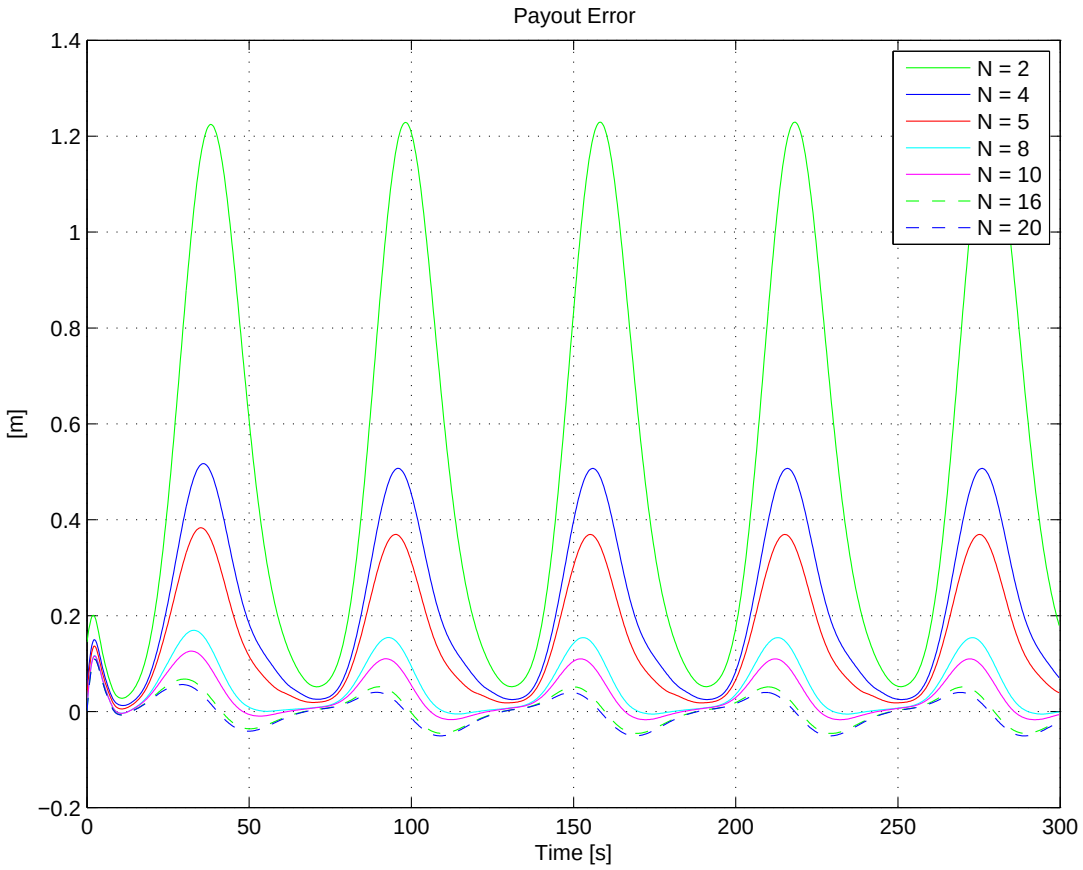

Figure 10.30: Relative payout error for harmonic TLP motions and Ormen Lange current.

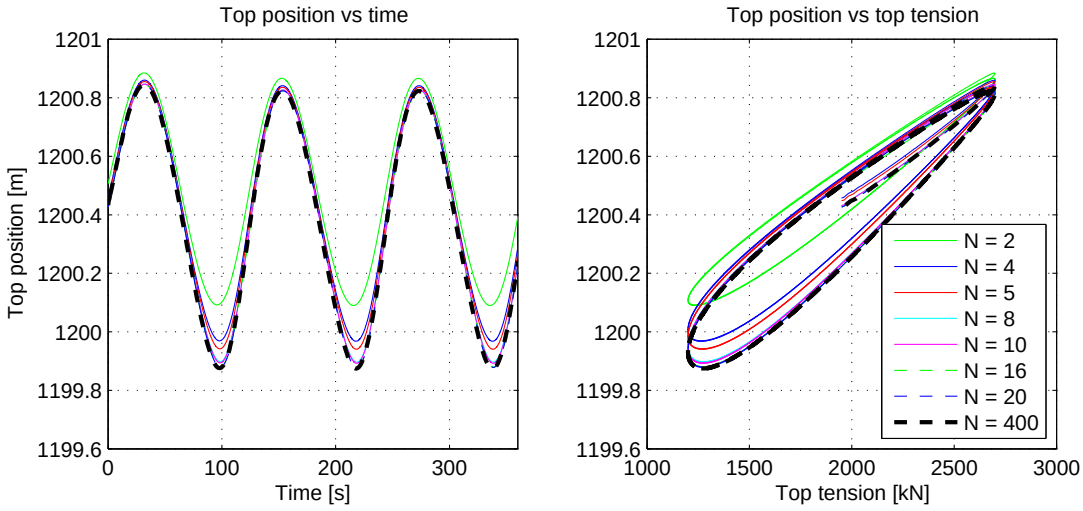

Figure 10.31: Riser tops as a function of time (a) and tension (b) exposed to the Ormen Lange current.

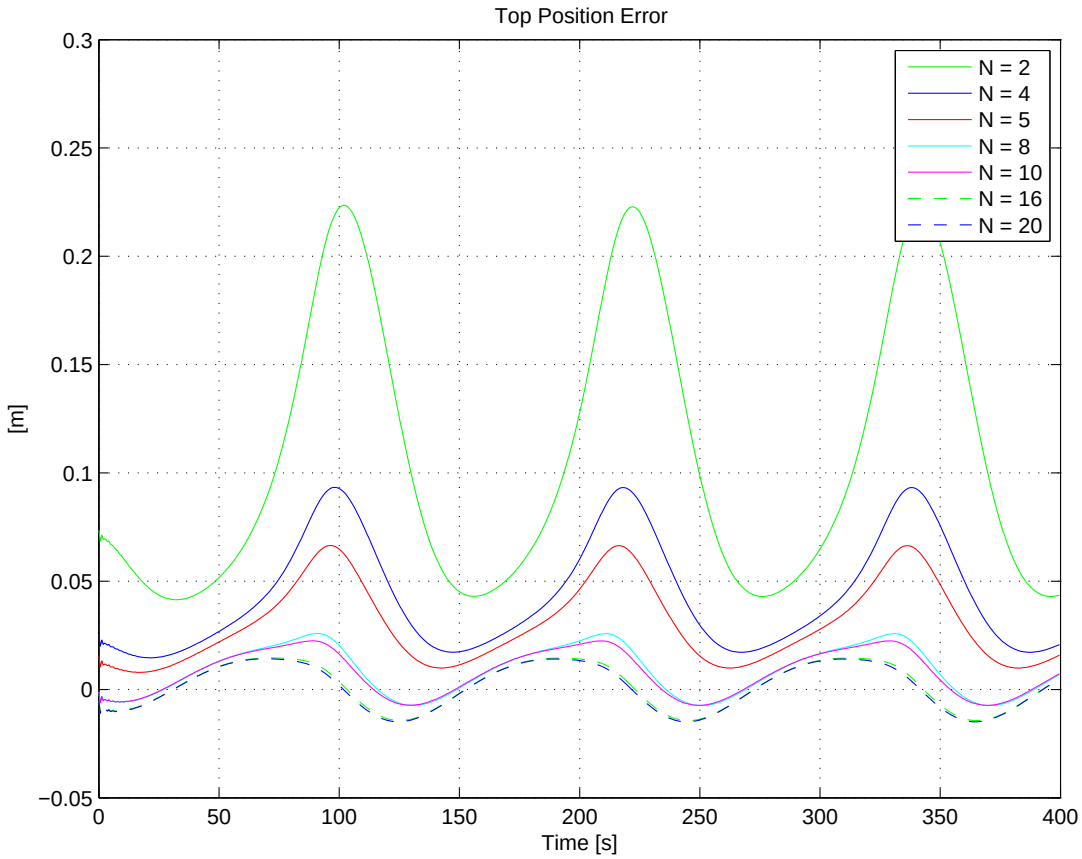

Figure 10.32: Relative payout error for a riser exposed to harmonic tension variations with periods 120s and the Ormen Lange current.

level plant control and *local optimization*. The first of these is the actual physical hardware system with local controllers, here represented by the *heave compensator* or *riser tensioner system*. The latter two are parts of the control system architecture or software solution. The local optimizer consists of a guidance block which decides the reference coordinates for the vertical top position for all risers. For each riser there is a reference block, calculating the feasible reference trajectory. The plant controller for each riser then calculates the necessary tension that the corresponding actuator will force on its riser system, according to the reference trajectory and the actual riser payout.

Controller objective

Today the top tension is kept close to constant by a passive heave compensation system for each riser

$$T_1 = T_2, \tag{10.125}$$

where T_j is the tension of riser $j = 1, 2$. Keeping the tensions constant and equal in both risers may lead to the following scenario: For the two risers in a tandem arrangement, R2 is in the wake of R1. Due to the shielding effects on R2, R1 will experience larger drag force than its

Type	N	QS error	Dyn error	Description
FCPM	4-6	5-10%	15-20%	Main physics used in control analysis
ACPM	8-12	2-5%	$< 8\%$	Good model for monitoring of the risers
PPM	≥ 15	$< 1\%$	$< 5\%$	High accuracy for the riser process model

Table 10.2: The categorized results of the CPM analysis.

downstream neighbor. If both risers have the same top tension, the deflection of R1 will exceed the deflection of R2, and the two risers may collide, shown in Figure 10.33 a).

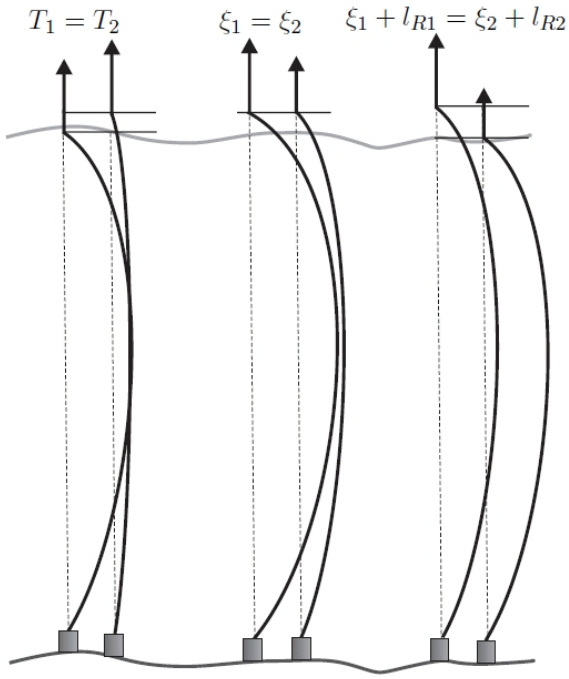

Figure 10.33: Effect of equal tension (a), equal payout (b), and equal effective length (c).

Another strategy is equal payout by connecting all risers to a common frame, proposed by Huse and Kleiven (2000), see Figure 10.33b). This will give varying top tension on the risers depending on the drag forces and the position in the riser array. Equal payout by adjusting the top tension through automatic control is studied in this work, with the control objective

$$\xi_1 = \xi_2, \tag{10.126}$$

where ξ_j is the payout of riser j. Further work proposed in Rustad (2007) has shown that due to this tension variation, two equal risers will experience different length due to axial strain

according to

$$\Delta l_R = \frac{\Delta T}{EA} l_{R0}, \quad \Delta T = T_1 - T_2, \tag{10.127}$$

where Δl_R is the length variation due to the difference in top tension ΔT of the two risers. l_{R0} is the untensioned initial riser length. Applying equal payout collision can still occur, but less frequent and in a smaller riser segment than for the equal tension strategy under the same environmental conditions. The risk of collision increases with increasing depth. In addition to the effect of axial strain increases for longer riser lengths and with larger tension variations.

We therefore propose a new control strategy letting the risers have equal effective length. By using automatic control of the heave compensators and top tension, the sum of payout and riser length should be equal such that the controller objective can be formulated as

$$\xi_1 + l_{R1} = \xi_2 + l_{R2}, \tag{10.128}$$

where l_{Rj} is the length of riser j. This means that in contrast to the strategy of equal payout we also compensate for the axial elasticity due to the tension variation, see Figure 10.33c). By introducing this way of controlling the top tension, the risers may be placed with closer spacing without increasing the risk of collision.

Equation (10.127) is a simplification valid for equal risers. For two or more risers with different characteristics with respect to diameter, riser material or filling, a more general expression is needed. The riser length can be formulated as

$$l_{Rj} = l_{Rj}\left(T_{0j}\right) + \Delta l_{Rj}, \quad \Delta l_{Rj} = \frac{T_j - T_{0j}}{EA} l_{R0}, \tag{10.129}$$

where $l_{Rj}\left(T_{0j}\right)$ is the initial length of riser j with the initial tension T_{0j}. Δl_{Rj} is the elongation of riser j relative to its initial tension. The riser material is assumed linear as long as the tension is much smaller than the yield stress. Hence, an increase ΔT in top tension will give the same increase for all elements along the riser, and (10.129) is a good estimate on the riser elongation due to tension. Equation (10.128) could be then be rewritten as

$$\xi_1 + l_{R1}\left(T_{0j}\right) + \Delta l_{R1} = \xi_2 + l_{R2}\left(T_{0j}\right) + \Delta l_{R2}. \tag{10.130}$$

The initial length and static payout can be found individually. However, note that the payouts need to have the same initial positions for the equation to be valid, otherwise this difference needs to be included in the equation.

To summarize, three different control objectives based on top measurements are proposed:

1. Equal tension: $T_1 = T_2$.
2. Equal payout: $\xi_1 = \xi_2$.
3. Equal effective length: $\xi_1 + l_{R1} = \xi_2 + l_{R2}$.

Guidance and reference model

The guidance block is used to calculate the reference trajectory or set point for payout for each riser tensioner system. If one risers position is used as a reference trajectory for the other in the two-riser-system, the length variation as given in (10.129) is compensated for with

$$\xi_{r,2} = \xi_1 + \Delta l_R, \tag{10.131}$$

where $\xi_{r,j}$ is the payout reference of riser j. The elongation term could be subtracted on both sides of (10.131) if ξ_2 is the reference. By this, the variation in riser length elongation is compensated for.

To provide high performance in tension control between various control modes and/or set-points, a reference model is introduced to calculate a feasible trajectory for the vertical position of the top node decided in the guidance block. The following third order filter is demonstrated appropriate

$$\ddot{\xi}_d + 2\zeta_d\omega_d\dot{\xi}_d + \omega_d^2\xi_d = \omega_d^2\xi_{ref} \tag{10.132}$$

$$\dot{\xi}_{ref} = -\frac{1}{t_d}\xi_{ref} + \frac{1}{t_d}\xi_r, \tag{10.133}$$

where ξ_d and its derivatives are the desired payout position, velocity and acceleration trajectories. ξ_r is the new reference coordinates in the same frame, and ξ_{ref} is the low pass filtered coordinate. ζ_d is the relative damping ratio, ω_d is natural frequency, and t_d is the cut-off period period of the low pass filter in (10.133). This provides a smooth transfer between different setpoints.

Plant controller

A PI-controller for each riser is introduced to adjust the top tension according to the reference trajectory and the actual position of the individual riser

$$\tau_{c,j} = -K_{P,j}e_j - K_{I,j}\int e_j dt \tag{10.134}$$

$$e_j = \xi_{d,j} - \xi_j \quad j = 1, 2, \tag{10.135}$$

where $K_{P,j}$ and $K_{I,j}$ are the positive control gains for riser j. The top tension in each riser is then the pretension, $T_{0,j}$, plus the contribution from the controller $\tau_{c,j}$

$$T_j = T_{0,j} + \tau_{c,j} \quad j = 1, 2. \tag{10.136}$$

10.3.7 Simulations

The riser model was verified with a variety of current profiles. However, in the simulations included in this section, a current profile with one year return period from the Ormen Lange field is used as a basis. In addition a variance in the current is made by filtering white noise through a low pass filter with a period of 100s, and an amplitude within the band of 5% of the current velocity in each node. The initial center-to-center distance between the risers is 15D in 1200m waters, and each riser model consists of 10 elements, unless otherwise specified. Some limitations and assumptions are made in relation to the shielding effect and the resulting current on R2 to keep the riser and current models valid.

- The current is coming from one direction only, such that the risers are always in a tandem position, with R2 in the wake of R1.
- Small TLP velocities such that the current is larger than the riser velocities and the relative velocity always positive, keeping R2 in the wake of R1.

The three different control objectives from Section 10.3.6 are tested and compared. The equal tension control objective is run with two different top tension levels and 0m or 30m offset. The equal payout and equal effective length control objectives are run with control of R2, using measurements from R1 as the reference. For the equal effective length control objective, control of R1 with the payout of R2 as a reference is also simulated.

Constant equal tension

In the first case, the top tension of the risers are constant and equal to a pretension. From (10.125) we have

$$T_1 = T_2 = T_{0,j}. \tag{10.137}$$

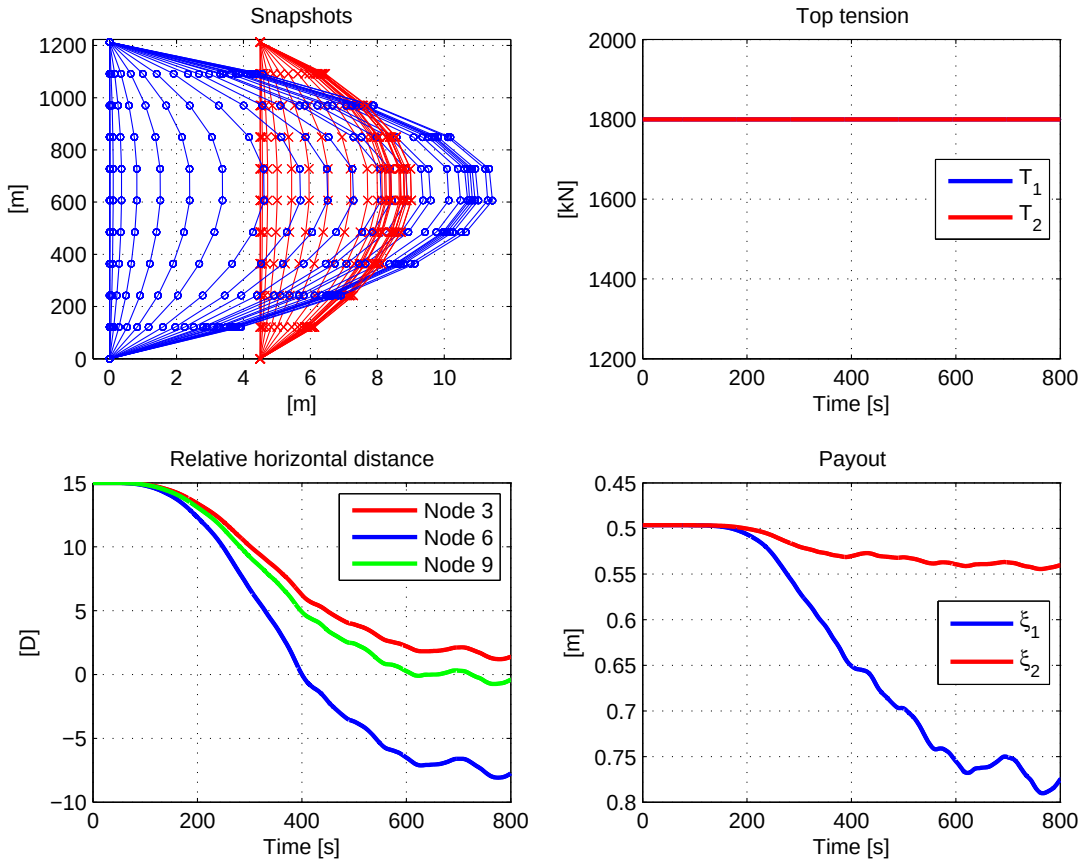

Figure 10.34: Incrementing current velocity from zero to the Ormen Lange design current. Snapshots of the riser configuration (top left), top tension (top right), relative horizontal distance (bottom left) and payout (bottom right).

A medium top tension of $T_{0,j} = 1800$kN is applied, and there is no TLP offset. The incoming current profile is increased as a second order low-pass filtered step from zero to the design current profile. As the current increases, the risers are seen to slide out to the right in Figure 10.34 (top left). The maximum horizontal deflection is seen at 600m above the seabed. Collision occurs along most of the riser (nodes 3 to 9), seen as relative horizontal distance smaller than

2D (bottom left). The payout of R1 is larger than for R2 due to the larger deflection (Figure 10.34, bottom right).

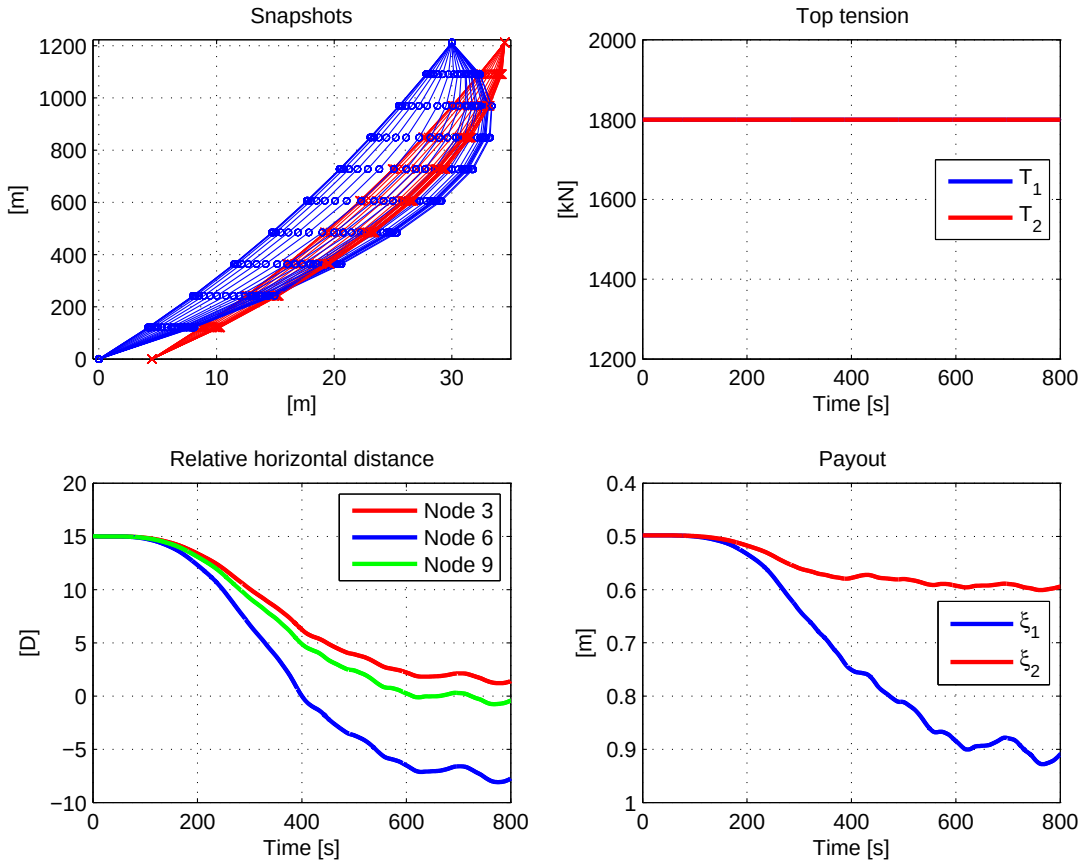

Figure 10.35: Incrementing current and 30m TLP offset. Snapshots of the riser configuration (top left), top tension (top right), relative horizontal distance (bottom left) and payout (bottom right).

The TLP is then put in an offset position of 30m, with increasing current, seen top left in Figure 10.35. The TLP is not very likely to have an offset in the opposite direction of the surface current, so offset is always simulated in the positive direction. Collision is seen to occur at the same nodes independent of the offset position. The relative horizontal distance between three selected nodes are shown in bottom left of Figure 10.35, where it is seen that collision occurs at the first node after approximately 400s. The corresponding payout due to deflection is seen bottom right in Figure 10.35. R1 has the largest deflection and hence setdown, which is clearly seen in the payout plot.

Increasing the top tension to the upper limit of $T_{0,j} = 2700kN$ and keeping the TLP in a no-offset position, no collision occurs at any nodes, seen in the snapshots (top left) and relative horizontal distance (bottom left) in Figure 10.36. Keeping the tension at the upper limit, collision could be avoided for these design currents. However, operation of the risers at this tension level is not desired due to increased stress in the riser and excessive wear of the tension system. The payouts (bottom right) are smaller than for the smaller top tensions.

For the rest of the simulations, the pretension is kept to $T_{0,j} = 1800kN$ for both risers. A

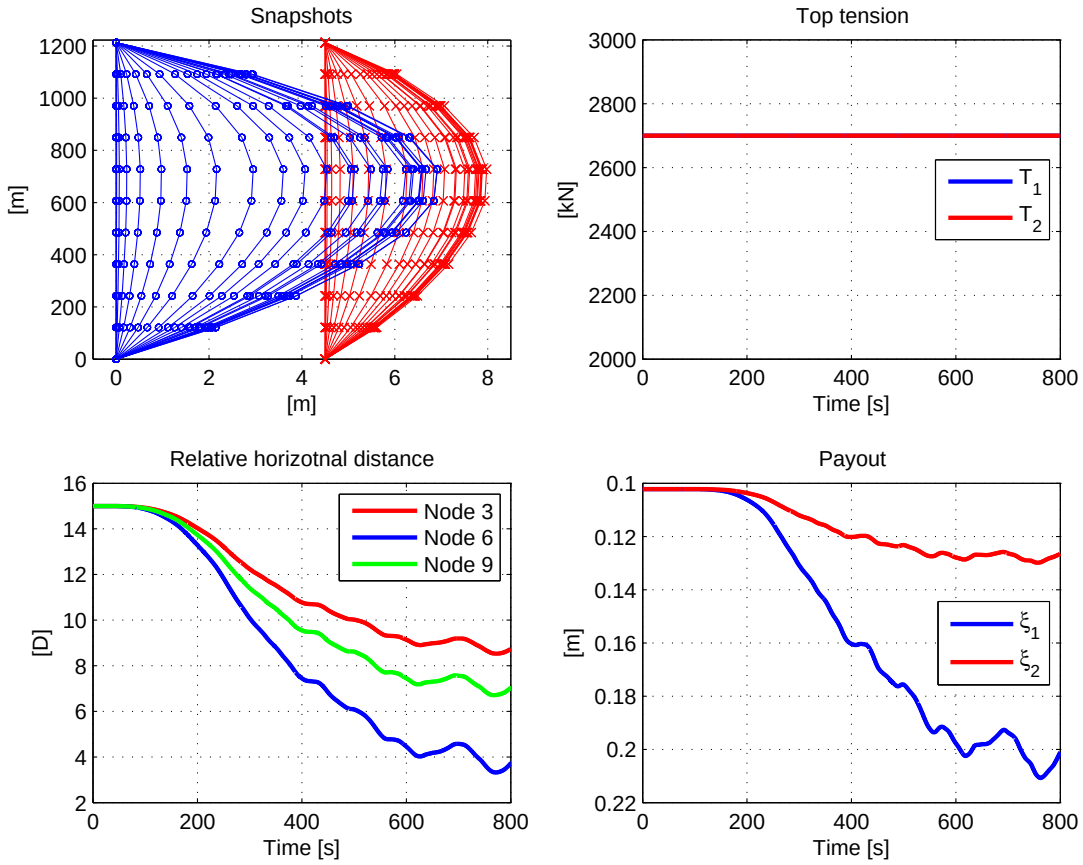

Figure 10.36: Incrementing current with top tension 2700kN. Snapshots of the riser configuration (top left), top tension (top right), relative horizontal distance (bottom left) and payout (bottom right).

fully developed current profile for the Ormen Lange field is used.

Equal payout

For the equal payout controller objective, the payout of all risers should be equal, see (10.126). Using the measured payout of R1 as a reference for R2, we have

$$\xi_{r,2}(t) = \xi_1(t). \tag{10.138}$$

Furthermore, a PI-controller for the top tension could be formulated from (10.134)-(10.136)

$$T_1 = T_{0,1}, \tag{10.139}$$
$$T_2 = T_{0,2} + \tau_{c,2}, \tag{10.140}$$
$$\tau_{c,2} = -K_{P,2}e_2 - K_{I,2}\int e_2 dt, \tag{10.141}$$
$$e_2 = \xi_{d,2} - \xi_2, \tag{10.142}$$

where $\xi_{d,2}$ is the guidance trajectory passed through the third order filter in (10.132)-(10.133). The results are found in Figure 10.37, with the top tension shown in the top right figure.

This control algorithm gives equal payout for the risers, seen bottom right in Figure 10.37. Top left shows how R2 slides out to the right due to decreased tension. However, collision still occurs, but in a smaller riser segment than with equal tension (nodes 5 and 6), also seen for the relative distance (bottom left). The collision is caused by the lower tension in R2 compared to R1, which in turn gives less axial elongation, and a shorter length of R2 than R1. Hence, due to the elasticity of steel, collision may still occur for long risers when using the equal payout control objective.

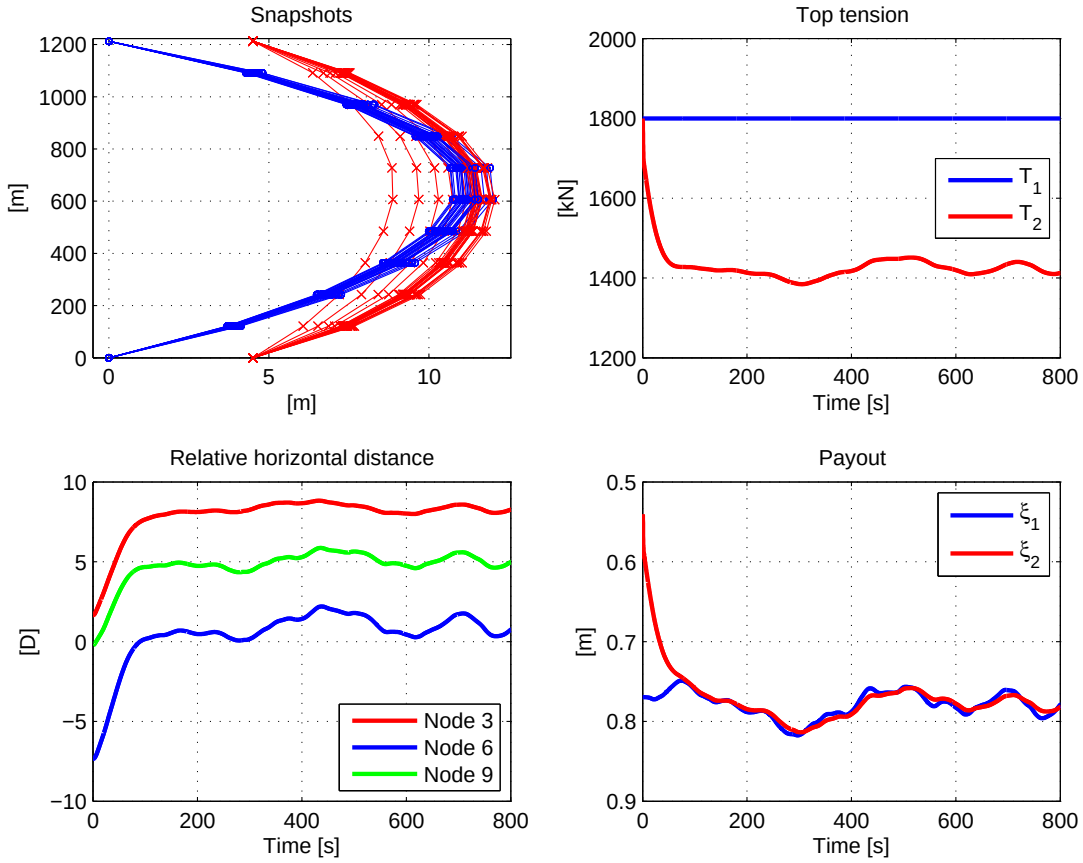

Figure 10.37: Equal payout algorithm and control of R2. Snapshots of the riser configuration (top left), top tension (top right), relative horizontal distance (bottom left) and payout (bottom right).

Equal effective length

In the next control objective, the elasticity of the riser material is included. This could be done by considering the riser length plus the payout. For equal risers with the same pretension, the guidance trajectory from (10.126), using (10.127) and (10.129) is simplified to

$$\xi_{r,2} = \xi_1 + \Delta l_R. \tag{10.143}$$

The controller is the same as for equal payout. The results are seen in Figure 10.38.

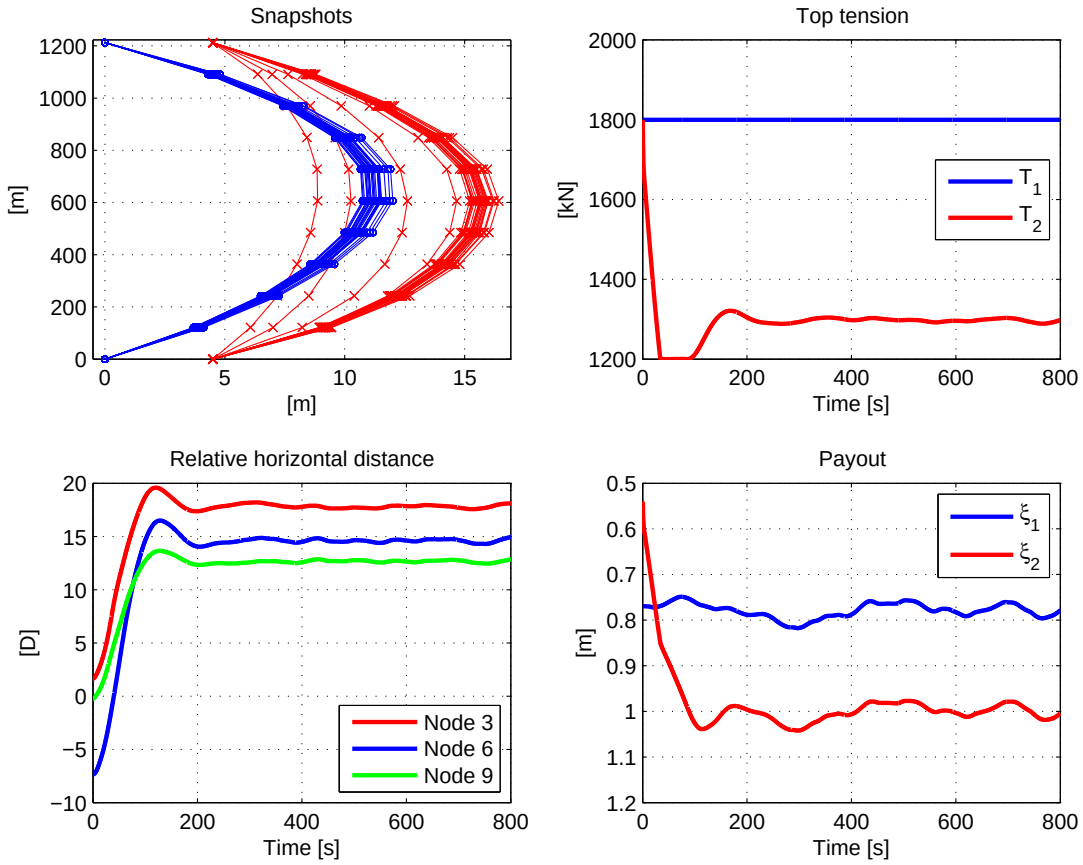

Figure 10.38: Equal effective length and control of R2. Snapshots of the riser configuration (top left), top tension (top right), relative horizontal distance (bottom left) and payout (bottom right).

The snapshots found top left show how the mid-position of R2 starts in front of R1 when the pretensions are equal. R2 then slides out to the right to avoid collision as the tension decreases, also seen in the relative horizontal distance to the lower left. The payout of R2 approaches the reference trajectory and both risers achieve similar deflection. The smaller variation in the horizontal position is due to variance in the current. To the bottom right in Figure 10.38 we clearly see that R2 has a larger payout to compensate for riser smaller elongation and achieves equal effective length.

The same algorithm is applied for 30m TLP offset (Figure 10.39). As before R2 slides out to the right with decreasing tension, increasing the horizontal distance between the risers to avoid collision, see Figure 10.39 top left. The payouts (bottom right) are larger in the offset case than without offset due to the effects from weight and current. The top tension T_2 is seen to stabilize about 1400kN for the offset case and 1300kN for the no-offset case, to the upper left in Figures 10.38 and 10.39, respectively. Hence, a smaller tension difference is needed in the offset position. This is due to a longer effective length (riser plus payout), and the relation between tension, payout and horizontal deflection. For a long riser with small tension, an increase in tension has larger effect on the lateral deflection than if the riser already has a high tension level.

Now the top tension of R1 is controlled using the payout of R2 as reference, compensated

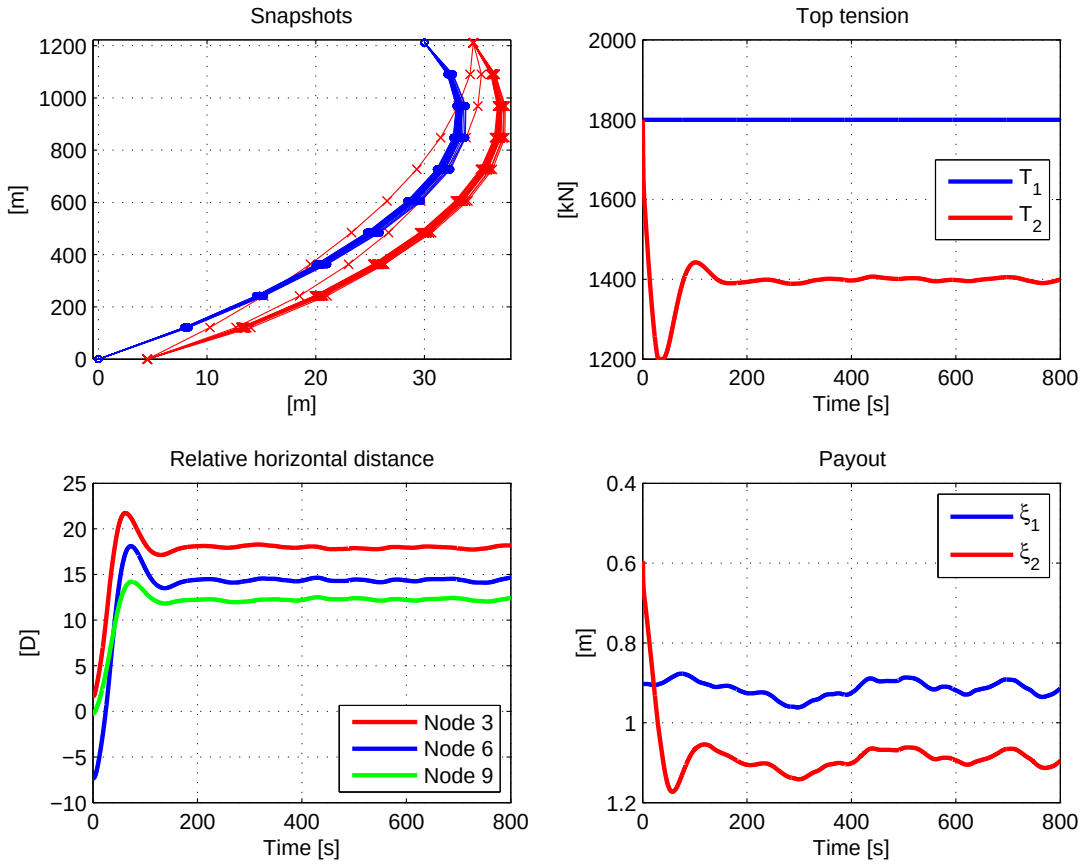

Figure 10.39: 30m TLP offset, equal effective length and control of R2. Snapshots of the riser configuration (top left), top tension (top right), relative horizontal distance (bottom left) and payout (bottom right).

for axial elasticity. R2 is not controlled. Hence,

$$\xi_{r,1} = \xi_2 - \Delta l_R, \tag{10.144}$$
$$T_1 = T_{0,1} + \tau_{c,1}, \tag{10.145}$$
$$T_2 = T_{0,2}, \tag{10.146}$$
$$e_1 = \xi_{d,1} - \xi_1. \tag{10.147}$$

The controller is the same as for Section 10.3.7.

Figure 10.40 shows the snapshots of the risers. As the tension in R1 increases and it is tightened up, the deflection decreases. In addition, R2 moves behind since R1 comes in front. This is due to the increased current and reduced shielding effect on R2 as the distance between the risers increases. It should be noted that the simulation is valid only when the downstream riser is more than 2D behind the upstream riser. The payouts, how the piston end of R1 is pulled in, and how the payout of R2 is slightly increased when the deflection increases, are seen (bottom right).

The TLP is placed at 30m offset. The risers behave similarly as for the case without offset, see snapshots and payouts in Figure 10.41. Top tension was seen to decrease compared to

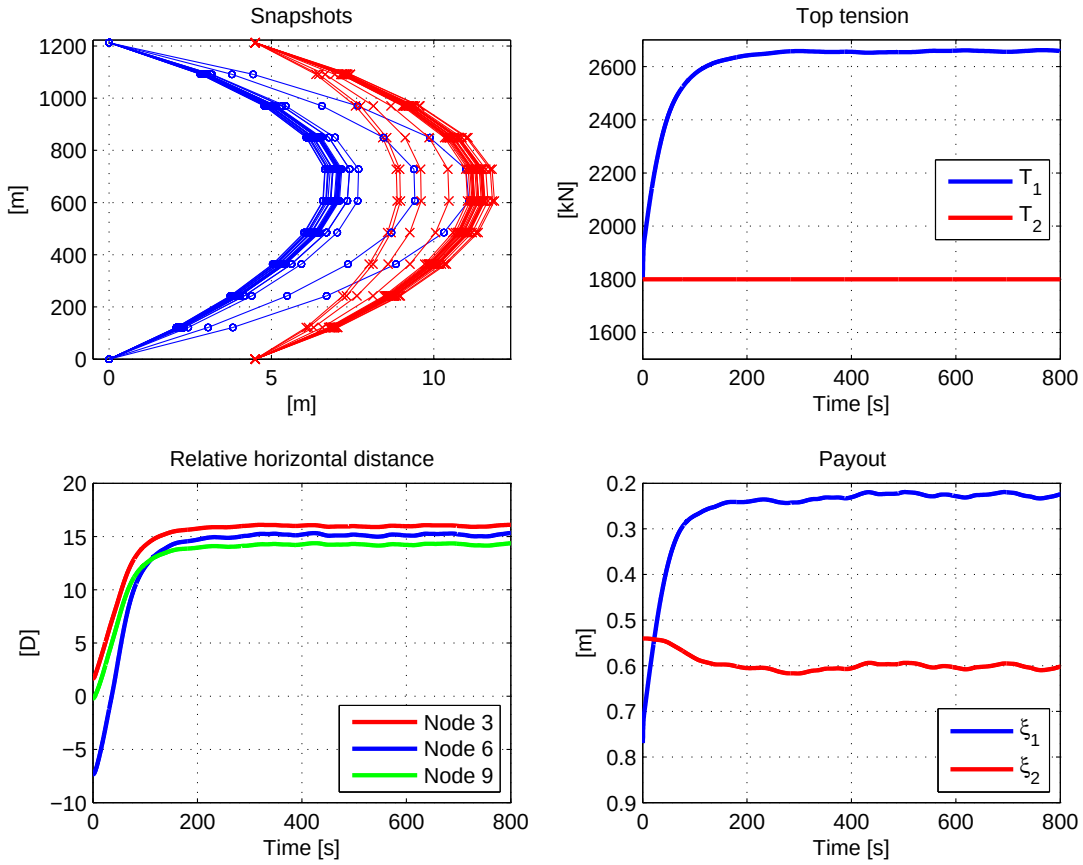

Figure 10.40: Equal effective length and control of R1. Snapshots of the riser configuration (top left), top tension (top right), relative horizontal distance (bottom left) and payout (bottom right).

the no-offset case and stabilize about 2650kN and 2400kN with tension differences of 850kN and 600kN, respectively shown in Figures 10.40 and 10.41. It should also be noted that the difference and payout is larger when controlling R1 than R2. This is caused by the more straightlined configuration at higher tension levels, and a need of even more tension to straighten up to prevent collisions, due to the nonlinear relationship (cf. $\frac{\Delta x}{\Delta T}$) between the tension and the deflection.

TLP dynamics

In this case the TLP moves with harmonic motions in surge direction about an offset of 30m. For the simulations with dynamic TLP motions, 1200m water depth is used. In this case, the TLP moves with harmonic motions in surge about a static offset of 30m. The period is 120s, and the peak-to-peak amplitude 40m.

The controllers are enabled after 400s. Figures 10.42 shows the horizontal positions for three selected nodes. It is seen in these plots, as expected, that the upper nodes are most influenced by the TLP motion. In this case where R2 is controlled, we see that the collision is avoided by increasing the horizontal position of R2. When R1 was controlled, the horizontal positions of

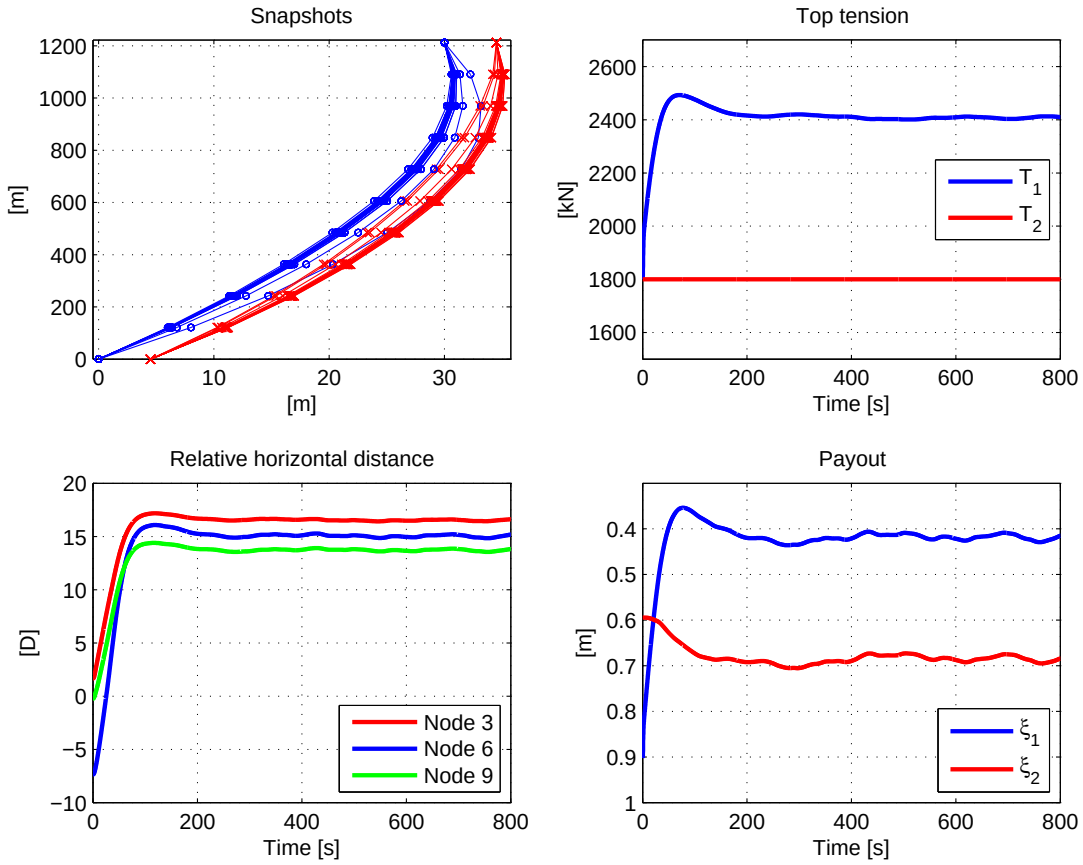

Figure 10.41: TLP offset of 30m, equal effective length and control of R1. Snapshots of the riser configuration (top left), top tension (top right), relative horizontal distance (bottom left) and payout (bottom right).

R1 decreased, and the horizontal positions for R2 increased at the same time due to reduced shielding, not shown here.

The riser slides out to the right when the payout ξ_2 increases, see Figure 10.43. The relative horizontal position between the same three nodes is seen in Figure 10.43 (bottom left). The effect of control is clearly seen. Before the controller is turned on, collision occurs twice for each cycle. After 400s, the controller is turned on, and the mean distance is about 15D, equal to the top and bottom distance, for all nodes, giving a similar configuration for the two risers. Also, the variation in distance between corresponding nodes decreases significantly. The payout with control of R1 and R2 are given in Figures 10.43 and 10.44, respectively. For the uncontrolled first 400s, the dynamic stroke of R1 is 1.6m and 0.8m for R2. This difference is caused by larger drag and deflection of R1. R2 has a more straightlined configuration due to reduced drag forces. Note that when R2 comes in front, the model is not valid and R2 keeps its straight configuration.

When R1 is the reference, the stroke of R2 is increased, and the stroke of R1 is slightly decreased, giving a dynamic stroke about 1.5m for both risers. The mean tension of R2 is decreased to about 1450kN, giving a tension difference of 350kN between the risers, see Figure 10.43. The smaller mean tension compared to the static case is due to longer payout and total effective length, such that a smaller tension difference is needed to avoid collision. The dynamic

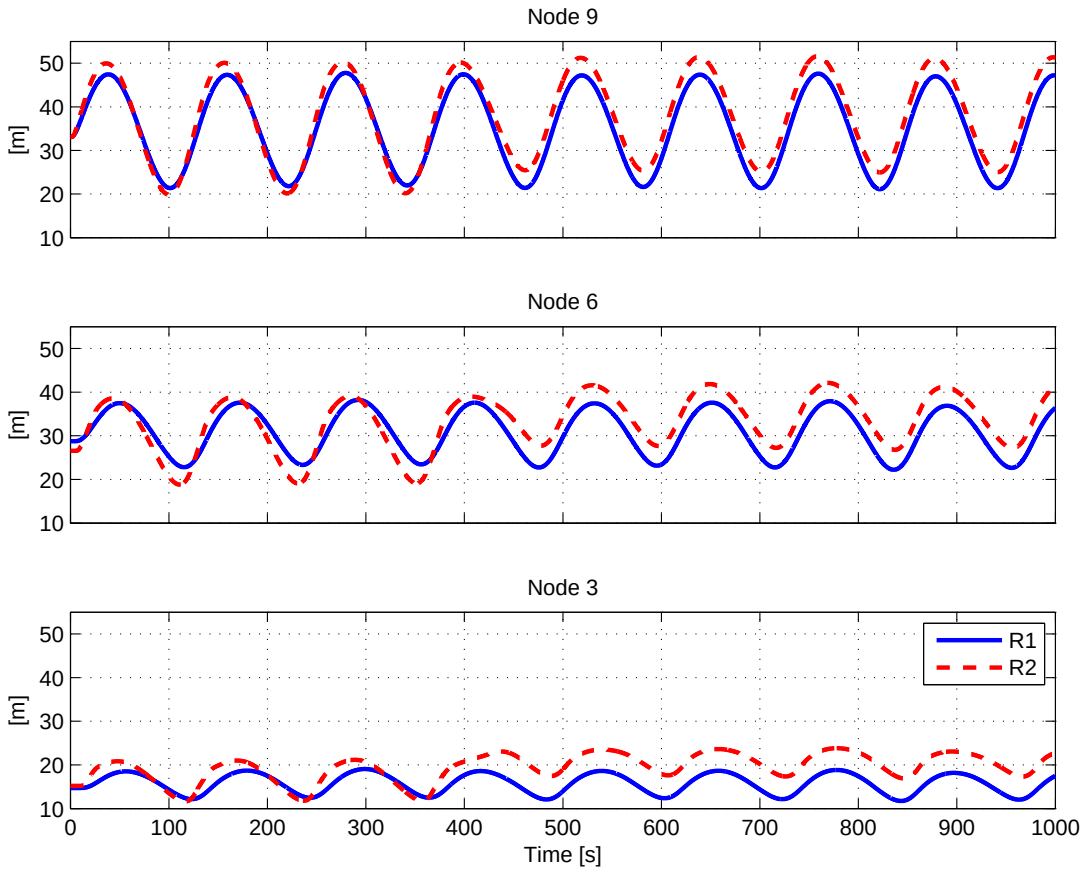

Figure 10.42: Dynamic TLP motions and control of R2 enabled after 400s. Horizontal positions for node 3, 6 and 9 for R1 and R2.

tension variation has a period of 120s as for the TLP motions, and a peak-to-peak amplitude about 120-140kN.

When R2 is the reference for R1, its dynamic stroke decreases, giving both R1 and R2 a dynamic stroke about 1m, see Figure 10.44. The mean tension level is increased with 400kN for T_1, seen in Figure 10.44. The dynamic tension variation was about 120-130kN. Increasing the TLP period to 300s, a more quasi-static riser behavior is seen with less dynamic deflection. This gives less need for stroke, a smaller payout and effective length and a larger tension difference closer to the static case.

10.3.8 Summary

In this section, controlling the top tension of risers to avoid collision is considered. The concept of tension legged platforms was introduced. A mathematical model of the system was made was proposed using the finite element method. Verification of the model was thereafter done with comparison to RIFLEX. The difference between a process plant model and the various control plant model was demonstrated. Three different control objectives was proposed and thereafter investigated in simulations. Automatic control of top tension to achieve equal effective length for two risers decreased the number of collision most efficiently, both in the static cases with

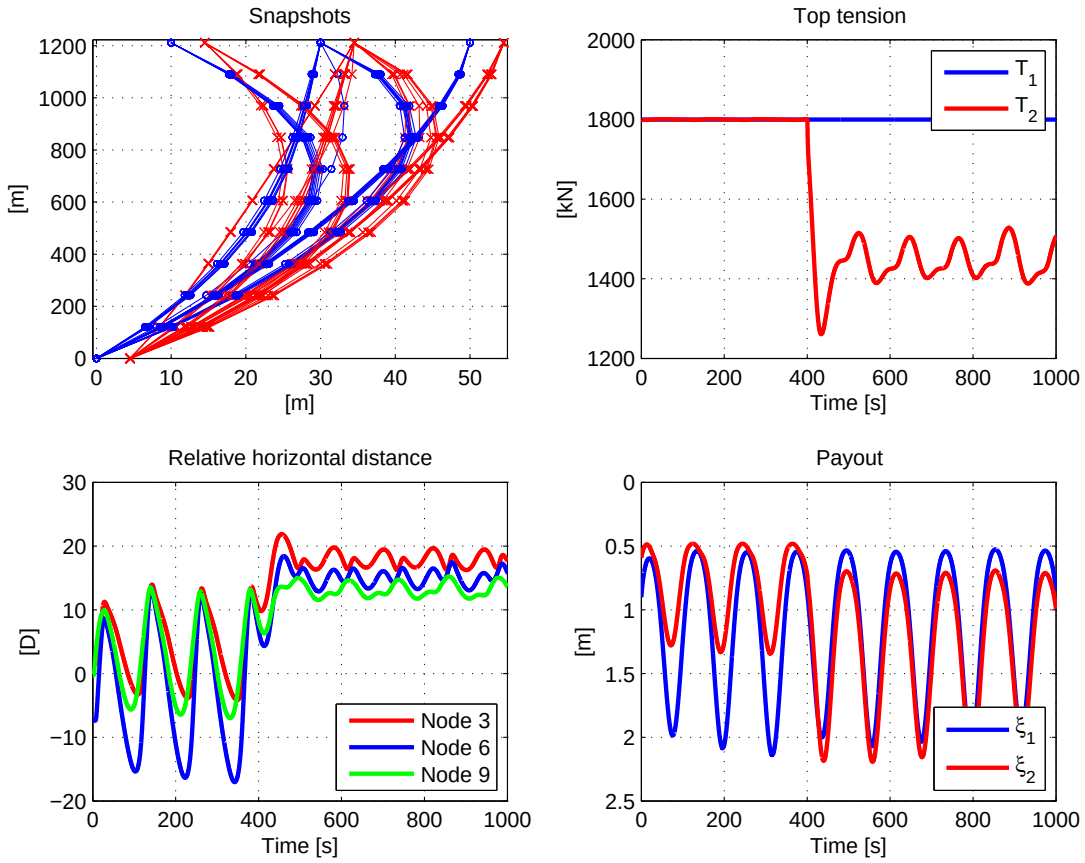

Figure 10.43: Dynamic TLP motions and control of R2 enabled after 400s. Snapshot of the riser configuration (top left), top tension (top right), relative horizontal distance (bottom left) and payout (bottom right).

and without offset, and in the cases with dynamic TLP motions.

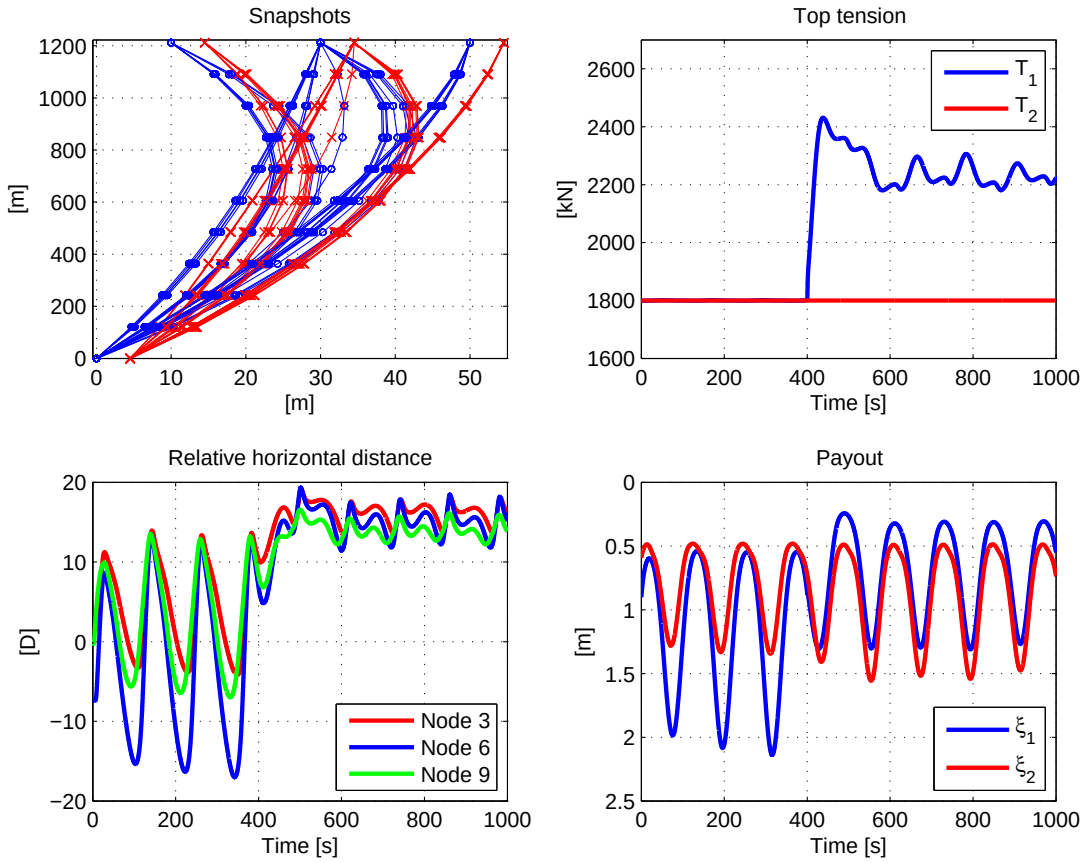

Figure 10.44: Dynamic TLP motions and control of R1 enabled after 400s. Snapshot of the riser configuration (top left), top tension (top right), relative horizontal distance (bottom left) and payout (bottom right).

10.4 Control of Drilling Riser Angles by Dynamic Positioning of Surface Vessels

10.4.1 Introduction

A dynamically positioned (DP) vessel maintains its position (fixed location or pre-determined track) exclusively by means of active thrusters. Position keeping means maintaining a desired position in the horizontal-plane within the normal excursions from the desired position and heading during the different environmental conditions.

The advantages of fully DP operated vessels are the ability to operate in deep-water, the flexibility to quickly establish position and leave location, and to start up in higher sea states than if a mooring system should be connected. In addition, there may be restrictions to deploy anchors due to already installed subsea structures on the seabed. Appropriate designed DP vessels, with high quality and capability on thruster/propulsion, power, control and instrumentation systems, are able to keep position and heading precisely and with satisfactory safety margin, even up to extreme weather conditions. For deep-water exploration and exploitation of hydrocarbons DP operated vessels may be the only feasibly solution.

However, drilling operations at water depths smaller than $200 - 300\ m$ have normally been done with moored semi-submersibles or fixed structures. Motivation for this has been the anticipation of lower investment costs and reduced operational risk compared to dynamic positioning. One reason for the skepticism to apply DP operated vessels for drilling at shallow water depth, especially performing in hot oil and gas wells, has been the risk for drive-off initiated damages of the well head, in worst case resulting in a open well. Drive-off is an uncontrolled excursion of the vessel, which may happen because of a failure in the DP system. The most limiting operational factor in drilling is the tolerance for riser angle deviation relatively to the well head and at the top joint. Ideally, the angle should be within $\pm\ 2°$. Deviations larger than $5° - 8°$ may be fatal. Hence, in case of a drive-off the available time windows to decide and execute a controlled disconnect becomes more limited at shallow water compared to deep-water. On the other hand, more complex riser dynamics is appearing for increasing water depth. A further step in ensuring a safe and high performance DP operation is to actively take the riser angle offsets and bending stresses into account in the DP control strategy.

Here the model-based DP controller presented Sørensen et al. (2001) accounting for riser angle offsets in 3 dimensions is shown. Numerical simulations with a drilling semi-submersible are carried out to demonstrate the performance of the proposed controller.

10.4.2 Mathematical Modeling

Vessel motions

Kinematics The different reference frames used are as presented in Section 6 and illustrated in Figure 10.45.

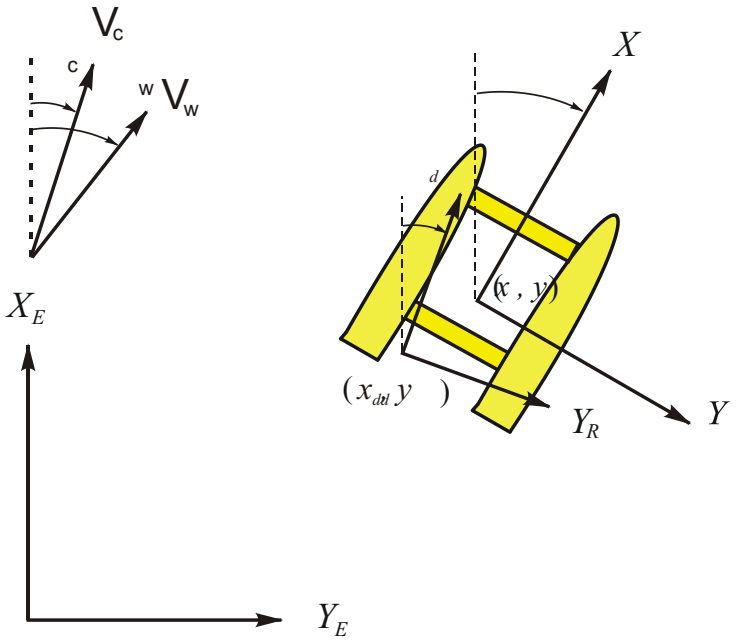

Figure 10.45: Vessel reference frames.

- The Earth-fixed reference frame is denoted as the $X_E Y_E Z_E$-frame. Measurements of the

vessel's position and orientation coordinates are done in this frame relatively to a defined origin.

- The reference-parallel $X_R Y_R Z_R$-frame is also Earth-fixed but rotated to the desired heading angle ψ_d. The origin is translated to the desired x_d and y_d position coordinates.
- The body-fixed XYZ-frame is fixed to the vessel body with the x-axis positive forwards, y-axis positive to the starboard and z-axis positive downwards.

The rotation matrix $\mathbf{J}$ gives the linear and angular velocity of the vessel in the body-fixed frame relative to the Earth-fixed frame

$$\dot{\eta} = \begin{bmatrix} \dot{\eta}_1 \\ \dot{\eta}_2 \end{bmatrix} = \begin{bmatrix} \mathbf{J}_1(\eta_2) & \mathbf{0}_{3\times 3} \\ \mathbf{0}_{3\times 3} & \mathbf{J}_2(\eta_2) \end{bmatrix} \begin{bmatrix} \nu_1 \\ \nu_2 \end{bmatrix} = \mathbf{J}(\eta_2)\,\nu. \tag{10.148}$$

The vectors defining the Earth-fixed vessel position and orientation, and the body-fixed translation and rotation velocities are given by

$$\eta_1 = [x \quad y \quad z]^T, \tag{10.149a}$$
$$\eta_2 = [\phi \quad \theta \quad \psi]^T, \tag{10.149b}$$
$$\nu_1 = [u \quad v \quad w]^T, \tag{10.149c}$$
$$\nu_2 = [p \quad q \quad r]^T. \tag{10.149d}$$

Nonlinear low-frequency vessel model The nonlinear six degrees of freedom (DOFs) body-fixed coupled equations of the low-frequency (LF) motions in surge, sway, heave, roll, pitch and yaw are written (Section 6.4)

$$\mathbf{M}\dot{\nu} + \mathbf{C}_{RB}(\nu)\nu + \mathbf{C}_A(\nu_r)\nu_r + \mathbf{D}_{NL}(\nu_r,\gamma_r)\nu_r + \mathbf{D}\nu + \mathbf{G}(\eta)\eta = \tau_{wind} + \tau_{wave2} + \tau_{thr}. \tag{10.150}$$

The effect of current is included in the relative velocity vector according to

$$\nu_r = [u - u_c \quad v - v_c \quad w \quad p \quad q \quad r]^T. \tag{10.151}$$

The current components are defined as

$$u_c = V_c \cos(\beta_c - \psi), \tag{10.152}$$
$$v_c = V_c \sin(\beta_c - \psi), \tag{10.153}$$

where V_c and β_c are the surface current velocity and direction respectively, see Figure 10.45. $\mathbf{C}_{RB}(\nu)$ and $\mathbf{C}_A(\nu_r)$ are the skew-symmetric Coriolis and centripetal matrices of the rigid body and potential induced added mass part of the current load. $\mathbf{D}_{NL}(\nu_r, \gamma_r)$ is the 6-dimensional nonlinear damping vector. The relative drag angle is found from the following relation $\gamma_r = a\tan(v_r, u_r)$. $\mathbf{M}$ is the 6×6 dimensional system inertial matrix including asymptotic added mass values for $\omega \to 0$, where ω is the wave frequency. $\mathbf{D}$ is the 6×6 dimensional strictly positive linear damping matrix caused by linear wave drift damping and laminar skin friction. $\mathbf{G}$ is the 6×6 dimensional generalized restoring coefficient matrix caused by buoyancy and gravitation. τ_{thr} is the 6-dimensional control vector consisting of forces and moments produced by the thruster system. τ_{wind} and τ_{wave2} are the 6-dimensional wind and second order wave load vectors.

Linear wave-frequency model The coupled equations of wave-frequency (WF) motions in surge, sway, heave, roll, pitch and yaw are assumed to be linear, and can in the reference-parallel frame be formulated as (Section 6.4)

$$\mathbf{M}(\omega)\dot{\nu}_w + \mathbf{D}_p(\omega)\nu_w + \mathbf{G}\eta_w = \tau_{wave1}. \tag{10.154}$$

Assuming small roll and pitch motions the Earth-fixed motion vector can be found by

$$\dot{\eta}_w = \mathbf{J}(\psi_d)\nu_w. \tag{10.155}$$

The 6-dimenaional WF motion vector is defined as:

$$\eta_w = \begin{bmatrix} \eta_{w1} & \eta_{w2} & \eta_{w3} & \eta_{w4} & \eta_{w5} & \eta_{w6} \end{bmatrix}^T. \tag{10.156}$$

τ_{wave1} is the 6-dimensional excitation vector, which will be modified for varying vessel heading relative to the incident wave direction. $\mathbf{M}(\omega)$ is the 6×6 wave-frequency system inertia matrix containing frequency dependent added mass coefficients in addition to the vessel mass and moment of inertia. $\mathbf{D}_p(\omega)$ is the 6×6 wave radiation (potential) damping matrix. $\mathbf{G}$ is the 6×6 linearized restoring coefficient matrix.

Drilling riser mechanics

Basic concepts A drilling riser behaves like a tensioned beam. The steel pipe provides some bending stiffness, but it is the geometric stiffness due to the effective tension distribution along the riser that gives the main contribution to lateral resistance against static and dynamic forces acting perpendicular to the beam axis. A key feature of a drilling riser is that the top end tension is kept close to constant under influence from floater motions by a heave compensating system at the upper end. The top tension must be sufficiently high to prevent the riser from global buckling, meaning that the effective tension must have a positive value at the lower end of the riser.

Some basic features of riser mechanics can for the 2-dimensional static case be illustrated with reference to Figure 10.46. The riser is seen to have an offset position of the upper end relative to the lower end. The angles between the riser and a vertical line at the top and bottom are denoted α_t and α_b, respectively. These angles are influenced by the tension at the riser ends, the offset and the current forces. Since both ends of a drilling riser are moment free, one can easily establish an equation that links most of these parameters

$$T_t \sin\alpha_t + T_b \sin\alpha_b = \int_b^t f_c(s)\cos\alpha(s)\, ds, \tag{10.157}$$

where $f_c(s)$ is the current force per unit length for a given position along the riser, and $\alpha(s)$ is the angle of the riser at the same position.

A successful drilling operation requires that both upper and lower riser angles are within certain limits. This can in principle be achieved by proper selection of the top tension and the vessel offset, where the latter is controlled by the dynamic positioning system. However, the top tension can for a given installation not exceed a predefined maximum level, meaning that successful angle control may become impossible under some current conditions. The objective of the dynamic position system is hence to keep the riser angles within the required limits for

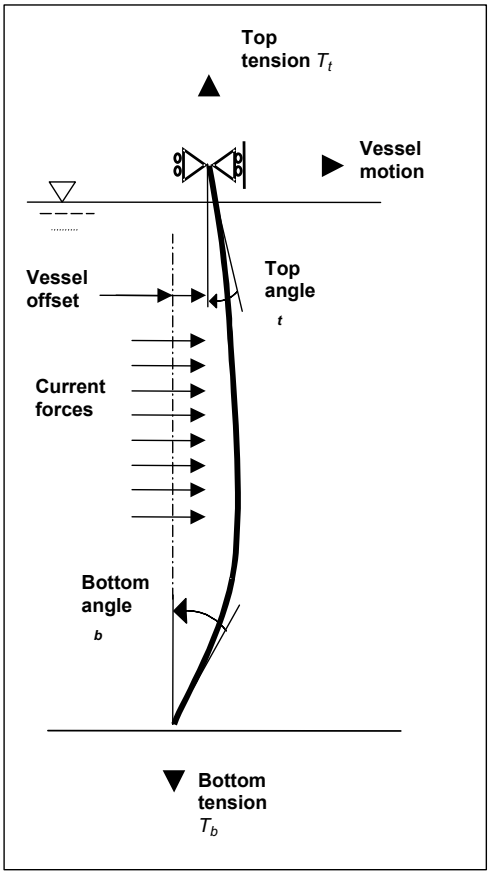

Figure 10.46: Riser mechanics.

drilling operations for the longest possible period of time by proper selection of the desired vessel position coordinates.

Compared to the 2-dimensional case, the 3-dimensional case is somewhat more complicated, and is illustrated in Figure 10.47. The current direction may vary through the water column, meaning that riser deflections will not take place in one well-defined plane. Rotation at riser ends must hence be defined by the direction of the inclination (β_b and β_t on Figure 10.47) and its magnitude (α_b and α_t on Figure 10.47).

Finite element modeling For the purpose of computing stresses in the riser, a quite refined Finite Element Model (FEM) is generally required. However, for the purpose of calculating top and bottom riser angles a less detailed model is necessary. A convergence study has indicated that 10 elements predicts the angles within a few percent of those obtained by application of several hundreds of elements, even for risers at water depths of 1000 m.

Accordingly, we presently apply a model as illustrated by Figure 10.48 with 10 elements. In reality, the model is 3-dimensional while only a 2-dimensional projection is shown in the figure. The local x-axis for each element passes through the two nodal points by which the element is defined. For each element a stiffness matrix is defined based on the local coordinate system. This stiffness matrix consists of two parts. The first part represents the elastic stiffness, $\mathbf{k}_{El}$, and the second represents the so-called geometric stiffness, $\mathbf{k}_G$. The latter is subsequently multiplied by

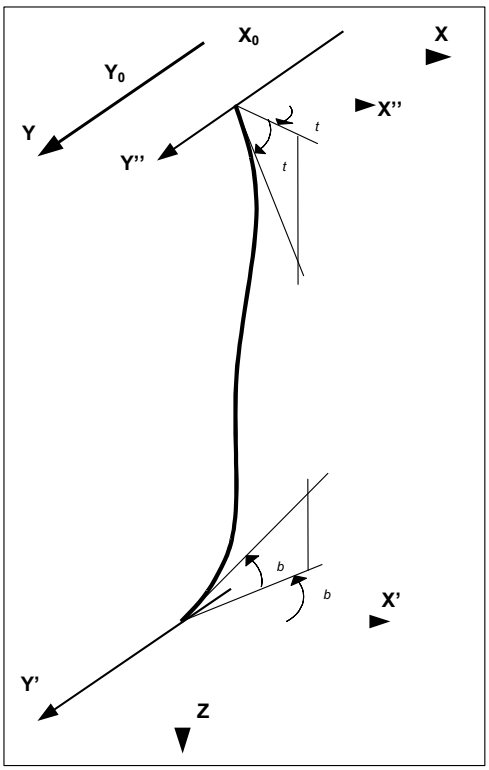

Figure 10.47: Riser kinematics.

the effective tension in the riser which acts at each particular element, P_i, where the subscript i denotes element number i. The resulting total stiffness matrix becomes for element i

$$\mathbf{k}_i = [\mathbf{k}_{EI} + P_i \mathbf{k}_G]_i \,. \tag{10.158}$$

The 6 kinematic components (i.e. 3 displacements and 3 rotations) at each end of the local elements (i.e. a total of 12 components for each element) are referred to the local coordinate system. All the 12 kinematic components for each element (number i) are collected in a vector $\mathbf{v}_i$. The elastic stiffness matrix is here expressed on the form

$$\mathbf{k}_{EI} = EI \begin{bmatrix} \frac{12}{l^3} & 0 & \frac{6}{l^2} & 0 & -\frac{12}{l^3} & 0 & \frac{6}{l^2} & 0 \\ 0 & \frac{12}{l^3} & 0 & -\frac{6}{l^2} & 0 & -\frac{12}{l^3} & 0 & -\frac{6}{l^2} \\ \frac{6}{l^2} & 0 & \frac{4}{l} & 0 & \frac{6}{l^2} & 0 & \frac{2}{l} & 0 \\ 0 & -\frac{6}{l^2} & 0 & \frac{4}{l} & 0 & \frac{6}{l^2} & 0 & \frac{2}{l} \\ -\frac{12}{l^3} & 0 & \frac{6}{l^2} & 0 & \frac{12}{l^3} & 0 & -\frac{6}{l^2} & 0 \\ 0 & -\frac{12}{l^3} & 0 & \frac{6}{l^2} & 0 & \frac{12}{l^2} & 0 & \frac{6}{l^2} \\ \frac{6}{l^2} & 0 & \frac{2}{l} & 0 & -\frac{6}{l^2} & 0 & \frac{4}{l} & 0 \\ 0 & -\frac{6}{l^2} & 0 & \frac{2}{l} & 0 & \frac{6}{l^2} & 0 & \frac{4}{l} \end{bmatrix}, \tag{10.159}$$

where E is the modulus of elasticity (Young's modulus), I is the moment of inertia (EI will then be the bending stiffness), and l is the length of each element. One should notice that (10.159) is only of dimension 8×8, and not of dimension 12×12 as explained above. This is due to the disregard of vertical displacements at the local nodes 1 and 2 of each element, and the same

applies to the rotation about the beam axis (torsion). The reason for this simplification is that these DOFs are not required for the studied case. Accordingly, a total of 4 DOFs are removed for each element, which reduces the total number from 12 to 8. The 8×8 geometric stiffness matrix is correspondingly expressed as

$$P_i \mathbf{k}_G = \frac{P_i}{30l} \begin{bmatrix} 36 & 0 & 3l & 0 & -36 & 0 & 3l & 0 \\ 0 & 36 & 0 & -3l & 0 & -36 & 0 & -3l \\ 3l & 0 & 4l^2 & 0 & -3l & 0 & -l^2 & 0 \\ 0 & -3l & 0 & 4l^2 & 0 & 3l & 0 & -l^2 \\ -36 & 0 & -3l & 0 & 36 & 0 & -3l & 0 \\ 0 & -36 & 0 & 3l & 0 & 36 & 0 & 3l \\ 3l & 0 & -l^2 & 0 & -3l & 0 & 4l^2 & 0 \\ 0 & -3l & 0 & -l^2 & 0 & 3l & 0 & 4l^2 \end{bmatrix} \tag{10.160}$$

The kinematic components entering the assembled dynamic equilibrium equation for the whole riser are referred to the global coordinate system (designated by XYZ in Figure 10.48. A transformation matrix $\mathbf{T}_i$ is accordingly introduced for each element. The corresponding kinematic components in the global system are for element number i expressed as

$$\mathbf{r}_i = \mathbf{T}_i \mathbf{v}_i. \tag{10.161}$$

These sub-vectors are finally assembled into a total riser displacement vector (containing both displacements and rotations), designated by $\mathbf{r}$. Note that the dimension of this vector is 4 times the number of nodes, rather than the number of elements. This is due to neighboring elements sharing common nodes.

Subsequently, a transformation of each element stiffness matrix from the local to the global XYZ-frame is performed by application of the transformation matrix $\mathbf{T}_i$ in (10.161) above. The corresponding element stiffness matrix for element number i in the global system is then expressed by a congruence transformation as

$$\mathbf{K}_i = \mathbf{T}_i^T \mathbf{k}_i \mathbf{T}_i, \tag{10.162}$$

$$= \begin{bmatrix} \mathbf{K}_{11}^i & \mathbf{K}_{12}^i \\ \mathbf{K}_{21}^i & \mathbf{K}_{22}^i \end{bmatrix}. \tag{10.163}$$

All the element matrices referred to the global coordinate frame are subsequently assembled to form the system stiffness matrix, $\mathbf{K}$. As explained below, this matrix depends on the positions of all the nodes. A more explicit expression for the system matrix is obtained by introducing the following notation, $\mathbf{K}_{jk}^i$, which designates sub-matrix jk for element number i. For each element, j and k run from 1 to 2 and refer to the local nodes of the elements. Hence, there are 4 such sub-matrices: $\mathbf{K}_{11}^i, \mathbf{K}_{12}^i, \mathbf{K}_{21}^i$ and $\mathbf{K}_{22}^i$ which are all of dimension 6×6, or more correctly here for the present modeling, 4×4. The first of these sub-matrices represents the stiffness terms for local node number 1 containing coupling terms between the 4 DOFs. The last sub-matrix represents the stiffness terms for the local node number 2. The two remaining sub-matrices $\mathbf{K}_{12}^i$ and $\mathbf{K}_{21}^i$ correspond to the stiffness coupling terms between the two local nodes. The global

system stiffness matrix will then take the form

$$\mathbf{K} = \begin{bmatrix} \mathbf{K}_{11}^1 & \mathbf{K}_{12}^1 & & & & \\ \mathbf{K}_{21}^1 & \mathbf{K}_{22}^1 + \mathbf{K}_{11}^2 & \mathbf{K}_{12}^2 & & & \\ & \mathbf{K}_{21}^2 & \mathbf{K}_{22}^2 + \mathbf{K}_{11}^3 & \cdots & & \\ \vdots & & & & & \\ & & & & \mathbf{K}_{22}^{N-1} + \mathbf{K}_{11}^N & \mathbf{K}_{12}^N \\ & & & & \mathbf{K}_{21}^N & \mathbf{K}_{22}^N \end{bmatrix}. \tag{10.164}$$

If we assume that node number 1 is located at the top of the riser, the two first DOFs correspond to the horizontal displacements of the surface floater ($x-$ and $y-$ coordinates in the global system). Furthermore, these correspond to the first two columns and rows of the system matrix $\mathbf{K}$. As observed from (10.164) there are at maximum 12 non-zero (here 8) elements in each of these rows or columns.

The boundary conditions at the upper and lower ends of the riser are subsequently introduced. The number of restrained kinematic components eliminates the equations corresponding to fixed and prescribed DOFs, which reduces the dimension of the global displacement vector. Taking the upper end as an example, the prescribed $x-$ and $y-$ displacements are taken into account by removing the first columns and rows of the system stiffness matrix (10.164). The first two columns of this matrix is stored in a separate matrix for later applications (see below) in connection with the prescribed vessel motions. The upper 2×2 sub-matrix is then removed, and the same applies to all the terms which correspond to the fixed DOFs at the last node of the model.

The resulting matrix will be of dimension $ndof \times 2$ (surge and sway DOFs are prescribed), where $ndof$ is the number of DOFs which are not fixed or prescribed. As shown later in the text (10.183b) this matrix is referred to as $\mathbf{K}_{Icoupl}$. Correspondingly, the main part of the remaining stiffness matrix is now of dimension $ndof \times ndof$. This is referred as $\mathbf{K}_I$ in (10.183b).

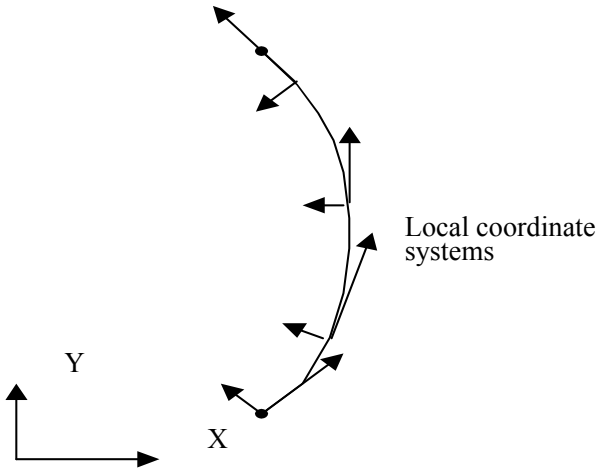

Figure 10.48: Two-dimensional projection of three-dimensional FEM riser model

The load vector for each element is also referred to the local coordinate frame initially. The force acting at each node of the element is obtained by integration of the force intensity multiplied by a proper "shape function". The static force intensity is the quadratic drag force based on the current velocity component, which is normal to the local element axis. The local

force vector at each node is subsequently transformed to the global system by an expression of the same type as in (10.161). The local force vector now replaces the local displacement vector in this equation, and the force vector referred to the global system replaces the displacement vector in the global system.

The transformation matrix and accordingly the stiffness matrix and load vector as referred to the global coordinate frame are functions of the nodal coordinates. These are in turn defined by the initial position and the subsequent total displacement of each node. It has been found that a two-step iteration gives accurate results: First the static riser displacements due to a given current profile and a given top end displacement are computed based on stiffness matrices and load vectors referring to a vertical riser. The new static configuration is subsequently applied for calculation of the updated transformation matrices. Based on these the system stiffness matrix and load vector is also updated. Finally, a more accurate static configuration is computed by means of these new matrices.

Example 10.7 *We consider a simplified two-dimensional example in order to illustrate the structure of the element and system matrices. Obviously, the resulting model is a gross oversimplification and does not reflect the physics of the riser behavior properly. Still, it may hopefully give useful insight to the various matrices and their properties. Specifically, the riser properties are given by the following data: Top tension is* $P_1 = 2500\,kN$*, tension at top of second element is* $P_2 = 1200\,kN$*, diameter is* $0.5\,m$*, wall thickness* $t = 2.5cm$*, modulus of elasticity is* $2.1 \times 10^8\,kN/m^2$*, water depth is* $1000\,m$ *(which implies an element length equal to* $500\,m$*). The resulting moment of inertia* $I = \pi r^3 t = 1.22656250 \times 10^{-3} m^4$*, where* r *designates the radius of the riser pipe.*

The elastic stiffness matrix for each of the two elements are now only of dimension 4×4 *since we retain only the in-plane degrees of freedom (i.e. one rotation and one translation at each node). For both elements, it is accordingly expressed as*

$$\mathbf{k}_{EI} = EI \begin{bmatrix} \frac{12}{l^3} & -\frac{6}{l^2} & -\frac{12}{l^3} & -\frac{6}{l^2} \\ -\frac{6}{l^2} & \frac{4}{l} & \frac{6}{l^2} & \frac{2}{l} \\ -\frac{12}{l^3} & \frac{6}{l^2} & \frac{12}{l^3} & \frac{6}{l^2} \\ -\frac{6}{l^2} & \frac{2}{l} & \frac{6}{l^2} & \frac{4}{l} \end{bmatrix}, \tag{10.165}$$

and the resulting numerical values become

$$\mathbf{k}_{EI} = \begin{bmatrix} .247e-1 & -6.182 & -.247e-1 & -6.182 \\ -6.182 & 2060.625 & 6.182 & 1030.313 \\ -.247e-1 & 6.182 & .2473e-1 & 6.182 \\ -6.182 & 1030.313 & 6.182 & 2060.625 \end{bmatrix}.$$

The unit of element $\mathbf{k}_{EI}(1,1)$ *is* $\frac{kN}{m}$*. The units of the other elements follow by scaling with respect to* l *as seen in (10.165). The geometric stiffness matrices are different for the two elements since the tension in the riser varies from top to bottom. However, the form of this matrix is the same for both elements, i.e.*

$$P_i \mathbf{k}_G = \frac{P_i}{30l} \begin{bmatrix} 36 & -3l & -36 & -3l \\ -3l & 4l^2 & 3l & -l^2 \\ -36 & 3l & 36 & 3l \\ -3l & -l^2 & 3l & 4l^2 \end{bmatrix}. \tag{10.166}$$

The numerical values of this matrix for element 1 (which corresponds to the upper half-length of the riser) becomes equal to

$$P_1\mathbf{k}_G = \begin{bmatrix} 6.00 & -250.00 & -6.00 & -250.00 \\ -250.00 & 166666.67 & 250.00 & -41666.67 \\ -6.00 & 250.00 & 6.00 & 250.00 \\ -250.00 & -41666.67 & 250.00 & 166666.67 \end{bmatrix},$$

and for the second element all the terms in the matrix are reduced in proportion to the tension in the element, which implies that

$$P_2\mathbf{k}_G = \begin{bmatrix} 2.88 & -120.00 & -2.88 & -120.00 \\ -120.00 & 80000.00 & 120.00 & -20000.00 \\ -2.88 & 120.00 & 2.88 & 120.00 \\ -120.00 & -20000.00 & 120.00 & 80000.00 \end{bmatrix},$$

The sum of the elastic and geometric stiffness matrix for the first and second elements hence become

$$\mathbf{k}_1 = \mathbf{k}_{EI} + P_1\mathbf{k}_G, \tag{10.167}$$

$$\mathbf{k}_2 = \mathbf{k}_{EI} + P_2\mathbf{k}_G. \tag{10.168}$$

As expected the geometric stiffness is much larger than the elastic stiffness. This is dependent of the length of each element. These two element matrices are subsequently added into the system matrix. For a deformed riser, non-trivial transformation matrices must first be applied. To establish the stiffness matrix, we consider initially the riser to have a straight and inclined shape between the seabed and with a relative lateral offset of 80m at the surface. Since the riser is undeformed (i.e. forms a straight line), the transformation matrices are identical for the top and bottom elements. The 4×4 *transformation matrix* $\mathbf{T}_i$ *for* $i = 1$ *to* 2 *is written*

$$\mathbf{T}_i = \begin{bmatrix} \mathbf{T}_o^i & \mathbf{0}_{2\times 2} \\ \mathbf{0}_{2\times 2} & \mathbf{T}_o^i \end{bmatrix}, \tag{10.169}$$

where

$$\mathbf{T}_0^1 = \mathbf{T}_0^2 = \begin{bmatrix} .987 & 0 \\ 0 & 1.0 \end{bmatrix}. \tag{10.170}$$

Using (10.162) the system matrix is of dimension 6×6 *and becomes*

$$\mathbf{K} = \begin{bmatrix} 6.022 & -256.134 & -6.022 & -256.134 & 0 & 0 \\ -256.134 & 168727.292 & 256.134 & -40636.354 & 0 & 0 \\ -6.022 & 256.134 & 8.926 & 129.976 & -2.904 & -126.158 \\ -256.134 & -40636.354 & 129.976 & 250787.917 & 126.158 & -18969.688 \\ 0 & 0 & -2.904 & 126.158 & 2.904 & 126.158 \\ 0 & 0 & -126.158 & -18969.688 & 126.158 & 82060.625 \end{bmatrix}. \tag{10.171}$$

Subsequently, the columns and rows corresponding to the prescribed degrees of freedom (i.e. one translation degree of freedom at the top corresponding to the surge motion of the vessel, and one fixed translation at the seabed) are removed. These correspond to the first row/column and the

next to the last row/column. The final stiffness matrix which corresponds to the non-prescribed degrees-of-freedom is now of dimension 4×4 *and is accordingly expressed as*

$$\mathbf{K} = \begin{bmatrix} 168727.292 & 256.134 & -40636.354 & 0 \\ 256.134 & 8.926 & 129.976 & -126.158 \\ -40636.354 & 129.976 & 250787.917 & -18969.688 \\ 0 & -126.158 & -18969.688 & 82060.625 \end{bmatrix}.$$

The vector which contains the coupling stiffness terms for the top end prescribed (non-zero) motion becomes

$$\mathbf{K}_{Icoupl} = \begin{bmatrix} -256.134 & -6.022 & -256.134 & 0 \end{bmatrix}^T.$$

This vector corresponds to part of the first column of (10.171), which was removed from the original 6×6 *stiffness matrix.*

Low-frequency model Considering LF riser motion, the driving excitation mechanism is due to forced motions caused by the surface vessel at the upper end of the riser. The direct hydrodynamic loading from waves on the riser can then be neglected, but forces from current and riser motions must be considered. These forces are proportional to the relative velocity squared and can hence not be separated into damping and driving terms. Since LF motions can become large, it is advantageous to take into account that geometrical changes will influence the system matrices. The dynamic equilibrium equation can then be written as

$$\mathbf{M}(\mathbf{r})\ddot{\mathbf{r}} + \mathbf{C}_s(\mathbf{r})\dot{\mathbf{r}} + \mathbf{K}(\mathbf{r})\mathbf{r} = \tau_{vessel_{LF}}(\mathbf{r}) + \tau_{current}(\mathbf{u}_c, \mathbf{r}, \dot{\mathbf{r}}), \tag{10.172}$$

where the nodal displacement vector is designated by $\mathbf{r}$. The mass matrix $\mathbf{M}$, structural damping matrix $\mathbf{C}_s$ and stiffness matrix $\mathbf{K}$ are all considered functions of the deformed configuration found from the displacements. Note that the mass matrix must include anisotropic added mass terms. Two loading terms $\tau_{vessel_{LF}}$ and $\tau_{current}$ are present, one containing contributions from LF vessel motions and the other with loads from the current velocity vector $\mathbf{u}_c$ and the riser velocity vector. The surface current velocity V_c will enter the first element of $\mathbf{u}_c$. Both terms will become functions of the displacements if LF motions are large. A generally applied simplification of (10.172) is to neglect the two dynamic terms related to inertia and damping forces. The model is then said to be quasi-static, meaning that the response model is static, but external loads are calculated by taking the riser motions into account. Such models will yield acceptable accuracy for shallow water applications, but dynamic effects will become more important in deep-water since the lowest eigenfrequency of the riser may approach the LF regime. A further simplification of (10.172) is to neglect the influence from riser velocity in the load due to the current. This type of model has been applied in the present study.

Wave-frequency model In the WF regime, the direct wave forces on the riser must be included. This loading vector τ_{hydro} contains a quadratic drag-term containing the relative velocity between the riser pipe and the surrounding fluid. For this case, the dynamic equilibrium equation accordingly is expressed as

$$\mathbf{M}(\mathbf{r})\ddot{\mathbf{r}} + \mathbf{C}_s(\mathbf{r})\dot{\mathbf{r}} + \mathbf{K}(\mathbf{r})\mathbf{r} = \tau_{vessel_{WF}}(\mathbf{r}) + \tau_{hydro}(\mathbf{u}_t, \dot{\mathbf{u}}, \mathbf{r}, \dot{\mathbf{r}}). \tag{10.173}$$

Again it is seen that all system matrices in principle should be functions of the displacements. The load terms are as for the LF model separated into one term from vessel motions (WF

motions only in this case) and a hydrodynamic load term. These forces must be found from a flow velocity profile $\mathbf{u}_t$ with contributions from current and waves, ant the wave induced flow accelerations $\dot{\mathbf{u}}$.

Two simplifications are frequently seen: The system matrices may be kept constant and represent the condition at static equilibrium. The model is then linear, but will still have nonlinear drag forces. The next simplification is to linearize the drag forces and split them into a damping and an exciting term. The linearized drag damping effect can subsequently be transferred to the left-hand side of the equilibrium equation and added to the pure structural damping term. This simplifies the analysis, and allows e.g. frequency domain analysis methods to be applied. However, linearizations also implies loss of accuracy in the numerical model. Note that for the WF case one should always apply a dynamic model since the eigenfrequencies of the riser in almost all cases will be found within the WF regime.

10.4.3 High Level Positioning and Riser Angle Controller

The horizontal-plane positioning controller consists of feedback and feedforward controller terms. The linear positioning control law including roll and pitch damping proposed in Section 7.3 is extended to also consider riser angle offsets. Motivated by the fact that the positioning controller has to reflect the nonlinear kinematics given in (10.148), the hybrid positioning and riser angle controller will be nonlinear. Applying a nonlinear formulation does also open up for further refinement of the control law.

Nonlinear horizontal-plane PID control law

The nonlinear horizontal-plane positioning feedback controller of PID type is formulated as

$$\tau_{PID} = -\mathbf{R}_e^T \mathbf{K}_p \mathbf{e} - \mathbf{R}_e^T \mathbf{K}_{p3} \mathbf{f}(\mathbf{e}) - \mathbf{K}_d \tilde{\nu} - \mathbf{R}^T \mathbf{K}_i \mathbf{z}, \tag{10.174}$$

where $\mathbf{e}$ is the 3-dimensional position and heading deviation vector, $\tilde{\nu}$ is the 3-dimensional velocity deviation vector, and $\mathbf{z}$ is the 3-dimensional integrator states defined as

$$\mathbf{e} = [e_1 \quad e_2 \quad e_3]^T = \mathbf{R}^T(\psi_d)(\hat{\eta} - \eta_d), \tag{10.175}$$

$$\tilde{\nu} = \hat{\nu} - \mathbf{R}^T(\psi_d)\dot{\eta}_d, \tag{10.176}$$

$$\dot{\mathbf{z}} = \hat{\eta} - \eta_d, \tag{10.177}$$

$$\mathbf{R}_e = \mathbf{R}(\psi - \psi_d) \triangleq \mathbf{R}^T(\psi_d)\mathbf{R}(\psi). \tag{10.178}$$

A third order stiffness term is also included for increasing the performance and robustness of the control system

$$\mathbf{f}(\mathbf{e}) = \begin{bmatrix} e_1^3 & e_2^3 & e_3^3 \end{bmatrix}^T. \tag{10.179}$$

An advantage of this is the possibility to reduce the first order proportional gain matrix, resulting in reduced dynamic thruster action for smaller position and heading deviations. Moreover, the third order term will make the thrusters work more aggressive for larger deviations. η_d is the 3-dimensional vector defining the desired Earth-fixed position and heading coordinates. $\hat{\eta}$ and $\hat{\nu}$ are the estimated position and velocity vectors computed by a nonlinear observer formulated as in Section 7.2. $\mathbf{K}_p, \mathbf{K}_{p3}, \mathbf{K}_d$ and $\mathbf{K}_i$ are the 3×3 non-negative controller gain matrices found by appropriate control synthesis methods.

One should notice that the integral action may be represented in Earth-fixed axes, in order to increase performance of the positioning controller for large rotating maneuvers.

Resulting control law

The resulting positioning control law is written

$$\tau_c = \tau_{wFF} + \tau_{PID} + \tau_{rpd}, \tag{10.180}$$

where the wind feedforward control law and the roll-pitch control law are as formulated in Section 7.3. The thruster allocation is as presented in Section 7.3.5.

10.4.4 Local Optimization: Optimal Setpoint Chasing

With reference to Figure 1.2 in Chapter 1 the optimal setpoint chasing will be on the local optimization level defining setpoints to the high level controller.

Reference model

A reference model is used for obtaining smooth transitions in the chasing of the optimal position setpoint minimizing the upper and lower riser angles, α_t and α_b, respectively. Let

$$\eta_r = [x_r \quad y_r \quad \psi_r]^T, \tag{10.181}$$

define the final Earth-fixed vector position and heading setpoint vector. This is input to the nonlinear third order reference model as presented in Section 7.3 and is given as

$$(\mathbf{x_{ref}}, \mathbf{x_d^e}, \mathbf{v_d^e}, \mathbf{a_d^e}) = \mathbf{f}(\eta_r, \mathbf{x_{ref}}, \mathbf{x_d^e}, \mathbf{v_d^e}, \mathbf{a_d^e}; t). \tag{10.182}$$

This model produces a smooth desired acceleration, velocity and position reference that are inputs to the positioning control law (10.180).

Riser control plant model

For simplicity it is assumed that all the natural periods for the riser are located away from the LF range. Thus the dynamic damping and inertia terms can be neglected. This leaves only the stiffness term in (10.172). Appropriate criteria that include dynamics and tilt and bearing are currently subject for further research. Hence, it is assumed that the increment in riser displacement vector $\mathbf{\Delta r}$ is related to the in-plane increment in surface vessel position vector $\mathbf{\Delta r}_{vessel}$ designated by

$$\mathbf{K}_I \mathbf{\Delta r} = -\mathbf{K}_{Icoupl} \mathbf{\Delta r}_{vessel}, \tag{10.183a}$$

$$\Updownarrow$$

$$\mathbf{\Delta r} = -\mathbf{K}_I^{-1} \mathbf{K}_{Icoupl} \mathbf{\Delta r}_{vessel}. \tag{10.183b}$$

$\mathbf{K}_I$ is the $ndof \times ndof$ incremental riser stiffness matrix at the present instantaneous vessel position corresponding to the given water current profile. $\mathbf{K}_{Icoupl}$ is the $ndof \times 2$ incremental stiffness matrix coupling the in-plane vessel motion (i.e. surge) to the remaining DOFs. Both matrices are obtained as sub-matrices of the system stiffness matrix given in (10.164).

The increments of top and bottom riser angles are expressed in terms of their x- and y-components. Typically, for the top angle these correspond to components 1 and 2 of the vector

in (10.164). For the bottom angle, components number $ndof-1$ and $ndof$ in the response vector are relevant. These are accordingly expressed as

$$\Delta\alpha_{tx} = -\left(\mathbf{K}_I^{-1}\mathbf{K}_{Icoupl}\right)_1 \Delta r_{vessel,x} = -c_{tx}\Delta r_{vessel,x}, \tag{10.184a}$$

$$\Delta\alpha_{ty} = -\left(\mathbf{K}_I^{-1}\mathbf{K}_{Icoupl}\right)_2 \Delta r_{vessel,y} = -c_{ty}\Delta r_{vessel,y}, \tag{10.184b}$$

$$\Delta\alpha_{bx} = -\left(\mathbf{K}_I^{-1}\mathbf{K}_{Icoupl}\right)_{ndof-1} \Delta r_{vessel,x} = -c_{bx}\Delta r_{vessel,x}, \tag{10.184c}$$

$$\Delta\alpha_{by} = -\left(\mathbf{K}_I^{-1}\mathbf{K}_{Icoupl}\right)_{ndof} \Delta r_{vessel,y} = -c_{by}\Delta r_{vessel,y}, \tag{10.184d}$$

where the scalar constants c_t and c_b are computed on-line.

Optimal criteria

A quadratic loss function L with the scalar weighting factors w_t and w_b is introduced

$$L = w_t\left[(\Delta\alpha_{tx}+\alpha_{tx})^2 + (\Delta\alpha_{ty}+\alpha_{ty})^2\right] + w_b\left[(\Delta\alpha_{bx}+\alpha_{bx})^2 + (\Delta\alpha_{by}+\alpha_{by})^2\right]. \tag{10.185}$$

By solving the equation where the partial derivatives of (10.185) with respect to the x- and y-components of the vessel increment are set equal to zero, the optimal direction for the increment of the vessel position is derived as

$$\theta_{opt} = \tan\left(\frac{\Delta y}{\Delta x}\right), \tag{10.186}$$

where

$$\Delta y = \left(w_b c_{bx}^2 + w_t c_{tx}^2\right) * \left(w_b c_{by}\alpha_{by} + w_t c_{ty}\alpha_{ty}\right), \tag{10.187}$$

and

$$\Delta x = \left(w_b c_{by}^2 + w_t c_{ty}^2\right) * \left(w_b c_{bx}\alpha_{bx} + w_t c_{tx}\alpha_{tx}\right). \tag{10.188}$$

For the optimal direction, the corresponding optimal vessel incremental position is computed as

$$\Delta r_{vessel}^* = \frac{w_t c_{tx}\alpha_{tx}\cos(\theta_{opt}) + w_t c_{ty}\alpha_{ty}\sin(\theta_{opt}) + w_b c_{bx}\alpha_{bx}\cos(\theta_{opt}) + w_b c_{by}\alpha_{bx}\sin(\theta_{opt})}{w_t c_{tx}^2\cos^2(\theta_{opt}) + w_t c_{ty}^2\sin^2(\theta_{opt}) + w_b c_{bx}^2\cos^2(\theta_{opt}) + w_b c_{by}^2\sin^2(\theta_{opt})}. \tag{10.189}$$

Then the x- and y-components of the optimal incremental vessel position vector are expressed as

$$\Delta r_x = \Delta r_{vessel}^*\cos(\theta_{opt}), \tag{10.190a}$$

$$\Delta r_y = \Delta r_{vessel}^*\sin(\theta_{opt}). \tag{10.190b}$$

Finally, in the general 3-dimensional case the updated Earth-fixed vector position and heading setpoint vector becomes

$$\eta_r^* = \eta_r + \Delta r_{vessel}^*\begin{bmatrix}\cos(\theta_{opt}) & \sin(\theta_{opt}) & 0\end{bmatrix}^T. \tag{10.191}$$

It is worthwhile to consider the special case that the current, wave and vessel motion takes place in a single vertical plane which passes through the x-axis. The optimal angle then obviously becomes zero, and the optimal vessel incremental position in the direction of the x-axis simplifies to:

$$\Delta r_{vessel}^* = \frac{w_t c_t\alpha_t + w_b c_b\alpha_b}{w_t c_t^2 + w_b c_b^2}. \tag{10.192}$$

Here, it is implicitly understood that the angles and coefficients refer to the in-plane quantities.

Water Depth:	**Surface** (**0** m)	**Middle** (500 m)	**Bottom** (1000 m)
Simulation 1	V_c, 30°	$0.75V_c$, 30°	$0.15V_c$, 30°
Simulation 2	V_c, 30°	$0.75V_c$, $-150°$	$0.15V_c$, $-150°$

Table 10.3: Current profile.

	Top Angle, w_t	**Bottom Angle,** w_b
Simulation 1	1	5
Simulation 2	1	1

Table 10.4: Weighting factors.

Weighting criteria

A key issue in the present algorithm is the relative weighting of the top and bottom riser angles. This weighting must reflect the maximum permissible limits for these angles. The permissible bottom angle is typically much smaller than the permissible top angle. This implies that the weighting factor for the lower angle should be much larger than for the upper angle. However, dynamic effects are different for the two angles. In particular, the dynamic response of the top angle due to wave-induced motion of the vessel and direct hydrodynamic loading on the riser is generally much larger than for the bottom angle. This acts in the opposite direction, i.e. the weighting factor for the top angle needs to be increased at the cost of the weighting factor for the bottom angle. A trade-off between the various considerations is hence required.

The present algorithm must also be supplemented with a maximum permissible radius of vessel motion for given values of the current magnitude and sea state parameters. If the vessel approaches the boundary of the permissible region, further increase of the offset must be restricted.

10.4.5 Numerical Simulations

In this Section a simulation study of a dynamic positioned semi-submersible conduction offshore drilling operations is carried out to demonstrate the effect of the setpoint chasing strategy. The semi-submersible, see Figure 10.49, is equipped with 4 azimuthing thrusters each able to produce 1000 kN located at the four corners at the two pontoons.

The operational draught is equal to 24 m, the vessel mass at operational draught is 45000 ton, the length is 110 m, and the breadth is 75 m. Radius of gyration in roll is 30 m, in pitch equal to 33 m and in yaw 38 m. The undamped resonance periods in roll and pitch are found to be equal to 55 sec and 60 sec, respectively.

The riser length used in the simulations is equal to 1000 m. The riser radius is 0.25 m, the riser wall thickness is 0.025 m and the modulus of elasticity (Young's modulus) is $E = 2.1 \times 10^8$ Pa. The top tension is 2500 Pa, and the tension of the lower part is 1200 Pa. In the simulation the riser is divided into only ten elements.

The positioning performance subject to two different current profiles will be considered, see Table 10.3.

The significant wave height is set equal to 7 m with peak period equal to 14 sec and direction equal to 20° The mean wind velocity is set equal 15 m/s with mean direction equal to 20°. The chosen weighting factors for the two simulations are given in Table 10.4.

Figure 10.49: Semi-submersible for oil and gas drilling.

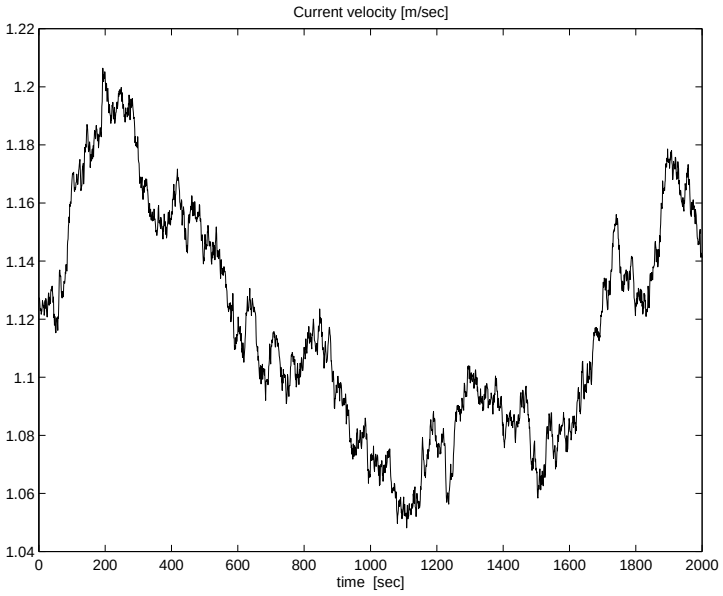

Figure 10.50: Surface current velocity.

Initially the semi-submersible is dynamically positioned over the well head with zero (field zero point) as the constant setpoint. After 1000 sec the optimal setpoint chasing is activated.

Figure 10.51 shows the LF position, reference and setpoint coordinates in North and East

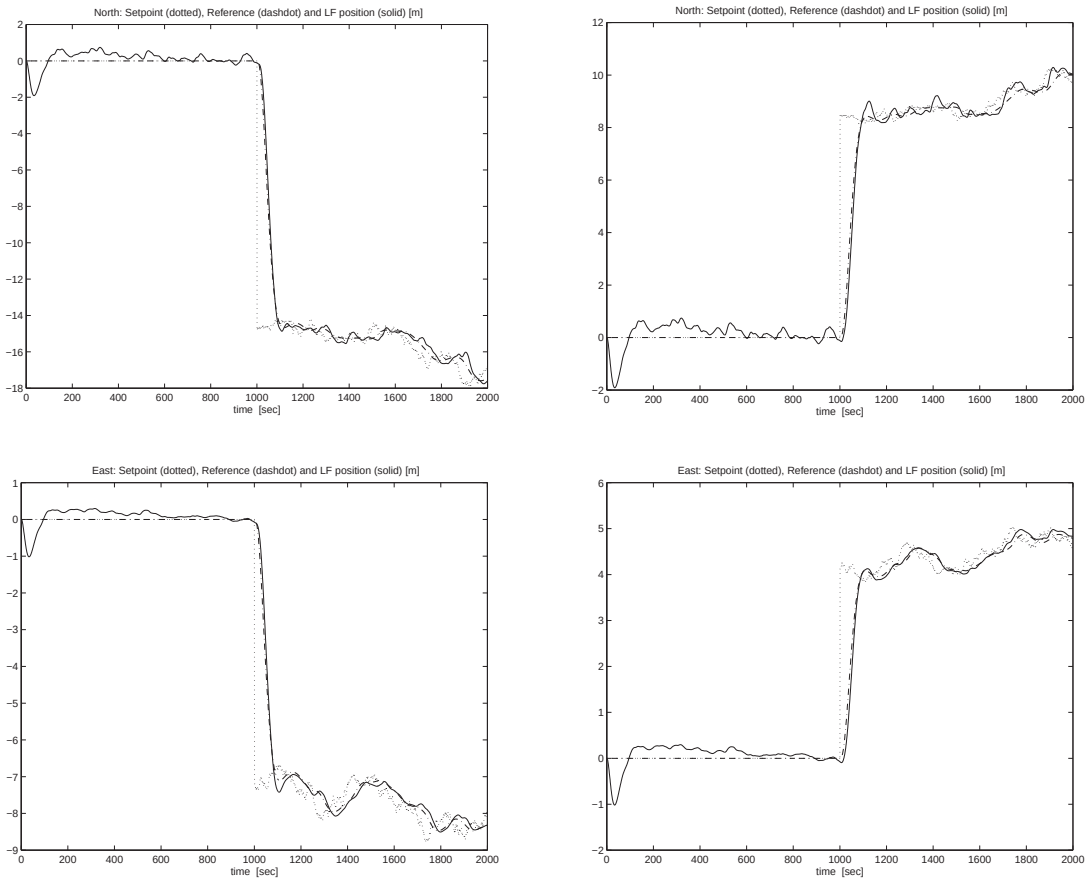

Figure 10.51: North and East positions for a dynamically positioned semi-submersible, where the optimal setpoint chasing is activated at 1000 sec. Simulation 1 is shown in left column (a) and Simulation 2 in right (b).

axes as function of the time for the two simulation cases. In simulation 1 with uniform current profile and with highest weight on the bottom riser angle, the optimal setpoint chasing forces the vessel about $16 - 18m$ to the South and $8 - 9m$ to the West. In simulation 2, with 180° change in the current direction from the middle to the bottom of the water column, and with equal weight on the bottom and top riser angles, the optimal setpoint chasing forces the vessel about $9 - 10$ m to the North and $4 - 5$ m to the East.

In Figure 10.52 the corresponding heading is shown for both simulations. The desired heading is set to 0° in both simulations. It can be seen that the heading control performance is satisfactory.

The effect of the optimal setpoint chasing on the riser angle offsets is clearly shown in Figure 10.53. In simulation 1, the lower riser angle decreases from 1.6° down to 0.4°, while the upper riser angle increases from 2.5° up to 3.5°. Since the lower riser angle offset is given higher weight compared to the upper riser angle, the opposite effect happens here. In simulation 2, the lower riser angle decreases from 1.0° down to 0.2°, while the upper riser angle changes from 0.15° down to $-0.4°$. Here, the weight on the lower riser angle is equal to the upper riser angle. Hence,

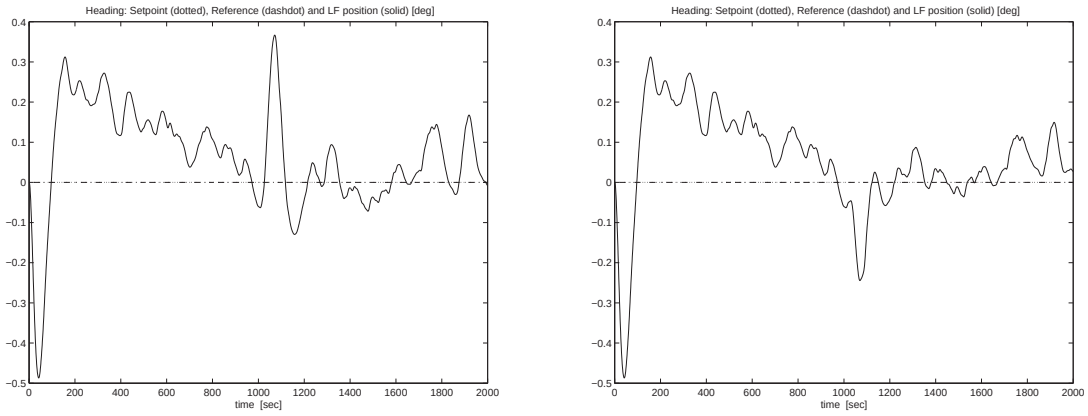

(a) Simulation 1 (b) Simulation 2

Figure 10.52: Heading angle for a dynamically positioned semi-submersible, where the optimal setpoint chasing is activated at 1000 sec. Simulation 1 is marked with (a) and simulation 2 is marked with (b).

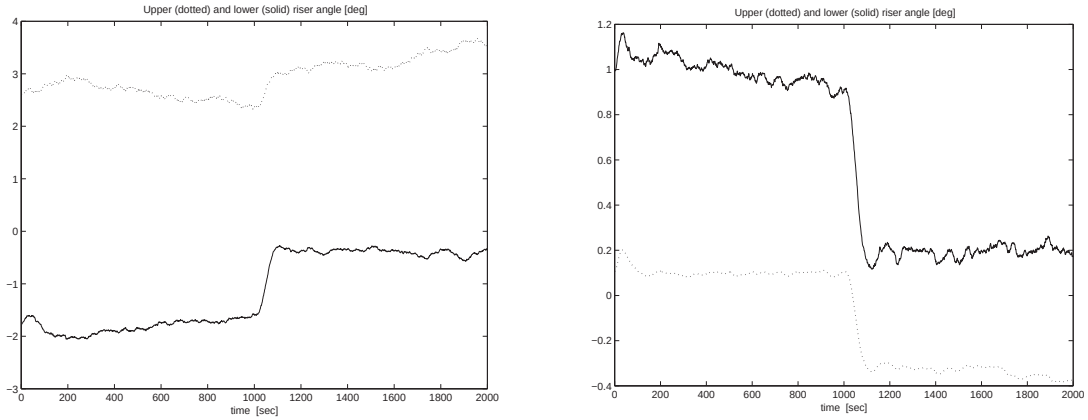

(a) Simulation 1 (b) Simulation 2

Figure 10.53: Lower α_t (solid) and upper α_b (dashed) riser angles, where the optimal setpoint chasing is activated at 1000 sec. Simulation 1 is marked with (a) and simulation 2 is marked with (b).

both angles are given equal priority. In an industrial system dynamic weights based on type of operation and magnitudes of the riser angle offsets have to be implemented.

In Figures 10.54 and 10.55 snapshots of the riser profile in 3-dimensions as function of time for simulation 1 and simulation 2 are shown. In the beginning the accumulation of riser profiles are found to be about the first desired setpoint defined to be over the field-zero-point equal to $(0, 0)$ in North-East coordinates. Then after 1000 sec, we observe that new accumulation areas appears corresponding to the new desired setpoint found by the optimal setpoint chasing algorithm. In Figure 10.56 the PID controller input in surge, sway and yaw are shown.

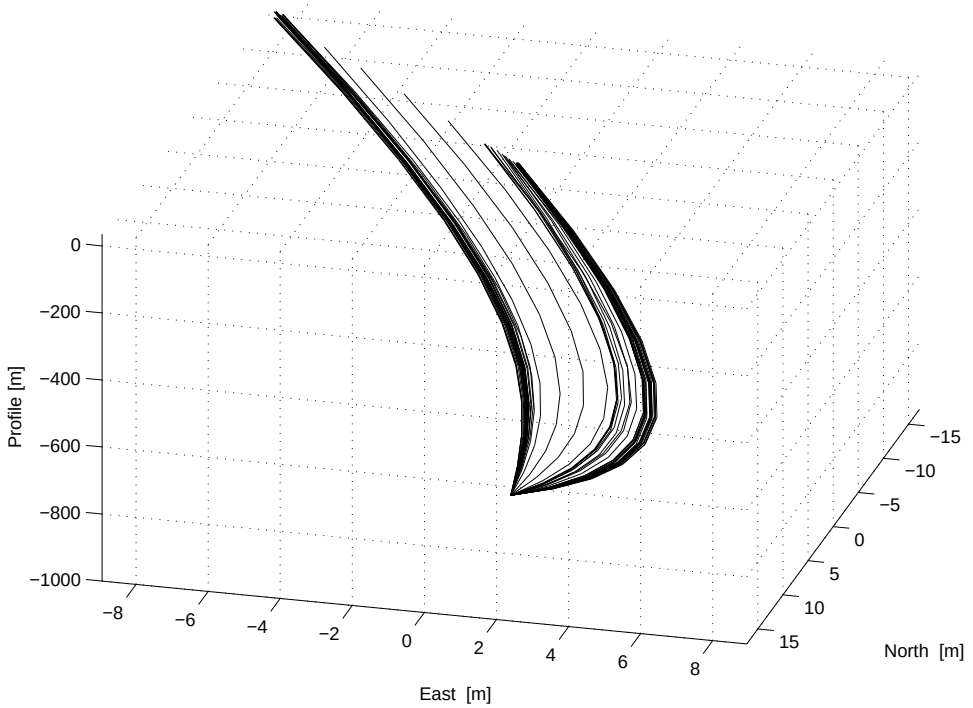

Figure 10.54: Snapshots of riser profile as function of time for uniform current profile, simulation 1, where the optimal setpoint chasing is activated at 1000 sec.

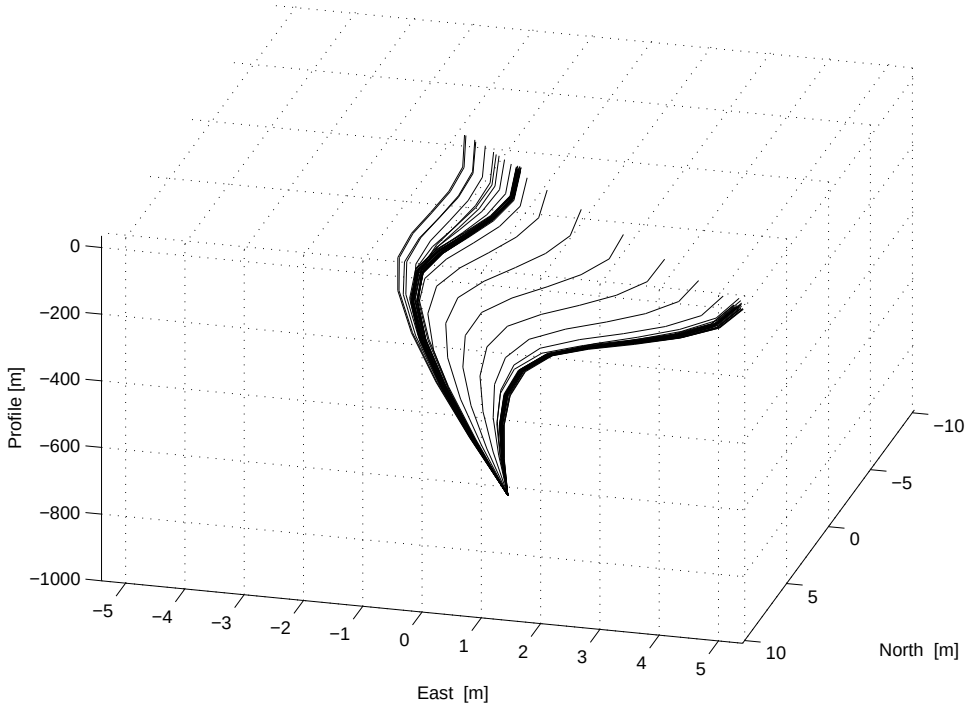

Figure 10.55: Snapshots of riser profile as function of time for change in current direction, simulation 2, where the optimal setpoint chasing is activated at 1000 sec.

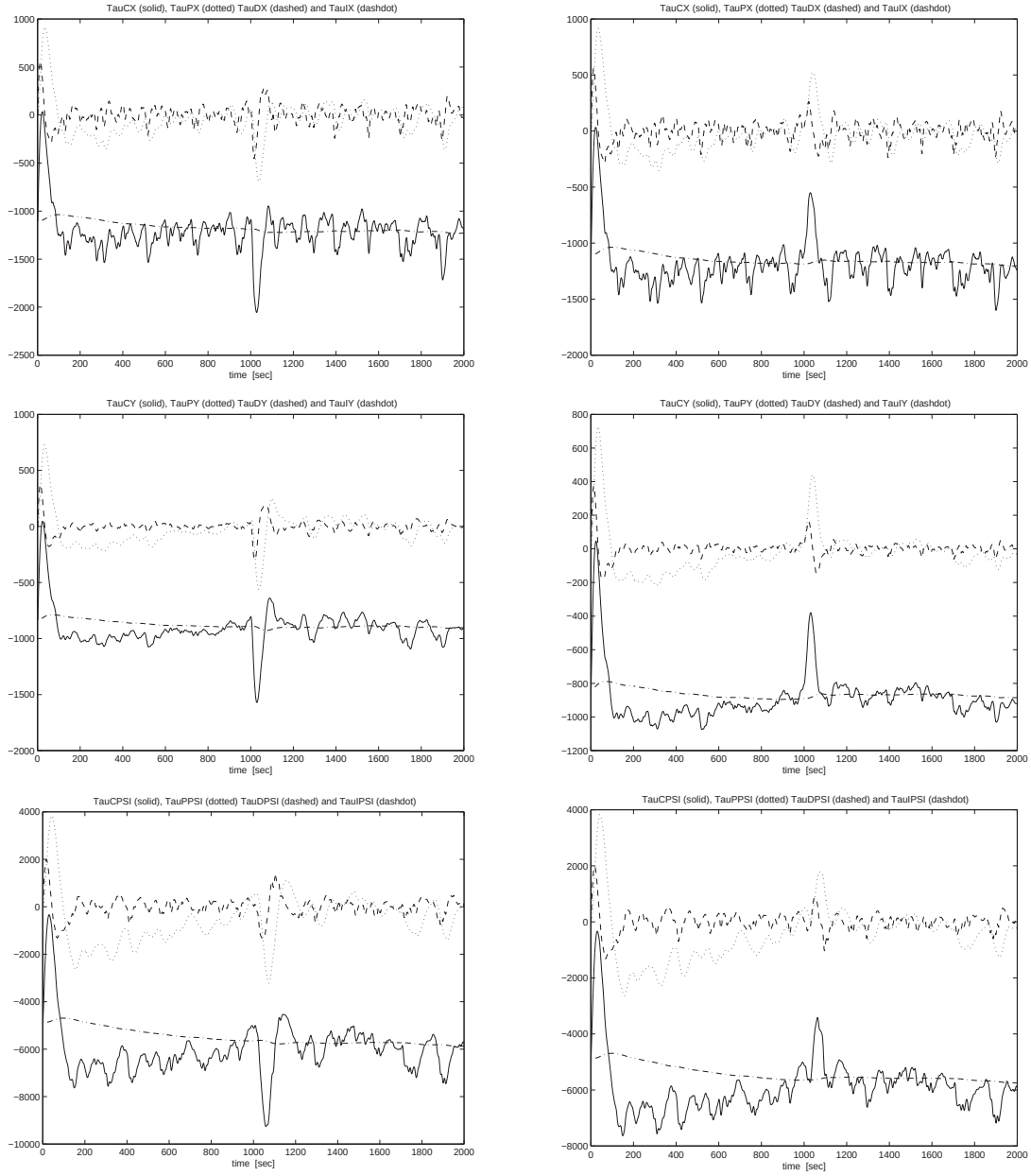

(a) Simulation 1

(b) Simulation 2

Figure 10.56: PID controller input in surge, sway and yaw, where the optimal setpoint chasing is activated at 1000 sec. Simulation 1 is shown in left column and Simulation 2 in right.

Chapter 11

Modeling and Control of High Speed Craft

This chapter is about ride control of a high speed craft concept denoted as *Surface Effect Ships* (SES). As described in Chapter 10, SES is also characterized with elastic dynamics described by partial differential equations (PDE) due to its spatial varying air pressure dynamics.

Learning outcome of the chapter: The reader shall understand:

- The physical principles for SES including the problem of vibrations modeled by the wave equation (class of PDE).
- How physical systems characterized as PDEs influence the controller design and analysis.
- The motivation for collocated sensor and actuator placement on flexible systems, and how this can be justified by the theory of passivity.
- How to solve a PDE by separation of variables and use this in the controller design.
- By a real example from the industry learn that nothing is as practical as a good theory. Hence, bridging theory and practice.

11.1 Introduction

SES has a catamaran type hull form which contains the air cushion with flexible structures called seals or skirts at the fore and aft ends of the air cushion. Pressurized air is supplied into the cushion by a lift fan system and is retained by rigid side-hulls and flexible skirt systems at the bow and the stern. The excess pressure lifts the craft and thereby reduces its calm water resistance. The major part of the craft weight (about 80%) is supported by the excess air cushion pressure, while the rest of the weight is supported by the buoyancy of the side-hulls. The most common stern seal system is the flexible rear bag system consisting of a loop of flexible material, open at both sides with one or two internal webs restraining the aft face of the loop into a two or three loop configuration. Pressurized air from the aft of the air cushion is supplied into the bag system. The bag pressure is about $10-15\%$ higher than the air cushion pressure. SES consist of catamaran hull equipped with skirt in the bow and a pressurized air bag in the stern. SES have

good seakeeping capabilities and offer a comfortable ride in moderate and heavy seas compared to conventional catamarans. However, in low sea states comfort problems due to high frequency vertical accelerations have been experienced. These high frequency vertical accelerations are denoted as the cobblestone effect. Full scale measurements of a $35\,m$ SES have indicated the existence of dominating vertical accelerations around three frequencies in the frequency range below $15\,Hz$. Later in the text we will show that the vibration about the first frequency is due to the resonance of the dynamic uniform pressure (*rigid body*) in the air cushion. For a $35\,m$ SES this frequency is typically around $2\,Hz$. This resonance may cause excessive vertical accelerations if a ride control system is not used. The resonances around the second and third frequency appear to be about $5\,Hz$ and $10\,Hz$ for a $35\,m$ SES having a flexible rear bag system. These resonances are related to the spatially varying pressure (*elastic modes*) in the air cushion.

11.2 Ride Control of Surface Effect Ships

Surface Effect Ships (SES), see Figure 11.1, are known for offering a high quality ride in heavy sea states compared to conventional catamarans. However, in low and moderate sea states there are comfort problems due to high frequency vertical accelerations induced by resonances in the pressurized air cushion and a high performance ride control system is required to achieve satisfactory passenger comfort and crew workability. To develop such a ride control system it is essential to use a sufficiently detailed dynamic model. Previous ride control systems have been based on the coupled equations of motion in heave and pitch as derived by Kaplan and Davis (1974), Kaplan and Davis (1978) and Kaplan et al. (1981). Their work were based on the assumption that the major part of the wave induced loads from the sea was imparted to the craft as dynamic uniform air pressure acting on the wetdeck, while a minor part of the wave induced loads from the sea was imparted to the craft as dynamic water pressure acting on the side-hulls. This work was extended by Sørensen et al. (1992), Sørensen et al. (1993) and Sørensen and Egeland (1995), who included the effect of spatial pressure variations in the air cushion. It was found that acoustic resonances in the air cushion excited by incident sea waves can result in significant vertical vibrations. To investigate the acoustic resonances a distributed model was derived from a boundary value problem formulation where the air flow was represented by a velocity potential subject to appropriate boundary conditions on the surfaces enclosing the air cushion volume. A solution was found using the *Helmholtz equation* in the air cushion region. In Sørensen et al. (1992) the first two acoustic modes were included in the mathematical model, while in Sørensen et al. (1993) and Sørensen and Egeland (1995) a more general model with an infinite number of acoustic modes was derived. In this chapter, the mathematical model presented Sørensen and Egeland (1995) is presented. This mathematical model is used to derive a ride control system, which provides active damping of both the dynamic uniform pressure and the acoustic resonances in the air cushion. Special attention is given to sensor and actuator placement to achieve robust stability and high performance. The stability of the control system is analyzed using the theory of passive systems as presented in Desoer and Vidyasager (1975) and in Vidyasager (1993). It is shown that under appropriate assumptions the dynamic system to be controlled is passive, and L_2^{n} stability can be achieved using a strictly passive controller with finite gain.

The chapter is organized as follows: In Section 11.2.1 the mathematical model is derived. Section 11.2.2 includes the controller design and the stability analysis. Finally, in Section 11.2.3 simulation results and power spectra of pressure variations and vertical accelerations obtained

Figure 11.1: Surface Effect Ship.

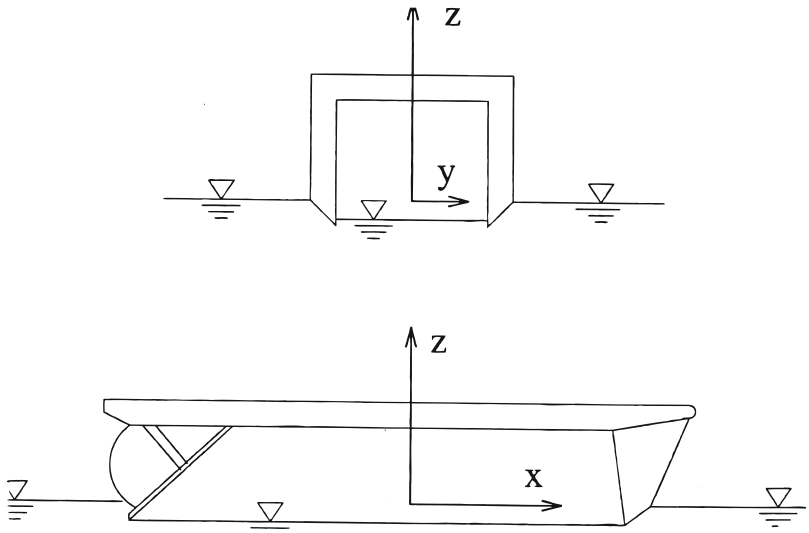

Figure 11.2: Surface Effect Ship (SES)—coordinate frame.

from full scale trials with a $35\,m$ SES are presented.

11.2.1 Mathematical Modeling

Kinematics

In this chapter a moving coordinate frame is defined so that the origin is located in the mean water plane below the centre of gravity with the x-, y- and z-axes oriented positive forwards, to the port, and upwards respectively, see Figure 11.2. This type of coordinate frame is commonly used in marine hydrodynamics to analyze vertical motions and accelerations Faltinsen (1993). The equations of motion are formulated in this moving frame. Translation along the z-axis is called heave and is denoted $\eta_3(t)$. The rotation angle about the y-axis is called pitch and is denoted $\eta_5(t)$. Heave is defined positive upwards, and pitch is defined positive with the bow down. We are mainly concerned about the high frequency vertical vibrations. In this frequency range the hydrodynamic loads on the slender side-hulls are of minor importance. Strip theory is used and hydrodynamic memory effects are assumed to be negligible due to the high frequency of oscillation. Furthermore, infinite water depth is assumed.

The global continuity equation

The craft is assumed to be advancing forward in regular head sea waves. The waves are assumed to have a small wave slope with circular frequency ω_0. The circular frequency of encounter ω_e is

$$\omega_e = \omega_0 + kU, \tag{11.1}$$

where $k = 2\pi/\lambda$ is the wave number, λ is the sea wave length and U is the craft speed. The circular frequency of encounter ω_e is the apparent wave frequency as experienced on the craft advancing forward at the speed U in head sea. The incident surface wave elevation $\zeta(x,t)$ for regular head sea is defined as

$$\zeta(x,t) = \zeta_a \sin(\omega_e t + kx), \tag{11.2}$$

where ζ_a is the wave elevation amplitude. In the case of calm water the wave elevation amplitude is equal to 0. The water waves are assumed to pass through the air cushion undisturbed. For simplicity a rectangular cushion is considered at the equilibrium condition with height h_o , beam b and length L, reaching from $x = -L/2$ at the stern (AP) to $x = L/2$ at the bow (FP). The beam and the height of the air cushion are assumed to be much less than the length. Hence, a one-dimensional ideal and compressible air flow in the x-direction is assumed. This means that the longitudinal position of the centre of air cushion pressure is assumed to coincide with the origin of the coordinate frame. The air cushion area is then given by $A_c = Lb$. The total pressure $p_c(x,t)$ in the air cushion is represented by

$$p_c(x,t) = p_a + p_u(t) + p_{sp}(x,t), \tag{11.3}$$

where p_a is the atmospheric pressure, $p_u(t)$ is the uniform excess pressure and $p_{sp}(x,t)$ is the spatially varying excess pressure.

The basic thermodynamic variations in the air cushion are assumed to be adiabatic. When neglecting seal dynamics, aerodynamics and viscous effects, the external forces are given by the water pressure acting on the side-hulls and by the dynamic air cushion pressure acting on the wetdeck. It is assumed that the dynamic cushion pressure is excited by incoming sea wave disturbances. In the absence of waves, the stationary excess pressure in the air cushion is equal to the equilibrium excess pressure p_0. This means that at equilibrium $p_{sp}(x,t) = 0$, such that (11.3) becomes

$$p_c(x,t) \approx p_a + p_0.$$

The rate of change of the mass of air inside the cushion is equal the net mass flux into the cushion. The global continuity equation for mass flow into and out of the cushion can then be written as

$$w_{in}(t) - w_{out}(t) = \frac{d}{dt}\left(\int_{-L/2}^{L/2} \rho_c(x,t) V_c(t) dx\right)\frac{1}{L}, \tag{11.4}$$

where $w_{in}(t)$ is the air flow into the air cushion from the lift fan system, $w_{out}(t)$ is the air flow out of the air cushion due to leakage, $V_c(t)$ is the cushion volume, and $\rho_c(x,t)$ is the density of the air at the pressure $p_c(x,t)$. The basic thermodynamic variations in the air cushion are assumed to be adiabatic. From the adiabatic pressure-density relation it follows that

$$\rho_c(x,t) = \rho_{co}\left[\frac{p_a + p_u(t) + p_{sp}(x,t)}{p_a + p_0}\right]^{\frac{1}{\gamma}}, \tag{11.5}$$

where γ is the ratio of specific heat for air, and ρ_{co} is the density of the air at the equilibrium pressure $p_a + p_0$. The nondimensional uniform pressure variations $\mu_u(t)$ and the nondimensional spatial pressure variations $\mu_{sp}(x,t)$ are defined according to

$$\mu_u(x,t) = \frac{p_u(t) - p_0}{p_0}, \tag{11.6}$$

$$\mu_{sp}(x,t) = \frac{P_{sp}(x,t)}{p_0}. \tag{11.7}$$

If we linearize (11.5) about the craft equilibrium operating point $\mu_u(t) = \mu_{sp}(x,t) = 0$ and differentiate with respect to the time t, we find an expression for the time derivative of $\rho_c(x,t)$ as

$$\dot{\rho}_c(x,t) = \frac{\rho_{c0}}{\gamma\left(1 + \frac{p_a}{p_0}\right)} \left(\dot{\mu}_u(t) + \dot{\mu}_{sp}(x,t)\right). \tag{11.8}$$

The rate of change of the air cushion volume can be written as

$$\dot{V}_c(t) = A_c \left(\dot{\eta}_3(t) - x_{cp}\dot{\eta}_5(t)\right) - \dot{V}_0(t). \tag{11.9}$$

The last term in (11.9) represents the wave volume pumping of the dynamic uniform pressure and can be written as

$$\dot{V}_0(t) = b \int_{-L/2}^{L/2} \dot{\zeta}(x,t)dx = A_c\zeta_a\omega_e \frac{\sin\frac{kL}{2}}{\frac{KL}{2}} \cos\omega_e t. \tag{11.10}$$

The air flow into the air cushion is given by a linearization of the fan characteristic curve about the craft equilibrium operating point, see Figure 11.3. It is assumed that q fans with constant RPM are feeding the cushion, where fan i is located at the longitudinal position x_{Fi}.

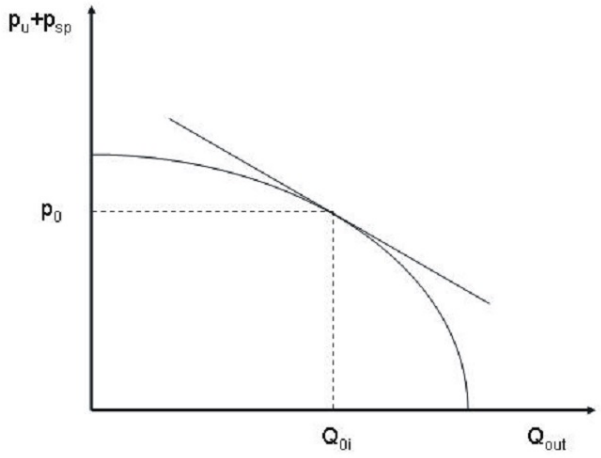

Figure 11.3: The fan characteristic curve.

Assuming no dynamic fan response, the fan characteristic curve can then be represented by

$$w_{in}(t) = \rho_{c0} \sum_{i=1}^{q} \left(Q_{0i} + p_0 \frac{\partial Q}{\partial p}|_{0i} \left(\mu_u(t) + \mu_{sp}(x_{Fi},t)\right)\right), \tag{11.11}$$

where Q_{0i} is the equilibrium air flow rate of fan i when $p_u(t) = p_o$, and $\frac{\partial Q}{\partial p}|_{0i}$ is the corresponding linear fan slope about the craft equilibrium operating point Q_{0i} and p_0. The total equilibrium air flow rate into the cushion is then

$$Q_0 = \sum_{i=1}^{q} Q_{0i} \tag{11.12}$$

The volumetric air flow out of the air cushion is proportional to the leakage area $A_L(t)$, which is defined as

$$A_L(t) = A_0 + A^{RCS}(t). \tag{11.13}$$

$A_L(t)$ represents the total leakage area and is expressed as the sum of an equilibrium leakage area A_o and a controlled variable leakage area $A^{RCS}(t)$. The equilibrium leakage area

$$A_0 = A_0^{AP} + A_0^{FP}, \tag{11.14}$$

will be divided into leakage areas under the bow and stern region or more precisely under the stern and bow seals. A_0^{AP} is the stern equilibrium leakage area at $x = -L/2$, and A_0^{FP} is the bow equilibrium leakage area at $x = L/2$. The controlled leakage area $A^{RCS}(t)$ of the ride control system is written

$$A^{RCS}(t) = \sum_{i=1}^{r} \left(A_{0i}^{RCS} + \Delta A_i^{RCS}(x_{si}, t) \right), \tag{11.15}$$

where r is the number of louvers. The louvers are variable vent valves located at the longitudinal position $x = x_{Li}$, which change the area of openings in the wetdeck for the purpose of leakage control. A_{oi}^{RCS} is defined as the mean operating value or bias of the leakage area and $\Delta A_i^{RCS}(x_{si}, t)$ is defined as the commanded variable leakage area of louver i. Pressure sensors are used to measure the pressure variations in the air cushion. Sensor i is placed at the longitudinal position $x = x_{si}$. Dynamic leakage areas under the side-hulls and the seals due to craft motion are assumed to be negligible in this analysis. This type of leakage is a hard nonlinearity and can be analyzed using describing functions Gelb and Vander Velde (1968). Computer simulations done in Sørensen et al. (1992) indicate that the dynamic leakage terms due to craft motion can be neglected for small amplitudes of sea wave disturbances and associated small amplitudes of heave and pitch motions as long as the sealing ability is good.

The air flow out of the air cushion is then represented by

$$w_{out}(t) = w_{AP}(t) + w_{FP}(t) + w_{RCS}(t), \tag{11.16}$$

where

$$w_{AP}(t) = c_n A_0^{AP} \sqrt{\frac{2\left(p_u(t) + p_{sp}(x_{AP}, t)\right)}{\rho_{c0}}} \rho_c(x_{AP}, t), \tag{11.17}$$

$$w_{FP}(t) = c_n A_0^{FP} \sqrt{\frac{2\left(p_u(t) + p_{sp}(x_{FP}, t)\right)}{\rho_{c0}}} \rho_c(x_{FP}, t), \tag{11.18}$$

$$w_{RCS}(t) = c_n \sum_{i=1}^{r} \left(\left(A_{0i}^{RCS} + \Delta A_i^{RCS}(x_{si}, t) \right) \sqrt{\frac{2\left(p_u(t) + p_{sp}(x_{Li}, t)\right)}{\rho_{c0}}} \rho_c(x_{Li}, t) \right). \tag{11.19}$$

ρ_a is the air density at the atmospheric pressure p_a, and c_n is the orifice coefficient varying between 0.61 and 1 depending of the local shape on the edges of the leakage area. In the numerical simulations $c_n = 0.61$ is used.

Using Taylor expansion about p_0 and A_0, the air flow out of the cushion $w_{out}(t)$, can be linearized and written

$$\begin{aligned} w_{out}(t) &= \left(\frac{1}{2} \sum_{i=1}^{r} A_{0i}^{RCS} \mu_{sp}(x_{Li}, t) + \frac{1}{2} A_0^{FP} \mu_{sp}(x_{FP}, t) + \frac{1}{2} A_0^{AP} \mu_{sp}(x_{AP}, t) + \right. \\ & \left. \frac{1}{2} \left(A_0 + \sum_{i=1}^{r} A_{0i}^{RCS} \right) \mu_u(t) + A_0 + \sum_{i=1}^{r} A_{0i}^{RCS} + \sum_{i=1}^{r} \Delta A_i^{RCS}(x_{si}, t) \right) \rho_{c0} c_n \sqrt{\frac{2p_0}{\rho_{c0}}}. \end{aligned} \tag{11.20}$$

At stationary equilibrium the air flow into and out of the cushion is equal to

$$Q_0 = c_n \left(A_0 + \sum_{i=1}^{r} A_{0i}^{RCS} \right) \sqrt{\frac{2p_0}{\rho_{c0}}}. \tag{11.21}$$

The global continuity equation given in (11.4) can be linearized and written as

$$\rho_{c0} \left(Q_{in}(t) - Q_{out}(t) \right) = \frac{V_{c0}}{L} \int_{-L/2}^{L/2} \dot{\rho}_c(x, t) dx + \rho_{c0} \dot{V}_c(t), \tag{11.22}$$

where $w_{in}(t) = \rho_{co} Q_{in}(t)$ and $w_{out}(t) = \rho_{co} Q_{out}(t)$. $Q_{in}(t)$ is the linear volumetric air flow into the air cushion from the lift fan system. $Q_{out}(t)$ is the linear volumetric air flow out of the air cushion due to leakage. $V_{c0} = Lbh_0$ is the equilibrium air cushion volume, where L is the cushion length, b is the cushion beam, and h_0 is the cushion height at equilibrium. Using the results from above, we find the uniform pressure equation given in equation (11.40) later in the text.

Boundary value problem for spatial pressure variations

Wave equation The effect of spatial pressure variations in the air cushion was investigated by Sørensen et al. (1992) and Sørensen et al. (1993) in the frequency domain using Helmholtz equation. Here, the wave equation is considered leading to a more general solution formulated in the time domain. A distributed model is derived from a boundary value problem formulation. A one-dimensional ideal and compressible air flow in the x-direction is assumed. The motion of the craft in the vertical plane is assumed to be small so the body boundary conditions and the free surface condition can be linearized. The air flow dynamics is formulated in terms of potential theory. The velocity potential $\phi_{sp}(x, z, t)$ for the spatially varying pressure is assumed to satisfy the wave equation in the cushion region and the boundary conditions enclosing the cushion volume, see Figure 11.4.

The wave equation is given by

$$\frac{\partial^2 \phi_{sp}(x, z, t)}{\partial t^2} - c^2 \left(\frac{\partial^2 \phi_{sp}(x, z, t)}{\partial x^2} + \frac{\partial^2 \phi_{sp}(x, z, t)}{\partial z^2} \right) = 0, \tag{11.23}$$

where c is the speed of sound in air. The one-dimensional approximation of the velocity potential is introduced as

$$\psi_{sp}(x, t) = \frac{1}{h_0} \int_0^{h_0} \phi_{sp}(x, z, t) dz. \tag{11.24}$$

By integrating the wave equation in the z-direction, the following partial differential equation of second order in the two variables x and t is obtained

$$\frac{c^2}{h_0 b}\int_{-b/2}^{b/2} dy \left(\left.\frac{\partial \phi_{sp}(x,z,t)}{\partial z}\right|_{z=h_0} - \left.\frac{\partial \phi_{sp}(x,z,t)}{\partial z}\right|_{z=0} \right) + c^2 \frac{\partial^2 \psi_{sp}(x,t)}{\partial x^2} - \frac{\partial^2 \psi_{sp}(x,t)}{\partial t^2} = 0. \quad (11.25)$$

It is then possible to derive an analytical solution of the boundary value problem. Because the louver area and the outflow area of the lift fan system do not cover the whole beam, we have to integrate these boundary conditions in the y-direction. The nondimensional spatial pressure variations $\mu_{sp}(x,t)$ can be found as

$$\mu_{sp}(x,t) = -\frac{\rho_{c0}}{p_0}\frac{\partial \psi_{sp}(x,t)}{\partial t}. \quad (11.26)$$

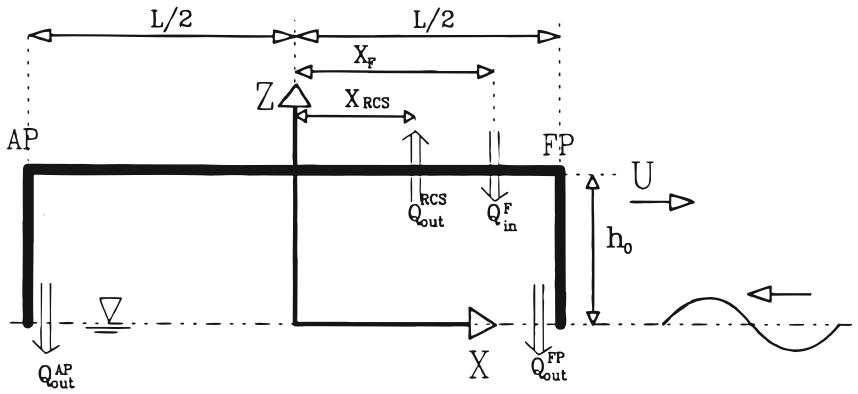

Figure 11.4: The boundary value problem.

The unbounded differential operator $\frac{\partial^2}{\partial x^2}$ with boundary conditions on the finite interval $x \in [-L/2, L/2]$ appearing in equation (11.25), has a set of discrete eigenvalues, called the discrete spectrum of the differential operator. $\frac{\partial^2}{\partial x^2}$ is a time-invariant smooth, self-adjoint differential operator which is dense in the infinite dimensional inner product space $L_2(\Omega)$, where Ω denotes the air cushion.$L_2(\Omega)$ is complete and hence a Hilbert space. The eigenvalue equation is given by

$$-c^2 \frac{\partial^2}{\partial x^2}\left(r_j(x)\right) = \omega_j^2 r_j(x), \qquad j = 1, 2, 3, ..., k, \quad (11.27)$$

where $r_j(x)$ is the eigenfunction or the mode shape function of mode j, and ω_j is the corresponding eigenfrequency. The eigenfunctions for $j \in \{1, 2, 3, .., k\}$ are orthonormal, that is

$$\left(r_i(x), r_j(x)\right) = \int_{-L/2}^{L/2} r_i(x) r_j(x) dx = \delta_{ij}, \quad (11.28)$$

where $(\cdot, \cdot)$ denotes the scalar product. The Kronecker delta is defined by $\delta_{ij} = 1$ when $i = j$ and $\delta_{ij} = 0$ when $i \neq j$. Letting $k \to \infty$, the eigenfunctions $r_j(x)$ for $j \in \{1, 2, 3, ...\}$ form an orthonormal basis of the Hilbert space $L_2(\Omega)$. Thus, $\mu_{sp}(x,t)$ has a unique modal representation for $k \to \infty$ given by

$$\mu_{sp}(x,t) = -\frac{\rho_{c0}}{p_0}\sum_{j=1}^{\infty} \frac{\partial \psi_{sp}^t(t)}{\partial t}\psi_{sp}^x(x) = \sum_{j=1}^{\infty} \dot{p}_j(t) r_j(x), \quad (11.29)$$

where $\dot{p}_j(t)$ is the modal amplitude function for mode j and $\psi_j^x(x) = r_j(x)$. Due to linearity and orthogonality between the modes, each mode can be considered separately and the contributions from each of them are superposed.

Boundary conditions We can set up the following boundary conditions on the surfaces enclosing the cushion air volume.

1. On the rigid part of the wetdeck ($z = h_0$)

$$\frac{\partial \phi_{sp}(x,z,t)}{\partial z} = \dot{\eta}_3(t) - x\dot{\eta}_5(t). \tag{11.30}$$

2. At the rigid bow and rear seal systems ($x = \pm\, L/2$)

$$\frac{\partial \phi_{sp}(x,z,t)}{\partial z} = 0. \tag{11.31}$$

3. At the fan outlet ($z = h_0, x = x_{Fi}$)

$$\frac{\partial \phi_{sp}(x,z,t)}{\partial z} = -p_0 \sum_{i=1}^{q} \frac{1}{A_{Fi}} \left.\frac{\partial Q}{\partial p}\right|_{0i} \left(\sum_{j=1}^{\infty} \dot{p}_j(t) r_j(x_{Fi}) + \mu_u(t) \right), \tag{11.32}$$

where A_{Fi} is the outlet area of fan i.

4. At the controlled leakage area ($z = h_0, x = x_{Li}$)

$$\frac{\partial \phi_{sp}(x,z,t)}{\partial z} = c_n \sqrt{\frac{2p_0}{\rho_{c0}}} \sum_{i=1}^{r} \left(\frac{1}{2} \sum_{j=1}^{\infty} \dot{p}_j(t) r_j(x_{Li}) + \frac{1}{2}\mu_u(t) - \frac{\Delta A_i^{RCS}(x_{si},t)}{A_{0i}^{RCS}} \right). \tag{11.33}$$

5. At the bow leakage area ($z = 0, x = x_{FP} = L/2$)
Assuming no motion induced leakage, we have

$$\frac{\partial \phi_{sp}(x,z,t)}{\partial z} = -\frac{c_n}{2} \sqrt{\frac{2p_0}{\rho_{c0}}} \left(\sum_{j=1}^{\infty} \dot{p}_j(t) r_j(x_{FP}) + \mu_u(t) \right). \tag{11.34}$$

6. At the stern leakage area ($z = 0, x = x_{AP} = -L/2$)
Assuming no motion induced leakage, we have

$$\frac{\partial \phi_{sp}(x,z,t)}{\partial z} = -\frac{c_n}{2} \sqrt{\frac{2p_0}{\rho_{c0}}} \left(\sum_{j=1}^{\infty} \dot{p}_j(t) r_j(x_{AP}) + \mu_u(t) \right). \tag{11.35}$$

7. At the mean free surface ($z = 0$)

$$\frac{\partial \phi_{sp}(x,z,t)}{\partial z} = \omega_e \zeta_a \cos\left(kx + \omega_e t\right). \tag{11.36}$$

The mode shape functions will be chosen so the boundary conditions on the seals are satisfied. The following mode shape functions, in general infinite many, will satisfy the boundary condition on the seals

$$r_j(x) = \cos\frac{j\pi}{L}\left(x + \frac{L}{2}\right), \quad j = 1, 2, 3, ... \quad \textit{and} \quad x \in \left[-\frac{L}{2}, \frac{L}{2}\right]. \tag{11.37}$$

From (11.27) we find that the corresponding eigenfrequency ω_j for mode j

$$\omega_j = c\frac{j\pi}{L}, \quad j = 1, 2, 3, ... \tag{11.38}$$

The modal amplitude functions will be determined according to (11.25) and the remaining boundary conditions. By taking the inner product of (11.25) with the mode shape function of mode j for $j \in \{1, 2, 3, ...\}$ and using (11.29), we find the spatially varying pressure equation for mode j for $j \in \{1, 2, 3, ...\}$, see (11.43) and (11.46) later in the text. The heave force and the pitch moment due to the spatially varying pressure are found in the following way

$$F_3^{sd}(t) = p_0 b \int_{-L/2}^{L/2} \sum_{j=1}^{\infty} \dot{p}_j(t) r_j(x) dx = 0, \quad j = 1, 2, 3, ..., \tag{11.39a}$$

$$F_5^{sd}(t) = -p_0 b \int_{-L/2}^{L/2} \sum_{j=1}^{\infty} \dot{p}_j(t) r_j(x) x dx = \begin{cases} 2p_0 b \sum\limits_{j=1,3,5,...} \left(\frac{L}{j\pi}\right)^2 \dot{p}_j(t), & j = 1, 3, 5, ... \\ 0, & j = 2, 4, 6, ... \end{cases} \tag{11.39b}$$

Due to symmetry about the origin, there is no contribution from the spatially varying pressure on the heave motion. However, the pitch moment $F_5^{sp}(t)$ is important to include in the pitch equation.

Equations of motion and dynamic cushion pressure

The coupling between the dynamic uniform pressure and the spatially varying pressure and hydrodynamic and hydrostatic coupling terms like $\{Z_{\dot{q}},\ M_{\dot{w}}\}$, $\{Z_q,\ M_w\}$, and $\{Z_\theta, M_z\}$-terms are assumed to be negligible regarding control system design. The equations of motions and the dynamic air cushion pressure are:

(1) Uniform pressure equation

$$K_1\dot{\mu}_u(t) + K_3\mu_u(t) + \rho_{c0}A_c\dot{\eta}_3(t) = K_2\sum_{i=1}^{r}\Delta A_i^{RCS}(x_{si}, t) + \rho_{c0}\dot{V}_0(t), \tag{11.40}$$

where $\dot{V}_0(t)$ is the wave volume pumping given by (11.10),and

$$K_1 = \frac{\rho_{c0}h_0A_c}{\gamma\left(1 + \frac{p_a}{p_0}\right)}, \tag{11.41a}$$

$$K_2 = c_n\sqrt{\frac{2p_0}{\rho_{c0}}}, \tag{11.41b}$$

$$K_3 = \rho_{c0}\sum_{i=1}^{q}\left(\frac{Q_{0i}}{2} - p_0\left.\frac{\partial Q}{\partial p}\right|_{0i}\right). \tag{11.41c}$$

(2) Spatially varying pressure equation

$$\mu_{sp}(x, t) = \sum_{j=1}^{\infty}\dot{p}_j(t)\cos\frac{j\pi}{L}\left(x + \frac{L}{2}\right), \quad x \in \left[-\frac{L}{2}, \frac{L}{2}\right]. \tag{11.42}$$

Odd modes about the centre of pressure, $j = 1, 3, 5, ...$

$$\ddot{p}_j(t) + 2\xi_j\omega_j\dot{p}_j(t) + \omega_j^2 p_j(t) = -c_{2j}\dot{\eta}_5(t) + c_1 \sum_{i=1}^{r} \cos\frac{j\pi}{L}\left(x_{Li} + \frac{L}{2}\right)\Delta A_i^{RCS}(x_{si}, t) + \rho_{c0}\dot{V}_j(t), \tag{11.43}$$

where

$$c_1 = \frac{2K_2c^2}{p_0V_{c0}}, \tag{11.44a}$$

$$c_{2j} = \frac{4\rho_{c0}Lc^2}{p_0h_0(j\pi)^2}. \tag{11.44b}$$

The wave volume pumping for regular head sea for $j = 1, 3, 5, ...$ is

$$\dot{V}_j(t) = -\frac{4c^2}{p_0h_0L}\frac{k\cos\frac{kL}{2}}{k^2 - \left(\frac{j\pi}{L}\right)^2}\omega_e\zeta_a\sin\omega_e t. \tag{11.45}$$

Even modes about the centre of pressure, $j = 2, 4, 6, ..$

$$\ddot{p}_j(t) + 2\xi_j\omega_j\dot{p}_j(t) + \omega_j^2 p_j(t) = c_1 \sum_{i=1}^{r} \cos\frac{j\pi}{L}\left(x_{Li} + \frac{L}{2}\right)\Delta A_i^{RCS}(x_{si}, t) + \rho_{c0}\dot{V}_j(t), \tag{11.46}$$

where the wave volume pumping for regular head sea for $j = 2, 4, 6, ...$ is

$$\dot{V}_j(t) = \frac{4c^2}{p_0h_0L}\frac{k\sin\frac{kL}{2}}{k^2 - \left(\frac{j\pi}{L}\right)^2}\omega_e\zeta_a\cos\omega_e t. \tag{11.47}$$

The relative damping ratio for $j = 1, 2, 3, 4, ..$ is

$$\zeta_j = \frac{\frac{c}{j\pi h_0 b}\left(\frac{K_2}{2p_0}A_0 + \frac{K_2}{2p_0}\sum_{i=1}^{r} A_{0i}^{RCS}\cos^2\frac{j\pi}{L}\left(x_{Li} + \frac{L}{2}\right) - \rho_{c0}\sum_{i=1}^{q}\left.\frac{\partial Q}{\partial p}\right|_{0i}\cos^2\frac{j\pi}{L}\left(x_{Fi} + \frac{L}{2}\right)\right)}{}. \tag{11.48}$$

(3) Heave equation

$$(m + Z_{\dot{w}})\ddot{\eta}_3(t) + Z_w\dot{\eta}_3(t) + Z_z\eta_3(t) - A_cp_0\mu_u(t) = F_3^e(t), \tag{11.49}$$

where m is the vessel mass.

(4) Pitch equation

$$(I_{33} + M_{\dot{q}})\ddot{\eta}_5(t) + M_q\dot{\eta}_5(t) + M_\theta\eta_5(t) - 2p_0b\sum_{j=1,3,5,...}\left(\frac{L}{j\pi}\right)^2\dot{p}_j(t) = F_5^e(t), \tag{11.50}$$

where I_{55} is the moment of inertia about the y-axis.

The hydrostatic $\{Z_z, M_\theta\}$-terms are found in the standard way by integration over the water plane area of the side-hulls. The hydrodynamic added-mass coefficients $\{Z_{\dot{w}}, M_{\dot{q}}\}$, the water wave radiation damping coefficients $\{Z_w, M_q\}$, and the hydrodynamic excitation force in heave $F_3^e(t)$ and moment in pitch $F_5^e(t)$, are derived from hydrodynamic loads on the side-hulls. The hydrodynamic loads on the side-hulls may be calculated as presented in Faltinsen (1993). However, since the main focus is on the high frequency range, we have used a simplified strip theory based on Salvesen et al. (1970) for calculation of the hydrodynamic loads. Neglecting the effects of transom stern and radiation damping, the hydrodynamic excitation forces on the side-hulls in heave and pitch are given by

$$F_3^e(t) = 2\zeta_a e^{-kd} \frac{\sin\frac{kL}{2}}{\frac{kL}{2}} \left(Z_z - \omega_0\omega_e Z_{\dot{w}}\right) \sin\omega_e t, \tag{11.51a}$$

$$F_5^e(t) = 2\zeta_a e^{-kd} \left[\left(\frac{1}{k}\cos\frac{kL}{2} - \frac{2}{k^2 L}\sin\frac{kL}{2}\right)\left(Z_z - \omega_0\omega_e Z_{\dot{w}}\right) - U\omega_e \frac{\sin\frac{kL}{2}}{\frac{kL}{2}} Z_{\dot{w}}\right] \cos\omega_e t, \tag{11.51b}$$

where d is the draft of the side-hulls. In the case studied here, the submerged part of side-hulls are assumed to have constant cross-section area. Examples of two-dimensional frequency depending added-mass and wave radiation damping coefficients are found in Faltinsen (1993). In the control system analysis constant two-dimensional added-mass and wave radiation damping values are assumed. The high frequency limit of the two-dimensional added-mass coefficient found in Faltinsen (1993) is used. The selected wave radiation damping coefficient in pitch corresponds to the value at the pitch resonance frequency determined from structural mass forces acting on the craft and hydrodynamic forces on the side-hulls. For heave we have chosen the wave radiation damping coefficient at the resonance frequency that will exist without the presence of the excess air cushion pressure. These simplifications are motivated by fact that the effect of damping is most pronounced about the corresponding resonance frequency.

Helmholtz equation

Above the boundary value problem was solved in the time domain, allowing us to study the transient behavior of the craft. If we assume that steady state conditions have been obtained, and that the time dependence is harmonic, the effect of spatial pressure variations in the air cushion may be investigated in the frequency domain using the Helmholtz equation (the Wave equation (11.23) transformed into frequency domain). We must then assume that the initial conditions of the dynamic variables are equal to zero. Furthermore, the craft is assumed to be exposed to regular sea waves where the transients are assumed to vanish quickly. This motivates the assumption of harmonic time dependence, $e^{i\omega_e t}$, where i is the complex unit. Hence, we write

$$\eta_3(t) = \eta_{3a}e^{i\omega_e t}, \eta_5(t) = \eta_{5a}e^{i\omega_e t}, \mu_u(t) = \mu_{ua}e^{i\omega_e t}, \mu_{sp}(t) = \mu_{spa}e^{i\omega_e t}, \tag{11.52}$$

where η_{3a} and η_{5a} are the heave and pitch motion amplitudes relatively to the coordinate frame located in the water plane below the centre of gravity, and μ_{ua} and μ_{spa} are the nondimensional uniform and spatially varying pressure amplitudes respectively. These amplitudes are generally complex and parametric functions of the frequency of encounter ω_e. Like in the ship motion problem, Salvesen et al. (1970), it is convenient to split the velocity potential $\phi_{sp}(x, z, t)$ in the air cushion into

$$\phi_{sp}(x,z,t) = \left(\phi_0(x,z)\mu_{ua} + \phi_3(x,z)\eta_{3a} + \phi_5(x,z)\eta_{5a} + \phi_7(x,z)\zeta_a + \sum_{i=1}^{r}\phi_{7+i}(x,z)\Delta A_i^{RCS}\right) e^{i\omega_e t}, \tag{11.53}$$

where $\phi_0(x,z)$, $\phi_3(x,z)$, $\phi_5(x,z)$, $\phi_7(x,z)$, $\phi_8(x,z)$, ... , ϕ_{7+r} are the spatially varying pressure potentials due to the effect of the dynamic uniform pressure, heave and pitch motion, the incident waves and the r control actions respectively. The subscript i must not be confused with the complex unit i. The frequency dependent modal amplitude functions will be determined according to the Helmholtz equation for $n = 0, 3, 5, 7, 8, ..., 7 + r$ according to

$$\left(\frac{\omega_e}{c}\right)^2 \phi_n(x,z) + \frac{\partial^2 \phi_n(x,z)}{\partial x^2} + \frac{\partial^2 \phi_n(x,z)}{\partial z^2} = 0. \tag{11.54}$$

Implicitly $\phi_n(x,z)$ is a function of the circular frequency of encounter ω_e, but this is considered as a parametric dependence. Similarly, eq. (11.25) transformed into frequency domain becomes

$$\frac{1}{h_0 b}\int_{-b/2}^{b/2} dy \left(\left.\frac{\partial \phi_n(x,z)}{\partial z}\right|_{z=h_0} - \left.\frac{\partial \phi_n(x,z)}{\partial z}\right|_{z=0} \right) + \frac{\partial^2 \psi_n(x)}{\partial x^2} + \left(\frac{\omega_e}{c}\right)^2 \psi_n(x) = 0. \tag{11.55}$$

$\psi_n(x; i\omega_e)$ is the one-dimensional spatially varying pressure for $n = 0, 3, 5, 7, 8, ..., 7 + r$ with modal representation given by

$$\psi_n(x; i\omega_e) = \sum_{j=1}^{\infty} P_{nj}(i\omega_e) r_j(x), \tag{11.56}$$

where $P_{nj}(i\omega_e)$ is the frequency dependent modal amplitude function for mode j due to action n. Due to linearity and orthogonality between the modes, we can consider each mode separately and superpose the contribution from each of them. As in the time domain, the frequency dependent modal amplitude functions have to be determined according to equation (11.55) and the remaining boundary conditions formulated in the frequency domain. By taking the inner product of equation (11.55) with the mode shape function of mode j for $j \in \{1, 2, 3, ...\}$ and using equation (11.56), we find the frequency dependent modal amplitude functions. However before doing so, it is convenient to divide the mode shape functions into even and odd modes around the origin of the coordinate frame. Thus, $j = 1, 3, 5, ...$ are representing the odd modes, while $j = 2, 4, 6, ...$ are representing the even modes. Denoting $s = i\omega_e$ to be the differential operator, equation (11.56) is written

$$\sum_{j=1}^{\infty} P_{nj}(s) r_j(x) = \sum_{j=1,3,5,..} A_{nj}(s) r_j(x) + \sum_{j=2,4,6,..} B_{nj}(s) r_j(x), \tag{11.57}$$

where $A_{nj}(s)$ and $B_{nj}(s)$ are the frequency dependent modal amplitude functions for the odd and the even modes respectively due to action n. Expressions for $A_{nj}(s)$, $B_{nj}(s)$ and the corresponding equations of motion and dynamic cushion pressure formulated in frequency domain are found in Sørensen (1993).

Discussion of the mathematical model

It is seen from (11.49) and (11.50) that the heave and pitch motions are coupled to the dynamic excess pressure in the air cushion region. This is to be expected since the major part of the SES mass is supported by the air cushion excess pressure. The dynamic air cushion pressure is expressed as the sum of the dynamic uniform pressure and the spatially varying pressure. An important question is how many acoustic modes should be included in the mathematical model.

Even if the solution is formally presented by an infinite number of acoustic modes, the modeling assumptions will not be valid in the high frequency range when two and three dimensional effects become significant. Then a more detailed numerical analysis is required, like for instance a boundary element or a finite element method. In the following we will use a finite number k acoustic modes in the mathematical model. The effect of higher order modes is assumed to be negligible. It is important to note that the air cushion dimensions and the forward speed affect the energy level of the vertical accelerations caused by the acoustic resonances. The acoustic resonance frequencies are inversely proportional to the air cushion length as seen from (11.38). The wave excitation frequency which is given by the circular frequency of encounter $\omega_e = \omega_0 + kU$, increase with the forward speed U. Thus waves of relatively low circular frequency ω_0 may excite the craft in the frequency range of the acoustic resonances when the speed U is high. This may result in more energy in the sea wave excitation about the resonance frequencies since the maximum sea wave height will tend to increase when the period of the sea waves increases. The relative damping ratio ξ_j given by (11.48) is an important parameter. As expected the leakage terms and the fan inflow term contribute to increased damping. One should notice that the fan slope $(\partial Q/\partial p)|_{oi}$, is negative. We also observe that the longitudinal placement of the fan and the louver systems strongly affects the relative damping ratio. In the case of a single fan system and a single louver system, it may seem natural to place the fan and the louver in the middle of the air cushion, that is $x_F = x_L = 0$. However, from (11.48) we observe that the relative damping ratio for the odd modes will be reduced significantly if x_L and x_F are equal to 0. Maximum damping of both the odd and even acoustic resonance modes in the case of a single lift fan system and a single louver system is obtained for x_F and x_L equal to $-L/2$ or$L/2$. The relative damping ratio of the first odd acoustic mode on a 35 m SES will increase from about 0.05 to 0.2 by placing the lift fan system at one of the ends of the air cushion instead in the middle. This gives a significant improvement in ride quality even when the ride control system is turned off. In the same manner the active damping due to the ride control system is maximized by placing the louver system at one of the ends of the air cushion.

Remark 11.1 *Here, the Faltinsen notation is used to define the coordinate frame. The hydrodynamic coefficients are written according to the SNAME (1950) notation.*

11.2.2 Robust Dissipative Controller Design

In this section a ride control system based on the mathematical model derived in the previous section is developed. The objective of the controller is to damp out pressure fluctuations about the equilibrium pressure p_0 in the presence of sea wave disturbances. This can be formulated in terms of the desired value of the nondimensional dynamic uniform pressure $\mu_u^d(t) = 0$ and the nondimensional spatially varying pressure $\mu_{sp}^d(x,t) = 0$, where the superscript d denotes the desired value.

The number of modes to be damped depends on the requirements related to established criteria for crew workability and passenger comfort. The mathematical model of the craft dynamics is of high order as it contains a high number of acoustic modes. A practical implementable controller has to be of reduced order. When designing a controller based on a reduced order model, it may happen that the truncated or residual modes give a degradation of the performance, and even instability of the closed loop system. This is analogous with the so-called spillover effect in active damping of vibrations in mechanical structures (Balas, 1978). The inadvertent excitation of the residual modes has been termed control spillover, while the unwanted contribution

of the residual modes to the sensed outputs has been termed observation-spillover, see Figure 11.5. Mode 0 is related to the uniform pressure, while the higher order modes are related to the spatially varying pressure.

The controller must be robust with respect to modeling errors and parametric and non-parametric uncertainties, nonlinearities in sensors and actuators and component failure. The use of collocated compatible actuators and sensors pairs and strictly passive controllers provides a design technique for circumventing these problems. Then louver and sensor pairs are distributed along the air cushion, preferentially in the longitudinal direction. The problem described here is closely related to the problem of vibration damping in large flexible space structures. Inspired by the work of Joshi (1989) we propose to use dissipative control for vibration damping of SES. Note that the problem of vibration damping of SES has significant differences as the dynamic system given by (11.40)-(11.51) is of third order as opposed to similar vibration damping problems of large flexible space structures that can be written as an equivalent second order mass, damper and spring system. Also here we use passivity theory in the following, whereas Joshi (1989) used Lyapunov theory. In dissipative controller synthesis using a linear design model it is possible to use standard linear synthesis methods, however, the design is complicated by the constraint that the resulting controller must satisfy appropriate passivity properties. Here, a static dissipative solution is presented where a passive controller with proportional feedback is used.

Preliminaries

The linear vector space L_2^n of real square-integrable n vector functions of time t is defined by

$$L_2^n = \left\{ \mathbf{z} : R_+ \to R^n \,\middle|\, \int_0^\infty \mathbf{z}(t)^T \mathbf{z}(t) dt < \infty \right\}. \tag{11.58}$$

Define the truncation operator P_T such that

$$\mathbf{z}_T = P_T \mathbf{z} = \begin{cases} \mathbf{z}(t) & 0 \le t \le T \\ 0 & t > 0 \end{cases}. \tag{11.59}$$

The extended spaceL_{2e}^n is then defined as

$$L_{2e}^n = \{ \mathbf{z} : R_+ \to R^n \,|\forall T \ge 0,\ \|\mathbf{z}\|_{T2} < \infty \}. \tag{11.60}$$

The respective norms $\|\cdot\|_2$ and $\|\cdot\|_{T2}$ are defined by

$$\|\mathbf{z}\|_2 = \lim_{T\to\infty} \|\mathbf{z}\|_{T2}, \tag{11.61}$$

where

$$\|\mathbf{z}\|_{T2} = (\mathbf{z},\mathbf{z})_T^{1/2} = \left(\int_0^T \mathbf{z}(t)^T \mathbf{z}(t) dt \right)^{1/2}. \tag{11.62}$$

The inner product $(\cdot,\cdot)$ of $\mathbf{x}, \mathbf{z} \in L_{2e}^n$ is

$$(\mathbf{x},\mathbf{z})_T = \int_0^T \mathbf{x}(t)^T \mathbf{z}(t) dt, \tag{11.63}$$

so that $\|\mathbf{z}\|_{T2}^2 = (\mathbf{z},\mathbf{z})_T$. If $\mathbf{x}, \mathbf{z} \in L_2^n$, then

$$(\mathbf{x},\mathbf{z}) = \lim_{t\to\infty} (\mathbf{x},\mathbf{z})_T, \tag{11.64}$$

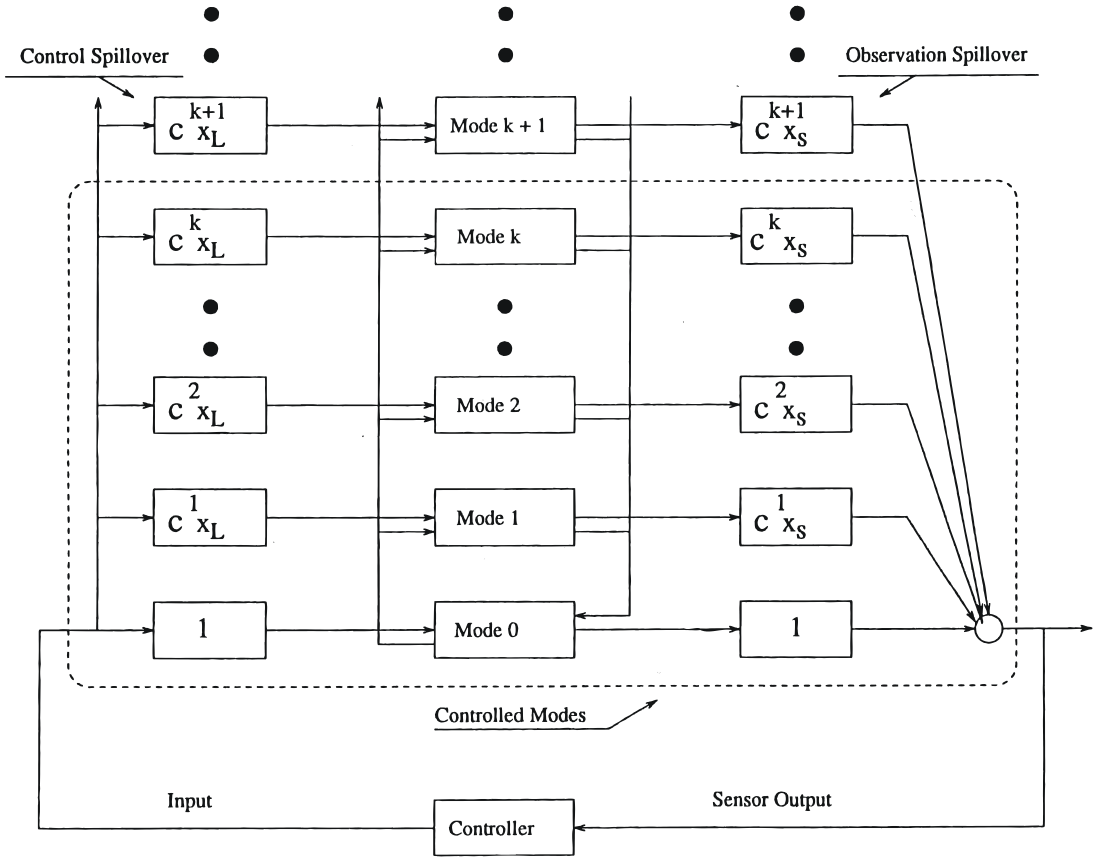

Figure 11.5: Observation and control spillover, where $C^k x_L = \cos k\pi(x_L + L/2)/L$ and $C^k x_s = \cos k\pi(x_s + L/2)/L$.

and hence $\|z\|_2^2 = (z, z)$. A function $z : R_+ \to R^n$ belongs to L_∞^n if

$$\|\mathbf{z}\|_\infty = ess \sup_{t\geq 0} |\mathbf{z}(t)| < \infty. \tag{11.65}$$

By essential supremum we mean

$$ess \sup_{t\geq 0} |\mathbf{z}(t)| = \inf_{t\geq 0} \{a|\ |\mathbf{z}(t)| < a \text{ almost everywhere}\}, \tag{11.66}$$

that is, $|\mathbf{z}(t)| \leq a$ except for a set of measure zero, and the *ess* sup is the smallest number which has that property. Notice that the L_∞^n space is a normed linear space but not an inner product space. Disturbances induced by irregular sea, and regular sea as well, are persistent for a long period of time and can be represented by sinusoids. This is the case in (11.40), (11.47), (11.45),and (11.51). Such disturbances belong to the L_∞^n space but not to the L_2^n space. On the other hand, in regular sea over a finite time interval when for example running the craft into

and out of a wave field set up by the craft itself or by other ships, the disturbances are transient and may belong to the L_2^n space. This may be modelled using the truncation operator given in (11.59) on the (11.40), (11.47), (11.45),and (11.51).

Passivity and strict passivity on L_{2e}^n are defined as:

Definition 11.1 *(Desoer and Vidyasager, 1975). Let $H : L_{2e}^n \to L_{2e}^n$. H is passive if there exist some constant β, such that*

$$(H\mathbf{u}, \mathbf{u})_T \geq \beta, \quad \forall \mathbf{u} \in L_{2e}^n, \quad \forall T \geq 0. \tag{11.67}$$

H is strictly $\mathbf{u}$-passive if there exist some $\delta_2 > 0$ and some constant β such that

$$(H\mathbf{u}, \mathbf{u})_T \geq \delta_2 \|\mathbf{u}\|_{T2}^2 + \beta, \quad \forall \mathbf{u} \in L_{2e}^n, \quad \forall T \geq 0. \tag{11.68}$$

Definition 11.2 *(Desoer and Vidyasager, 1975). Let $H : L_{pe}^n \to L_{pe}^n$. The mapping H is L_p^n stable with finite gain if $H\mathbf{u} \in L_p^n$ whenever $\mathbf{u} \in L_p^n$ and there exist finite constants γ and α such that*

$$\|H\mathbf{u}\|_p \leq \gamma \|\mathbf{u}\|_p + \alpha, \quad \forall \mathbf{u} \in L_p^n, \quad p \in [1, \infty]. \tag{11.69}$$

If $\alpha = 0$, the mapping H is L_p^n stable with finite gain and zero bias.

State space model

The dynamic system given by (11.40)-(11.51b) is written in standard state space form according to

$$\dot{\mathbf{x}}(t) = \mathbf{A}\mathbf{x}(t) + \mathbf{B}\mathbf{u}(t) + \mathbf{E}\nu(t), \tag{11.70a}$$

$$\mathbf{y}(t) = \mathbf{C}\mathbf{x}(t), \tag{11.70b}$$

where the n-dimensional state vector $\mathbf{x}(t)$ is

$$\mathbf{x}(t) = [\eta_3, \eta_5, \dot{\eta}_3, \dot{\eta}_5, \mu_u, p_1, p_2, ..., p_k, \dot{p}_1, \dot{p}_2, ..., \dot{p}_k]^T. \tag{11.71}$$

$v(t)$ is the $(3+k)$-dimensional disturbance vector defined as

$$\nu(t) = \left[F_3^e, F_5^e, \dot{V}_0, \dot{V}_1, \dot{V}_2, \cdots, \dot{V}_k\right]^T, \tag{11.72}$$

where $F_3^e(t)$, $F_5^e(t)$ and the time derivative $\dot{V}_i(t)$ for $i = 0, 1, 2, ..., k$ are found in Section 11.2.1. k is the number of acoustic modes. $\mathbf{u}(t)$ is the r-dimensional control input vector, and r is the number of louvers. The elements of $\mathbf{u}(t) = [u_1, u_2, .., u_r]^T$ are for $i = 1, 2, ..., r$

$$u_i(t) = \Delta A_i^{RCS}(x_{si}, t), \tag{11.73}$$

where $\Delta A_i^{RCS}(x_{si}, t)$ is defined in (11.15). $\mathbf{y}(t)$ is the m-dimensional measurement vector, and m is the number of pressure sensors. The symbolic expressions for the $n \times n$ system matrix $\mathbf{A}$, the $n \times r$ control input matrix $\mathbf{B}$, the $n \times (3+k)$ disturbance matrix $\mathbf{E}$, and the $m \times n$ measurement matrix $\mathbf{C}$ are defined below.

The $n \times n$ system matrix is given by

$$\mathbf{A} = \begin{bmatrix} \mathbf{A1}_{5\times5} & \mathbf{0}_{5\times k} & \mathbf{A2}_{5\times k} \\ \mathbf{0}_{k\times5} & \mathbf{0}_{k\times k} & \mathbf{I}_{k\times k} \\ \mathbf{A3}_{k\times5} & \mathbf{A4}_{4\times4} & \mathbf{A5}_{k\times k} \end{bmatrix}, \tag{11.74}$$

where $\mathbf{0}_{5\times k}$, $\mathbf{0}_{k\times 5}$ and $\mathbf{0}_{k\times k}$ are the $5\times k$, $k\times 5$ and $k\times k$ zero matrices respectively. $\mathbf{I}_{k\times k}$ is the $k\times k$ identity matrix. $\mathbf{A1}_{5\times 5}$ is defined as

$$\mathbf{A1}_{5\times 5} = \begin{bmatrix} 0 & 0 & 1 & 0 & 0 \\ 0 & 0 & 0 & 1 & 0 \\ -\frac{Z_z}{m+Z_{\dot{w}}} & 0 & -\frac{Z_w}{m+Z_{\dot{w}}} & 0 & \frac{A_c p_0}{m+Z_{\dot{w}}} \\ 0 & -\frac{M_\theta}{I_{55}+M_{\dot{q}}} & 0 & -\frac{M_q}{I_{55}+M_{\dot{q}}} & 0 \\ 0 & 0 & -\frac{\rho_{c0}A_c}{K_1} & 0 & -\frac{K_3}{K_1} \end{bmatrix}. \tag{11.75}$$

$\mathbf{A2}_{5\times k}$ is defined as

$$\mathbf{A2}_{5\times k} = \begin{bmatrix} 0 & 0 & 0 & 0 & 0 & \cdots & 0 \\ 0 & 0 & 0 & 0 & 0 & \cdots & 0 \\ 0 & 0 & 0 & 0 & 0 & \cdots & 0 \\ d_1 & 0 & d_3 & 0 & d_5 & \cdots & 0 \\ 0 & 0 & 0 & 0 & 0 & \cdots & 0 \end{bmatrix}, \tag{11.76}$$

where

$$d_j = \frac{2p_0 b}{I_{55}+M_{\dot{q}}}\left(\frac{L}{j\pi}\right)^2. \tag{11.77}$$

$\mathbf{A3}_{k\times 5}$ is defined as

$$\mathbf{A3}_{k\times 5} = \begin{bmatrix} 0 & 0 & 0 & g_1 & 0 \\ 0 & 0 & 0 & 0 & 0 \\ 0 & 0 & 0 & g_3 & 0 \\ \vdots & \vdots & \vdots & \vdots & \vdots \\ 0 & 0 & 0 & 0 & 0 \end{bmatrix}, \tag{11.78}$$

where

$$g_j = -\frac{4\rho_{c0}Lc^2}{p_0 h_0 (j\pi)^2}. \tag{11.79}$$

$\mathbf{A4}_{k\times k}$ and $\mathbf{A5}_{k\times k}$ are defined as

$$\mathbf{A4}_{k\times k} = \mathrm{diag}\left\{-\omega_j^2\right\}, \tag{11.80}$$

$$\mathbf{A5}_{k\times k} = \mathrm{diag}\left\{-2\xi_j\omega_j\right\}. \tag{11.81}$$

The $n\times(3+k)$ disturbances matrix is defined as

$$\mathbf{E} = \begin{bmatrix} 0 & 0 & 0 & 0 & 0 & \cdots & 0 \\ 0 & 0 & 0 & 0 & 0 & \cdots & 0 \\ \frac{1}{m+Z_{\dot{w}}} & 0 & 0 & 0 & 0 & \cdots & 0 \\ 0 & \frac{1}{I_{55}+M_{\dot{q}}} & 0 & 0 & 0 & \cdots & 0 \\ 0 & 0 & \frac{\rho_{c0}}{K_1} & 0 & 0 & \cdots & 0 \\ & & & \mathbf{0}_{k\times(3+k)} & & & \\ & \mathbf{0}_{k\times 3} & & & \rho_{c0}\mathbf{I}_{k\times k} & & \end{bmatrix}. \tag{11.82}$$

The $n \times r$ control input matrix is given by

$$\mathbf{B} = \begin{bmatrix} 0 & 0 & \cdots & 0 \\ 0 & 0 & \cdots & 0 \\ 0 & 0 & \cdots & 0 \\ 0 & 0 & \cdots & 0 \\ \frac{K_2}{K_1} & \frac{K_2}{K_1} & \cdots & \frac{K_2}{K_1} \\ & \mathbf{0}_{k\times r} & & \\ c_1 \cos\frac{\pi}{L}\left(x_{L1}+\frac{L}{2}\right) & c_1 \cos\frac{\pi}{L}\left(x_{L2}+\frac{L}{2}\right) & \cdots & c_1 \cos\frac{\pi}{L}\left(x_{Lr}+\frac{L}{2}\right) \\ c_1 \cos\frac{2\pi}{L}\left(x_{L1}+\frac{L}{2}\right) & c_1 \cos\frac{2\pi}{L}\left(x_{L2}+\frac{L}{2}\right) & \cdots & c_1 \cos\frac{2\pi}{L}\left(x_{Lr}+\frac{L}{2}\right) \\ \vdots & & & \\ c_1 \cos\frac{k\pi}{L}\left(x_{L1}+\frac{L}{2}\right) & c_1 \cos\frac{k\pi}{L}\left(x_{L2}+\frac{L}{2}\right) & \cdots & c_1 \cos\frac{k\pi}{L}\left(x_{Lr}+\frac{L}{2}\right) \end{bmatrix}, \tag{11.83}$$

where

$$c_1 = \frac{2K_2c^2}{p_0V_{c0}}. \tag{11.84}$$

The $m \times n$ measurement matrix is given by

$$\mathbf{C}^T = \begin{bmatrix} 0 & 0 & \cdots & 0 \\ 0 & 0 & \cdots & 0 \\ 0 & 0 & \cdots & 0 \\ 0 & 0 & \cdots & 0 \\ 1 & 1 & \cdots & 1 \\ & \mathbf{0}_{k\times m} & & \\ \cos\frac{\pi}{L}\left(x_{s1}+\frac{L}{2}\right) & \cos\frac{\pi}{L}\left(x_{s2}+\frac{L}{2}\right) & \cdots & \cos\frac{\pi}{L}\left(x_{sm}+\frac{L}{2}\right) \\ \cos\frac{2\pi}{L}\left(x_{s1}+\frac{L}{2}\right) & \cos\frac{2\pi}{L}\left(x_{s2}+\frac{L}{2}\right) & \cdots & \cos\frac{2\pi}{L}\left(x_{sm}+\frac{L}{2}\right) \\ \vdots & & & \\ \cos\frac{k\pi}{L}\left(x_{s1}+\frac{L}{2}\right) & \cos\frac{k\pi}{L}\left(x_{s2}+\frac{L}{2}\right) & \cdots & \cos\frac{k\pi}{L}\left(x_{sm}+\frac{L}{2}\right) \end{bmatrix}. \tag{11.85}$$

Consider the case where sensors and actuators are ideal, that is linear and instantaneous with no noise. It is assumed that the control input matrix $\mathbf{B}$ can be related to the measurement matrix $\mathbf{C}$ so that

$$\mathbf{C} = \mathbf{B}^T\mathbf{P}, \tag{11.86}$$

where $\mathbf{P}$ is a $n \times n$ symmetric positive definite matrix providing correct scaling of the $\mathbf{B}^T$ matrix to the $\mathbf{C}$ matrix. This is the case when there is perfect collocation between the sensors and the louvers, i.e. $x_{Li} = x_{si}$ for all i and $r = m$. We can derive the linear time-invariant operators between the outputs and the inputs of the dynamic system given by (11.70). Denote s to be the differential operator. Since the pair $(\mathbf{A}, \mathbf{B})$ is controllable, and the pair $(\mathbf{C}, \mathbf{A})$ is observable, the dynamic system can be represented by

$$\mathbf{y}(s) = H_p(s)\mathbf{u}(s) + H_d(s)\nu(s) = \mathbf{y}_u(s) + \mathbf{y}_\nu(s), \tag{11.87}$$

where

$$H_p(s) = \mathbf{C}(\mathbf{s}\mathbf{I}_n - \mathbf{A})^{-1}\mathbf{B}, \tag{11.88}$$

$$H_d(s) = \mathbf{C}(\mathbf{s}\mathbf{I}_n - \mathbf{A})^{-1}\mathbf{E}, \tag{11.89}$$

and $\mathbf{I}_n$ is the $n \times n$ identity matrix.

Stability properties of the control system

In this section a strictly passive controller with finite gain is proposed. Employing the definitions of passivity as presented in Desoer and Vidyasager (1975) and in Vidyasager (1993) on an interconnected system consisting of a two subsystems in a standard feedback configuration (Figure 11.6), robust stability of the feedback system can be shown for certain input-output properties of the subsystems. The following lemma showing that the $n \times n$ system matrix $\mathbf{A}$ is Hurwitz will then be utilized.

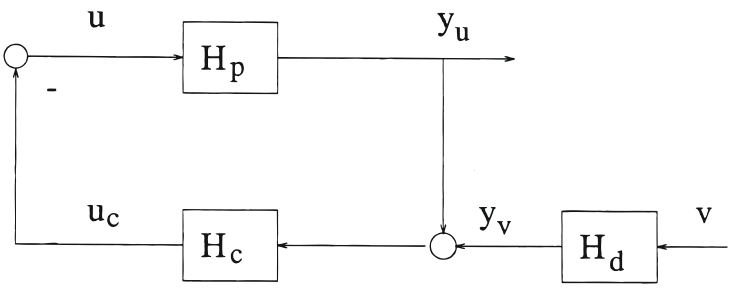

Figure 11.6: Feedback system.

Lemma 11.1 *The eigenvalues of the $n \times n$ system matrix $\mathbf{A}$ given in (11.70) have negative real parts.*

Proof. Consider the autonomous system of (11.70) with $\mathbf{u}(t) = \nu(t) = 0$. Define the Lyapunov function candidate

$$V(\mathbf{x}) = \frac{1}{2}\mathbf{x}^T\mathbf{P}\mathbf{x} > 0, \tag{11.90}$$

where the $n \times n$ diagonal positive definite matrix $\mathbf{P}$ is given below. $V(\mathbf{x})$ is positive definite. The time derivative of $V(\mathbf{x})$ along system trajectories is

$$\dot{V}(\mathbf{x}) = \frac{1}{2}\mathbf{x}^T\left(\mathbf{A}^T\mathbf{P} + \mathbf{P}\mathbf{A}\right)\mathbf{x} = -\frac{1}{2}\mathbf{x}^T\mathbf{Q}\mathbf{x} \leq 0. \tag{11.91}$$

The $n \times n$ diagonal positive semidefinite matrix $\mathbf{Q}$ is

$$\mathbf{Q} = diag\left\{\mathbf{0}_{2\times 2}, \mathbf{Q1}_{3\times 3}, \mathbf{0}_{k\times k}, \mathbf{Q2}_{k\times k}\right\}. \tag{11.92}$$

The 3×3 diagonal positive definite $\mathbf{Q1}_{3\times 3}$ matrix is defined

$$\mathbf{Q1}_{3\times 3} = diag\left\{q_{ii}\right\}, \quad i = 3, 4, 5,$$

where

$$q_{33} = p_{33}\frac{2Z_w}{m + Z_{\dot{w}}}, \tag{11.93a}$$

$$q_{44} = p_{44}\frac{2M_q}{m + M_{\dot{q}}}, \tag{11.93b}$$

$$q_{55} = p_{55}\frac{2K_3}{K_1}. \tag{11.93c}$$

The $k \times k$ diagonal positive definite $\mathbf{Q2}_{k\times k}$ matrix is

$$\mathbf{Q2}_{k\times k} = diag\left\{q_{ii}\right\}, \quad i = 5+k+1, 5+k+2, ..., 5+2k, \tag{11.94}$$

where

$$q_{(5+k+j)(5+k+j)} = p_{(5+k+j)(5+k+j)} 4\xi_j \omega_j, \quad j = 1, 2, 3, ..., k. \tag{11.95}$$

The $n \times n$ diagonal positive definite matrix $\mathbf{P}$ is found to be

$$\mathbf{P} = diag\left\{p_{ii}\right\}, \quad i = 1, 2, ..., 5+2k, \tag{11.96}$$

where

$$p_{11} = p_{33}\frac{Z_z}{m+Z_{\dot{w}}}, \tag{11.97a}$$

$$p_{22} = p_{44}\frac{M_\theta}{I_{55}+M_{\dot{q}}}, \tag{11.97b}$$

$$p_{33} = p_{55}\frac{\rho_{c0}\left(m+Z_{\dot{w}}\right)}{K_1 p_0}, \tag{11.97c}$$

$$p_{44} = -\frac{g_1}{d_1 c_1}, \tag{11.97d}$$

$$p_{55} = \frac{K_1}{\rho_{c0}}K_2, \tag{11.97e}$$

$$p_{jj} = \frac{\omega_j^2}{c_1}, \quad j = 6, 7, ..., 5+k, \tag{11.97f}$$

$$p_{jj} = \frac{1}{c_1}, \quad j = 6+k, 7+k, ..., 2k, \tag{11.97g}$$

and where c_1 is defined in (11.44a). From (11.70) it is seen that

$$\dot{V}(\mathbf{x}) = 0, \tag{11.98}$$

$$\Downarrow$$

$$\mathbf{x} = \mathbf{x}_0 = \left[\eta_3, \eta_5, 0, 0, 0, p_1, p_2, ..., p_k, 0, 0, ..., 0\right]^T. \tag{11.99}$$

Consequently

$$\ddot{\eta}_3 = \ddot{\eta}_5 = \dot{\mu}_u = \ddot{p}_1 = \ddot{p}_2 = \cdots = \ddot{p}_k = 0, \tag{11.100}$$

which implies

$$\eta_3 = \eta_5 = p_1 = p_2 = \cdots = p_k = 0. \tag{11.101}$$

Hence, by the invariant set theorem (Vidyasager, 1993) the equilibrium point $\mathbf{x}_0 = 0$ is asymptotically stable and the result of Lemma follows. ■

Define the linear time-invariant operators $H_p : L_{2e}^m \to L_{2e}^r (r = m)$ and $H_d : L_2^{3+k} \to L_2^m$, such that $\mathbf{y}_v \in L_2^m$ whenever $\mathbf{v} \in L_2^{3+k}$. In the following lemma it is shown that the process operator H_p is passive. This allows for the design of robust, stable output feedback controllers for ride control of SES.

Lemma 11.2 *The process operator H_p is passive.*

Proof. Set $\nu(t) = 0$ in (11.70) and use the Lyapunov function candidate as given in (11.90). $V(\mathbf{x})$ is positive definite. The time derivative $\dot{V}(\mathbf{x})$ along the system trajectories is

$$\dot{V}(\mathbf{x}) = \frac{1}{2}\mathbf{x}^T \left(\mathbf{A}^T\mathbf{P} + \mathbf{PA}\right)\mathbf{x} + \mathbf{x}^T\mathbf{PBu}. \tag{11.102}$$

The $n \times n$ diagonal positive semidefinite matrix $\mathbf{Q}$ is given in (11.92). Thus, if we assume perfect collocation between the sensor and actuator pairs, that is $\mathbf{C} = \mathbf{B}^T\mathbf{P}$, (11.102) becomes

$$\begin{aligned} \dot{V}(\mathbf{x}) &= \mathbf{x}^T\mathbf{C}^T\mathbf{u} - \frac{1}{2}\mathbf{x}^T\mathbf{Qx}, & (11.103)\\ &= \mathbf{y}_u^T\mathbf{u} - \frac{1}{2}\mathbf{x}^T\mathbf{Qx}. & (11.104) \end{aligned}$$

Integrating (11.104) from $t = 0$ to $t = T$ we obtain

$$(\mathbf{y}_u, \mathbf{u})_T = V(t = T) - V(t = 0) + \frac{1}{2}\int_0^T \mathbf{x}^T\mathbf{Qx}\, dt. \tag{11.105}$$

Since$\mathbf{Q} \geq 0$ and $V(t = T) > 0$, (11.105) can be written

$$(\mathbf{y}_u, \mathbf{u})_T \geq -V(t = 0) \triangleq \beta, \tag{11.106}$$

and the result of Lemma 2 follows. ■

Remark 11.2 *It is seen from (11.71) that if the initial conditions are equal to zero that is* $\mathbf{x}(t = 0) = 0$*, then* $\beta = -\mathbf{x}^T(t = 0)\mathbf{Px}(t = 0) = 0$.

Remark 11.3 *The transfer matrix* $H_d(s)$ *of the linear time-invariant operator* H_d *as defined by (11.89) is strictly proper and all the poles have negative real parts according to Lemma 1. Hence, if* $\nu \in L_2^{3+k}$*, then* $\mathbf{y}_v = H_d\mathbf{v} \in L_2^m \cap L_\infty^m$.

Let the controller be defined as the linear time-invariant operator H_c between the input $\mathbf{y} = \mathbf{y}_u + \mathbf{y}_v$ and the output $\mathbf{u}_c$. Connecting the H_c operator together with the H_p and H_d operators, we obtain the feedback system illustrated in Figure 11.6. The transfer matrix of H_c is denoted $H_c(s)$.

Proportional control law

A strictly **u**-passive proportional pressure feedback controller of dimension $r \times r$ with finite gain is proposed according to

$$\begin{aligned} \mathbf{u}_c(s) &= H_c(s)\mathbf{y}(s), & (11.107)\\ H_c(s) &= \mathbf{G}_p, \end{aligned}$$

where $\mathbf{G}_p = diag\{g_{pi}\} > 0$ is a constant diagonal feedback gain matrix of dimension $r \times r$. This control law provides enhanced damping of the pressure variations about the resonance frequencies.

The main result of this section is given by the following theorem.

Theorem 11.1 *Consider the following feedback system (see Figure 11.6)*

$$\begin{aligned} \mathbf{y}_u &= H_p\mathbf{u}, && (11.108)\\ \mathbf{y}_\nu &= H_d\nu, && (11.109)\\ \mathbf{y} &= \mathbf{y}_u + \mathbf{y}_\nu, && (11.110)\\ \mathbf{u} &= -\mathbf{u}_c = -H_c\mathbf{y}, && (11.111) \end{aligned}$$

where $H_p, H_c : L_{2e}^m \to L_{2e}^m$. *Assume that* $H_d : L_2^{3+k} \to L_2^m$, *so that* $\mathbf{y}_v \in L_2^m$ *whenever* $\nu \in L_2^{3+k}$. H_c *is strictly* $\mathbf{u}$*-passive with finite gain, and* H_p *is passive. Hence, the feedback system defined above is* L_2^m *stable, and since the feedback system given by* H_p, H_p *and* H_c *is linear,*L_2^m *stability is equivalent to* L_∞^m *(BIBO) stability.*

Proof. Set $\mathbf{v}(t) = 0$ in (11.70) and use the Lyapunov function candidate as given in (11.90). $V(\mathbf{x})$ is positive definite. If we assume perfect collocation between the sensor and actuator pairs, that is $\mathbf{C} = \mathbf{B}^T\mathbf{P}$, the time derivative $\dot{V}(\mathbf{x})$ along the closed loop system trajectory becomes

$$\begin{aligned} \dot{V}(\mathbf{x}) &= -\mathbf{y}_u^T\mathbf{G}_p\mathbf{y}_u - \frac{1}{2}\mathbf{x}^T\mathbf{Q}\mathbf{x},\\ &= -\mathbf{x}^T\left(\mathbf{C}^T\mathbf{G}_p\mathbf{C} + \frac{1}{2}\mathbf{Q}\right)\mathbf{x}, && (11.112) \end{aligned}$$

where the $n \times n$ diagonal positive semidefinite matrix $\mathbf{Q}$ is given in (11.92). It can be shown by inspection that

$$\mathbf{C}^T\mathbf{G}_p\mathbf{C} + \frac{1}{2}\mathbf{Q} \geq 0, \qquad (11.113)$$

since the first term in (11.112) is on quadratic form for diagonal $\mathbf{G}_p > 0$, and hence positive semidefinite. The time derivative $\dot{V}(\mathbf{x})$ is negative semidefinite. Using the invariant set theorem (Vidyasager, 1993) the equilibrium point of the closed-loop system is asymptotically stable and the result follows. ■

L_2^m and L_∞^m stability of the closed-loop system using collocated sensor and actuator pairs is maintained regardless of the number of modes, and regardless of the inaccuracy in the knowledge of the parameters. Thus the spillover problem is eliminated and the parameters do not have to be known in advance to obtain stability. Notice that there are no restrictions to the location of the collocated sensor and actuator pairs with respect to stability. However, optimizing the performance, the longitudinal location of the sensor actuator pairs is crucial as seen in (11.48). Robustness with respect to unmodelled dynamics and sector nonlinearities in the actuators are shown in Sørensen et al. (1993). It is further shown by Sørensen et al. (1993) that some imprecision in the collocated sensor and actuator pairs can be accepted without violating the stability properties of the closed-loop system

11.2.3 Simulation and Full Scale Results

In this section numerical simulations and results from full scale trials with a 35 m SES advancing forward at high speed in head sea waves are presented. The effect of collocation and noncollocation of the sensor and actuator pairs for the 35 m SES is investigated. The SES is equipped with one single fan and louver system. The number of acoustic modes considered in the simulation model is four, i.e. $k = 4$. Main dimensions and data of the SES craft are given in Table 11.1.

Length overall	35 m
Equilibrium fan flow rate	150 $m^3/\ s$
Linear fan slope	-140 $m^2/\ s$
Cushion length	28 m
Nom. cushion pressure	500 $mmWc$
Cushion beam	8 m
Cushion height	2 m
Weight	150 ton
Speed	50 knots

Table 11.1: SES main dimensions.

Remark 11.4 *One should notice that often* $mmWc$ *is used as unit for the pressure. The relation between* mmWc *and* Pa *(Pascal) is* $1\text{mm}Wc = \frac{1}{1000}\text{m} \cdot 1000\frac{\text{kg}}{\text{m}^3} \cdot 9.81\frac{\text{m}}{\text{s}^2} = 9.81\frac{\text{kg}}{\text{ms}^2} =$ 9.81Pa.

Numerical simulations

Figure 11.7 shows the Bode plot of $H_p(i\omega_e)$ between the pressure sensor $y_u(s)$ and the louver $u(s)$ when the pressure sensor and actuator pair is fully collocated. The sensor and louver pair is located at the fore end of the air cushion. When the frequency of encounter goes to zero, the dynamic pressure tends to a static value proportional to K_1/K_2. This indicates that the equilibrium pressure p_0 will decrease when the equilibrium leakage area increases and vice versa. about 0.1 Hz the response is close to zero. This is related to the structural mass forces acting on the SES and the hydrodynamic forces acting on the side-hulls. The high value about 2 Hz is due to the resonance of the dynamic uniform pressure. The high values about 6 Hz, 12 Hz, 18 Hz and 24 Hz are related to the four acoustic resonance modes. From the phase plot we observe that the phase is varying between 90° to −90° in the whole frequency range. This is to be expected when using collocated sensor and actuator pairs.

Figure 11.8 shows the Bode plots of $H_p(i\omega_e)$ for the case the pressure sensor is located at the fore end of the air cushion while the louver is located at the aft end of the air cushion. From the phase plot we observe that the sensed pressure signal at the fore end is 180° out of phase compared to the pressure signal at the aft end where the louver is located. This is to be expected with noncollocated sensor and louver pairs. Noncollocated sensor and actuator pairs introduce negative phase and may lead to instability.

Full scale results

The prototype ride control system used in the full scale experiments was based on the passive controller as presented in Section 11.2.2. The control algorithms in the ride control system were partly implemented on a personal computer (PC) and partly analog hardware devices were used. An outer feedback loop was implemented on the PC, while a faster inner feedback loop about the electro-hydraulic louver system was implemented by analog hardware devices. The lover system consisted of two vent valves located at the same longitudinal position $x_L = 8\ m$ side by side. The two vent valves were operated in parallel in the outer feedback loop. Two pressure sensors located at $x_{s1} = 10\ m$ and $x_{s2} = -10\ m$ were used to measure the excess pressure variations in the air cushion. One accelerometer located about 5 m aft of the centre of

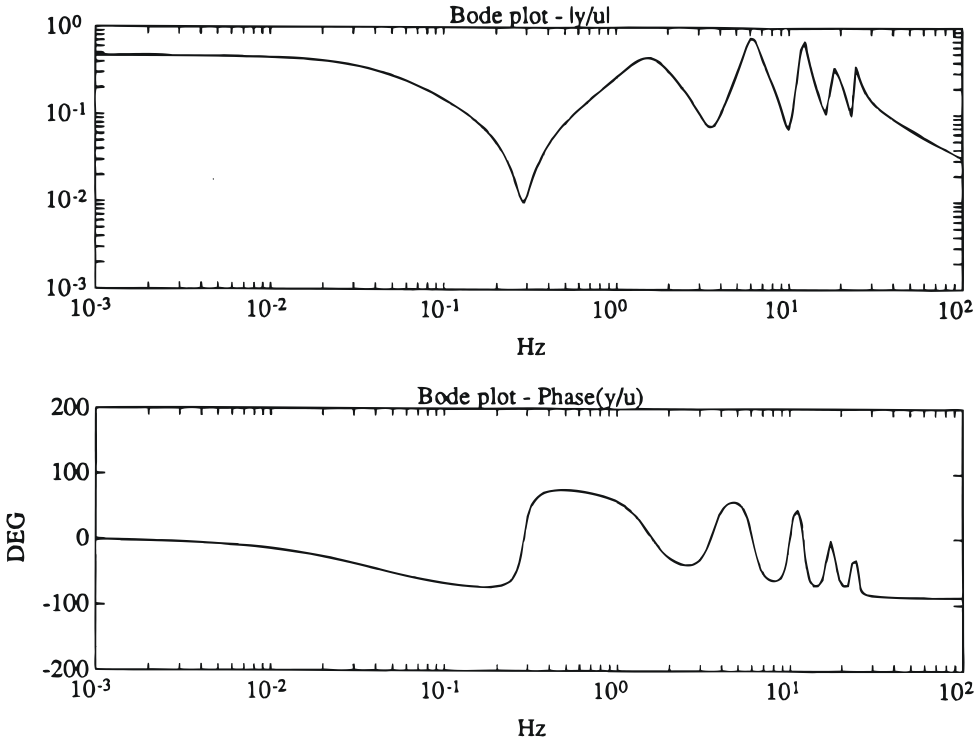

Figure 11.7: Collocated sensor and actuator pair; numerically calculated Bode plot of $H_p(i\omega_e)$; $x_L = x_s = 12\ m, x_F = 6m, U = 50$ knots, $p_0 = 500mmWc$.

gravity was used to measure the vertical accelerations. The inner analog controller loop around the louver system provided the necessary opening and closing actions of the vent valves. The experiment arrangement is illustrated in Figure 11.9. The full scale measurements were carried out in sea states with significant wave heights estimated to vary between $0.3 - 0.6\ m$. The power spectra of the vertical accelerations with and without the ride control system are presented.

Figure 11.10 shows the full scale power spectra of the vertical accelerations about 5 m aft of the centre of gravity with and without the ride control system activated. With the ride control system turned off, we observed significant response about 2 Hz, 5 Hz and 8 Hz. The response about 2 Hz is related to the resonance of the dynamic uniform pressure, while the response about 5 Hz and 8 Hz are related to the first odd and even resonance modes. Activating the ride control system the response about 5 Hz was significantly amplified, while the response about 2 Hz was only slightly reduced. In this case the pressure signal at $x_{s2} = -10\ m$ was used in the feedback loop. Hence, the actuator and sensor pair were completely noncollocated since the louver was located at $x_L = 8\ m$. This means that for the first odd mode, the noncollocation resulted in positive feedback for this particular mode because the pressure at the sensor location was 180° out of phase compared to the pressure at the actuator location in the frequency range dominated by the first odd acoustic resonance mode. The response about 8 Hz was more or less unchanged. Both time series were taken when the craft was advancing forward with the speed $U = 45\ knots$ in head sea waves with significant wave height estimated to be $H_s = 0.3\ m$.

Figure 11.11 shows the full scale power spectra of the excess pressure variations at $x_{s1} = 10\ m$ in the air cushion with and without the ride control system activated. The time series were taken

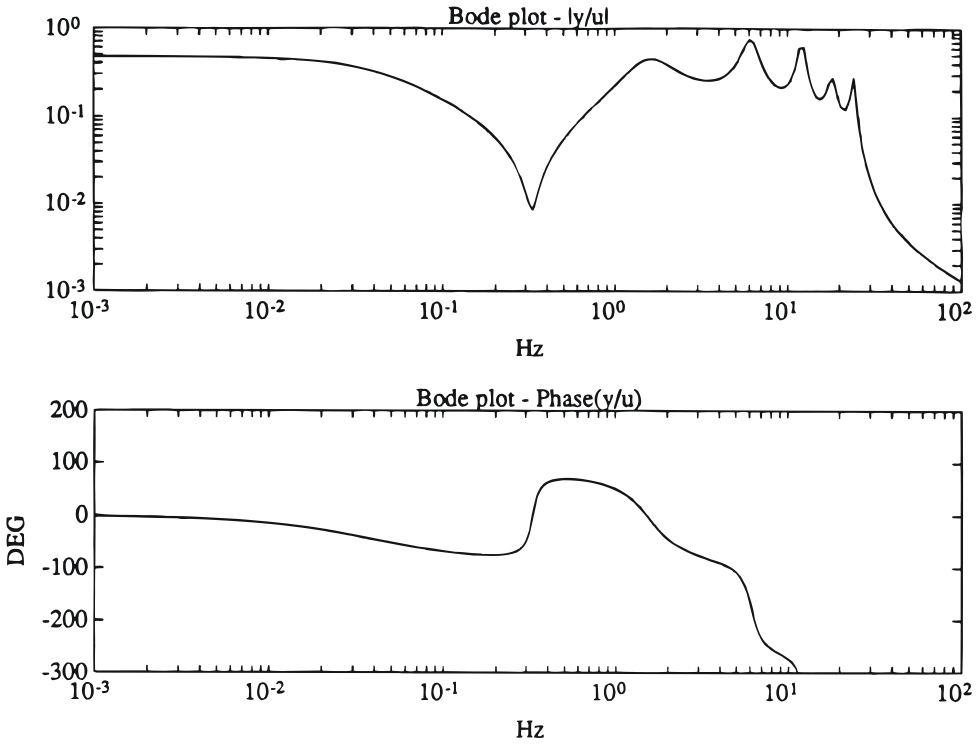

Figure 11.8: Noncollocated sensor and actuator pair; numerically calculated Bode plot of $H_p(i\omega_e)$; $x_s = 12\ m,\ x_L = -12\ m,\ x_F = 6\ ,\ U = 50$ knots $, p_0 = 500\ mmWc.$

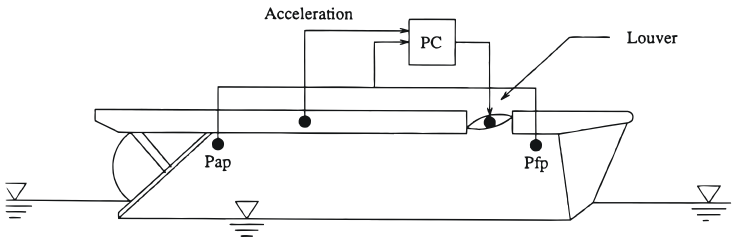

Figure 11.9: Experimental arrangement.

from the same run as above. The pressure signal at $x_{s3} = -10\ m$ was used in the feedback loop. Hence, the louvers and sensors were completely noncollocated. With the ride control system turned off, we observed response about 2 Hz and 5 Hz. Activating the ride control system the response about 5 Hz was significantly amplified. At the resonance of the dynamic pressure about 2 Hz the response level was reduced by the ride control system.

Figure 11.12 shows the full scale power spectra of the vertical accelerations about 5 m aft of the centre of gravity with and without the ride control system activated. In this case the pressure signal at $x_{s1} = 10\ m$ was used in the feedback loop. Hence, the louvers and sensors were "almost" collocated since the louver were located at $x_L = 8\ m$. With the ride control system turned off, we observed response about 2 Hz, 5 Hz and 8 Hz. Activating the ride control system the response about all three resonance frequencies were significantly reduced. These

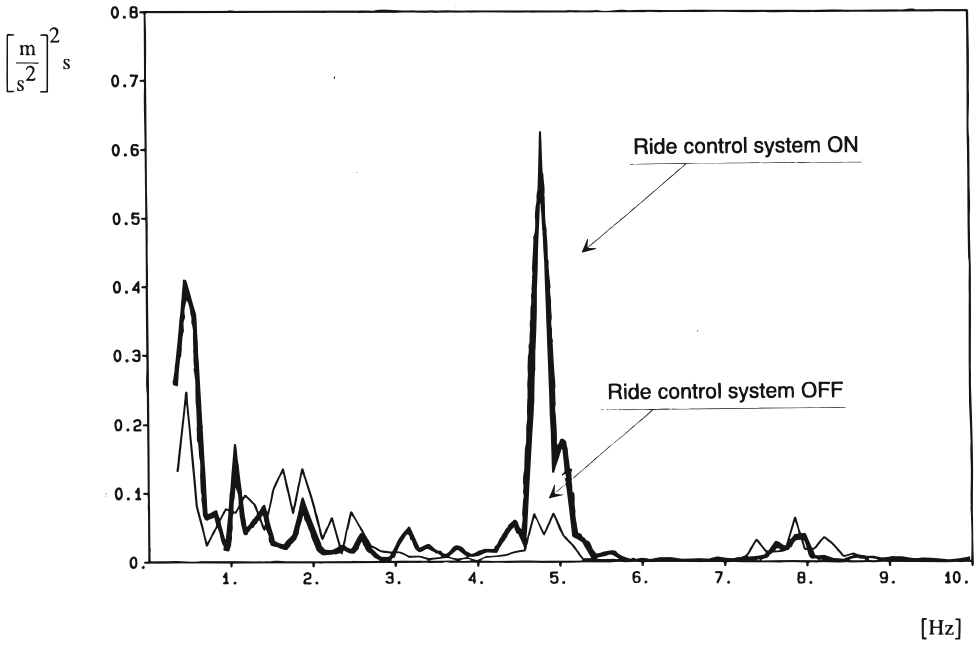

Figure 11.10: Noncollocated sensor and actuator pair; full-scale power spectra of the vertical accelerations at $x = -5\ m$ of a $35m$ SES with ride control system on and off; $p_0 = 450\ mmWc$.

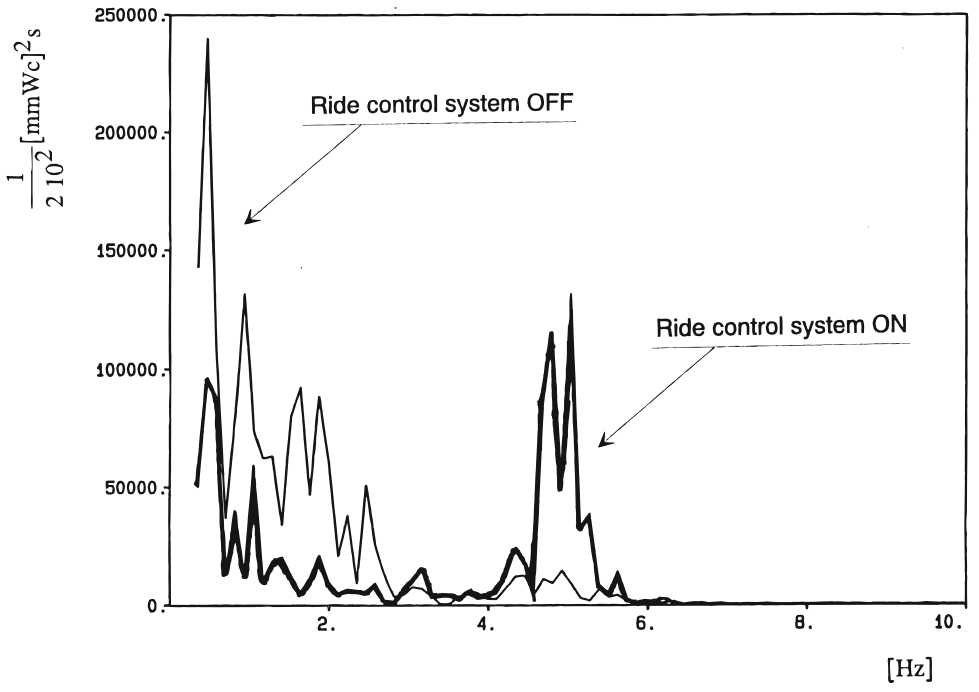

Figure 11.11: Noncollocated sensor and actuator pair; full-scale power spectra of the excess pressure at $x = 10\ m$ of a $35\ m$ SES with ride control system on and off; $p_0 = 450\ mmWc$.

time series were taken when the craft was advancing forward with the speed $U = 44$ knots in head sea waves with significant wave height estimated to be $H_s = 0.6m$.

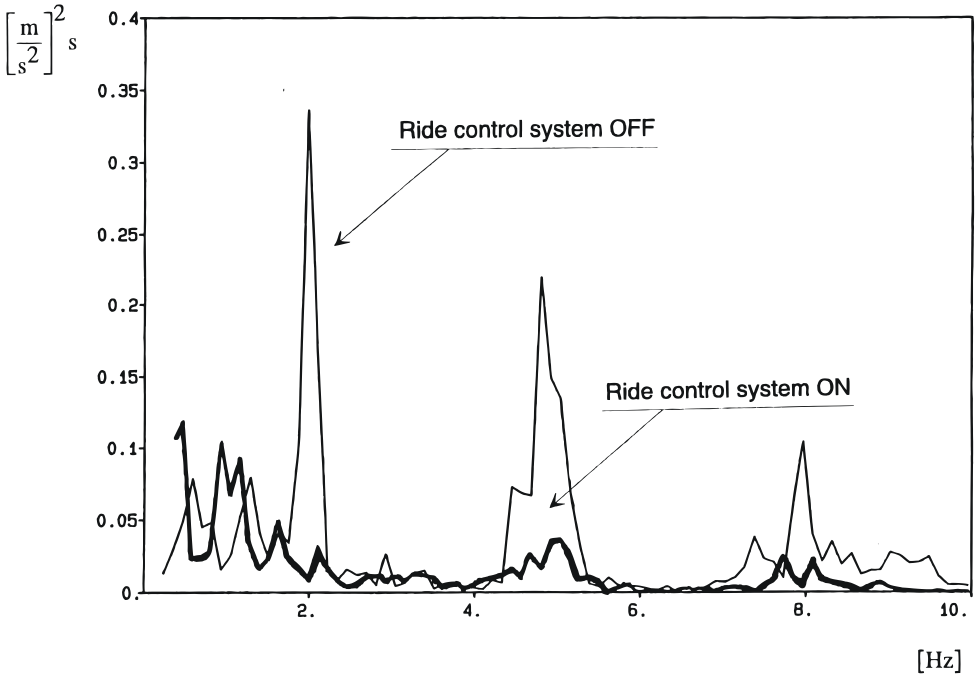

Figure 11.12: Collocated sensor and actuator pair; full-scale power spectra of the vertical accelerations at $x = -5$ m of a 35 m SES with ride control system on and off; $p_0 = 430$ $mmWc$.

Figure 11.13 shows the full scale power spectra of the excess pressure variations at $x_{s1} = 10$ m in the air cushion with and without the ride control system activated. The time series were taken from the same run as in Figure 11.12. The pressure signal at $x_{s1} = 10$ m was used in the feedback loop. Hence, the louvers and sensors were "almost" collocated. With the ride control system turned off, we observed response about 2 Hz and 5 Hz at the fore end of the air cushion. Activating the ride control system the response about all three resonance frequencies were significantly reduced.

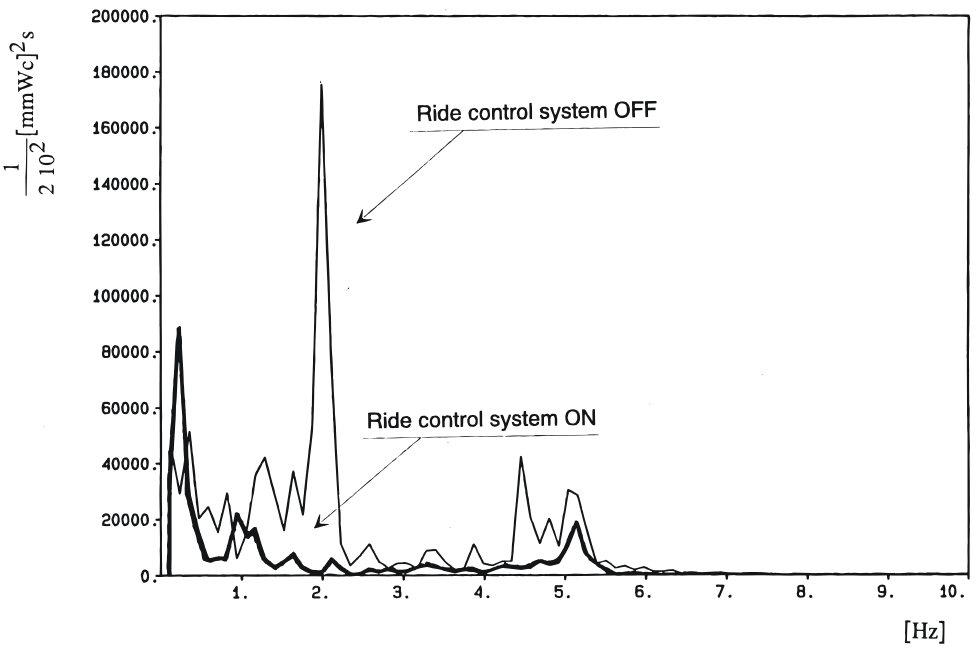

Figure 11.13: Collocated sensor and actuator pair; full-scale power spectra of the excess pressure at $x = 10\ m$ of a 35 m SES with ride control system on and off; $p_0 = 430\ mmWc$.

References

Anderson, B.D.O. and Moore, J.B. (1989). *Optimal Control: Linear Quadratic Methods*. Prentice-Hall, Englewood Cliffs, NJ.

Arcak, M., Meissen, C., and Packard, A. (2016). *Networks of Dissipative Systems Compositional Certification of Stability, Performance, and Safety*. Springer, Series: SpringerBriefs in Electrical and Computer Engineering. doi:10.1007/978-3-319-29928-0.

Åstrøm, K.J. and Wittenmark, B. (1997). *Computer-controlled systems, theory and design*. Prentice Hall Information and system sciences series.

Bachmayer, R., Whitcomb, L., and Grosenbaugh, M.A. (2000). An accurate four-quadrant nonlinear dynamical model for marine thrusters: Theory and experimental vaildation. *IEEE Journal of Oceanic Engineering*, 25, 146–159.

Bagchi, A. (1993). *Optimal Control of Stochastic Systems*. Prentice Hall International, UK.

Balas, M. (1978). Feedback control of flexible systems. *IEEE Transactions on Automatic Control*, 23(4), 673–679.

Balchen, J.G., Jenssen, N.A., Mathisen, E., and Sælid, S. (1980). A dynamic positioning system based on kalman filtering and optimal control. *Modeling, Identification and Control (MIC)*, 1(3), 135–163.

Bennet, S. (1979). *A History of Control Engineering 1800-1930*. Peter Peregrinus, London, UK.

Berge, S., Engseth, A., Fylling, I., Larsen, C.M., Leira, B.J., and Olufsen, A. (1992). *Handbook on Design and Operation of Flexible Pipes*. SINTEF, STF70 A92006, Trondheim, Norway.

Blanke, M., Kinnaert, M., Lunze, J., and Staroswiecki, M. (2003). *Diagnosis and Fault-tolerant Control*. Springer.

Blendermann, W. (1986). *Die Windkräfte am Shiff*. Technical Report Bericht Nr. 467. Institut für Schiffbau der Universit

Branicky, M.S. (1995). *Studies in Hybrid Systems; Modeling, Analysis and Control*. PhD Thesis, MiT, Cambridge, Masachusetts.

Brodtkorb, A.H., Nielsen, U.D., and Sørensen, A.J. (2015a). Sea state estimation using model-scale DP measurements. *MTS/IEEE OCEANS15 in Washington DC*, 1–7.

Brodtkorb, A.H., Sørensen, A.J., and Teel, A.R. (2014). Increasing the operation window of dynamic positioned vessels using the concept of hybrid control. *ASME. International Conference on Offshore Mechanics and Arctic Engineering, 33rd International Conference on Ocean, Offshore and Arctic Engineering (OMAE)*, 1A, V01AT01A046. doi:10.1115/OMAE2014-23601.

Brodtkorb, A.H., Teel, A.R., and Sørensen, A.J. (2015b). Sensor-based hybrid observer for dynamic positioning. *Proceedings of the IEEE Conference on Decision and Control (CDC 2015), Osaka, Japan*, 2015-December, 948–953. doi:10.1109/CDC.2015.7401995.

Brodtkorb, A.H., Teel, A.R., and Sørensen, A.J. (2016a). Hybrid observer combining measurements of different fidelities. *10th IFAC Conference on Control Applications in Marine Systems (CAMS), September 13-16 2016, Trondheim Norway*, 49(23), 506–511. doi: 10.1016/j.ifacol.2016.10.486.

Brodtkorb, A.H., Værnø, S.A.T., Teel, A.R., Sørensen, A.J., and Skjetne, R. (2016b). Hybrid observer for improved transient performance of a marine vessel in dynamic positioning. *10th IFAC Symposium on Nonlinear Control Systems (NOLCOS), August 23-25. 2016, Monterey, California, USA*, 49(18), 245–350. doi:10.1016/j.ifacol.2016.10.189.

Brodtkorb, A.H., Nielsen, U.D., and Sørensen, A.J. (2018a). Sea state estimation using vessel response in dynamic positioning. *Applied Ocean Research*, 70, 76 – 86. doi: https://doi.org/10.1016/j.apor.2017.09.005.

Brodtkorb, A.H., Værnø, S.A., Teel, A.R., Sørensen, A.J., and Skjetne, R. (2018b). Hybrid controller concept for dynamic positioning of marine vessels with experimental results. *Automatica*, 93, 489 – 497. doi:https://doi.org/10.1016/j.automatica.2018.03.047.

Bryne, T.H., Fossen, T.I., and Johansen, T.A. (2015). A virtual vertical reference concept for GNSS/INS applications at the sea surface. *10th Conference on Maneouvring and Control of Marine Craft, MCMC August 24-26 2015 Copenhagen, Denmark*, 48, 127–133. doi: 10.1016/j.ifacol.2015.10.269.

Bryne, T.H., Hansen, J.M., Rogne, R.H., Sokolova, N., Fossen, T.I., and Johansen, T.A. (2017). Nonlinear observers for integrated INS/GNSS navigation: Implementation aspects. *IEEE Control Systems Magazine*, 37(3), 59–86. doi:10.1109/MCS.2017.2674458.

Carlton, J.S. (1994). *Marine Propellers and Propulsion*. Oxford: Butterworth-Heinemann, UK.

Chen, C.T. (2004). *Signals and Systems*. Third Edition, Oxford University Press, Oxford, New York, US.

Chen, C.T. (2014). *Linear System Theory and Design*. Fourth Edition, Oxford University Press, Oxford, New York, US.

Christiansen, D. (1996). *Electronics Engineer's Handbook*. Fourth Edition, IEEE Press, McGraw-Hill, New York, US.

COLREG (1972). *Convention on the International Regulations for Preventing Collisions at Sea*. International Maritime Organization (IMO).

Desoer, C.A. and Vidyasager, M. (1975). *Feedback Systems: Input-Output Properties*. Academic Press, New York, US.

DNVGL (2018). Dnv gl rules and standards. URL `https://rules.dnvgl.com/ServiceDocuments/dnvgl`.

Dorf, R.C. and Bishop, R.H. (1998). *Modern Control Systems*. Eight Edition, Addision-Wesley, California, US.

Egeland, O. and Gravdahl, J.T. (2002). *Modeling and Simulation for Automatic Control*. Marine Cybernetics, Trondheim, Noway.

Faltinsen, O.M. (1993). *Sea Loads on Ships and Offshore Structures*. Cambridge University Press.

Fay, H. (1989). *Dynamic Positioning Systems, Principles, Design and Applications*. Editions Technip, Paris, France.

Fossen, T.I. (2011). *Handbook of Marine Craft Hydrodyamics and Motion Control*. Wiley.

Fossen, T.I. and Blanke, M. (2000). Nonlinear output feedback control of underwater vehicle propellers using feedback from estimated axial flow velocity. *IEEE Journal of Oceanic Engineering*, 25(2).

Fossen, T.I. and Perez, T. (2004). Marine systems simulator (MSS). URL `http://www.marinecontrol.org`.

Fossen, T.I. and Perez, T. (2009). Kalman filtering for positioning and heading control of ships and offshore rigs. *IEEE Control Systems Magazine*, 29(6), 32–46. doi: 10.1109/MCS.2009.934408.

Fossen, T.I. and Strand, J.P. (1999). Passive nonlinear observer design for ships using Lyapunov methods: full-scale experiments with a supply vessel. *Automatica*, 35(1), 3 – 16. doi:10.1016/S0005-1098(98)00121-6.

Fossen, T.I. and Strand, J.P. (2001). Weather optimal positioning control (wopc) system for ships and rigs: Experimental results. *Automatica*, 37(5), 701 – 715.

Gelb, A. and Vander Velde, W.E. (1968). *Multiple-Input Describing Functions and Nonlinear System Design*. McGraw-Hill, New York, US.

Godhaven, J.M. (1998). Adaptive tuning of heave filter in motion sensor. In *OCEANS '98 Conference Proceedings*, volume 1, 174–178 vol.1. doi:10.1109/OCEANS.1998.725731.

Goebel, R., Sanfelice, R., and Teel, A.R. (2009). Hybrid dynamical systems robust stability and control for systems that combine continuous-time and discrete-time dynamics. *IEEE Control Systems Magazine, April 2009*, 28–93. doi:10.1109/MCS.2008.931718.

Goebel, R., Sanfelice, R.G., and Teel, A.R. (2012). *Hybrid Dynamical Systems, Modelling, Stability and Robustness*. Princeton University Press.

Grimble, M.J. and Johnsen, M.A. (1988). *Optimal Control and Stochastic Estimation.* Vol. 1 - 2, John Wiley and Sons Ltd, UK.

Grip, H.F., Fossen, T.I., Johansen, T.A., and Saberi, A. (2015). Globally exponentially stable attitude and gyro bias estimation with application to GNSS/INS integration. *Automatica*, 51, 158–166. doi:10.1016/j.automatica.2014.10.076.

Hadamard, J. (1902). Sur les problèmes aux dérivés partielles et leur signification physique. *Princeton University Bulletin*, 13, 49–52.

Hansen, J.F. (2000). *Optimal Power Control of Marine Systems.* Ph.D. thesis, Dept. of Engineering Cybernetics, Norwegian University of Science and Technology, Trondheim, Norway.

Henzinger, T.A. (2000). *The Theory of Hybrid Automata*, 265–292. Springer Berlin Heidelberg, Berlin, Heidelberg. doi:10.1007/978-3-642-59615-5-13. URL `http://dx.doi.org/10.1007/978-3-642-59615-5-13`.

Hespanha, J.P. (2002). Tutorial on supervisory control. Lecture notes for the workshop Control using Logic and Switching, 40th conf. on Decision and Control, Orlando Florida.

Hespanha, J.P., Liberzon, D., and Morse, A.S. (2003). Hysteresis-based switching algorithms for supervisory control of uncertain systems. *Automatica*, 39(2), 263–272. doi:10.1016/S0005-1098(02)00241-8.

Hespanha, J.P. and Morse, A.S. (2002). Switching between stabilizing controllers. *Automatica*, 38(11), 1905–1917. doi:10.1016/S0005-1098(02)00139-5.

Hoffman, J.D. (2001). *Numerical Methods for Engineers and Scientists.* Second edition, Marcel Dekker, Inc.,New York, US.

Huse, E. (1993). Interaction in deep-sea riser arrays. In *Proc. of the 25th Annual Offshore Technology Conference (OTC), Houston, TX, US.*

Huse, E. and Kleiven, G. (2000). Impulse and energy in deepsea riser collisions owing to wake interference. In *Proc. of the 32nd Annual Offshore Technology Conference (OTC), Houston, TX, US.*

IMO (2011). *International convention for the prevention of pollution from ships (MARPOL) Annex VI.* International Maritime Organization (IMO).

Isherwood, M.A. (1972). Wind resistance of merchant ships. *Trans. Inst. Naval Arch., RINA*, 115, 327–338.

Johannessen, K., Meling, T.S., and S., H. (2002). Joint distribution for wind and waves in the northern north sea. *IJOPE*, 12(1).

Johansen, T.A. and Sørensen, A.J. (2009). Experiences with hil simulator testing of power management systems. In *Marine Technology Society, Houston, US.*

Johansson, R. (1993). *System Modeling & Identification.* Englewood Cliffs, New Jersey, US.

Joshi, S.M. (1989). *Control of Large Flexible Space Structures.* Springer, Berlin, Germany.

Kalleklev, A.J., Mørk, K.J., Sødahl, N., Nygård, M.K., and Horn, A.M. (2003). Design guidelines for riser collision. In *Proc. of the 35th Annual Offshore Technology Conference (OTC), Houston, TX, US.*

Kaplan, P., Bentson, J., and S., D. (1981). An accurate four-quadrant nonlinear dynamical model for marine thrusters: Theory and experimental vaildation. *Trans. SNAME*, 89, 211–247.

Kaplan, P. and Davis, S. (1974). A simplified representation of the vertical plane dynamics of ses craft. In *IAA Paper No. 74-314, AIAA/SNAME Adv. Marine Vehciles Conf. San Diego, CA, US.*

Kaplan, P. and Davis, S. (1978). System analysis techniques for designing ride control system for ses craft in waves. In *5th Ship Contr. Syst. Symp., Annapolis, MD, US.*

Khalil, H.K. (2002). *Nonlinear Systems, 3rd. edition.* Prentice Hall.

Kjerstad, Ø.K. (2016). *Dynamic Positioning of Marine Vessels in Ice.* PhD Thesis 2016:168, Department of Marine Technology, Faculty of Engineering Science and Technology, NTNU. Supervisor: Professor Roger Skjetne, NTNU.

Kreyszig, E. (1993). *Advanced Engineering Mathematics.* 7th edition, John Wiley and Sons, Inc.

Larsen, C.M. (1993). *Analysis of Tensioner System Stroke for Marine Risers.* SINTEF Structures and Concrete, STF70 F93011, Norway.

Larsen, C.M. (2000). *Dynamic Analysis of Structures.* Department of Marine Technology, NTNU.

Lehn, E. (1992). *Optimal Control and Stochastic Estimation.* Report MT51A92-003, 513003.00.06, MARINTEK, Trondheim, Norway.

Lygeros, J. (1996). *Hierarchical, hybrid control of large scale systems.* PhD Thesis University of California, Berkeley.

Minorsky, N. (1922). Directional stability of automatically steered bodies. *Journal of the American Society for Naval Engineers*, 34(2), 280–309. doi:10.1111/j.1559-3584.1922.tb04958.x.

Minsaas, K.J., Thon, H.J., and Kauczynski, W. (1987). Estimation of required thruster capacity for operation of offshore vessels under severe weather conditions. In *2PRADS 1987.*

Miyazaki, M.R. (2017). *Modeling and Control of Hybrid Marine Power Plants.* PhD thesis 2017:199, Department of Marine Technology, Faculty of Engineering, NTNU.

Miyazaki, M.R., Sørensen, A.J., and Vartdal, B.J. (2016). Reduction of fuel consumption on hybrid marine power plants by strategic loading with energy storage devices. *IEEE Power and Energy Technology Systems Journal*, 3(4), 207–217. doi:10.1109/JPETS.2016.2621117.

Newman, J.N. (1997). *Marine Hydrodynamics.* MIT Press, MA, US.

Nguyen, D.T. and Sørensen, A.J. (2009). Setpoint chasing for thruster-assisted position mooring. *IEEE Journal of Oceanic Engineering*, 34(4), 548–558. doi:10.1109/JOE.2009.2034553.

Nguyen, T.D. (2006). *Design of Hybrid Marine Control Systems for Dynamic Positioning*. PhD Thesis, Department of Civil Engineering, National University of Singapore (NUS).

Nguyen, T.D., Sørensen, A.J., and Quek, S.T. (2004). Observer for dynamic positioning of floating structures in extreme seas. *The Seventeenth KKCNN Symposium on Civil Engineering, December 13-15, Thailand*.

Nguyen, T.D., Sørensen, A.J., and Quek, S.T. (2007). Design of hybrid controller for dynamic positioning from calm to extreme sea conditions. *Automatica*, 43(5), 768–785. doi: 10.1016/j.automatica.2006.11.017.

Nguyen, T.D., Sørensen, A.J., and Quek, S.T. (2008). Multi-operational controller structure for station keeping and transit operations of marine vessels. *IEEE Transactions on Control Systems Technology*, 16(3), 491–498. doi:10.1109/TCST.2007.906309.

Nielsen, U.D., Brodtkorb, A.H., and Jensen, J.J. (2018). Response predictions for marine vessels using observed autocorrelation function. *Marine Structures*, 58(Supplement C), 31 – 52. doi: https://doi.org/10.1016/j.marstruc.2017.10.012.

Norsok (2018). Norsok standards. URL `https://www.standard.no/nettbutikk/norsok/`.

Oosterveld, M.W.C. and Oossanen, P.v. (1975). Further computer-analyzed data of the wageningen b-screw series. *Int. Shipbuilding Progress*, 22, 251–262.

Oppenheim, A.V. and Willsky, A.S. (2013). *Signals and Systems*. Second Edition, Pearson, US.

Perez, T., Sørensen, A., and Blanke, M. (2006). Marine vessel models in changing operational conditionsa tutorial. *14th IFAC Symposium on Identification and System Parameter Estimation, IFAC Proceedings Volumes*, 39(1), 309 – 314. doi:http://dx.doi.org/10.3182/20060329-3-AU-2901.00044.

Radan, D. (2008). *Integrated Control of Marine Electrical Power Systems*. PhD thesis 2008:37, Department of Marine Technology, Faculty of Engineering, NTNU.

Rensvik, E., Sørensen, A.J., and Rasmussen, M. (2003). Maritime industrial it. In *ICMES'03 International Conference on Marine Engineering Systems, Finland*, BF.

RIFLEX (2018). *RIFLEX User Manual*. SINTEF Ocean.

Rockafellar, R.T. and Wets, R.J.B. (1998). *Variational Analysis*. Springer Berlin Heidelberg, Series: Grundlehren der mathematischen Wissenschaften. doi:10.1007/978-3-642-02431-3.

Rustad, A.M. (2007). *Modeling and Control of Top Tensioned Risers*. PhD Thesis 2007:183, Department of Marine Technology, NTNU.

Rustad, A.M., Larsen, C.M., and Sørensen, A.J. (2007). Fem modelling and control for collision prevention of top tensioned risers. *Journal of Marine Structures, Elsevier*, 20.

Ruth, E. (2008). *Propulsion Control and Thrust Allocation on Marine Vessels*, volume 203. PhD Thesis 2008, Department of Marine Technology, Faculty of Engineering Science and Technology, NTNU.

Sagatun, S.I. (2001). The elastic cable under the action of concentrated and distributed forces. *Offshore Mechanics and Arctic Engineering*, 123, 43–45.

Salvesen, N., Tuck, E.O., and Faltinsen, O.M. (1970). Ship motions and sealoads. *Trans. SNAME*, 78, 334–356.

Sanfelice, R., Copp, D., and Nanez, P. (2013). A toolbox for simulation of hybrid systems in matlab/simulink: hybrid equations (hyeq) toolbox. *Conference: Proceedings of the 16th international conference on Hybrid systems: computation and control*, 101–106.

Sintef Ocean (2017). *ShipX*. Trondheim, Norway, `http://www.sintef.no/programvare/shipx/`.

Skjetne, R., Kjerstad, Ø.K., Værnø, S.A.T., Brodtkorb, A.H., Sørensen, A.J., Sørensen, M.E.N., Breivik, M., Calabrò, V., and Vinje, B.O. (2017). AMOS DP research cruise 2016: Academic full-scale testing of experimental dynamic positioning control algorithms onboard R/V Gunerus. *Proceedings of the 36th International Conference on Ocean, Offshore and Arctic Engineering (OMAE), Trondheim Norway, June 25-30*, (OMAE2017-62045).

Smogeli, O..M. (2010). Experiences from five years of dp software testing. In *European DP Conference, London, UK*.

Smogeli, Ø.N. (2006). *Control of Marine Propellers, From Normal to Extreme Conditions*. PhD Thesis 2006:187, Department of Marine Technology, Faculty of Engineering Science and Technology, NTNU.

Smogeli, Ø.N. and Sørensen, A.J. (2009). Antispin thruster control for ships. *IEEE Transactions on Control Systems Technology*, 17(6), 1362–1375. doi:10.1109/TCST.2008.2009065.

SNAME (1950). *Nomenclature for Treating the Motion of a Submerged Body Through a Fluid*. he Society of Naval Architects and Marine Engineers (SNAME), No. (1-5).

Sørdalen, O.J. (1997). Optimal thrust allocation for marine vessels. *Journal Control Engineering Practice (CEP)*, 5(9), 1223–1231.

Sørensen, A.J. (1993). *Modelling and Control of SES Dynamics in the Vertical Plane*. Dr. Ing. thesis, The Norwegian Institute of Technology, Trondheim, Norway, 1993.

Sørensen, A.J. (2005). Structural issues in the design and operation of marine control systems. *Annual Reviews in Control*, 29(1), 125–149. doi:10.1016/j.arcontrol.2004.12.001.

Sørensen, A.J. (2011). A survey of dynamic positioning control systems. *Annual Reviews in Control*, 35(1), 123–136. doi:10.1016/j.arcontrol.2011.03.008.

Sørensen, A.J., Ådnanes, A.K., Fossen, T.I., and Strand, J.P. (1997). A new method of thruster control in positioning of ships based on power control. *In Proc.: 4 th IFAC Conf. on Manoeuvring and Control of Marine Craft (MCMC'97). Brijuni, Croatia*, 172–179.

Sørensen, A.J. and Egeland, O. (1995). Design of ride control system for surface effect ships using dissipative control. *Automatica*, 31(2), 183–199.

Sørensen, A.J., Leira, B., Strand, J.P., and Larsen, C.M. (2001). Optimal setpoint chasing in dynamic positioning of deepwater drilling and intervention vessels. *International Journal of Robust and Nonlinear Control*, 11(13), 1187–1205. doi:10.1002/rnc.602. URL `http:https://dx.doi.org/10.1002/rnc.602`.

Sørensen, A.J., Nguyen, T.D., and Quek, S.T. (2004). Improved operability and safety of dp vessels using hybrid control concept. *International Conference on Technology & Operation of Offshore Support Vessels (OSV Singapore 2005), Jointly organized by Joint Branch of RINA-IMarEST Singapore and CORE, 20-21 September, Singapore.*

Sørensen, A.J., Pedersen, E., and Smogeli, Ø..M. (2003). Simulation-based design and testing of dynamically positioned marine vessels. In *International Conference on Marine Simulation and Ship Maneuverability, MARSIM'03, Kanazawa, Japan.*

Sørensen, A.J., Sagatun, S.I., and Fossen, T.I. (1996). The design of a dynamic positioning system using model-based control. *IFAC Journal of Control Engineering in Practice*, 4(3), 359–368. doi:10.1016/0967-0661(96)00013-5.

Sørensen, A.J. and Smogeli, Ø. (2009). Torque and power control of electrically driven marine propellers. *Journal Control Engineering Practice (CEP)*, 17(9), 1053–1064.

Sørensen, A.J., Steen, S., and Faltinsen, O.M. (1992). Cobbelstone effect on ses. In *High Performance Marine Vehicle Conf. (HPMV'92), ASNE, Washington D.C., US.*

Sørensen, A.J., Steen, S., and Faltinsen, O.M. (1993). Ses dynamics in the vertical plane. *Journal of Ship Technology Research*, 40, 71–94.

Sørensen, A.J. and Strand, J.P. (2000). Positioning of small-waterplane-area marine constructions with roll and pitch damping. *IFAC Journal of Control Engineering in Practice*, 8(2), 205–213. doi:10.1016/S0967-0661(99)00155-0.

Sørensen, A.J., Strand, J.P., and Nyberg, H. (2002). Dynamic positioning of ships and floaters in extreme seas. *In Proceedings of OCEANS'02 MTS/IEEE, Biloxi, Mississippi, US*, 3, 1850–1855. doi:10.1109/OCEANS.2002.1191913.

Steen, S., Selvik, Ø., and Hassani, V. (2016). Experience with rim-driven azimuthing thrusters on the research ship Gunnerus. *10th Symposium on High-Performance Marine Vessels (HIPER'16), October 17-19 2016, Cortona, Italy.*

Strand, J.P. (1999). *Nonlinear Position Control Systems Design for Marine Vessels.* Dr. Ing.-thesis 1999-6-W, Department of Engineering Cybernetics, NTNU.

Strand, J.P. and Fossen, T.I. (1999). *New Directions in Nonlinear Observer Design*, 113–134. Springer International Publishing.

Strand, J.P., Sørensen, A.J., and Fossen, T.I. (1998). Design of automatic thruster assisted mooring systems for ships. *Journal on Modeling, Identification and Control (MIC)*, 19(2), 61–75. doi:10.4173/mic.1998.2.1.

Strang, G. (1988). *Linear Algebra and its Applications*. Third Edition, Harcourt Brace Jovanovich, Publishers, Florida, US.

Triantafyllou, M.S. (1990). *Cable Mechanics with Marine Applications*. Lecture Notes, Dept. of Ocean Engineering, Massachusetts Institute of Technology (MIT).

Triantafyllou, M.S. (1994). Cable mechanics for moored floating systems. In *BOSS'94, Boston, MA, US*.

Tutturen, S.A. and Skjetne, R. (2015). Hybrid control to improve transient response of integral action in dynamic positioning of marine vessels. *10th IFAC Conference on Manoeuvring and Control of Marine Craft (MCMC2015)*, 56(7), 1636–1649. doi:10.1016/j.ifacol.2015.10.275.

Utne, I.B., Sørensen, A.J., and Schjølberg, I. (2017). Risk management of autonomous marine systems and operations. *Proceedings of the 36th Intenational Conference on Ocean, Offshore and Arctic Engineering, OMAE 2017,June 25-30, Trondheim, Norway*, (OMAE2017-61645).

van Lammeren, W.P.A. and van Manen, J.D. (1969). The wageningen b-screw series. *Transactions of SNAME*, 77, 269–317.

Vidyasager, M. (1993). *Nonlinear Sytem Analysis*. 2nd Ed., Prentice Hall, Englewood Cliffs, NJ, US.

Vik, B. and Fossen, T.I. (2001). Nonlinear observer design for integration of GPS and intertial navigation systems. *Proceedings of the Conference on Decision and Control (CDC'2001). Orlando, FL.*, 2956–2961. doi:10.1109/CDC.2001.980726.

WAMIT Inc. (2017). *WAMIT- State of the art in wave interaction analysis*. Massachusetts 02467-2504 USA, `http://www.wamit.com`.

Witsenhausen, H. (1966). A class of hybrid-state continuous-time dynamic systems. *IEEE Transactions on Automatic Control*, 11(2), 161–167. doi:10.1109/TAC.1966.1098336.

Appendix A

Linear Algebra

Some important linear algebra properties are listed below (Strang, 1988).

Definition A.1 *The matrix* $\mathbf{A} \in \mathbb{R}^{n \times n}$ *is symmetric if*

$$\mathbf{A} = \mathbf{A}^T. \tag{A.1}$$

Definition A.2 *The quadratic form is defined as*

$$\alpha = \mathbf{x}^T \mathbf{A} \mathbf{x}, \quad \forall \mathbf{x} \in \mathbb{R}^n, \tag{A.2}$$

where α *is a scalar.*

Definition A.3 *The matrix* $\mathbf{A} \in \mathbb{R}^{n \times n}$ *is skew-symmetric if*

$$\mathbf{A} = -\mathbf{A}^T. \tag{A.3}$$

The quadratic form of a skew-symmetric matrix is

$$\mathbf{x}^T \mathbf{A} \mathbf{x} = \mathbf{x}^T \left(\frac{1}{2} \left(\mathbf{A} + \mathbf{A}^T \right) + \frac{1}{2} \left(\mathbf{A} - \mathbf{A}^T \right) \right) \mathbf{x} = 0, \quad \forall \mathbf{x} \in \mathbb{R}^n. \tag{A.4}$$

Definition A.4 *A necessary and sufficient condition for the symmetric matrix* $A \in \mathbb{R}^{n \times n}$ *to be positive definite is*

$$\mathbf{x}^T \mathbf{A} \mathbf{x} > 0, \quad \forall \mathbf{x} \in \mathbb{R}^n. \tag{A.5}$$

All the eigenvalues of $\mathbf{A}$ *will be positive, that is* $\lambda_1, \lambda_2, ..., \lambda_n > 0$.

Definition A.5 *A necessary and sufficient condition for the symmetric matrix* $\mathbf{A} \in \mathbb{R}^{n \times n}$ *to be positive semidefinite is*

$$\mathbf{x}^T \mathbf{A} \mathbf{x} \geq 0, \quad \forall \mathbf{x} \in \mathbb{R}^n. \tag{A.6}$$

All the eigenvalues of $\mathbf{A}$ *will be positive or equal to zero, that is* $\lambda_1, \lambda_2, ..., \lambda_n \geq 0$.

Definition A.6 *The non-symmetric matrix* $\mathbf{A} \neq \mathbf{A}^T$, *where* $\mathbf{A} \in \mathbb{R}^{n \times n}$ *is positive if*

$$\mathbf{x}^T \mathbf{A} \mathbf{x} \geq 0, \quad \forall \mathbf{x} \in \mathbb{R}^n. \tag{A.7}$$

Definition A.7 *The non-symmetric matrix* $\mathbf{A} \in \mathbb{R}^{n \times n}$ *is strictly positive if*

$$\mathbf{x}^T \mathbf{A} \mathbf{x} > 0, \quad \forall \mathbf{x} \in \mathbb{R}^n. \tag{A.8}$$

Let the non-symmetric matrix, $\mathbf{A} \neq \mathbf{A}^T$, *be reformulated as* $\mathbf{A} = \frac{1}{2}\left(\mathbf{A} + \mathbf{A}^T\right) + \frac{1}{2}\left(\mathbf{A} - \mathbf{A}^T\right)$. *The non-symmetric matrix* $\mathbf{A}$ *is strictly positive if the symmetric matrix defined as*

$$\frac{1}{2}\left(\mathbf{A} + \mathbf{A}^T\right) \tag{A.9}$$

is positive definite, that is

$$\mathbf{x}^T \frac{1}{2}\left(\mathbf{A} + \mathbf{A}^T\right) \mathbf{x} > 0. \tag{A.10}$$

The matrix $\frac{1}{2}\left(\mathbf{A} - \mathbf{A}^T\right)$ *will be skew-symmetric matrix with the quadratic form equal to zero. Hence (A.8) can be reformulated as*

$$\mathbf{x}^T \mathbf{A} \mathbf{x} = \frac{1}{2} \mathbf{x}^T \left(\mathbf{A} + \mathbf{A}^T\right) \mathbf{x} > 0, \quad \forall \mathbf{x} \in \mathbb{R}^n. \tag{A.11}$$

Remark A.1 *In textbooks for notational simplicity* $\mathbf{x}^T \mathbf{A} \mathbf{x} > 0$ *is written* $\mathbf{A} > 0$.

Appendix B

Digital PID-Controllers

B.1 Continuous-Time PID-Controllers

It is well known from text books in control theory Åstrøm and Wittenmark (1997) and Dorf and Bishop (1998) that, a single-input single-output (SISO) continuous-time proportional-integral-derivative (PID) controller is often formulated as

$$u(t) = u_p(t) + u_d(t) + u_i(t), \tag{B.1}$$

where

$$\begin{aligned} u_p(t) &= k_p e(t), & \text{(B.2)} \\ u_d(t) &= k_d \dot{e}(t), & \text{(B.3)} \\ u_i(t) &= k_i \int_o^t e(s)ds. & \text{(B.4)} \end{aligned}$$

The deviation error between the state x and the desired setpoint x_d is defined as $e(t) = x_d(t) - x(t)$, and $\dot{e}(t) = \dot{x}_d(t) - \dot{x}(t)$. The controller gains are defined such that $k_p \geq 0$ is the proportional gain, $k_d \geq 0$ is the derivative gain, and $k_i \geq 0$ is the integrator gain. Often the proportional and integral gains are rewritten as

$$\begin{aligned} k_d &= k_p T_d, & \text{(B.5)} \\ k_i &= \frac{k_p}{T_i}, & \text{(B.6)} \end{aligned}$$

where T_d is the derivative time and T_i is the integration time.

Similarly, a multivariable PID controller can be written

$$\mathbf{u} = \mathbf{K}_p \mathbf{e} + \mathbf{K}_d \dot{\mathbf{e}} + \mathbf{K}_i \int_o^t \mathbf{e}(s)ds, \tag{B.7}$$

where $\mathbf{e} = \mathbf{x}_d - \mathbf{x}$ is the deviation error vector between the state vector $\mathbf{x}$ and the desired setpoint vector $\mathbf{x}_d$, and $\dot{\mathbf{e}} = \dot{\mathbf{x}}_d - \dot{\mathbf{x}}$. $\mathbf{K}_p \geq 0$, $\mathbf{K}_d \geq 0$ and $\mathbf{K}_i \geq 0$ are the corresponding proportional, derivative and integral gain matrices.

In the s-domain (Laplace) incorporating limitation on the derivative term and assuming that $0 \leq T_d \ll T_i$, the PID formulation becomes

$$u(s) = k_p e(s) + k_p \frac{T_d s}{(1 + \alpha T_d s)} e(s) + \frac{k_p}{T_i s} e(s), \tag{B.8}$$

where $0 < \alpha \leq 1$

B.2 Discrete-Time PID-Controllers

A simple approximation of (B.8) can be done in order to derive a digital PID controller. The proportional part can be written

$$u_p[k] = k_p e[k], \tag{B.9}$$

where

$$e[k] = x_d[k] - x[k]. \tag{B.10}$$

From (B.8) the derivative part can be rewritten according to

$$\begin{aligned} u_d(s) &= k_p \frac{T_d s}{(1 + \alpha T_d s)} e(s), & \text{(B.11)} \\ &\Updownarrow & \\ u_d(s) + \alpha T_d s u_d(s) &= k_p T_d s e(s). & \text{(B.12)} \end{aligned}$$

Using inverse Laplace transform we find the time domain formulation of (B.12) to be

$$\alpha T_d \dot{u}_d + u_d = k_p T_d \dot{e}. \tag{B.13}$$

If we apply Euler's backward difference method, we achieve a discrete approximation of the continuous-time derivative controller given in (B.13) to be

$$\frac{\alpha T_d}{T}(u_d[k] - u_d[k-1]) + u_d[k] = \frac{k_p T_d}{T}\left(e[k] - e[k-1]\right), \tag{B.14}$$

where T is the sampling period. Eq. (B.14) can be reformulated as

$$u_d[k] = \frac{T_d}{\left(T_d + \frac{T}{\alpha}\right)} u_d[k-1] + \frac{k_p T_d}{(\alpha T_d + T)}\left(e[k] - e[k-1]\right). \tag{B.15}$$

The integral term (B.4) is reformulated according to

$$T_i \, \dot{u}_i = k_p e(t), \tag{B.16}$$

and is approximated by a Euler's forward difference method according to

$$\frac{T_i}{T}\left(u_i[k] - u_i[k-1]\right) = k_p e[k-1]. \tag{B.17}$$

Eq. (B.17) is reformulated as

$$u_i[k] = u_i[k-1] + \frac{T k_p}{T_i} e[k-1]. \tag{B.18}$$

Thus the resulting discrete PID becomes by summarizing (B.9), (B.15) and (B.17)

$$u[i] = u_p[k] + u_d[k] + u_i[k]. \tag{B.19}$$

Remark B.1 *Several other formulations of digital PID controllers exist. These are based on other approximation methods. One example on this is to apply Tustin's bilinear transformation on (B.8) and then find the z-transform according to* $H_c(z) : h_c(s)$*, where*

$$s = \frac{2}{T}\frac{1 - z^{-1}}{1 + z^{-1}}. \tag{B.20}$$

Using shift-operator calculus the discrete PID controller is found.

Remark B.2 *Integrator anti-windup should be implemented in order to avoid that the integrator integrates up beyond the saturation limits of the actuators. A simple method to avoid this is to stop integrating when the integral term tends to a given percentage of the actuator saturation limit. More sophisticated algorithms are found in Åstrøm and Wittenmark (1997).*

Remark B.3 *For a constant setpoint* $\dot{e}(t) = \dot{x}_d(t) - \dot{x}(t)$ *simplifies to* $\dot{e}(t) = -\dot{x}(t)$ *as* $\dot{x}_d(t) = 0$.

Appendix C

Definition of Electro-Technical Terms

C.1 DC – Direct Current

The DC (Direct Current) voltage source is unipolar with a positive and negative voltage terminal. Examples of DC voltage sources are:

- Batteries.
- Static converters.
- DC generators.
- Fuel cells.

Connecting an electrically conductive load to the terminal forces a current to flow, Figure C.1. The polarity of the voltage source is annotated with + (positive) and – (negative). The arrow shows positive direction of current flow.

Figure C.1: Electrical circuit, with voltage source V_{dc} and a resistive load R.

If the DC voltage is V_{dc} and the electrical resistance in the load is R, the current I is found by Ohm's law

$$I = \frac{V_{dc}}{R}. \tag{C.1}$$

The power dissipated in the resistance equals the power delivered by the power source

$$P = V_{dc}I = \frac{V_{dc}^2}{R} = RI^2. \tag{C.2}$$

Example C.1 *: Flash-light bulb.*

A flash light is equipped with a 9 Volt (V) battery and 0.25 Watt (W) light bulb. The current in the bulb is then

$$I = \frac{P}{V_{dc}} = 27.8mA,$$

where $mA = milliampere$*, and the resistance in the bulb is*

$$R_{bulb} = \frac{V_{dc}^2}{P} = 324\Omega,$$

where $\Omega = Ohm$*. Here it is assumed that the battery is an ideal voltage source. Since such does not yet exist, the battery will normally be represented by an ideal voltage source, i.e. the no-load voltage, in series with an inner resistance, Figure C.2.*

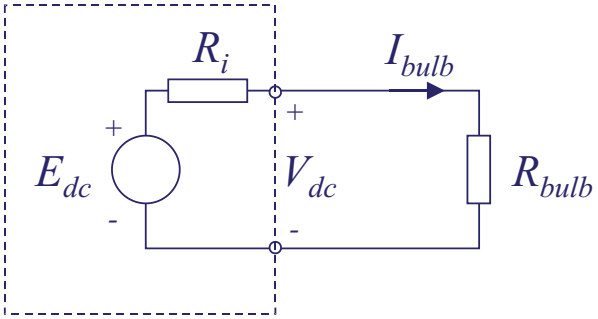

Figure C.2: Battery with no-load voltage E_{dc} and inner resistance R_i connected to a light-bulb with resistance R_{bulb}.

Example C.2 *: Flash-light bulb with non-ideal battery.*

If the battery in the previous example had an inner resistance of $R_i = 20\,\Omega$*, and a no-load voltage of* $E_{dc} = 9.2V$*, the current would be*

$$I_{bulb} = \frac{E_{dc}}{R_i + R_{bulb}} = 26.7mA.$$

The voltage on the battery terminals is then

$$V_{dc} = E_{dc} - R_i I_{bulb} = 8.67V.$$

The power dissipated in the bulb becomes

$$P_{bulb} = R_{bulb} I_{bulb}^2 = 0.23W.$$

The power loss in the battery is

$$P_{loss} = R_i I_{bulb}^2 = 14mW.$$

The efficiency of the battery is then

$$\eta = \frac{P_{bulb}}{P_{loss} + R_{bulb}} = 0.943 \qquad (94.3\%).$$

Example C.3 *: Short-circuited battery with inner resistance.*

A short circuit (direct connection of two conductive leads with different voltage potentials) gives a failure current which often is dimensioning for cable, terminations, etc. Upon short-circuit, the inner resistance in the battery and in the leads and short-circuit itself will limit the short-circuit current. With a low resistance short-circuit (0 Ω)*, the fault current of the battery in the example above is*

$$I_{sc} = \frac{V_{dco}}{R_i} = 0.46A.$$

C.2 AC – Alternating Current

C.2.1 One Phase AC Sources and Resistive Loads

The AC (Alternating Current) voltage source is bipolar and normally sinusoidal time varying. The frequency of the variations in European land network is $50Hz$ (Herz), i.e. 50 cycles per second, see Figure C.3. In US networks, the frequency is $60Hz$. In ship networks, both $50Hz$ and $60Hz$ are used. For some special equipment, especially in navy applications, 400Hz can be seen. Examples of AC voltage sources are:

- Generators (also called Alternators).
- Static converters.
- Uninterrupted Power Supplies (UPS), which are static converters supplied from batteries if supply voltage vanish, applied for power supply to critical equipment.

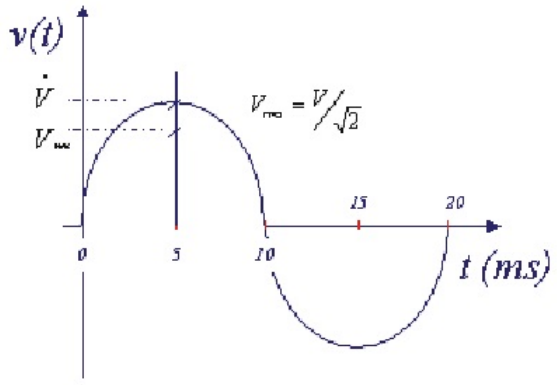

Figure C.3: AC voltages are sinusoidal time varying, 50 Hz voltages have a cycle time of 20 ms.

Figure C.3 shows a sinusoidal time varying voltage of frequency $f = 50Hz$. It can be expressed

$$v(t) = \hat{V} \sin 2\pi f t = \hat{V} \sin \omega t. \tag{C.3}$$

Here the $\omega = 2\pi f$ is the angular frequency, expressed in rad/s. If this voltage source is connected to a resistive load (ohmic load), as shown in Figure C.4, a current will flow through the circuit.

And assuming that there is no voltage drop in the voltage source, the current will be given by the resistance in the load

$$i(t) = \frac{v(t)}{R} = \frac{\hat{V}}{R}\sin\omega t. \tag{C.4}$$

From this it is seen, that the current is proportional to the voltage, and that the voltage and current are in phase, i.e. phase angle equals to zero. This is always true for a pure resistive load.

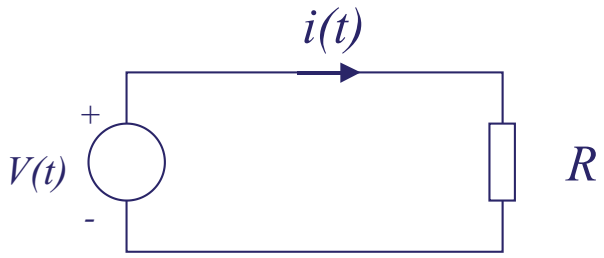

Figure C.4: AC voltage source connected to a resistive load.

Since the voltages and currents are time varying, the power consumed by the resistor is also time varying

$$p(t) = v(t)i(t) = \hat{V}\,\hat{I}\sin^2 2\pi ft = \hat{V}\,\hat{I}\frac{1}{2}\left(1-\cos 2\omega t\right). \tag{C.5}$$

Normally, the instantaneous power is less interesting than the average power. This is found by integrating the power and averaging it over e.g. one cycle time, T according to

$$\begin{aligned} P &= \overline{p(t)} = \overline{v(t)i(t)} = \frac{1}{T}\int_0^T \hat{V}\,\hat{I}\sin^2 2\pi ft\,dt \\ &= \frac{1}{2\pi}\hat{V}\,\hat{I}\int_0^{2\pi}\sin^2\omega t\,d\omega t = \frac{1}{2\pi}R\,\hat{I}^2\int_0^{2\pi}\sin^2\omega t\,d\omega t = R\frac{\hat{I}^2}{2}, \end{aligned} \tag{C.6}$$

where we have used $\omega = 2\pi/T$ and $d\omega t = td\omega + \omega dt = \omega dt$. Introducing the root mean square value (rms) for the current

$$I_{rms} = \sqrt{\frac{1}{2\pi}\hat{I}^2\int_0^{2\pi}\sin^2\omega t\,d\omega t} = \frac{\hat{I}}{\sqrt{2}}, \tag{C.7}$$

we can see that the power equation simplifies to a form similar as for DC systems

$$P = R\,I_{rms}^2. \tag{C.8}$$

With similar definition of rms value for the voltage, it yields

$$V_{rms} = R\,I_{rms}, \tag{C.9}$$

and

$$P = V_{rms}\,I_{rms}. \tag{C.10}$$

rms values for voltages and currents enable us to use well known formulas from DC systems in AC systems, when average power is concerned. This means almost always in analysis of electric network in this context.

Example C.4 *:A lamp connected to 230V AC network.*

A light bulb of $25W$ *is connected to a* $230V_{rms}$*,* $50Hz$ *voltage. The current in the bulb is then*

$$I_{rms} = \frac{P}{V_{rms}} = 0.11A,$$

and the resistance in the bulb is

$$R_{bulb} = \frac{V_{rms}}{I_{rms}} = 209\,\Omega.$$

C.2.2 Three Phase AC Sources and Resistive Loads

The power is in all larger installations generated as a three-phase voltage, because:

- Three-phase distribution systems give a better utilization of the material in the generator itself, cabling, and other distribution equipment and loads.
- Smooth torque in rotating electrical machines, i.e. motors and generators.
- Satisfactory start-up torque with proper design of rotating electrical machines.
- Smoother rectified voltage in static frequency converters.

A three-phase voltage generator can be regarded as three single-phase voltage sources connected in a common point called the neutral point, see Figure C.5.

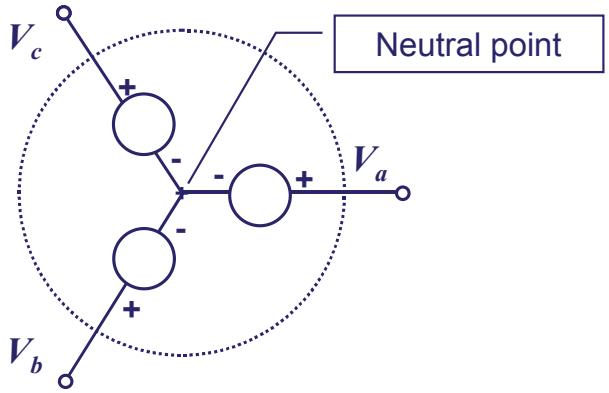

Figure C.5: Three phase voltage generator.

The voltages are called symmetrical if they all are sinusoidal with same amplitude and 120^o phase shift, see upper part of Figure C.6

$$\begin{aligned} v_a(t) &= \sqrt{2}V_{n,rms}\sin\omega t, \;\; v_b(t) = \sqrt{2}V_{n,rms}\sin\left(\omega t - 120^o\right), \\ v_c(t) &= \sqrt{2}V_{n,rms}\sin\left(\omega t - 240^o\right). \end{aligned} \tag{C.11}$$

In analysis of voltages and currents, it is convenient to express the sinusoidal time varying variables by using complex notation, which for voltage means

$$\begin{aligned} v_a(t) &= Re\left(\sqrt{2}V_{n,rms}e^{j\omega t}\right) = \sqrt{2}V_{n,rms}Re\left(e^{j\omega t}\right) \\ &= \sqrt{2}V_{n,rms}\sin\omega t, \end{aligned} \tag{C.12}$$

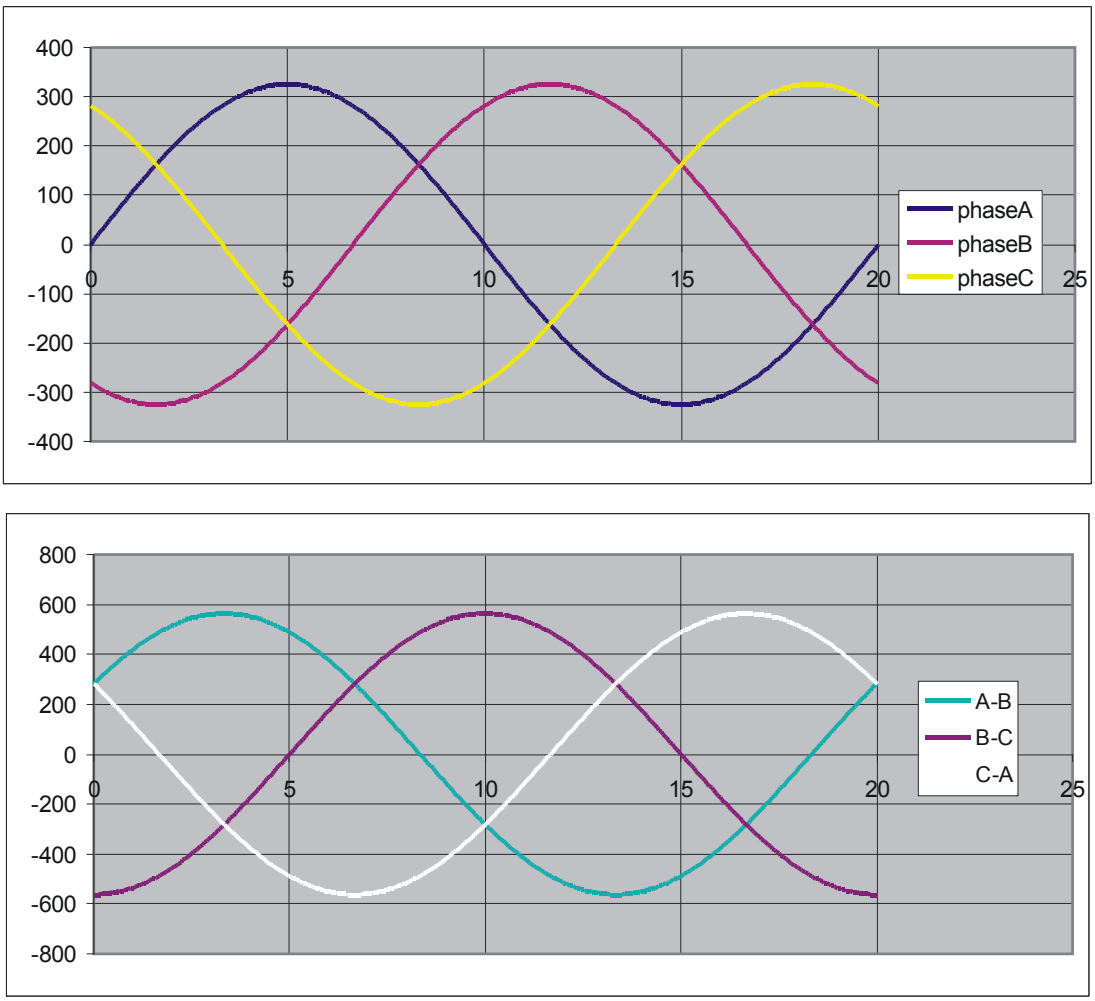

Figure C.6: (Upper) Phase voltages - phase to neutral, $V_n = 230V_{rms}$. (Lower) Line voltages - line to line, $V_{ll} = 400V_{rms}$.

$$\begin{aligned} v_b(t) &= Re\left(\sqrt{2}V_{n,rms}e^{j\omega t-\frac{2\pi}{3}}\right) = \sqrt{2}V_{n,rms}Re\left(e^{j\omega t-\frac{2\pi}{3}}\right) \\ &= \sqrt{2}V_{n,rms}\sin\left(\omega t - 120^o\right), \end{aligned} \tag{C.13}$$

$$\begin{aligned} v_c(t) &= Re\left(\sqrt{2}V_{n,rms}e^{j\omega t+\frac{2\pi}{3}}\right) = \sqrt{2}V_{n,rms}Re\left(e^{j\omega t+\frac{2\pi}{3}}\right) \\ &= \sqrt{2}V_{n,rms}\sin\left(\omega t - 240^o\right). \end{aligned} \tag{C.14}$$

The sinusoidal variables can be graphically presented in a complex vector diagram, see Figure C.8. The vectors are in electro-technical terms annotated phasors, which per definition is represented as a vector with length equal to the *rms* value of the variable and a phase angle which represents the angular phase to a reference value, e.g. one of the phases. For the voltages this notation gives

$$v_a(t) = V_{n,rms}e^{j\omega t}, \quad v_b(t) = V_{n,rms}e^{j\omega t-\frac{2\pi}{3}}, \quad v_c(t) = V_{n,rms}e^{j\omega t+\frac{2\pi}{3}}. \tag{C.15}$$

The line-voltages (line to line voltages) is found as the voltage difference between two phases, see lower part of Figure C.6

$$v_{ab}(t) = v_a(t) - v_b(t), \;\; v_{bc}(t) = v_b(t) - v_c(t), \;\; v_{ca}(t) = v_c(t) - v_a(t). \tag{C.16}$$

In the phasor diagram, the phasor of the line voltage is the vector difference between the phasors of the corresponding phases

$$V_{ab} = V_a - V_b, \;\; V_{bc} = V_b - V_c, \;\; V_{ca} = V_c - V_a. \tag{C.17}$$

Hence, the *rms* value which is the length of the phasor, for all the line voltages is the same and

$$V_{ll,rms} = |V_a - V_b| = 2V_{n,rms}\cos 30^o = \sqrt{3}V_{n,rms}. \tag{C.18}$$

If connecting a symmetrical load, i.e. equal load, to a symmetrical three-phase voltage source as shown in Figure C.7, there will flow symmetrical currents. The currents in each of the load branches are the same in amplitude but phase shifted. If the loads are resistive, as shown in Figure C.6, the currents in each of the branches are

$$i_a(t) = \sqrt{2}\frac{V_{n,rms}}{R}\sin\omega t, \tag{C.19}$$

$$i_b(t) = \sqrt{2}\frac{V_{n,rms}}{R}\sin\left(\omega t - 120^o\right), \tag{C.20}$$

$$i_c(t) = \sqrt{2}\frac{V_{n,rms}}{R}\sin\left(\omega t - 240^o\right). \tag{C.21}$$

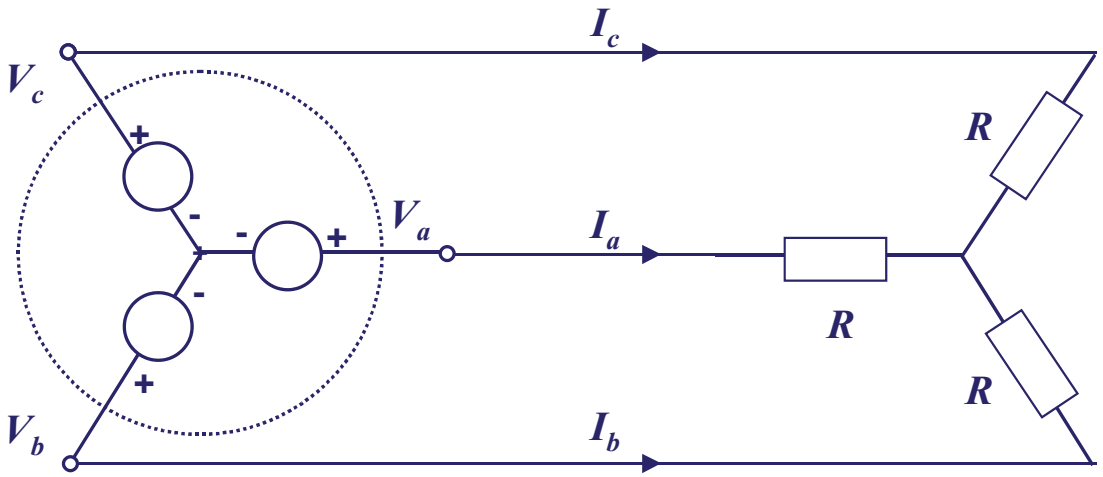

Figure C.7: Three-phase voltage source connected to three-phase resistive load.

In phasor notation

$$I_a = I_{rms}e^{j\omega t} = \frac{V_{n,rms}}{R}e^{j\omega t}, \tag{C.22}$$

$$I_b = I_{rms}e^{j\omega t - \frac{2\pi}{3}} = \frac{V_{n,rms}}{R}e^{j\omega t - \frac{2\pi}{3}}, \tag{C.23}$$

$$I_c = I_{rms}e^{j\omega t + \frac{2\pi}{3}} = \frac{V_{n,rms}}{R}e^{j\omega t + \frac{2\pi}{3}}. \tag{C.24}$$

The power dissipated by the load is

$$P = 3\,R\,I_{rms}^2 = 3\,R\,\frac{V_{n,rms}}{R} I_{rms} = 3\,V_{n,rms}\,I_{rms} = \sqrt{3} V_{ll}\,I_{rms}. \tag{C.25}$$

It is seen, that in a three-phase system, the power transfer capability of a three-phase cable is , i.e. 73% above a one phase transmission, with only 50% more conductor material, which means that three-phase transmission is more cost efficient than one-phase.

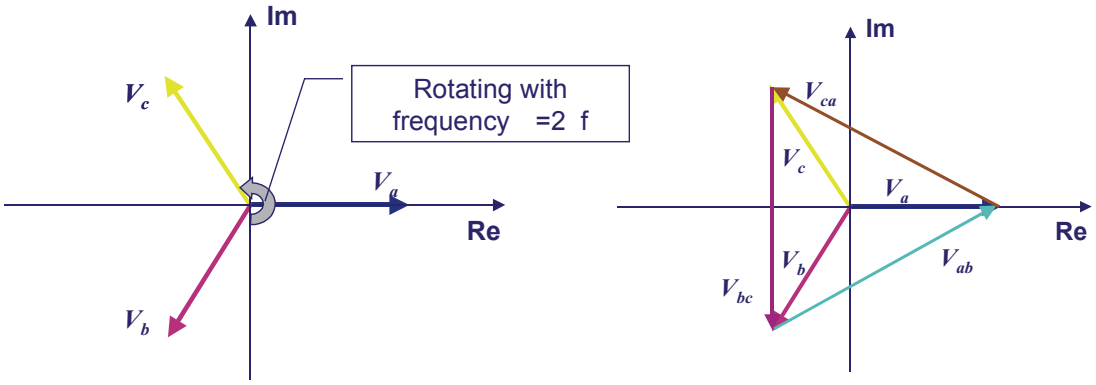

Figure C.8: Phasor diagram of three-phase voltages.

C.2.3 Impedance

The electric network on a ship will typically consist of a set of alternating generators (three-phase voltage sources), a distribution system with switchboards and transformers, and loads. For electrical analysis of the network, the components are modeled by use of equivalent parameters, such as voltage, or current sources and impedances.

In complex notation, the impedance of the circuit components are also expressed as complex values:

- Resistors: $Z_R = R$, i.e. positive real.
- Inductors: $Z_L = j\omega L = jX_L$, i.e. positive imaginary.
- Capacitors: $Z_C = \frac{1}{j\omega C} = -jX_C$, i.e. negative imaginary.

Ohm's law can be applied also to phasors. The relation between the current phasor I through an impedance, and the corresponding voltage phasor V over the impedance is

$$V = Z\,I. \tag{C.26}$$

One can now see that a current through a resistor will be in phase with the voltage, since the resistor is a positive real. An inductor is a positive imaginary, hence the current will lag the voltage by 90^o. For a capacitor, the current will lead the voltage by 90^o.

For a combination of resistors and inductors, the current's phase angle will be leading between 0 and 90^o, dependent on the R/L ratio. Similarly, the current's phase angle will be lagging between 0 and -90^o in a resistor-capacitor combination.

In phasor notation, the following definitions of power related terms apply:

- Apparent power (VA): $S = V\,I^* = P + jQ$.
- Power (W): $P = Re(S) = Re(V\,I)$.
- Reactive power (VA_r): $Q = Im(S) = Im(V\,I)$.

For a resistor, the apparent power equals to the power, since the voltage over the resistor and the current through it are in phase. This is also seen by calculating the apparent power

$$S = V\,I^* = Z_R\,I\,I^* = R\,|I|^2\,, \tag{C.27}$$

, which is a real value. For an inductor with only inductance, and an capacitor with only capacitance, the power is similarly zero, and hence apparent power and reactive power are equal.

Defining the phase angle between voltage and current as ϕ (phi), where positive phase angle means leading (capacitive) current and negative phase angle means lagging (inductive) current, it is seen that

$$P = |S|\,\cos\phi \tag{C.28}$$
$$Q = |S|\,\sin\phi \tag{C.29}$$

The $\cos\phi$ is called the power factor (PF) of the load. The power factor is 1.0 if the currents are in phase with the voltages, and lower if the load is inductive or capacitive.

Since reactive power is a measure of currents which load the network without contributing to usable power, but only gives losses in the distribution and generation system, it is usually desired to design and operate a system with highest possible power factor. If the load had been purely resistive, the power factor would be 1.0, but due to rotating machinery and transmission lines with inductances and capacitances, the power factor will in all practical applications be lower, normally lagging (inductive).

Example C.5 *: Single-phase voltage source with inductive-resistive load.*

A one phase, $230V\ \ 50Hz$ *voltage source is connected to an inductor with inductance* $L = 30mH$ *and resistance* $R = 2\Omega$*. The impedance of the load is*

$$Z = R + j\omega L = R + j\,2\pi f\,L = (2 + j15.7)\,\Omega.$$

Selecting $V = 230V$ *real, then the current in the circuit is*

$$I = \frac{V}{Z} = \frac{230V}{(2 + j15.7)\,\Omega} = (1.83 - j14.4)\,A = 14.5e^{-j1.44}A,$$

which is a current of magnitude $14.5A$*, and it is lagging the voltage with a phase angle of* 82.8^o*, which means that the power factor is* $\cos 82.8 = 0.125$*. The apparent power of the load is*

$$S = V\,I^* = 230\,(1.83 + j14.4)\,VA = (421 + j3312)\,VA.$$

The dissipated power is hence $P = 421W$ *and the reactive power,* $Q = 3312VA_r$*. Verifying the results by checking the power consumption in the resistor*

$$P_R = R\,|I|^2 = 2\,(14.5)^2W = 421W.$$

The inductor contributes to current and reactive power, but the power dissipation, or losses, only occur in the resistor and results in heat generation. The power factor is

$$PF = \cos\phi = \frac{P}{|S|} = \frac{P}{\sqrt{P^2 + Q^2}} = 0.126$$

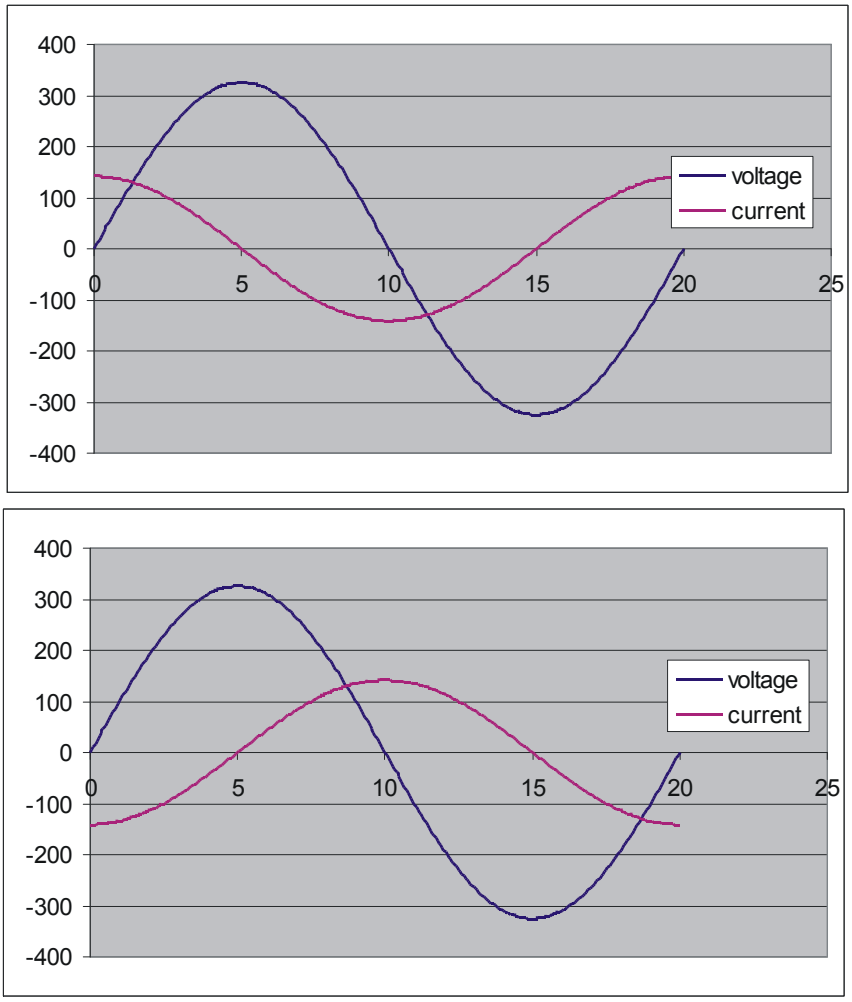

Figure C.9: (Upper) 90^o leading current - capacitive, and (Lower) 90^o lagging current - inductive. Voltage: $230V_{rms}$, Current: $100A_{rms}$.

Example C.6 *: Three-phase voltage source with inductive-resistive load.*

A three-phase, $400V$ *(line to line)* $50Hz$ *voltage source is connected to a three-phase inductor with inductance* $L = 30mH$ *and resistance* $R = 2\,\Omega$ *per phase. Comparing with Example C.5, it is seen that the loads will have the same voltage conditions, with a phase to neutral voltage of* $230V$*. Hence, in the three-phase system, the following applies:*

- *Apparent power:* $S = 3V_n\ I^* = (1263 + j9936)\ VA.$
  $|S| = 3\ |V_n|\ |I| = \sqrt{3}\ |V_{ll}|\ |I| = 10016\,VA = 10.016\,kVA.$
- *Power:* $P = Re(S) = 1263\,W.$
- *Reactive power:* $Q = Im(S) = 9936VA_r.$

The power factor is then $P/|S| = 0.126$*, which is the same as for the one-phase Example C.5, a fact that should not be too surprising, since the three-phase system actually is a triple of the one-phase system. Therefore, analysis of symmetrical three-phase systems is usually carried out by only regarding one of the phases, since all quantities are equivalent, and phase shifted by* 120^o *and* 240^o *in the remaining two phases. Such models are called* per phase representation *of*

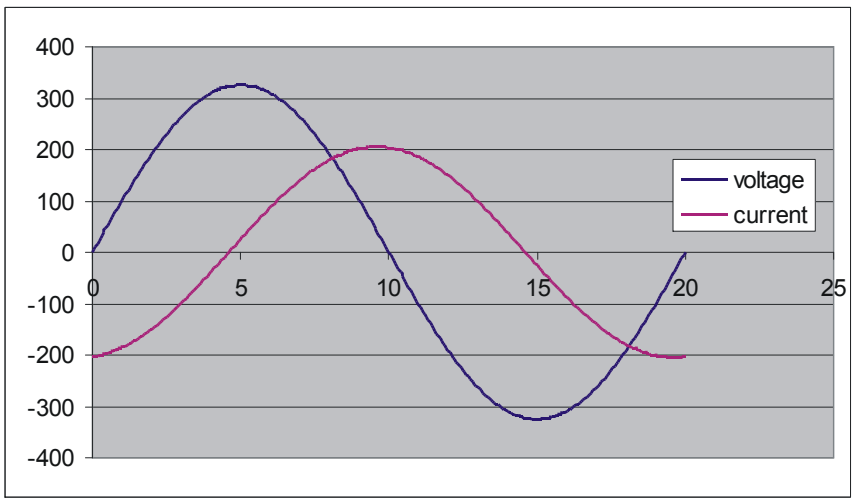

Figure C.10: Voltage and current waveforms of Example C.5. Note: currents magnified 10x. Current is lagging voltage by 82.8^o.

the three-phase system.

C.3 Modeling of Components in Electric Power Generation and Distribution

For analysis and calculation of electric components in the electric power generation and distribution system, simplified models consisting of voltage sources and impedances are used. For most calculations, linear models are used, which means that the discrete voltage sources and impedances are regarded to be constant, independent on voltage, current, and frequency. For more accurate analysis, one might need to model nonlinear phenomena, such as magnetic saturation of inductors and frequency dependent resistor due to current crowding. Nonlinear models are not regarded here.

C.3.1 Generator Model

The generator has a complex model. Physically, it is constructed of a rotating magnetization winding on the rotor, which also includes damper windings for dynamic stability. Stator consists of three-phase windings connected to a common neutral point. The induced voltage in the windings is proportional to the rotational speed of the magnetic flux (in stationary equal to the rotational speed of the rotor) and the magnitude of the magnetic flux. The total magnetic flux in the stator windings consists of magnetic flux from the magnetizing current in the rotor, and armature reaction, i.e. magnetic flux set up by the currents in the stator windings.

For accurate modeling of the generator, a time domain model with 7 degrees of freedom model must be applied, however, for most analysis, one represents the generator as a voltage source behind an inductor and a resistor. The inductance represents the inductive behavior of the windings and the resistance represents the ohmic losses in the windings. Usually, the resistance is small and can be neglected. One distinguish between stationary, transient, and sub-transient models of the generator. The reason is, that this simplified method of modeling

neglects dynamic behavior of the generator, and tries to represent it with stationary models. For fast transients, in the order of $10\,ms$ or shorter, the sub-transient model is applied. For transients in the order of $100\,ms - 500\,ms$, the transient model is used, and for stationary behavior, i.e. seconds and above, the stationary model is representative.

Typically, sub-transient models are used to find peak values of short circuit currents (in first period after short circuit), transient models are used for calculating voltage variations during start-up of motors and transformers, and stationary models are used to calculate stationary load flow. The motivation is to give an engineering tool which is representative and sufficiently simple for calculation by analytically means. Figure C.11 shows such three-phase equivalent diagram for a generator. Physically, the induced voltages represents magnetic flux that are characteristic and can be assumed quasi-constant for the transient period of interest and the stator inductance is representative for the dynamically induced voltages in this time period. It must be noted that the diagram is simplified by disregarding the effects of saliency in the rotor due to the non-cylindrical construction. Also, the capacitive coupling between the windings and the ground is neglected, for load flow calculations this is acceptable.

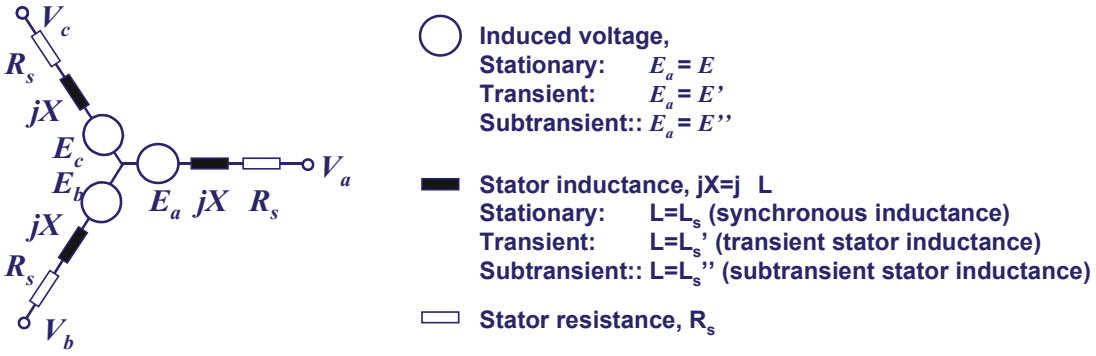

Figure C.11: Model of generators. Resistances are normally neglected (small, assumed zero).

Since the voltage and currents are equal, except of being phase shifted, in the three phases, it is normal only to draw the diagrams for the components in one of the phases, a so-called per phase diagram, as for the generator is shown in Figure C.12.

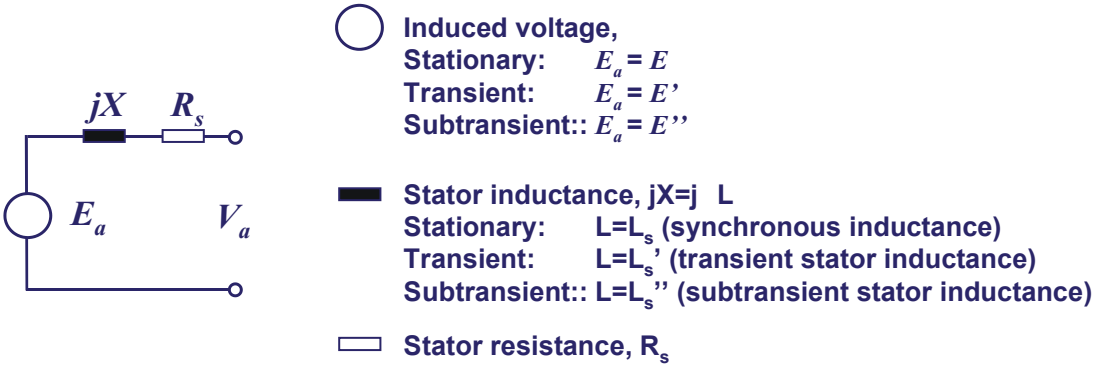

Figure C.12: Per phase diagram of generator.

The phasor diagram will then be as shown in Figure C.13. The stator voltage equals to the

induced voltage minus voltage drops over stator inductance and resistance, i.e.

$$E = V_a + R_s I_a + j\omega L_s I_a, \tag{C.30}$$
$$E' = V_a + R_s I_a + j\omega L'_s I_a, \tag{C.31}$$
$$E'' = V_a + R_s I_a + j\omega L''_s I. \tag{C.32}$$

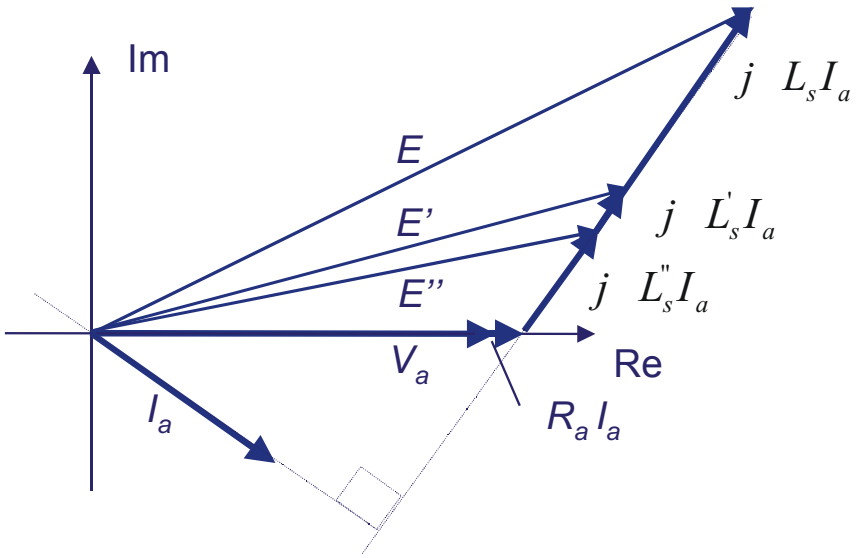

Figure C.13: Phasor diagram for generator, phase a only. The diagram is drawn for an arbitrary inductive current with power factor 0.8 (phase angle $\phi = 36.8^o$.

Transformers

The purpose of the transformer is normally to convert between different voltage levels. It also provides possibilities for isolating different parts of the system in order to reduce the spreading of electromagnetic and harmonic noise, and to operate with different earthing philosophy in different parts of the power system.

The equivalent per phase diagram for the transformer is shown in Figure C.14. For an accurate calculation of losses, the complete diagram should be used, which includes winding losses in stator primary and secondary (R_p and R_s), and magnetizing losses (R_m). L_p and L_s represents the so-called leakage inductance in primary and secondary windings, while L_m represents the magnetizing inductance.

From a load flow calculation, the magnetizing currents and losses are negligible and one can use the simplified diagram. Here, the primary and secondary resistances and inductances are represented by common equivalents, with subscript k. The voltage transformation ratio is described by the $n:1$ ratio, e.g. a $3300\,V$ to $690\,V$ transformer has $n = 4.8$.

C.3.2 Distribution Switchboards

Distribution switchboards are normally modeled as ideal conductors, without losses, inductance or capacitance. This is of cause a simplification, but valid for all practical considerations.

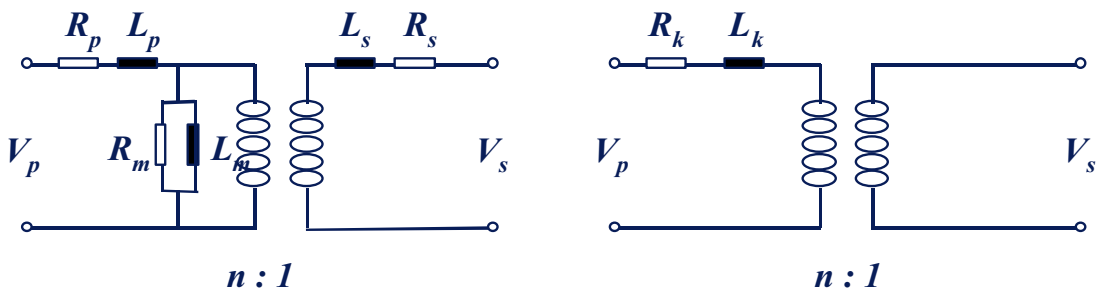

Figure C.14: Equivalent diagrams for transformer. Left: Complete diagram for loss calculations. Right: Simplified diagram for load flow and transient calculations.

C.3.3 Cables

The modeling of a cable depends on it's length. For shorter cables, such as up to the order of tens of meters, one can normally neglect the influence on load flow. It the length is higher, one must regard the losses, inductance in the conductor and some times also the capacitance to ground in the calculations. Figure C.15 describes the pi-equivalent of a cable, and the simplified model used for load flow calculations, neglecting capacitive coupling to ground.

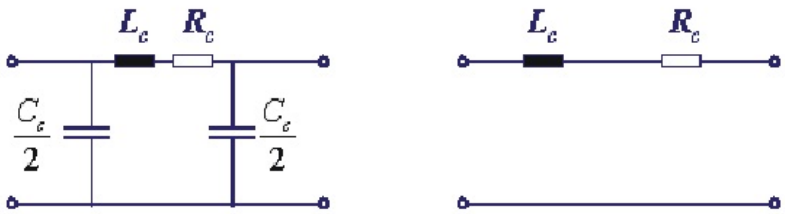

Figure C.15: Equivalent diagram for cable, pi-diagram (left) and simplified diagram for load flow calculations (right).

C.3.4 Synchronous Motors

Synchronous motors are basically a construction identically to the synchronous generator, and modeled similarly. Synchronous motors are rarely used on vessels, unless in connection with a variable speed drive.

C.3.5 Asynchronous Motors

Asynchronous (or induction) motors are used for direct driven or variable speed drives for most of the motor applications on a vessel. It has a rugged and cost efficient design, and low maintenance costs. Physically it is constructed by a stator similar to the synchronous machine. The rotor is constructed cylindrically, with short-circuited windings, normally not connected to stationary equipment. Hence, the currents in the rotor windings are induced by the magnetic flux in the air gap set up by the stator currents.

The equivalent diagram for the asynchronous motor is similar to a transformer with short circuited secondary. For most of the calculations, one is not interested in detailed behavior of the rotor windings, so the quantities in the rotor winding are referred to equivalent quantities at the stator side, and hence one can take the ideal transformer equivalent out of the diagram, as shown in Figure C.16.

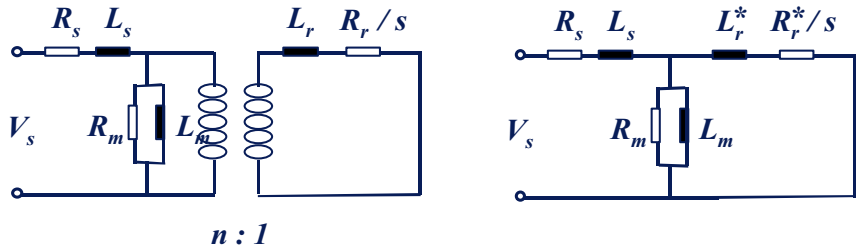

Figure C.16: Equivalent diagrams for asynchronous motors.

Appendix D

Vessel Parameters for R/V Gunnerus

The research vessel (R/V) Gunnerus is a NTNU-owned and operated ship which was put into operation in the spring of 2005, see Figure D.1. The vessel is a test platform for biologists, archeologists, marine robotics, and recently for DP and autopilot testing. In the winter of 2015 the main propulsion was changed from two conventional fixed-pitch propeller-rudder combinations to two Rolls Royce rim-driven azimuthing thrusters (Steen et al., 2016). The cruising speed of R/V Gunnerus is 9.4 knots (4.84 m/s). The values given in Table D.1 and a hull geometry file were inputs to ShipX for calculation of hydrodynamic parameters and motion transfer functions. This section gives the following parameters for R/V Gunnerus:

- Principle hull data
- Mass structure distribution for specific loading condition
- Rigid body and hydrodynamic parameters for zero forward speed
- Wave-induced motion and load coefficients, including plots of surge, sway and yaw motion and force transfer functions and wave drift force amplitudes.
- Wave resistance coefficients

Figure D.1: R/V Gunnerus.

D.1 Principle Hull Data

The principle hull data are given at the top of Table D.1. Parameters specific for the loading condition during DP tests in 2013 are given below the double line. Notice that the draught for this loading condition is smaller than the design draught. All data in the sections below are based upon the structure mass distribution given in Table D.1.

Table D.1: R/V Gunnerus principle hull data and structure mass distribution.

Principle hull data	
Length over all, L_{oa}	31.25 m
Length between perpendiculars, L_{pp}	28.90 m
Length in waterline, L_{wl}	29.90 m
Breadth middle, B_m	9.60 m
Breadth extreme, B	9.90 m
Depth mld. Main deck D_m	4.20 m
Draught (design), T	2.70 m
Dead weight	107 000 kg
Mast/antenna height	14.85 / 19.70 m
Block coefficient, C_B	0.56 [-]
Waterplane area coefficient, C_{WP}	0.837 [-]
Prismatic coefficient, C_p	0.653 [-]
Mid section area coefficient, C_m	0.855 [-]

Structure mass distribution during 2013 DP tests	
Displacement, Δ	418 000 kg
Wetted surface, S	353.24 m^2
Draught (loading condition), T	2.630 m
Vertical center of buoyancy, KB	1.591 m
Vertical center of gravity, VCG	2.630 m
Longitudinal center of buoyancy, LCB	13.202 m
Longitudinal center of gravity, LCG	13.202 m
Longitudinal metacentric height, GM_L	31.545 m
Transverse metacentric height, GM_T	2.663 m
Roll radius of gyration, r_{44}	3.840 m
Pitch radius of gyration, r_{55}	7.225 m
Yaw radius of gyration, r_{66}	7.225 m
Roll-yaw radius of gyration, r_{46}	0.000 m

D.2 Rigid Body and Hydrodynamic Parameters for Zero Forward Speed

Rigid body mass matrix:

$$\mathbf{M}_{\mathrm{RB}} = \begin{bmatrix} 418061 & 0 & 0 & 0 & 0 & 0 \\ 0 & 418061 & 0 & 0 & 0 & 0 \\ 0 & 0 & 418061 & 0 & 0 & 0 \\ 0 & 0 & 0 & 6164560 & 0 & 0 \\ 0 & 0 & 0 & 0 & 21823046 & 0 \\ 0 & 0 & 0 & 0 & 0 & 21823046 \end{bmatrix} \tag{D.1}$$

$m = 418061$ kg is the displacement of R/V Gunners, for this particular loading condition.

Added mass matrix:

For DP (zero forward speed), the added mass is selected for zero frequency $\mathbf{M}_{\mathrm{A}} = \mathbf{A}(0)$. For R/V Gunnerus this is:

$$\mathbf{M}_{\mathrm{A}} = 10^8 \cdot \begin{bmatrix} 0.0007 & 0 & 0 & 0 & 0 & 0 \\ 0 & 0.0034 & 0 & 0.0036 & 0 & -0.0023 \\ 0 & 0 & 0.0243 & 0 & 0.0591 & 0 \\ 0 & 0.0036 & 0 & 0.0202 & 0 & -0.0056 \\ 0 & 0 & 0.0591 & 0 & 1.2880 & 0 \\ 0 & -0.0023 & 0 & -0.0056 & 0 & 0.2024 \end{bmatrix} \tag{D.2}$$

See Figure D.2 for a selection of added mass terms as a function of wave frequency for zero forward speed. The total inertia matrix for R/V Gunnerus is $\mathbf{M} = \mathbf{M}_{\mathrm{RB}} + \mathbf{M}_{\mathrm{A}}$.

For high-speed craft, the added mass matrix is chosen for $\omega \to \infty$, for the desired speed. Figure D.3 shows a selection of terms in the added mass matrix as a function of frequency for forward speed 4.11 m/s. Notice how the added mass terms change for different forward speed.

Generalized Coriolis and centripetal matrices:

The Generalized Coriolis and centripetal forces, $\mathbf{C}_{\mathrm{RB}}(\boldsymbol{\nu})$ and $\mathbf{C}_A(\nu_{\boldsymbol{r}})$, are calculated from the inertia matrix and added mass matrix. They include the rotational speed, and therefore need to be calculated online in a simulation. The calculations are repeated from Section 6.4:

$$\mathbf{C}_{\mathrm{RB}}(\nu) = \begin{bmatrix} 0 & 0 & 0 & c_{41} & -c_{51} & -c_{61} \\ 0 & 0 & 0 & -c_{42} & c_{52} & -c_{62} \\ 0 & 0 & 0 & -c_{43} & -c_{53} & c_{63} \\ -c_{41} & c_{42} & c_{43} & 0 & -c_{54} & -c_{64} \\ c_{51} & -c_{52} & c_{53} & c_{54} & 0 & -c_{65} \\ c_{61} & c_{62} & -c_{63} & c_{64} & c_{65} & 0 \end{bmatrix}, \tag{D.3}$$

where

$$\begin{array}{llll} c_{41} = mz_G r & c_{42} = mw & c_{43} = m\left(z_G p - v\right) & \\ c_{51} = m\left(x_G q - w\right) & c_{52} = m(z_G r + x_G\, p) & c_{53} = m\left(z_G q + u\right) & c_{54} = I_{xz} p - I_z r \\ c_{61} = m\left(v + x_G r\right) & c_{62} = -mu & c_{63} = m x_G p & c_{64} = I_y q \\ c_{65} = I_x p + I_{xz} r. & & & \end{array} \tag{D.4}$$

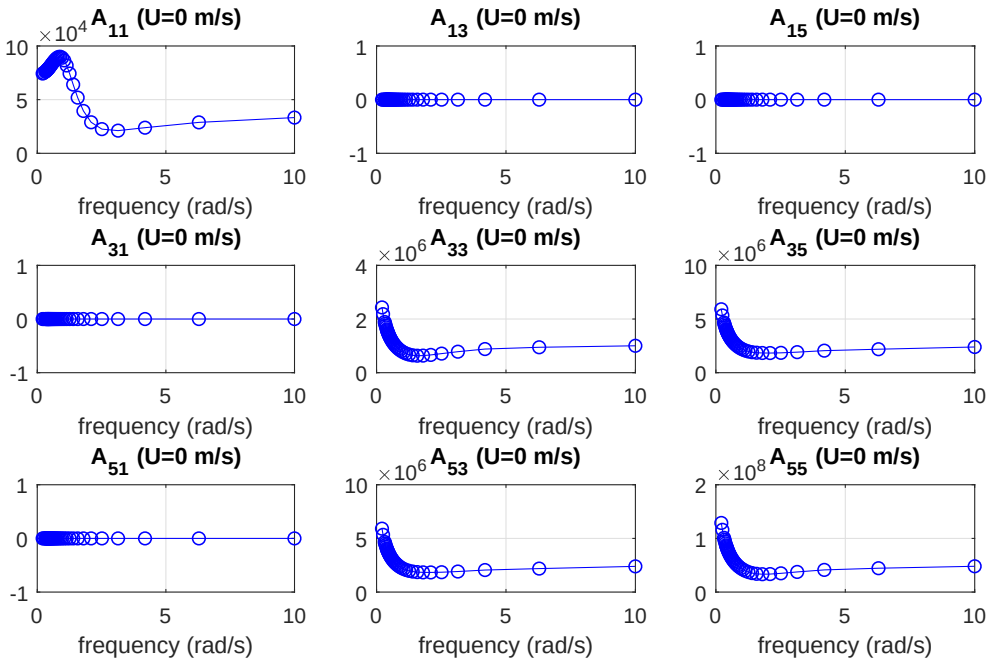

Figure D.2: Selected added mass coefficients for R/V Gunnerus for zero forward speed.

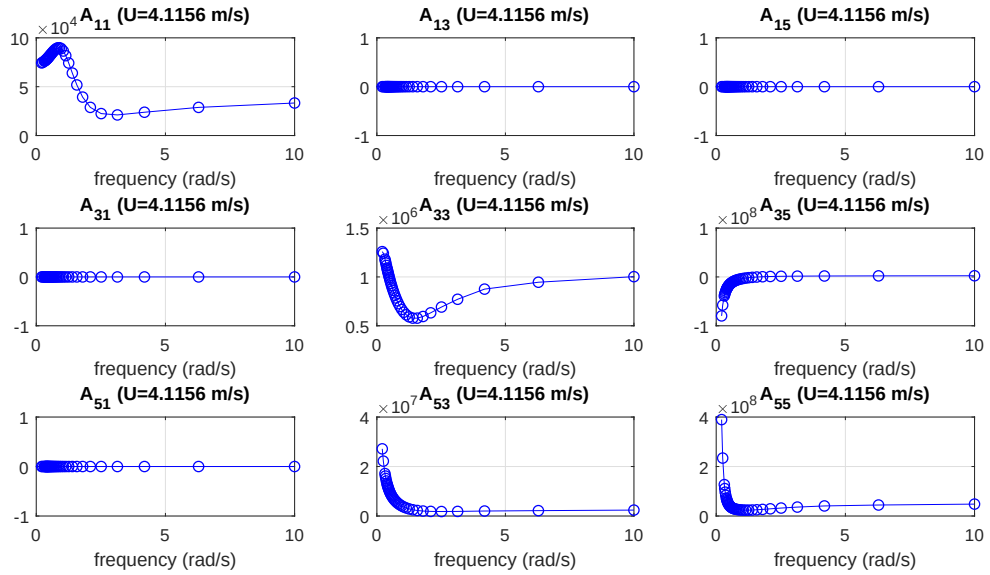

Figure D.3: Selected added mass coefficients for R/V Gunnerus for forward speed 4.11 m/s.

In Table D.1 the values for x_G and z_G are listed as the *longitudinal center of gravity* and *vertical center of gravity*.

$$\mathbf{C}_{\mathrm{A}}(\nu_{\mathrm{r}}) = \begin{bmatrix} 0 & 0 & 0 & 0 & -c_{a51} & -c_{a61} \\ 0 & 0 & 0 & -c_{a42} & 0 & -c_{a62} \\ 0 & 0 & 0 & -c_{a43} & -c_{a53} & 0 \\ 0 & c_{a42} & c_{a43} & 0 & -c_{a54} & -c_{a64} \\ c_{a51} & 0 & c_{a53} & c_{a54} & 0 & -c_{a65} \\ c_{a61} & c_{a62} & 0 & c_{a64} & c_{a65} & 0 \end{bmatrix}, \tag{D.5}$$

where

$$\begin{array}{lll} c_{a42} = -Z_{\dot{w}} w - X_{\dot{w}} u_r - Z_{\dot{q}} q & c_{a43} = Y_{\dot{p}} p + Y_{\dot{v}} v_r + Y_{\dot{r}} r & \\ c_{a51} = Z_{\dot{q}} q + Z_{\dot{w}} w + X_{\dot{w}} u_r & c_{a53} = -X_{\dot{q}} q - X_{\dot{u}} u_r - X_{\dot{w}} w & c_{a54} = Y_{\dot{r}} v_r + K_{\dot{r}} p + N_{\dot{r}} r \\ c_{a61} = -Y_{\dot{v}} v_r - Y_{\dot{p}} p - Y_{\dot{r}} r & c_{a62} = X_{\dot{u}} u_r + X_{\dot{w}} w + X_{\dot{q}} q & c_{a64} = X_{\dot{q}} u_r + Z_{\dot{q}} w + M_{\dot{q}} q \\ c_{a65} = Y_{\dot{p}} v_r + K_{\dot{p}} p + K_{\dot{r}} r & & \end{array} \tag{D.6}$$

See Section 6.4 for more details.

Linear damping matrix:

The linear damping matrix is made up of linear potential damping and linear viscous damping, $\mathbf{D}_{\mathrm{L}} \approx \mathbf{B}_p + \mathbf{B}_v$. The linear potential damping matrix is zero for zero forward speed. In the same way as the added mass matrix, for higher speed, the potential damping is chosen for $\omega \to \infty$, but for high forward speed the linear damping is dominated by nonlinear damping. See Figures D.4 and D.5 for examples of linear potential damping for zero and 6.17 m/s forward speed.

Linear viscous damping including skin friction (approximated by MSS toolbox (Fossen and Perez, 2004)):

$$\mathbf{B}_v = 10^6 \cdot \begin{bmatrix} 0.0174 & 0 & 0 & 0 & 0 & 0 \\ 0 & 0.0802 & 0 & 0 & 0 & 0 \\ 0 & 0 & 0 & 0 & 0 & 0 \\ 0 & 0 & 0 & 0.1951 & 0 & 0 \\ 0 & 0 & 0 & 0 & 0 & 0 \\ 0 & 0 & 0 & 0 & 0 & 4.9715 \end{bmatrix} \tag{D.7}$$

Generalized restoring matrix:

$$\boldsymbol{G}(\boldsymbol{\eta}) = 10^8 \cdot \begin{bmatrix} 0 & 0 & 0 & 0 & 0 & 0 \\ 0 & 0 & 0 & 0 & 0 & 0 \\ 0 & 0 & 0.0233 & 0 & 0.0347 & 0 \\ 0 & 0 & 0 & 0.1092 & 0 & 0 \\ 0 & 0 & 0.0347 & 0 & 1.2937 & 0 \\ 0 & 0 & 0 & 0 & 0 & 0 \end{bmatrix} \tag{D.8}$$

D.2.1 Wave Motion and Load Models

The vessel motion is often divided into first-order and second-order wave-frequency motion. The first-order wave-frequency vessel motion is often described using transfer functions, relating the amplitude of the wave to the vessel response; either to response amplitude directly, or to

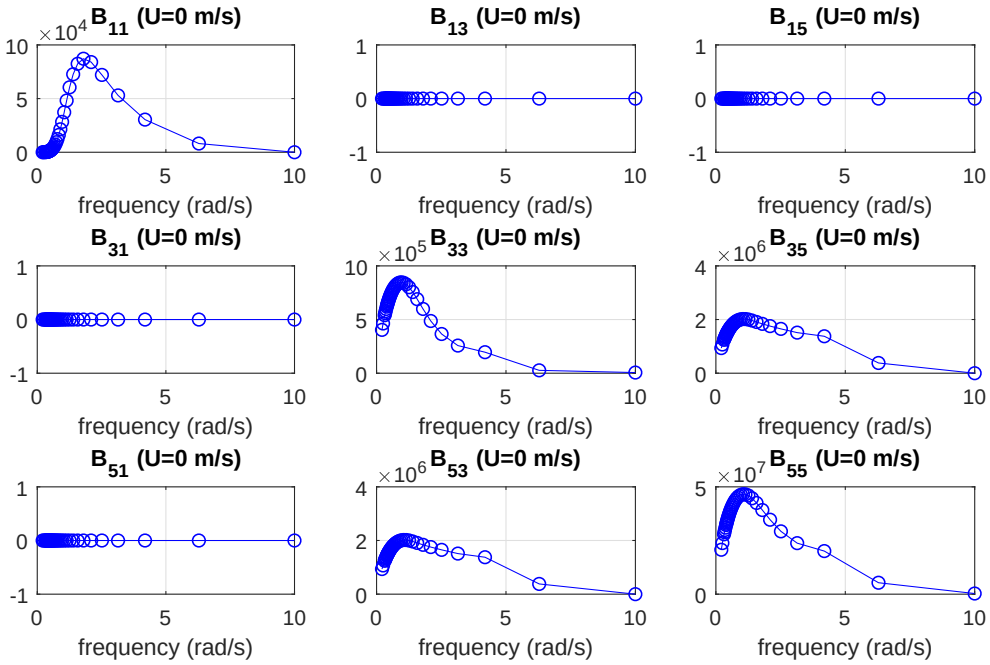

Figure D.4: Selected linear potential damping coefficients for R/V Gunnerus for zero forward speed.

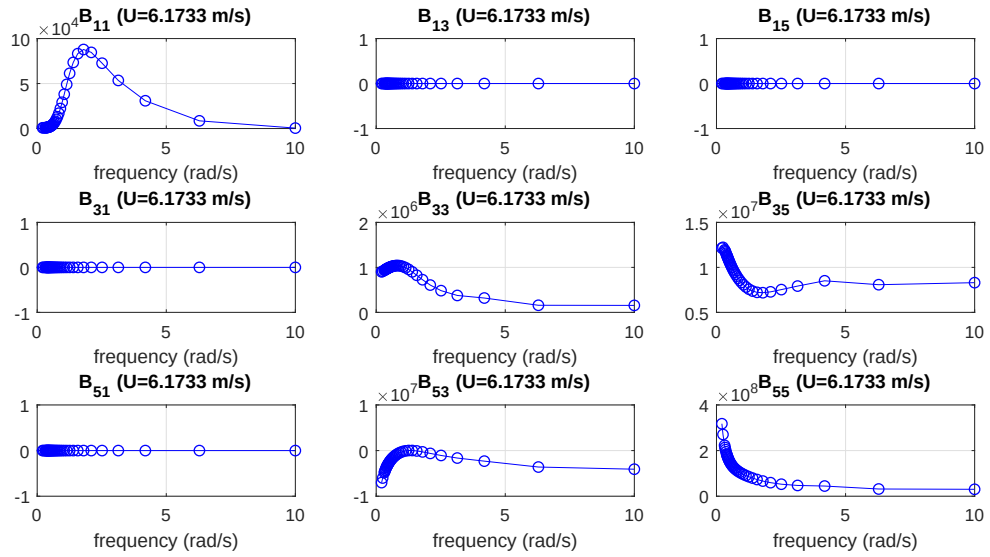

Figure D.5: Selected linear potential damping coefficients for R/V Gunnerus for forward speed 6.17 m/s.

(first-order) wave-induced loads $\boldsymbol{\tau}_{wave1}$. The second-order wave-frequency motion consists of mean wave drift, sum-frequency motion and difference-frequency motion. For ships, the mean and slowly varying motion is of interest, and this motion is computed using the second-order wave-induced loads $\boldsymbol{\tau}_{wave2}$.

D.2.2 First-order Wave-frequency Motion and Loads

The wave-frequency vessel motion can be modeled using two types of transfer functions:

- *Motion* transfer functions relate the wave amplitude to the response amplitude in each DOF.
- *Force* transfer functions relate the wave amplitude to the (first-order) wave-induced force amplitude in each DOF.

Applying the motion transfer functions, will give the first-order wave-frequency motion $\boldsymbol{\eta}_{Rw}$, see (6.100). In a simulator environment this may be an advantage, since $\boldsymbol{\eta}$ and $\boldsymbol{\eta}_w$ are calculated separately. Applying the force transfer functions, will give the first-order wave-induced loads $\boldsymbol{\tau}_{wave1}$, see (6.67).

The motion and force transfer functions can be calculated using hydrodynamic software codes, like ShipX (Sintef Ocean, 2017) (like applied here) or WAMIT (WAMIT Inc., 2017). They are functions of the wave frequency ω and relative wave direction β, and are complex-valued. In general a transfer function $X_i(\omega, \beta)$ can be written in terms of the amplitude $|X_i(\omega, \beta)|$ and phase $\angle X_i(\omega, \beta)$ as follows:

$$|X_i(\omega, \beta)| = \sqrt{Re[X_i(\omega, \beta)]^2 + Im[X_i(\omega, \beta)]^2} \tag{D.9}$$

$$\angle X_i(\omega, \beta) = \text{atan2}(Im[X_i(\omega, \beta)], Re[X_i(\omega, \beta)]) \tag{D.10}$$

The amplitude and phase of the motion transfer functions in surge, sway and yaw are shown in Figures D.7-D.9. Similarily, the amplitude and phase of the force transfer functions in surge, sway and yaw are shown in Figures D.10-D.12. The direction β is defined as $\beta = 0$ following sea, and $\beta = 180$ head sea, see Figure D.6 R/V Gunnerus is port/starboard symmetric.

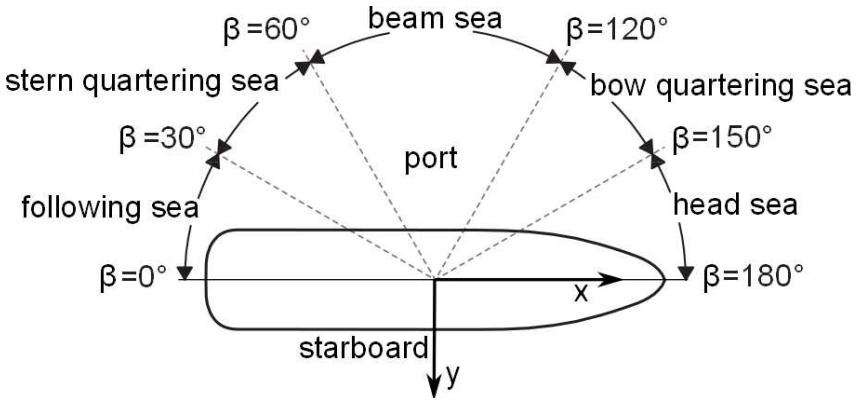

Figure D.6: Definition of relative wave direction β.

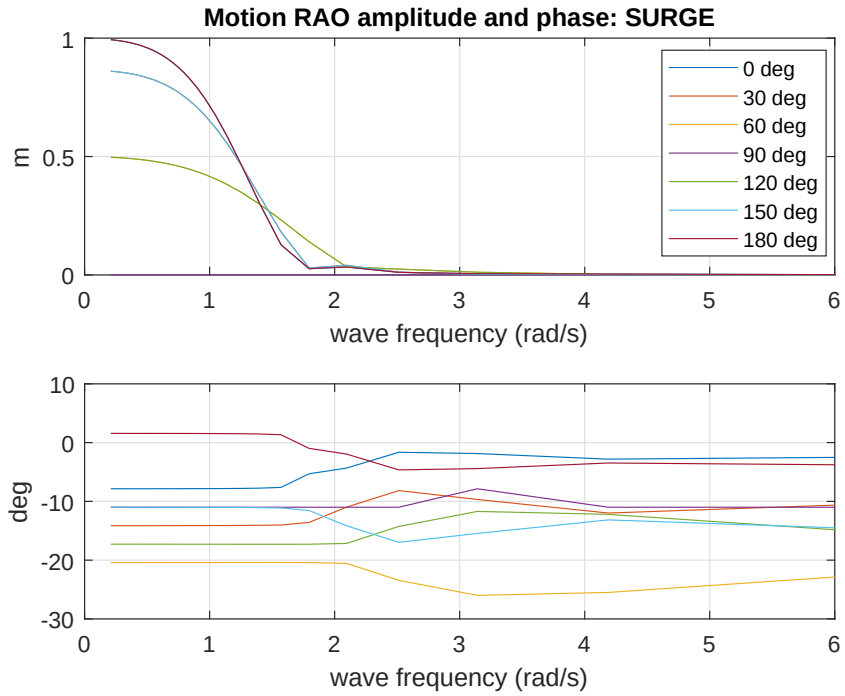

Figure D.7: Amplitude and phase of surge motion transfer function.

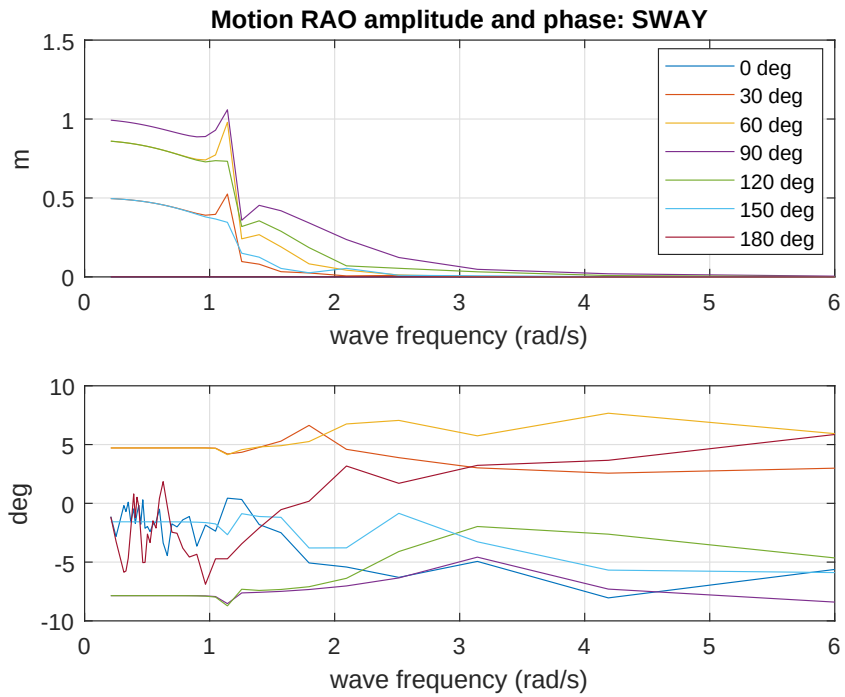

Figure D.8: Amplitude and phase of sway motion transfer function.

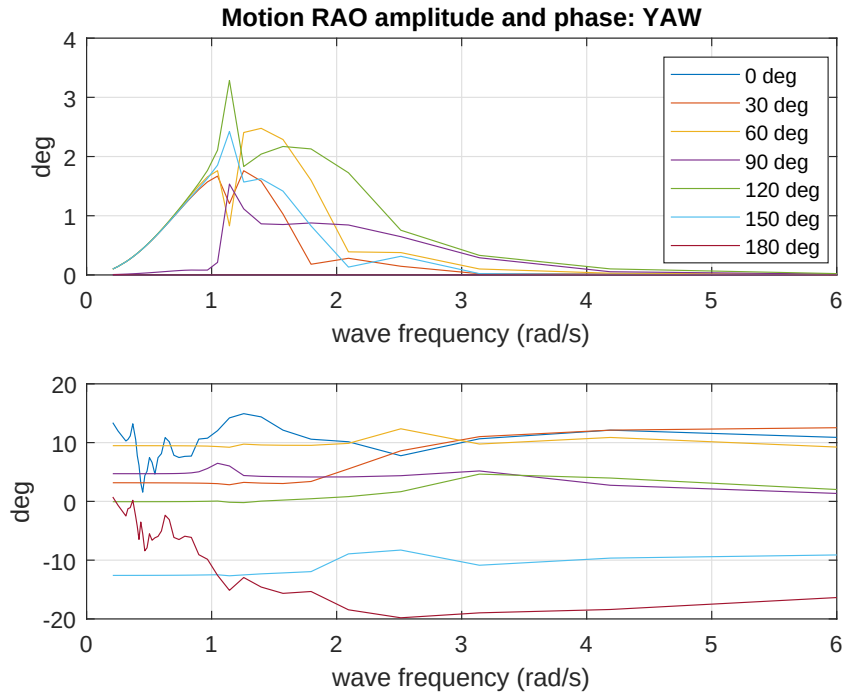

Figure D.9: Amplitude and phase of yaw motion transfer function.

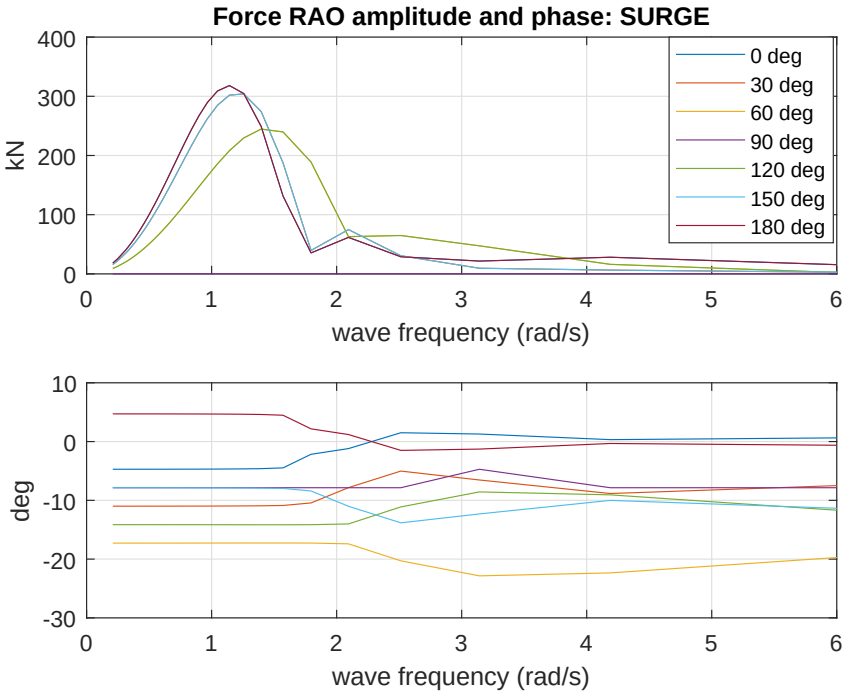

Figure D.10: Amplitude and phase of surge force transfer function.

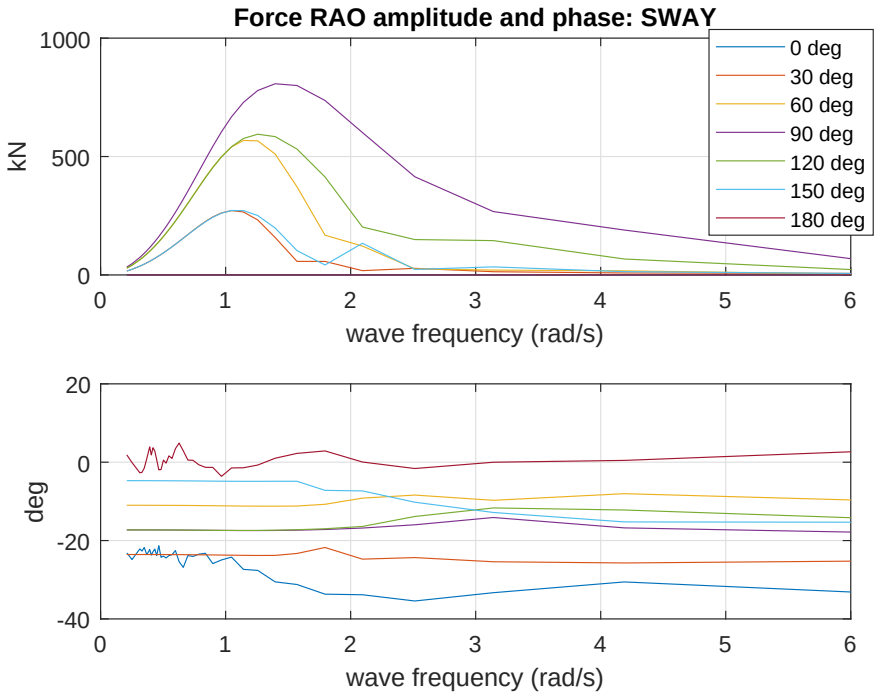

Figure D.11: Amplitude and phase of sway force transfer function.

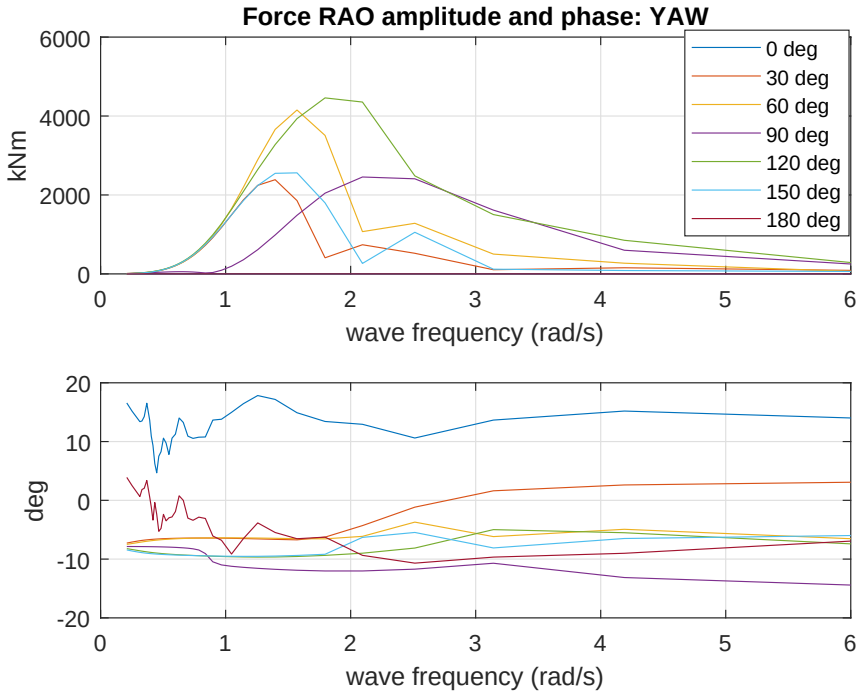

Figure D.12: Amplitude and phase of yaw force transfer function.

D.2.3 Wave Drift Force $\boldsymbol{\tau}_{wave2}$

The wave drift force amplitudes for R/V Gunnerus for surge, sway and yaw are given in Figure D.13. Again, the direction β is defined as $\beta = 0$ following sea, and $\beta = 180$ head sea. R/V Gunnerus is port/starboard symmetric.

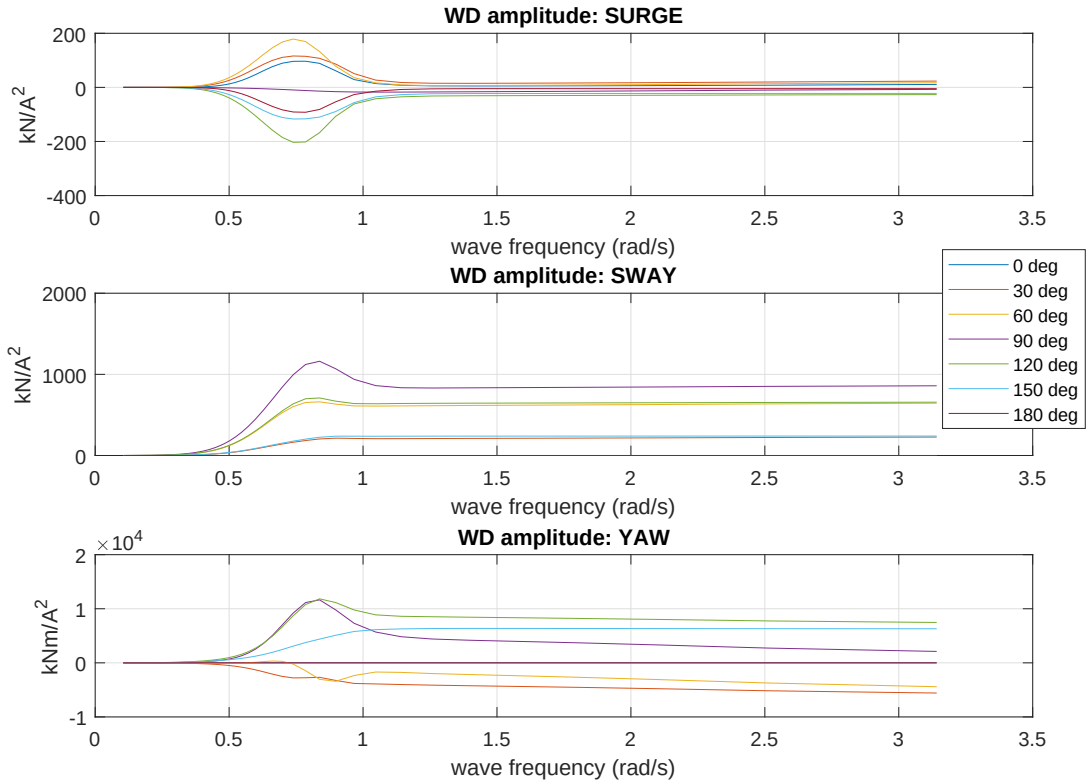

Figure D.13: Wave drift amplitudes in surge, sway and yaw.

D.2.4 Wave Resistance Coefficients

The wave resistance, wave coefficients, sinkage and trim were calculated, and are given in Tables D.2 and D.3. The calculations are done for the same structure mass distribution as given in Table D.1. An explanation of the parameters in Tables D.2 and D.3 is given below.

- $U_{s,n}$ - forward speed of the ship (knots).
- U_s - forward speed of the ship (m/s).
- F_N - Froude number $F_N = U_s/\sqrt{gL}$.
- C_w - wave resistance coefficient.
- $C_{r,c}$ - residual resistance coefficient (form factor calculated by program). In Table D.2 this coefficient is split into linear, nonlinear and total coefficient.
- $C_{r,u}$ - residual resistance coefficient (form factor input by user).
- C_f - frictional resistance coefficient for ship.
- F_{ds} - increase of wetted surface divided by nominal wetted surface.

The form factor calculated by the program is calculated as follows:

- For $C_B < 0.6$ Holtrop's form factor is applied.
- For $C_B > 0.7$ MARINTEK's form factor is applied.
- For $0.6 < C_B < 0.7$ a transition between the two are applied.

R/V Gunnerus has $C_B = 0.56$ (Table D.1), and hence the Holtrop's form factor was applied. The form factor calculated by the program was $(1 + k) = 1.3892$, and the form factor given by the user was $(1 + k) = 1.2353$.

- C_{33} - heave restoring coefficient.
- C_{55} - pitch restoring coefficient.
- AP - aft perpendicular.
- FP - fore perpendicular.

Table D.2: R/V Gunnerus wave resistance coefficients [-].

$U_{s,n}$ [kn]	U_s [m/s]	F_N	$C_{w,lin}$	$C_{w,nl}$	$C_{w,tot}$	$C_{r,c}$	$C_{r,u}$	C_f	F_{ds}
5.237	2.694	0.157	0.3766E-03	0.0000E+00	0.3766E-03	0.3920E-03	0.3903E-03	0.2192E-02	0.5046E-02
5.892	3.031	0.177	0.5710E-03	0.0000E+00	0.5710E-03	0.5904E-03	0.5883E-03	0.2154E-02	0.6472E-02
6.547	3.368	0.196	0.9830E-03	0.0000E+00	0.9830E-03	0.1007E-02	0.1004E-02	0.2121E-02	0.8156E-02
7.200	3.704	0.216	0.1086E-02	0.0000E+00	0.1086E-02	0.1115E-02	0.1112E-02	0.2091E-02	0.9950E-02
7.855	4.041	0.236	0.1739E-02	0.0000E+00	0.1739E-02	0.1773E-02	0.1770E-02	0.2065E-02	0.1205E-01
8.510	4.378	0.255	0.1724E-02	0.0000E+00	0.1724E-02	0.1765E-02	0.1760E-02	0.2042E-02	0.1426E-01
9.165	4.715	0.275	0.2952E-02	0.0000E+00	0.2952E-02	0.3000E-02	0.2995E-02	0.2020E-02	0.1714E-01
9.818	5.051	0.295	0.3834E-02	0.0000E+00	0.3834E-02	0.3892E-02	0.3886E-02	0.2000E-02	0.2067E-01
10.473	5.388	0.314	0.4184E-02	0.0000E+00	0.4184E-02	0.4248E-02	0.4241E-02	0.1982E-02	0.2329E-01
11.129	5.725	0.334	0.4665E-02	0.0000E+00	0.4665E-02	0.4736E-02	0.4728E-02	0.1965E-02	0.2620E-01

Table D.3: R/V Gunnerus running sinkage and trim, positive sinkage is up, and positive trim is bow up.

$U_{s,n}$ [kn]	C_{33} [kN/m]	C_{55} [kN/rad]	Sinkage [m]	Trim [deg]	Sinkage AP [m]	Sinkage FP [m]
5.237	0.2277E+04	0.1370E+06	-0.0297	-0.0527	-0.0164	-0.0430
5.892	0.2277E+04	0.1370E+06	-0.0381	-0.0671	-0.0212	-0.0551
6.547	0.2277E+04	0.1370E+06	-0.0481	-0.0830	-0.0271	-0.0690
7.200	0.2277E+04	0.1370E+06	-0.0586	-0.1068	-0.0317	-0.0856
7.855	0.2277E+04	0.1370E+06	-0.0710	-0.1240	-0.0397	-0.1023
8.510	0.2277E+04	0.1370E+06	-0.0840	-0.1557	-0.0448	-0.1233
9.165	0.2277E+04	0.1370E+06	-0.1010	-0.1680	-0.0587	-0.1434
9.818	0.2277E+04	0.1370E+06	-0.1218	-0.1358	-0.0876	-0.1561
10.473	0.2277E+04	0.1370E+06	-0.1372	-0.1503	-0.0993	-0.1751
11.129	0.2277E+04	0.1370E+06	-0.1544	-0.1846	-0.1078	-0.2009

Index